

Improved reservoir characterisation of a Chilean tight sandstone reservoir

Daniela Josefina Navarro Perez

Submitted in accordance with the requirements for the degree of
Doctor of Philosophy

The University of Leeds

School of Earth and Environment
Institute of Applied Geoscience

September, 2024

Declaration

The candidate confirms that the work submitted is her own, except where work which has formed part of jointly-authored publications has been included. The contribution of the candidate and the other authors to this work has been explicitly indicated below. The candidate confirms that appropriate credit has been given within the thesis where reference has been made to the work of others.

The work presented in Chapter 6 of this thesis appears in the publication:

Navarro-Perez, D., Fisher, Q., Allshorn, S., Grattoni, C., and Lorinczi, P. (2024). Multi-salinity core flooding study in clay-bearing sandstones, a contribution to geothermal reservoir characterisation. *Advances in Geosciences*, 62, 71-80. doi: [10.5194/adgeo-62-71-2024](https://doi.org/10.5194/adgeo-62-71-2024)

DNP, QF, SA, and CG designed the experiment, and DNP carried it out. DNP prepared the paper with contributions from all co-authors.

This copy has been supplied on the understanding that it is copyright material and that no quotation from the thesis may be published without proper acknowledgement.

The right of Daniela Josefina Navarro Perez to be identified as the Author of this work has been asserted by her in accordance with the Copyright, Designs and Patents Act 1988.

© 2024 The University of Leeds and Daniela Josefina Navarro Perez.

Acknowledgements

First and foremost, I would like to express my deepest gratitude to my supervisors, Piroska Lorinczi and Quentin Fisher, for their continuous support, invaluable guidance, and unending patience throughout my PhD journey. I have learnt so much from you.

I profoundly thank the Wolfson Laboratory group, Carlos Grattoni, Samuel Allshorn, and John Martin, for their technical training, mentoring, insightful feedback and constructive criticism, which greatly improved the quality of my research. Also, I thank Lesley Neve and John Wyn Williams for their technical training in sampling preparation for XRD/XRF and thin sections.

I want to acknowledge the financial support from the National Research and Development Agency of Chile (ANID), the scholarship programme Doctorado en el Extranjero Becas Chile (Grant No. 2018-72190176), and the 2024 Iaian Hillier Academic Award Scheme from the London Petrophysical Society. This research would not have been possible without the sponsorship of the Exploration and Production Management from ENAP Magallanes, Chile, for supplying sampling and data. My special thanks to my focal point, Martín Verdugo Dobronic, and the petrophysicists José Valderrama Puerto and Aníbal Velásquez Arauna, who supported me in further understanding the ZG reservoir.

My deepest thanks to my employer, Universidad de Magallanes, Chile, for sponsoring my PhD journey and providing endless support throughout these years. Special thanks to the Chemical Engineering Department and my dear colleagues, who always push me forward for professional growth and empowerment.

On a personal note, I am forever indebted to my family, especially my life partner Julio and son Ian, for their unwavering belief in me and their emotional support during the highs and lows of this journey. I also thank my Latina lunch buddies, Victoria, Silvia, Josefa, Junia, Ana, Adriana, Cristina and Anthony, for our conversations and advice. Lastly, I thank my GeoLatinas community for their support in many ways in growing as an integral professional in a safe space—my special thanks to the Mentoring and GeoTraductores team.

This PhD dissertation results from five years of hard work, including challenges faced during the COVID-19 pandemic, the loss of loved ones, and the 2019 social crisis in my country, Chile. As an educator, I acknowledge my efforts and perseverance in finishing this programme to transfer my knowledge to young generations of engineers and geoscientists. This dissertation is dedicated to those who embark on a new discipline, thus discovering new investigation frontiers and communicating science to the general public.

Abstract

This dissertation investigates the petrophysical characterization of a tight gas greensand, Zona Glauconitica (ZG), from the Magallanes basin in Tierra del Fuego island, Chile. The sandstones are mineralogically immature probably reflecting a source area that is rich in volcanics with a low rainfall. This has partly led to the samples containing a significant amount of iron-bearing glauconite and/or chlorite. These clays impact reservoir quality and pose challenges during petrophysical evaluation because they lead to a complex microstructure containing significant microporosity and impact various properties. Glauconite and chlorite have a moderate cation-exchange capacity (CEC), adding a second conductive water layer and decreasing the rock resistivity. Therefore, the classical Archie's (1942) model is unsuitable, and shaly-sand water saturation models are preferred.

Analysis of core and well-logs was used to study ZG's electrical, elastic and flow properties. The reservoir is divided into three distinct petrofacies (PRT1 – 3). PRT1 contains most of the producible gas; it lacks glauconite, has a bimodal pore size distribution, low permeability (0.01 – 1mD), moderate to high porosity (22 – 27%v/v), and low specific surface area (~3.4 m²/g). It has the highest iron (14 %wt) and CEC (72 meq/100g), which provide a photoelectric factor signature to quantify the clay volume. PRT1 has the best reservoir quality due to the presence of secondary porosity and the suppression of quartz cementation by the grain-coating chlorite. PRT 2-3 has ultra-low permeability (< 0.01 mD), low to high porosity (11 – 29%v/v), unimodal PSD of nanometric size, high specific surface area, moderate iron content and CEC values. Indicators of good reservoir quality are a V_p/V_s ratio > 1.75 and $\text{Log FZI} > -1.25$ using the Flow Zone Indicator method. The Indonesian and modified Simandoux models best fit ZG's water saturation profile, as it is a freshwater reservoir (12,000 NaCl) with significant clay mineral electrical contribution.

Abstract (Spanish version)

Translated by the author. Traducido por la autora.

Esta disertación investiga la caracterización petrofísica de una arenisca verde de tight gas, Zona Glauconítica (ZG), ubicado en la cuenca de Magallanes de la isla de Tierra del Fuego, Chile. Las areniscas son mineralógicamente inmaduras, lo que probablemente refleja una zona de origen rica en volcanes con bajas precipitaciones. Esta inmadurez mineralógica ha llevado a que las muestras contengan una cantidad significativa de glauconita y/o clorita con contenido de hierro. Estos minerales arcillosos impactan la calidad del reservorio y presentan desafíos durante la evaluación petrofísica debido a que generan una microestructura compleja, con microporosidad significativa, afectando varias propiedades. La glauconita y la clorita tienen una capacidad de intercambio catiónico (CIC) moderada, lo que añade una segunda capa de agua conductiva y disminuye la resistividad de la roca. Por lo tanto, el modelo clásico de Archie (1942) no es adecuado, y se prefieren modelos de saturación de agua en arenas arcillosas.

Se realizó un análisis de testigos y registros de pozos para estudiar las propiedades eléctricas, elásticas y de flujo de la ZG. El reservorio se divide en tres petrofacies distintas (PRT1 – 3). PRT1 contiene la mayor parte del gas a producir; no tiene glauconita, presenta una distribución de tamaño de poros bimodal, baja permeabilidad (0.01 – 1 mD), porosidad moderada a alta (22 – 27%v/v) y una baja área superficial específica (~3.4 m²/g). Tiene el contenido de hierro más alto (14 %wt) y la CIC más alta (72 meq/100g), lo que proporciona una firma de factor fotoeléctrico para cuantificar el volumen de arcilla. PRT1 tiene la mejor calidad de reservorio debido a la presencia de porosidad secundaria y la inhibición de la cementación de cuarzo por la clorita que recubre los granos. PRT2-3 tiene una permeabilidad ultra-baja (<0.01 mD), una porosidad baja a alta (11 – 29%v/v), una distribución unimodal de tamaño de poros de tamaño nanométrico, alta área superficial específica, y valores moderados de contenido de hierro y CIC. Los indicadores de buena calidad de reservorio son una relación $V_p/V_s > 1.75$ y $\text{Log FZI} > -1.25$, usando el método del Indicador de Zona de Flujo. Los modelos de Indonesio y modificado de Simandoux se ajustan mejor al perfil de saturación de agua de la ZG, ya que es un reservorio de agua dulce (12,000 NaCl) con una contribución eléctrica significativa de sus minerales arcillosos.

Table of Contents

Acknowledgements	iii
Abstract	iv
Abstract (Spanish version)	v
Table of Contents	vi
List of Tables	xii
List of Figures	xvi
Chapter 1 Overview	1
1.1 Introduction	1
1.2 Scope of research	3
1.3 Case study: ZG play, Tierra del Fuego island, Southern Chile.....	4
1.3.1 Background	4
1.3.2 Dataset.....	- 10 -
1.4 Study limitations	- 12 -
1.5 Thesis structure.....	- 12 -
Chapter 2 Petrophysical properties overview and the challenges in greensands reservoir characterisation	- 14 -
2.1 Petrophysics fundamentals	- 14 -
2.1.1 Petrophysical concepts review	- 14 -
2.1.2 Electrical parameters.....	- 19 -
2.1.2.1 Formation resistivity factor.....	- 21 -
2.1.2.2 Index resistivity and saturation exponent.....	- 23 -
2.1.2.3 Archie's (1942) saturation water formula	- 24 -
2.1.3 Rock microstructure	- 24 -
2.2 Clay minerals	- 27 -
2.2.1 Cation-exchange capacity	- 28 -
2.2.2 Clay swelling and migration.....	- 30 -
2.3 Greensand formation.....	- 33 -
2.3.1 Mineralogical analysis	- 38 -
2.3.2 Porosity estimation	- 39 -
2.3.3 Permeability estimation	- 40 -
2.3.4 Irreducible water saturation estimation.....	- 44 -
2.3.5 Greensand geomechanics	- 46 -
2.3.6 Greensand effect on well-logs.....	- 49 -
2.3.7 Water saturation modelling.....	- 52 -
2.4 Discussion.....	- 54 -

2.4.1 Estimating greensand petrophysical properties.....	54
2.4.2 Greensand petrophysical controls.....	58
2.5 Conclusion	59
Chapter 3 Core analysis methodology.....	61
3.1 Introduction	61
3.2 Condition of core plugs.....	61
3.3 Overview of the core analysis programme	62
3.4 Sampling cleaning.....	65
3.5 Digital imaging.....	65
3.5.1 Photography.....	65
3.5.2 X-ray computer tomography (CT) scanning	65
3.5.3 Scanning electron microscopy (SEM)	67
3.5.3.1 Sample preparation	67
3.5.3.2 Sample analysis	68
3.6 Mineralogy.....	68
3.6.1 X-ray diffraction (XRD)	68
3.7 Bulk chemistry.....	69
3.7.1 XRF methodology	69
3.8 Porosity	70
3.8.1 Bulk volume.....	70
3.8.1.1 Vernier calliper	70
3.8.1.2 Mercury immersion.....	70
3.8.2 Grain volume.....	71
3.8.2.1 Calibration	72
3.8.2.2 Grain volume measurement.....	72
3.8.3 Brine pore volume	73
3.8.4 Stressed helium pore volume.....	73
3.9 Permeability	76
3.9.1 Steady-state experiment	77
3.9.1.1 Klinkenberg correction.....	78
3.9.2 Pulse-decay gas permeameter	79
3.9.3 Pulse-decay brine permeameter	79
3.10 Mercury injection capillary pressure (MICP).....	80
3.10.1 Conformance correction	82
3.10.2 Fluid corrections.....	83

3.10.3 Key capillary pressure parameters	84
3.11 Nuclear magnetic resonance (NMR)	87
3.12 Electrical resistivities	90
3.12.1 Brine resistivity	90
3.12.2 Resistivity of brine-saturated core plugs.....	91
3.13 Specific surface area (SSA)	91
Chapter 4 Mineralogy, microstructure, porosity, and permeability of the ZG reservoir	94
4.1 Introduction	94
4.2 ZG mineralogy and chemistry	94
4.3 ZG microstructure.....	97
4.3.1 CT scan analysis.....	97
4.3.2 SEM analysis	99
4.4 ZG Specific surface area (SSA)	106
4.5 ZG densities	106
4.5.1 Bulk density.....	106
4.5.2 Grain density	107
4.6 ZG porosity.....	108
4.6.1 Porosity at ambient conditions	108
4.6.2 Stressed porosity	110
4.6 ZG permeability	111
4.6.1 Brine permeability	111
4.6.2 Klinkenberg corrected gas permeability	111
4.6.3 Gas and brine permeabilities relationship	113
4.8 ZG permeability and porosity relationships	115
4.8.1 Permeability and porosity cross-plot.....	115
4.8.2 Correlations with Klinkenberg b-values	118
4.9 Discussion.....	120
4.9.1 Clay minerals contribution to ZG microstructure	120
4.9.2 ZG total and interconnected porosity.....	121
4.9.3 Permeability and porosity correlations.....	125
4.9.4 Correlations based on Klinkenberg b-values.....	127
4.10 Summary.....	128
Chapter 5 Pore size distribution, permeability correlations with MICP and NMR data, and petrofacies units of the ZG reservoir .	131
5.1 Introduction	131

5.2 ZG Pore size distribution (PSD)	132
5.2.1 NMR T ₂ distribution	132
5.2.2 MICP distribution	133
5.3 NMR-MICP conversion.....	139
5.3.1 MICP inversion (workflow 1).....	139
5.3.2 Variable Kappa (workflow 2)	142
5.3.3 NMR-MICP conversion results	144
5.4 Permeability correlations	147
5.4.1 MICP as input data.....	147
5.4.1.1 Representative pore throat radius of ZG	153
5.4.2 NMR as input data	154
5.5 Discussion	158
5.5.1 MICP and NMR results.....	158
5.5.2 Petrofacies	161
5.6 Summary	165
Chapter 6 ZG electrical properties and ultrasonic velocities	167
6.1 Introduction	167
6.1.1 Waxman-Smiths model	168
6.2 Methodology.....	169
6.2.1 Sampling	169
6.2.2 Cation-exchange capacity	169
6.2.2.1. Chemical leaching method	169
6.2.2.2. Multisalinity core flooding method	170
6.2.3 Ultrasonic velocities.....	172
6.3 ZG electrical properties	173
6.3.1 Resistivity, formation factor, and cementation exponent	173
6.3.2 Cation-exchange capacity results	176
6.4 ZG ultrasonic velocities	178
6.5 Discussion.....	180
6.5.1 Rock resistivities comparison	180
6.5.2 Cementation exponent correlations and controls	181
6.5.3 Cation-exchange capacity comparison.....	188
6.5.4 ZG ultrasonic correlations and controls.....	191
6.6 Summary.....	199

Chapter 7 Improved petrophysical interpretation of the ZG.....	203
7.1 Introduction	203
7.2 Methodology.....	204
7.3 Petrophysical evaluation results	207
7.3.1 Environmental correction & qualitative control	207
7.3.2 Clay volume model.....	210
7.3.3 Porosity model	213
7.3.4 Permeability model.....	216
7.3.5 Water saturation model	218
7.3.6 ZG's net pay	221
7.4 Discussion.....	225
7.4.1 Controls on clay volume	225
7.4.2 Porosity and permeability estimates from log data	227
7.4.4 Estimates of water saturation from log data	229
7.5 Summary	238
Chapter 8 Conclusions and recommendations	241
8.1 Conclusions.....	241
8.2 Recommendations for further work	244
List of References	247
Appendix A: NMR empirical calibration curves.....	272
A.1 Number of scans.....	272
A.2 Signal-to-Noise	272
A.3 Hydrogen index correction	273
Appendix B: Core analysis data.....	274
B.1 Master list	274
B.2 QXRD and XRF trends versus depth.....	279
Appendix C: MICP and NMR data	281
C.1 Master list.	281
C.2 Apex position of the ZG dataset.	284
C.3 Cross-plot comparison on equivalent pore-throat radius correlations.....	285
Appendix D: Electrical and ultrasonic data	288
D.1 Electrical data at a confining pressure of 1,500 psig.....	288
D.2 Calibration information for ultrasonic velocities.....	289
D.3 Derived ultrasonic and geomechanical properties equations.....	290

Appendix E: Petrophysical evaluation data.....	293
E.1 Quick-look petrophysical interpretation of wells WX1 to WX10.	293
E.2 Clay volume equations.....	303
E.3 Clay volume estimation of wells WX1 to WX10.	305
E.4 Log porosity equations.....	315
E.5 Water saturation equations.	315
E.6 Petrophysical evaluation of wells WX1 to WX10.....	318

List of Tables

Table 1-1. The conventional logs used for petrophysical evaluation workflow.	11 -
Table 1-2. Documents provided by ENAP.	11 -
Table 1-3. Core sampling information of the wells ENAP1 and ENAP2. .	12 -
Table 2-1. Petrophysical primary properties formulas.	15 -
Table 2-2. Typical ranges of sedimentary rock resistivity (Palacky, 1988).	21 -
Table 2-3. Typical ranges of cementation exponent and the correlational factor from Worthington (1993).	23 -
Table 2-4. Cation exchange capacity range and total surface area for clay minerals (Van Olphen and Fripiat, 1979; McPhee et al., 2015).	29 -
Table 2-5. The ionic and hydrated radius of species involved in cation-exchange capacity (Haynes, 2016).	33 -
Table 2-6. Porosity and permeability reported data from some worldwide greensands reservoirs.	34 -
Table 2-7. Glauconite mineral properties (Webmineral, 2019; Hugget, 2021).	35 -
Table 2-8. Chlorite mineral properties (Webmineral, 2019; Alderton, 2021; Geology.com, 2023).	38 -
Table 2-9. Glauconite types classification of XRD spectrum (Burst, 1958).	38 -
Table 2-10. T ₂ cut-off guidelines for oilfield greensand formations according to the iron content (Dodge et al., 1996).	40 -
Table 2-11. Permeability estimation methods found in the literature review used on greensands reservoirs.	42 -
Table 2-12. Permeability equations applied for greensands reservoirs. ...	43 -
Table 2-13. Irreducible water saturation values found in worldwide greensands with the technique used to define them.	45 -
Table 2-14. Greensand reservoirs' elastic properties are found in the literature.	46 -
Table 2-15. Summary table showing how greensand affects well-log readings and which petrophysical properties are consequently under or overestimated.	50 -
Table 2-16. Average ranges of potassium, uranium and thorium concentrations on clays (Eslinger and Pevear, 1988).	51 -
Table 2-17. Water saturation models expressed in conductivity terms used in greensands.	53 -
Table 2-18. Water saturation models and parameters used on some greensands from the literature.	54 -

Table 2-19. Challenges and recommended tools choices for estimating reservoir properties in greensands.	57 -
Table 3-3. Contact angle and surface tension values used in this project (McPhee et al., 2015).	83
Table 4-1. Density of minerals identified in the XRD analysis and ZG mineralogy.	95
Table 4-2. Geochemical composition of ENAP1 and ENAP2 from XRF analysis.	96
Table 4-3. Average orthogonal views descriptive statistics.	97
Table 4-4. Superficial surface area descriptive statistics of dataset.	106
Table 4-5. ENAP1 set's bulk densities descriptive statistics.	107
Table 4-6. ENAP2 set's bulk densities descriptive statistics.	107
Table 4-7. Grain density descriptive statistics.	108
Table 4-8. ENAP1 set's porosities descriptive statistics.	108
Table 4-9. ENAP2 set's porosities descriptive statistics.	109
Table 4-10. Descriptive statistics of brine permeability measurements.	111
Table 4-11. Descriptive statistics of ENAP1 set derived Klinkenberg permeabilities.	111
Table 4-12. Descriptive statistics of ENAP2 set derived Klinkenberg permeabilities.	111
Table 4-13. Descriptive statistics of Klinkenberg and brine permeabilities ratio of the dataset.	114
Table 4-14. Facies lithological, porosity and permeability ranges.	117
Table 4-15. Statistical metrics and rank of Facies 1 and 2.	126
Table 4-16. Statistical metrics and rank of Facies 3.	126
Table 5-1. NMR T ₂ values comparison for the four distribution types.	133
Table 5-2. Pore-throat radius classification according to Hartmann and Coalson (1990).	134
Table 5-3. MICP key parameters range of the dataset.	137
Table 5-4. Key parameters range of the NMR-MICP conversion methods.	145
Table 5-5. NMR-MICP conversion error metrics range.	145
Table 5-6. Selected correlations that follow Poiseuille's theory and their results.	149
Table 5-7. Selected correlations that follow characteristic length models and their results.	150
Table 5-8. Ranking summary of selected correlations.	152
Table 5-9. Winland and Pittman (1992) empirical correlations.	153
Table 5-10. Ranking summary of selected correlations.	155

Table 5-11. Metrics comparison of selected correlations.	160
Table 6-1. Resistivity, formation factor, and cementation exponent metrics at 1,500 psig confining pressure and reservoir temperature (T_{res}).	174
Table 6-2. Cementation exponent metrics at 1,500 psig confining pressure using helium porosity.	174
Table 6-3. ENAP2 set resistivity metrics measured at three confining pressures.	176
Table 6-4. CEC results from multisalinity experiment (Navarro-Perez et al., 2024).	177
Table 6-5. CEC statistics from the destructive method.	177
Table 6-6. Ultrasonic velocity statistics from ENAP2 set.	179
Table 6-7. Statistical comparison of correlations 1 and 2.	182
Table 6-8. Fitted equations with the ERT workflow.	188
Table 6-9. Selected correlations of V_p as a function of porosity (ϕ) and clay content (C).	194
Table 6-10. ENAP2 geomechanical parameters statistics at a confining pressure of 4,350 psig.	198
Table 7-1. ZG wells formation depth interest and inclination angle.	206
Table 7-2. ZG wells grouping according to Carrizo et al.'s (2021) definitions.	207
Table 7-3. Gamma-ray (GR) average statistics from key and validator wells.	211
Table 7-4. Input parameters used at selected water saturation models. ...	219
Table 7-5. Net pay intervals with their average porosity, clay volume, and water saturation per well.	222
Table 7-6. Statistical metrics of clay volume estimation in key wells.	226
Table 7-7. Statistical metrics of porosity estimation in key wells ENAP1 and ENAP2.	228
Table 7-8. Statistical metrics of cementation exponent correlations with the average values in key wells ENAP1 and ENAP2.	230
Table 7-9. Absolute error in sensitivity analysis for sample ENAP1-2.	237
Table 7-10. Swi comparison of core and saturation models for ENAP1-2.	237
Table B-1. Master list table of ENAP1 core plugs XRD analysis and CT voxels standard deviation.	274
Table B-2. Master list table of ENAP2 core plugs XRD analysis and CT voxels standard deviation.	275
Table B-3. Master list table of ENAP1 core plugs XRF analysis.	275
Table B-4. Master list table of ENAP2 core plugs XRF analysis.	276

Table B-5. Master list table of ENAP1 core plugs specific surface area, bulk density, grain density, helium and brine porosities.	277
Table B-6. Master list table of ENAP2 core plugs specific surface area, bulk density, grain density, helium and brine porosities.	277
Table B-7. Master list table of ENAP1 core plugs MICP and NMR porosities, Klinkenberg permeability at three confining pressures (C.P.), and brine permeability measured at 1,500 psig C.P.	278
Table B-8. Master list table of ENAP2 core plugs MICP and NMR porosities, Klinkenberg permeability at three confining pressures (C.P.), and brine permeability measured at 1,500 psig C.P.	278
Table C-1. Master list table of ENAP1 core plugs NMR relevant output data.	281
Table C-2. Master list table of ENAP2 core plugs NMR relevant output data.	282
Table C-3. Master list table of ENAP1 core plugs MICP relevant output data.	282
Table C-4. Master list table of ENAP2 core plugs MICP relevant output data.	283
Table D-1. Master list table of ENAP1 core plugs electrical data.	288
Table D-2. Master list table of ENAP2 core plugs electrical data.	289
Table D-3. Calibration data.	290
Table D-4. Listed ω_{ij} coefficients.	291

List of Figures

Figure 1-1. Specific objectives overall scheme.	4
Figure 1-2. ZG formation location: maps showing continental location (left); Arenal block location in light blue and red rectangle indicating the ZG area on the northern area from Tierra del Fuego Island (right) (Gonzalez-Gonzalez et al., 2018).....	5
Figure 1-3. Core permeability vs core porosity cross-plot (Gonzalez-Gonzalez et al., 2018).	6
Figure 1-4. Mineralogical content of the ZG greensand formation (Britt et al., 2016).	6
Figure 1-5. Generalized geologic setting of Magallanes Basin, from left to right: geological age, formation unit, typical fossil and mineral content, tectonic phase and the two polygon fault systems which extend through the source in the Upper Cretaceous into and through the ZG formation in the early Eocene (Britt et al., 2016).	7
Figure 1-6. ZG logs: track #1 gamma-ray log; track #2 depth; track #3 lithology; track #4 petrofacies; track #5 ichnofossils: Thl=Thalassinodes isp., Hlm=Helminthopsigs isp., Z=Zoophycos isp. and Ch=Chondrites isp.; track #6 bioturbation index: red=high, yellow=moderate and green=low; track #7 induction log (Gonzalez-Gonzalez et al., 2018).....	8
Figure 1-7. Well-log interpretation results. Black and red dots are the core samples. Track #1 gamma-ray (GR) log; track #2 depth, track #3 subunits name; track #4 chlorite content; track #5 illite content; track #6 clay volume from chlorite and illite; track #7 mineral log; track #8 clay volume from GR log; track #9 corrected clay volume from PEF log; track #10 porosity from sonic log; track #11 porosity from density-neutron logs; track #12 porosity from NMR log and track #13 water saturation: light blue is water and red is hydrocarbon (Gonzalez-Gonzalez et al., 2018).	9
Figure 1-8. (a) Geolocalization of Tierra del Fuego island with political division (yellow lines): the left side locates the Magallanes and Chilean Antarctica region, and the right locates the Argentinian Tierra del Fuego province. (b) Geolocalization of the twelve wells north of Tierra del Fuego island, Chilean side.....	- 11 -
Figure 2-1. Fundamental constituents of a reservoir rock (Schlumberger, 2020).	- 14 -
Figure 2-2. Fundamental constituents of reservoir rock in terms of porosity and clay terms (modified after Hook, 2003).	- 16 -

- Figure 2-3. Diagram illustrating the interplay between capillary pressure and buoyancy as oil globule moves through a pore: (A) Pressure difference across oil-water interface resists distortion of globule required if it moves through pore throat. (B) The buoyant force is sufficient to distort the oil globule. However, the capillary pressure of the globule in the pore throat exceeds because the pore throat radius is smaller than the maximum pore radius. (C) Part of the buoyant force of the globule above the pore equals the capillary pressure in the pore throat. (D) Buoyant force above the pore is larger than capillary pressure in the pore throat, and the globule moves upwards. γ = interfacial tension, r = radius of the oil globule, D = grain radius, r_p = pore radius, r_t = pore-throat radius (Modified after Berg, 1975). - 17 -
- Figure 2-4. Fluid distribution in a conventional gas reservoir schematic. P_g and P_w are the gas and water column pressure, ΔP is the pressure difference between these fluids, P_c is the capillary pressure, FWL is the free-water level, GWC is the gas-water contact, and P_e is the entry pressure of the gas inside the first macropore of the rock. - 18 -
- Figure 2-5. Schematic illustration of capillary pressure and relative permeability relationships in traditional and low-permeability reservoir rocks. Critical water saturation (S_{wc}), critical gas saturation (S_{gc}), and irreducible water saturation (S_{wirr}) are shown (Shanley et al., 2004). - 19 -
- Figure 2-6. Basic log interpretation, identifying the sandstone reservoir rock in the gamma-ray log, the oil-bearing and water-bearing zone in the resistivity log, and the gas, oil, and brine zones with density-neutron cross-plot logs (Schlumberger, 2016). - 20 -
- Figure 2-7. Relation of porosity and permeability to formation factor for consolidated sandstone cores of the Gulf Coast (Archie, 1942). - 22 -
- Figure 2-8. Formation factor as a function of porosity according to Archie's first law. The negative gradient of each curve provides the cementation exponent with $a=1$ (Glover, 2015). - 22 -
- Figure 2-9. Resistivity index as a function of water saturation for a rock saturated with water and oil. Solid lines indicate drainage. The dark blue line, representing Archie's second law ($n=2$), is only valid for clean, water-wet, moderately well-connected rocks. Rocks with higher connectivity due to intergranular water films tend to follow the red curve, while low connectedness or oil-wet rocks follow the green and purple trends. It should be noted that imbibition can often produce a nonlinear curve (dashed) due to the development of oil-wet patches in the rock (Glover, 2015). - 24 -
- Figure 2-10. Sandstone microstructure impacts the porosity-permeability trends (Ethier and King, 1991). - 25 -
- Figure 2-11. Effect of grain size and sorting in the porosity-permeability trends (Cade et al., 1994). - 25 -

Figure 2-12. Mode of shale and clay occurrences in sandstones (Asquith, 1990).....	- 26 -
Figure 2-13. Modes of occurrence of authigenic clay in sandstone (Wilson and Pittman, 1977).....	- 26 -
Figure 2-14. Porosity-permeability trends of clay-free and clay-bearing sandstones (Wilson, 1982).....	- 26 -
Figure 2-15. General dispersed clay types within sandstone reservoirs (Neasham, 1977).	- 27 -
Figure 2-16. Silica and alumina sheets structure units (above) and main clay mineral groups structure, distances not scaled (modified from Elementary Engineering Library, 2020).	- 28 -
Figure 2-17. Pore and clay ion mobility in a shaly sand (McPhee et al., 2015).....	- 28 -
Figure 2-18. Electrical double layer. (a) TOT structure of clay minerals, where T=tetrahedral layer and O=octahedral layer. (b) The surface of 2:1 clay minerals in contact with water is charged because of amphoteric sites on the edges of the clay crystal and basal negative sites associated with isomorphic substitutions in the crystalline framework. (c) the mineral charge is compensated by cations (M ⁺) and anions (A ⁻), forming a double layer. This double layer comprises a sorbed cations (Stern) layer and a diffuse layer where the Coulombic interactions between the charged mineral surface and the ions prevail. The subscript f denotes the fraction of the counter charge located in the Stern layer (Revil and Mahardika, 2013).	- 30 -
Figure 2-19. Clay mechanisms in sedimentary rocks with fresh water: (a) migration, (b) swelling (adapted from Khilar and Fogler, 1983; Daneshfar and Moghadasi, 2017; Xiao et al., 2017).	- 32 -
Figure 2-20. Morphological transformation from nascent to highly evolved glauconite (from Hugget al., 2021; modified from Odin and Letolle, 1980).	- 36 -
Figure 2-21. (a) BSE image of the North Sea greensand, scale bar for greensand is 100 μm, and the image represents macroporosity, quartz, and glauconite grains. (b) BSE glauconite grain image from Arnager greensand, scale bar for glauconite grain is 1 μm. Micropores reside within glauconite grain (Hossain et al., 2009). ...	- 37 -
Figure 2-22. Diagram of greensand major grains and clay distribution types as grain coating and filling pore throats, glauconite contains microporosity.....	- 37 -
Figure 2-23. Variations in potassium atoms as functions of structural regularity (Burst, 1958).....	- 39 -

Figure 2-24. NMR T_2 curve distribution on greensands samples (a) Nini field, North Sea (Hossain, 2011a), and (b) Late Paleocene/Early Eocene sandstone, North Sea (Rueslatten et al., 1998). A peak close to 1 ms represents microporosity, and a peak close to 100 ms represents macroporosity.	39 -
Figure 2-25. Total porosity and air permeability cross-plot showing the different trends of clay-free sandstones and greensands.	41 -
Figure 2-26. Relationship between pore-filling berthierine (chlorite) content of North Sea greensands samples with (a) helium porosity and (b) core permeability (Hossain and Zhou, 2015).	41 -
Figure 2-27. Capillary pressure and water saturation cross-plot comparing clay-free sandstones and greensands trend.	44 -
Figure 2-28. NMR T_2 distribution diagram comparing clay-free sandstones and greensands distribution.	45 -
Figure 2-29. Macroporosity and microporosity determination of a North Sea greensand sample (a) from NMR T_2 distribution and (b) from the capillary pressure curve. The dashed vertical line shows a cut-off of 5.21 ms. The capillary pressure of 100 Psig corresponds to a microporosity of 9.1% (Hossain et al., 2011a).	45 -
Figure 2-30. Gas-water relative permeability and water saturation cross-plot comparing the trend of clay-free sandstones (continuous line) and greensands (dashed line). K_{rg} is gas relative permeability, K_{rw} is water relative permeability, S_{wirr} is irreducible water saturation, and S_{rg} is residual gas saturation.	46 -
Figure 2-31. P-impedance versus Poisson's ratio plot, discriminated by the Putumayo Basin, Colombia's lithology (colour bar). Dark blue: quartz sandstones, light blue: calcareous-glaucconitic sandstones, green: glauconitic sandstones, orange: quartz-siltstones, and red: glauconitic wackestones (Diaz et al., 2003).	47 -
Figure 2-32. Modelling of porosity and velocity relations using rock physics diagnostics. Blue circles are Fontainebleau sandstone from the Ile De France, black circles are clay-bearing sandstone, and green circles are greensands from the North Sea (Hossain and Zhou, 2015).	48 -
Figure 2-33. Schematic rock-physics model for the North Sea greensand shows the link between the rock-physics model and greensand diagenesis. (1) Depositional stage, no diagenesis occurs. (2.1) Lack of silica cementation, some greensand is not influenced by the silica flux. (2.2) Early silica cementation, the first diagenetic mineral to form. (3.1) Pore-filling berthierine cementation: berthierine precipitation occurs because microcrystalline-quartz cement is absent. (3.2) Berthierine in early silica-cemented greensand that causes major porosity reduction. (4.) Late diagenetic phase where berthierine continues to grow (Hossain et al., 2011b).	49 -

Figure 2-34. Nini-1 well logs showing the greensand reservoirs intervals (Hermod and Ty sands from the North Sea), (a) gamma-ray log; (b) porosity logs: bulk density, neutron porosity and helium porosity from core analysis; (c) resistivity log and, (d) permeability log (using Kozeny’s equation) from core analysis (Hossain et al., 2011b).	- 52 -
Figure 2-35. Diagram of conventional well-logs responses in a quartz sandstone and greensand formations, from left to right: gamma-ray log (GR), deep resistivity log (Rdeep), neutron log (NEU), bulk density log (DEN), and photoelectric factor log (PEF).	- 52 -
Figure 2-36. Mind map of controls on greensands petrophysics according to the literature review conducted.	59
Figure 3-1. Sample ENAP1-9 was classified as accepted (left), and sample ENAP1-10 was classified as rejected (right) before core preservation—pictures supplied by ENAP.	61
Figure 3-2. Example of the labelling of whole core samples (ENAP2 set). The red line refers to the liner's right side, and the blue line refers to the left side of the liner. T refers to the top, and B to the bottom depths. The number marked in black is the well depth in metres, and the one marked in blue is the tag number.	62
Figure 3-3. Core analysis programme workflow.	63
Figure 3-4. Flowchart of laboratory experiments undertaken in the core analysis programme, divided into nine categories: digital imaging, mineralogy, bulk volume, pore volume, permeability, capillary pressure, electrical measurements, and others. The properties estimation and identification of main rock features are listed at the end of each category.	64
Figure 3-5. Wolfson CT Scanner with seven core plugs of ENAP2 set.	66
Figure 3-6. Pixel colour map used in final CT scan images.	66
Figure 3-7. Signals resulting from the interaction between a primary electron beam and specimen (extracted from MyScope, 2023).	67
Figure 3-8. Scanning electron microscopy model Tescan VEGA3 XM consists of a tungsten source machine with a large chamber and high sample throughput, equipped with X-max 150 Energy Dispersive X-ray spectroscopy (EDS) and Aztec 3.3 software. Also RGB filtered cold-cathode (CL) system (reference photograph from TARR, 2023).	68
Figure 3-9. Archimedes mercury immersion diagram (API RP40, 1998).	71
Figure 3-10. Diagram of the stereopycnometer. V_{inle} = helium inlet valve, $V_{connect}$ = connecting valve of chambers, V_{vent} = cell cent valve, P_g = sample chamber pressure transducer.	72
Figure 3-11. Auto porosity diagram. V_1 = upstream reservoir, V_2 = downstream reservoir, P_1 = upstream pressure transducer, P_2 = downstream pressure transducer, P_c = confining pressure gauge.	74

Figure 3-12. Scheme of sleeve conformance pressure and pore volume detection: (1) the dry core plug is initially confined at low pressure; as the confining pressure increases, the helium surrounding gas between the sample and the rubber sleeve enters the space. (2) The rubber sleeve will progressively conform to the sample surface, pushing the helium gas to enter inside the pore space. Here is the stress point at which the sleeve exactly conforms to the sample surface, known as Sleeve Conformance Pressure (SCP) and Conformance Pore Volume ($PV_{\text{conformance}}$). (3). From this point onwards, the measurements are considered to derive the stressed pore volume of the sample.....	75
Figure 3-13. Permeability ranges of unconventional reservoirs rocks and measurements ranges of different experimental methods. Some methods' gradients across the measurement range highlight the range over which they are most effective; the solid bracket indicates the typical permeability range; the dashed line bracket indicates the possible permeability range (modified after Sander et al., 2017).....	77
Figure 3-14. Klinkenberg plot with laboratory core data (McPhee et al., 2015).....	78
Figure 3-15. Diagram of the apparatus for gas pulse-decay experiment. $V_0 = V_3$ large reservoir, $V_1 =$ upstream reservoir, $V_2 =$ downstream reservoir, $\Delta P =$ differential pressure transducer, $P_c =$ confining pressure gauge, $P_{dn} =$ downstream pressure transducer.....	79
Figure 3-16. Diagram of the apparatus for liquid pulse-decay experiment. $V_{up} =$ upstream reservoir, $V_{dn} =$ downstream reservoir, $P_p =$ pore pressure transducer, $\Delta P =$ differential pressure transducer, $P_c =$ confining pressure gauge, and $T_{ch} =$ chamber temperature.....	80
Figure 3-17. Micromeritics Autopore IV series model (AZO materials, 2023).....	81
Figure 3-18. Schematic of the conformance or closure effect on a sample outer surface (Svendsen, 2019).	82
Figure 3-19. Conformance correction examples from ENAP1 and ENAP2 sets (a) and (b) display the capillary pressure curves as mercury intrudes. (c) and (d) display the pore size distribution range as incremental mercury intrusion rate. The conformance or closure effect is shown as a dashed green circle.	83
Figure 3-20. Schematic diagram of the mercury injection capillary curve displaying the entry, displacement, and threshold pressures location (DNPUq, 2023).....	85
Figure 3-21. Cross-plot of mercury saturation vs mercury saturation/capillary pressure ratio to obtain the apex parameter (Pittman, 1992).....	85
Figure 3-22. Example of finding the displacement pressure in sample ENAP1-31.	85

Figure 3-23. Example of finding the threshold pressure in samples ENAP1-31 and ENAP2-54.	86
Figure 3-24. During polarisation, protons in fluid align parallel to a static magnetic field. A sequence of radio-frequency pulses excites the protons, causing them to generate a decaying signal (echo train). The wait time can be as much as 12 seconds, whereas echo trains typically are several hundred milliseconds long. T_1 = longitudinal relaxation; T_2 = transversal relaxation; T_e = inter echo spacing (modified from Menger and Prammer, 2002).	87
Figure 3-25. Theoretical relaxation time distributions for a range of pore sizes. The pores are black for square panels, whereas the solid matrix is white (modified from Mohnke and Yaramanci, 2008).	88
Figure 3-26. A typical NMR T_2 distribution trace and how this corresponds to the volume of fluids in place (Coates et al., 1999).	89
Figure 3-27. Workflow to compute incremental and cumulative T_2 distribution.	90
Figure 3-28. Custom-made sample tube vessel for BET technique in Wolfson laboratory.	92
Figure 4-1. XRD mineral grouping as clay minerals + quartz + plagioclase in %v/v. ENAP1 (left) and ENAP2 (right) compared with their overall average indicated in Table 4-1 and ENAP reference of 43% v/v clay minerals, 23% v/v quartz and 34% v/v feldspar (Britt et al., 2016).	95
Figure 4-2. Cross-plot of XRF and XRD compositions: (a) potassium vs glauconite, (b) sodium vs plagioclase, (c) iron vs clay minerals (chlorite + glauconite), and (d) glauconitic mica and smectite mineral distribution.	96
Figure 4-3. CT scan images from the dataset in an increasing trend of voxel standard deviation (from left to right). A black-and-white voxel intensity distribution histogram is shown for each orthogonal view (0° and 90°).	98

Figure 4-4. ZG greensand SEM images: (A) Sample ENAP1-2 (pay sand) is a grain-supported sandstone with plagioclase and chlorite dominance in the matrix and overgrowth of glauconitic smectite grains. There are large secondary pores present (red arrows). (B) Sample ENAP1-18 is a matrix-supported siltstone with chlorite and plagioclase grains. (C) Sample ENAP2-19 is a grain-supported sandstone with overgrowth of glauconitic smectite and mica grains. Pore-lining chlorite and authigenic albite are in the isolated pores (red arrows). (D) Sample ENAP1-27 is poorly sorted with plagioclase, chlorite matrix dominance, and glauconitic smectite grains. There are two artificial micro fractures (green arrows). (E) Sample ENAP2-12 with artificial micro fractures (green arrows) around the edges of glauconitic grains. There is a chlorite grain with illite presence on the top left. (F) Sample ENAP2-12 shows a major presence of pyrite mineral in the matrix with different shapes. (G) Sample ENAP1-6 shows a pyrite layer with framboidal distribution of a length of ~400 μm . There are mixed chlorite-illite and glauconitic mica grains. (H) Sample ENAP1-23 has framboidal pyrite in the matrix; this sample has the highest XRD pyrite content of 1.8%v/v. pIC = pore-lining chlorite, g=glauconitic grain, ch=chlorite grain, Al= albite, Pl=plagioclase, py=pyrite..... 101

Figure 4-5. ZG greensand pore structure types: (A) Authigenic albite in sample ENAP1-22. (B) Chlorite pore lining a secondary pore in sample ENAP1-2 (pay sand). (C) Ingrowth of chlorite inside the pore of sample ENAP1-13. (D) Glauconitic grain with two isolated pores in sample ENAP2-53 with plastic deformation in its edges (green arrow). (E) Chlorite pore-filling in sample ENAP2-65. (F) Chlorite pore-lining and pore-bridging in sample ENAP2-54 (pay sand). (G) Pore-bridging of mixed-layer illite-smectite in sample ENAP1-13. (H) Chlorite pore-lining and pore-bridging in sample ENAP2-54 (pay sand). Al= albite, Ch=chlorite, G= glauconite, I/S= illite-smectite. 102

Figure 4-6. ZG greensand glauconitic grain types: All the glauconitic grains presented plastic deformation on their edges (red arrows). (A) Sample ENAP1-28 has slightly evolved grains. The big grain has internal fissures, indicating secondary generation growth. It is classified as glauconitic mica. (B) Sample ENAP1-27 shows two nascent glauconitic grains well-rounded with ghost fossils. It is classified as glauconitic micas. (C) Sample ENAP1-21 has two slightly evolved glauconitic grains. It is classified as glauconitic mica. (D) Sample ENAP1-31 has an evolved glauconitic grain. It is classified as glauconitic mica. It has secondary pores on its edges (orange arrows). (E) Sample ENAP1-1 shows slightly evolved glauconitic mica grains with second-generation growth. The one in the centre is an evolved grain since it is divided into two grains. (F) Sample ENAP1-15 shows evolved glauconitic mica grains. Two of them have an isolated internal pore. (G) Sample ENAP2-17 shows a slightly evolved glauconitic mica grain with second-generation growth. (H) Sample ENAP2-17 has a slightly evolved glauconitic illite-smectite grain with second-generation growth. (I) Sample ENAP2-24 has an evolved glauconitic smectite grain. (J) Sample ENAP2-46 shows an evolved glauconitic mica grain with secondary pores on its edges (orange arrows). (K) Sample ENAP1-1 shows slightly evolved glauconitic mica grains. (L) Sample ENAP1-15 shows evolved glauconitic mica and smectite grains. Al= albite, g=glauconitic, Pl= plagioclase. 105

Figure 4-7. Cross-plot of XRD clay minerals content and SSA. 106

Figure 4-8. Cross-plot of dataset bulk density derived from Vernier calliper on the X-axis and mercury immersion on the Y-axis..... 107

Figure 4-9. Bar chart of dataset derived porosities: (a) ENAP1 set, (b) ENAP2 set. The samples labelled with a coloured line indicate they are outliers in the porosity type measurement..... 109

Figure 4-10. Cross-plot of core helium porosity (x-axis) and stressed helium porosity (y-axis) at 3,500 psig..... 110

Figure 4-11. Cross-plot of stressed and ambient core helium porosity ratio (x-axis) and applied confining pressure (y-axis). 110

Figure 4-12. Examples of cross-plot of measured gas permeability vs the inverse mean pore pressure to derive the Klinkenberg permeability..... 112

Figure 4-13. Cross-plot of Klinkenberg permeability at three confining pressures of the dataset..... 113

Figure 4-14. Cross-plot of Klinkenberg permeability ratio at 1,500 psigg and 3,500 psigg confining pressures of the dataset. 113

Figure 4-15. Klinkenberg and brine permeability ratio. 114

Figure 4-16. Scatter plot of brine against Klinkenberg gas permeability.... 114

Figure 4-17. Core helium porosity vs core Klinkenberg permeability at 3,500 psig confining pressure cross-plot..... 116

Figure 4-18. Porosity and permeability cross-plot discriminated by facies 1, 2, and 3..... 117

Figure 4-19. Exponential and power-of-law correlations for Facies 1 and 2 together (left side) and Facies 3 separately (right side). 117

Figure 4-20. Log k/Φ vs Log FZI cross-plot with linear correlation of Facies 1 and 2 and Facies 3 separately. Facies 3 separates from the rest at coordinate [-1.9, -1.9]. 118

Figure 4-21. Core permeability vs predicted permeability from the FZI method for Facies 1 and 2 together (left side) and Facies 3 (right side). 118

Figure 4-22. Cross-plots: (a) slippage factor b against Klinkenberg permeability, (b) the ratio of Klinkenberg permeability and helium porosity, and (c) the ratio of Klinkenberg permeability and MICP porosity. Sample ENAP2-19 is an outlier since its permeabilities were measured at steady-state, while the rest of the dataset was measured with the pulse-decay method..... 119

Figure 4-23. Cross-plots comparing core helium porosity type: (a) Helium porosity versus brine porosity. (b) Helium porosity versus MICP porosity. (c) Helium porosity versus NMR porosity..... 124

Figure 4-24. Cross-plot of core porosity types: (a) NMR porosity versus brine porosity. (b) Delta Helium and NMR porosities versus Delta Helium and brine porosities. (c) Delta Helium and NMR porosities versus clay mineral type. (d) Delta porosities versus core permeability at 3,500 psig C.P. 124

Figure 4-25. Cross-plot of core porosity types: (a) MICP porosity vs NMR porosity. (b) MICP porosity vs Brine porosity. 125

Figure 4-26. Core permeability vs predicted permeability from the (a) exponential, (b)power-law, and (c)FZI correlations of the ZG dataset. 126

Figure 4-27. Log-log cross-plot of Φ_z (pore-volume to grain-volume ratio) and RQI (reservoir quality index) with isolines of Log FZI separating Facies 1, 2, and 3..... 127

Figure 4-28. Porosity vs permeability cross-plot with isolines of Log FZI discriminated by Facies 1, 2, and 3. The black line corresponds to the exponential correlation to predict permeability using porosity as input of Facies 1 and 2. 127

Figure 5-1. NMR T_2 distributions of the dataset grouped by the average of the T_2 geometric mean. 133

Figure 5-2. MICP curve distribution of the dataset, black lines represent Group I and red lines represent Group II. ENAP1 set capillary curve (a) and PSD (b); three samples from Group II are tagged as 'A' for the accepted sample and as 'R' for the rejected sample. ENAP2 set capillary curve (c) and PSD (d). 134

Figure 5-3. MICP dataset statistics. (a) Entry pressure histogram. (b) Threshold pressure histogram. (c) Pore throat radius weighted geometric histogram. (d) Displacement pressure histogram. (e) Capillary pressure at 50% mercury saturation histogram. (f) Apex pore-throat radius histogram.	138
Figure 5-4. MICP dataset statistics. (a) Pore-throat sorting with quartiles histogram. (b) Pore-throat sorting with 16,50,84 method histogram. (c) MICP curve skewness histogram. (d) MICP curve kurtosis histogram.	139
Figure 5-5. NMR-MICP conversion workflow 1 (MICP inversion method).	141
Figure 5-6. NMR-MICP conversion cross-plots from workflow 1.	142
Figure 5-7. Newton-Raphson method used for the variable Kappa method.	143
Figure 5-8. NMR-MICP conversion workflow 2 (variable Kappa).	144
Figure 5-9. NMR-MICP conversion results in pay sands ENAP1-2 and ENAP2-54.	146
Figure 5-10. NMR-MICP conversion results in samples ENAP1-18 and ENAP2-24.	146
Figure 5-11. Surface relaxivity vs XRF Fe ₂ O ₃ cross-plot.	147
Figure 5-12. Capillary pressure prediction comparison cross-plot. The MICP inversion 1, 2, and 3 corresponds to the groups 1, 2, and 3 reported in Table 5-5.	147
Figure 5-13. Predicted pore throat radius vs Pore throat radius from MICP at a 25 %v/v mercury saturation cross-plot comparing the dataset with Pittman's (1992) correlation.	154
Figure 5-14. Cross-plot used to find the Timur-Coates constant with the least square method.	156
Figure 5-15. Klinkenberg permeability versus NMR predicted permeability from (a) T ₂ distribution summation, (b) SDR using the T ₂ geometric mean, (c) SDR using the T ₂ cut-off at MICP threshold pressure, (d) Timur-Coates using the T ₂ geometric mean cut-off, and (e) Timur-Coates using the T ₂ cut-off at MICP threshold pressure.	157
Figure 5-16. Pore throat radius and permeability cross-plot of ZG reservoir cores comparing selected correlations with the dataset: (a) at 25%v/v mercury saturation with Pittman's, (b) at 35%v/v mercury saturation with Winland's, (c) at Apex radius with Wells and Amaefule's, and (d) at Apex radius with Pittman's.	160
Figure 5-17. Best correlations found with MICP data analysis: (a) MICP displacement pressure vs. the Weighted geometric mean and Apex pore throat radius. (b) MICP threshold pressure vs. Capillary pressure at 50% mercury saturation. (c) NMR T ₂ geometric mean vs. Capillary pressure at 50% mercury saturation.	161

Figure 5-18. NMR T ₂ distribution trend per petrofacies.	162
Figure 5-19. Derived PSD from MICP data discriminated per petrofacies.	162
Figure 5-20. Permeability-porosity cross-plot with Pittman's (1992) isolines at equivalent R ₂₅ values.	163
Figure 5-21. Petrofacies 1 features: (A) SEM image of ENAP2-54. (B) NMR T ₂ distribution where the average T ₂ geometric mean of the cores is indicated. (C) Permeability-porosity cross-plot. (D) Capillary pressure curve as an air-mercury system. (E) XRD mica, illite-smectite, and chlorite content distribution. (F) Average XRF Fe ₂ O ₃ content and SSA. (G) CT image with voxel standard deviation of ENAP1-2.....	164
Figure 5-22. Petrofacies 2 features: (A) SEM image of ENAP2-62. (B) NMR T ₂ distribution where the average T ₂ geometric mean of the cores is indicated. (C) Permeability-porosity cross-plot. (D) Capillary pressure curve as an air-mercury system. (E) XRD mica, illite-smectite, and chlorite content distribution. (F) Average XRF Fe ₂ O ₃ content and SSA. (G) CT image with voxel standard deviation of ENAP2-44.....	164
Figure 5-23. Petrofacies 3 features: (A) SEM image of ENAP1-28. (B) NMR T ₂ distribution where the average T ₂ geometric mean of the cores is indicated. (C) Permeability-porosity cross-plot. (D) Capillary pressure curve as an air-mercury system. (E) XRD mica, illite-smectite, and chlorite content distribution. (F) Average XRF Fe ₂ O ₃ content and SSA. (G) CT image with voxel standard deviation of ENAP1-30.....	165
Figure 6-1. Diagram of the multi-salinity experiment. Pp: pore pressure transducer, Pc: confining pressure indicator, ΔP: pressure difference transducer, T _{ch} : chamber temperature, Ro: rock resistance meter, V ₁ : pump downstream valve, and V ₂ : bypass valve (Navarro-Perez et al., 2024).	171
Figure 6-2. Determination of Qv from multiple salinity tests (McPhee et al., 2015).	171
Figure 6-3. Compressive testing machine (maximum of 250 KN) located in the Wolfson Multiphase Flow Laboratory at the University of Leeds, UK.....	172
Figure 6-4. Diagram showing compressional or P-wave velocity (V _p) and shear or S-wave velocities (S1 and S2) directions.	173
Figure 6-5. Apparent formation factor vs helium porosity cross-plot discriminated by the PRT units.....	174
Figure 6-6. Calculated cementation exponent vs helium porosity cross-plot with linear correlation.	175
Figure 6-7. Cementation exponent (m) cross-plot: calculated vs predicted from linear correlation, the dark blue data points belong to the pay sands in the PRT3 unit.	175

Figure 6-8. Resistivity measurements of ENAP2 set at three confining pressures: (a) cross-plot of rock resistivity to reservoir temperature discriminated by the PRT unit, and (b) cross-plot of the confining pressure resistivities at reservoir temperature vs ENAP2 well depth.	176
Figure 6-9. Rock (C_o) and brine (C_w) conductivities cross-plot from the multisalinity experiment on ENAP1-2 core (Navarro-Perez et al., 2024).	177
Figure 6-10. Cation contribution in total CEC per sample bar chart with the chemical leaching method.	178
Figure 6-11. Total derived CEC measurements per PRT unit from the chemical leaching method. The black line indicates the average value of 23 meq/100g. Samples ENAP2-12, ENAP2-19, and ENAP2-27 were grouped as fracture samples.	178
Figure 6-12. Ultrasonic velocities for Petrofacies 1 (ENAP2-54) and 2: (a) P-wave velocity, (b) S1-wave velocity, and (c) S2-wave velocity.	179
Figure 6-13. P-wave and S1-wave velocities cross-plots at different confining pressures: (a) 500 psig, (b) 1450 psig, (c) 2900 psig, and (d) 4350 psig.	180
Figure 6-14. Plot comparing the deep and shallow resistivities logs with core resistivity at reservoir temperature per depth and discriminated per PRT (petrofacies) unit (of well ENAP2 with R_o measured at a confining pressure of 3,500 psig.	181
Figure 6-15. Cementation exponent (m) cross-plots with (a) logarithm of core helium porosity with empirical correlation following Cluff et al. (2009); (b) core helium porosity discriminated by PRT units. Correl1 in the black line corresponds to the empirical correlation found in Figure 6-6, and Correl2 in the red dashed line corresponds to the empirical correlation found following Cluff et al. (2009).	182
Figure 6-16. Cementation exponent (m) cross-plot (a) calculated vs predicted from correlation found in Figure 6-6; (b) calculated vs predicted from correlation found in following Cluff et al. (2009).	182
Figure 6-17. Cementation exponent (m) with porosity cross-plots discriminated by (a) XRF iron content and (b) XRD chlorite content.	183
Figure 6-18. Cross-plot of cementation exponent (m) with porosity discriminated by standard deviation counting of voxels from CT scan images. Some CT images are displayed to visualize the trend of the degree of heterogeneity as m increases.	184
Figure 6-19. Cross-plot of cementation exponent (m) with porosity discriminated by the specific surface area (SSA). Some SEM images are displayed to visualize the grain and pore distribution trend.	184

Figure 6-20. Cross-plot of MICP pore-throat radius at 25% mercury saturation (r_{25}) with $(F \cdot K_g)^{0.5}$ following Ziarani and Aguilera (2012) correlation discriminated by (a) the cementation exponent and (b) the specific surface area.	185
Figure 6-21. (a) Normal probability plot of $(1/\eta_e)$ of the dataset. (b) frequency and cumulative histogram.....	186
Figure 6-22. (a) Electrical efficiency vs porosity for all ERTs. (b) Cementation exponent vs $1/\ln(\phi_{He})$ for the identified electrical rock types (ERTs).	186
Figure 6-23. Electrical efficiency (η_e) cross-plots with (a) core porosity, (b) iron content, (c) clay content, (d) chlorite content, (e) quartz content, and (f) plagioclase content.	187
Figure 6-24. Cross-plots of ENAP2 set: (a) cementation exponent (m) vs rock resistivity at the measured three confining pressures and (b) comparison of measured cementation exponent at 1,500 psig C.P. vs 3,500 psig C.P.	188
Figure 6-25. Plots from multisalinity experiment on ENAP1-2: (a) permeability ratio reduction trend, (b) NMR T_2 distribution trend (modified from Navarro-Perez et al., 2024).	189
Figure 6-26. Pore water conductivity (C_w) cross-plots from multisalinity experiment in ENAP1-2: (a) apparent formation factor, (b) cementation exponent.	190
Figure 6-27. (a) V_s1 vs V_p discriminated at confining pressures of 2,900 and 4,350 psig, respectively, and compared with Castagna et al. (1985) mudrock line. (b) Cross-plot of measured vs predicted V_p at 2,900 psig CP with Castagna et al. (1985) mudrock line. (c) Cross-plot of measured vs predicted V_p at 4,350 psig CP with Castagna et al. (1985) mudrock line.....	191
Figure 6-28. V_s and V_p for worldwide mudrocks from in-situ sonic and field seismic measurements from Castagna et al.'s (1985) study.	192
Figure 6-29. (a) Core porosity vs V_p cross-plot discriminated by lithological units at 4,350 psig C.P. and compared with Wyllie et al. (1958) and Raymer et al. (1980) correlations. A linear empirical correlation is shown. (b) Cross-plot of measured vs predicted V_p with Raymer et al. (1980) correlation. (c) Cross-plot of measured vs predicted V_p with linear empirical correlation. (d) Cross-plot of measured vs predicted V_p with Wyllie et al. (1958) correlation. The chloritic sample ENAP2-54 was not added in the cross-plots (b), (c), and (d).	193
Figure 6-30. (a) Core porosity vs V_p cross-plot discriminated by glauconitic sandstone cores at 4,350 psig C.P. and compared with selected correlations. (b) Cross-plot of measured vs predicted V_p with Han et al. (1986) correlation. (c) Cross-plot of measured vs predicted V_p with Castagna et al. (1958) correlation. (d) Cross-plot of measured vs predicted V_p with Tosaya (1982) correlation.	194

Figure 6-31. (a) Core porosity vs Vp cross-plot discriminated by glauconitic sandstone cores at 4,350 psig C.P. and compared with multilinear regression (MLR) equation. (b) Cross-plot of measured vs predicted Vp with MLR correlation. 194

Figure 6-32. Core helium porosity vs Vp cross-plots at a confining pressure of 4,350 psig discriminated by (a) XRD clay minerals and (b) XRF iron content. 195

Figure 6-33. Core helium porosity vs Vp cross-plot with some SEM images at a scale of 200 μ m and CT scan images of cores. 196

Figure 6-34. Vp/Vs1 ratio cross-plots at a confining pressure of 4,350 psig: (a) cementation exponent vs Vp/Vs1 discriminated by the plagioclase content; (b) rock resistivity vs Vp/Vs1 discriminated by the iron content; (c) clay content vs Vp/Vs1 discriminated by the Poisson's ratio; (d) core permeability vs Vp/Vs1 discriminated by the chlorite content. 198

Figure 6-35. Geomechanical properties cross-plots at a confining pressure of 4,350 psig: (a) plagioclase content vs Poisson's ratio discriminated by clay content; (b) core helium porosity vs Impedance from Vp discriminated by bulk density. 199

Figure 7-1. Petrophysical evaluation workflow diagram. 206

Figure 7-2. Bulk density and neutron porosity cross-plot of calibration (a), validation (b), and propagation (c) groups. 208

Figure 7-3. Quick-look interpretation of ENAP1 well. Track1: ZG formations name. Track2: True vertical depth (m). Track3: Measured depth (m). Track4: Borehole, BS= Bit size 6.12", HCAL= calliper. Track5: GrC=gamma-ray, SP=spontaneous potential. The preliminary cutoff value for greensand and claystone is 80 API. Track6: AT90=deep resistivity, RXOZ=invaded formation resistivity, and RXOZ/Rdeep ratio. Porous rock shading occurs in the crossover from RXOZ to AT90. Track7: DTSM=compressional transit time, DTCO=shear transit time, VPVS< 1.75 identifies the pay zone (ENAP cut-off). Track8: SDR permeability model from NMR tool. Track9: mineralogy logs derived from the CMR tool. 209

Figure 7-4. Quick-look interpretation of ENAP2 well. Track1: ZG formations name. Track2: True vertical depth (m). Track3: Measured depth (m). Track4: Borehole, BS= Bit size 6.12", HCAL= calliper. Track5: GrC=gamma-ray, SP=spontaneous potential. The preliminary cutoff value for greensand and claystone is 80 API. Track6: AT90=deep resistivity, RXOZ=formation resistivity, and RXOZ/Rdeep ratio. Porous rock shading occurs in the crossover from RXOZ to AT90. Track7: DTSM=compressional transit time, DTCO=shear transit time, VPVS< 1.75 identifies the pay zone (ENAP cut-off). Track8: mineralogy logs derived from the CMR tool. 210

Figure 7-5. Gamma-ray readings of wells ENAP1 (blue), ENAP2 (light blue), WX1 (green), WX2 (purple), and WX3 (red-brown) histogram. The average minimum, maximum, and mean values lines are shown.	211
Figure 7-6. Neutron porosity (v/v) and bulk density (kg/m ³) cross-plot of key and validators wells per subzone. The pay sands are coloured in magenta and were not considered to establish the clean sandstone line.	212
Figure 7-7. Clay volume estimation of ENAP1 well. Track 1: True vertical depth (m). Track 2: ZG subzones name. Track 3: Gamma-ray log (API). Track 4: Photoelectric factor log (barns/e). Track 5: Bulk density (kg/m ³) and neutron porosity (v/v) logs. Track 6: Clay volume estimation from each selected indicator. Track 7: Final clay volume in black line (VCL). XRD core data in red dots. Clay volume derived from the CMRPlus tool (kgf/kgf).	213
Figure 7-8. Clay volume estimation of ENAP2 well. Track 1: True vertical depth (m). Track 2: ZG subzones name. Track 3: Gamma-ray log (API). Track 4: Photoelectric factor log (barns/e). Track 5: Bulk density (kg/m ³) and neutron porosity (v/v) logs. Track 6: Clay volume estimation from each selected indicator. Track 7: Final clay volume in black line (VCL). XRD core data in red dots. Clay volume derived from the CMRPlus tool (kgf/kgf).	213
Figure 7-9. Porosity logs vs core porosity of ENAP1 well. Track 1: True vertical depth (m). Track 2: ZG subzones name. Track 3: Density porosity (red), NMR porosity (blue), core helium porosity (black dot), core NMR porosity (blue dot). Track 4: Neutron porosity (green). Track 5: Sonic porosity (purple).	214
Figure 7-10. Porosity logs vs core porosity of ENAP2 well. Track 1: True vertical depth (m). Track 2: ZG subzones name. Track 3: Density porosity (red), NMR porosity (blue), core helium porosity (black dot), core NMR porosity (blue dot). Track 4: Neutron porosity (green). Track 5: Sonic porosity (purple).	215
Figure 7-11. Porosity logs vs core porosity of WX1 and WX2 wells. Track 1: True vertical depth (m). Track 2: ZG subzones name. Track 3: Density porosity (blue), NMR porosity (red). Track 4: Sonic porosity (purple), NMR porosity (red).	216
Figure 7-12. Permeability model of ENAP1 well. Track 1: True vertical depth (m). Track 2: ZG subzones name. Track 3: NMR porosity log from Timur-Coates (black), NMR porosity log from SDR (blue), core permeability (black dot). Track 4: Synthetic permeability log (red). Track 5: Computed Log FZI (black) with a cutoff value - 1.25.	217
Figure 7-13. Permeability model of ENAP2 well. Track 1: True vertical depth (m). Track 2: ZG subzones name. Track 3: core permeability (black dot), synthetic permeability log (black). Track 4: Computed Log FZI (black) with a cutoff value -1.25.	217

- Figure 7-14. Permeability model of WX2 (validator) and WX9 (propagation) wells. Track 1: True vertical depth (m). Track 2: ZG subzones name. Track 3: Synthetic permeability log (black). Track 4: Computed Log FZI (black) with a cutoff value -1.25..... 218
- Figure 7-15. Pickett's plot of well ENAP1. The left side shows the glauconitic sandstone subzones with $m=2.02$, and the right side shows the chloritic sandstone subzone with $m=3.0$. The X-axis shows the deep resistivity log, and the Y-axis shows the total porosity log, which is discriminated by gamma-ray log readings from 40 to 120 API. 219
- Figure 7-16. Water saturation models in well ENAP2. Track1: Measured depth (m). Track2: ZG Subzones name. Track3: Gamma-ray (green) and photoelectric factor (purple). Track4: Reservoir markers Log FZI (black) displays the PTR1 facies location shading in blue, and Vp/Vs ratio (blue) displays the PTR1 facies location shading in lime. Track 5: Porous rock shading in light brown occurs in the crossover from RXOZ to AT90. Track6: Cation-exchange capacity curves used in the Waxman-Smits model, from core data (black) and log data (blue). Track7: total gas production from mudlogging data (red triangles). Track8: Sw Archie's model. Track9: Sw Indonesian model. Track10: Sw Modified Simandoux model. Track11: Sw Waxman-Smits model. 220
- Figure 7-17. Net pay (red) and reservoir (green) location in well ENAP1. Track 1: True vertical depth (m). Track 2: ZG subzone name. Track 3: Gamma-ray (green) and photoelectric factor (purple) logs. Track 4: Porosity (v/v). Track5: Water saturation (v/v). Track6: Clay volume (v/v)..... 221
- Figure 7-18. Petrophysical evaluation of well ENAP1: Track 1: True vertical depth (m). Track 2: Subzone name. Track 3: Gamma-ray (green) and photoelectric factor (purple) logs. Track 4: Deep resistivity (red) and formation resistivity (magenta) logs. Porous rock shading in light brown occurs in the crossover from RXOZ to AT90. Track5: Neutron porosity (green) and bulk density (red) logs. Gas effect shading in light grey occurs in the crossover from RHOC to NPHI. Track6: Reservoir markers Log FZI (black) displays the PTR1 facies location shading in blue, and Vp/Vs ratio (blue) displays pay sand location shading in lime. Track7: Clay and sandstone lithology. Track8: Total porosity (black). A cut-off value of 18%v/v in shading gold. Track9: Permeability (black). A cut-off value of 0.01 mD in shading red. Track10: Water saturation (black). Gas saturation shading in green, water saturation in light blue, and a cut-off value of $Sw= 65\%v/v$ in red. 223

Figure 7-19. Petrophysical evaluation of well ENAP2: Track 1: True vertical depth (m). Track 2: Subzone name. Track 3: Gamma-ray (green) and photoelectric factor (purple) logs. Track 4: Deep resistivity (red) and formation resistivity (magenta) logs. Porous rock shading in light brown occurs in the crossover from RXOZ to AT90. Track5: Neutron porosity (green) and bulk density (red) logs. Gas effect shading in light grey occurs in the crossover from RHOC to NPHI. Track6: Reservoir markers Log FZI (black) displays the PTR1 facies location shading in blue and Vp/Vs ratio (blue) displays pay sand location shading in lime. Track7: Clay and sandstone lithology. Track8: Total porosity (black). A cut-off value of 18%v/v in shading gold. Track9: Permeability (black). A cut-off value of 0.01 mD in shading red. Track10: Water saturation (black). Gas saturation shading in green, water saturation in light blue, and a cut-off value of $S_w = 65\%v/v$ in red. 224

Figure 7-20. Clay volume plot comparison of XRD (X-axis) with log data (Y-axis). 226

Figure 7-21. Well ENAP1. Track 1: True vertical depth (m). Track 2: ZG subzone name. Track 3: Gamma-ray (green) and photoelectric factor (purple) logs. Track 4: Deep resistivity (ohm·m). Track5: Vp/Vs ratio log with grey shading below 1.70. Track6: Vp/Vs ratio log with grey shading below 1.75. Track7: Clay volume (v/v). 226

Figure 7-22. Porosity plots comparison: core porosity (X-axis) with porosity log data (Y-axis): (a) density method, (b) neutron method, (c) sonic method, and (d) NMR tool. 228

Figure 7-23. Bar chart comparison of pay sand samples' core and log porosity data: (a) ENAP1-2, (b) ENAP2-54. 229

Figure 7-24. Well ENAP2. Track 1: True vertical depth (m). Track 2: ZG subzone name. Track 3: cementation exponent m (black) log from correlation 1 (linear). Track 4: Water saturation log using correlation 1 and the modified Simandoux model. Track5: cementation exponent m (black) log from average values. Track6: Water saturation log using average values of m and the modified Simandoux model. Track7: cementation exponent m (black) log from correlation 2 (natural logarithmic). Track8: Water saturation log using correlation 2 and the modified Simandoux model. 230

Figure 7-25. Cross-plot comparison of water saturation log values with the average m values (X-axis) and on the Y-axis: (a) Correlation 1 (linear). (b) Correlation 2 (ERT). 231

Figure 7-26. Well ENAP1. Track 1: True vertical depth (m). Track 2: ZG subzone name. Track 3: Photoelectric factor (purple), Vp/Vs ratio (blue), and Log FZI (black) logs. Track 4: Deep (red) and formation (magenta) resistivity logs. Track5: Water saturation log with Archie's model. Track6: Water saturation log with the Indonesian model. Track7: Water saturation log with the modified Simandoux model. Track8: Water saturation log with the Waxman-Smiths model. 232

Figure 7-27. Wells ENAP2 (a) and WX1 (b). Track 1: True vertical depth (m). Track 2: ZG subzone name. Track 3: Photoelectric factor (purple) and gamma-ray (green) logs. Track 4: Reservoir markers Log FZI (black) displays the PTR1 facies location shading in blue, and the Vp/Vs ratio (blue) displays the PTR1 facies location shading in lime. Track 5: Porous rock shading in light brown occurs in the crossover from RXOZ to AT90. Track6: Cation-exchange capacity curves used in the Waxman-Smiths model, from core data (black) and log data (blue). Track7: total gas production from mudlogging data (red triangles). Track8: Sw Archie's model. Track9: Sw Indonesian model. Track10: Sw Modified Simandoux model. Track11: Sw Waxman-Smiths model. 234

Figure 7-28. $1/\Phi_T$ vs Q_{vapp} , cross-plot of wells ENAP1 (left) and ENAP2 (right), discriminated by gamma-ray log readings..... 234

Figure 7-29. $1/\Phi_T$ vs Q_{vapp} cross-plot of well ENAP2 with core data. Linear correlation does not consider the PTR1 unit. 235

Figure 7-30. Computed Indonesian Sw (X-axis) vs computed modified Simandoux Sw (Y-axis) of key wells ENAP1 (left) and ENAP2 (right), discriminated by subzones. Note the underestimation of the Indonesian in subzone ZG bottom2, which corresponds to the pay sand location. 236

Figure 7-31. Cross-plot of Sw log profiles of modified Simandoux (X-axis) vs Indonesian (Y-axis) of the pay sand area of key wells. 236

Figure 7-32. Sensitivity analysis cross-plots: (a) varying clay resistivity, Rcl. (b) varying water resistivity, R_w. (c) varying clay volume, Vcl. 237

Figure A-1. Cross-plot of number of scans versus water volume. 272

Figure A-2. Cross-plot of signal per scan versus water volume. 272

Figure A-3. Cross-plot of hydrogen index and salt concentration..... 273

Figure B-1. ENAP1 mineralogy (top) and major chemical components (bottom) against depth. The green rectangle indicates the location of the pay sand core..... 279

Figure B-2. ENAP2 mineralogy (top) and major chemical components (bottom) against depth. The green rectangle indicates the location of the pay sand core..... 280

Figure C-1. Apex position of the ZG dataset using Pittman's (1992) workflow. 284

Figure C-2. (a) Predicted vs actual pore-throat radius at 35%v/v mercury saturation with MLR in MS Excel. (b) Predicted vs actual pore-throat radius at 35% mercury saturation with Winland's correlation. (c) Predicted vs actual pore-throat radius at 35%v/v mercury saturation with Kolodzie's correlation. (d) Predicted vs actual pore-throat radius at 15%v/v mercury saturation with Pittman's correlation. (e) Predicted vs actual pore-throat radius at 20%v/v mercury saturation with Pittman's correlation. (f) Predicted vs actual pore-throat radius at 25%v/v mercury saturation with Pittman's correlation..... 285

Figure C-3. (g) Predicted vs actual pore-throat radius at 30%v/v mercury saturation with Pittman's correlation. (h) Predicted vs actual pore-throat radius at 35%v/v mercury saturation with Pittman's correlation. (i) Predicted vs actual pore-throat radius at 40%v/v mercury saturation with Pittman's correlation. (j) Predicted vs actual pore-throat radius at 45%v/v mercury saturation with Pittman's correlation. (k) Predicted vs actual pore-throat radius at 50%v/v mercury saturation with Pittman's correlation. (l) Predicted vs actual pore-throat radius at 55%v/v mercury saturation with Pittman's correlation..... 286

Figure C-4. (m) Predicted vs actual pore-throat radius at 60%v/v mercury saturation with Pittman's correlation. (n) Predicted vs actual pore-throat radius at 65%v/v mercury saturation with Pittman's correlation. (o) Predicted vs actual pore-throat radius at 70%v/v mercury saturation with Pittman's correlation. (p) Predicted vs actual pore-throat radius at 75%v/v mercury saturation with Pittman's correlation..... 287

Figure D-1. Calibration cross-plot with aluminium alley bars..... 290

Figure E-1. Diagram of bulk density (g/cc) and neutron porosity (v/v) cross-plot to define the clean sandstone endpoints 1 and 2 with the clay point (Geoactive Ltd., 2024)..... 304

Figure E-2. Clay volume estimation of WX1 well. Track 1: Depth (m). Track 2: ZG subzones name. Track 3: Gamma-ray log (API). Track 4: Photoelectric factor log (barns/e). Track 5: Bulk density (kg/m³) and neutron porosity (v/v) logs. Track 6: Clay volume estimation from each selected indicator. Track 7: Final clay volume in black line (VCL). Clay volume derived from the CMRPlus tool (kgf/kgf). 305

Figure E-3. Clay volume estimation of WX2 well. Track 1: Depth (m). Track 2: ZG subzones name. Track 3: Gamma-ray log (API). Track 4: Photoelectric factor log (barns/e). Track 5: Bulk density (kg/m³) and neutron porosity (v/v) logs. Track 6: Clay volume estimation from each selected indicator. Track 7: Final clay volume in black line (VCL). Clay volume derived from the CMRPlus tool (kgf/kgf). 306

Figure E-4. Clay volume estimation of WX3 well. Track 1: Depth (m). Track 2: ZG subzones name. Track 3: Gamma-ray log (API). Track 4: Photoelectric factor log (barns/e). Track 5: Bulk density (kg/m ³) and neutron porosity (v/v) logs. Track 6: Clay volume estimation from each selected indicator. Track 7: Final clay volume in black line (VCL). Clay volume derived from the CMRPlus tool (kgf/kgf).	307
Figure E-5. Clay volume estimation of WX4 well. Track 1: Depth (m). Track 2: ZG subzones name. Track 3: Gamma-ray log (API). Track 4: Photoelectric factor log (barns/e). Track 5: Bulk density (kg/m ³) and neutron porosity (v/v) logs. Track 6: Clay volume estimation from each selected indicator. Track 7: Final clay volume in black line (VCL).	308
Figure E-6. Clay volume estimation of WX5 well. Track 1: Depth (m). Track 2: ZG subzones name. Track 3: Gamma-ray log (API). Track 4: Photoelectric factor log (barns/e). Track 5: Bulk density (kg/m ³) and neutron porosity (v/v) logs. Track 6: Clay volume estimation from each selected indicator. Track 7: Final clay volume in black line (VCL).	309
Figure E-7. Clay volume estimation of WX6 well. Track 1: Depth (m). Track 2: ZG subzones name. Track 3: Gamma-ray log (API). Track 4: Photoelectric factor log (barns/e). Track 5: Bulk density (kg/m ³) and neutron porosity (v/v) logs. Track 6: Clay volume estimation from each selected indicator. Track 7: Final clay volume in black line (VCL).	310
Figure E-8. Clay volume estimation of WX7 well. Track 1: Depth (m). Track 2: ZG subzones name. Track 3: Gamma-ray log (API). Track 4: Photoelectric factor log (barns/e). Track 5: Bulk density (kg/m ³) and neutron porosity (v/v) logs. Track 6: Clay volume estimation from each selected indicator. Track 7: Final clay volume in black line (VCL).	311
Figure E-9. Clay volume estimation of WX8 well. Track 1: Depth (m). Track 2: ZG subzones name. Track 3: Gamma-ray log (API). Track 4: Photoelectric factor log (barns/e). Track 5: Bulk density (kg/m ³) and neutron porosity (v/v) logs. Track 6: Clay volume estimation from each selected indicator. Track 7: Final clay volume in black line (VCL).	312
Figure E-10. Clay volume estimation of WX9 well. Track 1: Depth (m). Track 2: ZG subzones name. Track 3: Gamma-ray log (API). Track 4: Photoelectric factor log (barns/e). Track 5: Bulk density (kg/m ³) and neutron porosity (v/v) logs. Track 6: Clay volume estimation from each selected indicator. Track 7: Final clay volume in black line (VCL).	313

Figure E-11. Clay volume estimation of WX10 well. Track 1: Depth (m). Track 2: ZG subzones name. Track 3: Gamma-ray log (API). Track 4: Photoelectric factor log (barns/e). Track 5: Bulk density (kg/m³) and neutron porosity (v/v) logs. Track 6: Clay volume estimation from each selected indicator. Track 7: Final clay volume in black line (VCL). 314

Figure E-12. Screenshot of the Porosity tab from the Basic Log Analysis Function module in IP (Geoactive Ltd., 2024). 315

Figure E-13. Petrophysical evaluation of well WX1: Track 1: True vertical depth (m). Track 2: Subzone name. Track 3: Gamma-ray (green) and photoelectric factor (purple) logs. Track 4: Deep resistivity (red) and formation resistivity (magenta) logs. Porous rock shading in light brown occurs in the crossover from RXOZ to AT90. Track5: Neutron porosity (green) and bulk density (red) logs. Gas effect shading in light grey occurs in the crossover from RHOC to NPHI. Track6: Reservoir markers Log FZI (black) displays the PTR1 facies location shading in blue, and Vp/Vs ratio (blue) displays pay sand location shading in lime. Track7: Clay and sandstone lithology. Track8: Total porosity (black). A cut-off value of 18%v/v in shading gold. Track9: Permeability (black). A cut-off value of 0.01 mD in shading red. Track10: Water saturation (black). Gas saturation shading in green, water saturation in light blue, and a cut-off value of Sw= 65%v/v in red. 318

Figure E-14. Petrophysical evaluation of well WX2: Track 1: True vertical depth (m). Track 2: Subzone name. Track 3: Gamma-ray (green) and photoelectric factor (purple) logs. Track 4: Deep resistivity (red) and formation resistivity (magenta) logs. Porous rock shading in light brown occurs in the crossover from RXOZ to AT90. Track5: Neutron porosity (green) and bulk density (red) logs. Gas effect shading in light grey occurs in the crossover from RHOC to NPHI. Track6: Reservoir markers Log FZI (black) displays the PTR1 facies location shading in blue, and Vp/Vs ratio (blue) displays pay sand location shading in lime. Track7: Clay and sandstone lithology. Track8: Total porosity (black). A cut-off value of 18%v/v in shading gold. Track9: Permeability (black). A cut-off value of 0.01 mD in shading red. Track10: Water saturation (black). Gas saturation shading in green, water saturation in light blue, and a cut-off value of Sw= 65%v/v in red. 319

Figure E-15. Petrophysical evaluation of well WX3: Track 1: True vertical depth (m). Track 2: Subzone name. Track 3: Gamma-ray (green) and photoelectric factor (purple) logs. Track 4: Deep resistivity (red) and formation resistivity (magenta) logs. Porous rock shading in light brown occurs in the crossover from RXOZ to AT90. Track5: Neutron porosity (green) and bulk density (red) logs. Gas effect shading in light grey occurs in the crossover from RHOC to NPHI. Track6: Reservoir markers Log FZI (black) displays the PTR1 facies location shading in blue, and Vp/Vs ratio (blue) displays pay sand location shading in lime. Track7: Clay and sandstone lithology. Track8: Total porosity (black). A cut-off value of 18%v/v in shading gold. Track9: Permeability (black). A cut-off value of 0.01 mD in shading red. Track10: Water saturation (black). Gas saturation shading in green, water saturation shading in light blue, and a cut-off value of Sw= 65%v/v in red. 320

Figure E-16. Petrophysical evaluation of well WX4: Track 1: True vertical depth (m). Track 2: Subzone name. Track 3: Gamma-ray (green) and photoelectric factor (purple) logs. Track 4: Deep resistivity (red) and formation resistivity (magenta) logs. Porous rock shading in light brown occurs in the crossover from RXOZ to AT90. Track5: Neutron porosity (green) and bulk density (red) logs. Gas effect shading in light grey occurs in the crossover from RHOC to NPHI. Track6: Reservoir markers Log FZI (black) displays the PTR1 facies location shading in blue, and Vp/Vs ratio (blue) displays pay sand location shading in lime. Track7: Clay and sandstone lithology. Track8: Total porosity (black). A cut-off value of 18%v/v in shading gold. Track9: Permeability (black). A cut-off value of 0.01 mD in shading red. Track10: Water saturation (black). Gas saturation shading in green, water saturation in light blue, and a cut-off value of Sw= 65%v/v in red. 321

Figure E-17. Petrophysical evaluation of well WX5: Track 1: True vertical depth (m). Track 2: Subzone name. Track 3: Gamma-ray (green) and photoelectric factor (purple) logs. Track 4: Deep resistivity (red) and formation resistivity (magenta) logs. Porous rock shading in light brown occurs in the crossover from RXOZ to AT90. Track5: Neutron porosity (green) and bulk density (red) logs. Gas effect shading in light grey occurs in the crossover from RHOC to NPHI. Track6: Reservoir markers Log FZI (black) displays the PTR1 facies location shading in blue, and Vp/Vs ratio (blue) displays pay sand location shading in lime. Track7: Clay and sandstone lithology. Track8: Total porosity (black). A cut-off value of 18%v/v in shading gold. Track9: Permeability (black). A cut-off value of 0.01 mD in shading red. Track10: Water saturation (black). Gas saturation shading in green, water saturation in light blue, and a cut-off value of Sw= 65%v/v in red. 322

Figure E-18. Petrophysical evaluation of well WX6: Track 1: True vertical depth (m). Track 2: Subzone name. Track 3: Gamma-ray (green) and photoelectric factor (purple) logs. Track 4: Deep resistivity (red) and formation resistivity (magenta) logs. Porous rock shading in light brown occurs in the crossover from RXOZ to AT90. Track5: Neutron porosity (green) and bulk density (red) logs. Gas effect shading in light grey occurs in the crossover from RHOC to NPHI. Track6: Reservoir markers Log FZI (black) displays the PTR1 facies location shading in blue, and Vp/Vs ratio (blue) displays pay sand location shading in lime. Track7: Clay and sandstone lithology. Track8: Total porosity (black). A cut-off value of 18%v/v in shading gold. Track9: Permeability (black). A cut-off value of 0.01 mD in shading red. Track10: Water saturation (black). Gas saturation shading in green, water saturation in light blue, and a cut-off value of Sw= 65%v/v in red. 323

Figure E-19. Petrophysical evaluation of well WX7: Track 1: True vertical depth (m). Track 2: Subzone name. Track 3: Gamma-ray (green) and photoelectric factor (purple) logs. Track 4: Deep resistivity (red) and formation resistivity (magenta) logs. Porous rock shading in light brown occurs in the crossover from RXOZ to AT90. Track5: Neutron porosity (green) and bulk density (red) logs. Gas effect shading in light grey occurs in the crossover from RHOC to NPHI. Track6: Reservoir markers Log FZI (black) displays the PTR1 facies location shading in blue, and Vp/Vs ratio (blue) displays pay sand location shading in lime. Track7: Clay and sandstone lithology. Track8: Total porosity (black). A cut-off value of 18%v/v in shading gold. Track9: Permeability (black). A cut-off value of 0.01 mD in shading red. Track10: Water saturation (black). Gas saturation shading in green, water saturation in light blue, and a cut-off value of Sw= 65%v/v in red. 324

Figure E-20. Petrophysical evaluation of well WX8: Track 1: True vertical depth (m). Track 2: Subzone name. Track 3: Gamma-ray (green) and photoelectric factor (purple) logs. Track 4: Deep resistivity (red) and formation resistivity (magenta) logs. Porous rock shading in light brown occurs in the crossover from RXOZ to AT90. Track5: Neutron porosity (green) and bulk density (red) logs. Gas effect shading in light grey occurs in the crossover from RHOC to NPHI. Track6: Reservoir markers Log FZI (black) displays the PTR1 facies location shading in blue, and Vp/Vs ratio (blue) displays pay sand location shading in lime. Track7: Clay and sandstone lithology. Track8: Total porosity (black). A cut-off value of 18%v/v in shading gold. Track9: Permeability (black). A cut-off value of 0.01 mD in shading red. Track10: Water saturation (black). Gas saturation shading in green, water saturation in light blue, and a cut-off value of Sw= 65%v/v in red. 325

Figure E-21. Petrophysical evaluation of well WX9: Track 1: True vertical depth (m). Track 2: Subzone name. Track 3: Gamma-ray (green) and photoelectric factor (purple) logs. Track 4: Deep resistivity (red) and formation resistivity (magenta) logs. Porous rock shading in light brown occurs in the crossover from RXOZ to AT90. Track5: Neutron porosity (green) and bulk density (red) logs. Gas effect shading in light grey occurs in the crossover from RHOC to NPHI. Track6: Reservoir markers Log FZI (black) displays the PTR1 facies location shading in blue, and Vp/Vs ratio (blue) displays pay sand location shading in lime. Track7: Clay and sandstone lithology. Track8: Total porosity (black). A cut-off value of 18%v/v in shading gold. Track9: Permeability (black). A cut-off value of 0.01 mD in shading red. Track10: Water saturation (black). Gas saturation shading in green, water saturation in light blue, and a cut-off value of Sw= 65%v/v in red. 326

Figure E-22. Petrophysical evaluation of well WX10: Track 1: True vertical depth (m). Track 2: Subzone name. Track 3: Gamma-ray (green) and photoelectric factor (purple) logs. Track 4: Deep resistivity (red) and formation resistivity (magenta) logs. Porous rock shading in light brown occurs in the crossover from RXOZ to AT90. Track5: Neutron porosity (green) and bulk density (red) logs. Gas effect shading in light grey occurs in the crossover from RHOC to NPHI. Track6: Reservoir markers Log FZI (black) displays the PTR1 facies location shading in blue, and Vp/Vs ratio (blue) displays pay sand location shading in lime. Track7: Clay and sandstone lithology. Track8: Total porosity (black). A cut-off value of 18%v/v in shading gold. Track9: Permeability (black). A cut-off value of 0.01 mD in shading red. Track10: Water saturation (black). Gas saturation shading in green, water saturation in light blue, and a cut-off value of Sw= 65%v/v in red. 327

Chapter 1 Overview

This chapter introduces the research topic, highlighting the current state of the art and the contribution of this work. It then follows by explaining the investigation scope and presenting the case study. Then, it describes the project limitations and finishes with this dissertation's structure.

1.1 Introduction

Glauconitic sandstones, also known as greensands, are a complex rock type that produces oil or gas worldwide reservoirs, e.g. Lower Senonian Matulla in the Gulf of Suez, Egypt (Patchett et al., 1993), Caballos Formation, Colombia (Diaz et al., 2003), Mardie Greensand, Australia (Hatcher et al., 1996), North Sea Greensand (Thomas et al., 2003), the Upper T Napo Formation, Ecuador (Yang et al., 2019), the Magallanes Formation, Argentina (Aimar et al., 2018). These reservoirs are clastic quartz rocks characterised by a considerable amount of glauconite and other clay minerals such as illite-smectite mixed layer, chlorite, and pyrite. They typically have poor to moderate porosity ($< 15\%v/v$) and ultra-low to low permeability (< 1 mD for tight gas), often classifying them as tight formations. Due to these characteristics, hydraulic fracturing is frequently the only viable technology to make them producible.

The presence of glauconite and other clay minerals in greensands results in several unique properties, such as a bimodal pore size distribution due to the presence of macropores between framework grains and micropores between clay minerals (Dodge et al., 1996). Chemical analysis suggests they have a high iron, potassium (Odin and Letolle, 1980) and boron content (Harder, 1969). They also have a considerable cation-exchange capacity (Patchett et al., 1993). These features significantly affect main wire-line log readings (e.g. gamma-ray, density, neutron, and resistivity), making standard well-log interpretation techniques unreliable for estimating petrophysical properties. Hence, a core analysis programme is crucial for accurately determining petrophysical properties, calibrating the petrophysical model, and estimating producing hydrocarbons-in-place.

Archie's (1942) model is still used to interpret electrical logs to determine water saturation in tight gas sandstones, TGS henceforth, including clayey formations. Usually, the correlational factor (a), the cementation (m), and saturation (n) exponents are fitted to laboratory measurements of the sandstone samples' resistivity with varying brine saturation. The values obtained are then used to estimate the water

saturation of reservoirs from wire-line log data. Unfortunately, there often exists a significant uncertainty in the hydrocarbon saturation because the original Archie model does not take into account how clay minerals impact electrical logs, particularly at low water salinity. Glauconites alter the rock's deep resistivity, and other water saturation models, such as Waxman and Smits (1968) or the Dual-Water (Clavier et al., 1977, 1984), which includes the clayey conduction term, need to be applied.

Cut-off criteria to define net pay in TGSs are challenging due to poor quality rock property measurements and potentially inaccurate readings of traditional logging tools; as such, the traditional well-log interpretation methods are unsuitable. Also, due to the high heterogeneity of TGSs, variable cut-off values are more likely to be used than fixed ones (Worthington, 2009). Nuclear magnetic resonance (NMR) technology counteracts such factors by measuring the net magnetisation of hydrogen nuclei inside a core with a transverse relaxation time, T_2 , without interfering with the rock microstructure. The NMR response to gas is shorter than in oil, which is shorter than that of brine, and the fluids volume and pore size distribution (PSD) can be estimated from NMR logs. An empirical T_2 cut-off may assist in defining the ratio of mobile to immobile fluids (e.g. Coates et al., 1999).

Similarly, laboratory mercury injection capillary pressure (MICP) data can be used to build the saturation-height distribution, which can be used to estimate how gas saturation varies in function of the height above the free water level (e.g. McPhee et al., 2015). Also, permeability can be derived from NMR and MICP techniques using empirical correlations (Coates et al., 1999; Comisky et al., 2007). This is an advantage when no good quality core is acquired from the field, as these analyses use side wall cores and cuttings, respectively. Furthermore, it is common practice to convert NMR T_2 data to MICP data and vice versa with a scaling factor since the pore-body size may be derived from the NMR T_2 data and the pore-throat radius may be derived from MICP data (Marshall et al., 1995). Hence, a customised workflow with the scaling factor assists in deriving PSDs and permeability at the log scale when capillary data is unavailable, but NMR logging is.

Few published works propose innovative workflows in estimating the petrophysical properties of greensand reservoirs (e.g. Patchett et al., 1993; Hatcher et al., 1996; Zhang et al., 2000; Thomas et al., 2003; Klein et al., 2006; Hossain, 2011a; Prayoga et al., 2018). However, these studies often focus on specific geological and sedimentary settings and do not fully answer the question: how does the presence of glauconite and other clay minerals impact the petrophysical properties, especially for estimating water saturation?

Understanding this impact is crucial because glauconite can significantly alter the electrical properties of the rock, potentially leading to inaccurate estimates of water

saturation and, consequently, hydrocarbon reserves. This knowledge gap presents a significant challenge in accurately characterising greensand reservoirs.

This research project investigates the petrophysical properties (e.g. porosity, permeability, electrical resistivity, ultrasonic velocities and capillary pressure) and their microstructural controls for the Zona Glauconítica (ZG) from the Magallanes basin in Tierra del Fuego island, Chilean Patagonia. This reservoir is often referred to as tight greensand as it often contains a high concentration of glauconite. The work combines laboratory analyses of the ZG reservoir with wire-line log data to create a calibrated workflow to aid reservoir characterisation. The work increases understanding of formation petrophysics, particularly the ability to accurately estimate the porosity, permeability, clay volume, and water saturation.

1.2 Scope of research

This research project aims to increase the quality of the petrophysical characterisation and well-log interpretation of a greensand tight gas, defined as the ZG formation, in Southern Chile by completing the following specific objectives (SOs):

SO1. Identify the key controls on the petrophysical properties of the ZG tight sandstone and establish their relationship to the microstructure.

SO2. Compare empirical and theoretical water saturation models that include the electrical behaviour of clays and select the best fit for the ZG formation.

SO3. Propose an integrated workflow for establishing a suitable petrophysical model in the ZG formation.

Each specific objective is executed with a different approach, and by combining them, an integrated workflow develops to fulfil the overall aim (**Figure 1-1**). The core analysis programme (**SO1**) follows the Wolfson Multiphase Flow Laboratory protocols at the School of Earth and Environment, University of Leeds, divided into petrographic and petrophysical analysis. On the one hand, the petrographic analysis determines the mineral and chemical composition and rock microstructure (e.g. heterogeneity, porosity type, clay minerals particles location and distribution). On the other hand, the petrophysical analysis measures the porosity, permeability, water saturation, capillary pressure, and rock resistivity, among other parameters, in unstressed and stressed conditions, respectively.

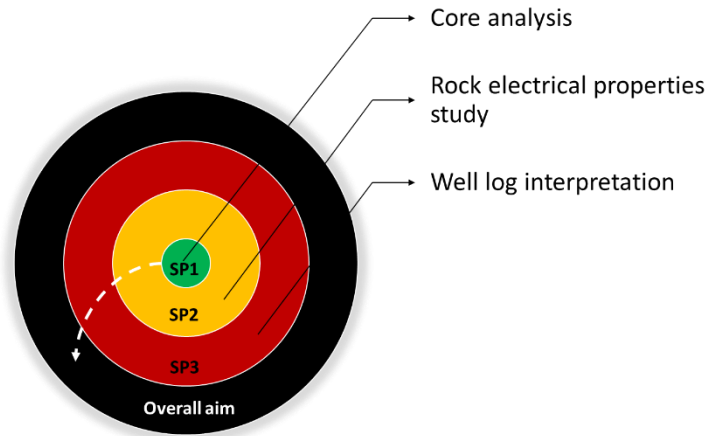


Figure 1-1. Specific objectives overall scheme.

SO2 consists of studying the electrical rock properties of the ZG formation and finding any correlation with the results from **SO1**. Two techniques are selected to understand the clay minerals' contribution to the rock microstructure; in other words, to test which water saturation model best describes the ZG reservoir. The results from **SO1** and **SO2** help calibrate and build a robust petrophysical model through well-log interpretation (**SO3**), thus defining the clay volume, porosity, water saturation and permeability estimation.

1.3 Case study: ZG play, Tierra del Fuego island, Southern Chile

1.3.1 Background

Chilean gas and oil exploration and production only occurs in the Magallanes basin (Austral basin on the Argentinian side), located in the southern part of the country, the Chilean Patagonia. ENAP is the state-owned national oil company in the Magallanes basin since the 1950s. It has initiated a roadmap of fossil fuel production by applying conventional and unconventional technologies and providing port logistics services to its clients (ENAP, 2022).

In 2015, ENAP began its exploration phase of the Zona Glauconítica Formation, shortened as ZG, in the Magallanes basin. ZG is a glauconite-rich sandstone that contains chlorite-rich subzones; in other words, it is a greensand formation located in the Arenal Block field north of Tierra del Fuego island (**Figure 1-2**). Garay et al. (2022) reported that 140 ZG producer wells, out of 320 active wells operated by ENAP, produced 70% of the overall gas over the last seven years in the Magallanes basin. The Arenal Block is in a remote location, which presents several challenges for producing gas, such as transporting equipment, materials and personnel and the

logistics of the different play development phases (Alqatrani et al., 2016; Britt et al., 2016).

The ZG formation, located between 2 to 3 km below the sea level, has a gross thickness between 50 to 150 metres. It features an ultra-low-to-low permeability (0.001 – 0.1 mD) and a low-to-moderate porosity between 10 – 25 %v/v (**Figure 1-3**). The reservoir's mineralogical immaturity is attributed to the rapid accumulation of volcanoclastics from the western Andean orogeny and continental lowlands, likely deposited in a low-energy, middle-to-outer shelf environment during a transgressive phase. This immaturity is reflected in its average composition of 43% clay (primarily glauconite and chlorite minerals), 34% feldspar, 23% quartz, and 3% tuff (**Figure 1-4**). The high proportion of unstable minerals (clay and feldspar) relative to quartz indicates minimal weathering and transportation of the sediments before deposition. Diagenetic processes, such as calcite cementation and grain compaction, reduced the original porosity, though some porosity was preserved through the leaching of labile grains (Pinto et al., 2022). Stratigraphically, it belongs to the Eocene epoch of the Paleogene period, situated below the Bahía Inutil Group Formation (**Figure 1-5**).

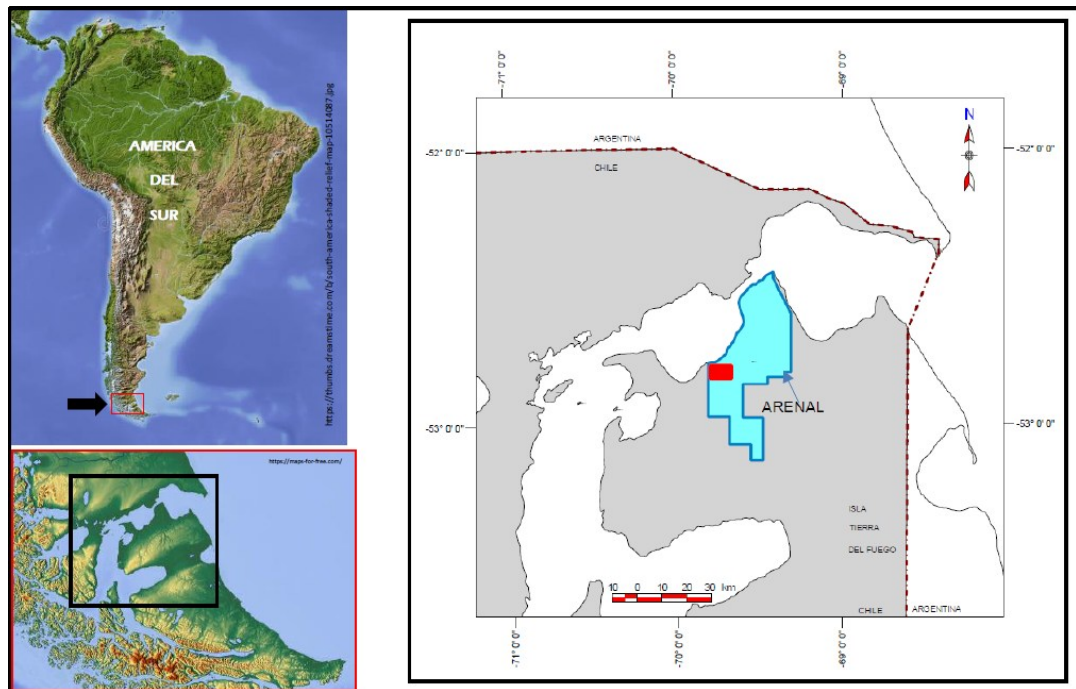


Figure 1-2. ZG formation location: maps showing continental location (left); Arenal block location in light blue and red rectangle indicating the ZG area on the northern area from Tierra del Fuego Island (right) (Gonzalez-Gonzalez et al., 2018).

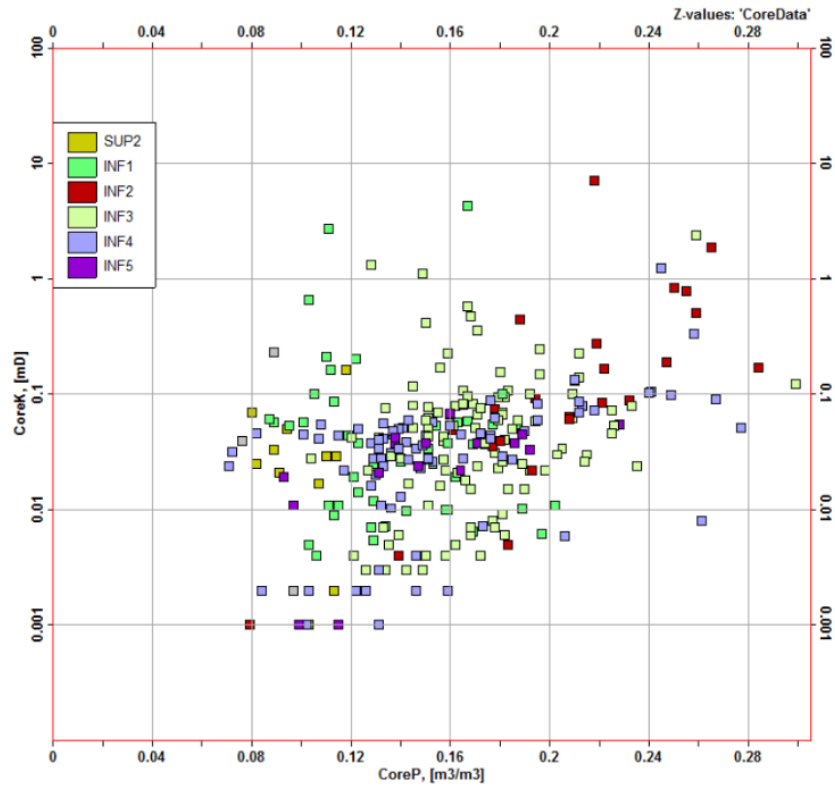


Figure 1-3. Core permeability vs core porosity cross-plot (Gonzalez-Gonzalez et al., 2018).

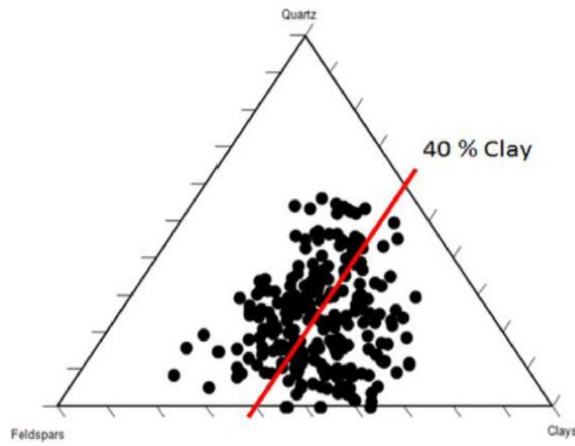


Figure 1-4. Mineralogical content of the ZG greensand formation (Britt et al., 2016).

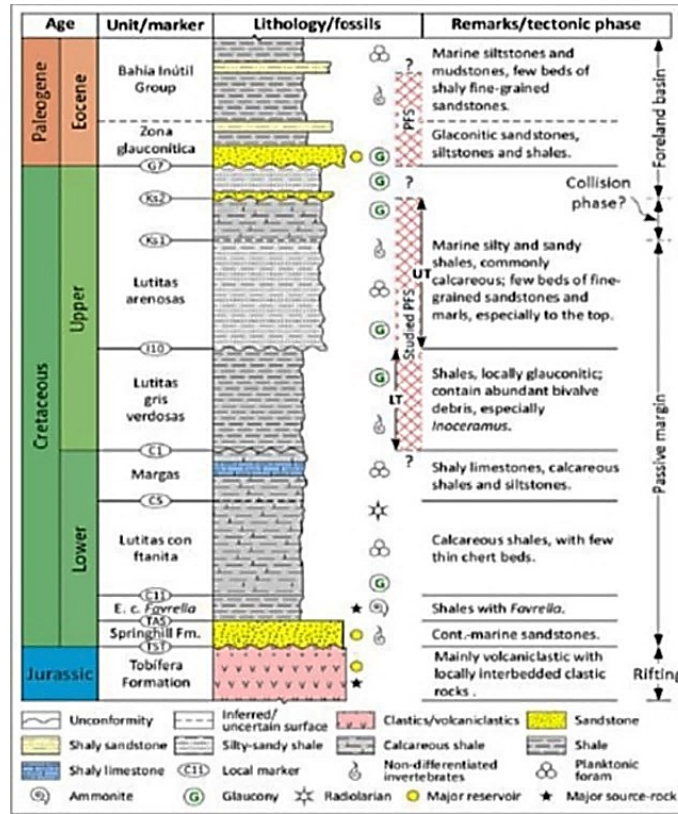


Figure 1-5. Generalized geologic setting of Magallanes Basin, from left to right: geological age, formation unit, typical fossil and mineral content, tectonic phase and the two polygon fault systems which extend through the source in the Upper Cretaceous into and through the ZG formation in the early Eocene (Britt et al., 2016).

The ZG formation has peculiar gamma-ray and induction log trends attributed to its high clay minerals. **Figure 1-6** shows the gamma-ray (green line) and induction (red line) logs of a ZG well divided into seven subunits. The pay sand is located between the ZG_SUP-2 and ZG_INF-4 subunits. On one side, the gamma-ray log has a bell pattern, from ZG_INF-2 to ZG_SUP-2, and a funnel pattern, from ZG_INF-2 to ZG_SUP-2, where it is evident that the formation is more in a clayey sequence than a sandstone sequence. Conversely, the induction log contrasts the gamma-ray log shape throughout the depth. Alqatrani et al. (2018) used the gamma-ray log to identify the formation lithology. They defined the criteria of less than 65 API units to be considered glauconitic sand, between 65 and 100 API units to be considered siltstone and higher than 100 API units to be shale.

The modified Simandoux model was used to estimate the water saturation, assuming $m= 2.09$, $n= 1.66$, and $a= 1$. The reservoir water formation salinity and resistivity are 12,000 ppm and 4 ohms·m, respectively, meaning the formation water is fresh to brackish (Carpenter, 1978).

Finally, **Figure 1-7** displays the well-interpretation of clay volume, porosity and water saturation of a ZG well. Gamma-ray and the photoelectric factor logs defined the sandstone and clayey zones (chlorite and glauconite presence) for clay volume. The

porosity model based on the nuclear magnetic resonance (NMR) tool is contrasted with core porosity. Finally, the water saturation in the last track (modified Simandoux model) shows gas stores between the ZG_INF-2 and ZG_INF-4.

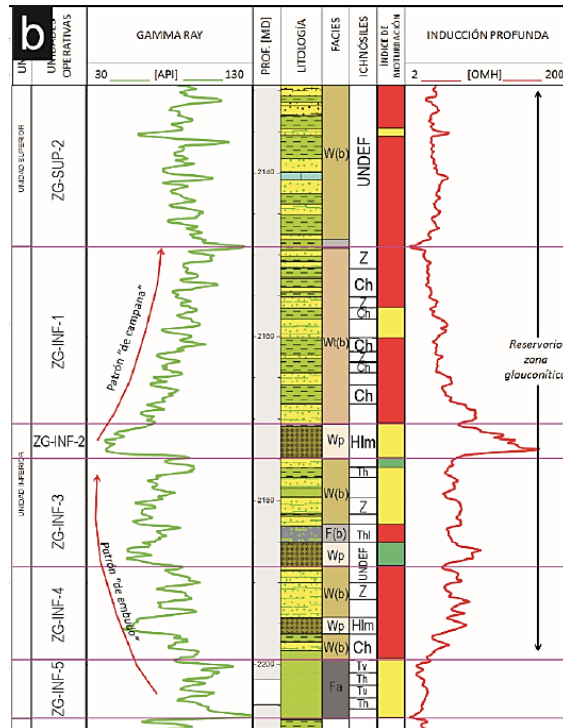


Figure 1-6. ZG logs: track #1 gamma-ray log; track #2 depth; track #3 lithology; track #4 petrofacies; track #5 ichnofossils: Thl=Thalassinodes isp., Hlm=Helminthopsis isp., Z=Zoophycos isp. and Ch=Chondrites isp.; track #6 bioturbation index: red=high, yellow=moderate and green=low; track #7 induction log (Gonzalez-Gonzalez et al., 2018).

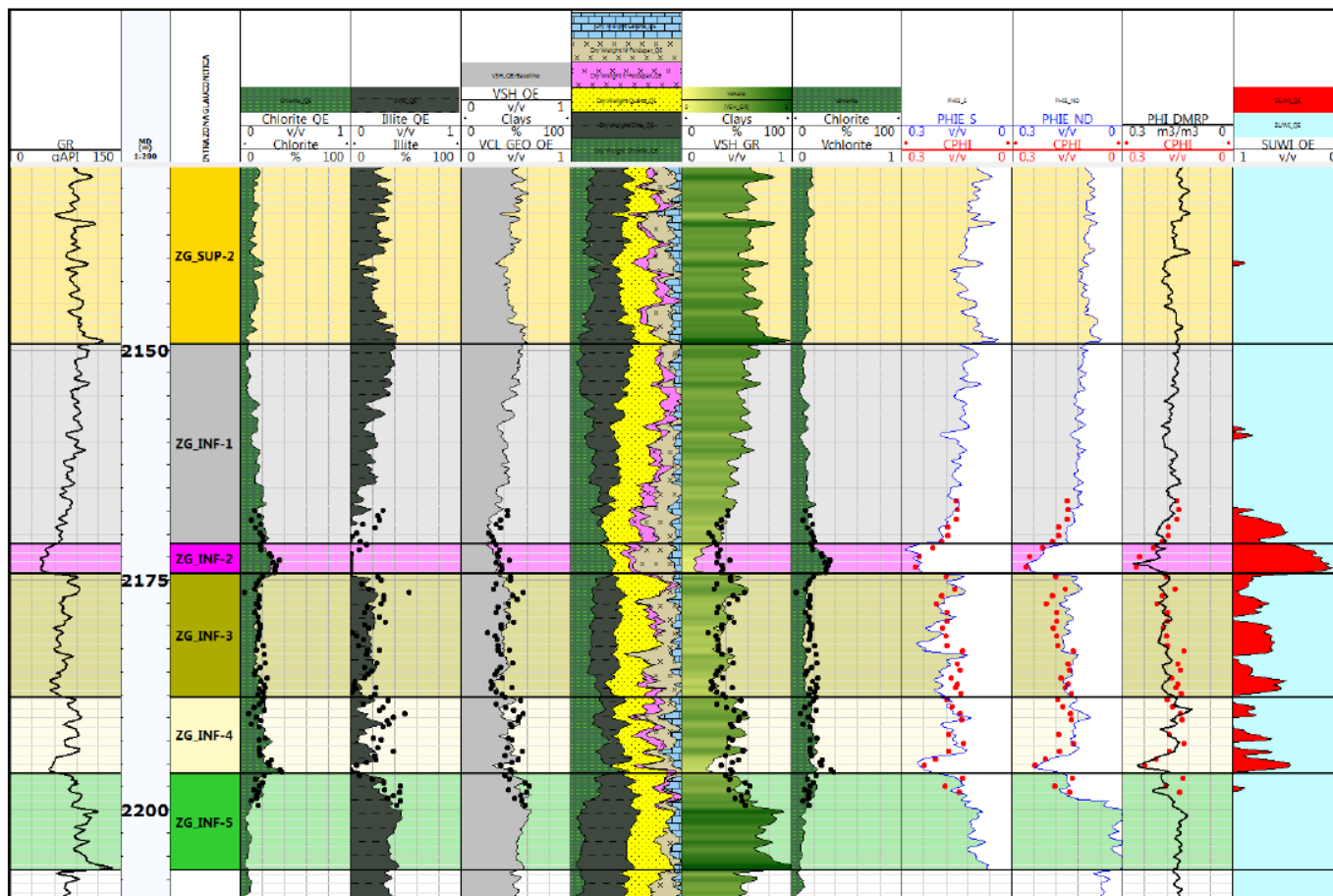


Figure 1-7. Well-log interpretation results. Black and red dots are core data from laboratory analysis of ENAP. Track #1 gamma-ray (GR) log; track #2 depth, track #3 subunits name; track #4 chlorite content; track #5 illite content; track #6 clay volume from chlorite and illite; track #7 mineral log; track #8 clay volume from GR log; track #9 corrected clay volume from PEF log; track #10 porosity from sonic log; track #11 porosity from density-neutron logs; track #12 porosity from NMR log and track #13 water saturation: light blue is water and red is hydrocarbon (Gonzalez-Gonzalez et al., 2018).

1.3.2 Dataset

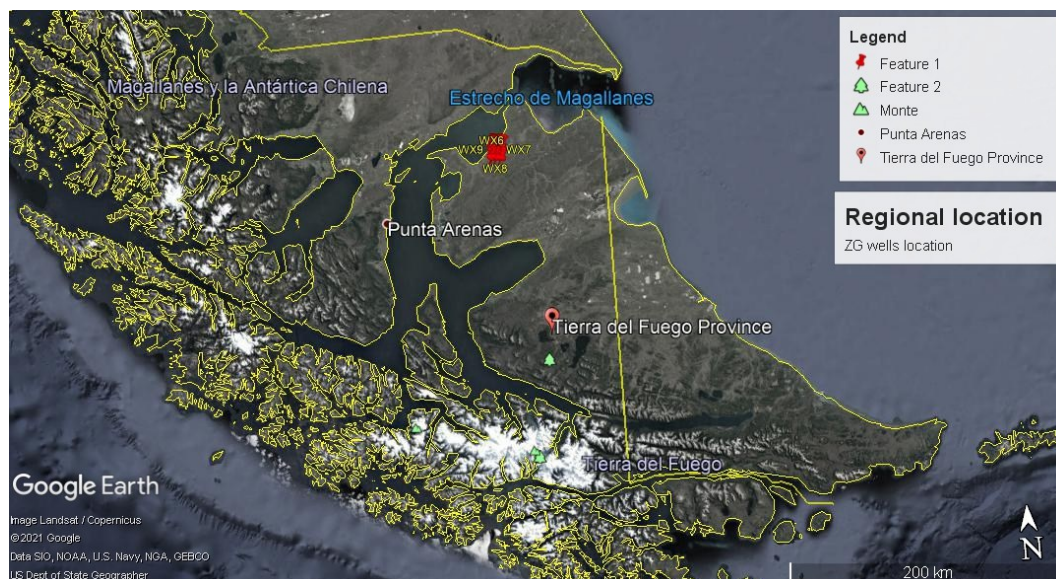
The dataset consists of well-log data and documentation of ZG's twelve vertical wells, two of which have core samples available (**Figure 1-8**). The labelling for these wells is ENAP1 and ENAP2, while the rest are labelled from WX1 to WX10. This dataset corresponds to 5.5% of the 220 wells that produced tight gas from ZG in 2019. The selection criteria for these wells are that they have the most complete log tracks and some with core availability. Also, they are strategically located in the extend of the Arenal block from north to south and west to east, creating an imaginary irregular rectangle with an area of 96.2 km².

Table 1-1 shows the conventional logs from Schlumberger's PEX (Platform Express) technology used in this project. All logs were received in LAS format. The following logging tools from Schlumberger complemented the petrophysical calibration process of the wells ENAP1 and ENAP2, and also WX1 to WX3, respectively:

- The ECS (Elemental Capture Spectroscopy) tool provided lithological logs from elements and matrix properties.
- The CMR (Combinable Magnetic Resonance) tool provided the NMR estimation of permeability, water cut, and hydrocarbon pore volume.
- The NGS (Natural Gamma-ray Spectrometry) tool provided uranium, thorium, and potassium spectral gamma-ray logs.

ENAP's documentation includes conference papers, mudlogging reports, and PVT data (**Table 1-2**). Here, the gas chromatography of each well (except ENAP1) was converted into a LAS file. The supplied samples for laboratory testing are side wall core plugs of 1-inch diameter and whole cores of 10 cm diameter (

Table 1-3).



(a)



(b)

Figure 1-8. (a) Geolocalization of Tierra del Fuego island with political division (yellow lines): the left side locates the Magallanes and Chilean Antarctica region, and the right locates the Argentinian Tierra del Fuego province. (b) Geolocalization of the twelve wells north of Tierra del Fuego island, Chilean side.

Table 1-1. The conventional logs used for petrophysical evaluation workflow.

Log name	Tag name	Unit
Gamma-ray	GR	API
Bit size	BS	inches
Calliper	CALI	inches
Spontaneous potential	SP	mV
Deep resistivity	AT90	ohm·m
Invaded formation resistivity	RXOZ	ohm·m
Bulk density	RHOC	kg/m ³
Density standoff correction	HDRA	kg/m ³
Neutron porosity	NPHI	v/v
Photoelectric factor	PEF	barns/e
Temperature	TEM	Celsius degrees
Delta-T Compressional	DTCO	µs/ft
Delta-T Shear	DTS	µs/ft
Compression and Shear velocity ratio	VPVS	unitless

Table 1-2. Documents provided by ENAP.

Document Type	Quantity	Purpose
Conference paper	8	Information about published works from the Reservoir Development Department regarding the ZG formation.
Mudlogging report	12	Description of the formation top, geological information, well deviation, and drilling stages.
PVT study	2	Information about the gas thermodynamic properties.

Table 1-3. Core sampling information of the wells ENAP1 and ENAP2.

Well	Sample type and size	Quantity	Depth interval (MD)	Gross thickness (MD)
ENAP1	Sidewall cores. Diameter of 23 mm and length range between 25 to 33 mm.	32	2,127.00 – 2,185.00	58.00
ENAP2	Whole cores. Diameter and length of 100 mm.	15	2,218.40 – 2,248.96	30.56

MD = measured depth in metres.

1.4 Study limitations

This PhD project has potential limitations due to the laboratory's available timing and sampling size. The project started on June 1st, 2019. Access to the laboratories was suspended from March 2020 to November 2020 due to the COVID-19 pandemic, delaying all experimental work for eight months. Nonetheless, all the planned work was conducted but delayed the data processing and analysis. The original project proposed undertaking a history-matching simulation of the ZG formation production in ECLIPSE, and because of the delayed data acquisition, this objective could not be achieved. On another hand, the ENAP1 well sampling size was small (sidewall core plugs) compared to the whole cores of the ENAP2 well, presenting a sampling bias in terms of quantity availability and not repeatability in measurements at the laboratory.

The time constraint attributed to an external factor (COVID-19) was handled by drawing an alternative pathway towards a more robust investigation in the laboratory by selecting specific techniques to be applied in tight clayey sandstones. In addition, ultrasonic velocities measurements. This new study route, presented in this dissertation, contributes to best practices in laboratory protocols when dealing with moderate clay minerals portion in tight rocks.

Finally, the potential sampling bias was identified early in this project before the arrival of ENAP1 core plugs. Following the Wolfson laboratory training and guidelines, a workflow involving careful handling, order of analysis selection, and quantity distributed per core plugs were planned. Moreover, identifying biased measurements and their contribution to uncertainty was executed when undertaking data processing and interpretation.

1.5 Thesis structure

This dissertation comprises eight chapters, following the logical order of an investigation: introduction, literature review, methodology, results and discussions, conclusions, and recommendations.

Chapter 1 (current) introduces the overview of the main research topic, describes the case study and establishes the study limitations.

Chapter 2 presents the fundamentals of petrophysical concepts, the state-of-the-art on the petrophysical properties in greensands, its challenges in estimating them, and findings in their controls.

Chapter 3 describes the laboratory experiments and techniques undertaken in the core analysis programme.

Chapter 4 presents the results of the ZG mineralogy, microstructure, porosity and permeability—empirical correlations between them and their petrophysical controls.

Chapter 5 presents the results of the ZG pore size distribution derived from MICP and NMR data. It also presents identified petrofacies units and their distinctive features.

Chapter 6 presents the results of the ZG electrical and ultrasonic velocities, the methods used, findings related to its cation-exchange capacity, and elastic parameters.

Chapter 7 presents the results of the ZG petrophysical model with an integrative methodology fitted to the coring results, findings in the clay volume, porosity, water saturation and permeability estimation at the logging scale.

Chapter 8 provides the investigation's conclusions according to defined objectives and recommendations for future work.

Chapter 2

Petrophysical properties overview and the challenges in greensands reservoir characterisation

This chapter overviews the petrophysical fundamentals, including rock microstructure and clay minerals. It then describes the petrophysical properties of worldwide greensands, their primary clay minerals, and the challenges in petrophysically characterising this reservoir formation. Finally, it discusses how to counteract these challenges by recommending tools and identifying petrophysical controls from the literature review.

2.1 Petrophysics fundamentals

Petrophysics studies the physical, chemical and electrical properties of rocks and their interactions with fluids within petroleum systems (e.g. Archie, 1942). The fundamental petrophysical properties characterise the many aspects of the porous rock media in terms of void space, mobility, pressure gradient, rock-fluid interaction, electrical behaviour, and fluid type, phase and content. This section briefly defines the main petrophysical properties, their interrelationships, and key features of rock microstructure.

2.1.1 Petrophysical concepts review

Reservoir rocks are deposited and buried for millions of years in the subsurface, storing organic matter and fluids that interact with the rock matrix. Chemical and biological reactions occur in such media, altering the rock-type formation as sedimentation advances, e.g. clay or shale presence. The reservoir rock comprises grains, mineral coatings, fluids (water and petroleum), and a complex pore network. Water may flow as a free fluid or be clung to the clay-bound and capillary-bound zones (**Figure 2-1**). The latter two are water between the grains' surface and mineral interlayers; capillary-bound water represents the thin water layers physically bound to the rock by capillary forces, while clay-bound water (CBW) refers to the thin water layers electrochemically bound to the clay lattice.

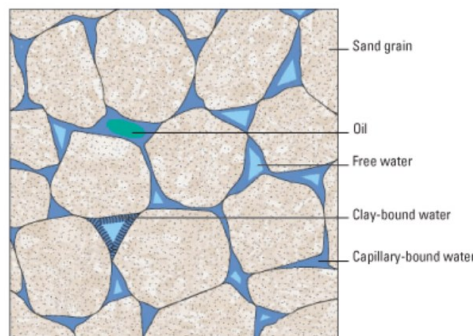


Figure 2-1. Fundamental constituents of a reservoir rock (Schlumberger, 2020).

Porosity, permeability, saturation, and capillary pressure are the four main petrophysical properties used to characterise reservoir rocks (**Table 2-1**) in terms of void space, fluids mobility or transmissibility, fluid content, and the pressure difference between immiscible fluids within the pore-throat radius, respectively. These are interrelated, and their magnitude depends on the rock microstructure and environmental conditions such as in-situ stress, pressure and temperature; thus, by comprehending which rock properties control or govern these petrophysical properties, the calibration and prediction from core to log data will be more reliable.

Table 2-1. Petrophysical primary properties formulas.

Property	Formula	Reference
Porosity	$\phi_T = \frac{\text{Pore Volume}}{\text{Bulk Volume}} = \frac{PV}{BV}$ <p>ϕ_T: total porosity (v/v), PV: pore volume (cc), BV: bulk volume (cc).</p>	API RP40 (1998)
Permeability	$k = \frac{q \mu L}{\Delta P A}$ <p>k: permeability (Darcy), q: flowrate (cc/s), μ: fluid viscosity (cP), L: rock length (cm), A: rock cross-sectional area (cm), ΔP: pressure difference across the rock (atm).</p>	Darcy's Law (1856)
Saturation	$S_i = \frac{\text{Fluid } i \text{ volume}}{\text{Pore Volume}} = \frac{V_i}{PV}$ <p>S_i: gas, oil or water saturation (v/v), V_i: fluid volume (cc), PV: pore volume (cc).</p>	API RP40 (1998)
Capillary pressure	$P_c = P_{nw} - P_w$ <p>P_c: capillary pressure, P_{nw}: non-wetting phase pressure, P_w: wetting phase pressure.</p> $P_c = (\rho_w - \rho_{hyd})g_c h$ <p>P_c: capillary pressure (Pa), ρ_w: water density (kg/m³), ρ_{hyd}: hydrocarbon density (kg/m³), g_c: gravity acceleration constant 9.8 m²/s, h: liquid height difference (m).</p>	Young (1805); Laplace (1806)

Porosity (ϕ) is referred to as total porosity (ϕ_T) when it includes free mobile and enclosed fluids. In contrast, effective porosity is defined in petrophysics as "*the total porosity less any water associated with clay minerals in the rock*" (Dodge et al., 1996, p. 2), visually explained in **Figure 2-2**. In addition, Pittman (1979) classified four basic types of sandstone porosity: intergranular, dissolution, micro and fracture porosities. The first three porosity types are related to the rock texture; intergranular porosity is the pore volume between grains. Dissolution porosity results from the dissolution of mineral grains during diagenesis; its values range from excellent to poor depending on the connection between pores. Microporosity is related to pore sizes less than 0.5 μm , commonly associated with detrital and authigenic clay minerals; the portion rock here has a high surface area, low permeability, high irreducible water saturation and increased sensitivity to freshwater. Conversely, fracture porosity represents the pore spaces in natural or artificial fractures that could enhance the interconnected pore throats.

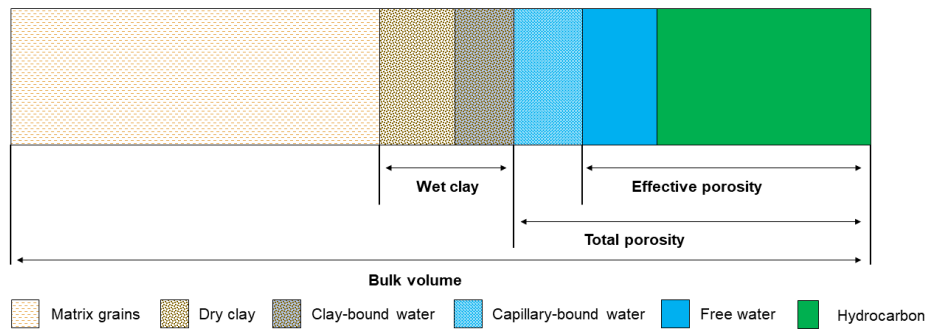


Figure 2-2. Fundamental constituents of reservoir rock in terms of porosity and clay terms (modified after Hook, 2003).

Permeability (k) measures the rocks' ability to transmit the fluids, and it is expressed in area units, typically one millidarcy or mD, i.e. approximately $0.986923 \times 10^{-12} \text{ m}^2$. In petrophysics, three permeability types are used in terms of the fluids involved (i.e. oil, gas or water), expressed in Equation 2–1 and defined according to API RP40 (1998):

- a) Absolute permeability represents the rock's permeability to a single-phase fluid.
- b) Effective permeability represents the permeability of a single fluid in a multi-phase system.
- c) Relative permeability is the ratio between the effective permeability of a particular fluid and the absolute permeability in a multi-phase system. It is unitless and generally varies from 0 to 1. The relative permeability to different phases is defined as:

Equation 2–1

$$k_{rg} = \frac{k_{eg}}{k}, \quad k_{ro} = \frac{k_{eo}}{k}, \quad k_{rw} = \frac{k_{ew}}{k}$$

where k_{rg} , k_{ro} and k_{rw} are the gas, oil and water relative permeability, respectively (unitless); k_{eg} , k_{eo} and k_{ew} are the gas, oil and water effective permeability, respectively (mD); k is the absolute permeability (mD).

Saturation (S_i) describes the fraction of a particular fluid phase in the void spaces of a rock. A rock may contain a combination of water, oil and gas, and the sum of their saturations equals 1 or 100%. Additionally, two water saturations are defined according to the minimum amount available in the rock formation; the connate water (S_{wc}) refers to the water formation trapped inside the rock throughout its geologic history. On the other hand, the irreducible water saturation (S_{wirr}) is the maximum amount of immobile water trapped inside the pores. Sometimes, it is referred to as critical water saturation, and typically, it is the term used in laboratory measurements and empirical correlations (Tiab and Donaldson, 2012).

In a water-wet system, while buoyancy or gravitational forces push the water column downwards, capillary forces push it upwards. Since oil and water cannot mix because

they are immiscible, a pressure is generated between them known as the capillary pressure (P_c). This pressure is a driving force for water (or other fluid) to flow into narrow spaces; it rises because it adheres to the walls of the solid until gravitational forces balance it. The Young-Laplace equation (**Table 2-1**) describes this phenomenon, which involves the pressure difference between the wetting and non-wetting phases, the interfacial tension, the interface radius, and the wetting angle of the liquid on the surface of the capillary. Therefore, the buoyancy and capillary pressure driving forces govern which fluid will flow inside the pore throat networks (**Figure 2-3**).

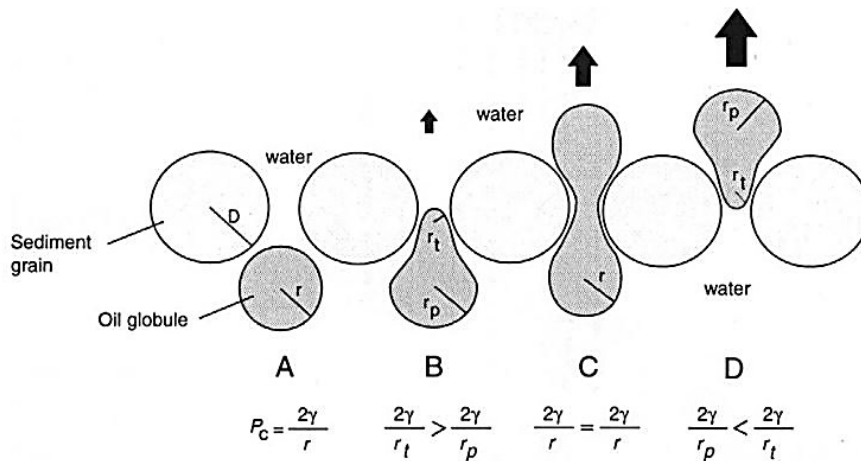


Figure 2-3. Diagram illustrating the interplay between capillary pressure and buoyancy as oil globule moves through a pore: (A) Pressure difference across oil-water interface resists distortion of globule required if it moves through pore throat. (B) The buoyant force is sufficient to distort the oil globule. However, the capillary pressure of the globule in the pore throat exceeds because the pore throat radius is smaller than the maximum pore radius. (C) Part of the buoyant force of the globule above the pore equals the capillary pressure in the pore throat. (D) Buoyant force above the pore is larger than capillary pressure in the pore throat, and the globule moves upwards. γ = interfacial tension, r = radius of the oil globule, D = grain radius, r_p = pore radius, r_t = pore-throat radius (Modified after Berg, 1975).

In a petroleum reservoir, the location of fluids depends on how they have been distributed inside the pore networks and on their in-situ density. Since oil (and gas) density is lower than water, hydrocarbon will be located on the top of the water zone. Conventional gas reservoirs will have a free-gas level, transition zone, gas-water contact, and free-water level (FWL). Following the gas pathway of secondary migration (drainage capillary pressure curve) from a seal to a reservoir rock in **Figure 2-4**:

1. The reservoir rock is fully water-saturated. Regarding fluids and column pressure, the pressure difference (capillary pressure) between gas and water is zero, and only water is produced. This point is known as the free-water level (FWL).
2. Gas starts to push forward and achieves the first entry in the larger pore throats (displacement pressure, P_D); this point is the gas-water contact (GWC).

3. Gas continues to migrate through the reservoir rock over water, known as the transition zone, into smaller pore throats.
4. Gas fully saturates the effective pore volume of the reservoir rock, and the water left is trapped inside enclosed pore throats, i.e. capillary and bound-water zones (irreducible water saturation).

As can be seen, there is an inverse relationship between capillary pressure and the water saturation of a reservoir rock; the higher the capillary pressure, the lesser the water saturation and vice versa (in a water-wet rock). Since the gas (or oil) migrates from large to small pore-throats, the capillary pressure curve moves towards the left as permeability increases and the entry pressure decreases; hence, the irreducible water saturation decreases.

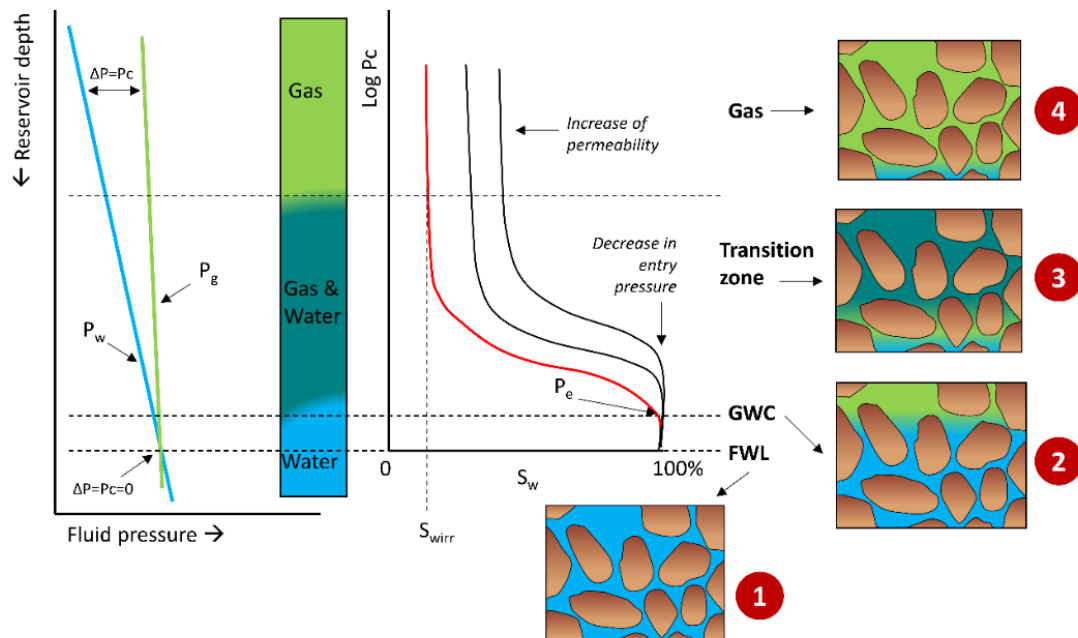


Figure 2-4. Fluid distribution in a conventional gas reservoir schematic. P_g and P_w are the gas and water column pressure, ΔP is the pressure difference between these fluids, P_c is the capillary pressure, FWL is the free-water level, GWC is the gas-water contact, and P_e is the entry pressure of the gas inside the first macropore of the rock. The $\log P_c$ vs S_w plot shows three lines indicating the increase in permeability when shifting towards the left side; the red line highlights the position of the irreducible water saturation S_{wirr} in the plot.

In TGS, the capillary pressure curves are steeper with higher pressure due to their narrow pore size distribution. Hence, the gas movement depends on capillary forces (e.g. Mo et al., 2020). TGSs are stress- and salt-sensitive and present gas slippage (e.g. Gong et al., 2022; Mo et al., 2020; Farahani et al., 2019). Their gas-water relative permeability curve is peculiar. In a specific water (and gas) saturation range at a gas and water relative permeability below 0.02, there is no capacity flowing of either gas or water, and both are jailed or trapped in the pore volume. This concept is known as "permeability

jail" (Shanley et al., 2004; Cluff and Byrnes, 2010) and explains the effective permeability decrease of gas and water as a function of saturation history (**Figure 2-5**).

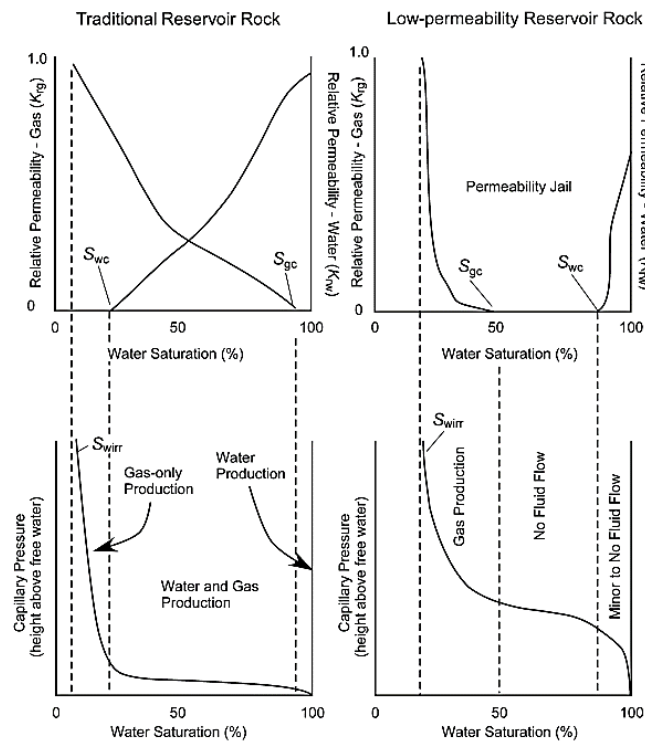


Figure 2-5. Schematic illustration of capillary pressure and relative permeability relationships in traditional and low-permeability reservoir rocks. Critical water saturation (S_{wc}), critical gas saturation (S_{gc}), and irreducible water saturation (S_{wirr}) are shown (Shanley et al., 2004).

2.1.2 Electrical parameters

Resistivity logs measure the electrical behaviour of rock formations. Several theoretical and empirical formulations are used to estimate the water saturation within the rock based on its resistivity (or conductivity). This subsection summarises the electrical parameters needed to estimate water saturation with Archie's (1942) worldwide accepted empirical model.

Resistivity measures the ability of a substance to impede electrical flow and is expressed in $\text{ohm}\cdot\text{m}^2/\text{m}$, or simply $\text{ohm}\cdot\text{m}$; it can be calculated using:

Equation 2-2

$$R = \frac{\rho A}{L}$$

where R is the electrical resistivity expressed ($\text{ohm}\cdot\text{m}$), ρ is the electrical resistance (ohms), A is the cross-sectional area of rock material exposed to the current flow (m^2), and L is the length of the material (m).

Conductivity measures a substance's ability to transmit electrical flow, and it is the resistivity reciprocal, expressed in mhos/m or Simens/m .

Two electrical current components in the reservoir rock contribute to its conductivity: the in-situ water and the clay minerals surrounding the bound water. Hydrocarbons have practically zero conductivity, which makes them relatively easy to identify on the resistivities log as their resistivity is very high (**Figure 2-6**). The resistivity of water or brine in the subsurface varies significantly depending upon the salt concentration (NaCl) it contains. For example, freshwater contains <1 g/L of salt and will have a resistivity of >5 ohm·m at 25°C. On the other hand, a brine in equilibrium with halite will have a salt concentration of around 360 g/l and a resistivity of 0.5 ohm·m at 25°C (Schlumberger, 1997). In addition, consolidated or sedimentary rocks are much more resistive in a rock-fluid system than unconsolidated ones (**Table 2-2**). The more clay-rich minerals in the sedimentary rock, the less the rock resistivity (i.e. more conductive), which is why shale is less resistive than sandstone—summing up with the formation water salinity, the higher the concentration of salts like NaCl, the less resistive and more conductive the reservoir rock may be. Therefore, interstitial water and clay minerals contribute to the electrical properties of reservoir rocks.

Several authors have studied the rock’s resistivity with natural or synthetic core plugs, agreeing that pore geometry (interconnectivity and pore-throat size), saturation distribution, clay/shale content, wettability, and temperature control the rock’s resistivity (e.g. Sweeny and Jennings, 1960, Swanson, 1985, Worthington et al., 1989, Abousrafa et al., 2009).

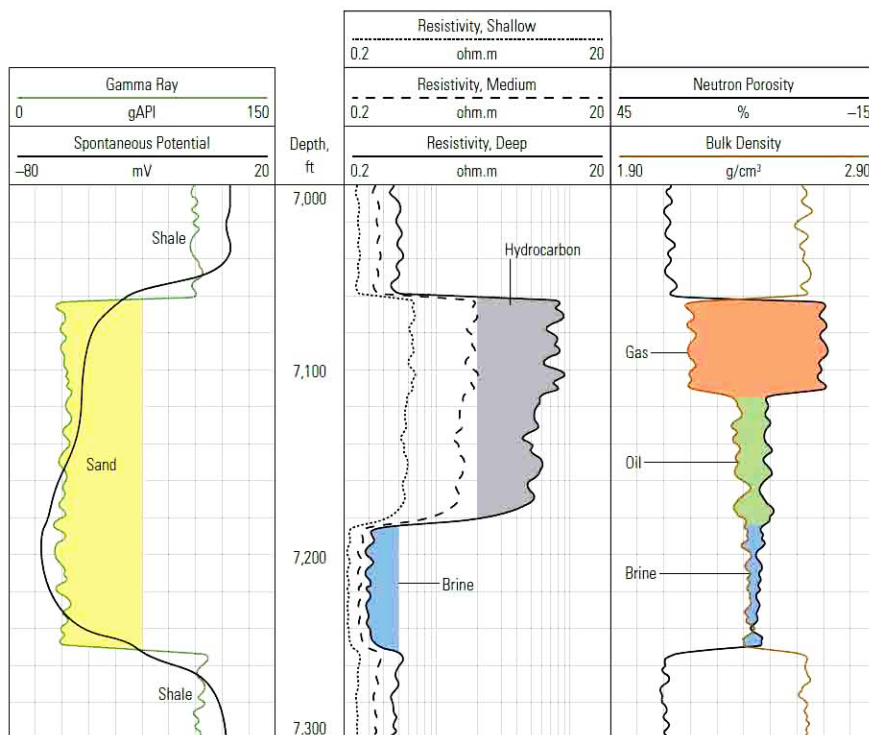


Figure 2-6. Basic log interpretation, identifying the sandstone reservoir rock in the gamma-ray log, the oil-bearing and water-bearing zone in the resistivity log, and the gas, oil, and brine zones with density-neutron cross-plot logs (Schlumberger, 2016).

Table 2-2. Typical ranges of sedimentary rock resistivity (Palacky, 1988).

Sedimentary rock	Range (Ohm·m)
Argillite	74-840
Conglomerate	2,000-13,000
Dolomite	700-2,500
Greywacke	400-1,200
Limestone	350-6,000
Sandstone	1,000-4,000
Shale	20-2,000
Slate	340-1,600
Coal	1-200,000

2.1.2.1 Formation resistivity factor

The formation resistivity factor, F , is the ratio of the electrical resistivity of a rock (R_o) fully water-saturated and the electrical resistivity of the water (R_w), defined by Archie (1942) as:

Equation 2–3

$$F = \frac{R_o}{R_w} = \frac{1}{\phi^m}$$

where F is the formation resistivity factor (unitless), R_o is the rock resistivity (ohm.m), R_w the water resistivity (ohm·m); ϕ the rock porosity (fraction), and m is the cementation exponent (unitless).

It is important to note that Archie's experiments were conducted on clean sandstones from the Gulf Coast region (**Figure 2-7**), and, as he highlighted in his abstract: "*It should be remembered that the equations given are not precise and represent only approximate relationships*". Therefore, care must be taken when applying this equation on argillaceous sandstones, carbonates or shales, where the rock matrix contributes to the electrical current throughout the rock. Thus, a correlational factor, a , is added to counteract the data calibration on formation rocks with clay minerals or shale (Hossain and Zhou, 2015):

Equation 2–4

$$F = \frac{a}{\phi^m}$$

where F is the formation resistivity factor (unitless), a is the tortuosity or correctional factor (unitless), ϕ the rock porosity (fraction), and m is the cementation exponent (unitless).

The formation factor and Archie exponents are called apparent or intrinsic to differentiate them from Archie's foundational definition, and in this case, the Archie model is denominated as Pseudo-Archie.

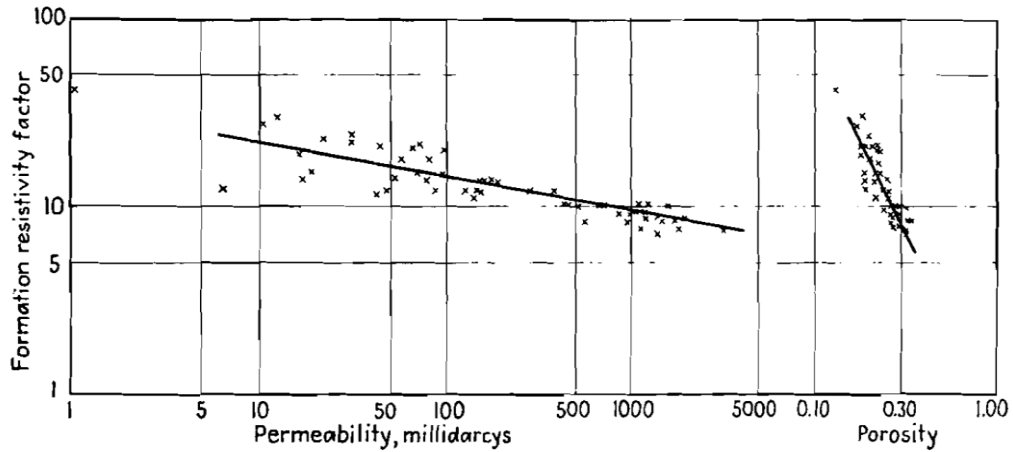


Figure 2-7. Relation of porosity and permeability to formation factor for consolidated sandstone cores of the Gulf Coast (Archie, 1942).

The cementation exponent, m , is determined from a log-log plot of the formation factor vs porosity obtained from cores (**Figure 2-8**). F is derived from the electrical resistivities from the rock and formation water resistivity, measured in the laboratory at in-situ stress when the rock is fully brine-saturated. Several authors have reported different values of a ranging from 0.4 to 2, while m can vary from unity to as high as five for specific rock formations (**Table 2-3**). The common practice of calibrating a is somewhat controversial as it does not follow Archie's formation factor empirical correlation, meaning that the formation factor is not equal to 1 for 100% of porosity but instead to the a best-fit value. Worthington (1993) studied the deviation of a and m for clean and shaly sandstones, concluding that the inclusion and variation of the correlational a factor must be to compensate for the clay or shale effect in shaly formations.

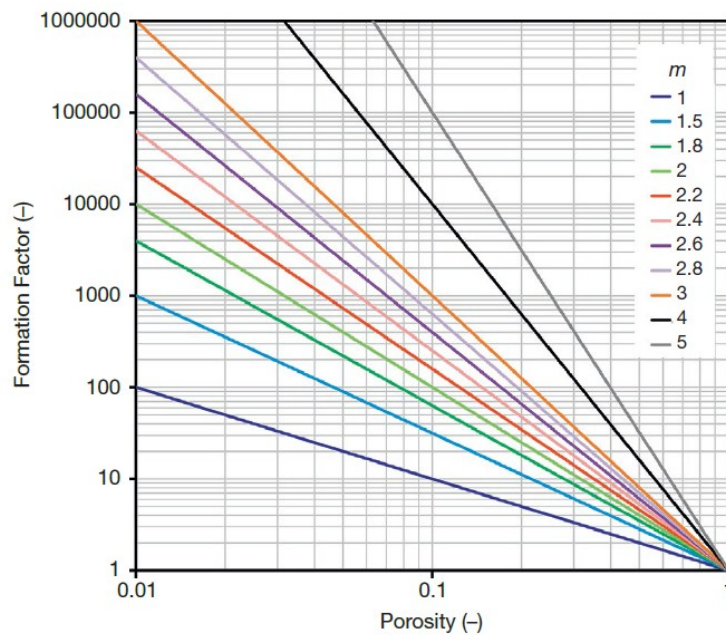


Figure 2-8. Formation factor as a function of porosity according to Archie's first law. The negative gradient of each curve provides the cementation exponent with $a=1$ (Glover, 2015).

Table 2-3. Typical ranges of cementation exponent and the correlational factor from Worthington (1993).

Lithology	<i>m</i>	<i>a</i>	References
Sandstone	1.64-2.23	0.47-1.8	Hill and Milburn (1956)
	1.3-2.15	0.62-1.65	Carothers (1968)
	0.57-1.95	1.0-4.0	Porter and Carothers (1970)
	1.2-2.21	0.48-4.31	Timur et al. (1972)
	0.02-5.67	0.004-17.7	Gomez-Rivero (1976)
Carbonates	1.64-2.10	0.73-2.3	Hill and Milburn (1956)
	1.78-2.38	0.45-1.25	Carothers (1968)
	0.39-2.63	0.33-78.0	Gomez-Rivero (1977)
	1.7-2.3	0.35-0.8	Schön (2004)

2.1.2.2 Index resistivity and saturation exponent

Archie's second law relates the ratio of the resistivity of the partially saturated rock (R_t) and the resistivity of the formation water (R_w) to its water saturation (S_w). In particular:

Equation 2-5

$$I_R = \frac{R_t}{R_w} = S_w^{-n}$$

where I_R is the resistivity index (unitless), R_t is the true rock resistivity (ohm·m), R_w is the formation water resistivity, S_w is the water saturation (unitless), and n is the saturation exponent (unitless).

The saturation exponent, n , is estimated from a log-log plot of I_R vs S_w derived by conducting resistivity measurements on core plugs whose water saturation has been changed using various methods (e.g. porous plate, centrifuge, clean). For clean unconsolidated and consolidated sandstones, n is found to be around 2. However, it has been demonstrated that n depends on the degree of saturation since it relates to the amount of water in the rock voids, the rock formation type and wettability (Figure 2-9). It is strongly preferred for water-wet rocks with $n=2\pm0.5$, while for oil-wet rocks, n can reach values up to 5 (Montaron, 2008; Sweeney and Jennings, 1960).

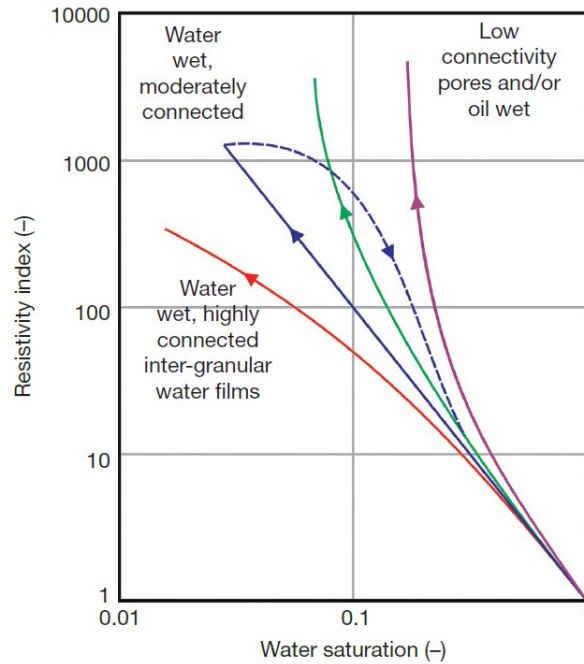


Figure 2-9. Resistivity index as a function of water saturation for a rock saturated with water and oil. Solid lines indicate drainage. The dark blue line, representing Archie's second law ($n=2$), is only valid for clean, water-wet, moderately well-connected rocks. Rocks with higher connectivity due to intergranular water films tend to follow the red curve, while low connectedness or oil-wet rocks follow the green and purple trends. It should be noted that imbibition can often produce a nonlinear curve (dashed) due to the development of oil-wet patches in the rock (Glover, 2015).

2.1.2.3 Archie's (1942) saturation water formula

By combining Equation 2-4 and Equation 2-5, Archie's well-known equation is obtained for determining the water saturation of a clean sandstone reservoir rock:

Equation 2-6

$$S_w = \left(\frac{aR_w}{\phi^m R_t} \right)^{1/n}$$

Those rock formations that fulfil Archie's criteria are denominated Archie reservoirs, and Equation 2-6 describes the electrical behaviour and water saturation tendency throughout the reservoir. On the other hand, formation rocks with a significant clay portion or oil-wet are denominated as non-Archie reservoirs (e.g. Worthington, 1985).

2.1.3 Rock microstructure

The term microstructure is used to describe the basic texture of the rock and includes grain shape, roundness, size, sorting, and fabric. Different measurement techniques are used to quantify these properties, such as optical microscopy and scanning microscopy (SEM). The microstructure of the rocks controls the petrophysical properties; however,

the relationship between them is difficult to find due to the rock complexity and the measurement technique selected (Pettijohn et al., 1973).

Through the visual and statistical analyses, researchers have found evidence of the impact of grain size, sorting, and rock texture on the porosity-permeability relationship. For example, Ethier and King (1991) portrayed the surface texture factors found by Sneider et al. (1983) and Sneider and King (1984) in sandstones (**Figure 2-10**), taking into account clay, micropores, and consolidation presence. On the other hand, Cade et al. (1994) developed a relationship between grain size/sorting on porosity-permeability trends through numerical simulation of grains packing as spheres and comparisons with case studies in sandstone (**Figure 2-11**).

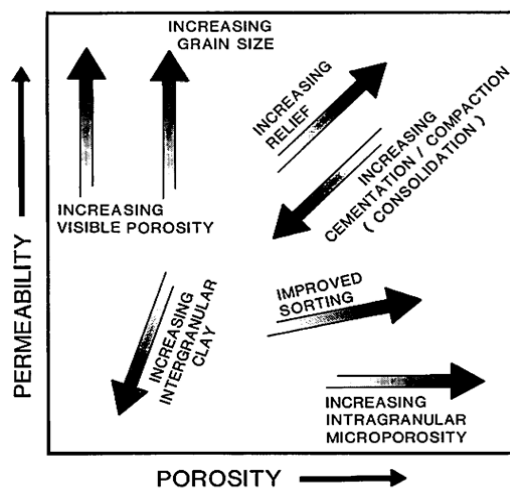


Figure 2-10. Sandstone microstructure impacts the porosity-permeability trends (Ethier and King, 1991).

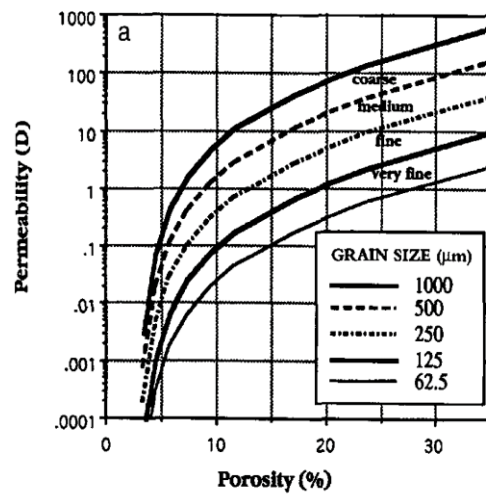


Figure 2-11. Effect of grain size and sorting in the porosity-permeability trends (Cade et al., 1994).

The rock fabric is controlled by sedimentation and diagenesis, significantly impacting petrophysical properties. For example, these processes control the quality and distribution of clay. Clay may be distributed as laminated, structural or dispersed (**Figure 2-12**). Laminated shale or clay is distributed as interbedded with sandstone. Structural shale, or detrital clay, means they are within the rock framework as grains. Dispersed clay refers to clay particles disseminated in the pore walls, choking pore-throat networks and thus decreasing effective porosity and permeability (Thomas and Stieber, 1975; Asquith, 1990).

Wilson and Pittman (1977) and Wilson (1982) studied how dispersed authigenic clays impacted porosity and permeability relationships (**Figures 2-13** and **2-14**). Neasham (1977) also considered how the type of clay mineral impacted flow properties (**Figure 2-15**). Pore-lining, pore-filling, and pore-bridging are the most frequently used to describe clay minerals occurrence. Pore-lining refers to clay coatings growing at the grain surface

outwards, blocking pore-throats; pore-filling (discrete particles) refers to clays filling the pores partially; pore-bridging refers to clay that extends further into the pore-throats, creating a bridge which encloses pore space (microporosity).

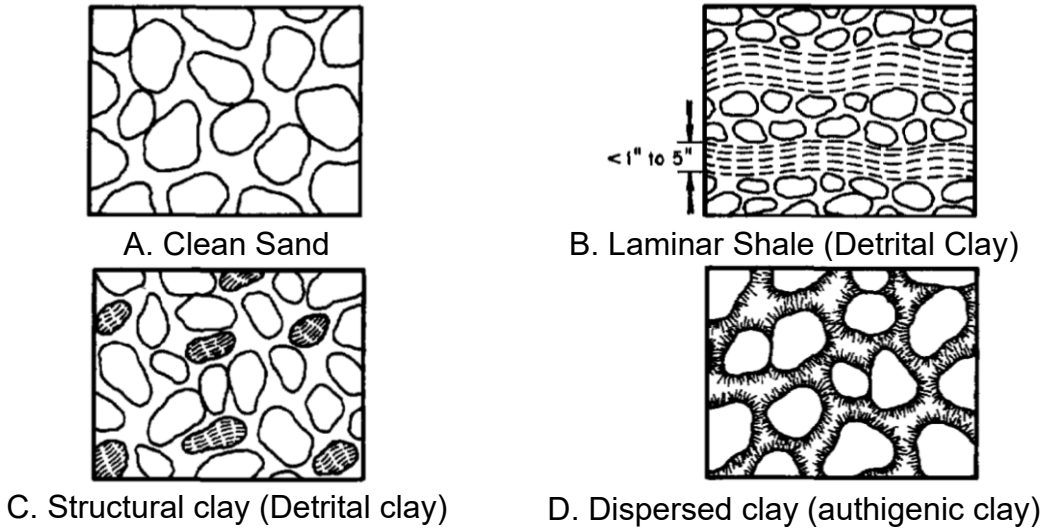


Figure 2-12. Mode of shale and clay occurrences in sandstones (Asquith, 1990).

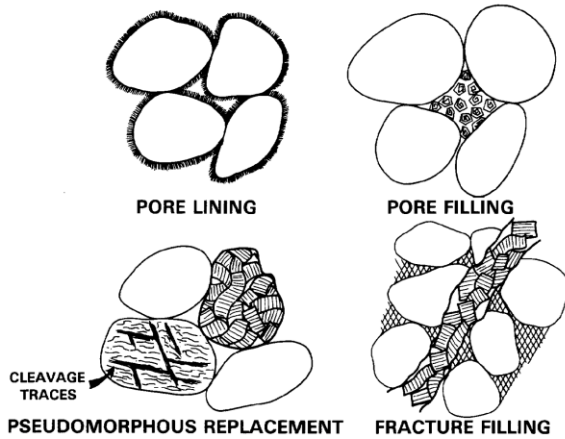


Figure 2-13. Modes of occurrence of authigenic clay in sandstone (Wilson and Pittman, 1977).

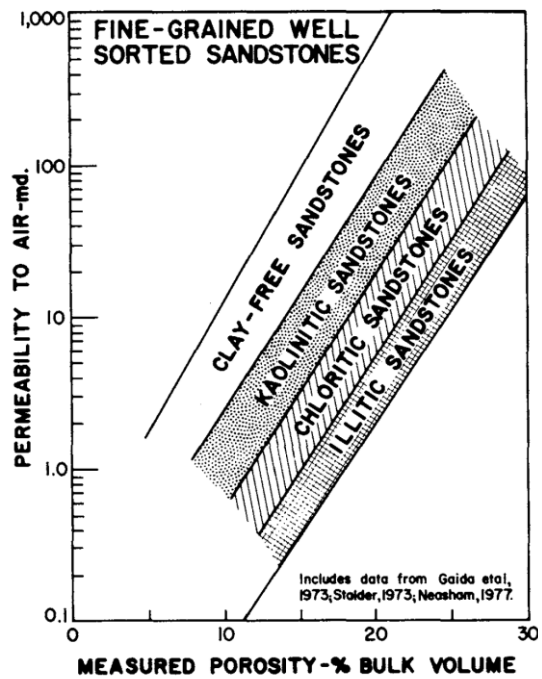


Figure 2-14. Porosity-permeability trends of clay-free and clay-bearing sandstones (Wilson, 1982).

FIGURE 1a. - "DISCRETE PARTICLE" KAOLINITE

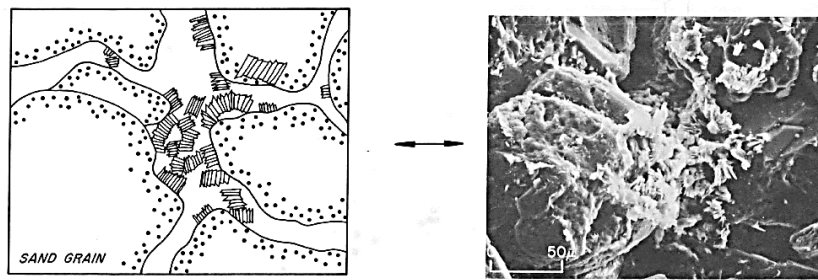


FIGURE 1b. - "PORE-LINING" CHLORITE

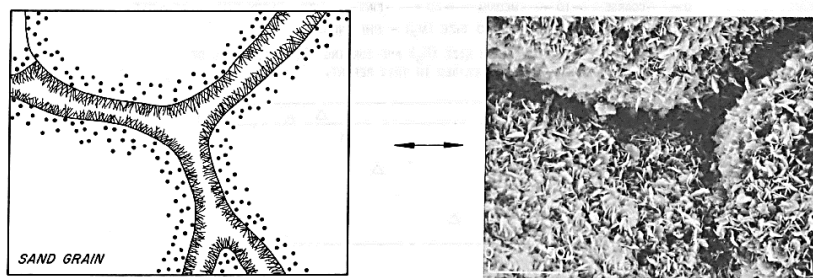


FIGURE 1c. - "PORE-BRIDGING" ILLITE

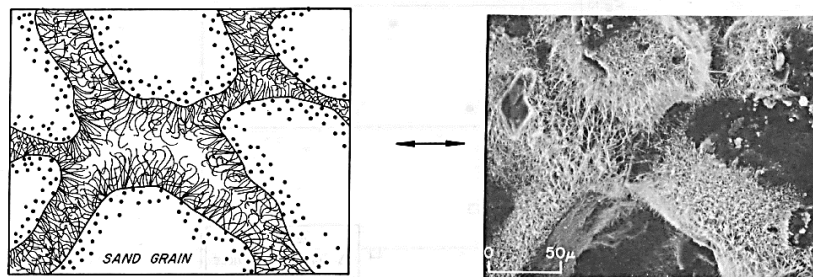


Figure 2-15. General dispersed clay types within sandstone reservoirs (Neasham, 1977).

2.2 Clay minerals¹

In terms of grain sizing, the clay fraction of rock consists of very fine particles of less than 2 μm (Wentworth, 1922). These fine particles comprise diverse minerals where the clay minerals predominate. The clay minerals are grouped into families related to their chemical composition and crystal structure. They consist of two main sheets: a tetrahedral sheet of silica (SiO_2) and an octahedral alumina sheet (Al_2O_3), also known as a gibbsite. The principal clay mineral groups are kaolinite, illite, mica, chlorite, and smectite (Figure 2-16). The following subsections describe clay electrical properties and phenomena in subsurface rock formations and their relevance to this investigation.

¹ Clay minerals or clay is used interchangeably throughout this dissertation and refers to the clay minerals portion present within a rock.

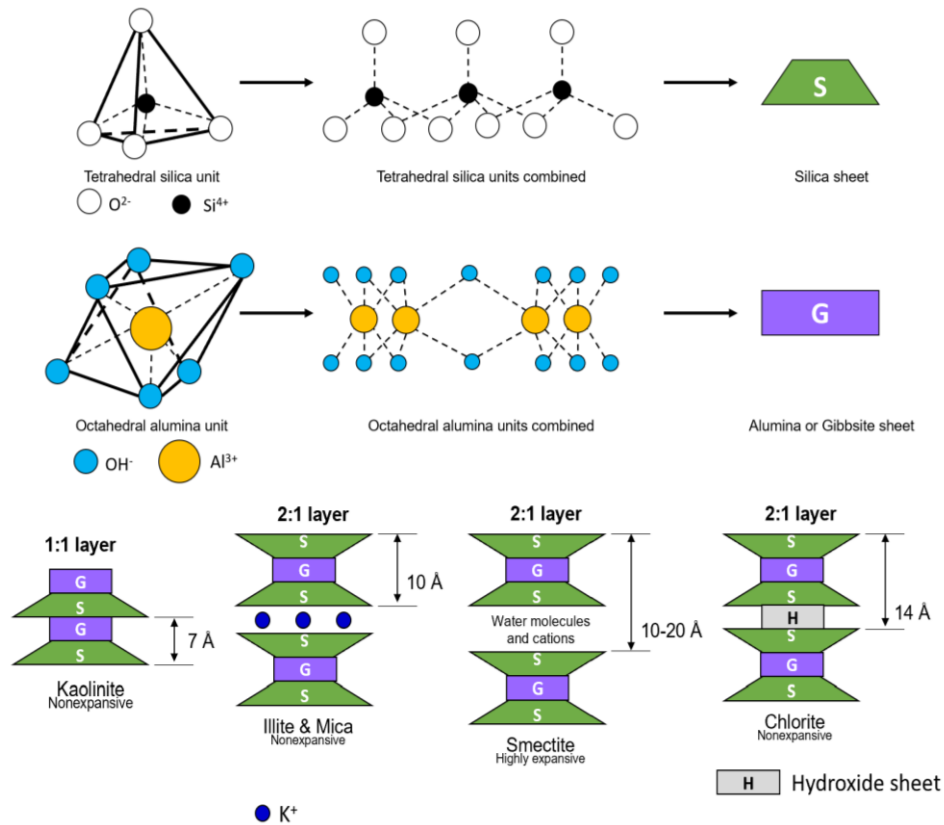


Figure 2-16. Silica and alumina sheets structure units (above) and main clay mineral groups structure, distances not scaled (modified from *Elementary Engineering Library*, 2020).

2.2.1 Cation-exchange capacity

Clays have the property to interexchange cation species as surface adsorption to neutralise its negative layer charge, i.e. cation-exchange capacity. An ion-exchange reaction occurs through selectivity in the cation size, charge or valence between the clay pore wall and the cations flowing inside the rock pores. Thus, the selectivity order for alkali-metal ions is Li⁺, Na⁺, K⁺, Rb⁺, and Cs⁺, while for alkaline-earth ions is Mg²⁺, Ca²⁺, Sr²⁺, and Ba²⁺ (in order of decreasing electronegativity). This ion exchange, known as an isomorphous substitution in the clay lattice, occurs by selecting a substituting a cation with a lower charge of the free mobile water with a clay lattice-bound cation, which increases the rock's net negative charge (**Figure 2-17**).

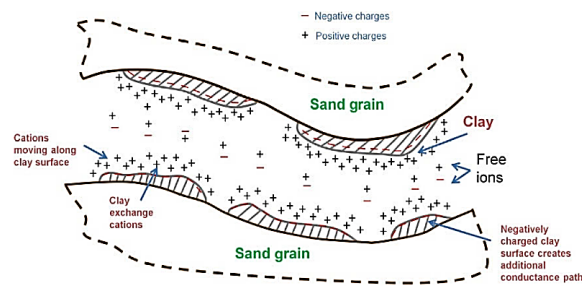


Figure 2-17. Pore and clay ion mobility in a shaly sand (McPhee et al., 2015).

The cation-exchange capacity or *CEC*, defined by Allaby (2019), is: "... the amount of exchangeable cations that a particular material or soil can absorb at a given pH". In rock-fluid interaction, *CEC* measures the concentration of cations available relative to mass, expressed in milli-equivalents of exchangeable ions per 100 g of dry rock (meq/100 g). **Table 2-4** displays the *CEC* range values for the principal clays group, directly proportional to the surface area.

Table 2-4. Cation exchange capacity range and total surface area for clay minerals (Van Olphen and Fripiat, 1979; McPhee et al., 2015).

Clay mineral group	CEC (MEQ/100 g)	Surface area (m ² /g) ¹
Smectite	70-130	800
Illite	25-40	30
Chlorite	10-40	15
Kaolinite	3-15	15

¹ Summation of internal (interlayer) and external surface area.

The diffuse double layer (DDL) theory explains this electrochemical mechanism (**Figure 2-18**). Two layers form: an inner layer at the clay surface known as the Stern layer, i.e. adsorbed water, and an outer layer with the charged cations distributed as a cloud-diffuse layer (Van Olphen, 1977). The Waxman and Smits (1968) model is based on the DDL, and it adds the *CEC* parameter volumetrically (Q_v in meq/ml) to include the clay effect of the rock. The ZG formation (**Section 1.3**) contains an average of 43%v/v of clays where glauconite is the primary mineral, meaning the clay component impacts when estimating the petrophysical properties. ENAP uses the modified Simandoux model (Bardon and Pied, 1969) to build the water saturation profile; this model is widely used for shaly sandstones since it adds a term to counteract the clay or shale content. Furthermore, there are no precise cation-exchange capacity measurements of the ZG formation to apply the Waxman-Smits (1968) or other shaly-sand models accurately. This investigation aims to measure the *CEC* with different methods to evaluate this parameter inclusion to best fit the reservoir water saturation profile.

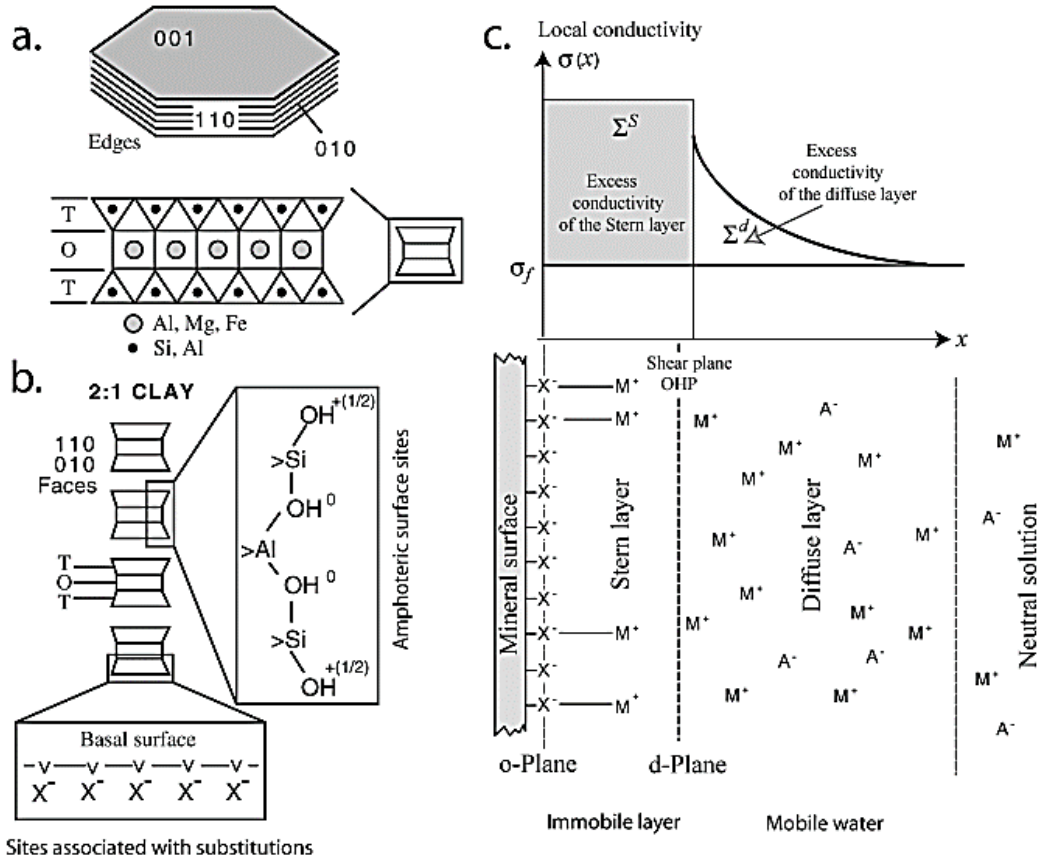


Figure 2-18. Electrical double layer. (a) TOT structure of clay minerals, where T=tetrahedral layer and O=octahedral layer. (b) The surface of 2:1 clay minerals in contact with water is charged because of amphoteric sites on the edges of the clay crystal and basal negative sites associated with isomorphous substitutions in the crystalline framework. (c) the mineral charge is compensated by cations (M⁺) and anions (A⁻), forming a double layer. This double layer comprises a sorbed cations (Stern) layer and a diffuse layer where the Coulombic interactions between the charged mineral surface and the ions prevail. The subscript *f* denotes the fraction of the counter charge located in the Stern layer (Revil and Mahardika, 2013).

2.2.2 Clay swelling and migration

Two clay phenomena may occur within reservoir formations: migration and swelling (Figure 2-19). Fines migration results from dragging forces that release clay particles from the pore wall to the pore space, plugging the pore throats, while the swelling results from the water adsorption capacity that distinct clay particles have, increasing their size and blocking pore throats. Both phenomena are a problem for the oil and gas industry. They are highly costly if not handled with chemical inhibitors to prevent damaging drilling operations (e.g. de Carvalho et al., 2015).

The drag forces to release the clay particles from the pore wall combine fluid viscosity, flow velocity and regime (turbulence). Together with the rock environmental conditions (mineralogy, water salinity and pH), clay migration can happen. Kaolinite is the easiest to migrate due to its booklet shape, followed by illite, mica, and non-clay fines (Gray and Rex, 1966). Flow rate, wettability, cation-exchange capacity, pH increase, and acidising

treatments promote clay migration (Xiao et al., 2017). Furthermore, water sensitivity is the leading cause of fines migration. As salinity decreases to a very low concentration, the cation exchange site increases its negative charge since it will prefer monovalent cations (Na^+) instead of divalent ones such as Ca^{+2} , and the silicate surfaces become strongly negative. Hence, the repulsive electrostatic forces increase, providing enough electrochemical energy to release particles (Jones, 1964; Gray and Rex, 1966; Lever and Dawe, 1987). Khilar and Fogler (1983) defined a critical salt concentration (CSC) in which clay fines migrate and cause permeability impairment; a water shock test is conducted from core flooding a high to very low salinity to determine whether a rock formation is water sensitive.

Clay swelling has been long studied for permeability impairment and water sensitivity on formations by core flooding brine such as NaCl or KCl (e.g. Baptist and Sweeny, 1954; Jones, 1964; Bush and Jenkins, 1970; Khilar and Fogler, 1983; Lever and Dawe, 1987). The swelling is directly related to the water salinity, cation-exchange capacity, and clay type, resulting in poorer effective permeability and porosity. Clays may present two swelling types according to their structure and environmental conditions: intercrystalline and osmotic (Bush and Jenkins, 1970; Madsen and Muller-Vonmoos, 1989). The intercrystalline swelling occurs in the clay interlayer, so its crystal lattice expands; this is a mechanism commonly seen in the montmorillonite mineral from the smectite group since it has the affinity for interchange water molecules and cations (i.e. hydrophilic clays). It has been found to increase more than twice its dry size. In osmotic swelling, as the name implies, water adsorption occurs between clay platelet surfaces with a significant ionic concentration gradient. Montmorillonite has the strongest swelling capacity in clay, followed by mixed-clay illite/smectite or mica/smectite, then chlorite and illite. In contrast, kaolinite has a lesser swelling capacity since it does not have an interlayer (Tao et al., 2019).

Clay migration and swelling identification are keys for formation damage prevention in clayey reservoir formations. While clay swelling involves water adsorption and internal expandability, clay migration is about fine particle detachment and suspension. Both phenomena will emerge with a combination of clay mineral type, cationic species flowing in the pore space and salinity concentration, i.e. the ion exchange equilibrium in the diffuse double-layer (DDL). The clay-water boundary, in the DDL, has a negative charge in the clay surface holding weak bonds of hydrated cations (ion-dipole bonds), and it will exchange those cations with the same valence or those with different valence but a close hydrated radius flowing near the clay surface. As shown in Equation 2–7, a reverse equilibrium reaction forms where the clay sorbs cations interchangeably. The binding strength increases inversely to the hydrated ionic radius of the cationic species (Table

2-5). Lithium has the strongest bond with clay particles for the monovalent alkali cations, while magnesium has the strongest bond for the divalent cations alkaline earth group. Furthermore, in terms of the cation-exchange capacity values of the clay mineral groups (Table 2-4), kaolinite has the lowest capacity magnitude due to its 1:1 (tetrahedral-octahedral) configuration not leaving enough interlayer space for isomorphic substitution for Si⁴⁺ or Al³⁺ species. In contrast, the remaining clay groups have a 2:1 (tetrahedral-octahedral-tetrahedral) configuration and moderate to high CEC magnitude. The chlorites interchange cations in their hydroxide interlayer sheet, and micas and illites interchange their K⁺ cations with Ca²⁺ in their interlayer and Fe²⁺/Fe³⁺ cations in their octahedral sheets. Finally, smectites substitute Mg²⁺ for Al³⁺ in the octahedral sheets (Barton and Karathanasis, 2002).

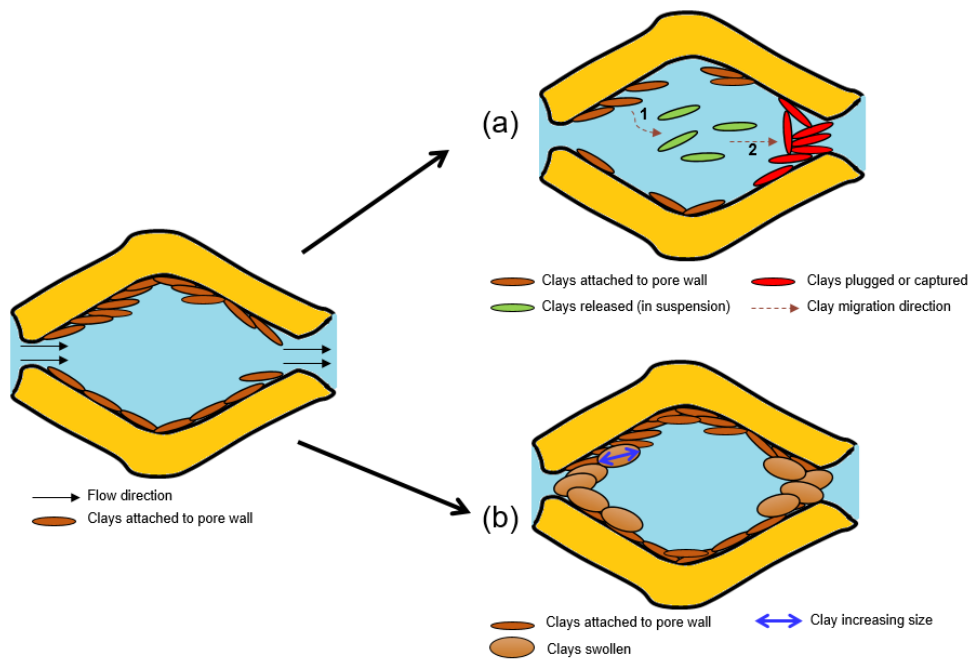
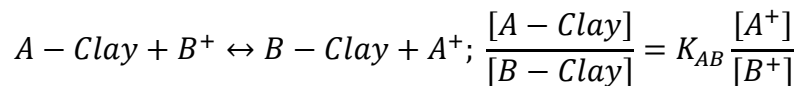


Figure 2-19. Clay mechanisms in sedimentary rocks with fresh water: (a) migration, (b) swelling (adapted from Khilar and Fogler, 1983; Daneshfar and Moghadasi, 2017; Xiao et al., 2017).

Equation 2-7



where *A* and *B* represent different atomic metals, *A*⁺ and *B*⁺ represent different cationic metals, *Clay* represents the clay mineral, and *K*_{AB} is the exchangeable constant written as a function of the species concentrations.

Table 2-5. The ionic and hydrated radius of species involved in cation-exchange capacity (Haynes, 2016).

Ion	Ionic radius (Å)	Hydrated radius (Å)
Li ⁺	0.59	3.82
Na ⁺	0.95	3.58
K ⁺	1.37	3.31
Mg ²⁺	0.57	4.28
Ca ²⁺	1.00	4.12
Ba ²⁺	1.35	4.04
Fe ²⁺	0.63	4.28
Fe ³⁺	0.49	4.57
Al ³⁺	0.39	
Si ⁴⁺	0.26	

2.3 Greensand formation

The name *greensand* stems from the colour of the sandstone, which is generally attributed to the presence of glauconite but also could include other clay minerals such as chlorite and illite/smectite (Hossain, 2011a). Greensand reservoirs have been discovered worldwide to produce hydrocarbons; their permeability ranges from moderate to ultra-low but with moderate porosity (Table 2-6). Likewise, greensand deposits are exploited to produce potash minerals for fertilisers, where glauconite content enhances crop growth (Tedrow, 2002). Also, greensands are used to soften water treatments as an adsorbent filter media to remove iron and manganese ions (Abd El-Rahman, 2006).

Table 2-6. Porosity and permeability reported data from some worldwide greensands reservoirs.

Reference	Reservoir type	Reservoir name	Location	Geological period or epoch	Porosity* (%v/v)	Permeability* (mD)	Glaucanite content*(%v/v)
Patchett et al. (1993)	Tight oil	Matulla Formation from Nezzazat Group	Lower Senonian, Gulf of Suez, Egypt	Upper Cretaceous	3.5 to 25	<1 to 90	20 to 45
Broger and Syhlonyk (1995)	Tight oil & gas	Glaucanite member from Mannville Group	Lake Newell, Southern Alberta, Canada	Lower Cretaceous	9 to 33	10 to 10,200	Not available
Taber et al. (1995)	Tight oil	Albian 'A' Sand Formation from Greensand Group	North Celtic Sea Basin	Lower Cretaceous	≤ 30	≤ 50	≤ 45
Garamendi and Atau (1999)	Tight oil	Pona reservoir, Chonta Formation	Peruvian forest region	Cretaceous	1 to 20	1 to 1,000	Not available
Diaz et al. (2003)	Tight oil	Caballos Formation	Putumayo Basin, Colombia	Lower Cretaceous	2 to 19	0.01 to 1,200	10 to 60
Hatcher et al. (1996); Zhang et al. (1996, 2000)	Tight oil	Mardie Greensand Formation	Carnarvon Basin, Australia	Early Cretaceous	15 to 28	0 to 100	Not available
Hossain (2011a)	Tight oil	Hermod and Ty Formations	Siri Canyon, Danish North Sea	Palaeocene	25 to 40	60 to 1,000	20 to 30
Aimar et al. (2018); Jait et al. (2018)	Tight gas	Magallanes Formation	Campo Indio field, Austral Basin, Argentina	Upper Cretaceous	15 to 35	0.01 to 1	Not able to determine**
Yang et al. (2019)	Tight oil	Upper T of Napo Formation	Oriente Basin, Ecuador	Cretaceous	5 to 20	≤ 500	10 to 40

* Reported either from core analysis or reservoir evaluation.

** XRD analysis could not identify glauconite since it overlapped with illite presence.

Glaucanite is the predominant clay mineral with a high potassium and iron content. It belongs to the mica group and may contain smectite that forms silicate interlayers referred to as glauconite/smectites (or G/S) or mixed layers with illite (Thompson and Hower, 1975). It frequently develops in open-marine and oxidising environments (Van Houten and Purucker, 1984; Newman and Brown, 1987; Odin and Fullager, 1988). **Table 2-7** shows the main properties of glauconite mineral, where the density and photoelectric factor are higher than typical quartz or sandstone (e.g. 2.65 g/cc and 1.8 barns/electron). Patchett et al. (1993) reported that greensand density ranges from 2.40 to 2.95 g/cc, depending on the presence of glauconite. The higher the glauconite presence, the higher the bulk rock density.

Table 2-7. *Glauconite mineral properties (Webmineral, 2019; Hugget, 2021).*

Property	Description or value
Formula	$K_{(x+y)}(Si_{4-x}, Al_x) \sim 4(Fe^{3+}, Al, Mg, Fe^{+2}) \sim 2O_{10}(OH)_2$ where x is 0.2-0.6 and y is 0.4-0.6.
Molecular weight	426.93
Lustre	Dull, Earthy
Hardness	2 (Mohs scale)
Density	2.4 – 2.95 g/cm ³ (Measured)
Member of	Mica group (dioctahedral interlayer-deficient micas)
Colour	Blue-green, yellow-green, green, rarely colourless
Recorded ages	Mesoproterozoic to Carboniferous: 1175 Ma to 354 Ma – based on 18 recorded ages
Photoelectric factor	PEF = 7.42 barns/electron
Radioactivity	GR = 78.31 API

The glauconite formation process is called glauconitization, described by Odin and Letolle (1980) from the morphological and mineralogical perspective (**Figure 2-20**) into four stages:

1. Nascent: after deposition at the sea floor or other marine environment, the grain forms in a semi-confined microenvironment where pores networks start creating together with accommodation of detrital clay minerals, dissolution of carbonate and formation of Fe³⁺ smectite.
2. Slightly evolved: the grain starts maturing by re-accommodating the ions of the seafloor, i.e. formation water, feeding the crystals of glauconitic smectites (G/S); the detrital minerals disappear, and Fe and K ions start to increase their presence and Fe oxides to Fe²⁺ and Fe³⁺.
3. Evolved: the grain evolves by rearranging the mineral composition and recrystallising into more closed minerals resulting in superficial cracks with faster crystal growth in the grain's centre.

4. Highly evolved: the grain grows a new glauconitic minerals generation in its periphery, wrapping around the glaucony pellet, and new recrystallisation creates glauconitic micas.

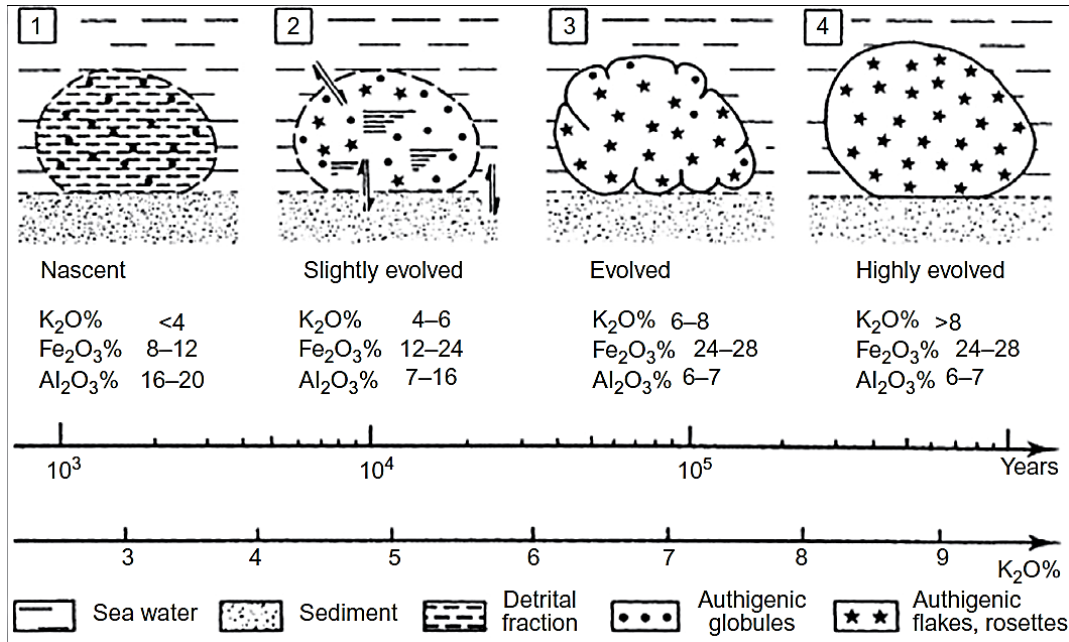


Figure 2-20. Morphological transformation from nascent to highly evolved glauconite (from Hugget al., 2021; modified from Odin and Letolle, 1980).

Glauconite grains vary in shape, such as a sphere, ovoid, tabular, vermiform or lobate, and may occur in microfossils (Wilson et al., 2014); they tend to be part of the rock framework rather than pore-filling, reducing the pore throats volume and connectivity. Silica cement is typically found in glauconitic sandstones that strengthen the pore network and reduce the overall porosity to some extent; carbonate, calcite or berithierine cement can also show up in some intervals, blocking intergranular pore throats. Some authors describe the glauconitic grains with angular and subangular shapes (i.e. irregular) with a high roughness degree on the surface. The sorting may range from locally poor to moderate, and the packing can be moderately poor to a tight arrangement (e.g. Hossain et al., 2009; Atahualpa, 2013; Guanochanga, 2013; Yang et al., 2019).

Greensands have a dual porosity system: macro- or inter-granular porosity and microporosity – pore size less than 0.5 μm (Pittman, 1979). For example, **Figure 2-21** shows the macropores (right side) and micropores (left side) of two greensands BSE images where it is worth noting that the scale used to show the microporosity is 1 μm. Hossain et al. (2009) and Diaz et al. (2003) agree that compacted glauconite grains create microporous networks under high or moderate overburden pressure; since glauconite is ductile, the microporosity results from permanent or non-elastic deformation.

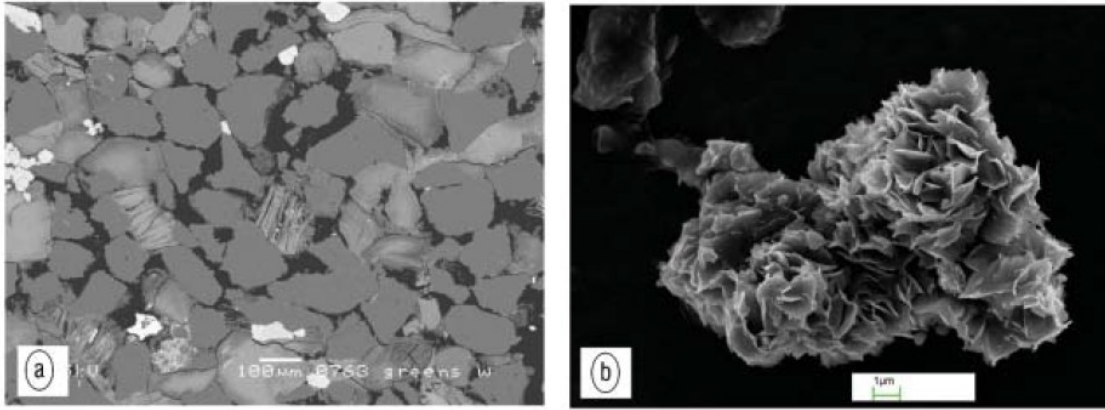


Figure 2-21. (a) BSE image of the North Sea greensand, scale bar for greensand is 100 μm , and the image represents macroporosity, quartz, and glauconite grains. (b) BSE glauconite grain image from Arnager greensand, scale bar for glauconite grain is 1 μm . Micropores reside within glauconite grain (Hossain et al., 2009).

Chlorite may also be present within greensand formations as an authigenic (Dodge et al., 1995; Rueslatten et al., 1998; Durand et al., 2000; Bansal et al., 2020). Due to the high presence of iron and magnesium, chlorite clay types such as clinochlore (magnesium-rich) or chamosite (iron-rich) can develop as a mixed layer in the glauconitic micas or glauconitic smectites, contributing to an increase in the rock heterogeneity (Durand et al., 2000). The chlorite within greensands has been found as grain coating, pore-lining in the form of plates or honeycombs or pore filling in rosette or cabbage head shapes (e.g. Rueslatten et al., 1998; Dodge et al., 1996). The latter two increase micropore networks and enhance bi- and even tri-modal pore size distribution (**Figure 2-22**). **Table 2-8** displays the chlorite group properties, which vary depending on the ionic substitution in its 2:1 layer. Compared to glauconite, theoretically, chlorite does not contain potassium, uranium, or thorium and thus is not radioactive as a pure component (Worden et al., 2020).

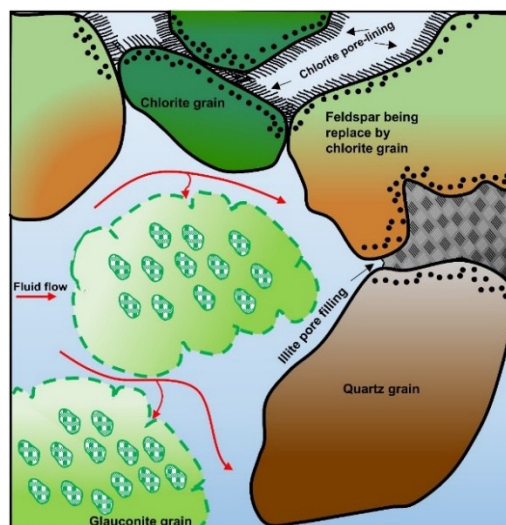


Figure 2-22. Diagram of greensand major grains and clay distribution types as grain coating and filling pore throats, glauconite contains microporosity.

Table 2-8. Chlorite mineral properties (Webmineral, 2019; Alderton, 2021; Geology.com, 2023).

Property	Description or value
Formula	$(X,Y)_{4-6}(\text{Si}, \text{Al})_4\text{O}_{10}(\text{OH}, \text{O})_8$ X and Y represent ions that include: Fe^{+2} , Fe^{+3} , Mg^{+2} , Mn^{+2} , Ni^{+2} , Zn^{+2} , Al^{+3} , Li^{+1} , or Ti^{+4} .
Molecular weight	595.22, 664.18, 300.61, 546.77
Lustre	Vitreous, pearly, dull
Hardness	2 – 2½ (Mohs scale)
Density	2.6 – 3.3 g/cm ³ (Measured)
Common species	Clinochlore, chamosite, odinite, sudoite
Colour	Various shades of green
Recorded ages	Paleoproterozoic to Neogene: 2211 Ma to 15.7 ± 0.2 Ma – based on 7 recorded ages

2.3.1 Mineralogical analysis

The glauconitic grains' microstructure is complex, and it presents difficulties in identifying them correctly since they can be easily confused with other minerals. For instance, there are other greenish clays, such as odinite, clinochlore, or chamosite (all from the chlorite group), and berthierine (from the kaolinite group), all have in common with glauconite, which develops in a slow sedimentary deposition rate (Hugget, 2021).

Burst (1958) identified four types of glauconites based on their XRD spectrum (**Table 2-9**), and he compared the structural and chemical relation of clay mineral groups with their potassium content (**Figure 2-23**); he shows that glauconite can be confused for muscovite, illite and mixed layer clays when using XRD techniques because all have a 10 Å lattice spacing. Several authors agreed with Burst's work and pointed out that the pure glauconite lattice peaks at ~10Å spacing while mixed-layer glauconitic grains may range from 10Å to 14Å due to smectite (montmorillonite) expandable interlayer (Hower, 1961; Cimbalnikova, 1971a, 1971b; Abudelgawad et al., 1975; El-Amamy et al., 1982; López-Quirós et al., 2020).

Table 2-9. Glauconite types classification of XRD spectrum (Burst, 1958).

Type	Description
1	Well-ordered, non-swelling, high-potassium, mica-type lattice. It corresponds to the glauconite mineral.
2	Disordered, non-swelling, low-potassium, mica-type lattice of 10 Å.
3	Extremely disordered, expandable, low-potassium, montmorillonite-type lattice.
4	Mixtures of two or more clay minerals as normal pellet constituents of unrelated structures, i.e. kaolinite and illite or chlorite and glauconite.

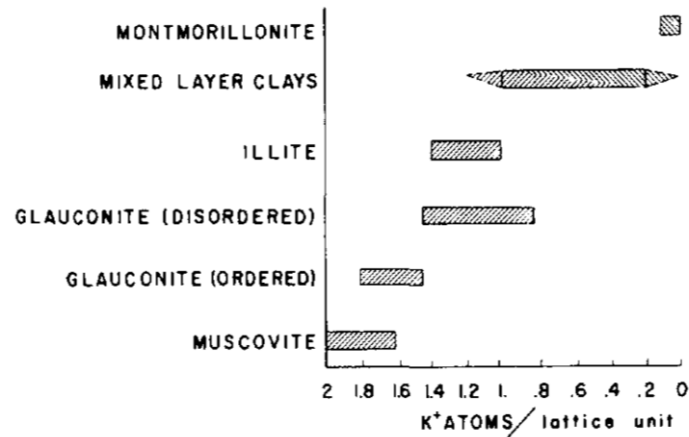


Figure 2-23. Variations in potassium atoms as functions of structural regularity (Burst, 1958).

2.3.2 Porosity estimation

Greensands have a bimodal pore-size distribution (**Figure 2-24**) where the meso- or macropores range associates with the effective porosity, and the micro- or nanopores range associates with the enclosed pores storing bound water, i.e. irreducible water (Slot-Petersen et al., 1998; Markley et al., 2010).

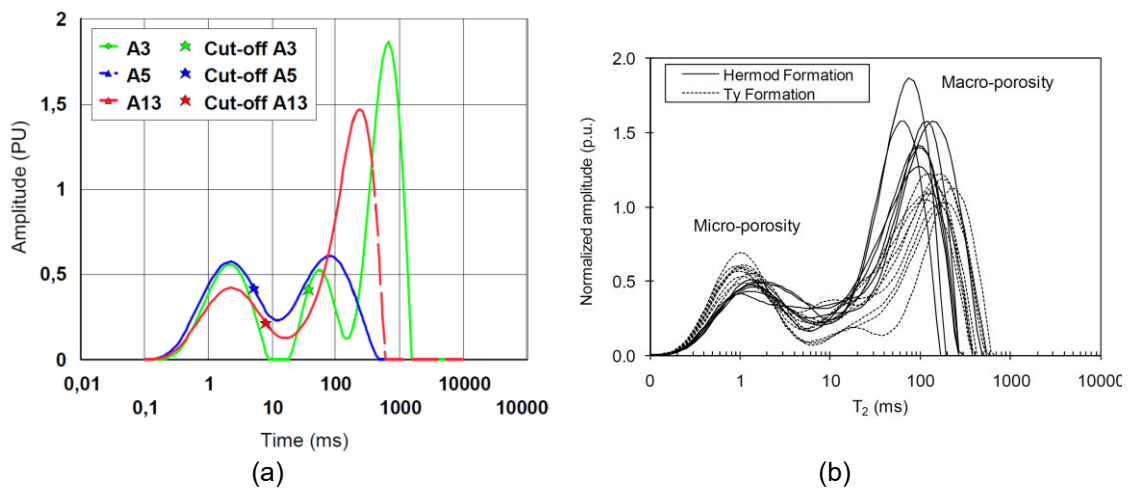


Figure 2-24. NMR T_2 curve distribution on greensands samples (a) Nini field, North Sea (Hossain, 2011a), and (b) Late Paleocene/Early Eocene sandstone, North Sea (Rueslatten et al., 1998). A peak close to 1 ms represents microporosity, and a peak close to 100 ms represents macroporosity.

Dodge et al. (1996), Rueslatten et al. (1998), Slot-Petersen et al. (1998), and Hossain et al. (2011a) measured the NMR T_2 distribution of greensand samples and identified three critical features:

- 1) The iron minerals have *paramagnetic properties*² which increase surface relaxivity and reduce T_2 decay times (LaTorraca et al., 1995; Saidian and Prasad, 2015). Dodge et al. (1996) reported a 3.9 $\mu\text{m}/\text{sec}$ surface relaxivity for a glauconitic sandstone (14% iron content). The authors agree to lower the T_2 cut-off for oilfields, such as values between 30 to 10 ms (**Table 2-10**), to separate the irreducible water from the mobile bulk fluids.

Table 2-10. T_2 cut-off guidelines for oilfield greensand formations according to the iron content (Dodge et al., 1996).

Fe (wt%)	T_2 cut-off (ms)
0 – 4	30
4 – 6	20
> 6	10

- 2) Core NMR porosity tends to underestimate total porosity due to the iron paramagnetic effect. However, the authors agree that this method is preferable for measuring effective porosity rather than helium porosity. Rueslatten et al. (1998) recommend re-calibrating the NMR logging tool to an inter-echo spacing of 0.3 ms for a better effective porosity log.
- 3) Rueslatten et al. (1998) and Slot-Petersen et al. (1998) concluded that chlorite is directly related to the core NMR porosity underestimation rather than glauconite. Hossain and Zhou (2015) found a linear correlation factor of 0.7 between core helium porosity and pore-filling berthierine (chlorite) within sixteen North Sea greensand samples (**Figure 2-26 a**).

In addition, Hossain et al. (2011a) point out that the core helium porosity measures the total porosity since this inert gas molecular size is small enough to sweep the micropores network and the clay-bound water. In contrast, the Archimedes method with fully brine-saturated core plugs measures the effective porosity since the water molecule size is higher than helium. Their core NMR porosity was similar to the brine porosity and significantly lower than the core helium porosity.

2.3.3 Permeability estimation

Compared to clay-free sandstones, the permeability-porosity cross-plot of greensands is scattered and shifted to the right (**Figure 2-25**). The considerable amount and distribution

² A paramagnetic substance is attracted and aligned to an external magnetic field, and its atoms or molecules present unpaired electrons, such as aluminium or iron (A Dictionary of Chemistry, 2020). In the reservoir rocks, paramagnetic components are considered impurities that affect NMR hydrogen protons relaxation measurements. Examples are iron components such as pyrite, siderite, illite or chlorite (Saidian and Prasad, 2015).

of clay minerals in the rock framework result in poorer effective permeability and porosity, higher microporosity content, lower pore-throats interconnectivity, and decreased flow capacity. Clay minerals have a moderate to high specific surface area – SSA – (Table 2-4), which explains the low permeability and high irreducible water saturation. Hossain et al. (2011a) reported a range of SSA from 17 to 23 m²/g through nitrogen adsorption (SSA of quartz is ~2.5 m²/g) and found an inverse relationship with the macroporosity and permeability. Hossain and Zhou (2015) show a relationship between the porosity and permeability with the SSA discriminated by the greensand's pore-filling clay distribution (Figure 2-26).

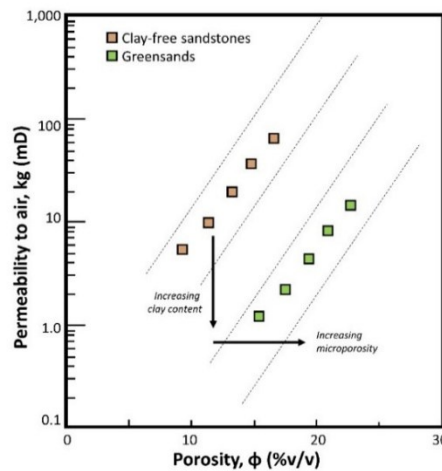


Figure 2-25. Total porosity and air permeability cross-plot showing the different trends of clay-free sandstones and greensands.

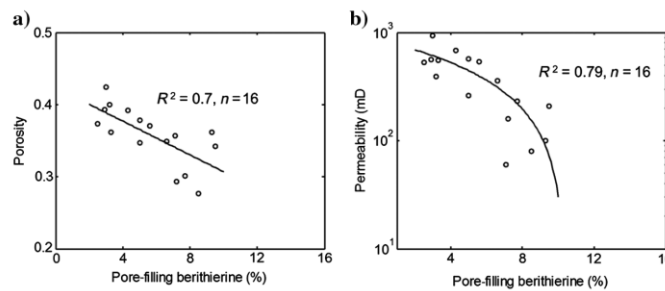


Figure 2-26. Relationship between pore-filling berthierine (chlorite) content of North Sea greensands samples with (a) helium porosity and (b) core permeability (Hossain and Zhou, 2015).

Several researchers have created innovative methodologies to determine greensand permeability assertively by calibrating the core data with well logs (Table 2-11). The discrimination of iron content, matrix density, and NMR parameters is important to define an optimised permeability prediction. Table 2-12 displays the permeability equations in the literature used for greensands. Kozeny's, Timur-Coates, and SDR equations are the most frequently used either in their classic style or modified.

Table 2-11. Permeability estimation methods found in the literature review used on greensands reservoirs.

Reference	Method	Comments
Dodge et al. (1996)	Log NMR permeability with Schlumberger (SRD) and Timur-Coates (TC) equations.	<ul style="list-style-type: none"> ▪ Iron content underestimates NMR-derived permeability for the TC equation; care must be taken to define the T₂ cut-off value. ▪ The fitted factors of the formulas used were enough for good calibration. ▪ Suggested T₂ cut-off values according to the iron content in greensand formations.
Zhang et al. (1996)	Electrofacies pattern linked to permeability transforms algorithm using core porosity and permeability as database.	<ul style="list-style-type: none"> ▪ Log synthetic permeabilities used as input were litho-density, neutron, sonic and gamma-ray spectrometry logs. ▪ Grouping the electrofacies (lithological units) is extremely important.
Rueslatten et al. (1998)	NMR permeability with the Timur-Coates equation.	<ul style="list-style-type: none"> ▪ T₂ cut-off values below 10 ms for chloritic greensands and 33 ms when chlorite and glauconite are present (oil production).
Slot-Petersen et al. (1998)	Log NMR permeability with the Timur-Coates (TC) equation.	<ul style="list-style-type: none"> ▪ Chlorite presence influences the irreducible bulk volume when using the TC equation. ▪ Density-derived porosity log replaced the FFI/BVI term in the TC formula, increasing permeability estimation.
Zhang et al. (2000)	Artificial neural network technique to estimate permeability using four parameters as decision criterion of well wireline logs.	<ul style="list-style-type: none"> ▪ 147 log response sets were trained with core permeability from eight wells. ▪ The synthetic permeability log shown as an example gave good consistency results.
Klein et al. (2006)	Density Constrained Stochastic Modelling (DCSM).	<ul style="list-style-type: none"> ▪ Method based on a random selection of core bulk density values and matched it with an apparent matrix density log. ▪ The average density tolerance between the two parameters is less or equal to 0.05 g/cm³.
Hossain et al. (2011a)	Modified Kozeny's equation to include the whole macroporosity range of T ₂ times.	<ul style="list-style-type: none"> ▪ Kozeny's factor C=8.3 was estimated from the Mortensen et al. (1998) porosity model. ▪ Surface relaxivity derived from specific surface area from Kozeny's BET and image analyses. ▪ The BET-specific surface area takes into account the microporosity range. While the image and Kozeny's specific surface area are associated with the macroporosity range.
Hossain and Cohen (2012)	Empirical correlation of permeability with the electrical formation factor – Worthington's (1997) modified Kozeny's equation.	<ul style="list-style-type: none"> ▪ The formation factor was estimated using the equation $F=a/\phi^m$, with a=1.67 and m=1.9. ▪ A linear relationship between permeability and formation factor was found by varying the specific surface area. ▪ The diagenesis of the greensands needs to be known to replicate this method.
Hossain and Zhou (2015)	Modified Kozeny's equation by including two factors, a and b, dependent on the rock type instead of the specific surface area or surface relaxivity and as a function of porosity.	<ul style="list-style-type: none"> ▪ Factors a and b are constants derived from a linear relationship between the specific surface area and porosity. ▪ For clean sandstone, a=-1.0 and b=2.2; for clay-bearing sandstone, a=-2.5 and b=-2.3. ▪ For greensand with pore-filling cementation, a=-5.5 and b=3.0. ▪ A linear relationship between Kozeny's constant c and porosity is proposed.

Table 2-12. Permeability equations applied for greensands reservoirs.

Name	Reference	Equation
Timur and Coates (TC)	Timur (1968)	$k = (\phi_{NMR})^4 (FFI/BVI)^2$
Schlumberger-Doll-Research (SRD)	Kenyon (1997)	$k = 4.5(\phi_{NMR})^4 (T_{2.g})^2$
Kozeny	Kozeny (1927)	$k = c \frac{\phi^3}{S^2}$
Modified Kozeny's to include macroporosity range	Hossain et al. (2011a)	$k = c\phi\rho_2^2 \sum_{i=1}^N f_i(T_{2i})^2$
Worthington's (1997) modified Kozeny's equation.	Hossain and Cohen (2012)	$k = \left(\frac{B}{F}\right)^{1/C}$
Modified Kozeny's as a function of rock type	Hossain and Zhou (2015)	$k = c \frac{\phi^{3-2a}}{10^{2b}}$

Nomenclature: k = permeability (mD), ϕ_{NMR} = NMR porosity (v/v), FFI = NMR log free fluid index (v/v), BVI = NMR bulk volume irreducible fluid (v/v), $T_{2.g}$ = geometric mean of T_2 distribution time (ms), c = Kozeny's constant, S = specific surface area of bulk ($1/\mu\text{m}$), ρ_2 = surface relaxivity ($\mu\text{m}/\text{ms}$), f_i = fraction of the total amplitude of each T_{2i} , F = electrical formation factor ($F=a/\phi^m$), B , C , a and b are fitting constants.

2.3.4 Irreducible water saturation estimation

Since greensands have a complex microstructure due to clays' presence, it is expected that the irreducible water saturation (S_{wirr}) and the capillary pressure curves to be high (Figure 2-27). Indeed, the glauconitic grains are water-wet (Thomas et al., 2003), favouring storing water in the micropores range and leaving hydrocarbon in the macropores range (Figure 2-28). Table 2-13 shows the reported irreducible water saturation for greensands with values up to 78%v/v in the literature. The standard technique used is the NMR T_2 distribution, and the T_2 cut-off values are below the typical value of 33 ms used for clean sandstones (Coates et al., 1999).

As previously stated in Section 2.3.2, the iron content in greensands affects the NMR T_2 readings and hence the estimated irreducible water saturation; that is why the authors in Table 2-13 use lower T_2 cut-off values. Dodge et al. (1996) suggest that the T_2 cut-off value needs to be lower than 10 ms to quantify S_{wirr} (Slot-Peterson, 1998). Typical T_2 cut-off values of 33 ms for free mobile fluid and 3 ms for the clay-bound water for greensands reservoirs are incorrect. The T_2 decays faster due to the iron paramagnetic properties and narrower pore size distribution; thus, the T_2 cut-off value must be lowered (e.g. Simpson et al., 2018). Hossain et al. (2011a) went further down, and using the capillary pressure curves, they defined a cut-off value of 100 psig to separate the microporosity from the meso- and macroporosity zone equivalent to a T_2 cut-off value of 5.21 ms (Figure 2-29).

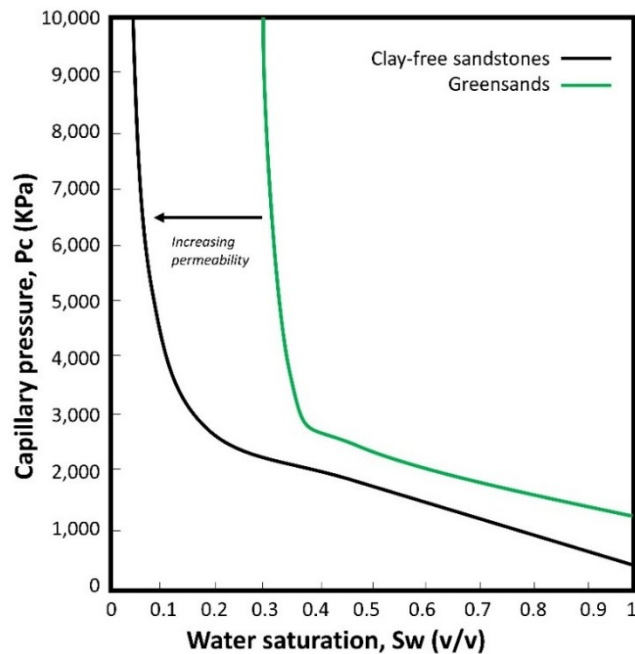


Figure 2-27. Capillary pressure and water saturation cross-plot comparing clay-free sandstones and greensands trend.

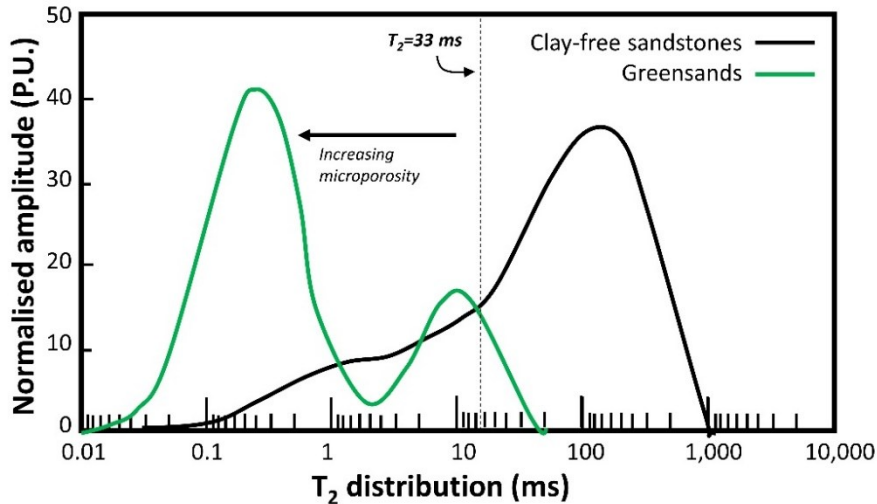


Figure 2-28. NMR T_2 distribution diagram comparing clay-free sandstones and greensands distribution.

Table 2-13. Irreducible water saturation values found in worldwide greensands with the technique used to define them.

Reference	S_{wirr} (%v/v)	T_2 cut-off value (ms)	Technique used
Dodge et al. (1996)	12 – 78	10 to 30	Centrifuge air/brine drainage capillary pressure and NMR T_2 distribution.
Rueslatten et al. (1998)	27 – 55	33	Decane-brine saturation, Karl Fischer titration, and NMR T_2 distribution
Slot-Peterson et al. (1998)	27 – 41	33 and 10 for chlorite zones	Karl Fischer titration and NMR T_2 distribution
Hossain et al. (2011a)	22 – 41	5.2 and 3.7	Centrifuge air/brine drainage capillary pressure and NMR T_2 distribution.

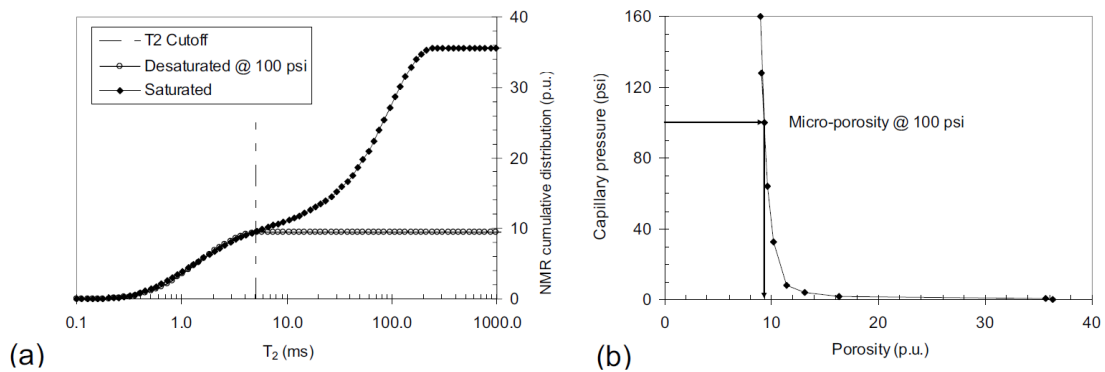


Figure 2-29. Macroporosity and microporosity determination of a North Sea greensand sample (a) from NMR T_2 distribution and (b) from the capillary pressure curve. The dashed vertical line shows a cut-off of 5.21 ms. The capillary pressure of 100 Psig corresponds to a microporosity of 9.1% (Hossain et al., 2011a).

Finally, the gas-water permeability curve of greensands is expected to shift to the right (Figure 2-30) due to the high S_{wirr} reported values and its microporosity portion. The water relative permeability curve will start at a moderate to high S_{wirr} and effectively flow from 2% of k_{rw} onwards (Cluff and Byrnes, 2010). In comparison, the gas relative permeability

curve will start at 100% k_{rg} to a small value of residual gas saturation ($1-S_{rg}$), where the remaining hydrocarbon gets trapped.

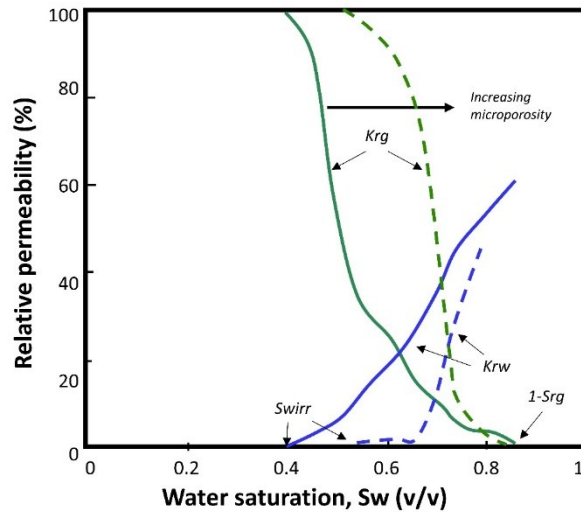


Figure 2-30. Gas-water relative permeability and water saturation cross-plot comparing the trend of clay-free sandstones (continuous line) and greensands (dashed line). K_{rg} is gas relative permeability, K_{rw} is water relative permeability, S_{wirr} is irreducible water saturation, and S_{rg} is residual gas saturation.

2.3.5 Greensand geomechanics

Only a few studies have been published on the greensands geomechanics and its relationship with reservoir quality. **Table 2-14** shows some geomechanical properties of two greensands reservoirs in Canada and Ecuador, respectively. The only geomechanical reported data from the ZG formation (case study) is the static Young's Modulus of 32.1 GPa (Britt et al., 2016) that can be compared with the literature. Following reported typical ranges for Young's modulus as a function of lithology (Ahmed, 2019), greensands formation is classified as medium to hard sandstone (~34.5 to 69 GPa).

Table 2-14. Greensand reservoirs' elastic properties are found in the literature.

Location	Parameters	Reference
Glauconite formation of the Willesden Green Field, Western Canada Sedimentary Basin.	Poisson's ratio = 0.229 (dynamic) and 0.225 (static). Young's modulus = 44.8 GPa (dynamic) and 36.2 GPa (static). Shear modulus = 18.2 GPa Overburden stress = 47.684 MPa Pore pressure = 13.753 MPa	Urban and Aguilera (2015)
Upper T formation in Tarapoa Block, Oriente Basin, Ecuador	Bulk modulus = 20.2 GPa Shear modulus = 18.5 GPa Young's modulus = 29.5 GPa (dynamic) Poisson's ratio = 0.25 (dynamic) Uniaxial compressive strength = 149.4 GPa	Yang et al. (2019)

Diaz et al. (2001; 2003) analysed the effects of lithology, porosity and permeability of Colombian greensand and its relationship with the Poisson's ratio and P-impedance³. They identified a pattern to determine the quality of reservoir rock using the P-impedance as a discriminator, where the values above 12 Mrayls correspond to a non-reservoir quality rock (glaucconitic wackestones, calcareous-glaucconitic sandstones and siltstones) and below 12 Mrayls corresponds to a reservoir quality rock (glaucconitic and quartz sandstones) as shown in **Figure 2-31**. Also, the Poisson's ratio range of glauconitic sandstones is from 0.17 to 0.24, and the reported values in **Table 2-14** are within this range. These studies confirm that glauconite presence reduces the P- and S wave velocity and P-impedance besides decreasing the rock permeability. Hossain and Zhou (2015) found a variety of petrophysical relationships with the P- and S- wave velocities compared to the diagenetic distribution type, and they agree that when glauconite is present in the rock, the wave velocities are lower (**Figure 2-32**).

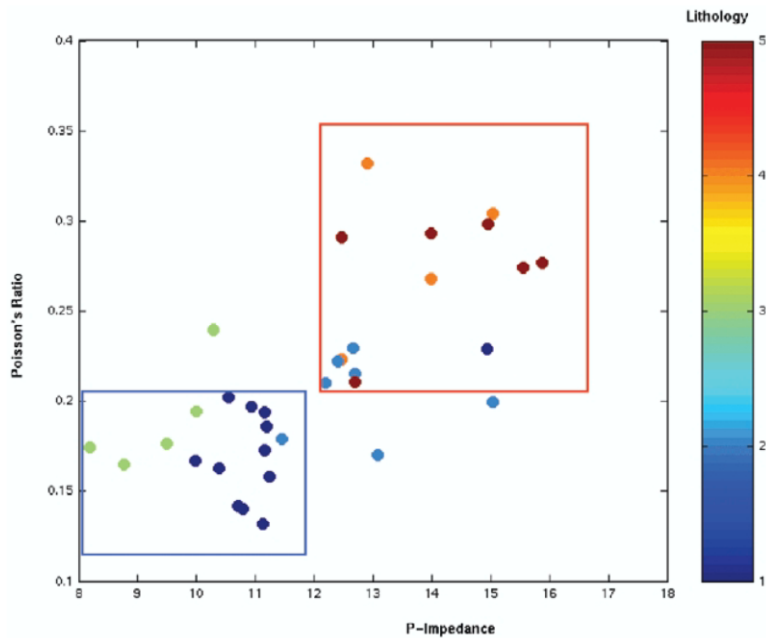


Figure 2-31. P-impedance versus Poisson's ratio plot, discriminated by the Putumayo Basin, Colombia's lithology (colour bar). Dark blue: quartz sandstones, light blue: calcareous-glaucconitic sandstones, green: glauconitic sandstones, orange: quartz-siltstones, and red: glauconitic wackestones (Diaz et al., 2003).

³ Impedance is the product of density (Kg/m^3) and the wave of speed (m/s) of a material and typically is expressed in Mrayl unit that equals $1 \times 10^6 \text{ Kg/m}^2 \cdot \text{m/s}$ (Jaeger et al., 2007).

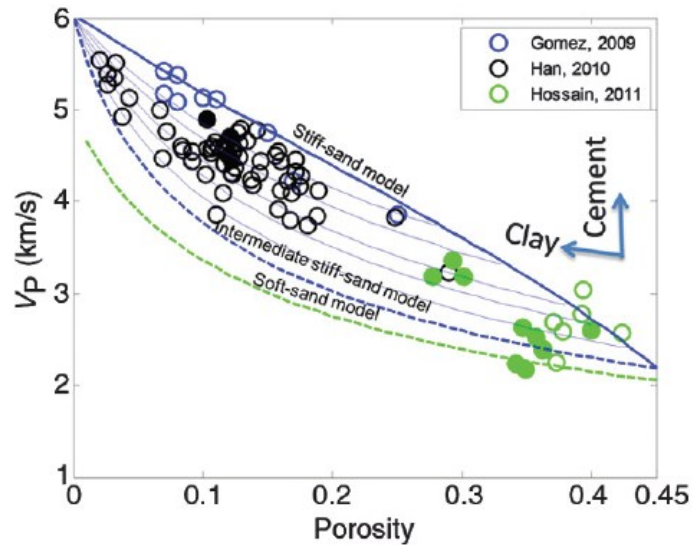


Figure 2-32. Modelling of porosity and velocity relations using rock physics diagnostics. Blue circles are Fontainebleau sandstone from the Ile De France, black circles are clay-bearing sandstone, and green circles are greensands from the North Sea (Hossain and Zhou, 2015). The mentioned models are rock physics proposed by Mavko et al. (2009) for intermediate stiff-sand and stiff-sand models and by Dvorking and Nur (1996) for the soft-sand model.

Hossain et al. (2009) demonstrated, through image analysis and in mechanical testing under 15 MPa uniaxial conditions for greensand, that the permanent deformation results from the glauconite grains microporosity while the macroporosity is unchanged, e.g. quartz grains are elastic. They also found that the dynamic Young's modulus is 1.3 times higher in the static one and that the dynamic Poisson's ratio is 1.2 higher than the static one. These findings are important when deriving elastic properties from the laboratory (static) or well-logs (dynamic).

Furthermore, Hossain et al. (2011b) developed a rock physics model integrating elastic properties and porosity from logging and coring analysis to identify the diagenetic alterations of the North Sea greensands (Figure 2-33). They found that silica and berthierine cementation occurs in the greensand diagenetic alterations; when weakly cemented, the formation has low elastic moduli and is modelled by the Hertz-Mindlin contact model (Mindlin, 1949). The intermediate-stiff-sand or stiff-sand model (Mavko et al., 2009) can be used when the formation has silica cement because it has a higher elastic modulus, while the soft-sand (Dvorking and Nur, 1996) or intermediate stiff-sand model can be used when the formation has berthierine cement.

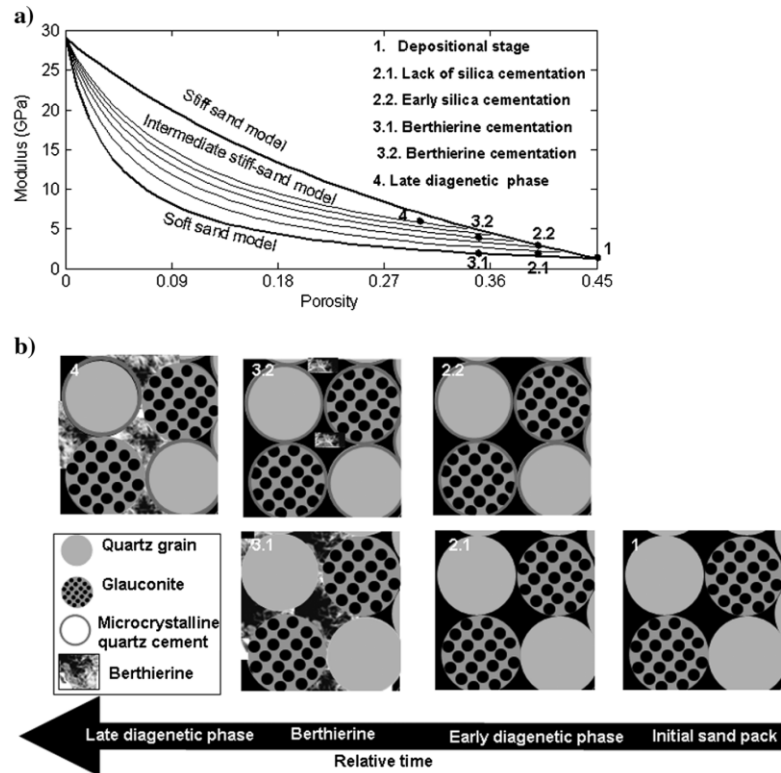


Figure 2-33. Schematic rock-physics model for the North Sea greensand shows the link between the rock-physics model and greensand diagenesis. (1) Depositional stage, no diagenesis occurs. (2.1) Lack of silica cementation, some greensand is not influenced by the silica flux. (2.2) Early silica cementation, the first diagenetic mineral to form. (3.1) Pore-filling berthierine cementation: berthierine precipitation occurs because microcrystalline-quartz cement is absent. (3.2) Berthierine in early silica-cemented greensand that causes major porosity reduction. (4.) Late diagenetic phase where berthierine continues to grow (Hossain et al., 2011b).

2.3.6 Greensand effect on well-logs

Table 2-15 summarises the effects of greensand on different well-logs and which petrophysical properties are impacted. As can be seen, the primary logs used for well-log interpretation are affected, meaning that a different approach must be implemented to estimate the petrophysical properties accurately. As previously stated, greensands are radioactive due to their high potassium content; hence, spectral gamma-ray logs are extremely helpful if available. Particularly the K/Th ratios combined with the photoelectric factor log can be used to identify glauconite (Table 2-16).

Table 2-15. Summary table showing how greensand affects well-log readings and which petrophysical properties are consequently under or overestimated.

Well-log	Greensand effect	Causes	Petrophysical estimation or consequence	Reference
Gamma-ray	Higher response than clean and shaly sandstone	High presence of potassium. Greensands can have other clay minerals such as chlorite, siderite and pyrite. Higher boron content than other clay minerals.	The shale or clay volume calculated is overestimated.	Klein et al. (2006); Atahualpa (2013); Yang et al. (2019).
Deep resistivity	Lower response similar to freshwater zones	High cation cation-exchange capacity (CEC), meaning lower resistivity. Large amount of bound water in the glauconitic grains.	The hydrocarbon zone is not easily identified. The water saturation is overestimated.	Patchett et al. (1993); Hossain et al. (2011b); Atahualpa, (2013).
Neutron porosity	Higher response than sandstone	Large thermal neutron absorption cross-section because of its high iron content. Higher boron content than other clay minerals.	Neutron porosity is overestimated.	Patchett et al. (1993) ; Klein et al. (2006).
Bulk density	Higher response than sandstone	Glauconite is denser than sandstone. Iron presence.	Density porosity is underestimated.	Patchett et al. (1993); Diaz et al. (2001); Klein et al. (2006); Hossain et al. (2011b).
Photoelectric factor	Higher response than sandstone	Relatively high molecular weight. Iron presence.	It can be used to identify the glauconitic sandstone lithology.	Patchett et al. (1993); Atahualpa (2013).
NMR tool	T ₂ decays faster	Paramagnetic effect of the iron content of greensand.	Bulk mobile fluid underestimated. T ₂ cut-off value needs to be lower than 30 ms.	Dodge et al. (1996); Slot-Peterson et al. (1998); Rueslatten et al. (1998)

Table 2-16. Average ranges of potassium, uranium and thorium concentrations on clays (Eslinger and Pevear, 1988).

Clay mineral	K (wt%)	U (ppm)	Th (ppm)
Glaucanite	3.2 – 5.8	0	2 – 8
Muscovite	7.9 – 9.8	0	6 – 22
Biotite	6.2 – 10.1	0	0
Kaolinite	0.1 – 1.49	0	18 – 26
Smectite	0 – 0.60	0	10 – 24
Illite	3.51 – 8.31	0	6 – 22
Chlorite	0	0	6 – 22
Illite/Smectite	2 – 8 (as K ₂ O)	0	0

Due to the greensand effect in well-logs, the core analysis programme is critical for accurate calibration and petrophysical model building. An example is shown below (**Figure 2-34**) where the greensands formations Hermod and Ty present the lowest resistivity readings and shorter density-neutron separations, even though the core helium-porosity and permeability indicate that these zones are permeable (permeability higher than 200 mD) and porous (porosity between 38 – 43%v/v). Finally, a schematic summary of the typical well-log responses is displayed below (**Figure 2-35**), highlighting clay-free sandstone's gas effect (Neutron-Density crossover) and the no-gas effect in greensands.

The multimineral analysis is the widely used procedure for building a petrophysical model, which is a mathematical inversion method (e.g. Doveton, 2018) that finds the best fit by knowing the outputs (i.e. core data) and by altering the input variables (i.e. the number of minerals and fluids constituents, and well-logs). Patchett et al. (1993) conducted a multimineral analysis using the Wiley and Patchett (1990) nuclear log model for greensands; they combine two to four minerals - including glauconite as a major mineral - and bulk density, neutron porosity, and PEF logs as input. They compare the statistical correlation R^2 and porosity standard error to define the best regression equation to estimate porosity. This study shows that the photoelectric factor log contributes to a better porosity estimation since this can better identify the glauconite presence similar to illite.

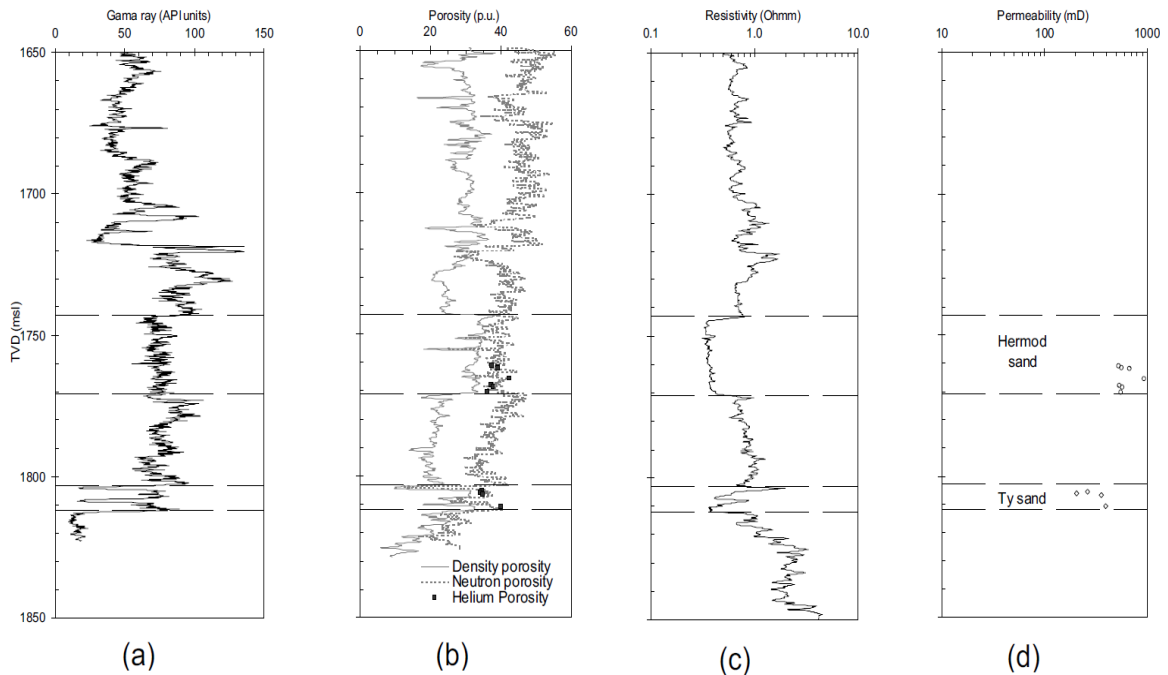


Figure 2-34. Nini-1 well logs showing the greensand reservoirs intervals (Hermod and Ty sands from the North Sea), (a) gamma-ray log; (b) porosity logs: bulk density, neutron porosity and helium porosity from core analysis; (c) resistivity log and, (d) permeability log (using Kozeny's equation) from core analysis (Hossain et al., 2011b).

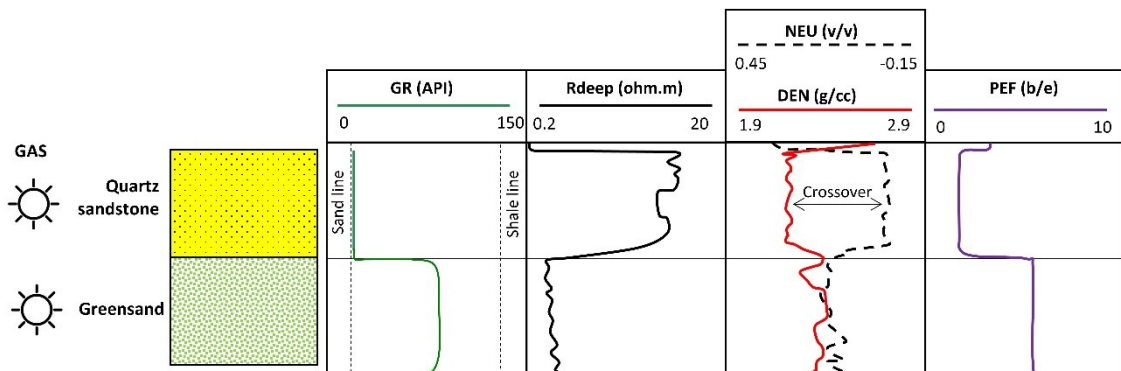


Figure 2-35. Diagram of conventional well-logs responses in a quartz sandstone and greensand formations, from left to right: gamma-ray log (GR), deep resistivity log (Rdeep), neutron log (NEU), bulk density log (DEN), and photoelectric factor log (PEF).

2.3.7 Water saturation modelling

Greensands present high rock conductivity due to the significant cation-exchange capacity of glauconitic grains. Weaver (1989) reports values from 5 to 12 meq/100gr for glauconites with up to 5% expandable clays, and with 50% expandable layers, a CEC values up to 40 meq/100gr. Patchett et al. (1993) report values from 7.8 to 32.4 meq/100gr (13 to 81% glauconite). In contrast, values of greensand deep resistivity log range from 1 to 5 ohm·m (Slot-Peterson et al., 1998; Pratama et al., 2017; Prayoga et al., 2018). Since these values are low, the formation can be confused with freshwater rather than a hydrocarbon zone.

Greensands are referred to as low-resistivity pays, according to the definition by Worthington (2000, p.78), “a lack of useful positive contrast in measured electrical resistivity between zones that contain and produce hydrocarbons in commercial quantities and zones that contain and produce only water, within the same reservoir system”. Sneider (2003) uses the term low-resistivity, low-contrast (LRLC) to refer to sandstones with very low resistivities (< 2 ohms·m) that have low contrast in resistivity with adjacent shales. The excess clay minerals, fine grains and microporosity are some of the leading causes of low-resistivity pays, which are greensands features.

Archie (1942) (see **Section 2.1.2.3**), Waxman-Smits (1968) and Simandoux (Bardon and Pied, 1969) are the three models used frequently in worldwide greensands (**Table 2-18**). Waxman-Smits is the main representative of the double-layer models and uses the cation-exchange capacity parameter. Simandoux represents V_{sh} models since it adds a shaley term. The V_{sh} models are based on the wetted-shale/clay volume fraction, meaning that they implicitly assume that the electrical properties of clays, independent of how they are distributed in sandstones, are the same as the layers of the detrital clay adjacent to the sandstones. The advantage of using them is that shale/clay parameters can be estimated from log data alone (Worthington, 1985).

The double-layer models offer a better scientific understanding of the rock’s electrical behaviour. However, they require core data to calibrate their terms, such as Q_v , for log-derived parameters (e.g. McPhee et al., 2015). It is important to note that these water saturation models – Archie, Simandoux, and Waxman-Smits – did not use glauconitic sandstones as empirical data for their postulates, so care should be taken when applying them to other rock-type formations such as greensands.

Table 2-17. Water saturation models expressed in conductivity terms used in greensands.

Model	Equation	Reference
Archie	$C_t = \frac{C_w \phi^m S_w^n}{a}$	Archie (1942); Kennedy and Herrick (2012)
Simandoux	$C_t = \frac{C_w}{F} S_w^n + V_{sh} C_{sh}$	Bardon and Pied (1969); Worthington (1985)
Waxman-Smits	$C_t = \frac{C_w}{F^*} S_w^n + \frac{B Q_v}{F^*} S_w^{n-1}$	Waxman and Smits (1968); Worthington (1985)

Nomenclature: S_w = water saturation (v/v), C_w = water conductivity (S/m), C_t = true rock conductivity (S/m), F = Archie formation factor, a = tortuosity factor constant, ϕ = porosity (v/v), m = Archie cementation exponent, n = Archie saturation exponent, F^* = Apparent formation factor, Q_v = cation-exchange capacity per unit pore volume (meq/ml), B = equivalent conductance of clay (mho·ml/(meq·m)), C_{sh} = shale conductivity (S/m), V_{sh} = shale or clay volume (v/v).

Table 2-18. Water saturation models and parameters used on some greensands from the literature.

Location	Model	Reference
Trimble Field, Mississippi, USA	Pseudo-Archie using $m=1.8$ and $n=1.77$	Worthington, 2000
Nini Field, North Sea	Pseudo-Archie using $a=1.67$, $m=1.18$, $n=2.4$ and $R_w=0.077$ ohm.m.	Hossain et al., 2012
Trembul Field, Indonesia	Waxman-Smits using $a=1.0$, $m^*=1.76$, $n^*=1.79$ and $R_w=0.19$ ohm.m @148°F.	Prayoga et al., 2018
Glauconite Formation, Southern Chile	Simandoux using $a=1$, $m=2.09$, $n=1.66$.	Gonzalez-Gonzalez et al., 2018
Magallanes Formation, Southern Argentina	Pseudo-Archie using $a=0.8-0.82$, $m=1.4-1.6$, $n=1.4-1.6$ and $R_w=0.3$ ohm.m @150°F.	Aimar et al., 2018

2.4 Discussion

2.4.1 Estimating greensand petrophysical properties

Table 2-19 summarises the challenges to characterise greensand reservoirs petrophysically and recommends which tools or techniques to select when undertaking well-log interpretation, divided into four categories: (1) pay thickness and lithology, (2) porosity, (3) fluids saturation, electrical properties and pressures, and (4) permeability.

Pay thickness and lithology are typically defined with gamma-ray, spontaneous potential, density-neutron separation and photoelectric factor logs. However, some of these log readings get altered for greensands because of glauconite and other clay minerals' presence. Litho-density or photoelectric factor logs and spectral gamma-ray logs are recommended for identifying clayey formations. Additionally, there are commercial logging tools that detect the minerals portion, such as the ECS (Elemental Capture Spectroscopy Sonde), which measures and processes gamma-ray readings to define elements portion such as silicon, iron, calcium, sulphur, titanium, gadolinium, chlorine, barium, and hydrogen (Schlumberger, 2006). Indeed, with core mineralogical data, lithology is enhanced. However, the permeability-porosity cross-plot is scattered, and petrofacies grouping can be difficult to define using only logs or core porosity and permeability. Pore size distribution - PSD - can help review the pore-throats radius range and frequency; if capillary pressure curves are available, threshold and entry pressures can be used as input, too. Finally, geomechanical-derived logs (acoustic) can help as reservoir quality discriminators (Diaz et al., 2003).

Porosity can be determined with logs such as neutron, bulk density or sonic combined with core porosity. Since greensands have complex microstructures and present a bimodal porosity in their pore size distribution, the effective porosity is challenging to estimate with conventional workflows. NMR logs can help define the free fluid and bound water zones per depth and identify the microporosity range. For instance, the CMR

(Combinable Magnetic Resonance) commercial logging tool measures and processes nuclear magnetic resonance to derived lithology-dependent porosity, free- and bound-fluid volumes, permeability derived from SDR, and Timur-Coates equations, among other NMR-derived properties (Schlumberger, 2014). Also, core analysis plays a vital role in determining effective porosity using, for instance, NMR T_2 distribution curves, helium or NMR porosity, and image analysis. However, as Rueslatten et al. (1998) point out, glauconite is paramagnetic because of the iron presence, which induces the magnetic field in the NMR scanners, causing a shortened NMR T_2 relaxation time. Hence, caution must be taken in defining a realistic T_2 cut-off value for greensands decreases as the iron content increases (Dodge et al., 1996).

Fluid content, electrical properties, and capillary pressures are estimated using resistivity logs and core analysis. Greensands are conductive because glauconite and other clay minerals interact with the formation water in their pore walls, adding an extra current throughout the rock; this alters the electric logs and presents high electrical properties (i.e., formation factor and cementation exponent). Also, greensands are water-wet, so they store large amounts of water in their micropores rather than macropores, reflected in high irreducible water saturation and high capillary curve distributions. Core analysis is critical for these properties. Some laboratory techniques that can help understand the electric properties and determine water saturation are cation-exchange capacity determination through a multi-salinity test or destructive method, NMR T_2 distribution curves, and capillary pressure techniques such as MICP (e.g. McPhee et al., 2015). Additionally, it is most likely to use shaly-sands water-saturation models instead of Archie's since these take into account the extra electrical current of clays.

Permeability can be estimated using the Timur-Coates or SDR correlation if NMR logging is available. The interconnected pore-throats in greensands are poor due to their significant cementation degree and high clay mineral presence. The latter may increase permeability impairment due to clay swelling and migration. Core permeability is mandatory by using gas or brine permeability; additionally, NMR T_2 distribution curves are recommended. However, care is needed when applying empirical permeability correlations such as Kozeny's (1927); their applicability and limitations must be comprehended before use.

Additionally, geomechanical analysis complements petrophysics by indicating how stresses behave throughout the rock formation. The in-situ pore pressure, elastic properties, in which direction the fracture propagation will go when performing hydraulic fracturing, rock brittleness, and others. Greensands reservoirs are medium to hard

sandstones; using acoustic logging, the geomechanics features can be derived and used as reservoir quality discriminators like Diaz et al. (2001; 2003) did with the P-impedance.

Table 2-19. Challenges and recommended tools choices for estimating reservoir properties in greensands.

Reservoir property	Challenges in greensand for property estimation	Recommended tools or techniques
Pay thickness and lithology/rock type.	<ul style="list-style-type: none"> - Gamma-ray, bulk density and neutron logs read high values. - Low deep resistivity readings may be confused by a freshwater zone. - Moderate heterogeneity. - Severe scattered porosity-permeability data that difficult to define petrofacies with traditional workflows. 	<ul style="list-style-type: none"> - Elemental, spectral gamma ray and photoelectric factor logs to identify greensand. - Core mineralogical data (e.g. QXRD, XRF or CT scan) to contrast with logs. - Geomechanical properties derived logs can help as discriminators (e.g. P-impedance from acoustic logs). - Pore size distribution from core data (e.g. NMR or capillary pressure curves).
Porosity	<ul style="list-style-type: none"> - The higher the glauconite and/or other clay presence, the more complex the microstructure. - Neutron and density-derived porosity logs readings alteration. - Bimodal porosity distribution (macro- and microporosity). - High microporosity content. 	<ul style="list-style-type: none"> - NMR logs can help in identifying the microporosity zone. - Core porosity data (e.g. helium porosity, NMR porosity, image analysis). - Porosity derived from acoustic logs (e.g. sonic). - Use of lower NMR T₂ cut-off value according to iron presence.
Fluids saturations, electrical properties and pressures	<ul style="list-style-type: none"> - High irreducible water-saturations. - Difficulty in selecting the appropriate water-saturation model. - High capillary pressure curves. - Deep-resistivity log readings are low. - High apparent formation factors and cementation exponents (range from 2.3 to 2.5). - Clay cations create an additional conductivity path inside bound water zones (e.g. cation-exchange capacity high). 	<ul style="list-style-type: none"> - Core analysis data (e.g. electrical properties, NMR, MICP). - Cation-exchange capacity factor determination through core analysis (e.g. destructive or non-destructive method). - Apply a shaly-sand water saturation model or Pseudo-Archie.
Permeability	<ul style="list-style-type: none"> - The higher the glauconite or other clay presence, the less interconnected the pore throats. - Significant cementation degree (silica, carbonate, calcite or berthierine). - Potential clay swelling and migration causing permeability impairment. 	<ul style="list-style-type: none"> - NMR permeability derived-log. - Core permeability data (e.g. gas permeability, brine permeability, MICP derived-permeability, BET analysis). - Pore size distribution data (e.g. NMR tools or capillary pressure curves)

2.4.2 Greensand petrophysical controls

Four controls have been identified in the literature review, which control or govern greensands petrophysical properties (**Figure 2-36**):

- 1) *Glauconite and other clay minerals*, especially chlorite and illite/smectite, may be incorporated into the rock matrix or as pore fillings, increasing the anisotropy (heterogeneity) in the rock properties. Therefore, from the mineralogical standpoint, greensand clays control the lithology, pay thickness, porosity and permeability.
- 2) *Microporosity* since the glauconitic grains form pore throats diameter below 1 μm . These micropores frequently are isolated from the macropores, decreasing the effective porosity, i.e., the interconnectivity of pores. The advantage is that these pores range will store water rather than hydrocarbon (water-wet rock), so greensands are economically feasible reservoirs. From the pore volume standpoint, greensands microporosity controls the capillary pressure, pay thickness, porosity, permeability, and water saturation.
- 3) Due to the significant presence of clays, greensands tend to have *high specific surface areas* because their grain size distribution is small, with poor to moderate sorting. This rock property controls all petrophysical properties since it is directly related to the pore size. The higher the surface area, the poorer the petrophysical properties.
- 4) *Clay minerals' conductivity* adds a second electrical component to the rock formation. These clays' distribution and quantity may electrochemically react with the reservoir formation water electrolytes. Glauconite and other clay minerals present a cation-exchange phenomenon if they are present in the walls of the pores, interchanging cations of the same or lesser valence of the free water. This rock property controls the electrical properties and the water saturation estimation.

These four identified controls from the literature review will be contrasted with this project-specific objectives findings.

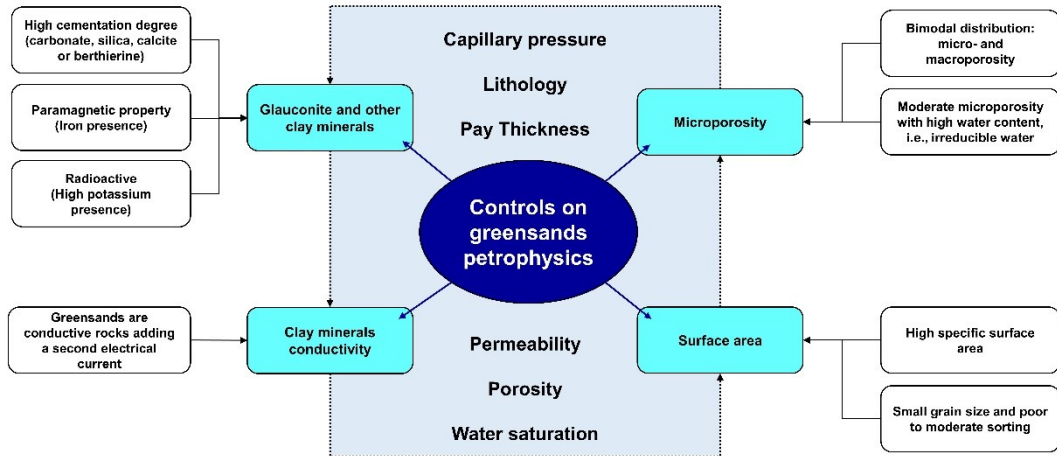


Figure 2-36. Mind map of controls on greensands petrophysics according to the literature review conducted.

2.5 Conclusion

The petrophysical model of a rock formation gives relevant information on the quantity and distribution of petroleum within a rock and its economic productivity. Fundamental petrophysical parameters that must be incorporated into the model are porosity, permeability, saturation and capillary pressure. Predicting these properties at the well-log scale is achieved with innovative logging technology and workflows. Petrophysicists can determine the rock properties that control the petrophysical properties, such as pore size distribution, fabric or texture components, and shale or clay portion presence. Through statistical or computational analysis with experimental data (core and logs), interrelationships between a rock and petrophysical properties are found, contributing to the decision criteria of potential net reservoirs.

The petrophysical characterisation may be challenging when clay minerals are present in sandstones as a matrix or cement. Mechanisms such as clay swelling or migration may occur depending on the presence of clays and their type and distribution, impairing rock permeability. It is noteworthy that clay minerals exchange cations with formation water. Depending on the electrochemical reactions, a second electrical current path is created inside the water formation, which impacts water saturation estimations.

Greensands are iron-rich sandstones whose main clay mineral is the glauconite from the mica group; other clays such as chlorite, smectite, and illite are frequently present. Glauconitic pellets are formed through the glauconitization process where sedimentary buried sandstones evolved from K-poor smectite to K-rich glauconite mica pellets; as glauconitization develops, the content of potassium and iron increases while aluminium decreases. Due to the green colour of glauconite, it may

be confused with other clays, such as clinocllore. Also, its identification from the XRD spectrum may be confused with other clays, such as illite, which also have a 10 Å lattice spacing.

Greensands present a combination of moderate to high porosity, low to high permeability, and high irreducible water saturation, capillary pressure, and specific surface area. They have a bimodal pore size distribution, micro-and macropores, with a significant microporosity portion, meaning that the effective porosity decreases. Since they are water-wet, the water formation will likely be stored in the micropores zone, leaving hydrocarbons mobile in the free-fluid zone.

Further challenges arise when performing a well-logging interpretation for greensands reservoirs since they are radioactive and have high iron and boron content, altering the gamma-ray, neutron, and bulk density log readings. Additionally, greensands are conductive rocks because the clay minerals in the rock wall electrochemically react with the formation of water, adding a second current to the rock and decreasing the deep resistivity log reading. They are expressed as a clay conductivity term in shaly-sands water saturation models. It depends on the cation-exchange capacity (*CEC*) and its maximum cation mobility (*B*) related to the formation of water salinity. Thus, care must be taken when undertaking the petrophysical and mineralogy interpretation, and other logs, such as NMR and PEF, are preferable. Innovative techniques need to be conducted to determine the petrophysical controls on greensands, such as image analysis, machine learning, and statistical or probabilistic techniques.

Four petrophysical controls have been identified in the literature review for greensands: (1) glauconite and other minerals content, (2) microporosity, (3) surface area, and (4) clay minerals conductivity. These controls must be detected through core analysis and logs so the decision criteria of reservoir pay zones can be reliable. Moreover, the water-saturation model must best represent the water content and movable hydrocarbon throughout the rock formation. Archie's model (1942) does not comply with it, and shaly water-saturation models have to be applied, such as the Waxman and Smits (1968) or the Simandoux (Bardon and Pied, 1969) models. The main reason Archie's does not work for greensands is that it does not include the additional clay-bound water electrical current that the mentioned models consider.

Some knowledge gaps in the literature are studies on permeability stress-dependency, experimental relative permeabilities curves, glauconite identification and quantification with laboratory analysis, and electrical properties. This project aims to investigate these knowledge gaps to improve the petrophysical characterisation of the ZG greensand reservoir and to report the findings for contributing to academia and the industry.

Chapter 3 Core analysis methodology

This chapter describes the laboratory analyses and techniques conducted in the core analysis programme. It starts by explaining the cores' arrival state, programme workflow and sampling preparation. It then briefly depicts each technique categorised by the parameter measured.

3.1 Introduction

Much of this research project has involved analysing the petrophysical properties of tight sandstone samples from the study area (

Table 1-3). The methods followed the recommendations provided by McPhee et al. (2015) guidelines and the expertise of the Wolfson laboratory research group at the University of Leeds.

It should be noted that several measurements (e.g. permeability and electrical properties) were under confining pressures. In particular, these measurements were conducted at net confining stresses of up to 3,500 psig. This net pressure was the maximum allowable since the estimated net confining pressure at the ZG greensand formation bottom vertical depth of 2,300 m (Gonzalez-Gonzalez et al., 2018) was around 3,508 psig – assuming a hydrostatic gradient of 0.465 psig/ft. The sampling selection was conducted by ENAP company.

3.2 Condition of core plugs

Core samples were carefully preserved on the same drilling date within a time frame of 16 hours. The sidewall core plugs (ENAP1 set) were inspected and classified as accepted or rejected (broken). The drilling mud was a water-based potassic with a density of 10.2 ppg.

ENAP1 set had 32 core plugs divided into 21 intact samples with cylindrical shapes classified as accepted and 11 broken samples classified as rejected (**Figure 3-1**). ENAP2 set had 15 core sections. Both core plugs and whole cores arrived sealed with cling film, then aluminium foil and waxed (**Figure 3-2**).

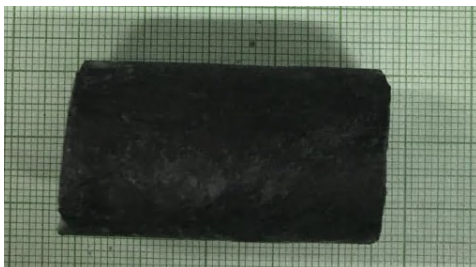


Figure 3-1. Sample ENAP1-9 was classified as accepted (left), and sample ENAP1-10 was classified as rejected (right) before core preservation—pictures supplied by ENAP.

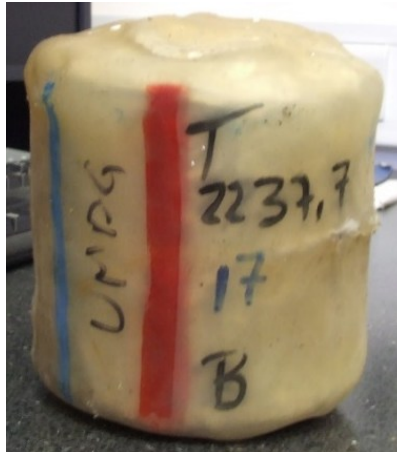


Figure 3-2. Example of the labelling of whole core samples (ENAP2 set). The red line refers to the liner's right side, and the blue line refers to the left side of the liner. T refers to the top, and B to the bottom depths. The number marked in black is the well depth in metres, and the one marked in blue is the tag number.

3.3 Overview of the core analysis programme

The core analysis programme (**Figure 3-3**) workflow involved receiving and checking the core condition when they arrived at the laboratory. The samples were then photographed and labelled. Sealed core plugs were analysed using the Nuclear Magnetic Resonance (NMR) instrument to estimate their initial bulk fluid content and the T_2 distribution, indicating the pore-size distribution. If samples were whole cores, they were horizontally cored at 38 and 25 mm diameter plugs and trimmed; small cuttings or trim ends were also collected.

The samples were then cleaned (**Section 3.4**). Then, the end trimmed and cuttings were distributed to the scanning electron microscopy (**Section 3.5.3**), mercury injection capillary pressure (**Section 3.10**), X-ray diffraction (**Section 3.6.1**), and X-ray fluorescence (**Section 3.7.1**) analyses. Finally, the core plugs were sent to a routine core analysis programme.

The core analysis programme was divided into eight categories related to the analysis type and output data (**Figure 3-4**). Digital imaging (**Section 3.5**) involves a visual interpretation of the rock macro-and microstructure, heterogeneity, and identification of fractures or cracks and clay minerals groups. Mineralogy characterisation (**Section 3.6**) provides rock composition in minerals identification and chemical elements. Pore volume (**Section 3.8**) is derived into porosity and grain density. Permeability (**Section 3.9**) was measured with a single phase (gas and brine), where steady-state and pulse-decay methods were applied, depending on the core's permeability range. NMR spectroscopy (**Section 3.11**) derives into pore size distribution and immobile fluid fraction. Electrical measurements (**Section 3.12**) were

used to determine the rock resistivity and synthetic formation water resistivity (brine) to derive the cementation exponent m . Finally, the BET (Brunauer-Emmett-Teller) technique (**Section 3.13**) was used to measure the specific surface area (SSA).

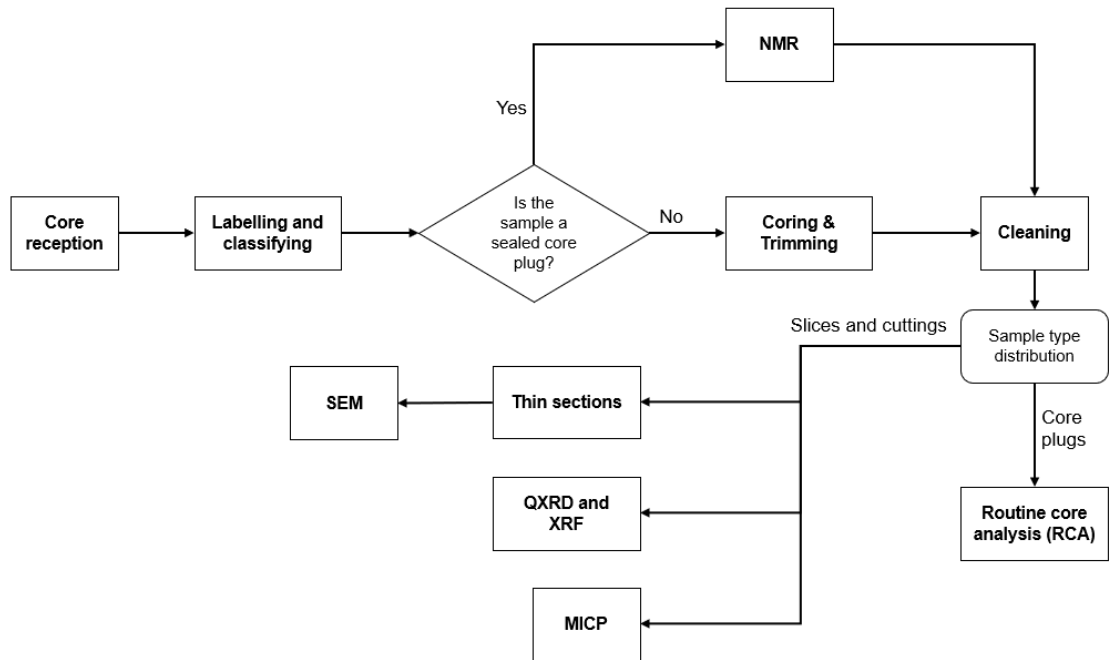


Figure 3-3. Core analysis programme workflow.

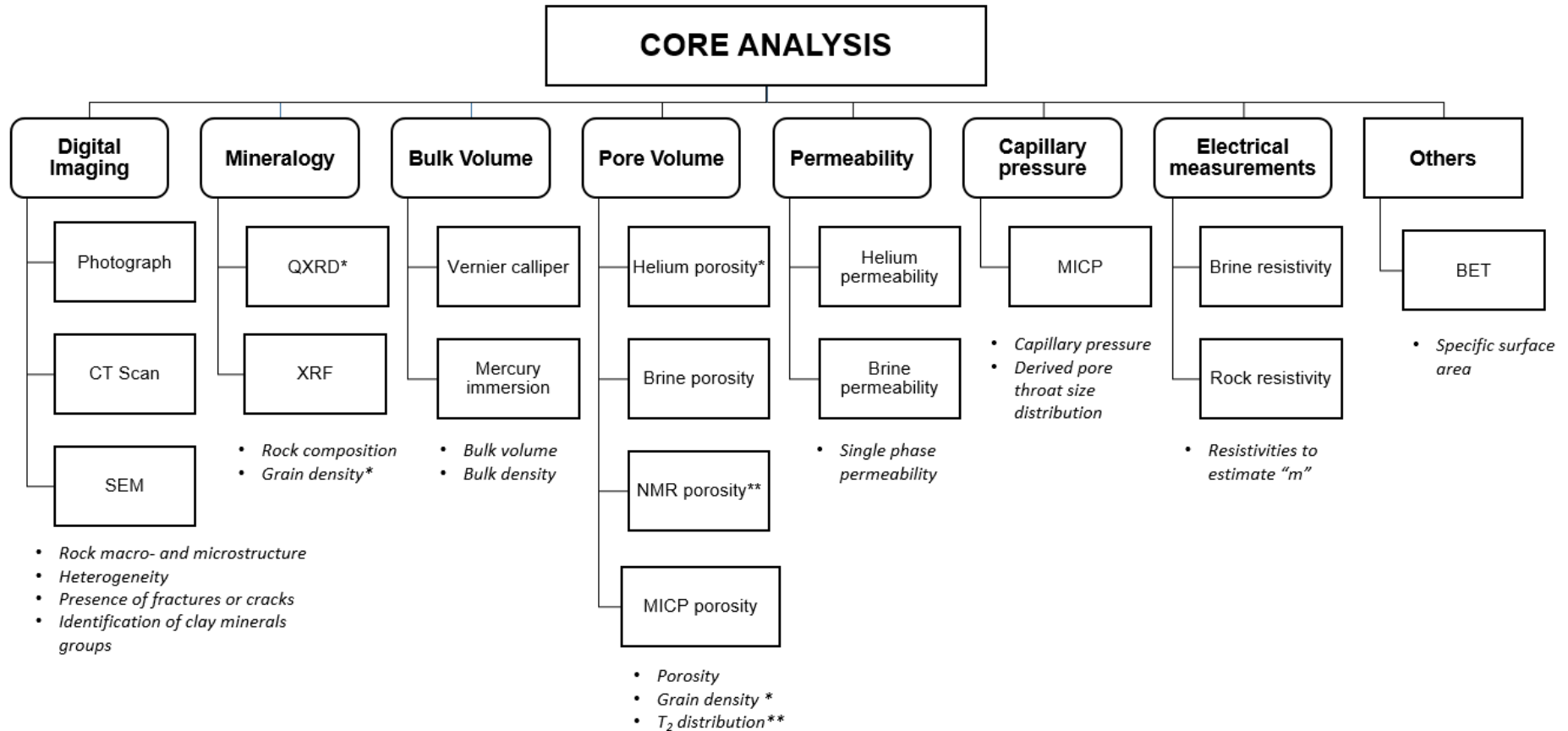


Figure 3-4. Flowchart of laboratory experiments undertaken in the core analysis programme, divided into nine categories: digital imaging, mineralogy, bulk volume, pore volume, permeability, capillary pressure, electrical measurements, and others. The properties estimation and identification of main rock features are listed at the end of each category.

3.4 Sample cleaning

All samples were cleaned in three stages: Soxhlet extraction, methanol immersion, and oven-drying to remove in-situ hydrocarbons and water, mud filtrates, and salts. Soxhlet extraction is a distillation-extraction process which removes organic matter inside the core with a selected solvent that flushes in cycles until it changes into a darkish colour. The samples were cleaned with dichloromethane (DCM) as a solvent with a normal boiling point of 40°C (Merck, 2023). All the samples were then immersed in methanol to remove any salt present; the conductivity of the solution was constantly measured to assess when the salt dissolution was complete. The methanol was replaced several times until no significant increase in conductivity was detected. Once cleaned with methanol, the samples were air-dried before placing them in an oven for 1 to 3 days at no more than 65°C to prevent dehydration of the interlayers of clay minerals (Soeder, 1986). The weight of the samples was measured repeatedly to ensure the drying process was complete. Samples were then stored in a desiccator.

3.5 Digital imaging

The structure of samples was recorded digitally at a range of scales using a range of techniques. In particular, optical photographs were taken of each sample to record their overall structure (**Section 3.5.1**). The heterogeneity degree of the samples was assessed using a medical-type CT scanner (**Section 3.5.2**). The microstructure of the samples was assessed using scanning electron microscopy (**Section 3.5.3**).

3.5.1 Photography

Each core plug was photographed, showing the longitudinal and cross-sectional views to have visual evidence. Each sample was photographed with its tag, depth location and scale bar. Typically, white and ultraviolet lights display the rock structure and features. At the Wolfson laboratory, white lights were available.

3.5.2 X-ray computer tomography (CT) scanning

CT scanning involves measuring the absorption of an X-ray beam after it has passed through the sample. Medical CT scanners have been adapted for these purposes. Computer software processes the CT scan information into a pixelated image. Each image pixel has X, Y, and Z values, forming a cuboid called a voxel and a grey scale intensity value (Hounsfield unit, HU). HU brightness is proportional to the material density. Higher-density materials absorb more X-ray energy and show as white (3700

HU), while lower-density materials absorb less X-ray energy and show as black (-1000 HU); hence the original colour palette is greyscale. CT images can provide information about the core structure, heterogeneity, bedding planes, and mineralogical and lithological changes. They can also be used for other applications, such as fluid distribution, formation damage, saturation monitoring, fracture mapping, and mud invasion (Withjack et al., 2003).

The CT scanner used in this study was a BRIVO CT385 model (**Figure 3-5**). The effective resolution of the CT images was approximately $200\ \mu\text{m} \times 200\ \mu\text{m} \times 625\ \mu\text{m}$ (X \times Y \times Z directions), which corresponds to the minimum size of an identifiable feature. Core plugs were CT scanned in two orthogonal views parallel to the length of the plug. The output DICOM (Digital Imaging and Communications in Medicine) files were processed using ImageJ Fiji software (<https://imagej.nih.gov/ij/index.html>). Data analysis included grouping the samples by their heterogeneity degree through visual interpretation and statistical analysis. Each DICOM file was cropped in a region of interest (ROI), excluding the margins of the CT scan image, which are black colour, and the ROI's statistics (area, mean, minimum, maximum, and standard deviation) were printed out of the grey scale pixels counting. The grey pixels were coloured in a brown scale based on a look-up table to display variations in density within the sample. Hence, a black pixel indicates pores/lowest density; white indicates high-density minerals, and pixels displayed in brown scale indicate the rock portion (**Figure 3-6**). Finally, the two orthogonal images per sample were merged for montage side-by-side and converted into an 8-bit TIFF image file.



Figure 3-5. Wolfson CT Scanner with seven core plugs of ENAP2 set.



Figure 3-6. Pixel colour map used in final CT scan images.

3.5.3 Scanning electron microscopy (SEM)

The SEM produces images by scanning a focussed beam of electrons on the surface sample and recording the various signals (electrons, photons or X-rays) produced by the interaction of the emitted electrons with the sample (**Figure 3-7**). BSEs (back-scattered electrons) and SEs (secondary electrons) are the most relevant in obtaining high-resolution sample images—both result from scattering interactions between the electron beam and the sample's atomic nuclei. BSEs collide elastically, i.e. they maintain their primary energy and back out of the sample as back-scattered electrons with high energy (>50 eV) and can navigate into deeper regions of the sample, reaching 100-1,000 nanometres. In contrast, SEs collide inelastically, i.e. they lose kinetic energy and may be transformed into X-ray radiation and only navigate in the sample's near-surface region. SEs are helpful for the topography surface of the sample with only a few nanometres, while BSEs give detailed information on the sample microstructure and minerals identification. Other signals, such as the cathodoluminescence (CL) photons and Auger electrons, can be detected. The first is a radiation phenomenon in the visible wavelength due to the recombination of excited electrons of the valence band to their ground state. The second is surface electrons with lower depth exploration than SEs. Finally, if an EDX (energy dispersive X-ray) detector is attached to SEM, a chemical micro-analysis can be conducted to identify the chemical elements in a region of interest in the sample (Vanderlinde, 2019; Krishnan, 2021).

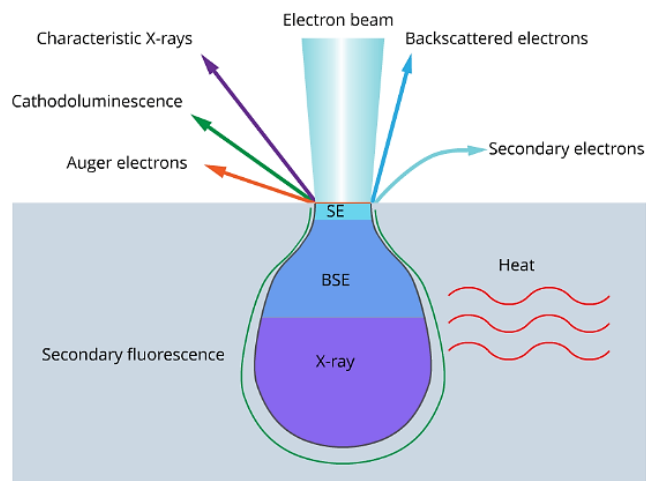


Figure 3-7. Signals resulting from the interaction between a primary electron beam and specimen (extracted from MyScope, 2023).

3.5.3.1 Sample preparation

Sample preparation substantially influences the quality of BSE images; therefore, the rock lithology must be examined before making thin block sections to determine the appropriate preparation process (Krinsley et al., 1998). The project samples were prepared with low-viscosity epoxy in a polished block and thin sections. A four-stage

grinding and polishing with 6- μm , 3- μm , 1- μm and $\frac{1}{4}$ - μm diamond paste were applied. Additionally, core slices were dyed with blue epoxy to fill and highlight the pore spaces on the glass microscope slides visible. The thin sections were carbon coated prior to SEM analysis to prevent charging. In addition, fractured bits from geomechanical tests were collected, mounted, and gold coated for analysing and capturing magnified resolution BSE images.

3.5.3.2 Sample analysis

Whole thin-section images were scaled at 10 mm and 5 mm, while detailed microstructure features were scaled at 500 μm , 200 μm , 100 μm or 50 μm . Confirmation of minerals was checked with Back-scattered Scanning Electron software. All the BSE images were obtained using the TESCAN VEGA3 XM equipment from the School of Chemical and Process Engineering, University of Leeds (Figure 3-8) and stored as TIFF files in the project folder server.



Figure 3-8. Scanning electron microscopy model Tescan VEGA3 XM consists of a tungsten source machine with a large chamber and high sample throughput, equipped with X-max 150 Energy Dispersive X-ray spectroscopy (EDS) and Aztec 3.3 software. Also RGB filtered cold-cathode (CL) system (reference photograph from TARR, 2023).

3.6 Mineralogy

A quantitative indication of the mineralogy of the samples was determined using X-ray diffraction analysis. Care was taken to ensure the results were consistent with the minerals identified using SEM.

3.6.1 X-ray diffraction (XRD)

XRD involves irradiating a solid powder material with incident X-rays, generating a diffraction pattern that can identify the minerals present (i.e. Eslinger and Pevear, 1988). The XRD analyses followed the X-ray laboratory protocols of the Earth Sciences Department at the University of Leeds. Bulk and clay-XRD analyses were undertaken. The first characterises the bulk mineralogy of the rock. The second identifies the clay minerals groups' presence in the clay fraction of the sample.

The rock sample was prepared for the bulk-XRD technique by grinding it in a mortar and pestle with 20% wt. of corundum ($\alpha\text{-Al}_2\text{O}_3$) as the internal standard. Then, a slurry mix is prepared using an XRD-Mill McCrone by rinsing a 0.5%wt PVA solution and 0.1 ml (two drops) of octanol into a McCrone vial and ground for 12 minutes to disaggregate more of the grains ($< 1\mu\text{m}$). The slurry was placed in a spraying bottle; deionized water may be used to recover part of the slurry inside the vial to enter into a spray-drying oven preheated to 130°C . The dry sample is collected with paper at the bottom of the oven, then placed into a tube holder and ready for the XRD analysis. The Philips PW1050 diffractometer has a Cu $K\alpha$ source with a secondary graphite monochromator and a scanning range of 3 to 105° . The Rietveld (1969) method obtained the output results with a 95% confidence level of $\pm X0.35$, where X is the concentration in %wt.

The clay-XRD technique separates the clay fraction from the bulk rock sample by sedimentation-decantation after grinding. 10 g of fine grain sample was placed into a graduated tube and filled with tap water to cover 22 cm of marked height to settle for 17 hours with sodium hexametaphosphate solution as a dispersing agent to prevent flocculation. Afterwards, the suspended solution was separated by vacuum filtering with a filter paper of $0.4\mu\text{m}$ and placed in a slide. One or two slides per sample were prepared for the XRD. Four scans were run per prepared slide: (1) air-dried, (2) ethylene glycol treatment to expand swelling clays, and heat treatment at (3) 300°C and (4) 550°C to help identify clay minerals by changes in the crystal structure or loss of structure. The four scans were compared using the traces package load and the peaks d-spacing in the Bruker EVA software. All the slides were run at the same conditions: a start angle of $3^\circ 2\theta$ and an end angle of $35^\circ 2\theta$ with a rotation of $0.6^\circ/\text{min}$ and a step size of 0.02.

3.7 Bulk chemistry

The bulk chemistry of samples was determined using X-ray fluorescence (XRF) as described below.

3.7.1 XRF methodology

XRF is a non-destructive analytical procedure. X-rays or gamma rays emitted to the sample produce fluorescent or secondary X-rays as fingerprints, unique for each chemical element. The CPU processes these fluorescent X-rays and converts the spectral data to detailed compositional data (Seyama et al., 2006). The Department of Geology, University of Leicester, undertook the XRF analysis for trace elements with a PANalytical Axios Advanced WD-XRF spectrometer and major elements with the Rigaku ZSX PrimusIV WD-XRF spectrometer. The reported major elements were SiO_2 , TiO_2 , Al_2O_3 , Fe_2O_3 , MnO , MgO , CaO , Na_2O , K_2O , P_2O_5 , Cr_2O_3 and LOI (loss on

ignition). The latter represents the mass loss on sample powders ignited. The reported traces elements were As, Ba, Ce, Co, Cr, Cs, Cu, Ga, La, Mo, Nb, Nd, Ni, Pb, Rb, Sb, Sc, Se, Sn, Sr, Th, U, V, W, Y, Zn and Zr.

3.8 Porosity

Porosity, ϕ , is not measured directly but is calculated from two of the three properties: bulk volume (BV), pore volume (PV) or grain volume (GV), using:

Equation 3–1

$$\phi = \frac{PV}{BV} = \frac{BV - GV}{BV} = 1 - \frac{GV}{BV}$$

where ϕ is expressed as fractional volume (v/v), which can be multiplied by 100 to provide the percentage value (%v/v). Techniques used to measure bulk volume, grain volume and pore volume are described in **Sections 3.8.1, 3.8.2, 3.8.3** and **3.8.4**, respectively.

3.8.1 Bulk volume

Bulk volume was determined using two methods. First, the dimensions of the sample were measured using the Vernier calliper (**Section 3.8.1.1**), and then the mercury immersion method was used (**Section 3.8.1.2**).

3.8.1.1 Vernier calliper

Vernier calliper was used when the core plugs had a uniform cylindrical shape for determining the bulk volume. Six diameter and length measurements were taken, and the arithmetic mean defined the average diameter and length. These were then used to calculate the core plug bulk volume (cylindrical shape).

Equation 3–2

$$BV = \pi \frac{\bar{D}^2}{4} \bar{L}$$

where \bar{D} is average diameter and \bar{L} is the average length (cm), BV is the bulk volume (cm³).

3.8.1.2 Mercury immersion

This technique applies Archimedes' mercury immersion method (**Figure 3-9**). The core plugs were immersed in mercury, and the bulk volume was calculated by the volume of the mercury displaced using:

Equation 3–3

$$BV = \frac{W_{Hg_displ}}{\rho_{Hg}}$$

where W_{Hg_displ} is the mass of mercury displaced (g), ρ_{Hg} is mercury density at room temperature (g/cm^3), and BV is the bulk volume (cm^3).

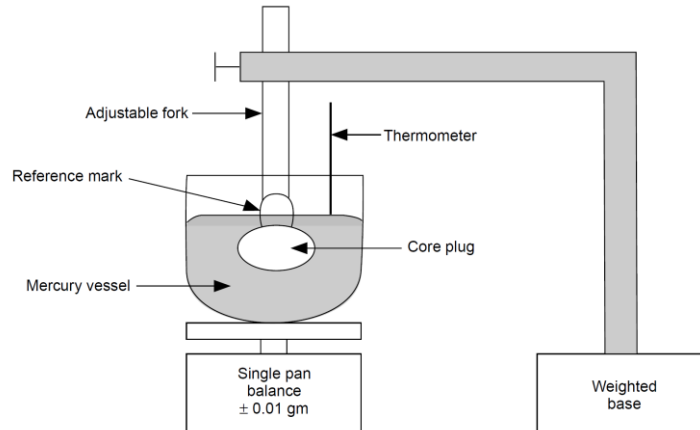


Figure 3-9. Archimedes mercury immersion diagram (API RP40, 1998).

The bulk density can be obtained as:

Equation 3-4

$$\rho_{Bulk} = \frac{W_{dry}}{BV}$$

where ρ_{Bulk} is bulk density (g/cm^3), W_{dry} is the dry sample weight (g), and BV is the bulk volume (cm^3).

Note: the mercury immersion bulk volume was used for further derived calculations since it presents an accuracy of $\pm 0.01 \text{ cm}^3$ compared to the calliper measurement reaching 0.15 cm^3 . The latter assumes a cylindrical regular shape of cores, so it does not consider uneven shapes and surface irregularities (API RP40, 1998).

3.8.2 Grain volume

Grain volume was determined using helium pycnometry, a technique based on Boyle's law in which helium gas is expanded into a chamber containing the sample and allowed to equilibrate. A valve is then opened to allow gas to expand into an empty reference chamber. The grain volume is then calculated based on the change in pressure, as explained below. The measurement is made at ambient stress, assuming constant temperature. A stereopycnometer Quantachrome Spy-2 model (**Figure 3-10**) was used at the Wolfson laboratory to undertake this experiment.

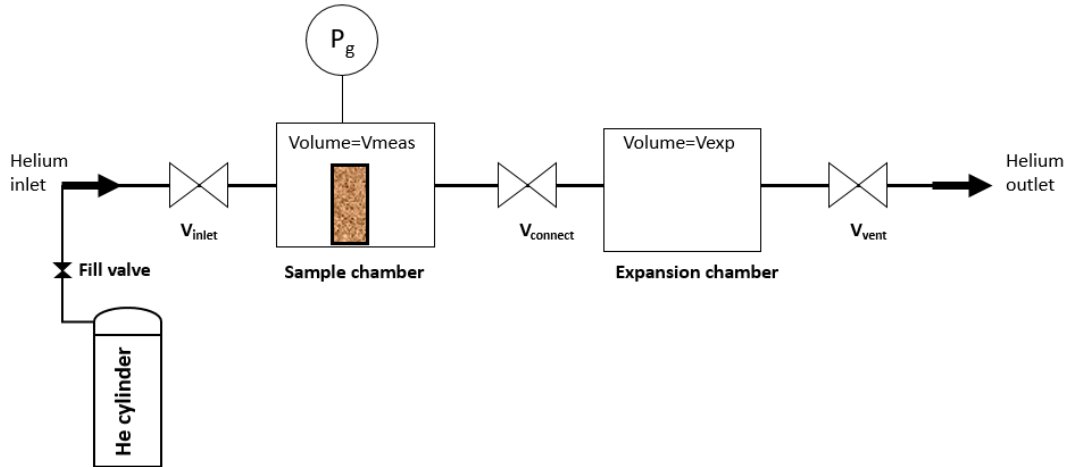


Figure 3-10. Diagram of the stereopycnometer. V_{inlet} = helium inlet valve, $V_{connect}$ = connecting valve of chambers, V_{vent} = cell vent valve, P_g = sample chamber pressure transducer.

3.8.2.1 Calibration

The calibration is run first with the sample cup empty ($V_s=0$) and then with a ball-bearing calibration volume (V_c), whose volume is close to the bulk volume range of the dataset. Each test is run six times, and with the $P1/P2$ ratio, the reference chamber volume (V_{meas}) and the expanded volume from the sample chamber (V_{exp}) are used:

Equation 3–5

$$V_{exp} = \frac{V_c}{\frac{1}{\left[\left(\frac{P1}{P2}\right)_{V_s=0} - 1\right]} - \frac{1}{\left[\left(\frac{P1}{P2}\right)_{V_c} - 1\right]}}$$

Equation 3–6

$$V_{meas} = V_c + \frac{V_{exp}}{\left[\left(\frac{P1}{P2}\right)_{V_s=0} - 1\right]} = \frac{V_{exp}}{\left[\left(\frac{P1}{P2}\right)_{V_c} - 1\right]}$$

where V_g is the grain volume of the core sample, V_c is the sample chamber volume (matrix cup), V_r is the reference chamber volume, $P1$ is the reference chamber pressure, and $P2$ is the sample chamber pressure.

3.8.2.2 Grain volume measurement

After calibration, the test was ready for the core plugs by measuring the reference chamber and the sample chamber pressures, $P1$ and $P2$. Equation 3–7 calculates the grain volume of the core sample, and Equation 3–8 calculates the grain density. Finally, the pore volume was obtained by subtracting the grain volume from the bulk volume (Equation 3–1), and thus the grain volume can be calculated using:

Equation 3–7

$$GV = V_c - V_r \left(\frac{P_1}{P_2} - 1 \right)$$

where GV is the grain volume of the core sample, V_c is the sample chamber volume (matrix cup), V_r is the reference chamber volume, P_1 is the reference chamber pressure, and P_2 is the sample chamber pressure.

Equation 3–8

$$\rho_{grain} = \frac{W_{dry}}{GV}$$

where W_{dry} is the dry core plug mass (g) and ρ_{grain} is the grain density (g/cm³).

3.8.3 Brine pore volume

Brine porosity was determined by weighing the dry core plug, then saturating it with a brine solution representing the reservoir's formation of water (SWF) and weighing the saturated core plug. Each core plug was submerged in the SWF, and a vacuum was applied to remove the air bubbles inside the rock for at least 8 hours; as the vacuum was released, the SWF flowed into the evacuated pore volume. Brine pore volume was calculated by weight difference and brine density (Equation 3–9), and the brine porosity was calculated (Equation 3–1).

Equation 3–9

$$PV_{brine} = \frac{W_{sat} - W_{dry}}{\rho_{brine}}$$

Where W_{sat} is the saturated core plug mass (g), W_{dry} is the dry core plug mass (g), ρ_{brine} is the brine density (g/cm³), and PV_{brine} is the brine pore volume (cm³).

3.8.4 Stressed helium pore volume

Custom-made auto porosity equipment at the Wolfson laboratory measures the helium pore volume at stress conditions (**Figure 3-11**). This setup is a modified version of the grain volume equipment (**Section 3.8.2**), with the difference that it directly measures the pore volume of the sample space by applying Boyle's law.

The experiment starts by placing a dry sample on the Hassler core holder, where the confining pressure is applied and monitored. It is connected with an upstream and downstream reservoir (V_1 and V_2) with known volumes, and their pressures are measured. The upstream valve of the Hassler is closed. Helium enters the upstream reservoir at a defined pressure of 150 psig and known volume, and then the helium cylinder valve is closed. The helium stored at the upstream reservoir is expanded to the Hassler core holder by opening its downstream valve so that helium penetrates the sample's pore-empty space. The pressure difference is monitored until stabilisation, where the upstream and downstream pressures are equal, with no change in the pressure greater than 0.05 psig/hour. The pore volume is derived from the initial and final pressure ratio using the calibration correlation from standards of known pore volume (Equation 3–10). This process is a forward cycle, and since it creates a pressure pulse that decays, the core permeability can be derived (**Section 3.9.2**). Finally, two reverse cycles are performed to vent the helium gas (needle valve open) before subsequent pore volume measurements with increased confining pressure. The calibration involves measuring the pore volume of stainless steel plugs with defined grain size and the upstream and downstream pressure ratio. An empirical correlation (linear trend) results from cross-plotting these two parameters. In addition, reference and system dead volumes are defined (API RP40, 1998).

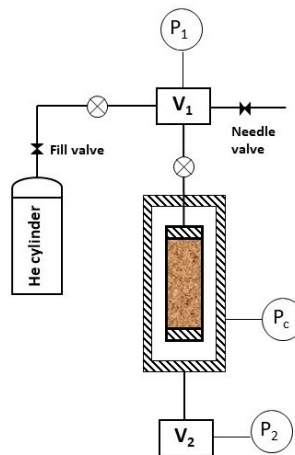


Figure 3-11. Auto porosity diagram. V_1 = upstream reservoir, V_2 = downstream reservoir, P_1 = upstream pressure transducer, P_2 = downstream pressure transducer, P_c = confining pressure gauge.

Equation 3–10

$$PV_i = \frac{\left(\frac{P_{up}}{P_{dn}} - Intercept \right)}{Slope}$$

This technique measures all space, including the platens dead volume of the Hassler core holder and the annulus pore volume between the sample and the internal rubber sleeve (McPhee et al., 2015). This volume is known as conformance pressure and pore volume (Figure 3-12), and it is empirically determined per sample. The annulus pore volume (Equation 3-11) is calculated to correct the actual stressed pore volume (Equation 3-12) and derive the stressed porosity (Equation 3-13).

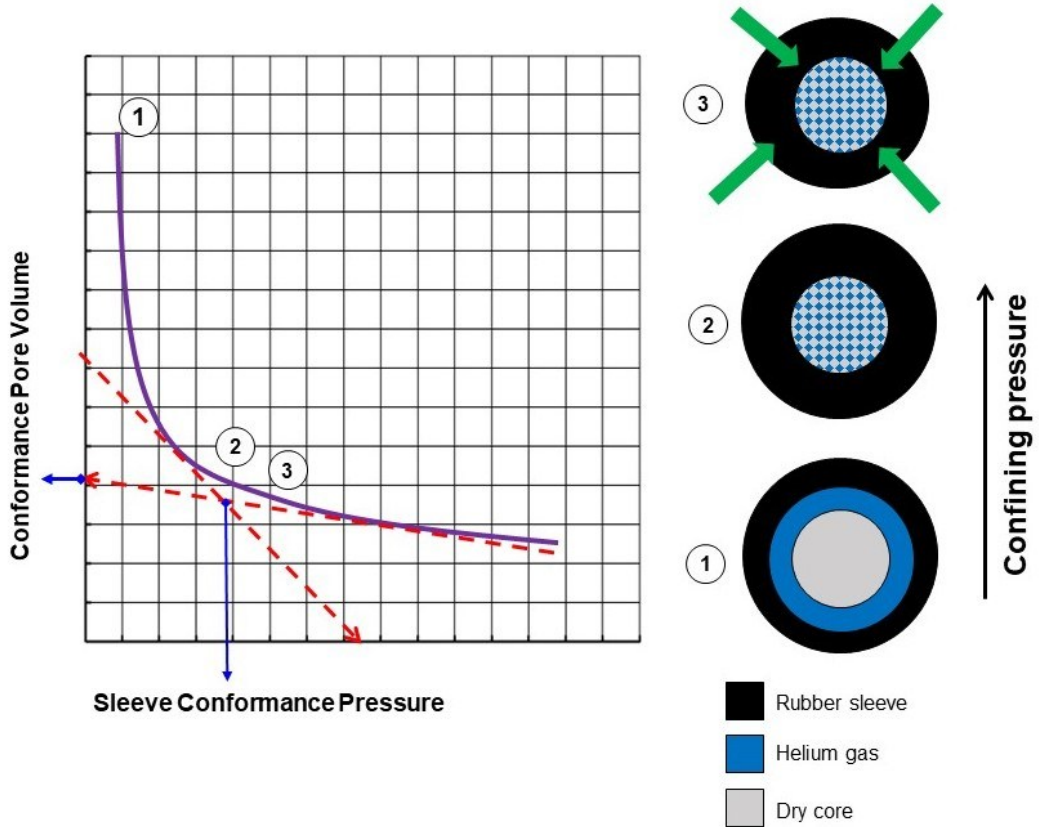


Figure 3-12. Scheme of sleeve conformance pressure and pore volume detection: (1) the dry core plug is initially confined at low pressure; as the confining pressure increases, the helium surrounding gas between the sample and the rubber sleeve enters the space. (2) The rubber sleeve will progressively conform to the sample surface, pushing the helium gas to enter inside the pore space. Here is the stress point at which the sleeve exactly conforms to the sample surface, known as Sleeve Conformance Pressure (SCP) and Conformance Pore Volume ($PV_{conformance}$). (3). From this point onwards, the measurements are considered to derive the stressed pore volume of the sample.

Equation 3-11

$$PV_{annulus} = PV_{initial} - PV_{conformance}$$

Equation 3-12

$$PV_{stress} = PV_i - PV_{annulus}$$

Equation 3-13

$$\phi_{stress} = \frac{PV_{stress}}{GV + PV_{stress}}$$

where $PV_{annulus}$ is the annulus pore volume (cm^3), $PV_{initial}$ is the initial pore volume in the experiment (cm^3), $PV_{conformance\ i}$ is the conformance pore volume shown in **Figure 3-12** (cm^3), PV_{stress} is the stressed pore volume in the measurement i (cm^3), PV_i is the pore volume of the measurement i (cm^3), and ϕ_{stress} is the stressed core porosity (v/v).

3.9 Permeability

Several laboratory techniques are available to measure the permeability of rocks depending on their permeability range value (**Figure 3-13**). These techniques are named after the flowing state of the fluid inside the rock, that is, steady- and unsteady-state (or transient). Unsteady-state techniques include the oscillating pressure, GRI (Gas Research Institute) protocol, and pulse-decay, while steady-state techniques are based on Darcy's law.

For low permeability rocks (<0.1 mD), the steady-state flow permeability measurement is not practical because of the time needed for the initial pressure equilibrium, and the steady-state is very long, decreasing the measurement accuracy (Cui et al., 2009). Hence, unsteady-state techniques are preferred, whereas, for tight rocks, the pulse-decay is the most frequently used (e.g. Chen and Stagg, 1984; Haskett et al., 1988).

In the Wolfson laboratory, helium gas was used to measure gas permeability, while brine (synthetic reservoir water) measured the liquid permeability. The steady-state and pulse-decay techniques were used on the project core plugs. The samples were loaded into a Hassler-type core holder with a stress load applied with an oil pump.

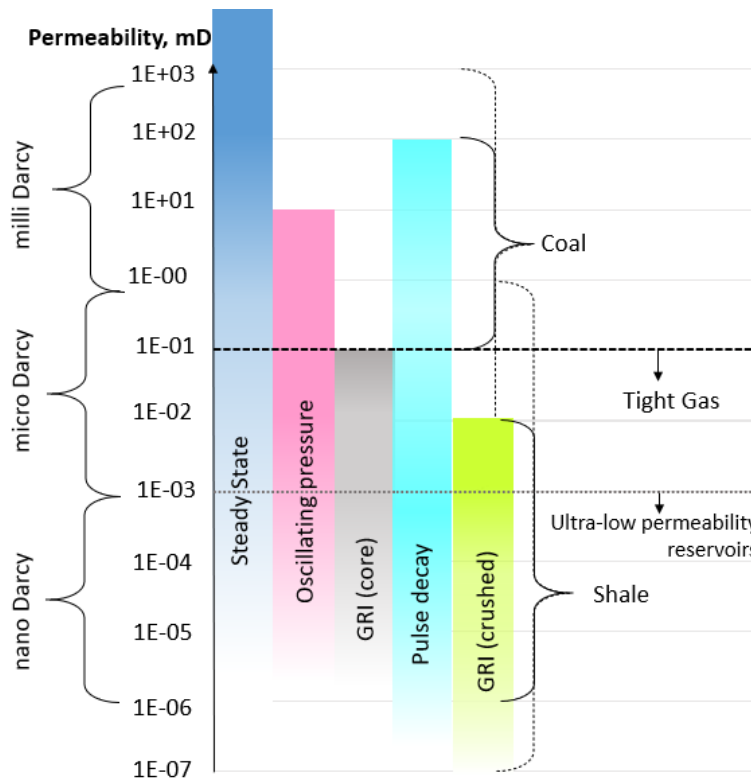


Figure 3-13. Permeability ranges of unconventional reservoir rocks and measurements ranges of different experimental methods. Some methods' gradients across the measurement range highlight the range over which they are most effective; the solid bracket indicates the typical permeability range; the dashed line bracket indicates the possible permeability range (modified after Sander et al., 2017).

3.9.1 Steady-state experiment

This technique applies Darcy's Law, where a single fluid (gas or liquid) flows throughout the core plug at a constant flow rate and confining pressure. The pressure drop and flow rate are the output data to measure the core plug permeability. There are four assumptions when applying Darcy's law:

- The fluid must saturate the core plug entirely and in a single phase.
- The selected fluid must not interact with the porous media walls -i.e., inert.
- The flowing of the fluid must be laminar; that is, smooth particle layers do not mix.
- The permeability must be constant throughout the cylindrical core plug.

Equation 3–14

$$k = \frac{Q\mu L}{(P_1 - P_2)A}$$

where k is the permeability (Darcy), Q is the fluid flowrate (cm^3/s), μ is the fluid viscosity (cP), L is the core plug length (cm), A is the core plug cross-sectional area in (cm^2), and P_1 and P_2 are the inlet and outlet pressure (atm).

An important aspect is the compressibility of fluid when a gas is selected to measure permeability, like helium or nitrogen, and laboratories use the atmospheric gas pressure and flowrate and the mean pressure in a modified Darcy's formula valid for high flow rates using:

Equation 3–15

$$k_g = \frac{Q_a P_a \mu L}{(P_1^2 - P_2^2) A}$$

where k_g is the gas permeability (Darcy), Q_a is the gas flow rate in (cm³/s), and P_a is atmospheric gas pressure (atm).

3.9.1.1 Klinkenberg correction

A slippage effect occurs when using low pressures for gas permeability measurements, known as the Klinkenberg effect. The gas molecules travel faster when contacting the pore walls of tiny pore throats, affecting the precision measurement, which is crucial for low-permeability rocks. Klinkenberg (1941) postulated that the slippage effect is corrected by interpolating the permeability to an infinite mean pressure, meaning that the gas molecules are together with no space to slip, behaving as a liquid. Typically, three to four measurements at different flow rates are undertaken. Then, the measured gas permeability against the inverse mean pressure is plotted (**Figure 3-14**), and the Klinkenberg permeability is determined (intercept point on the y-axis) using:

Equation 3–16

$$k_g = k_{\infty} \left(1 + \frac{b}{p_{av}} \right)$$

where k_g is the gas-measured permeability (mD), k_{∞} is the absolute or Klinkenberg permeability (mD), b is the Klinkenberg constant, and P_{av} is the mean flow pressure (atm), equal to $(P_1 + P_2)/2$.

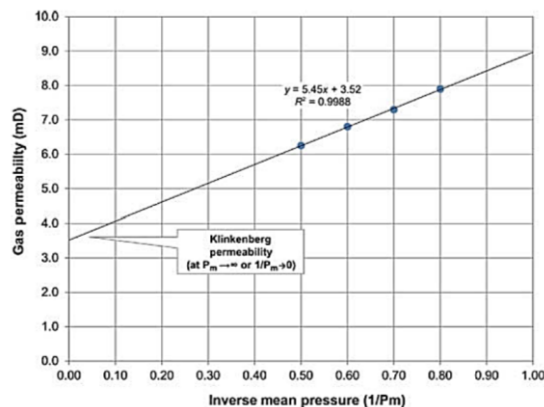


Figure 3-14. Klinkenberg plot with laboratory core data (McPhee et al., 2015).

3.9.2 Pulse-decay gas permeameter

The pulse-decay experiment setting (**Figure 3-15**) follows the method presented by Jones (1997). The first step is establishing the pressure equilibration throughout the system by adding two large reservoirs (V_0 and V_3) connected to the upstream and downstream main reservoirs (V_1 and V_2). Therefore, differential pressure decay is faster to produce. The pressure pulse is generated by bleeding off the gas through the shut-off valve with the needle valve slightly open.

The experiment is automated and uses software that applies the calculation presented in Jones (1997) to measure the gas permeability and the constant mean pressure. Five to six runs with decreasing mean pressure at specific confining pressure were conducted, and the actual gas permeability was obtained using Equation 3-16 to consider the Klinkenberg correction. The final permeability reported was the Klinkenberg permeability at three confining pressures (1,500, 2500, and 3,500 psigg). In addition, the effective pressure was calculated by subtracting the confining pressure minus the mean pore pressure at each confining pressure to review the trend in the low-permeability range of the project core plugs.

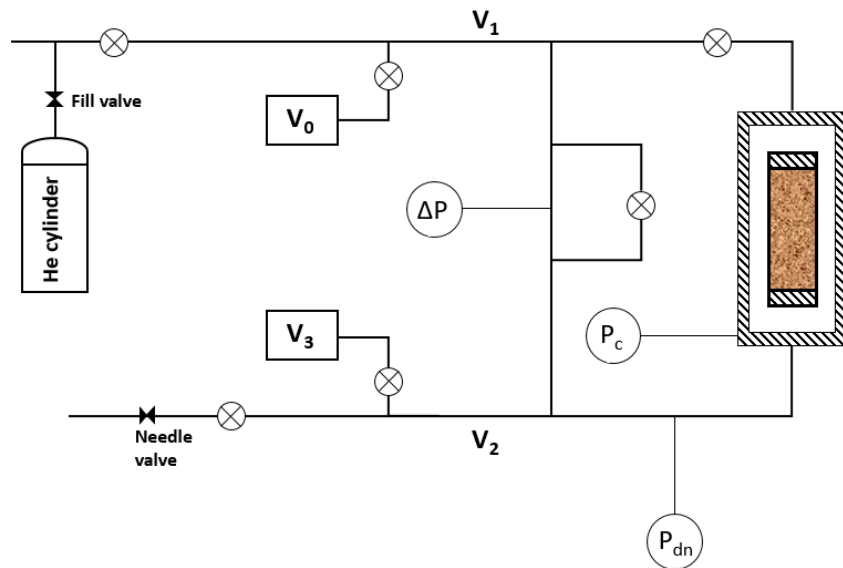


Figure 3-15. Diagram of the apparatus for gas pulse-decay experiment. $V_0=V_3$ large reservoir, $V_1=$ upstream reservoir, $V_2=$ downstream reservoir, $\Delta P=$ differential pressure transducer, $P_c=$ confining pressure gauge, $P_{dn}=$ downstream pressure transducer.

3.9.3 Pulse-decay brine permeameter

The pulse-decay experiment setting (**Figure 3-16**) follows Amaefule et al. (1986) technique and calculation. The upstream reservoir (V_{up}) is small, around 10 cm³ of brine, and the downstream reservoir is a large compressible volume of gas pressurised at 120 psigg. That way, when the pressure pulse decay is generated, the downstream reservoir pressure is constant while the upstream reservoir pressure is depleted.

The pore pressure of the whole system was at 120 psig with a confining pressure of 1,500 psig in the core holder. Before producing the pulse, valves 4 and 2 must be closed, and the differential pressure transducer must be zero. Then, by closing valve 3 and opening valve 1, the pump increases the pressure in V_{up} to ~196 psig. Valve 1 is then closed. Finally, opening valve 3 increases the differential pressure across the core plug. Differential pressure and time were recorded and processed in an automated spreadsheet. The brine permeability is estimated by applying the calculation outlined in Amaefule et al. (1986).

Each core sample was left one day at 120 psig pore pressure to allow pressure equilibrium across the core plug, and at least two runs were conducted per sample to ensure repeatability.

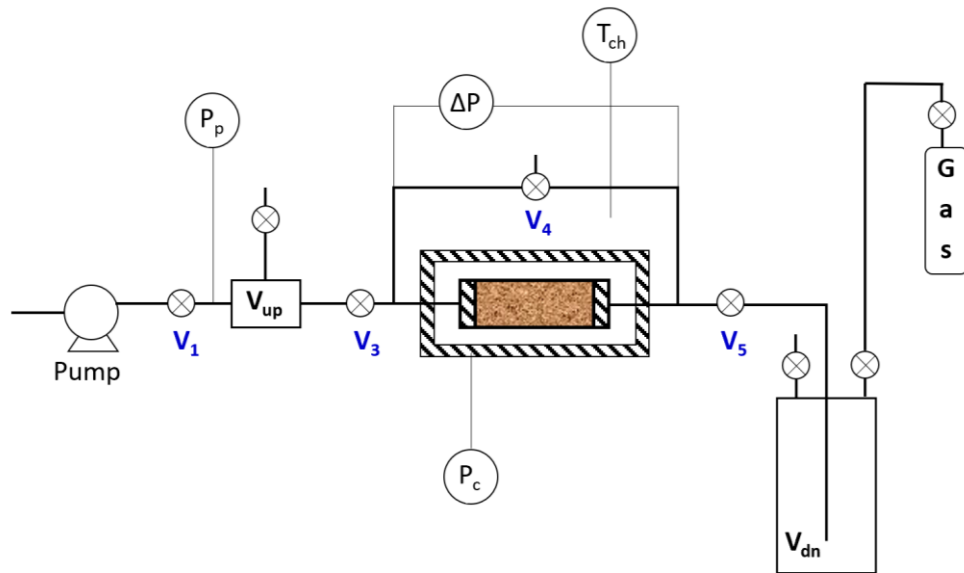


Figure 3-16. Diagram of the apparatus for liquid pulse-decay experiment. V_{up} = upstream reservoir, V_{dn} = downstream reservoir, P_p = pore pressure transducer, ΔP = differential pressure transducer, P_c = confining pressure gauge, and T_{ch} = chamber temperature.

3.10 Mercury injection capillary pressure (MICP)

MICP was used to estimate the capillary pressure and pore throat size distribution by injecting mercury (non-wetting phase) into air-dried (wetting phase) core samples. The Micromeritics Autopore IV 9520 apparatus was used (Figure 3-17), which has a high-pressure automated system reaching up to 60,000 psig into small samples of ~3 cm³.



Figure 3-17. Micromeritics Autopore IV series model (AZO materials, 2023).

Washburn's (1921) equation and the pore size distribution equation derived from Young-Laplace (Lenormand, 2003) were applied to determine the radius and pore size distribution, using:

Equation 3-17

$$r_i = \frac{WASHCON\gamma(-4 \cos \theta)}{2P_i}$$

where *WASHCON* is the Washburn constant to express the pore radius in microns (μm):

$$WASHCON = \frac{10^4[\mu\text{m}/\text{cm}]}{68947.6[\text{dynes}/\text{cm}^2] \cdot [\text{Psia}]}$$

where γ is the interfacial tension (dynes/cm^2), θ is the contact angle (degrees), and P_i is the entry mercury pressure (psia). For the mercury-air system, 485 dynes/cm^2 and 140° values were used as the interfacial tension and angle contact, respectively.

Equation 3-18

$$f(r) = -\frac{dS}{dr} = \frac{P^2}{2\gamma \cos \theta} \frac{dS}{dP}$$
$$\int_{\infty}^0 f(r) \cdot dr = \int_0^1 dS = 1$$

where $f(r)$ is the pore size distribution function, dS is the mercury saturation derivative, dr is the radius derivative, and dP is the capillary pressure derivative.

From this technique, the bulk volume and pore volume can be calculated as:

Equation 3-19

$$BV_{MICP} = V_{pen} - V_{Hg}$$

where V_{pen} is the penetrometer volume (cm^3) and V_{Hg} is the intruded mercury volume (cm^3).

Equation 3–20

$$PV_{MICP} = Int_{Total}W_{sample}$$

where Int_{Total} is the total mercury intrusion volume throughout the sample after conformance correction –explained in the following subsection (cm^3/g), and W_{sample} is the dry weighted sample (g).

3.10.1 Conformance correction

In the initial stages of a MICP test, the mercury will conform to the sample surface irregularities, resulting in an apparent intrusion often referred to as conformance or closure. From this point onwards, the mercury truly starts to intrude inside the largest pore throats of the sample (**Figure 3-18**). Therefore, the conformance correction arises within the MICP data's low-pressure region (Newsham et al., 2004). If the output MICP data is not corrected due to this conformance or closure effect, the data will be misleading and not representative. Therefore, the conformance correction was performed by subtracting the apparent volume of mercury intruded prior to the actual displacement pressure within the low-pressure range (Guise et al., 2017). Even though there are more rigorous methods, such as Comisky et al. (2011) or Peng et al. (2018), the conformance correction for TGS is very intuitive because the capillary pressure curves start at very high pressure. The conformance effect is displayed as small tails in the derived pore size distribution, PSD, shown in **Figure 3-19** (e.g. Newsham et al., 2004; Guise et al., 2017).

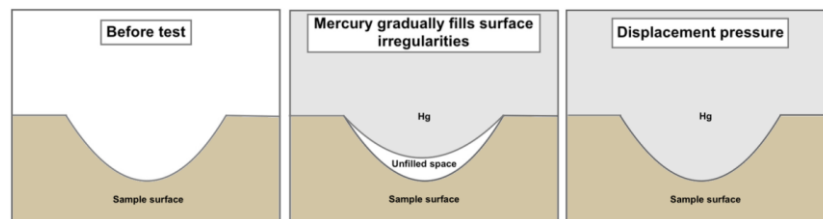


Figure 3-18. Schematic of the conformance or closure effect on a sample outer surface (Svendsen, 2019).

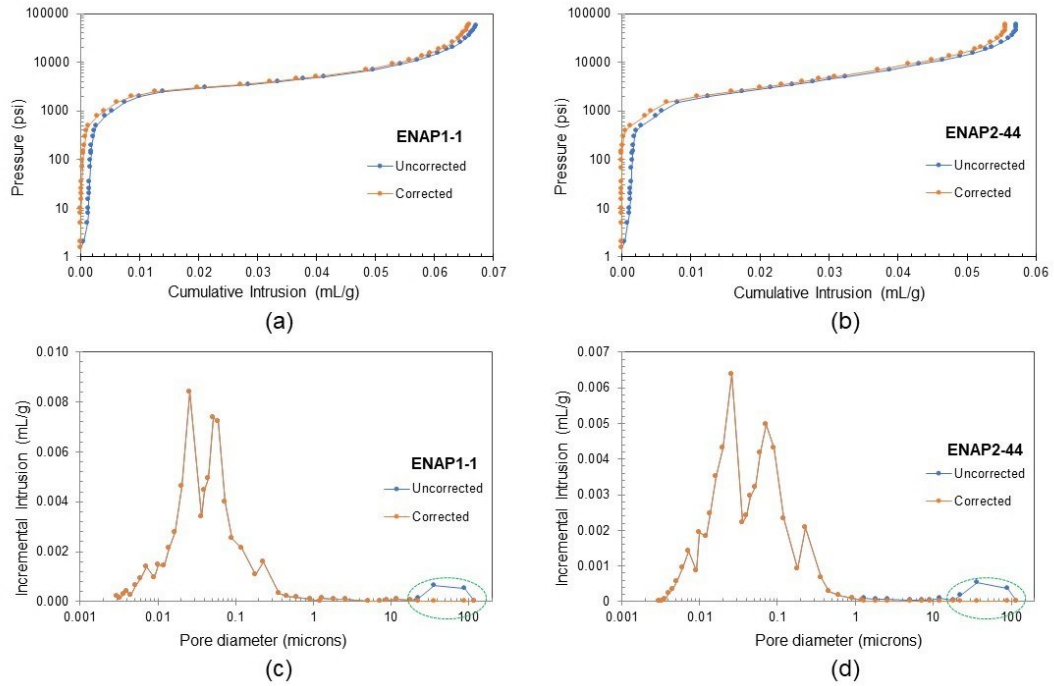


Figure 3-19. Conformance correction examples from ENAP1 and ENAP2 sets (a) and (b) display the capillary pressure curves as mercury intrudes. (c) and (d) display the pore size distribution range as incremental mercury intrusion rate. The conformance or closure effect is shown as a dashed green circle.

3.10.2 Fluid corrections

Fluid corrections must be applied to the air-mercury capillary pressure data through a conversion equation (Equation 3–21) according to the fluids inside the rock pore volume. This work used air-brine and gas-brine systems to analyse and interpret the MICP data (Table 3-1). The air-brine system was used to convert the MICP curves to NMR T₂ distribution curves and define T₂ cut-offs (Chapter 5).

Equation 3–21

$$P_{C_{New}} = P_{C_{AM}} \left(\frac{\sigma_{New} \cos \theta_{New}}{\sigma_{AM} \cos \theta_{AM}} \right)$$

where $P_{C_{New}}$ is the pseudo capillary pressure of a new binary system (psig), $P_{C_{AM}}$ is the air-mercury capillary pressure (psig), σ_{New} is the interfacial tension of a new binary system (dynes/cm²), σ_{AM} is the air-mercury interfacial tension (dynes/cm²), θ_{New} is the contact angle of a new binary system (°), and θ_{AM} is the air-mercury contact angle (°).

Table 3-1. Contact angle and surface tension values used in this project (McPhee et al., 2015).

Parameter	Air-Brine	Air-Mercury	Gas-Brine
Contact angle (°)	0	140	0
Interfacial tension (dynes/cm ²)	72	485	50

3.10.3 Key capillary pressure parameters

Four capillary pressure parameters are of interest for petrophysical correlations to estimate the permeability (e.g. Comisky et al., 2007): entry pressure, displacement pressure, threshold pressure and apex, as shown in **Figures 3-20** and **3-21**. In this work, the definition of these parameters is:

- a. Entry pressure (P_e): the pressure at which mercury initially enters the largest pore throats of the sample pore space.
- b. Displacement pressure (P_d): the pressure at which mercury actually enters the sample in the largest pore throats, forming the first continuous filament of mercury inside the rock (Schowalter, 1979). In other words, mercury intrudes into the first interconnected pore throats of the sample pore network. The P_d cannot be readily estimated for highly altered and heterogeneous rocks, such as TGS, since their capillary pressure curves are stepped (not a steady plateau). Therefore, P_d was estimated by plotting the first three data points after the entry pressure with a linear correlation and extrapolating the intercept to the Y-axis (**Figure 3-22**).
- c. Threshold pressure (P_{thr}): the pressure at which mercury first forms a connected filament across the span of the sample; in other words, it is the breakthrough pressure (Pittman, 1992). Katz and Thompson (1986, 1987) point out that P_{thr} is the inflexion point at which the capillary pressure curve becomes convex upward and steeper since, from this pressure, the mercury intrusion rate decreases. The procedure involves identifying the characteristic length, L_c , which is the equivalent pore throat diameter at the threshold pressure using Washburn's expression (Equation 3-17). However, this is not true for TGS since their curve shape does not clearly present an inflexion point due to its complex microstructure and mercury intrusion takes longer to penetrate throughout the sample. Amann-Hildenbrand et al. (2016) applied the Schlöemear and Krooss (1997) method in TGS samples from the southern North Sea to derive the P_d and P_{thr} . This method plots the mercury intrusion volume versus the logarithm of the capillary pressure; the P_d is the curve's inflexion point, while the P_{thr} is the intersection of the tangent to that inflexion point. The Schlöemear and Krooss (1997) method was applied for the P_{thr} estimation, compared with Katz and Thompson's method, and by visually selecting a pressure with a visible plateau start in the MICP curve (**Figure 3-23**).
- d. Apex: the capillary curve's highest mercury saturation and capillary pressure ratio. This term was presented by Swanson's (1981) correlation to estimate the absolute permeability. The physical explanation is that this apex point is the effective mercury saturation at which the pore throat aperture interconnects the main part of the pore network. Hence, permeability correlations should be more

accurate. Pittman (1992) suggested a better approach to readily find it by plotting the ratio of mercury saturation and capillary pressure against mercury saturation (Figure 3-21). The data point located at the peak of the resulting curve is the apex; this procedure was followed in the dataset.

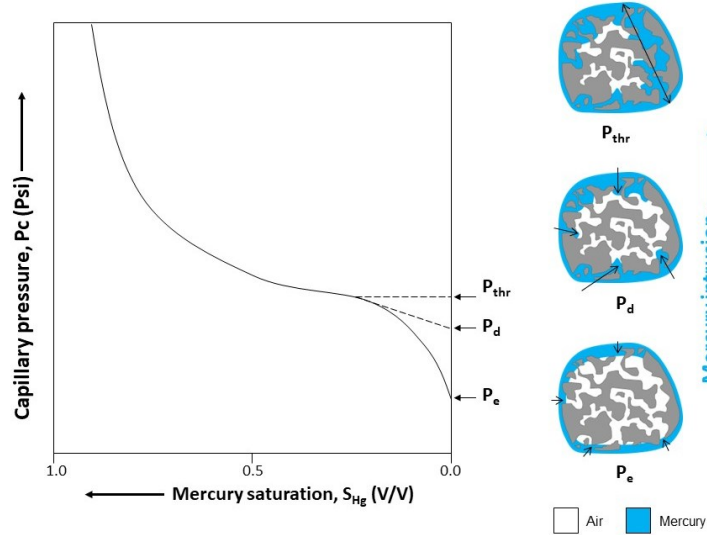


Figure 3-20. Schematic diagram of the mercury injection capillary curve displaying the entry, displacement, and threshold pressures location (DNPuq, 2023).

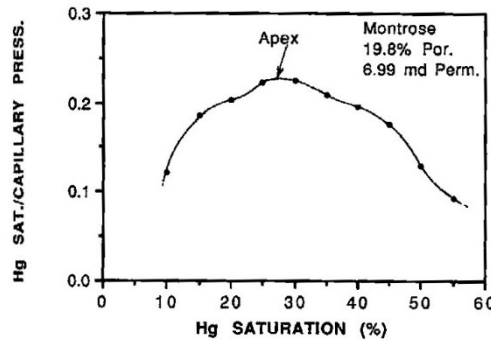


Figure 3-21. Cross-plot of mercury saturation vs mercury saturation/capillary pressure ratio to obtain the apex parameter (Pittman, 1992).

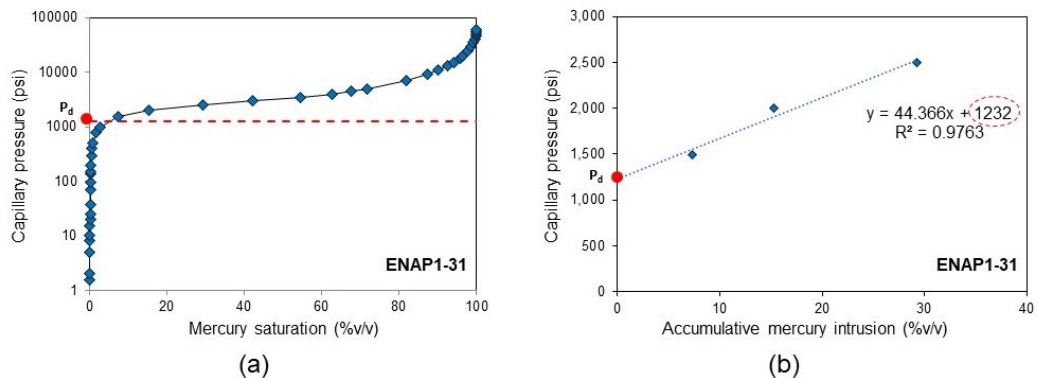


Figure 3-22. Example of finding the displacement pressure in sample ENAP1-31.

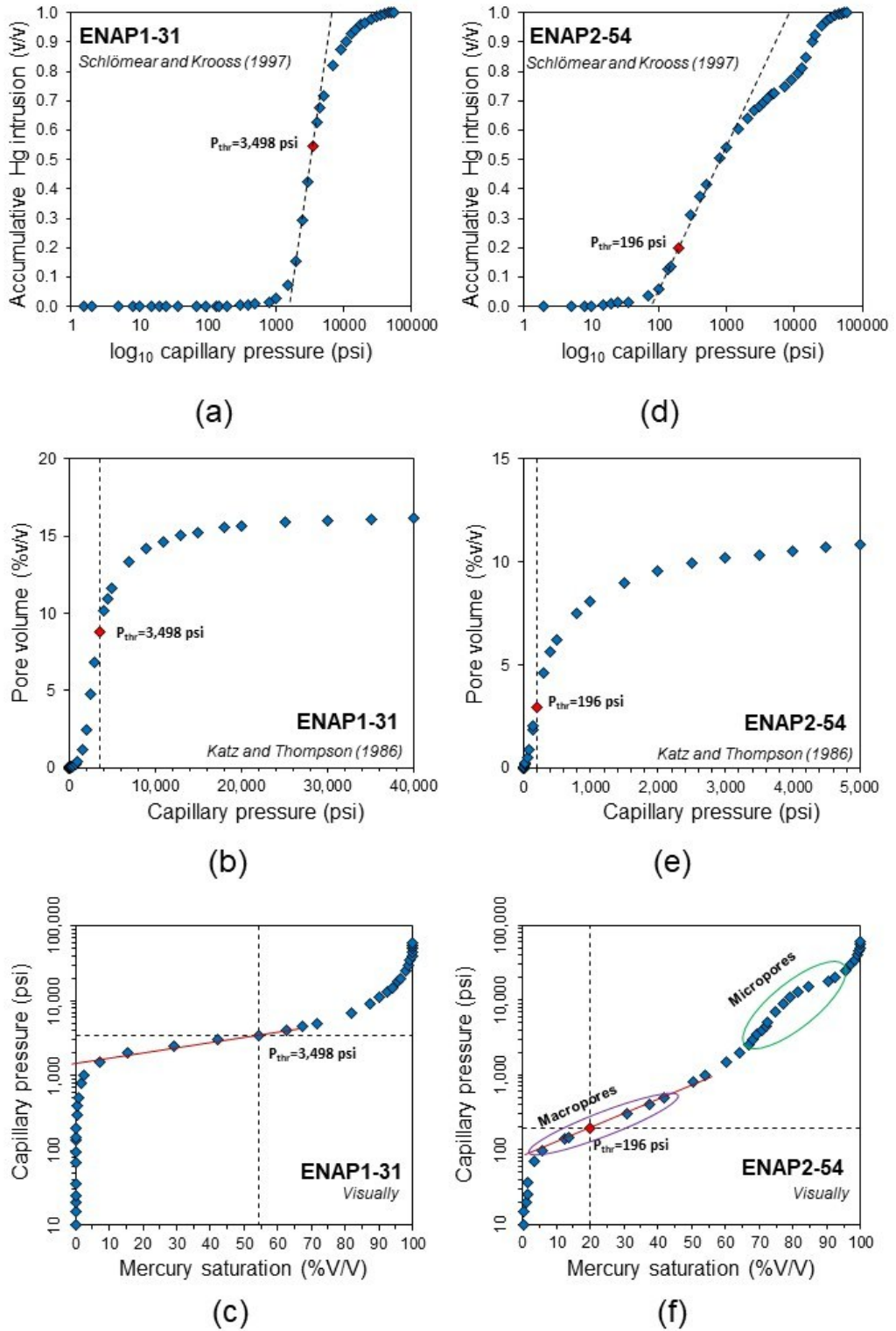


Figure 3-23. Example of finding the threshold pressure in samples ENAP1-31 and ENAP2-54.

3.11 Nuclear magnetic resonance (NMR)

NMR is a non-invasive technique that measures the net magnetisation of hydrogen nuclei inside a rock sample by applying a magnetic field (Coates et al., 1999). Since water and hydrocarbons are fluids with hydrogen atoms inside a reservoir, the volume of the fluids and the pore size distribution can be estimated.

In an NMR spectrometer, a radio-frequency (RF) pulse interacts with the hydrogen nuclei atoms within a core sample in a constant magnetic field. The nuclei absorb energy from a low to a higher energy state, affecting the net magnetic moment and angular momentum of electrons (spin quantum number, $m_s = -\frac{1}{2}$ and $+\frac{1}{2}$). Then, the RF is switched off, and the nuclei lose excess energy, returning to their original state. The electrons return by spinning, a process known as the relaxation phenomenon.

The electrons will flip from bottom to top in a three-dimensional plane and transversally like a spinning top. The relaxation time in the z-plane (i.e. from bottom to top) is called longitudinal relaxation time or T_1 . It quantifies the rate of energy transfer from the nuclei spin system to their neighbouring molecular, also known as spin-lattice. On the other hand, the relaxation time in the XY plane is called transverse relaxation time or T_2 , and it quantifies the magnetisation decay, also known as spin-spin (Figure 3-24).

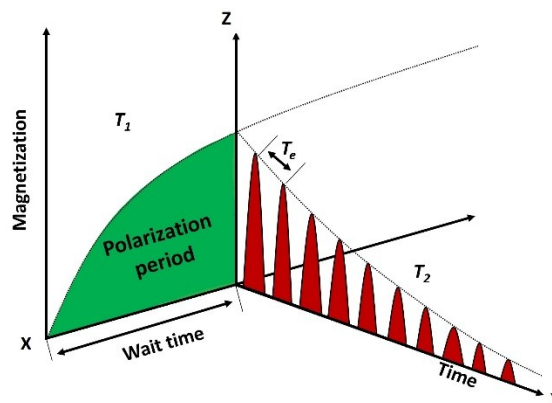


Figure 3-24. During polarisation, protons in fluid align parallel to a static magnetic field. A sequence of radio-frequency pulses excites the protons, causing them to generate a decaying signal (echo train). The wait time can be as much as 12 seconds, whereas echo trains typically are several hundred milliseconds long. T_1 = longitudinal relaxation; T_2 = transversal relaxation; T_e = inter echo spacing (modified from Menger and Prammer, 2002).

NMR relaxation time is shorter in the micropores where bound water is trapped within the clay portion, while it is larger where free fluids flow inside larger pores. This indicates a relationship between the pore size distribution and the NMR relaxation time (**Figure 3-25**). The terminology “bound” and “free” fluids is often used interchangeably with “non-mobile” and “mobile” fluids. “Mobile” refers to fluids that can move under the influence of pressure gradients and within interconnected pores, while “non-mobile” fluids are either genuinely sorbed to mineral surfaces or confined in tiny small pores that are impossible to flow.

Also, T_2 is faster to measure than T_1 for solid bodies since it proceeds faster, so the oil and gas industry prefers to use T_2 in core and logs. By transforming the decay time into an NMR T_2 distribution amplitude in time, typically from 0.3 milliseconds to 3 seconds, the signal width and height display the pore size distribution of the rock, including the bound fluid and free fluid, by defining a T_2 cut-off value separating the non-mobile and mobile fluids (**Figure 3-26**). Typical values of 33 ms and 92 ms are used for sandstones T_2 cut-off and carbonates T_2 cut-off, respectively (Coates et al., 1999).

The relaxation time for hydrocarbons is larger than that for water (**Figure 3-26**). This difference arises because hydrocarbons tend to occupy larger pores, where relaxation times are inherently longer due to reduced surface interactions than micropores. Alternatively, the relaxation time for hydrocarbons can be greater for a given pore than for water due to differences in fluid properties such as viscosity and molecular interactions with the pore surfaces. These factors influence the NMR response and should be considered when interpreting T_2 distributions (Coates et al., 1999).

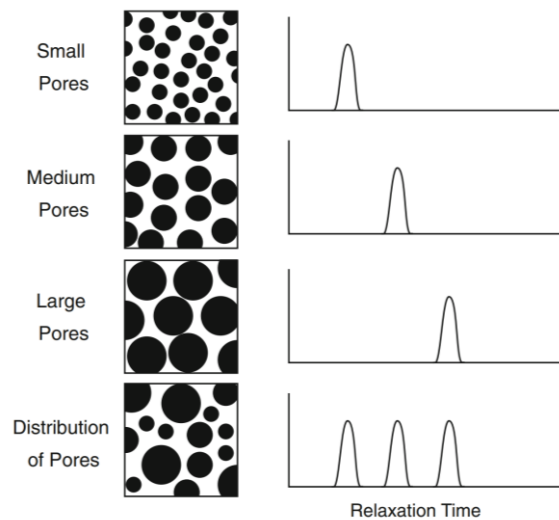


Figure 3-25. Theoretical relaxation time distributions for a range of pore sizes. The pores are black for square panels, whereas the solid matrix is white (modified from Mohnke and Yaramanci, 2008).

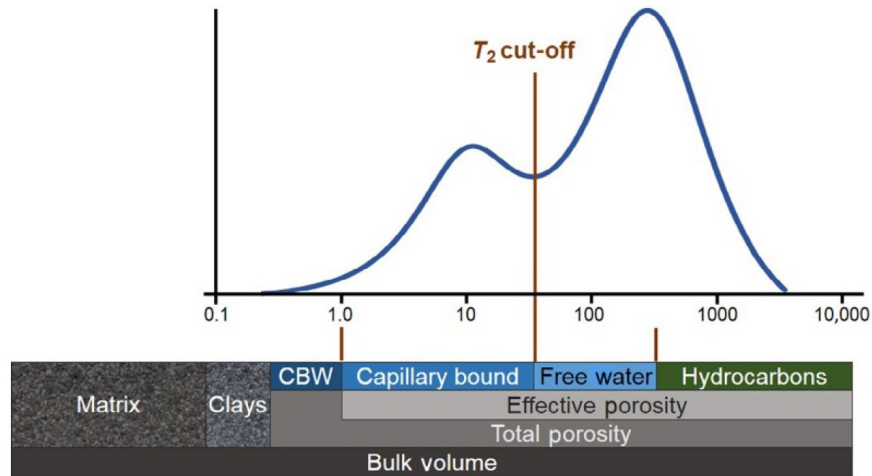


Figure 3-26. A typical NMR T_2 distribution trace and how this corresponds to the volume of fluids in place (Coates et al., 1999).

The Oxford MARAN Ultra NMR spectrometer in the Wolfson laboratory was used to obtain T_2 NMR distribution curves. This equipment runs at 35°C with an operating frequency of 2 MHz. Carr-Purcell-Meiboom-Gill (CPMG) pulse sequence was employed to measure the amplitude in T_2 fixed times ranging from 0.01 to 10,000 ms with 100 data points. The output data was processed with WinFIT (<https://www.novocontrol.de/php/winfit.php>) to fit the raw data best according to the multi-exponential decay trend within the CPMG (Equation 3–22). An inter-echo spacing time (TE) of 100 μ s and a wait time (TW) of 10 s was used. The scans varied from 50 to 1,000 depending on the pore volume determined by the weight difference of the dry and brine-saturated sample (**Section 3.8.3**) and a reference curve built in the laboratory (**Appendix A.1**). Before entering the NMR spectrometer, all core plugs were fully brine saturated with the synthetic water formation and wrapped with cling film.

Equation 3–22

$$M(t) = \sum M_i(0)e^{-\frac{t}{T_{2i}}}$$

where $M(t)$ is the measured magnetization at time t , $M_i(0)$ is the initial magnetization from the i component of relaxation, and T_{2i} is the decay constant of the i component of transverse relaxation (Coates et al., 1999).

The T_2 distribution was calculated as normalised cumulative and incremental amplitude with an automatic spreadsheet per sample (**Figure 3-27**). To estimate the NMR pore volume of samples, a calibration cross-plot between the NMR spectrometer signal-to-noise ratio (SNR) and pore volume of pure water is up-to-date and maintained that follows a linear trend (**Appendix A.2**). The slope and intercept are used together with the sample final signal amplitude, number of scans, and received gain factor in Equation 3-23 to calculate the NMR pore volume. Note that

the resulting NMR pore volume needs to be corrected (Equation 3–24) with a hydrogen index correction to convert from pure water to brine pore volume. The hydrogen index correction results from an empirical plot of a NaCl concentration in ppm and hydrogen index built in the laboratory (**Appendix A.3**).

Equation 3-23

$$NMR PV_{raw} = \left[\left(\frac{A}{NS/Rg} \right) + Intercept \right] \cdot \frac{1}{Slope}$$

where $NMR PV_{raw}$ is the calculated NMR pore volume of pure water, A is the sample final signal amplitude, NS is the number of scans, RG is the gain received factor, $Intercept$ and $Slope$ are the linear parameters of the calibration curve.

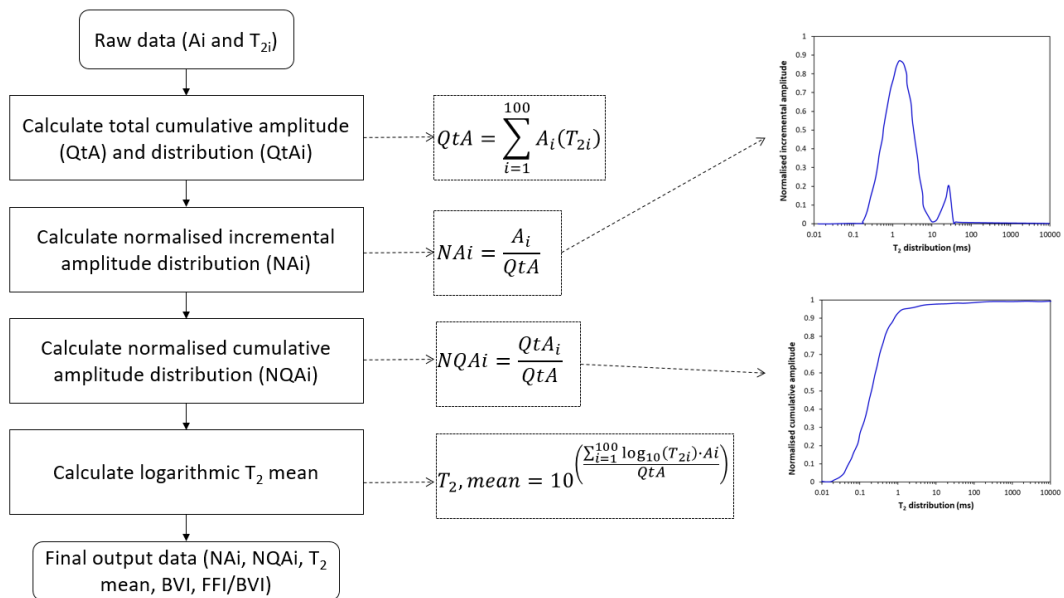


Figure 3-27. Workflow to compute incremental and cumulative T_2 distribution.

Equation 3–24

$$NMR PV_{corr} = \frac{NMR PV_{raw}}{HI(salinity)}$$

where $NMR PV_{corr}$ is the corrected NMR pore volume, $NMR PV_{raw}$ is the calculated NMR pore volume, and $HI(salinity)$ is the hydrogen index correction calculated from the Wolfson NMR scanner as a function of NaCl salinity.

3.12 Electrical resistivities

3.12.1 Brine resistivity

The oil company reported a reservoir water formation estimated at 12,000 ppm NaCl; therefore, a brine solution of this concentration was prepared as the synthetic water

formation (SWF). The Mettler Toledo Seven Excelente multiparameter meter was used to measure the brine conductivity at laboratory conditions, then converted to resistivity by using Arps (1953) equation to standard conditions (1 atm and 25°C):

Equation 3–25

$$R_2 = R_1 \frac{(T_1 + 21.5)}{(T_2 + 21.5)}$$

where R_1 and R_2 are the laboratory brine resistivity and brine resistivity at standard conditions (ohm·m), T_1 is the laboratory temperature, and T_2 is the standard temperature (°C).

In addition, each brine solution was deaerated before use; density and viscosity were measured by weight difference in a pycnometer and Ostwald viscometer, respectively.

3.12.2 Resistivity of brine-saturated core plugs

The core plug resistivity was measured before the brine permeability test was performed at a confining pressure of 1,500 Psig for the ENAP1 set and 1,500-2,500-3,500 psig for the ENAP2 set. The core plugs were brine-saturated and put into a Hassler-type core holder at the desired confining pressure inside a cabinet to ensure a constant temperature.

An AC multifrequency meter RS PRO LCR-600 model with a four-electrode system was used to measure the resistance and phase angle at nine data points: 100 – 500 – 1,000 – 2,000 – 5,000 – 7,500 – 10,000 – 15,000 – 20,000 Hz. Calibration was done to ensure a phase angle of less than 0.5°, and the resistance measured at 2,000 Hz was selected to represent the rock resistivity (e.g. McPhee et al., 2015). The chamber temperature and rock resistance were monitored to ensure measurement stability. Using Equation 2–2 and Arps (1953), the rock resistance measured in ohms was converted to rock resistivity at 25°C in ohm·m.

3.13 Specific surface area (SSA)

The method to estimate the SSA was nitrogen adsorption isotherms based on the BET (Brunauer-Emmett-Teller) theory (Brunauer et al., 1938), which is an extended version of the classic Langmuir (1918) adsorption equation. All samples were oven-dried at 65°C to constant weight before entering the nitrogen absorption equipment – Gemini VII 2.00 from Micromeritics – to measure the surface area by applying the BET theory.

The procedure consisted of cooling the sample under vacuum conditions at -195.8°C to ensure no gas was present. At this temperature, liquid nitrogen (adsorbate) easily

flows since it condenses onto the solid surface. Incremental pressure steps of about 22 mmHg were applied, and the absorbed mass was calculated. The nitrogen gas molecule (N₂) size was considered 0.1620 nm². The functional equipment settings were a running time of 16 min for evacuation, at a rate of 1,000 mmHg/min, and an equilibration time of 15 s. A complete analysis took around 4 hours.

Standard sampling consists of powdered samples less than 3 g that enter into a sample tube with a limited capacity of about 2.0 cm³ (for the Wolfson equipment). The issue with crushing samples is that the measurement can be biased by breaking the quartz grains' bonds, severing amorphization, and increasing the surface area; for this reason, the Wolfson laboratory has a custom-made sample tube vessel for using intact small core plugs (**Figure 3-28**). This analysis was the last step of the core plugs before being destroyed for the ENAP1 set, while small plugs of 23 mm (1-inch) diameter and 25 mm of ENAP2 set were cored.



Figure 3-28. Custom-made sample tube vessel for BET technique in Wolfson laboratory.

BET theory assumes that the surface is homogeneous, the adsorbate physically adsorbs in infinite layers at saturated pressure, and no interaction in the adsorption layer occurs, among others. The output data is the cross-plot of relative pressure (p/p_0) and left-side term (y-axis) of the BET function (Equation 3–26), the slope S and intercept I derive the monolayer adsorbed gas and BET constant (Equations 3–27 and 3–28).

Equation 3–26

$$\underbrace{\frac{1}{v \left[\left(\frac{p_0}{p} \right) - 1 \right]}}_{\text{Y-axis}} = \underbrace{\frac{c-1}{v_m c}}_S \underbrace{\left(\frac{p_0}{p} \right)}_{\text{X-axis}} + \underbrace{\frac{1}{v_m c}}_I$$

where p and p_0 are the equilibrium and saturation pressure of the nitrogen at the adsorption temperature (Pa), v is the adsorbed gas quantity (mL), v_m is the monolayer adsorbed gas volume (mL), and c is the BET constant (unitless).

Equation 3–27

$$v_m = \frac{1}{S + I}$$

Equation 3–28

$$c = 1 + \frac{S}{I}$$

The BET-specific surface area is calculated by using the following formula:

Equation 3–29

$$S_{BET} = \frac{v_m N s}{V m}$$

where S_{BET} is the specific surface area (m^2/g), N is Avogadro's number (6.02×10^{23} 1/mol), s is the adsorption cross-section of the absorbing species (0.162 nm^2 for nitrogen), V is the adsorbate molar volume (m^3/mol), and m is solid sample mass (g).

Chapter 4

Mineralogy, microstructure, porosity, and permeability of the ZG reservoir

This chapter presents the mineral content, microstructure, porosity and permeability data from the core analysis programme (Chapter 3). It then discusses the key relationships between petrophysical properties and their controls, supported by empirical correlations, and ends with a summary.

4.1 Introduction

From the petrophysical standpoint, greensands contain significant microporosity and have high mineral density and specific surface (**Section 2.5**). Glauconite and chlorite are the clay minerals common in these rock formations, with high iron content, and their distribution within the rock may result in poor reservoir quality. This chapter presents data on the mineralogy, microstructure, specific surface area, bulk and grain density, porosity, and permeability of the cores from the ENAP1 and ENAP2 wells. The dataset's similarities, discrepancies, and outliers are highlighted and discussed using the principal parameters of descriptive statistics and linear correlation. For further information, **Appendix B** provides the master list of the petrophysical parameters and additional figures and tables.

This chapter reports the findings related to the first specific objective (**SO1**): *identify the key controls on the petrophysical properties of a glauconitic tight sandstone and establish their relationship to the microstructure (Section 1.2)*. The discussion and summary sections respond to **SO1** by examining empirical relationships between the mentioned parameters and the rock microstructure features.

4.2 ZG mineralogy and chemistry

The principal minerals present in the ZG reservoir are quartz, plagioclase, and clay minerals. The predominant clay mineral groups are chlorite, mica, and illite-smectite—in decreasing order (**Table 4-1**). ENAP1 and ENAP2 sets' average mineralogy comprises 66% v/v quartz and plagioclase with 33% v/v clay minerals (**Figure 4-1**). Geochemical analysis from XRF indicates that ZG consists mainly of SiO₂, Al₂O₃, Fe₂O₃, Na₂O, and MgO, with a significant amount of K₂O with traces of CaO, TiO₂, SO₃, P₂O₅, and MnO (**Table 4-2**). The high iron oxide content combined with the magnesium and potassium oxides is consistent with glauconitic mica, smectite, and chlorite minerals (**Figure 4-2 b**). Glauconite was not adequately identified in the bulk-XRD analysis. Instead, the mica and illite-smectite groups were classified as glauconitic mica and glauconitic smectite (**d**). For further details, refer to

the discussion **Section 4.9.1**. The XRD results on the clay-sized fraction (<2 μm) identified albite and microcline (feldspar group), muscovite (mica group), and clinochlore (chlorite group) as the main clay minerals and only in sample ENAP2-8, a mixed-layer of illite-montmorillonite. Mineral and geochemical components trend versus the depth of each well is displayed in **Appendix B.2**.

Table 4-1. Density of minerals identified in the XRD analysis and ZG mineralogy.

Component	Mineral	Density (g/cm ³) ^{1,2}	ENAP1 average (%v/v)	ENAP2 average (%v/v)
Quartz	Quartz	2.65	29.8	26.5
Feldspar	Plagioclase	2.68	38.4	37.2
	Mica	2.90	7.3	8.0
Clay minerals	Illite-Smectite	2.75	3.6	4.8
	Chlorite	2.95	19.8	21.1
	Pyrite	5.01	0.6	0.7
Minor minerals	Barite	4.48	0.1	0.0
	Calcite	2.71	0.4	1.7

¹ Taken from Deer et al., 2013.

² Taken from Webmineral, 2019.

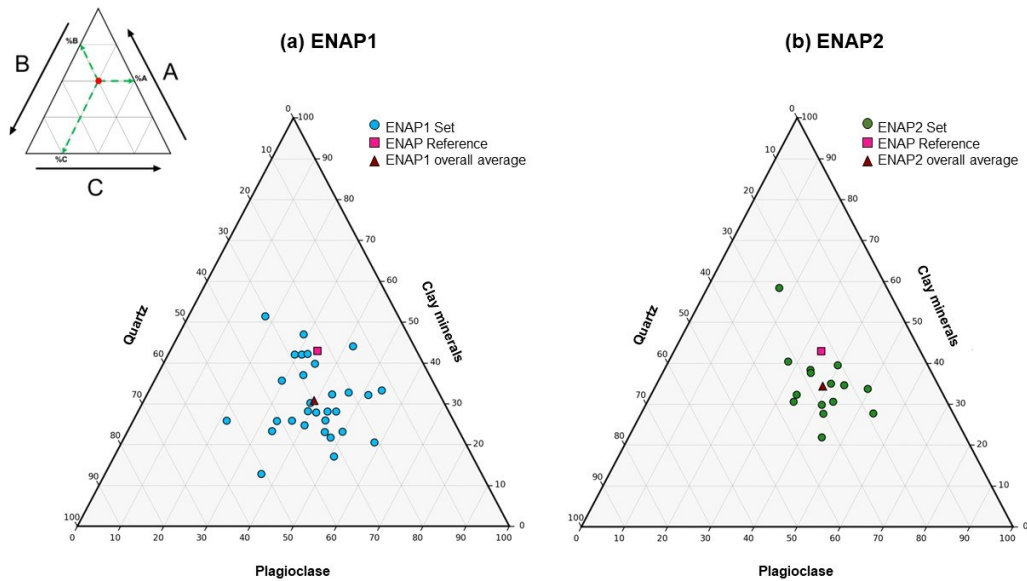


Figure 4-1. XRD mineral grouping as clay minerals + quartz + plagioclase in %v/v. ENAP1 (left) and ENAP2 (right) compared with their overall average indicated in **Table 4-1** and ENAP reference of 43% v/v clay minerals, 23% v/v quartz and 34% v/v feldspar (Britt et al., 2016).

Table 4-2. Geochemical composition of ENAP1 and ENAP2 from XRF analysis.

Component	ENAP1		ENAP2	
	Range (%wt)	Average (%wt)	Range (%wt)	Average (%wt)
SiO ₂	58.0 – 77.8	64.3	48.4 – 67.1	62.5
Al ₂ O ₃	9.5 – 16.2	13.4	8.7 – 16.2	13.5
Fe ₂ O ₃	2.8 – 14.5	8.0	4.4 – 13.6	8.0
Na ₂ O	2.6 – 5.6	3.9	1.8 – 5.2	3.7
MgO	0.9 – 3.2	2.3	1.7 – 3.4	2.6
K ₂ O	0.5 – 2.6	1.7	0.1 – 2.2	1.6
CaO	0.7 – 2.8	1.6	1.6 – 13.4	2.9
TiO ₂	0.4 – 0.8	0.7	0.5 – 0.9	0.7
SO ₃	0.1 – 1.0	0.5	0.1 – 1.6	0.5
P ₂ O ₅	0.1 – 0.1	0.1	0.1 – 0.4	0.2
MnO	0.0 – 0.1	0.1	0.0 – 0.1	0.1
LOI ¹	2.0 – 4.4	3.3	2.6 – 8.7	3.7
SiO ₂ /Al ₂ O ₃	3.6 – 8.1	4.9	3.6 – 5.6	4.7

¹ Loss of ignition.

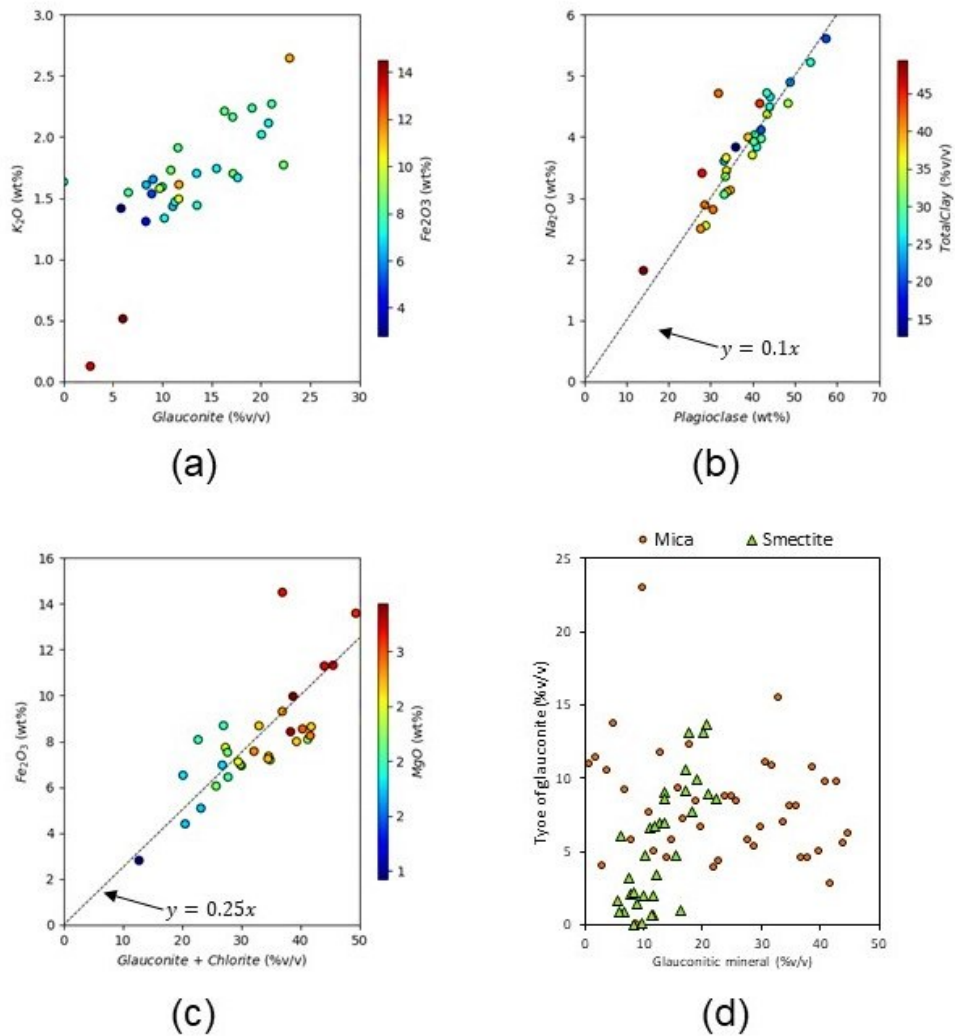


Figure 4-2. Cross-plot of XRF and XRD compositions: (a) potassium vs glauconite, (b) sodium vs plagioclase, (c) iron vs clay minerals (chlorite + glauconite), and (d) glauconitic mica and smectite mineral distribution.

4.3 ZG microstructure

4.3.1 CT scan analysis

CT scans were used to determine the degree of heterogeneity in ZG. **Table 4-3** shows the average descriptive statistics from the cropped region of interest (ROI) of the two orthogonal parallel views (0° and 90°) from the CT images. The standard deviation of the CT number was used to measure the cores' heterogeneity (**Section 3.5.2**). The heterogeneity was classified into four categories: low, moderately, highly and extremely heterogeneous based on the standard deviation, black and white voxel intensity distribution, and visual CT image in brown scale.

In the images presented in **Figure 4-3**, the low heterogeneous cores presented a uniform brown colour; the moderately heterogeneous cores contained a few high-density minerals such as pyrite as white dots and a few low-density materials in black that could be regions with higher porosity. The highly heterogeneous cores presented higher white and black voxels in the CT images. These samples have higher pyrite and clay content; the only one with barite is ENAP1-1. Finally, the extremely heterogeneous cores are ENAP1-2, with the highest standard deviation of 168 HU units and the highest grain density of 2.74 g/cm³ from the ENAP1 set. Samples ENAP2-12, ENAP2-27, and ENAP2-54, with a standard deviation of 231, 296 and 279 HU units, respectively, from the ENAP2 set, also have the highest grain density (2.74-2.76 g/cm³). The CT scans of these four cores show the dataset's highest pyrite and clay content.

Table 4-3. Average orthogonal views descriptive statistics.

Parameter	ENAP1 set	ENAP2 set
Minimum (HU)	2,090	1,942
Maximum (HU)	2,511	2,596
Average (HU)	2,253	2,208
Standard deviation (HU)	30	87

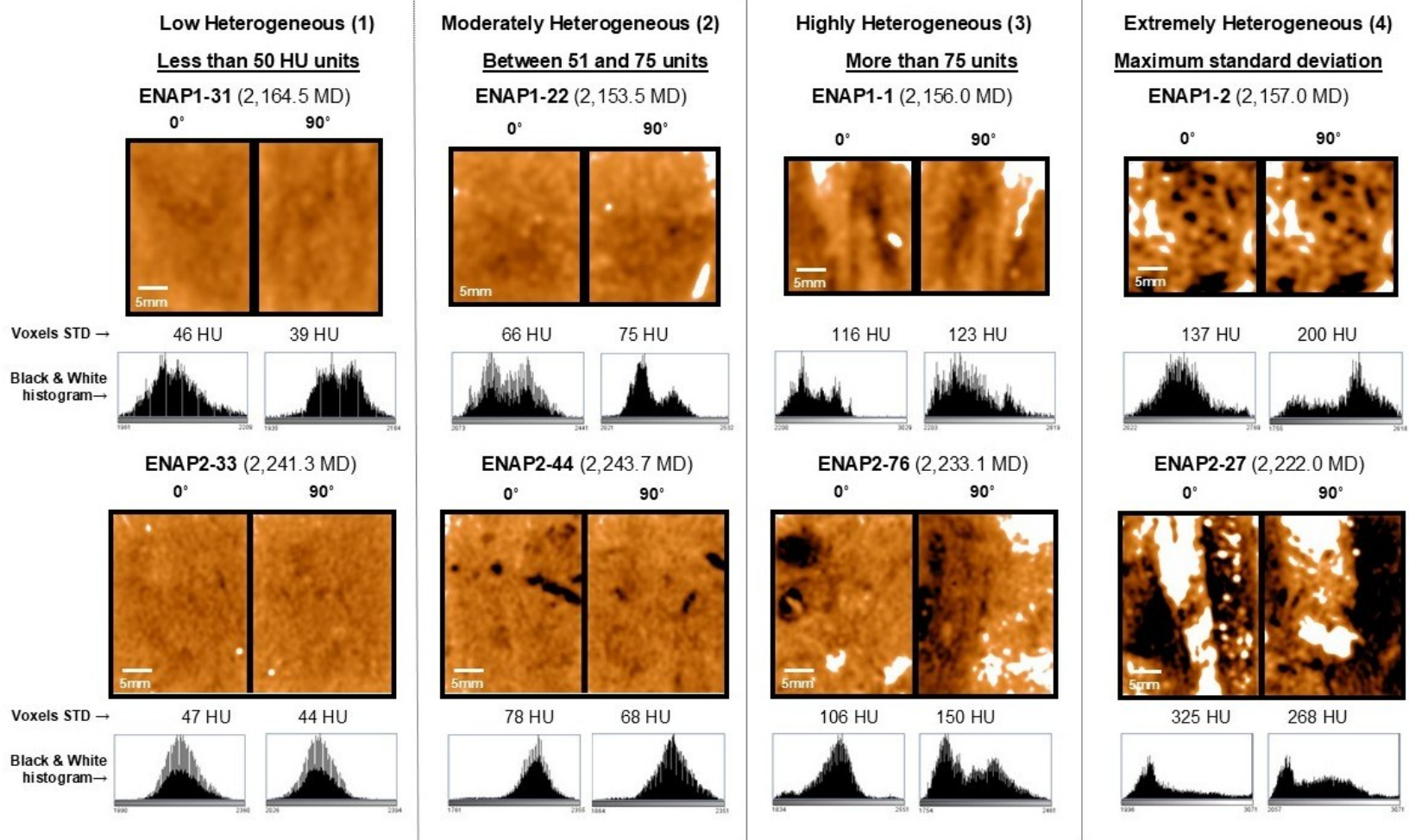


Figure 4-3. CT scan images showing the density heterogeneity of cores classified as Low Heterogeneous (<50 HU std), Moderately Heterogeneous (51–75 HU std), Highly Heterogeneous (>75 HU std), and Extremely Heterogeneous (maximum standard deviation). Images are presented in two orthogonal views (0° and 90°). The colour represents variations in material density: black indicates pores (low density), white represents high-density minerals, and shades of brown indicate the rock matrix. Below each image, the histograms show the grey-scale distribution corresponding to voxel densities (measured in HU). The voxel standard deviation (STD) quantifies density variations within each sample—scalebar: 5 mm.

4.3.2 SEM analysis

The ZG formation comprises a combination of moderately to very poorly sorted sandstone and siltstone. The SEM interpretation indicated that ZG contains glauconitic grains that vary from angular to subrounded. The clayey matrix is fine to very fine and composed of chlorite, glauconitic smectite and mica, and a mixed layer of illite-smectite (**Figure 4-4**). Most of the analysed samples are matrix-supported siltstone, except for samples ENAP1-2 and ENAP2-54, which are grain-supported sandstone with plagioclase and chlorite dominant in the matrix. These latter represent the pay sands of both cored wells (**Figure 4-4 A**).

Above the pay sands, the ZG lithology contains more silty claystone (80-60%) than glauconitic sandstone, while below them, the presence of glauconitic sandstone increases (60-80%). Several samples above the pay sands contained microfractures, probably resulting from changes in the stress state during or following coring (**Figure 4-4 D**). Also, there is plastic deformation around the glauconitic grains, resulting in fissured or cracked grains (**Figure 4-4 E**). This deformation likely occurred as a result of the dehydration of the clays after the core was brought to the surface.

Clay minerals are sometimes distributed between quartz and plagioclase grains as clasts, but most are as dispersed as coating or pore filling. Dispersed clay minerals can be found as pore-lining, pore-bridging and pore-filling. Chlorite was found to be pore-lining (**Figure 4-5 A, B, F, and H**), particularly in the pay sand samples (**Figure 4-5 B and H**) – increasing the pore preservation and enhancing reservoir quality. Chlorite was also found to be occasionally pore-bridging (**Figure 4-5 C, F, and H**) and even pore-filling (**Figure 4-5 E**). The mixed-layer illite-smectite was pore-bridging (**Figure 4-5 G**). Framboidal pyrite was identified in all the samples (**Figure 4-4 F, G, and H**).

Significant mineral dissolution was identified as secondary porosity in pay sands (**Figure 4-4 A**), while glauconitic samples presented notable microporosity content. The secondary porosity in the pay sands is characterised by pores ranging from 20-250 µm, which were likely formed by mineral dissolution processes rather than being part of the original sedimentary structure. This criteria used to infer these as secondary pores include irregular shapes, association with the depositional texture of the rock. In contrast, several pores within glauconitic grains appear to be isolated (**Figure 4-5 D**), and their distribution suggests they are primary pores formed during deposition and compaction.

Glauconitization increased with core depth as more mature glauconitic grains were identified in deeper samples (**Figure 4-6**). This process contributes to the reservoir heterogeneity by enhancing microporosity in glauconitic samples.

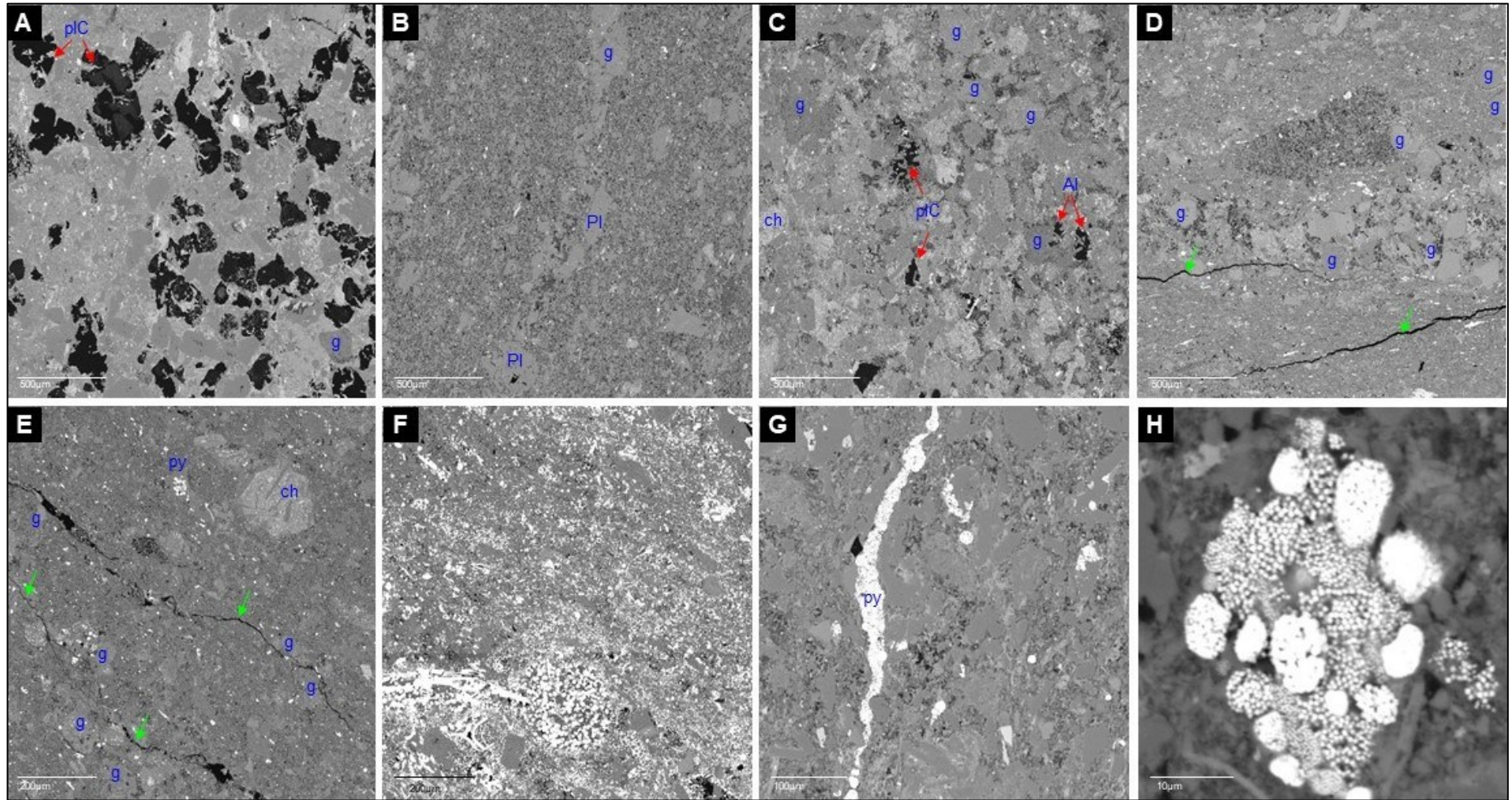


Figure 4-4. ZG greensand BSEM images: (A) Sample ENAP1-2 (pay sand) is a grain-supported sandstone with plagioclase and chlorite dominance in the matrix and overgrowth of glauconitic smectite grains. There are large secondary pores shown in black areas (red arrows). (B) Sample ENAP1-18 is a matrix-supported siltstone with chlorite and plagioclase grains. (C) Sample ENAP2-19 is a grain-supported sandstone with overgrowth of glauconitic smectite and mica grains. Pore-lining chlorite and authigenic albite are in the isolated pores (red arrows). (D) Sample ENAP1-27 is poorly sorted with plagioclase, chlorite matrix dominance, and glauconitic smectite grains. There are two artificial micro fractures (green arrows). (E) Sample ENAP2-12 with artificial micro fractures (green arrows) around the edges of glauconitic grains. There is a chlorite grain with illite presence on the top left. (F) Sample ENAP2-12 shows a major presence of pyrite mineral in the matrix with different shapes. (G) Sample ENAP1-6 shows a pyrite layer with framboidal distribution of a length of $\sim 400 \mu\text{m}$. There are mixed chlorite-illite and glauconitic mica grains. (H) Sample ENAP1-23 has framboidal pyrite in the matrix; this sample has the highest XRD pyrite content of 1.8%v/v. pIC = pore-lining chlorite, g=glauconitic grain, ch=chlorite grain, Al= albite, Pl=plagioclase, py=pyrite.

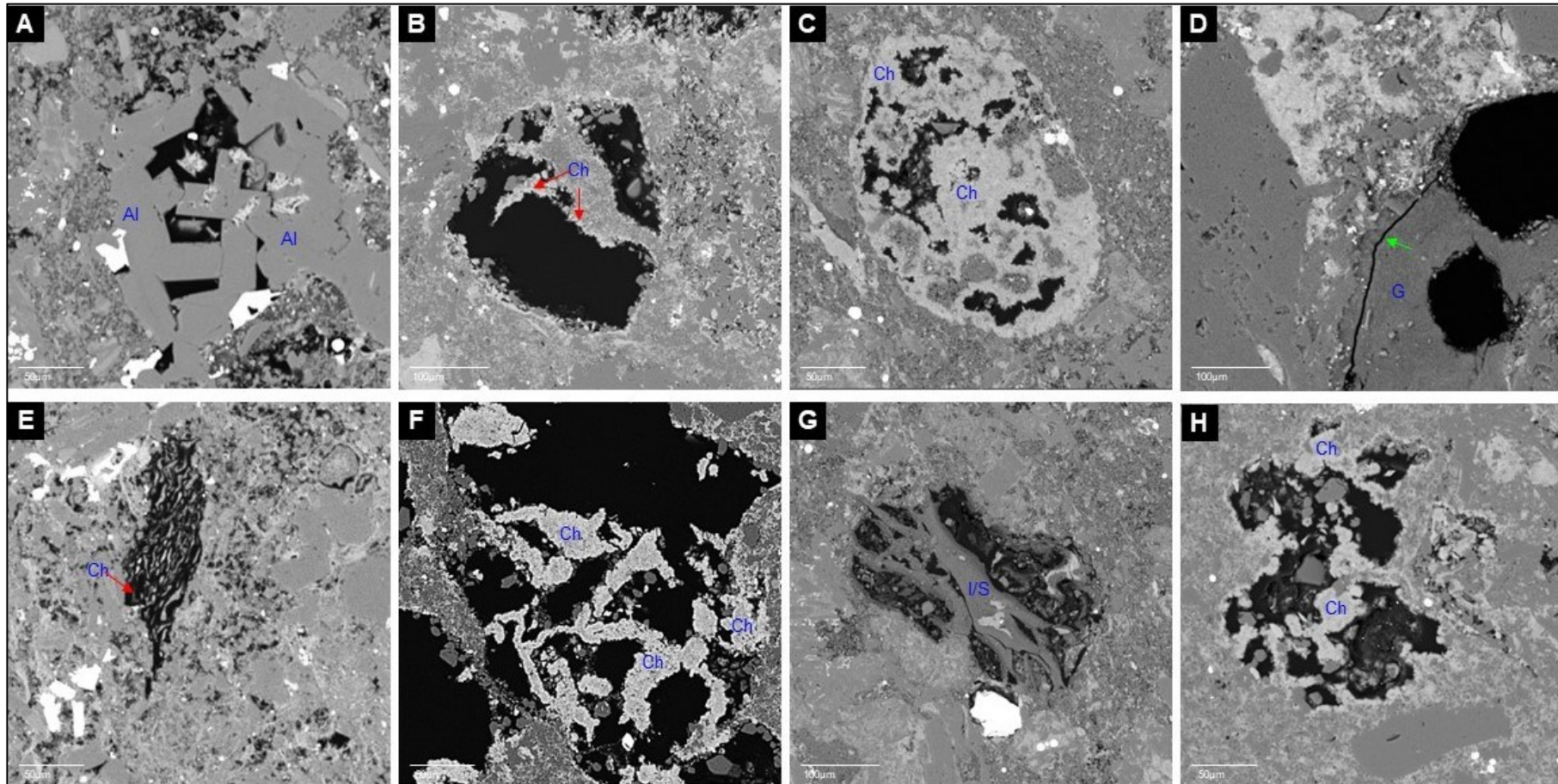
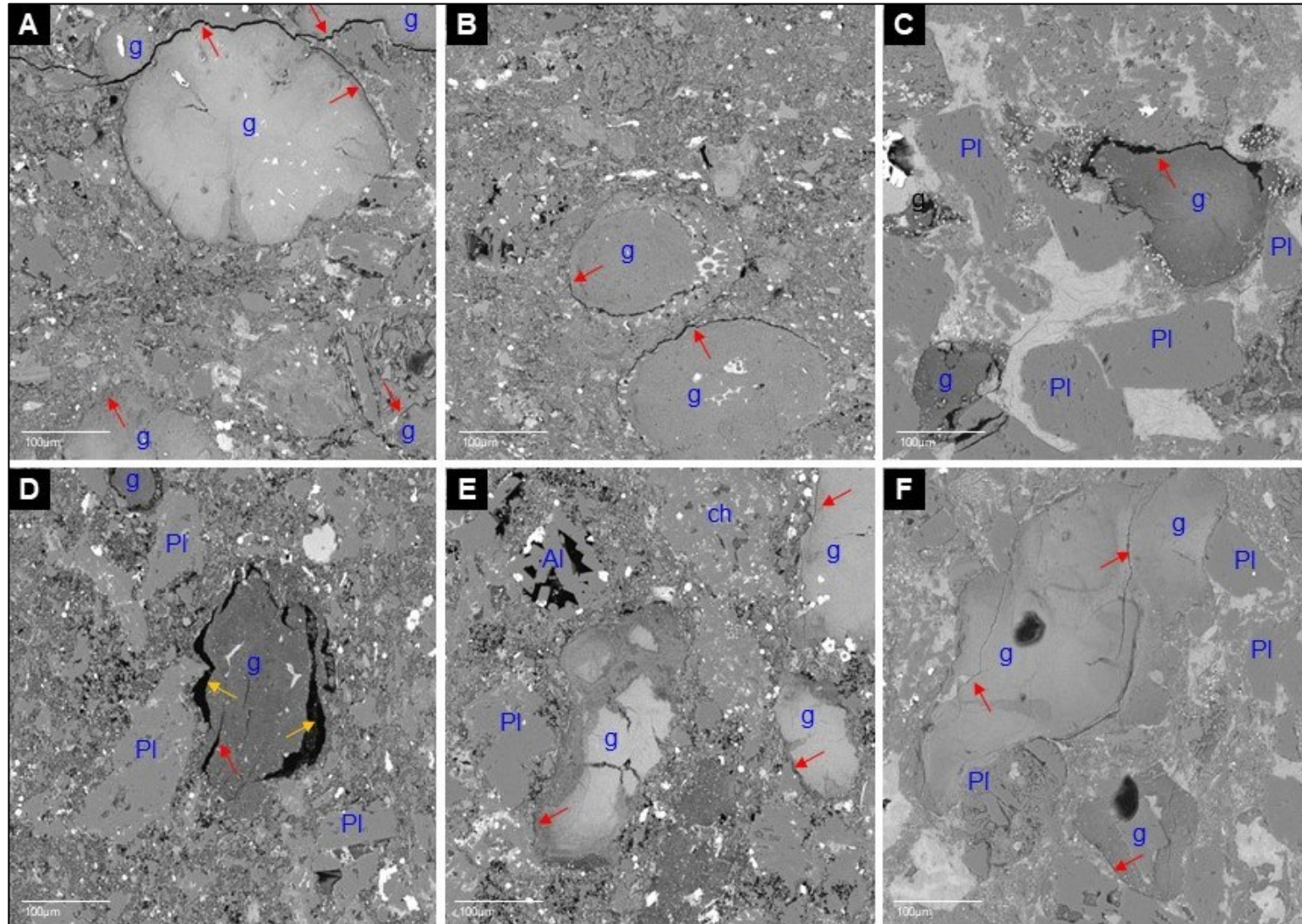


Figure 4-5. ZG greensand pore structure types: (A) Authigenic albite in sample ENAP1-22. (B) Chlorite pore lining a secondary pore in sample ENAP1-2 (pay sand). (C) Grain/alterated ingrowth of chlorite inside the pore of sample ENAP1-13. (D) Glauconitic grain with two isolated pores in sample ENAP2-53 with plastic deformation in its edges (green arrow). (E) Chlorite pore-filling in sample ENAP2-65. (F) Chlorite pore-lining and pore-bridging in sample ENAP2-54 (pay sand). (G) Pore-bridging of mixed-layer illite-smectite in sample ENAP1-13. (H) Chlorite pore-lining and pore-bridging in sample ENAP2-54 (pay sand). Al= albite, Ch=chlorite, G= glauconite, I/S= illite-smectite.



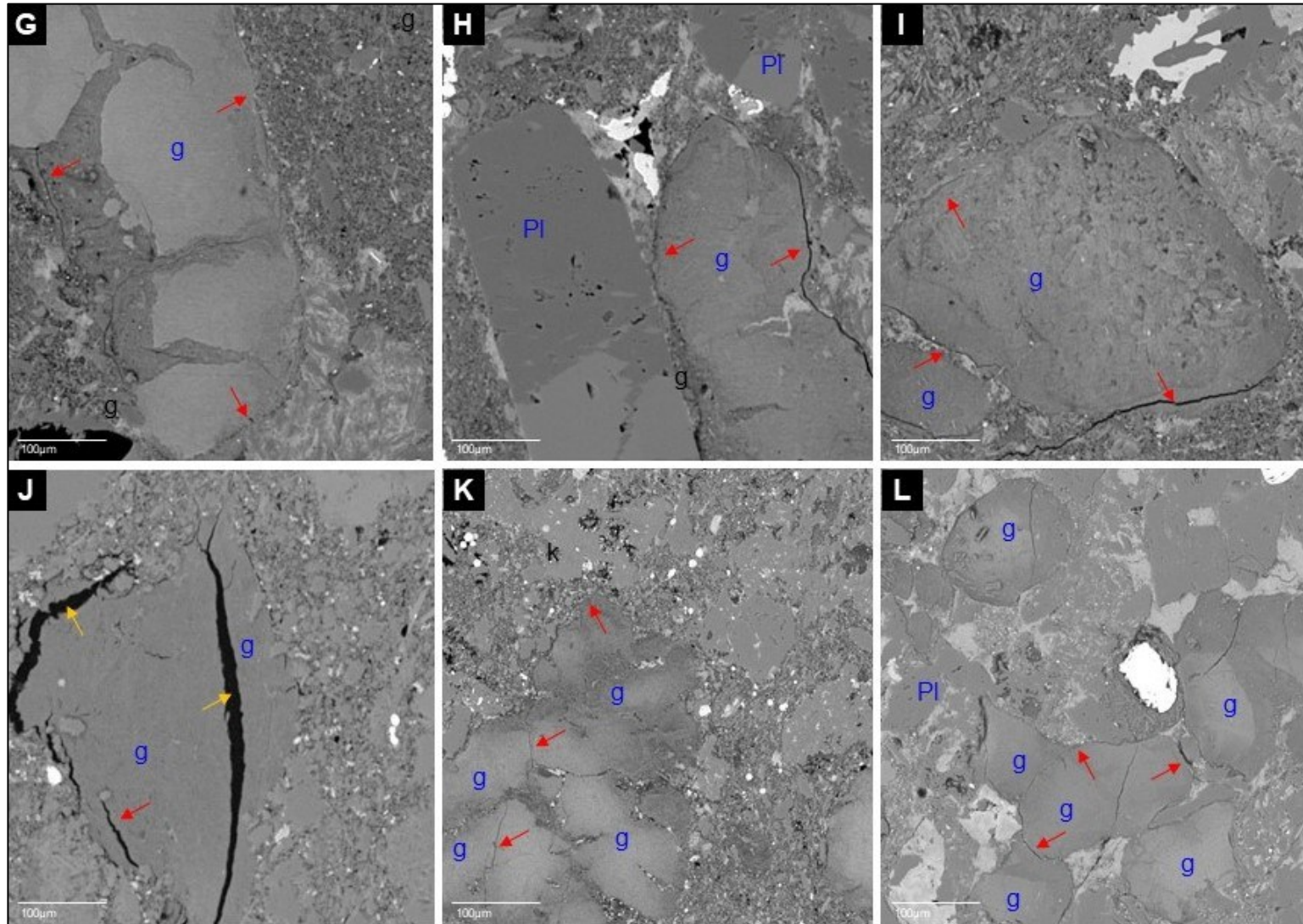


Figure 4-6. ZG greensand glauconitic grain types: All the glauconitic grains presented plastic deformation on their edges (red arrows). (A) Sample ENAP1-28 has slightly evolved grains. The big grain has internal fissures, indicating secondary generation growth. It is classified as glauconitic mica. (B) Sample ENAP1-27 shows two nascent glauconitic grains well-rounded with ghost fossils. It is classified as glauconitic micas. (C) Sample ENAP1-21 has two slightly evolved glauconitic grains. It is classified as glauconitic mica. (D) Sample ENAP1-31 has an evolved glauconitic grain. It is classified as glauconitic mica. It has secondary pores on its edges (orange arrows). (E) Sample ENAP1-1 shows slightly evolved glauconitic mica grains with second-generation growth. The one in the centre is an evolved grain since it is divided into two grains. (F) Sample ENAP1-15 shows evolved glauconitic mica grains. Two of them have an isolated internal pore. (G) Sample ENAP2-17 shows a slightly evolved glauconitic mica grain with second-generation growth. (H) Sample ENAP2-17 has a slightly evolved glauconitic illite-smectite grain with second-generation growth. (I) Sample ENAP2-24 has an evolved glauconitic smectite grain. (J) Sample ENAP2-46 shows an evolved glauconitic mica grain with secondary pores on its edges (orange arrows). (K) Sample ENAP1-1 shows slightly evolved glauconitic mica grains. (L) Sample ENAP1-15 shows evolved glauconitic mica and smectite grains. Al= albite, g=glauconitic, Pl= plagioclase The grain terminology related to slightly evolved and evolved glauconitic grains was conducted following Odin and Letolle's (1980) classification (**Figure 2-20**).

4.4 ZG Specific surface area (SSA)

The SSA values range from 3.2 to 19.8 m²/g with an average of 9.8 m²/g (Table 4-4) – as a reference, pure quartz has a SSA value of 2.5 m²/g (EU Joint Research Centre, n.d.). Plotting the XRD total clay content with the measured SSA of 28 samples from the dataset showed a linear trend with a correlation coefficient (R²) of 0.76 (Figure 4-7). Five samples were classified as outliers, including the extremely heterogeneous pay sands (Figure 4-3), which are chloritic sandstones with few glauconitic grains.

Table 4-4. Superficial surface area descriptive statistics of dataset.

Parameter	ENAP1	ENAP2
Minimum (m ² /g)	3.5	3.2
Maximum (m ² /g)	19.8	15.2
Average (m ² /g)	9.8	9.9
Median (m ² /g)	8.8	10.4
Standard deviation (m ² /g)	4.1	3.1

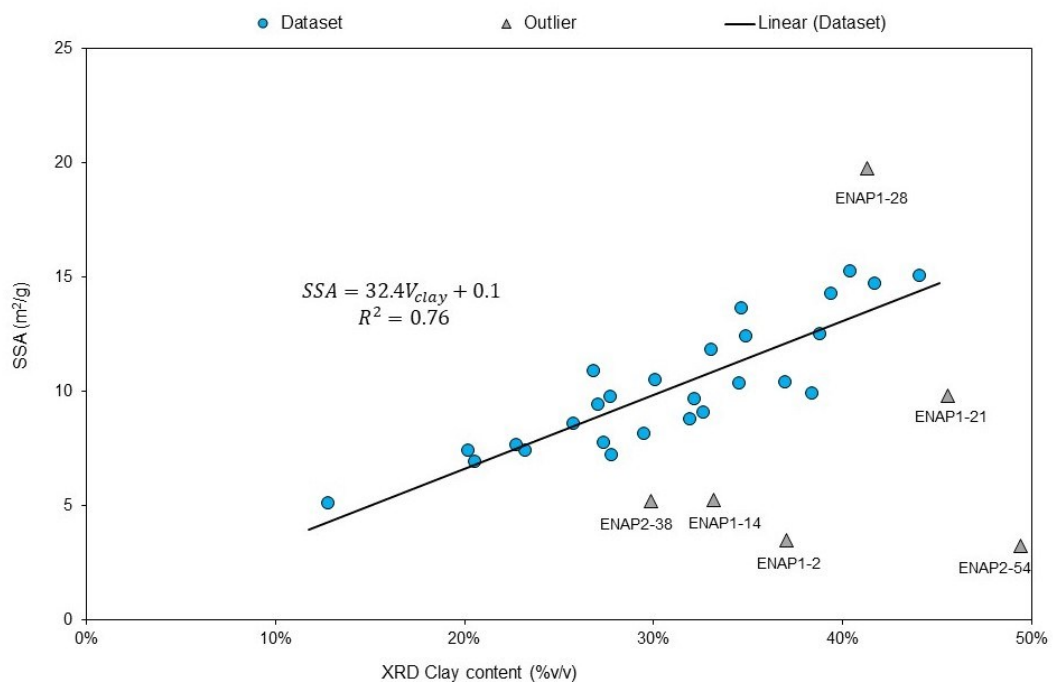


Figure 4-7. Cross-plot of XRD clay minerals content and SSA.

4.5 ZG densities

4.5.1 Bulk density

The bulk density (ρ_{Bulk}) of the ZG ranges from 2.02-2.41 g/cm³, with an average of 2.29 g/cm³. The bulk density measured by Vernier calliper is higher than that determined by mercury immersion (Section 3.8) by around +1.5% absolute difference (Figure 4-8). Three samples from ENAP1 (13, 24, and 27) and one from ENAP2 (27) are outliers from the dataset, where the Vernier calliper overestimated the BV due to the irregular shapes of the core plugs. The standard deviation of each

method per well indicates that the mercury immersion has better precision (**Tables 4-5 and 4-6**).

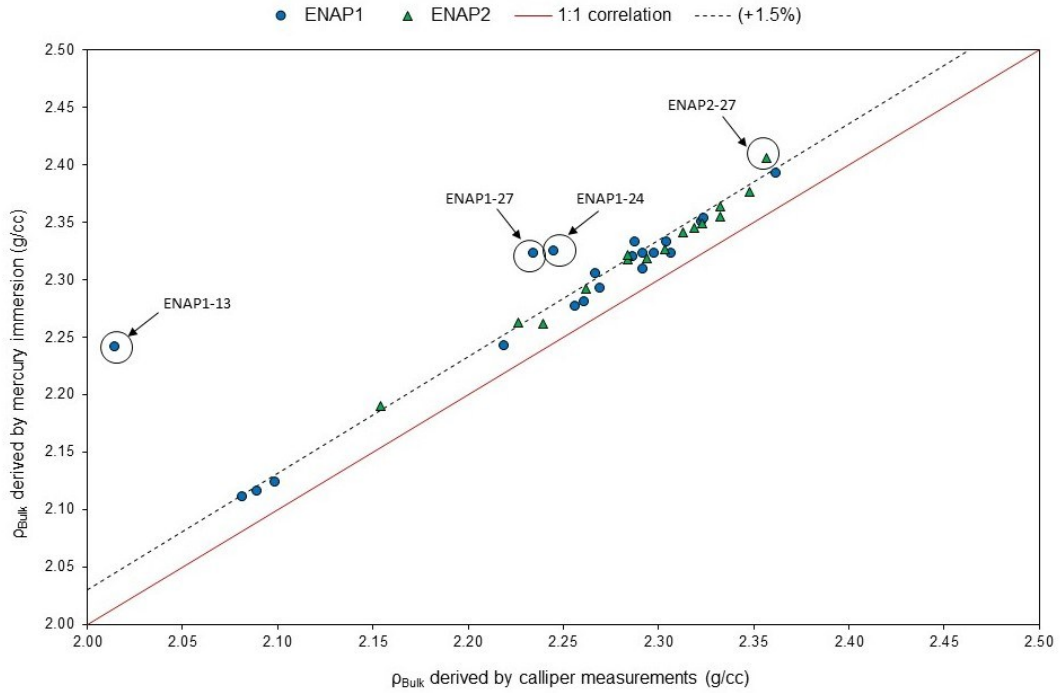


Figure 4-8. Cross-plot of dataset bulk density derived from Vernier calliper on the X-axis and mercury immersion on the Y-axis.

Table 4-5. ENAP1 set’s bulk densities descriptive statistics.

Parameter	ρ_{Bulk} derived from Vernier calliper	ρ_{Bulk} derived from mercury immersion
Minimum (g/cm ³)	2.02	2.11
Maximum (g/cm ³)	2.36	2.39
Average (g/cm ³)	2.24	2.29
Median (g/cm ³)	2.27	2.32
Standard deviation (g/cm ³)	0.09	0.08

Table 4-6. ENAP2 set’s bulk densities descriptive statistics.

Parameter	ρ_{Bulk} derived from Vernier calliper	ρ_{Bulk} derived from mercury immersion
Minimum (g/cm ³)	2.15	2.19
Maximum (g/cm ³)	2.36	2.41
Average (g/cm ³)	2.29	2.32
Median (g/cm ³)	2.30	2.33
Standard deviation (g/cm ³)	0.05	0.05

4.5.2 Grain density

The measured grain volume (GV) was used in Equation 3–8 to calculate the ρ_{Grain} from helium porosimetry (**Section 3.8.2**). The overall range of the ρ_{Grain} dataset is 2.48-2.97 g/cm³, with an average of 2.73 g/cm³ (**Table 4-7**).

Table 4-7. Grain density descriptive statistics.

ρ_{Grain} (g/cm ³)	ENAP1	ENAP2
Minimum	2.48	2.67
Maximum	2.97	2.80
Average	2.75	2.73
Median	2.74	2.74
Standard deviation	0.13	0.04

4.6 ZG porosity

4.6.1 Porosity at ambient conditions

Four porosity types were derived and grouped based on the fluid type used in the measurements:

- Brine solution at 12,000 ppm NaCl: porosity using pore volume measurements following brine saturation (Equation 3–9) and NMR (Equation 3–24) with bulk volume from mercury immersion (**Section 3.8.1.2**). These are referred to as brine and NMR porosity, respectively.
- Helium gas: porosity using grain volume measurements (**Section 3.8.2**) with bulk volume from mercury immersion (Equation 3–1), referred to as helium porosity.
- Mercury liquid: porosity derived from the mercury injection capillary pressure technique using Equations 3–19 and 3–20 for pore and bulk volumes, respectively, and referred to as MICP porosity.

The overall range of porosities for the ENAP1 set is 11.3-28.9 %v/v, with an average of 16.2 %v/v (**Table 4-8**), while the overall range of porosities for the ENAP2 set is 10.9-22.3 %v/v, with an average of 14.3 %v/v (**Table 4-9**). The standard deviation of each porosity type per well indicates that the brine porosity has the best precision for the ENAP1 set. In contrast, the NMR porosity has the best precision for the ENAP2 set. Helium porosity has the highest standard deviation for the ENAP1 set (5.2 %v/v) compared with the ENAP2 set (2.1 %v/v). The porosity types were compared per core set. Seven measurements from the ENAP1 set and three from the ENAP2 set were discarded due to laboratory measurement errors (**Figure 4-9**).

Table 4-8. ENAP1 set's porosities descriptive statistics.

Parameter	Brine (%v/v)	NMR (%v/v)	Helium (%v/v)	MICP (%v/v)
Minimum	12.4	12.1	11.3	12.2
Maximum	21.2	20.8	28.9	20.6
Average	16.1	14.9	18.5	15.3
Median	15.7	14.1	16.9	14.5
Standard deviation	2.0	2.7	5.2	2.5

Table 4-9. ENAP2 set's porosities descriptive statistics.

Parameter	Brine (%v/v)	NMR (%v/v)	Helium (%v/v)	MICP (%v/v)
Minimum	13.3	12.0	13.1	10.9
Maximum	22.3	16.0	21.8	16.6
Average	15.2	13.6	15.1	13.4
Median	14.7	13.2	14.4	13.3
Standard deviation	2.1	1.4	2.1	1.6

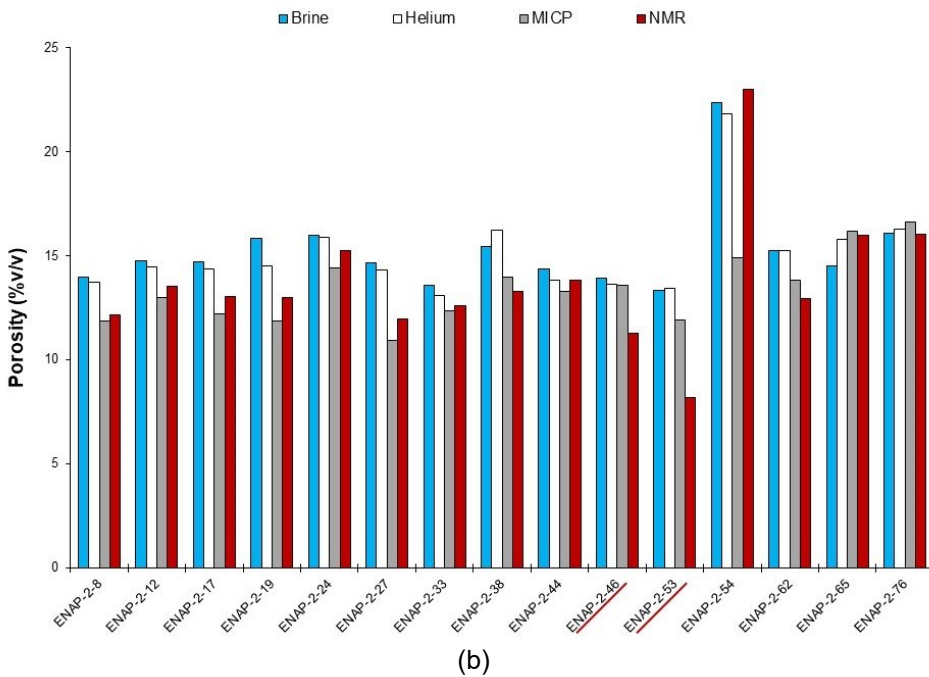
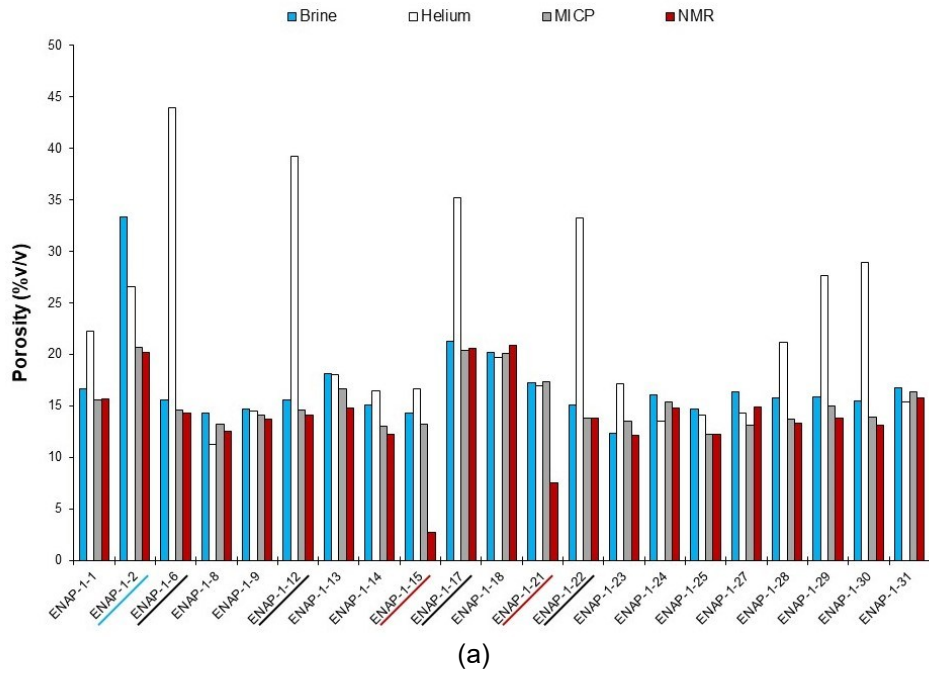


Figure 4-9. Bar chart of dataset derived porosities: (a) ENAP1 set, (b) ENAP2 set. The samples labelled with a coloured line indicate they are outliers in the porosity type measurement.

4.6.2 Stressed porosity

Stressed porosity derived from the autoporosity equipment (**Section 3.8.4**) of four samples of the ENAP2 set was obtained. The stressed core porosity at 3,500 psig confining pressure– the closest value to the reservoir pressure of 3,508 psig @2,300 m of vertical depth (Gonzalez-Gonzalez et al., 2018), was selected to be compared at ambient conditions (**Figure 4-10**). Both porosities match very well, with the stressed porosity being 2 %v/v points lower than the ambient helium porosity. In addition, the stressed porosity and ambient porosity ratio trend at increasing confining pressure were compared (**Figure 4-11**). Samples ENAP2-27 and ENAP2-44 were more stress-sensitive than ENAP2-76 and ENAP2-12. Still, their stressed porosity decreased by no more than a 3 % ratio from its original porosity.

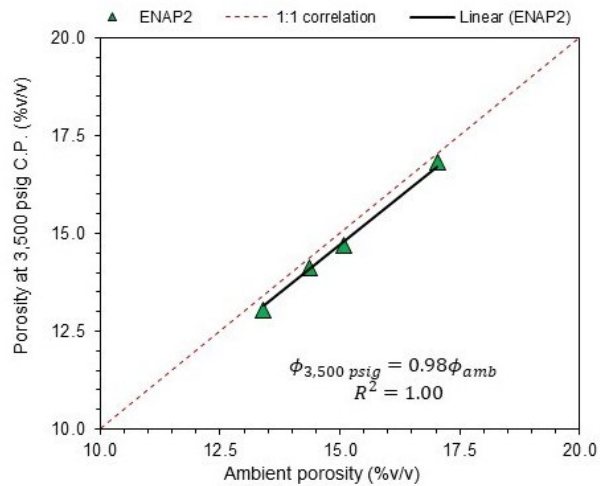


Figure 4-10. Cross-plot of core helium porosity (x-axis) and stressed helium porosity (y-axis) at 3,500 psig.

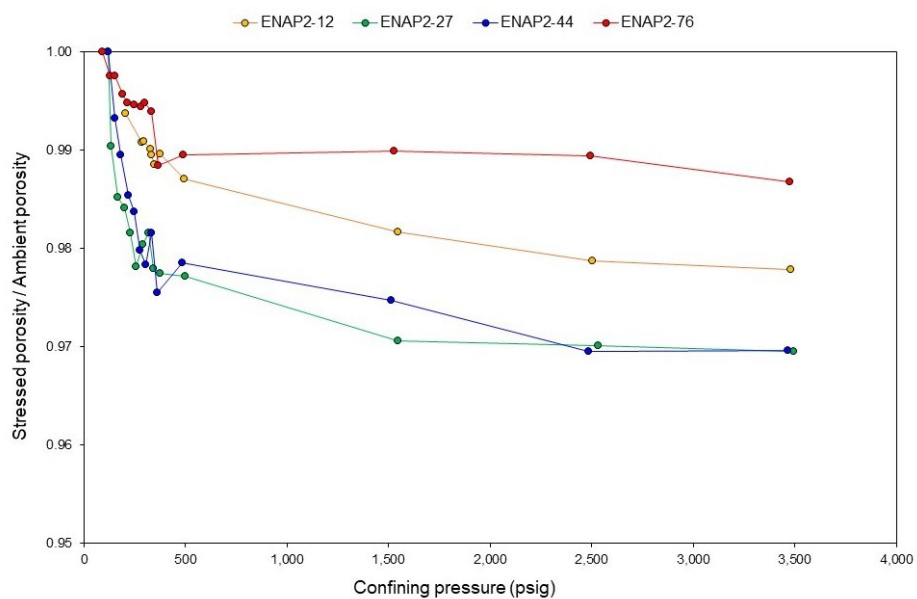


Figure 4-11. Cross-plot of stressed and ambient core helium porosity ratio (x-axis) and applied confining pressure (y-axis).

4.7 ZG permeability

4.7.1 Brine permeability

The range of the ZG brine permeability is 20 nD (nano Darcy) to 2.86 mD with a geometric average of 600 nD. ENAP1 set samples seem less permeable than the ENAP2 set samples, where the permeabilities of the latter have a significantly higher standard deviation (Table 4-10).

Table 4-10. Descriptive statistics of brine permeability measurements.

Parameter	ENAP1 set	ENAP2 set
Minimum (mD)	0.00011	0.00002
Maximum (mD)	0.065	2.86
Geometric average (mD)	0.00067	0.00080
Median (mD)	0.00041	0.00040
Standard deviation (mD)	0.014	0.74

4.7.2 Klinkenberg corrected gas permeability

Klinkenberg permeability was derived at three confining pressures: 1,500, 2500, and 3,500 psig (Figure 4-12). The Klinkenberg permeability ranges from 790 nD to 2.15 mD with a geometric average of 380 nD (between the three confining pressures). Only sample ENAP2-19 was measured using steady-state permeametry, and the rest were measured with the pulse-decay method (Section 3.9). The standard deviation of both core sets is high, indicating a widespread dispersion in permeability within ZG (Tables 4-11 and 4-12).

Table 4-11. Descriptive statistics of ENAP1 set derived Klinkenberg permeabilities.

Parameter	1,500 psigg C.P.	2,500 psigg C.P.	3,500 psigg C.P.
Minimum (mD)	0.00079	0.00098	0.00096
Maximum (mD)	0.56	0.55	0.54
Geometric average (mD)	0.0070	0.0058	0.0047
Median (mD)	0.0037	0.0025	0.0022
Standard deviation (mD)	0.14	0.13	0.12

Table 4-12. Descriptive statistics of ENAP2 set derived Klinkenberg permeabilities.

Parameter	1,500 psigg C.P.	2,500 psigg C.P.	3,500 psigg C.P.
Minimum (mD)	0.0021	0.0010	0.0009
Maximum (mD)	2.15	1.56	1.14
Geometric average (mD)	0.0082	0.0087	0.0068
Median (mD)	0.019	0.0039	0.0036
Standard deviation (mD)	0.60	0.30	0.23

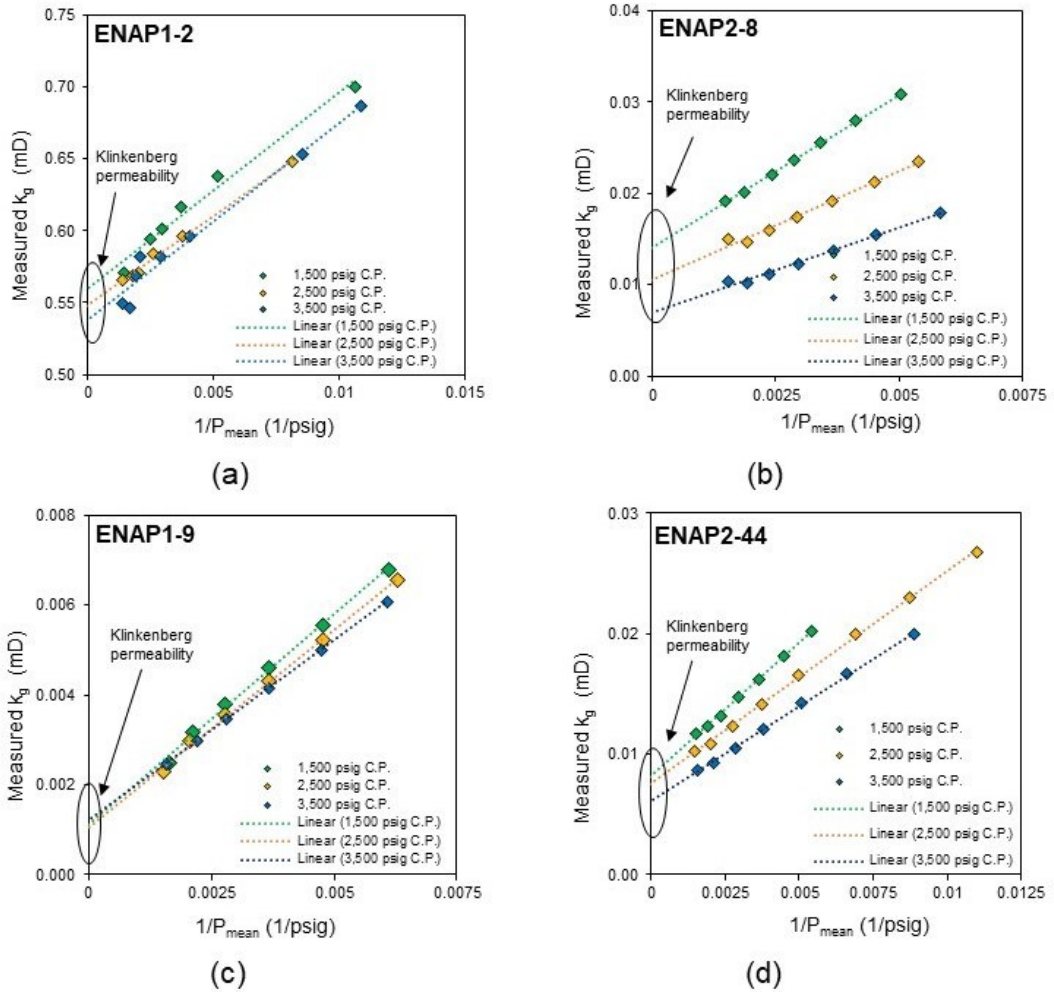


Figure 4-12. Examples of cross-plot of measured gas permeability vs the inverse mean pore pressure to derive the Klinkenberg permeability.

Klinkenberg permeabilities (k_{∞}) at a confining pressure of 1,500 psig were compared against those at confining pressures of 2,500 and 3,500 psig (**Figure 4-13**), finding empirical correlations by the power-of-law, with R^2 of 0.99 and 0.96, respectively. The stress sensitivity is noted at low permeabilities ($k_{\infty} < 0.01$ mD), which is further noticeable with the ratio of the highest and lower confining pressures (**Figure 4-14**).

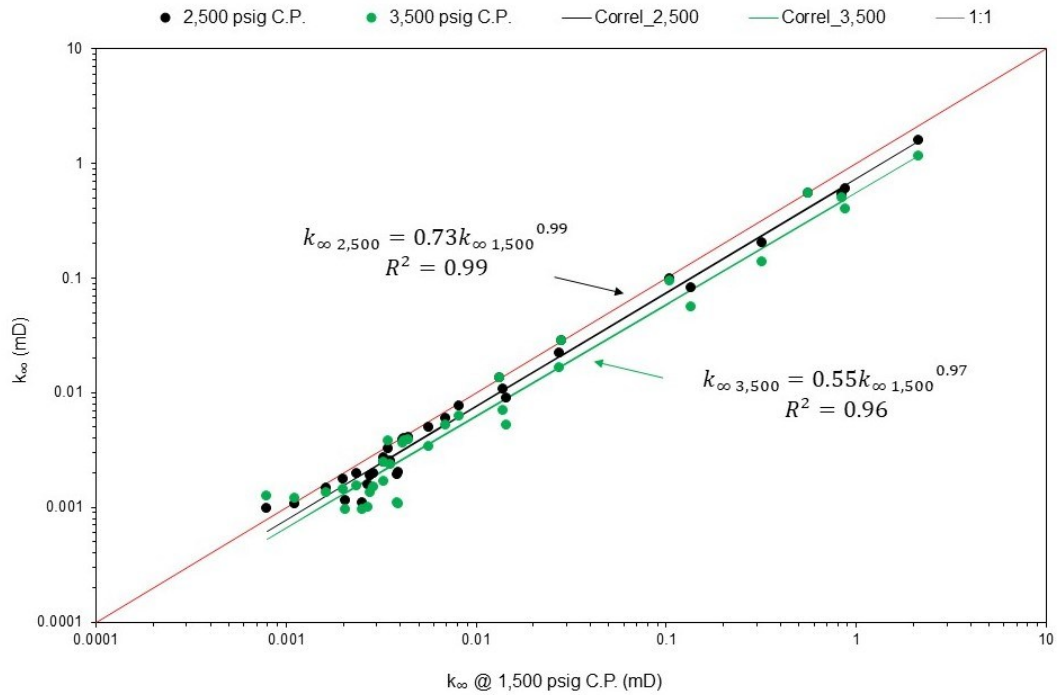


Figure 4-13. Cross-plot of Klinkenberg permeability at three confining pressures of the dataset.

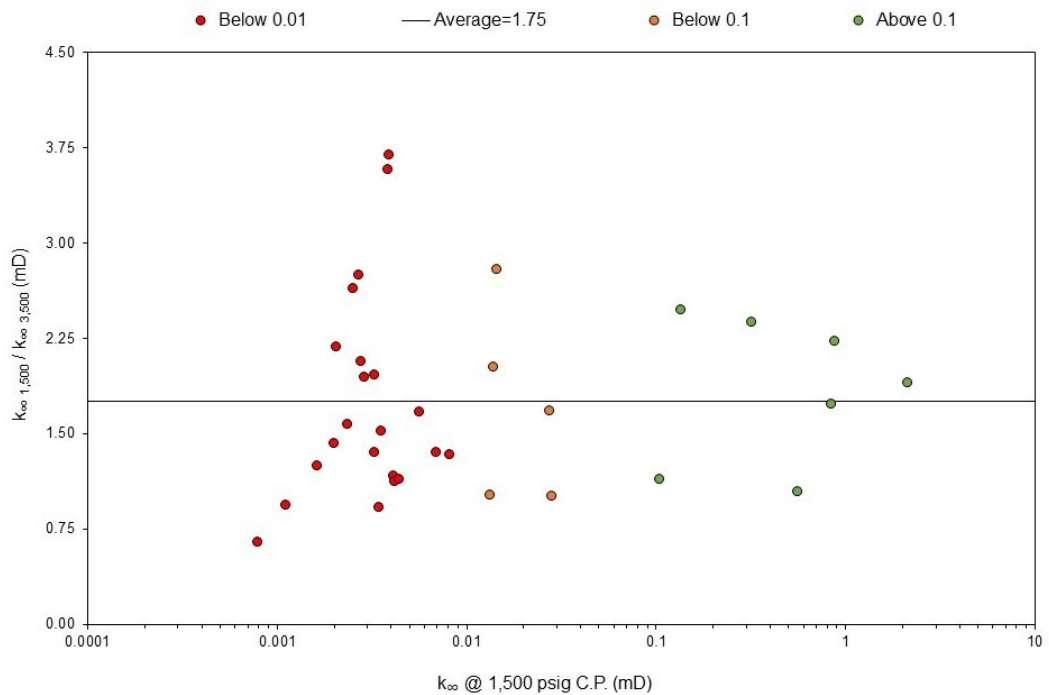


Figure 4-14. Cross-plot of Klinkenberg permeability ratio at 1,500 psig and 3,500 psig confining pressures of the dataset.

4.7.3 Gas and brine permeabilities relationship

The Klinkenberg permeabilities reported in **Section 4.7.1** were compared to the brine permeabilities reported in **Section 4.7.2** as a ratio (k_{∞}/k_W). The overall range of the dataset ratio is from 2 to 305, with an average of 12 (**Table 4-13**). ENAP2 set ratios are higher than 10 (12 of 15 samples), while ENAP1 set ratios are lower than 10 (12

of 21 samples) (Figure 4-15). These ratios indicate that Klinkenberg permeability is higher than the absolute brine in the whole dataset (Figure 4-16).

Table 4-13. Descriptive statistics of Klinkenberg and brine permeabilities ratio of the dataset.

Parameter	ENAP1 set	ENAP2 set
Minimum (mD)	2	2
Maximum (mD)	250	305
Average (mD)	24	70
Median (mD)	9	25
Standard deviation (mD)	53	83

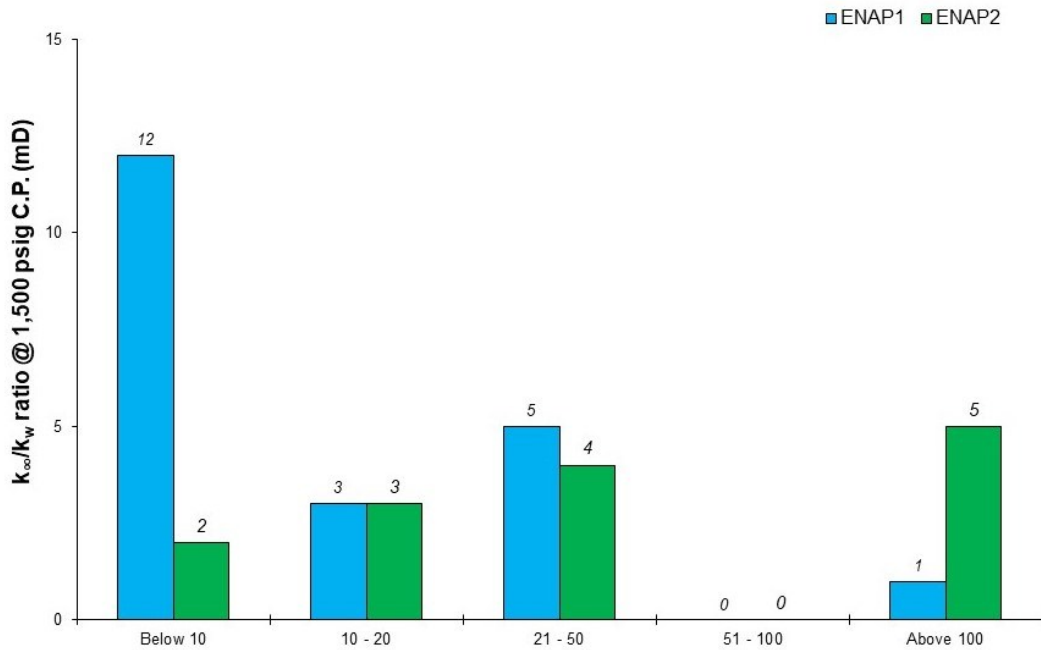


Figure 4-15. Klinkenberg and brine permeability ratio.

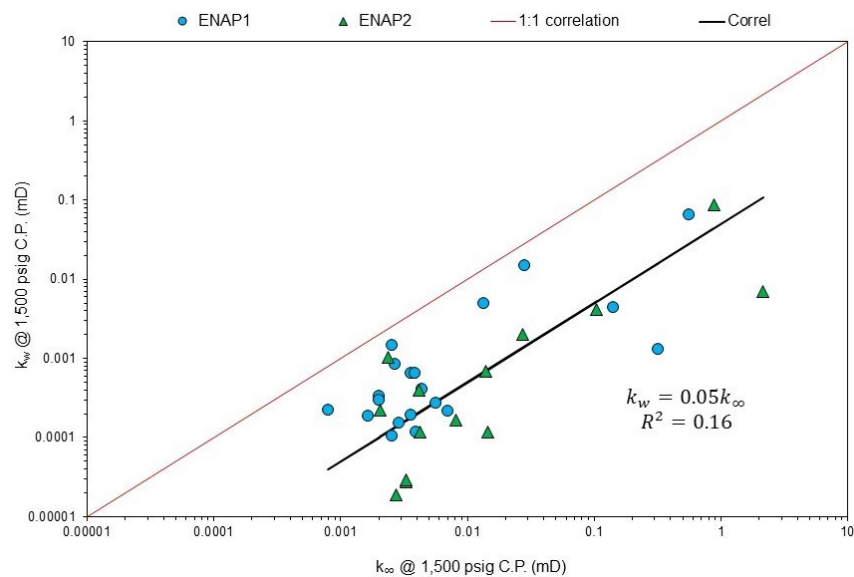


Figure 4-16. Scatter plot of brine against Klinkenberg gas permeability.

4.8 ZG permeability and porosity relationships

4.8.1 Permeability and porosity cross-plot

The conventional permeability-porosity cross-plot was first analysed to identify outliers, potential facies and empirical relationships. According to the SEM image analysis, five cores from the dataset were categorised as fractured samples since their permeability measurements do not represent their matrix permeability (**Figure 4-17**). Two samples (ENAP1-2 and ENAP2-54) were unique to the dataset. They contain large pores, high permeability, a lack of glauconite, and high chlorite; hence, these cores are called pay sand (chloritic sandstones).

Three facies were grouped according to lithology, porosity and permeability (**Figure 4-18** and **Table 4-14**). Facies 1 corresponds to the pay sands with the highest permeability, while Facies 2 corresponds to glauconitic sandstones with low to ultra-low permeability that follows Facies 1's positive trend. Facies 3 corresponds to glauconitic sandstones with ultra-low permeability with high porosity.

Three empirical correlations to predict gas permeability as a function of ambient helium porosity were used: exponential and power-law correlations were derived with R^2 of 0.64 and 0.57, respectively, for Facies 1 and 2 (**Figure 4-19 a**) and with R^2 of 0.63 and 0.61, respectively for Facies 3 (**Figure 4-19 b**). The third correlation was derived from the Flow Zone Indicator concept (Amaefule et al., 1993) and based on the Kozeny-Carman permeability (e.g. Wyllie and Gardner, 1958) theoretical expression, assuming that the pore throat radius is like a cylindrical capillary tube (Equation 4-1). Three parameters were calculated to find a correlation as hydraulic units: RQI (Equation 4-2), ϕ_z (Equation 4-3), and FZI (Equation 4-4). The log-log cross-plot found a linear correlation between the FZI and k/ϕ , with $R^2= 0.92$ for Facies 1 and 2 from $\text{Log } FZI > -1.9$ and $R^2= 0.96$ for Facies 3 (**Figure 4-20**). Finally, a new correlation was developed from this method (Equation 4-5), with an R^2 of 0.58 for Facies 1 and 2 and an R^2 of 0.62 for Facies 3 (**Figure 4-21**).

Equation 4-1

$$k_{KC} = \frac{\phi^3}{(1 - \phi)^2} \left[\frac{1}{F_S \tau^2 S_{gv}^2} \right]$$

where F_S is the shape factor (2 for circular cylinder), τ is the tortuosity factor defined as the effective length from the total length ratio of the flow paths in the pore space (e.g. Adisoemarta et al., 2000), and S_{gv} is the specific surface area to grain volume ratio in μm^{-1} .

Equation 4-2

$$RQI = 0.0314 \sqrt{\frac{k}{\phi}}$$

Equation 4-3

$$\phi_z = \frac{\phi}{1 - \phi}$$

Equation 4-4

$$FZI = \frac{1}{F_S \tau^2 S_{gv}^2} = \frac{RQI}{\phi_z}$$

where RQI is the reservoir quality index (μm), ϕ_z is the pore-volume to grain-volume ratio, and FZI is the flow zone indicator (μm).

Equation 4-5

$$k = \phi_{He} \left[\frac{10^b}{0.0314} \left(\frac{\phi_{He}}{1 - \phi_{He}} \right) \right]^{(0.5-m)}$$

where m and b are the slope and intercept of the FZI cross-plot. For Facies 1 and 2, $m= 0.38$ and $b= -0.96$, while for Facies 3, $m= 0.81$ and $b= -0.34$, respectively.

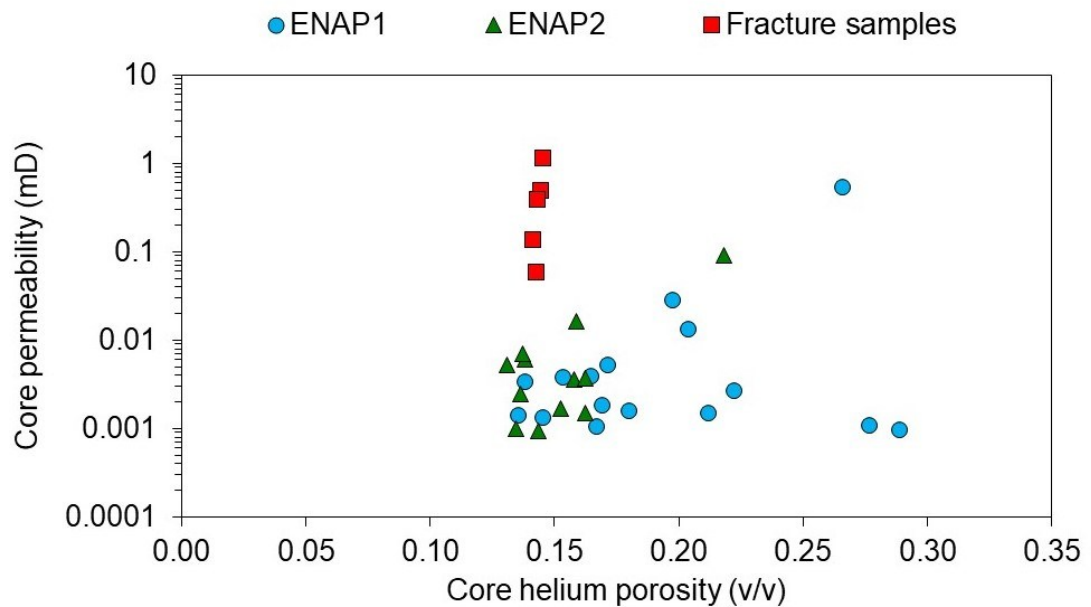


Figure 4-17. Core helium porosity vs core Klinkenberg permeability at 3,500 psig confining pressure cross-plot.

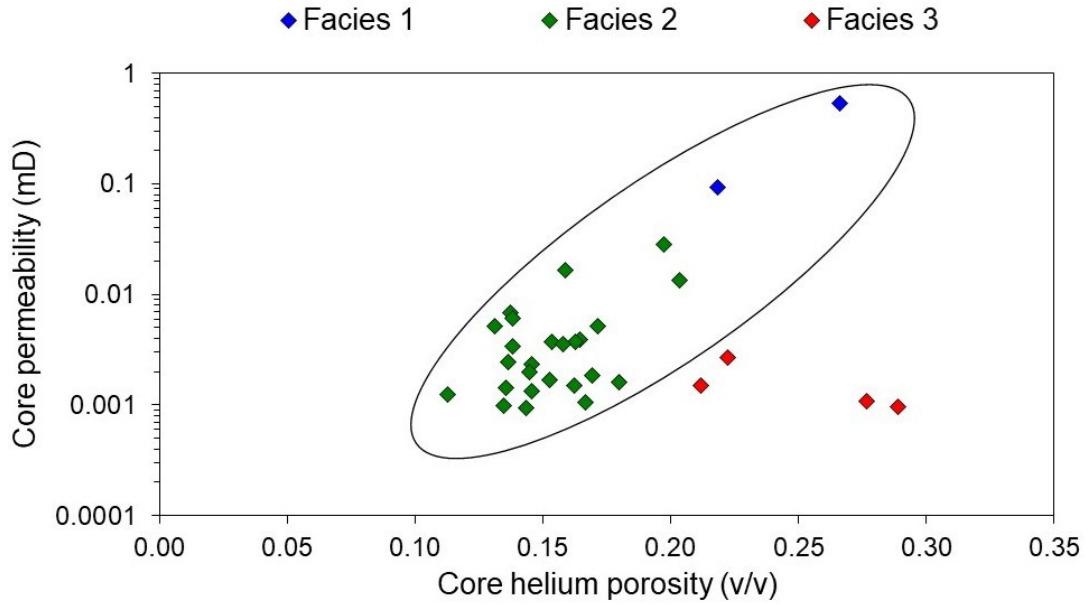


Figure 4-18. Porosity and permeability cross-plot discriminated by facies 1, 2, and 3.

Table 4-14. Facies lithological, porosity and permeability ranges.

Facies	Lithology	Core helium porosity range (%v/v)	Core absolute permeability range (mD)
1	Chloritic sandstones (pay sands)	22 – 27	0.093 – 0.54
2	Glaucconitic sandstones from low to ultra-low permeability	11 – 20	0.001 – 0.028
3	Glaucconitic sandstones with ultra-low permeability	21 – 29	0.001 – 0.0027

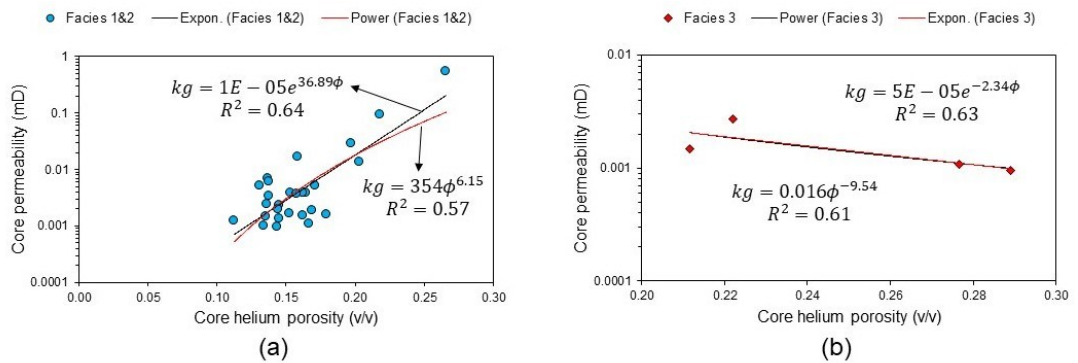


Figure 4-19. Exponential and power-law correlations for Facies 1 and 2 together (left side) and Facies 3 separately (right side).

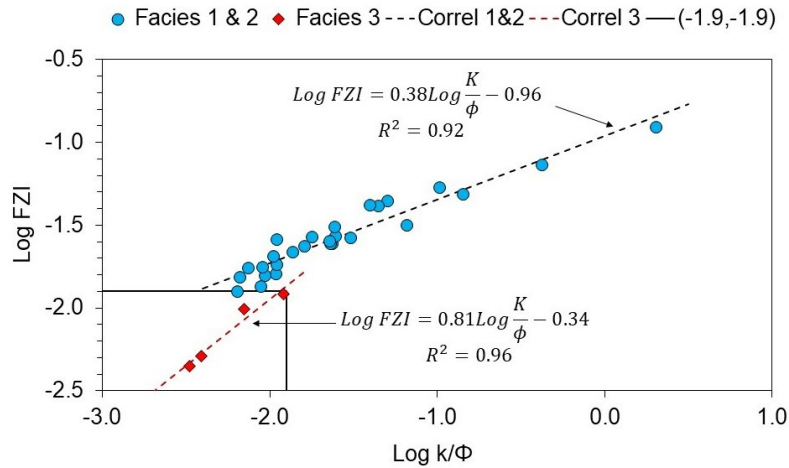


Figure 4-20. Log k/Φ vs Log FZI cross-plot with linear correlation of Facies 1 and 2 and Facies 3 separately. Facies 3 separates from the rest at coordinate [-1.9, -1.9].

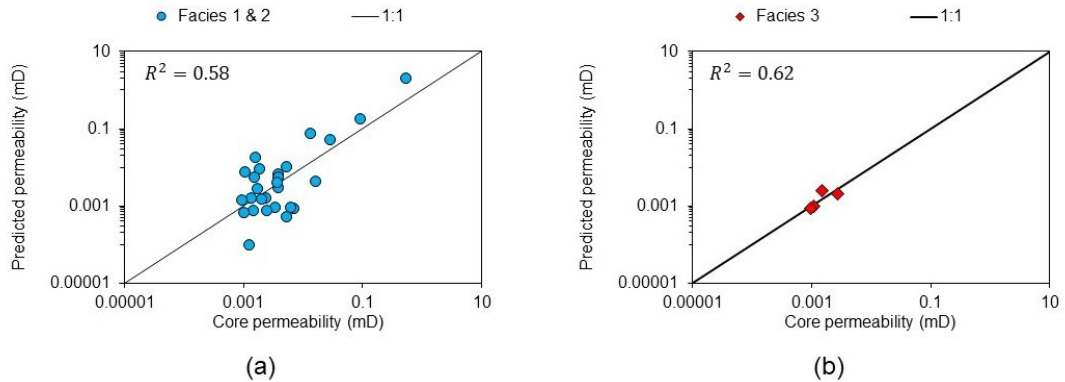
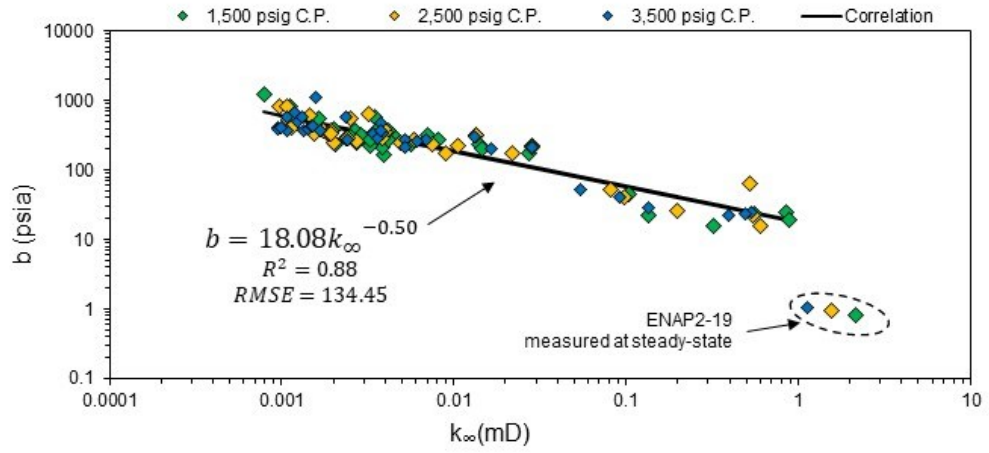


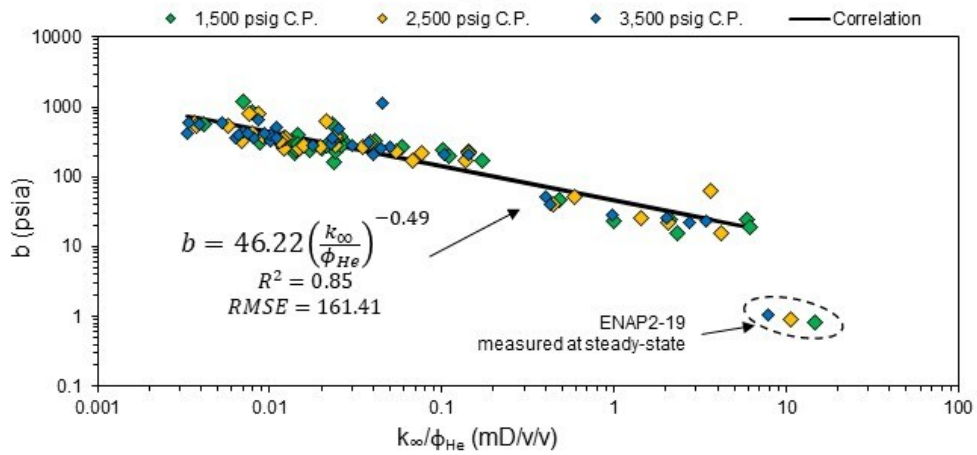
Figure 4-21. Core permeability vs predicted permeability from the FZI method for Facies 1 and 2 together (left side) and Facies 3 (right side).

4.8.2 Correlations with Klinkenberg b-values

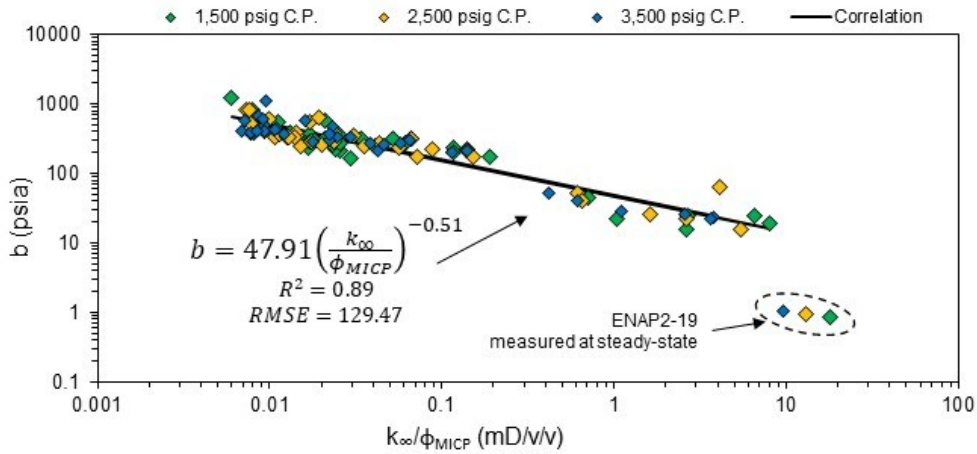
The gas slippage factor was further analysed using the least-square method since the ZG cores are in the low-permeability range. Sample ENAP2-19 was not considered as it was the only sample measured with the steady-state method. Three empirical correlations were found to correlate the slippage factor b with the Klinkenberg permeabilities, including the helium and MICP porosities shown in **Figure 4-22**. The first correlation followed Jones and Owens's (1980) workflow, where the slope value was -0.50. The second and third correlations followed Sampath and Keighin's (1982) workflow, which includes the porosity as a third parameter. The helium and MICP porosities gave the best correlations, obtaining slope values of -0.49 and -0.51.



(a)



(b)



(c)

Figure 4-22. Cross-plots: (a) slippage factor b against Klinkenberg permeability, (b) the ratio of Klinkenberg permeability and helium porosity, and (c) the ratio of Klinkenberg permeability and MICP porosity. Sample ENAP2-19 is an outlier since its permeabilities were measured at steady-state, while the rest of the dataset was measured with the pulse-decay method.

4.9 Discussion

4.9.1 Clay minerals contribution to ZG microstructure

A third of the ZG reservoir comprises clay minerals (32 %v/v in ENAP1 and 34 %v/v in ENAP2). The XRD interpretation software could not identify glauconite at the first-order basal reflection of the 10 Å peak since it overlaps between illite and expandable mixed layers (**Section 2.3.1**). Nevertheless, since glauconite belongs to the mica group (Hugget, 2021) and is mixed layered with other 2:1 clay minerals (e.g. Thompson and Hower, 1975; Baker et al., 1997), the combination of XRD mica and illite-smectite is considered as glauconitic mica and glauconitic smectite following Odin and Matter (1981) glauconitization guidelines on XRD interpretation. Further investigation needs to be conducted on the X-ray diffractogram interpretation to confirm the presence of glauconite. Regardless, the XRF analysis indicated a high presence of iron (an overall average of 13.5%wt Fe₂O₃), and the clay-XRD analysis confirmed the presence of clinocllore minerals.

Likely, the high grain density of ZG formation (~2.71 g/cm³) is due to the presence of the iron-rich clays; this interpretation agrees with the reported greensand grain densities by Cimbalnikova (1970), Odin and Matter (1981), and Patchett et al. (1993).

SEM analysis confirmed the presence of grains that have a chemical composition consistent with glauconite; these have ovoid, subangular, and vermiform shapes that agree with those reported by Odin and Letolle (1980), Odin and Matter (1981), Krinsley et al. (1998), and López-Quirós et al. (2020). The high iron content identified in XRF is due to the significant presence of framboidal pyrite, glauconite and chlorite distributed as pore-lining, pore-bridging and within the matrix and also confirmed by the CT scan analysis, where the higher the HU standard deviation, the higher the heterogeneity degree and high-density minerals presence (i.e., pyrite).

In addition, ENAP characterises the pay sands as a porous tuffaceous wacke with fine to medium volcanic lithics, plagioclase, and minor quartz embedded in a clayey matrix deposited in a mid-to outer shelf environment. Pinto et al. (2022) describe the ZG diagenetic process as transforming much of glauconite to chlorite during mesogenesis. In this context, chlorite is interpreted as primarily diagenetic, formed during mesogenesis through the alteration of unstable minerals such as feldspar or volcanic grains. Evidence for this include its association with zones of significance microporosity, where labile minerals have been replaced.

The secondary porosity is likely a result of carbonate mineral dissolution, driven by acidification associated with increased CO₂ flux. This process involves the dissolution of primary grains such as bioclasts, feldspar, or volcanic particles, and the subsequent formation of mouldic pores. The presence of CO₂ enhances the

dissolution of minerals, it is not derived directly from carbonate dissolution but from external sources or hydrocarbons, as carbonate dissolution consumes acid (Pinto et al., 2022). This secondary porosity was identified only in chlorite-rich sandstones SEM images, samples ENAP 1-2 and ENAP2-54 (**Figure 4-4 A**), i.e. pay sands. In contrast, glauconite-rich sandstones do not undergo the same degree of dissolution or porosity generation. Even though there is secondary porosity in the pay sands, the permeability remains low (**Section 4.7**) because the pores generated by dissolution and chlorite microporosity are not well-connected, thus restricting fluid flow.

These findings indicate that chlorite rather than iron content is the mineralogical marker to separate the pay sands, which agrees with the company petrophysicists' hypothesis. Glauconite grains are distinguishable for the non-expert eye as with fissured or cracks on its grain edges (Krinsley et al., 1998), as observed in SEM images (**Figure 4-6 D and J**). Such fissures may be formed due to displacive growth in the glauconitization process (Odin and Matter, 1981) or shrinkage when the grain loses interlayered water (Odom, 1976). Since the ZG greensand have tiny pore throats (significant microporosity), they store a high amount of irreducible water, further addressed in **Chapter 5**.

Finally, a good linear correlation ($R^2=0.76$) was found between the clay content and specific surface area within 3 to 15 m²/g (**Section 4.4**). In comparison, Hossain et al. (2011a) reported a range of 17 to 23 m²/g for the Hemond and Ty greensand reservoirs of the North Sea located at a vertical depth of ~1,770 m with a permeability range of 60 to 1,000 mD and porosity of 25 to 40 %v/v. They converted SSA to a specific surface of pores (i.e. surface to volume ratio of pores), finding a linear correlation with the XRD clay minerals content ($R^2= 0.68$) for sixteen samples. The correlation found for ZG can replace the SSA term, expressed as S_{gv} , in Kozeny-Carman's permeability formula (Equation 4-1). A new correlation can be used to predict permeability using porosity and clay content as a dependent variable. This suggestion is analysed in **Section 4.9.4**.

4.9.2 ZG total and interconnected porosity

As described in **Section 2.1.1**, the total porosity includes free mobile and enclosed fluids, and the effective porosity can be defined as "*the total porosity less any water associated with clay minerals in the rock*" (Dodge et al., 1996, p. 2). This section discusses the four derived porosity types from the core analysis programme (**Section 4.6.1**) and those that can be referred to as the ZG total and effective core porosity.

The helium core porosity was first compared with brine, MICP, and NMR core porosities (**Figure 4-23**). For the samples from ENAP2, helium porosity has a fairly good match with brine ($R^2= 0.92$) and NMR ($R^2= 0.88$) porosities but a poor match ($R^2= 0.33$) with MICP porosity. In contrast, for the ENAP1 samples, helium porosity is higher than its brine ($R^2= 0.03$), MICP ($R^2= 0.14$) and NMR ($R^2= 0.09$) porosities. The CT images suggest that the ENAP1 samples are more heterogeneous than those from ENAP2 (**Figure 4-3**). Typically, helium-derived porosity is used as total porosity to calibrate the porosity log since the helium molecule (diameter of 0.064 nm) is tiny enough to pass through the microporosity clay portion (e.g. McPhee et al., 2015). So, it might be that the helium effectively navigated through the clay portion in ENAP1.

The high values in helium porosity observed in the ENAP1 set can be attributed to the sampling size. The cores of the ENAP1 set were sidewall core plugs of 23 mm (~1 inch) diameter with an average length of 28 mm, while for ENAP2 set were core plugs of 37 mm (~1.5 inch) with an average length of 45 mm. This logic is supported by the standard deviation values of the porosity types in ENAP1 (**Table 4-8**); helium porosity was +5.2 %v/v, about two times higher than the rest of the standard deviation porosities. Complementary, the derived grain density of both sets is similar, with an average of 2.73 g/cm³, where the ENAP1 set presented a standard deviation three times higher than the ENAP2 set (**Table 4-7**). Therefore, the ENAP1 helium porosities presented measurement errors. Nonetheless, considering the overall data indicates that the ENAP1 set is more heterogeneous and microporous than the ENAP2 set, it is plausible to hypothesise that helium porosity from both sets can be used as total core porosity.

Following the previous hypothesis, the brine and NMR porosities were compared and subtracted from the helium porosity (**Figure 4-24 a and b**) because both measured pore volume from fully brine-saturated core plugs. Brine and NMR porosities match fairly well ($R^2=0.83$), and the difference with helium porosity presents a very good match ($R^2=0.92$). The ENAP1 set presents the highest delta values, and for both sets, 25% (9 of 36 cores) present a delta with helium from 0 to 15%v/v units following a linear trend. In addition, the helium and NMR porosity delta presented a broad positive correlation with glauconite and chlorite minerals (**Figure 4-24 c**). This finding disagrees with Rueslatten et al. (1998), who found only a positive correlation with the chlorite of North Sea greensand wells. Finally, both deltas were compared with core permeability – Klinkenberg at 3,500 psig C.P. (**Figure 4-24 d**), finding that the high deltas are within permeability below 0.01 mD indicating that brine did not penetrate the tiny pore throats at ultra-low permeability. This analysis sustains the hypothesis of using core helium porosity as total porosity.

Brine porosity is an interconnected porosity (API RP, 1998) since its technique measurement is based on liquid saturation. NMR porosity is a measurement of NMR T_2 decay distribution by counting hydrogen atoms in a fully saturated core, including the clay-bound water zone, so it should correspond to total porosity. Nonetheless, for greensands, the porosity derived from NMR logs has proven to serve as an effective porosity for well-log interpretation because of the paramagnetic properties of iron minerals that cause shorter T_2 distributions (Dodge et al., 1996; Rueslatten et al., 1998; Slot-Petersen et al., 1998). MICP technique measures interconnected porosity, where mercury intrudes from the largest pores to the tiniest under pressure (**Section 3.10**). So, a comparison between NMR and brine porosities with MICP porosity was done to identify which is a potentially interconnected porosity (**Figure 4-25**). A very good match was found between NMR and MICP porosities ($R^2=0.89$), except for sample ENAP2-54. The discrepancy is most likely that the measured sample size ($\sim 3 \text{ cm}^3$) with the MICP technique was not representative. These results show that brine, MICP and NMR porosities can be referred to as interconnected porosities. An effective porosity at this stage cannot be defined, as there was no laboratory experiment to measure bound water. An alternative is to define a T_2 cut-off value to separate the clay microporosity from deriving effective porosity, as defined by Dodge et al. (1996). This suggestion is addressed in **Chapter 5**.

Finally, the autoporosity results (**Section 4.6.2**) indicate a stressed porosity decreased of no more than 3% from its original porosity at 3,500 psig of confining pressure, concluding that the porosity is not stress-dependant and that ambient porosity values can be used as reservoir porosity for ZG. Therefore, the porosities derived from helium porosimetry, NMR technology, and brine saturation are selected to build the porosity model in the well-log calibration process.

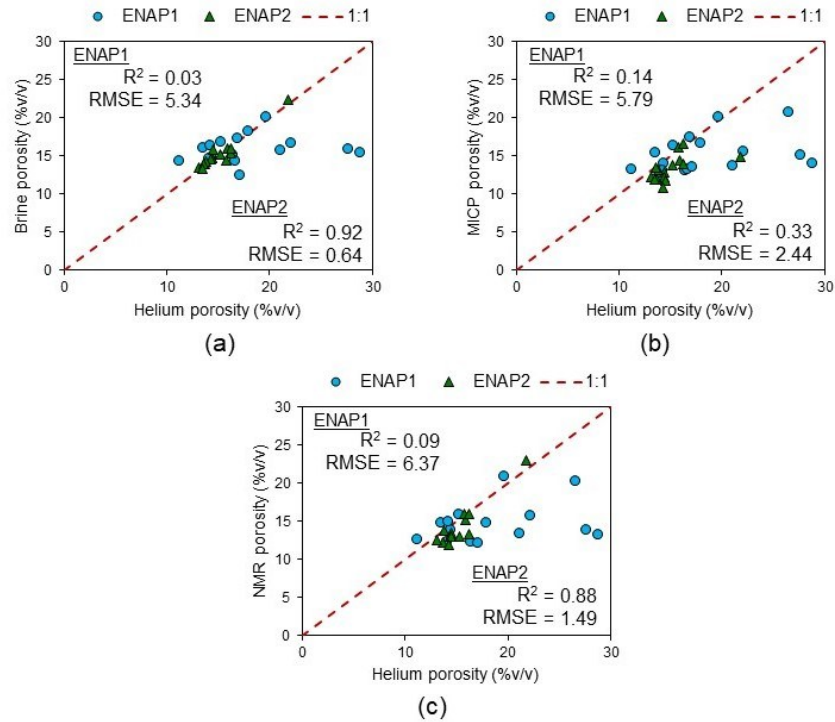


Figure 4-23. Cross-plots comparing core helium porosity type: (a) Helium porosity versus brine porosity. (b) Helium porosity versus MICP porosity. (c) Helium porosity versus NMR porosity.

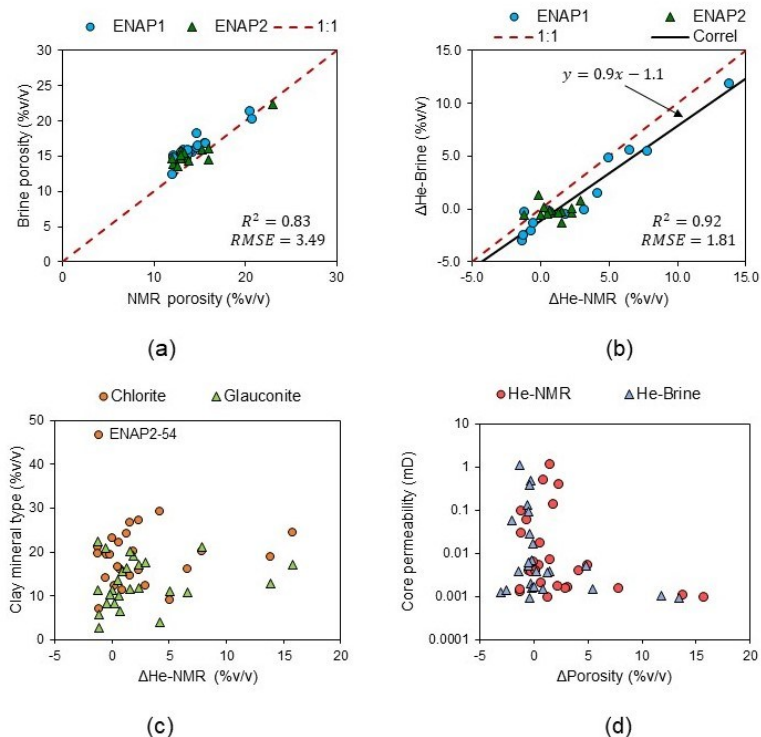


Figure 4-24. Cross-plot of core porosity types: (a) NMR porosity versus brine porosity. (b) Delta Helium and NMR porosities versus Delta Helium and brine porosities. (c) Delta Helium and NMR porosities versus clay mineral type. (d) Delta porosities versus core permeability at 3,500 psig C.P.

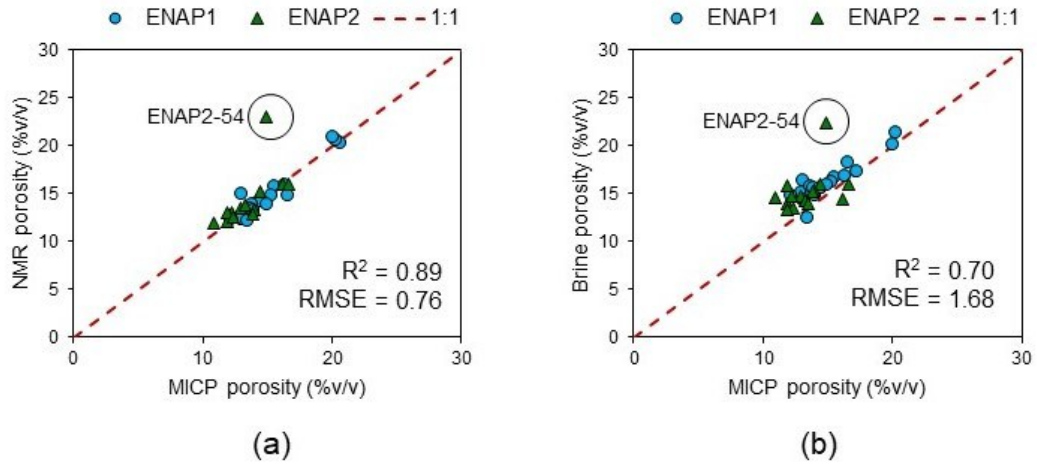


Figure 4-25. Cross-plot of core porosity types: (a) MICP porosity vs NMR porosity. (b) MICP porosity vs Brine porosity.

4.9.3 Permeability and porosity correlations

An excellent correlation ($R^2 = 0.96$) was found to convert Klinkenberg permeabilities from 1,500 to 3,500 psigg, which is close to a ratio of 2:1 ($\sim k_{\infty @ 3,500} = 0.55 k_{\infty @ 1,500}$) (**Section 4.7.2**). This finding indicates that reservoir permeability must be corrected (e.g. Akai et al., 2016). The overall gas and brine permeabilities ratio was 12 (**Section 4.7.3**), meaning that the Klinkenberg permeabilities are higher than the brine permeability in the ZG cores. From the laboratory standpoint, this significant difference may be due to the sampling brine saturation process, clay particle rearrangement, rehydration or flocculation since the formation water is very low in salinity, i.e. 12,000 ppm NaCl (e.g. McPhee et al., 2015). Six fracture samples were categorised as outliers when cross-plotting total porosity with permeability (**Figure 4-17**). Interestingly, these are located in the same depth range per well, indicating that the rock in those zones is stiff and, in laboratory permeability measurements, was prone to damage due to gas expansion, causing artificial fractures.

Three correlations were found to predict permeability from total core porosity (**Section 4.8.1**). An extended statistical workflow from Comisky et al. (2007) was followed to rank the correlations by calculating the RMSE, R^2 and a standard error (STDx) of the predicted log permeability value (y) for each core log permeability (x) in the correlation (Equation 4–6).

Equation 4–6

$$STDx = \sqrt{\frac{1}{(n-2)} \left[\sum (y - \bar{y})^2 - \frac{[\sum (x - \bar{x})(y - \bar{y})]^2}{\sum (x - \bar{x})^2} \right]}$$

where n is the sample size, y is the predicted value, x is the original value, \bar{x} is the average of the original values and \bar{y} is the average of the predicted values.

The final rank resulted from the sum of the three rank metrics (Tables 4-15 and 4-16) combined with a visual comparison of the actual and predicted permeability (Figure 4-26) for the three Facies. The exponential correlation is best followed closely by the power-of-law and FZI correlation (Equation 4-5). However, the FZI method can be used as a criterion to separate all facies with Log FZI isolines (Figure 4-27), thus $-1.25 < \text{Log FZI} < -0.8$ for Facies 1, $-1.9 < \text{Log FZI} < -1.25$ for Facies 2, and $-2.4 < \text{Log FZI} < -1.9$ for Facies 3 (Figure 4-28). In other words, three hydraulic units are defined.

Chapter 5 Chapter 6
ZG electrical properties and ultrasonic velocities, the NMR and MICP data will be added to confirm if these three facies are correctly grouped.

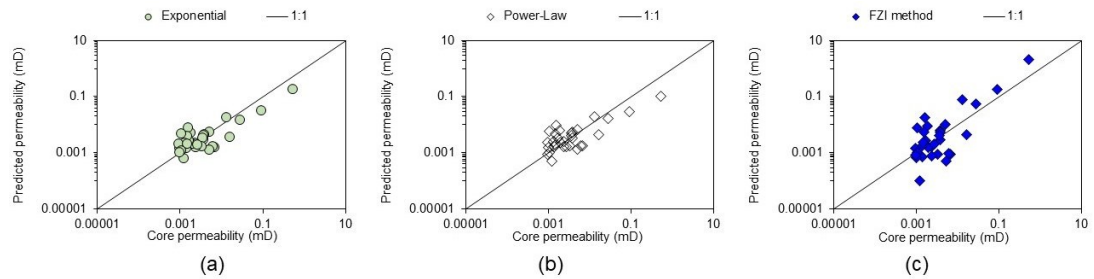


Figure 4-26. Core permeability vs predicted permeability from the (a) exponential, (b) power-law, and (c) FZI correlations of the ZG dataset.

Table 4-15. Statistical metrics and rank of Facies 1 and 2.

Correlation	R ²	R ² rank	RMSE	RMSE rank	STD	STD rank	Sum ranks
Exponential	0.64	1	0.38	1	0.31	1	3
Power-law	0.57	3	0.41	2	0.32	2	7
FZI method	0.58	2	0.57	3	0.59	3	8

Table 4-16. Statistical metrics and rank of Facies 3.

Correlation	R ²	R ² rank	RMSE	RMSE rank	STD	STD rank	Sum ranks
Exponential	0.63	1	0.11	1	0.12	1	3
Power-law	0.61	3	0.11	2	0.12	2	7
FZI method	0.62	2	0.12	3	0.17	3	8

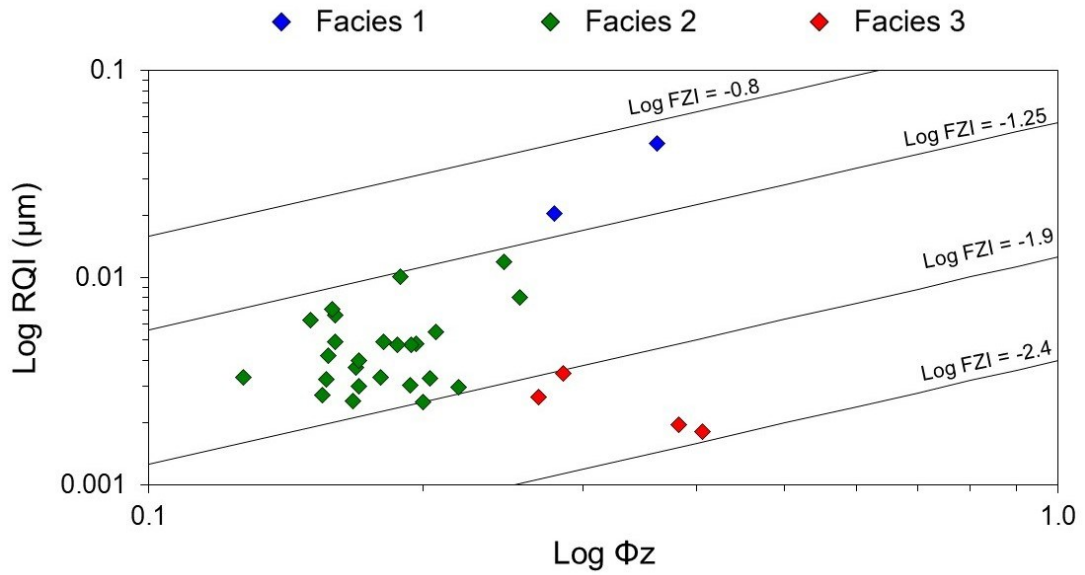


Figure 4-27. Log-log cross-plot of Φ_z (pore-volume to grain-volume ratio) and RQI (reservoir quality index) with isolines of Log FZI separating Facies 1, 2, and 3.

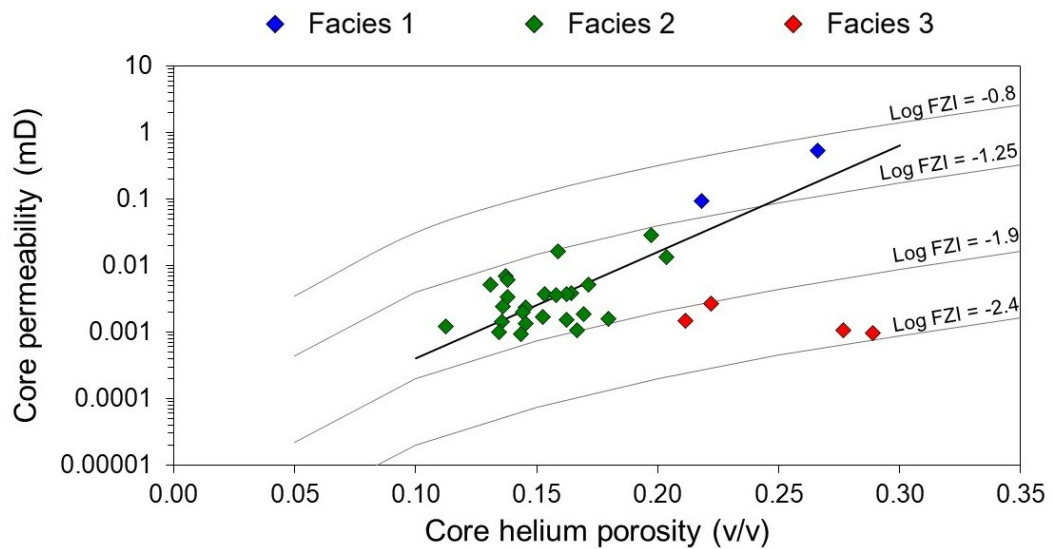


Figure 4-28. Porosity vs permeability cross-plot with isolines of Log FZI discriminated by Facies 1, 2, and 3. The black line corresponds to the exponential correlation to predict permeability using porosity as input of Facies 1 and 2.

4.9.4 Correlations based on Klinkenberg b-values

Three correlations were found between the Klinkenberg slippage factor b and permeabilities, where two added core porosity as a third term (**Section 4.8.2**). The first correlation followed Jones and Owens's (1980) workflow using only b and k_{∞} . The obtained slope value is -0.50, which agrees with the theoretical value of pore throat radius modelled as parallel capillary bundles (Kundt and Warburg, 1875). The other two correlations resulted in slope values of -0.49 and -0.51 that agree with the theoretical derivation of a square-root correlation presented by Florence et al. (2007):

Equation 4–7

$$b = \beta \frac{k_{\infty}^{-0.50}}{\phi}$$

where β is a coefficient that depends on the gas type used for the permeability core measurements.

Finally, three derived empirical correlations for the ZG reservoir are presented to estimate Klinkenberg permeability (k_{∞}) given core helium permeability and pore average pressure (Equation 4–8), total porosity (Equation 4–9) or interconnected porosity, NMR or MICP core porosity (Equation 4–10). These are valid for core permeabilities between 0.0008 and 1 mD and confining pressures between 1,500 to 3,500 psig. The Newton-Raphson iterative method can solve these non-linear equations (e.g. McPhee et al., 2015).

Equation 4–8

$$k_{\infty} + \frac{18.08}{P_{av}} k_{\infty}^{0.50} - k_g = 0$$

Equation 4–9

$$k_{\infty} + \frac{46.22 \phi_{total}^{0.49}}{P_{av}} k_{\infty}^{0.51} - k_g = 0$$

Equation 4–10

$$k_{\infty} + \frac{47.91 \phi_{int}^{0.51}}{P_{av}} k_{\infty}^{0.49} - k_g = 0$$

where k_g is the gas-measured permeability (mD), k_{∞} is the Klinkenberg permeability (mD), P_{av} is the mean flow pressure (psiga) equal to $(P_1+P_2)/2$, ϕ_{total} is the total porosity (v/v), and ϕ_{int} is the interconnected porosity (v/v).

4.10 Summary

The following summarises the chapter's key findings and informs the subsequent chapters by providing a detailed understanding of the lithofacies and their petrophysical characteristics. The identified lithofacies are the key controls on the pore systems, porosity, and permeability relationships, underpinning the analysis in the upcoming chapter on pore size distribution and other properties.

- Clay minerals, namely chlorite and glauconite are confirmed as significant factors influencing the ZG reservoir porosity and permeability relationships (**Section 4.9.3**). However, chlorite alone does not control; secondary porosity also plays a key role, particularly in chlorite-rich pay sands.

- Approximately one-third of the ZG comprises clay minerals, accounting for 32 %v/v in ENAP1 and 34 %v/v in ENAP2, respectively.
- The predominant clay minerals identified are chlorite, mica, and illite-smectite. The amalgamation of XRD-detected mica and illite-smectite was interpreted as glauconitic mica and glauconitic smectite by Odin and Matter's (1981) guidelines for glauconitization (**Section 4.9.1**).
- The XRF analysis showed a notably high range of Fe₂O₃ content, from 2.8 to 14.5 %wt Fe₂O₃. When considered alongside the presence of MgO and K₂O, this showed consistency with identifying glauconite and chlorite mineral groups in XRD and SEM image analyses. Consequently, the ZG reservoir is identified as greensand comprising predominantly glauconitic micas and smectites, with a significant proportion of chlorite.
- SEM image analysis corroborated the existence of glauconitic grains exhibiting ovoid, subangular, and vermiform shapes, with deeper core locations indicating a more advanced glauconitization process. Elevated iron content is attributed to framboidal pyrite, glauconite, and chlorite, distributed as pore-lining, pore-bridging, and within the matrix. This finding was consistent with CT scan images of high-dense minerals and low to extreme heterogeneity (**Figure 4-3**).
- From a microstructural perspective, two distinct groups are observed: matrix-supported siltstone in most samples and grain-supported sandstone with albite and chlorite dominance in the matrix for the samples from the pay sands. These latter exhibited chlorite pore-linings, aiding secondary pore preservation and contributing to reservoir quality. However, chlorite does not enhance secondary porosity but lines them. This finding indicates that chlorite, rather than iron content, serves as the mineralogical marker for distinguishing the pays sands, aligning with the hypothesis of company petrophysicists.
- The ZG reservoir has a total porosity ranging from 11 to 28 %v/v (derived from helium porosimetry) and a Klinkenberg permeability ranging from 0.001 to 1 mD (confining pressure of 3,500 psig).
- Core-derived helium porosity is assigned as total porosity, while core brine, MICP and NMR-derived porosities are assigned as interconnected porosity (**Section 4.9.2**).
- Stressed porosity at 3,500 psig of confining pressure, i.e., close to reservoir conditions, is approximately 97% of the ambient porosity. Hence, there is no need for stressed correction in porosity for reservoir modelling (**Section 4.6.2**).
- ZG gas permeability is stress-dependent, especially in $k_{\infty} < 0.01$ mD for the whole dataset at increasing confining pressure (**Figure 4-14**). Therefore, a conversion factor of 0.55 needs to be applied to convert Klinkenberg permeabilities from 1,500 to 3,500 psig (**Figure 4-13**).

- Three potential facies were grouped according to lithology, porosity, and permeability (**Table 4-14**). Facies 1 corresponds to chloritic pay sands, while Facies 2 and 3 correspond to glauconitic sandstones. The latter presented ultra-low permeability and high porosity.
- An exponential correlation with core helium porosity predicted the best gas permeability in all Facies (**Tables 4-15** and **4-16**).
- FZI method can be used as a criterion to separate all facies as hydraulic units as $-1.25 < \text{Log FZI} < -0.8$ for Facies 1, $-1.9 < \text{Log FZI} < -1.25$ for Facies 2, and $-2.4 < \text{Log FZI} < -1.9$ for Facies 3 (**Figure 4-27**).
- Three correlations were presented to derive ZG Klinkenberg permeabilities using core helium permeability and pore average pressure (Equation 4–8), total porosity (Equation 4–9) or interconnected porosity (Equation 4–10). These correlations are valid for core permeabilities between 0.0008 and 1 mD and confining pressures between 1,500 to 3,500 psig.

Chapter 5

Pore size distribution, permeability correlations with MICP and NMR data, and petrofacies units of the ZG reservoir

This chapter reports the pore size distribution derived from the MICP and NMR techniques, two conversion methods and permeability-derived correlations. A Petrophysical Rock Typing workflow is presented to categorise the cores into petrofacies units. Key relationships between the results, their controls and petrofacies features are discussed.

5.1 Introduction

Greensands have a dual porosity system, macropores and micro- or nano-pores, where the latter store bound water (**Section 2.3.2**). The pore size distribution, PSD, of these formations is in the lower range of NMR T_2 distribution (<100 ms) due to the small pores size, which are in the higher range of capillary pressure curves due to high irreducible water (**Table 2-13**). Consequently, the reported NMR T_2 cut-off values are lower than 33 ms – the typical sandstone value (**Section 2.3.2**). Furthermore, several authors have extended the use of NMR and MICP conversion workflows to obtain empirical correlations to predict permeability (**Table 2-12**). Although MICP and NMR analysis are expensive, they give essential information about pore and pore-throat size distribution and complement the reservoir characterisation process.

It is common practice to convert NMR T_2 data to MICP water saturation distribution to derive the immobile water saturation and other properties such as permeability (Marshall et al., 1995). NMR T_2 is controlled by the pore body size (r_{body}) distribution throughout the rock, including the pore throats. In contrast, the MICP capillary pressure measures the pore throat radius (r_{pore}) distribution through mercury intrusion. Therefore, if the NMR and MICP analyses display the same PSD, a scaling factor can be defined between r_{body} and r_{pore} (Marshall et al., 1995; Volokitin et al., 1999).

However, for heterogeneous rocks such as carbonates, finding a single scaling factor has been proven to be problematic due to their microstructure and the presence of paramagnetic minerals (e.g. Rios et al., 2015; Pires et al., 2017; Knapp et al., 2018; Simpson et al., 2018); this is also the case for greensands such as the ZG formation that have a very high iron content (Dodge et al., 1996; Hossain et al., 2011a). Considering this issue, two methods were selected from the literature to convert NMR T_2 distribution data to MICP capillary pressure data: the MICP inversion (Marshall et al., 1995) and the variable Kappa (Moss et al., 2019), which are described in **Sections 5.3.1** and **5.3.2**.

Petrophysical Rock Typing (PRT) is commonly used for classifying reservoir rocks as units according to their distinct petrophysical properties and geological microstructure (Gunther et al., 2012). PRT includes the pore attributes as petrophysical facies or petrofacies (Doveton, 2014). Porras et al. (1999, p. 2) define petrofacies as “*ranges of rock fluid flow and storage properties with a similar average pore throat radius, thus having similar fluid flow characteristics.*” They aim to correlate the pore structure with the physical properties of the rock, such as porosity, permeability, and capillary pressure (Porras and Campos, 2001).

This chapter presents the derived PSD curve types, key capillary pressures - permeability correlations, and NMR-MICP scaling conversion factors using MICP and NMR data of the ENAP1 and ENAP2 cored wells. The MICP and NMR data were added to the grouped facies from Chapter 4 to extend these as petrofacies units. Also, this chapter continues in reporting findings related to the first specific objective (SO1): *identify the key controls on the petrophysical properties of a glauconitic tight sandstone and establish their relationship to the microstructure (Section 1.2)*. The discussion and summary sections respond to SO1 by examining empirical relationships between the mentioned parameters, the ZG petrofacies units and NMR-MICP conversion workflows. For further information, **Appendix C.1** provides the master list of the derived parameters and additional figures and tables.

5.2 ZG Pore size distribution (PSD)

5.2.1 NMR T_2 distribution

Four NMR T_2 distribution curve types were categorised on the dataset using their T_2 geometric mean as criteria (**Figure 5-1**). Group 1 comprised 12 cores, with the lowest geometric mean of 1.6 ms, with an unimodal small pores trend and predominantly within the 0.1 to 10 ms range. Group 2 comprised 20 cores with a T_2 geometric mean of 2.9 ms and an unimodal small pores trend, predominantly within the 0.3 to 20 ms range. Group 3 comprised two cores, with a T_2 geometric mean of 7.9 ms, with a bimodal small pores trend and predominantly within the 0.3 to 25 ms range. Finally, Group 4 comprised the pay sands, ENAP1-2 and ENAP2-54, with a T_2 geometric mean of 18.6 ms, with a bimodal big pores trend and predominantly within the 0.1 to 350 ms range. Three T_2 values were selected to compare per distribution curve types: the highest peak, geometric mean, and threshold capillary pressure (P_{thr}) (**Table 5-1**). The T_2 value at P_{thr} was calculated with the variable Kappa method from MICP data (**Section 5.3.2**).

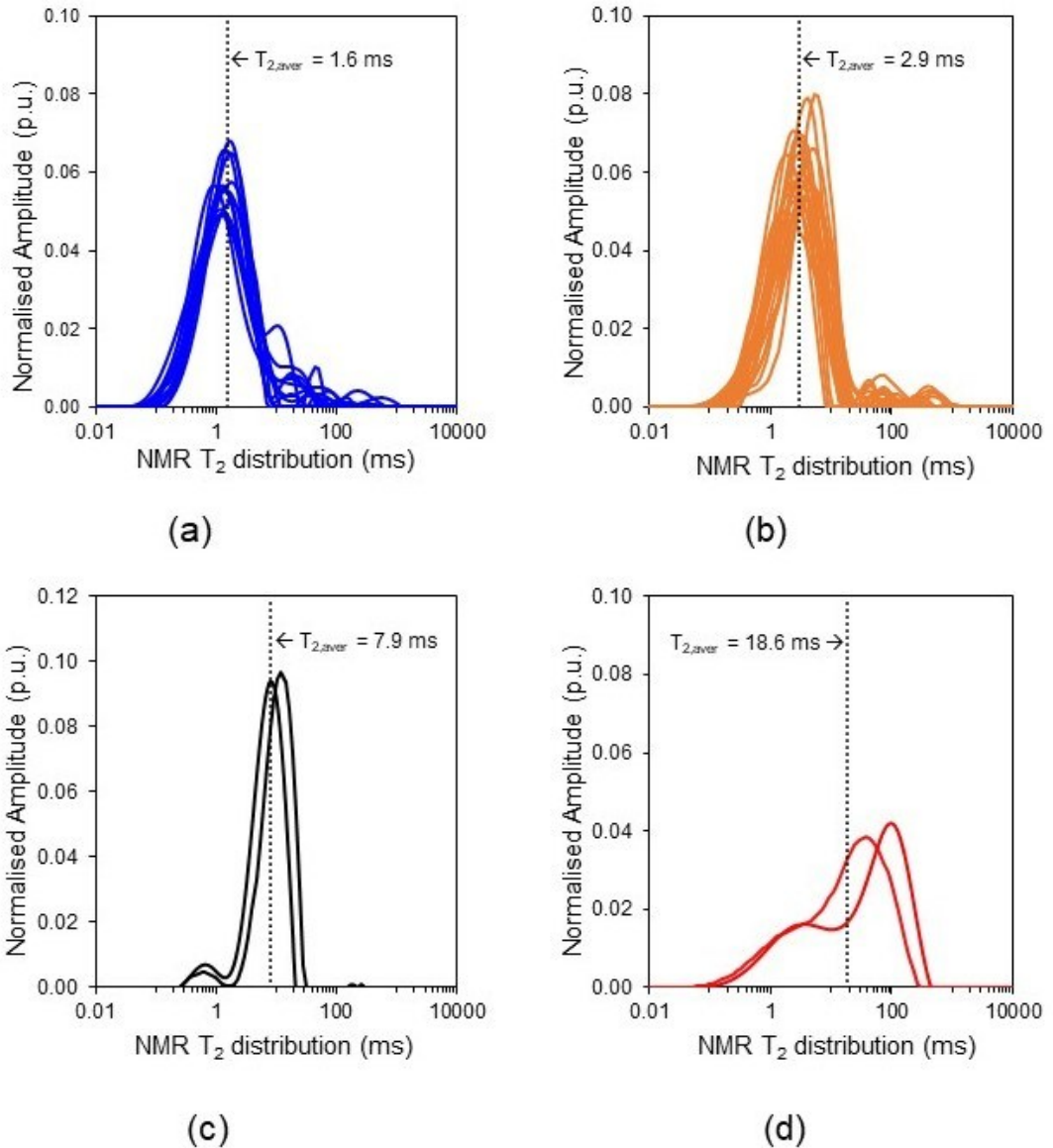


Figure 5-1. NMR T_2 distributions of the dataset grouped by the average of the T_2 geometric mean. a) Group I, b), Group II, c) Group III, and d) Group IV.

Table 5-1. NMR T_2 values comparison for the four distribution types.

Parameter	Group 1	Group 2	Group 3	Group 4
Number of samples	12	20	2	2
Average T_2 highest peak (ms)	1.7	3.3	10.2	68.8
Average T_2 geometric mean (ms)	1.6	2.9	7.9	18.6
Average T_2 at threshold pressure (ms)	1.5	3.2	6.6	124.2

5.2.2 MICP distribution

Forty-six MICP curves were obtained including ten rejected core plugs from the ENAP1 set (Figure 5-2). There are two groups (I and II) of MICP curves. Group I includes 42 samples that presented a typical TGS capillary pressure curve trend, and their PSD distribution is unimodal, AA:with small pores within the range of nanopores

($r_{pore} > 0.1 \mu\text{m}$). Group II consists of 4 pay sand samples that presented a lower capillary pressure curve. Their PSD distribution is bimodal within the range of mesopores and nanopores ($0.1 \mu\text{m} < r_{pore} < 2 \mu\text{m}$). The second group is highlighted in a red line in **Figure 5-2**, where it can be seen that the threshold pressure is less than 200 psig, while for Group I in the black line, the plateau starts at threshold pressures up to 2,000 psig. The pore-throat radius classification is indicated in **Table 5-2**.

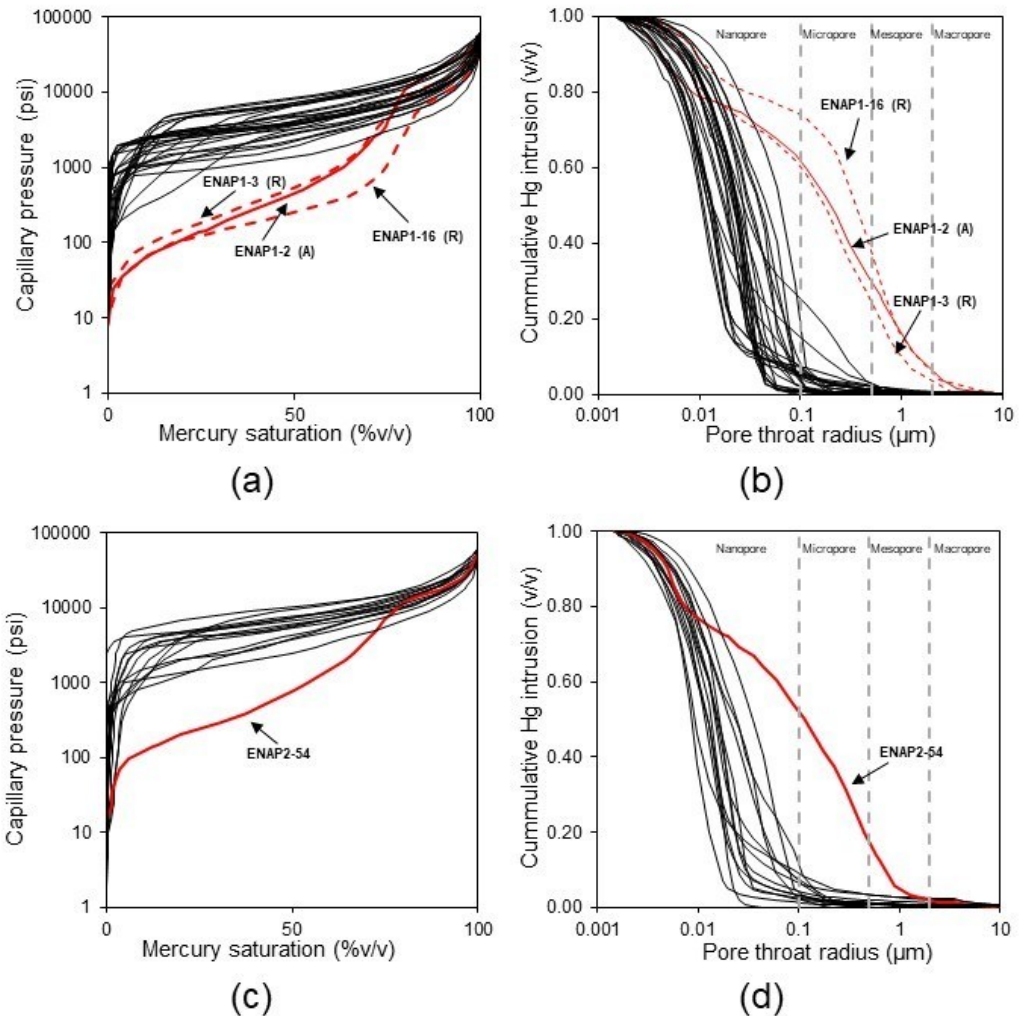


Figure 5-2. MICP curve distribution of the dataset, black lines represent Group I and red lines represent Group II. ENAP1 set capillary curve (a) and PSD (b); three samples from Group II are tagged as ‘A’ for the accepted sample and as ‘R’ for the rejected sample. ENAP2 set capillary curve (c) and PSD (d). The rejected samples were broken sidewall core plugs.

Table 5-2. Pore-throat radius classification according to Hartmann and Coalson (1990).

Pore-throat type	Pore-throat radius (μm)
Megapore	$r_{pore} > 10$
Macropore	$2 < r_{pore} < 10$
Mesopore	$0.5 < r_{pore} < 2$
Micropore	$0.1 < r_{pore} < 0.5$
Nanopore	$r_{pore} < 0.1$

Ten key capillary pressure parameters were identified through statistical analysis and visual interpretation: entry pressure (P_e), displacement pressure (P_d), threshold pressure (P_{thr}), capillary pressure at 50%v/v mercury saturation, apex pore throat radius (R_{apex}), and five additional parameters derived from the MICP data. These parameters were selected because they provide insights into the PSD and the storage and flow properties of the ZG reservoir.

The weighted geometric mean of the pore throat radius R_{wgm} (Equation 5–1); two pore throat sorting coefficients, $PTS_{quartiles}$ (Equation 5–2) and $PTS_{16.50.84}$ (Equation 5–3); the capillary pressure curve kurtosis (Equation 5–4) and skewness (Equation 5–5).

Equation 5–1

$$R_{wgm} = \exp\left(\frac{\sum w_i \ln R_i}{\sum w_i}\right); \quad w_i = \frac{a_i}{a_t}$$

where R_{wgm} is the weighted geometric mean of the pore throat radius (μm), R_i is the pore throat radius at the i^{th} capillary pressure (μm), a_i is the incremental volume of mercury intruded into the sample at the i^{th} capillary pressure, and a_t is the total volume of mercury intruded, and w_i is the ratio of the latter two (Comisky et al., 2007).

The R_{wgm} reflects the effective flow paths in the pore network by averaging the pore-throat sizes weighted by the incremental mercury volumes, making it particularly useful for assessing fluid flow capacity,

The two PTSs selected are typically used for pore geometry and capillary pressure curve shaping analysis (Chehrazi et al., 2011). The $PTS_{quartiles}$ is the squared root of the third and first capillary pressure quartiles (Equation 5–2). If its value is 1.0, the curve has a perfect horizontal plateau; if it is above 5.0, it lacks plateau development. A lower $PTS_{quartiles}$ indicates a more uniform PSD, which correlates with more efficient fluid storage and flow, while higher values indicate heterogeneity and potentially reduced connectivity. The $PTS_{16.50.84}$ uses three capillary pressures at the extremes and the centre (Equation 5–3); its magnitude represents an arithmetic average of the curve plateau.

Equation 5–2

$$PTS_{quartiles} = \left(\frac{3rd \text{ quartile } Pc}{1st \text{ quartile } Pc}\right)^{1/2}$$

where $PTS_{quartiles}$ is the pore throat sorting coefficient ($\text{psiga}^{1/2}$), and the first and third quartile capillary pressures correspond to the 25% and 75% mercury saturation of the curve (psig).

Equation 5–3

$$PTS_{16.50.84} = \frac{P_{16} + P_{50} + P_{84}}{3}$$

where $PTS_{16.50.84}$ is the pore throat sorting coefficient (psig); P_{16} , P_{50} , and P_{84} correspond to capillary pressures at 16%, 50% and 84% of mercury saturation of the curve.

The $PTS_{16.50.84}$ provides a broader representation of the PSD and is useful for characterising the average geometry and heterogeneity of the pore network,

The kurtosis characterises the relative peakedness (positive value) or flatness (negative value) of a data distribution compared with the normal distribution (Equation 5–4). High kurtosis values indicate a narrow range of dominant pore sizes, which may concentrate fluid flow, while low kurtosis suggests a broader size distribution with potentially less efficient flow. The skewness of a data distribution characterises the asymmetry degree around its mean (Equation 5–5); positive values indicate an asymmetric tail extending toward more positive values and vice versa.

Equation 5–4

$$Kurtosis = \frac{\sum(x_i - \bar{x})^4}{(n - 1)s^4}$$

Equation 5–5

$$Skewness = \frac{\sum(x_i - \bar{x})^3}{(n - 1)s^3}$$

where n is the number of data, x_i is the data value, \bar{x} is the mean of the dataset, and s is the standard deviation.

Skewness provides information on the asymmetry of pore sizes, where a positive value indicates the presence of larger pores capable of enhancing fluid flow, while a negative value suggests a dominance of smaller pores that might impede flow.

These parameters collectively describe the pore structure, fluid storage capacity, and flow characteristics of the material, offering essential insights into reservoir quality and petrophysical behaviour.

Overall, the ENAP2 set presents higher capillary pressure parameter values than the ENAP1 set since the pore sizes are smaller (**Table 5-3**). The dataset distribution of the ten selected parameters of the MICP data analysis highlights the TGS features (**Figures 5-3** and **5-4**). The entry pressures are below 50 psig (**Figure 5-3 a**). The threshold pressure is between 2,500 and 7,500 psig (**Figure 5-3 b**). The displacement pressure rises from 2,000 to 4,000 psig (**Figure 5-3 d**). The capillary pressure at 50% mercury saturation is near the threshold pressure (**Figure 5-3 e**). The R_{wgm} mainly falls between 0.011 to 0.025 μm , while the R_{Apex} predominantly falls below 0.025 μm

(Figure 5-3 c and f). The dataset $PTS_{quartiles}$ ranges from 1.3 to 5.5 $\text{psig}^{1/2}$ with a mean of 1.8 $\text{psig}^{1/2}$ (Figure 5-4 a), indicating that the MICP curves present a horizontal plateau. The dataset $PTS_{16.50.84}$ ranges from 2,330 to 13,000 psig with a mean of 8,000 psiga, confirming that the MICP curves present a solid horizontal plateau (Figure 5-4 c). The dataset kurtosis ranges from -1.9 to -1.2, indicating that the data distribution is flat rather than normal (Figure 5-4 d). The dataset skewness ranges from -0.9 to -0.3, indicating that the dataset has a left-long tail (Figure 5-4 b).

Table 5-3. MICP key parameters range of the dataset.

Parameter	ENAP1	ENAP2
Range P_e (psig)	2 – 800	5 – 2,500
Range P_d (psig)	50 – 4,000	70 – 5,500
Range P_{thr} (psig)	200 – 9,000	200 – 9,000
Range P_C at $S_{Hg}=50\%v/v$ (psig)	500 – 9,000	800 – 11,000
Range R_{wgm} (μm)	0.012 – 0.12	0.009 – 0.082
Range R_{Apex} (μm)	0.012 – 1.11	0.008 – 0.36
$PTS_{quartiles}$ ($\text{psig}^{1/2}$)	1.3 – 5.2	1.3 – 5.5
$PTS_{16.50.84}$ (psig)	2,330 – 13,000	5,000 – 12,000
Kurtosis	-1.9 – -1.3	-1.9 – -1.2
Skewness	-0.7 – 0.5	-0.9 – 0.3

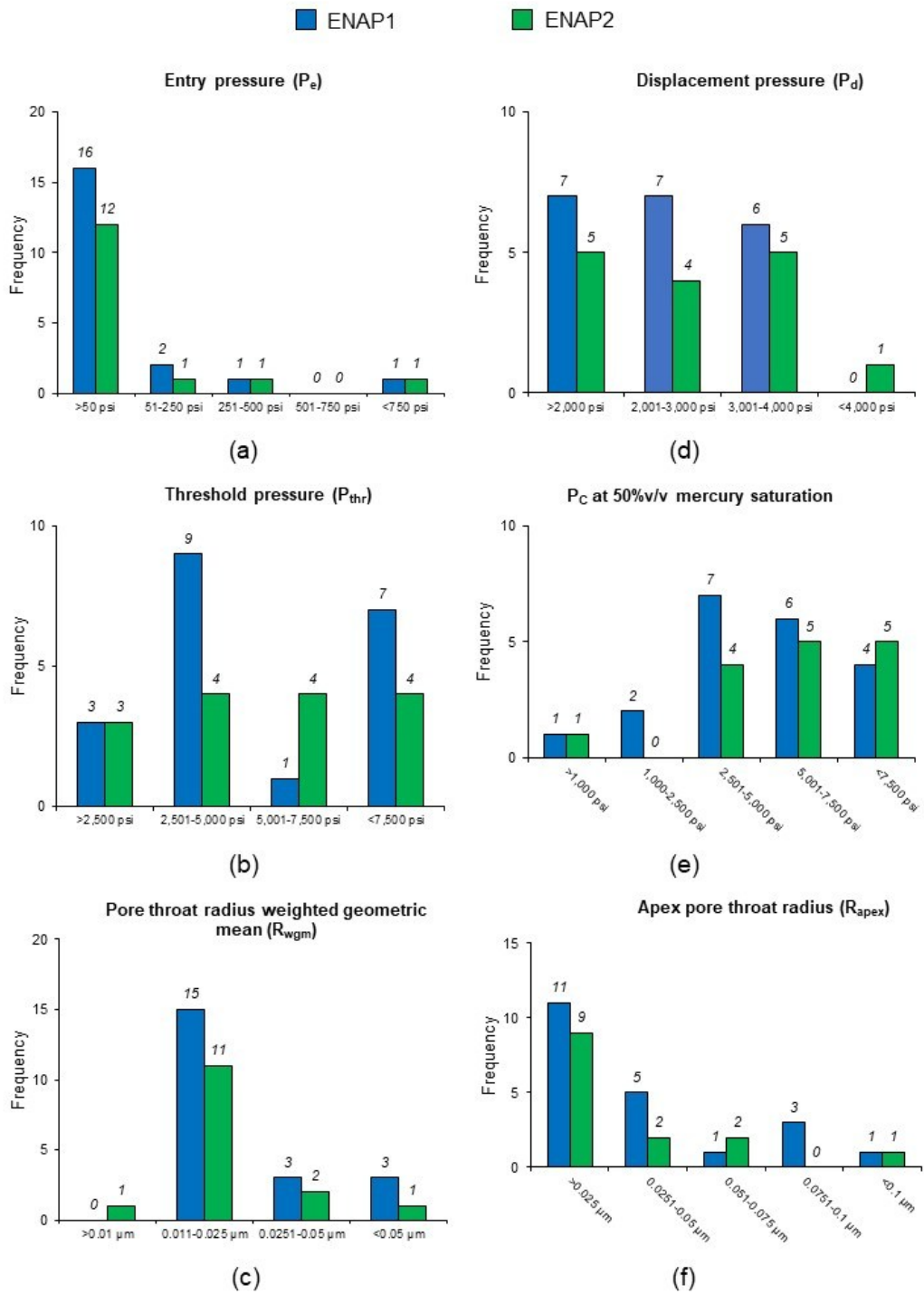


Figure 5-3. MICP dataset statistics. (a) Entry pressure histogram. (b) Threshold pressure histogram. (c) Pore throat radius weighted geometric histogram. (d) Displacement pressure histogram. (e) Capillary pressure at 50% mercury saturation histogram. (f) Apex pore-throat radius histogram.

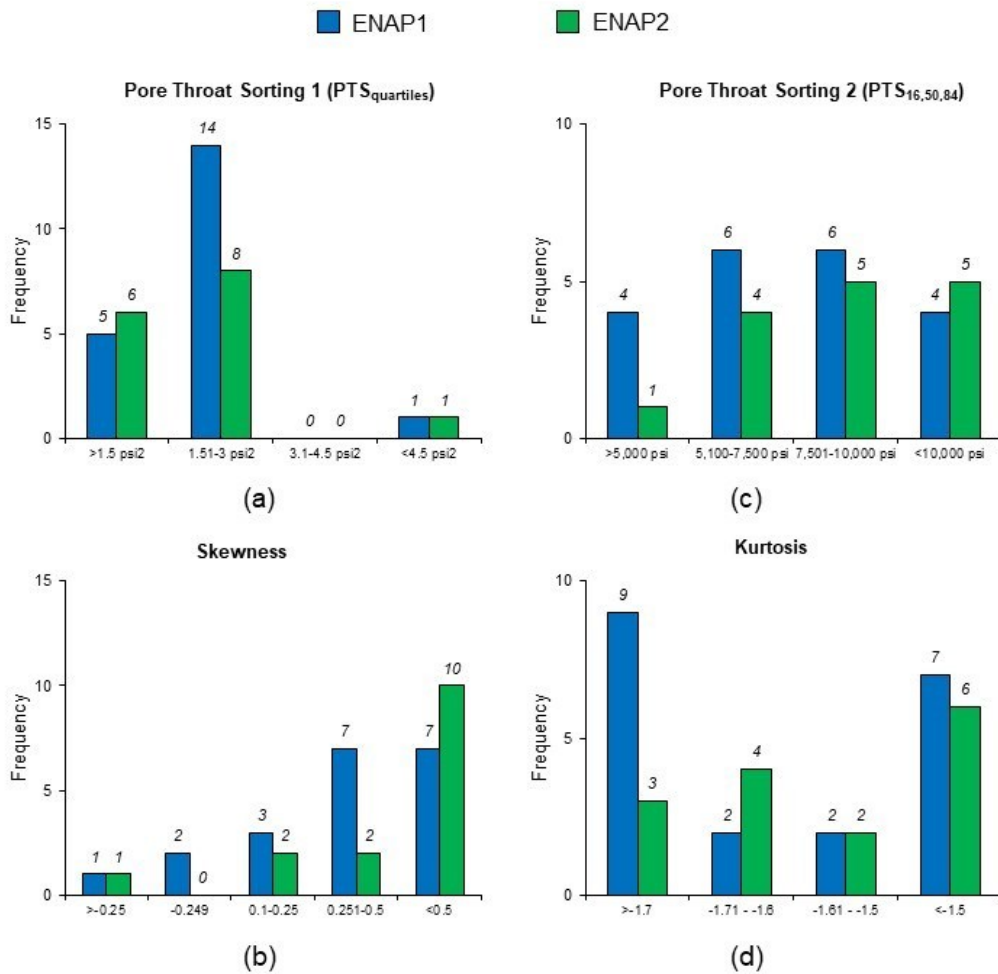


Figure 5-4. MICP dataset statistics. (a) Pore-throat sorting with quartiles histogram. (b) Pore-throat sorting with 16,50,84 method histogram. (c) MICP curve skewness histogram. (d) MICP curve kurtosis histogram.

5.3 NMR-MICP conversion

5.3.1 MICP inversion (workflow 1)

This method is the most used in petrophysics, proposed by Marshall et al. (1995). The assumptions for the conversion formulas (Equations 5–6 and 5–7) are that (i) the T_2 of a water-saturated rock correlates with its surface relaxivity (ρ_2) and with the pore volume-pore surface ratio (V/S); (ii) the pore throats geometry is a cylindrical tube; hence the V/S is simplified to $2/r$; and (iii) the Washburn’s expression is valid to derive the capillary pressure or pore throat radius (Equation 3–17).

A cross-correlation function was used to optimize the value of ρ_2 (Equation 5–8). The workflow sequence used for the ZG formation involved an iterative process to fit best the scaling factor K and ρ_2 (Figures 5-5 and 5-6). In addition, the RMSE (Root-mean square error) and a linear correlation were used to evaluate the accuracy of capillary pressure prediction.

Equation 5–6

$$\frac{1}{T_2} = \rho_2 \frac{V}{S} = \frac{2\rho_2}{Kr_{MICP}}$$

where ρ_2 is the surface relaxivity factor ($\mu\text{m/ms}$), V/S is the pore volume-pore surface ratio (equivalent to $2/r$ if the pore has a cylindrical shape), and K is the scaling factor (equal to 1,000 using Marshall et al.'s (1995) original value).

Equation 5–7

$$K = \frac{2\rho_2}{T_2 r_{MICP}} = \frac{-C 4\sigma \cos \theta}{T_2 P_{C_{MICP}}}$$

where C is a unit conversion constant.

Equation 5–8

$$C(\rho_2) = \sum a_{NMR}(T_2) \cdot a_{MICP} \left(\frac{1000r_{MICP}}{2\rho_e} \right)$$

where a_{NMR} and a_{MICP} are the amplitude incremental of pore size distribution calculated from NMR T_2 and MICP, respectively.

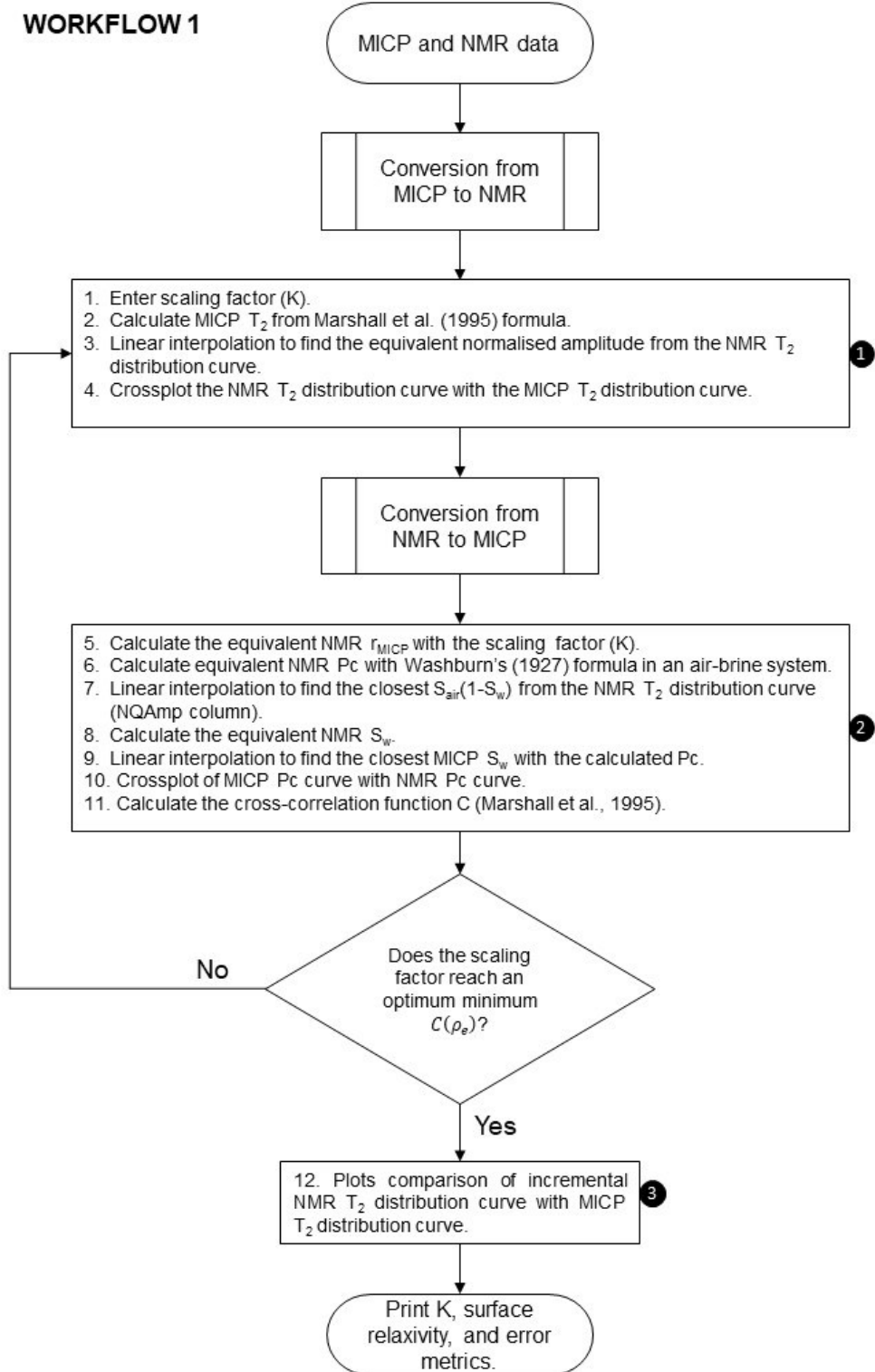
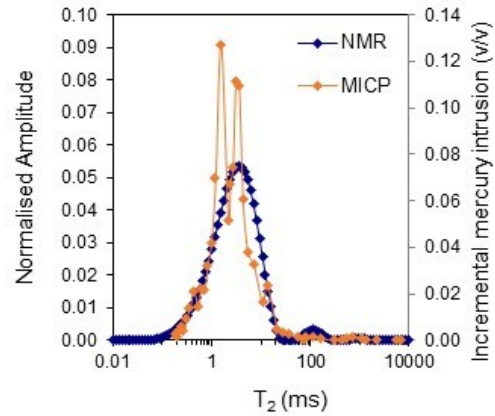


Figure 5-5. NMR-MICP conversion workflow 1 (MICP inversion method).

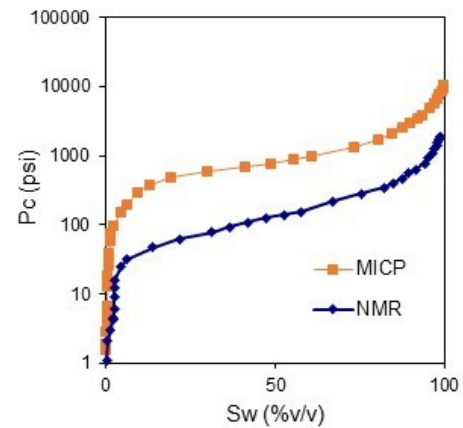
Step 4. Plots comparison the NMR T_2 distribution curve with the MICP T_2 distribution curve.

1



Step 10. Plots comparison of MICP P_c curve with NMR P_c curve.

2



Step 12. Plots comparison of incremental NMR T_2 distribution curve with MICP T_2 distribution curve.

3

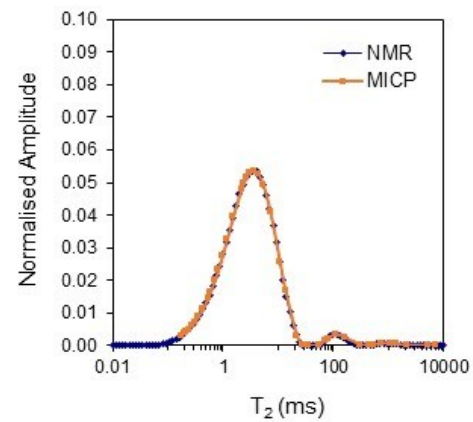


Figure 5-6. NMR-MICP conversion cross-plots from workflow 1.

5.3.2 Variable Kappa (workflow 2)

The variable Kappa method is an extension of the MICP inversion that includes the variability of the multiple pore volume-pore surface ratio (V/S) that a water-saturated rock can have, thus being more suitable for a heterogeneous core (Moss et al., 2018). Kappa is a proportional constant between the capillary pressure and NMR T_2 curves (Equation 5–9). The workflow process starts with the MICP inversion workflow outputs since the equivalent NMR T_2 distribution matches the MICP pore throat size distribution. The iterative Newton-Raphson method was used to find the Kappa value per data point with a tolerance of 0.0001 (Figure 5-7) with a defined objective function

and its derivative (Equations 5–10 and 5–11). The workflow sequence used for the ZG formation involves the mentioned iterative process and linear regression of a log-log cross-plot correlation of Kappa vs NMR T_2 (**Figure 5-8**) to compare Moss et al. (2018) correlation. In addition, the RMSE and a linear correlation were used to evaluate the accuracy of capillary pressure prediction.

Equation 5–9

$$Kappa = \frac{Pc}{T_2}$$

where *Kappa* is the scaling factor (psig/ms).

Equation 5–10

$$f(Kappa) = \frac{T_2}{Pc} Kappa - 1$$

Equation 5–11

$$f'(Kappa) = \frac{T_2}{Pc}$$

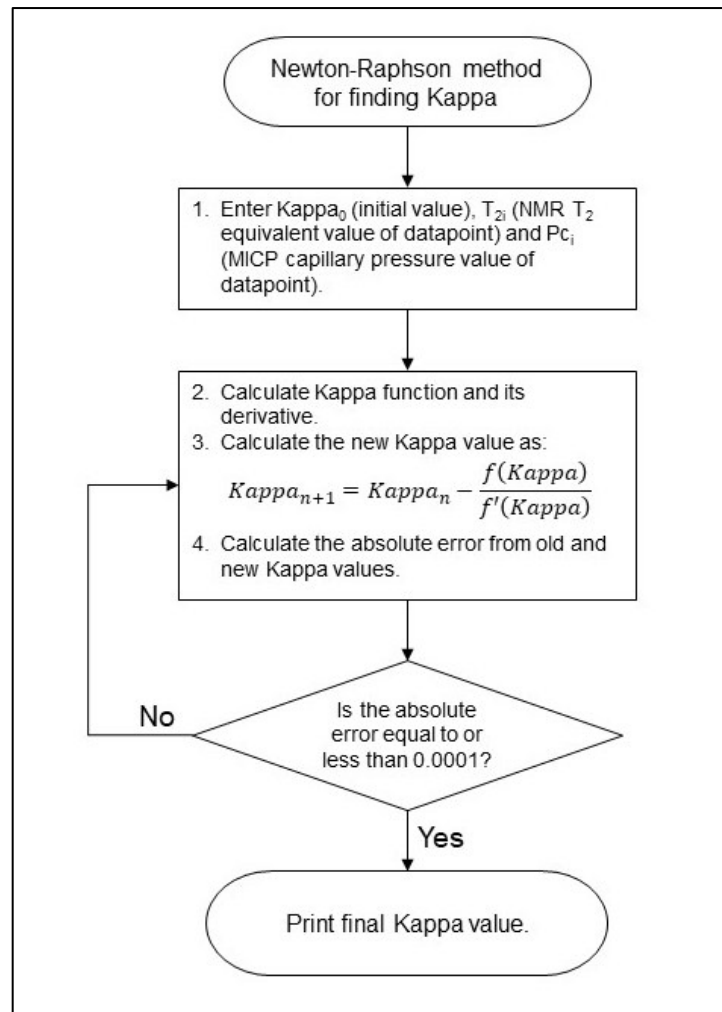


Figure 5-7. Newton-Raphson method used for the variable Kappa method.

WORKFLOW 2

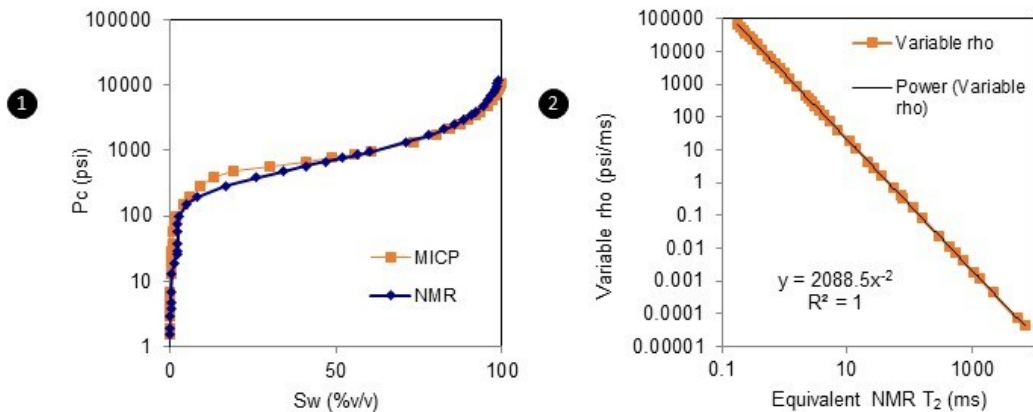
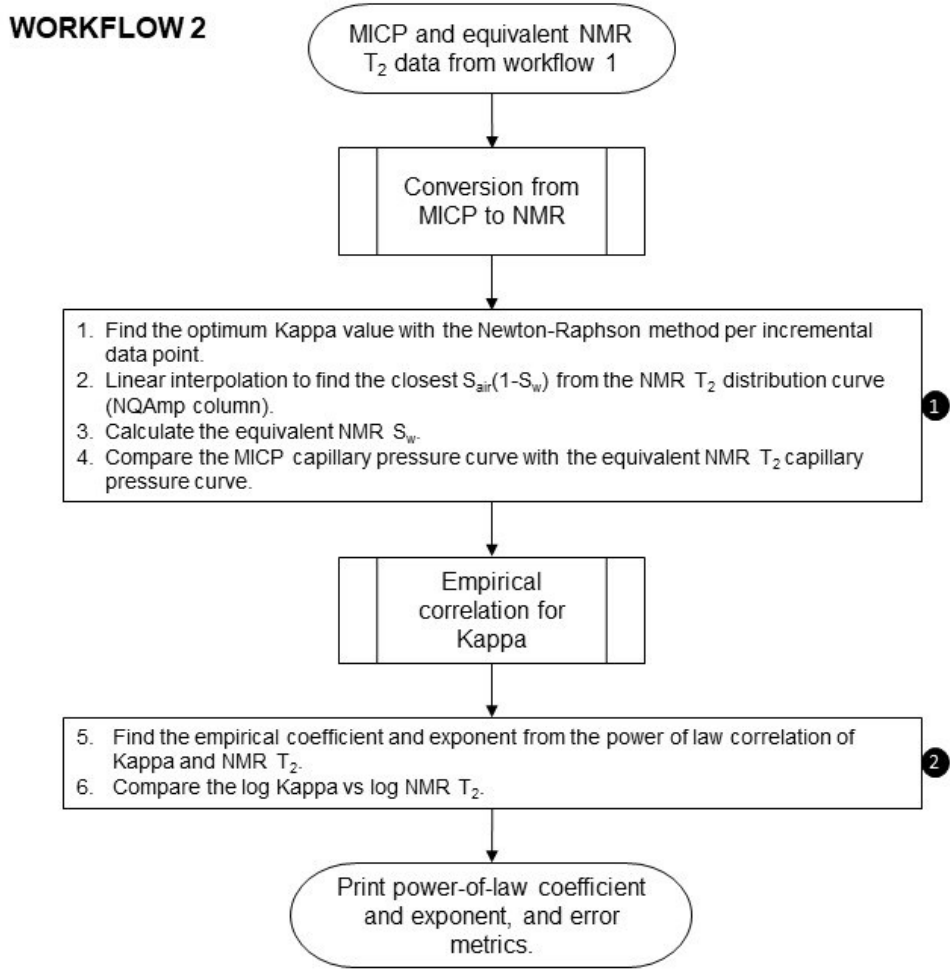


Figure 5-8. NMR-MICP conversion workflow 2 (variable Kappa).

5.3.3 NMR-MICP conversion results

The NMR-MICP conversion methods were applied to thirty-five samples of the dataset. From the MICP inversion method, the surface relaxivity values ranged from

2.0 to 10.0 $\mu\text{m}/\text{ms}$ with an overall average of 3.5 $\mu\text{m}/\text{ms}$. Likewise, the scaling factor ranged from 0.002 to 0.010 $\mu\text{m}/\text{ms}$ with an overall average of 0.003 $\mu\text{m}/\text{ms}$. The variable Kappa method proved to be a perfect match following a power-law trend with an inverse squared root of NMR T_2 , with empirical coefficients ranging between 1,044 to 6,266 (Tables 5-4 and 5-5). The pay sands have the lowest surface relaxivity from the dataset; ENAP1-2 had the farther mismatch from both conversion methods, and ENAP2-54 had a very good match with the variable Kappa method (Figure 5-9). The variable Kappa method better fits the rest of the dataset (Figure 5-10). ENAP2-46, with the highest XRF Na_2O (5.2 wt%) and XRD plagioclase (53.8%v/v) content of the dataset, presented the highest surface relaxivity of 10.0 $\mu\text{m}/\text{ms}$. The surface relaxivity average of 3.5 $\mu\text{m}/\text{ms}$ represents the glauconitic sandstone core with iron content up to 12 %wt; however, no correlation was found between these two parameters (Figure 5-11). Finally, three groups were generated by the MICP inversion method when comparing the predicted capillary pressure from NMR and the original MICP capillary pressure, where the second group (slope = 0.161) is the closest to the variable Kappa method (Table 5-5 and Figure 5-12).

Table 5-4. Key parameters range of the NMR-MICP conversion methods.

Method	Parameter	ENAP1 set	ENAP2 set
MICP inversion	Surface relaxivity ρ_e ($\mu\text{m}/\text{ms}$)	2.0-10.0	1.7-10.0
	Scaling factor K ($\mu\text{m}/\text{ms}$)	0.002-0.010	0.002-0.010
Variable Kappa	Correlation	Kappa=Coeff* T_2^{Exp}	
	Coefficient (psig-ms)	1,044-4,177	1,044-6,266
	Exponent (dimensionless)	-2	-2

Table 5-5. NMR-MICP conversion error metrics range.

Method	Parameter	ENAP1 set	ENAP2 set
MICP inversion	Cross-correlation	0.02-0.06	0.02-0.05
	RMSE	977 ¹ -3,945	3,936-3,978
	Group 1 slope	0.161 ²	0.161 ³
	Group 2 slope	0.158 ⁴	
	Group 3 slope	0.792 ⁵	
Variable Kappa	RMSE	0	0
	Slope	1	1

¹ The minimum RMSE of 977 corresponds only to sample ENAP1-2.

² All the 15 samples from the ENAP2 set.

³ 5 samples from ENAP1 set.

⁴ 13 samples from the ENAP1 set.

⁵ 1 sample from the ENAP1 set.

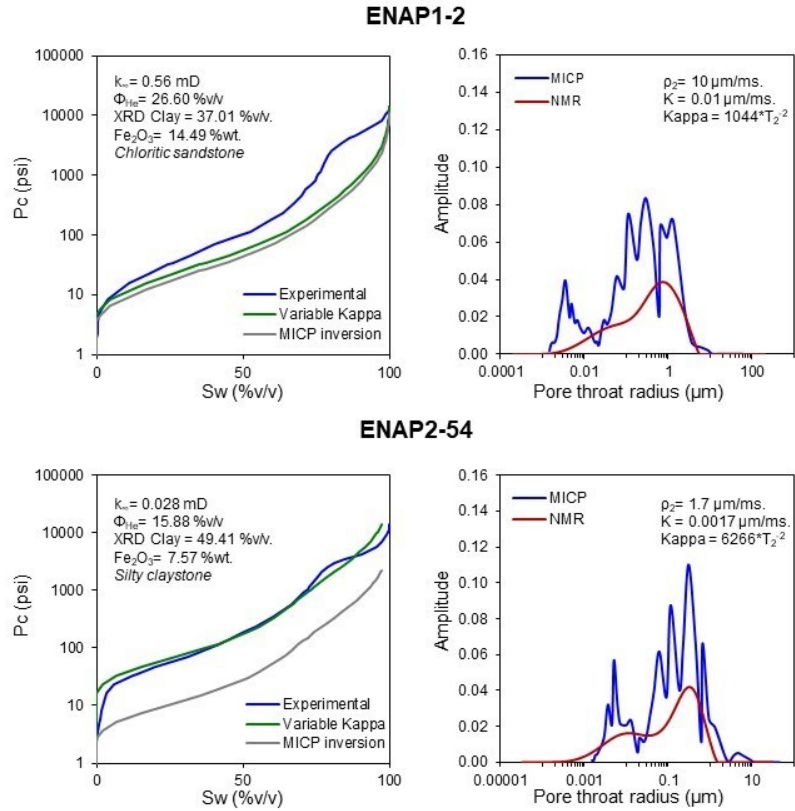


Figure 5-9. NMR-MICP conversion results in pay sands ENAP1-2 and ENAP2-54.

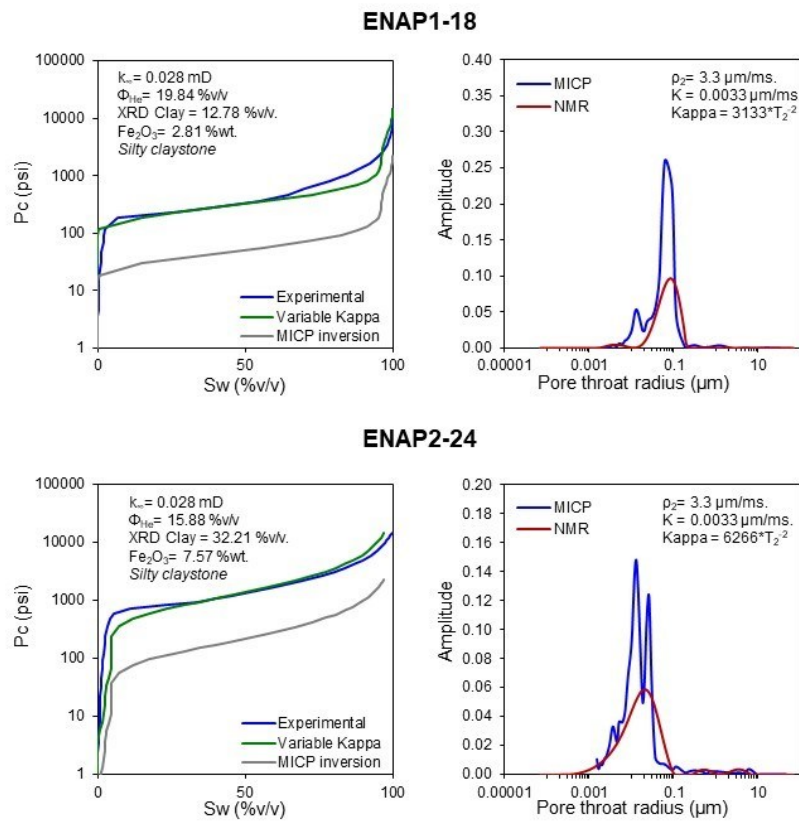


Figure 5-10. NMR-MICP conversion results in samples ENAP1-18 and ENAP2-24.

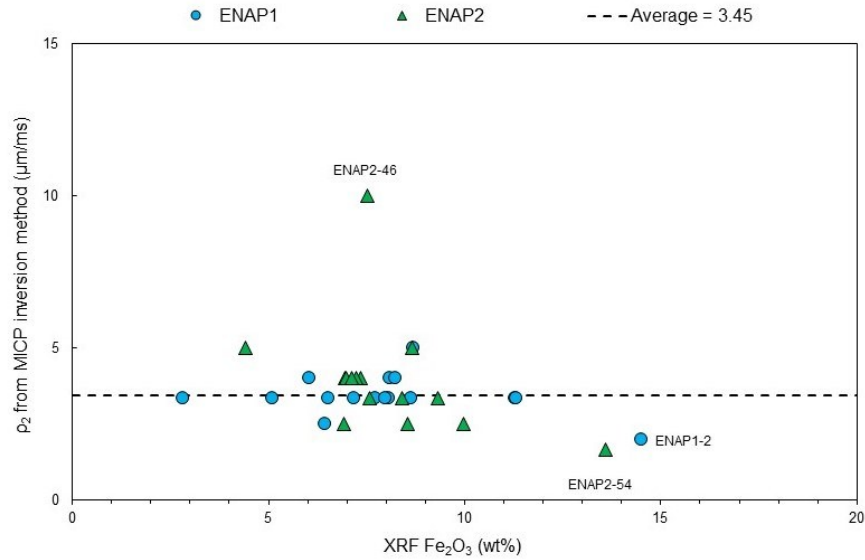


Figure 5-11. Surface relaxivity vs XRF Fe₂O₃ cross-plot.

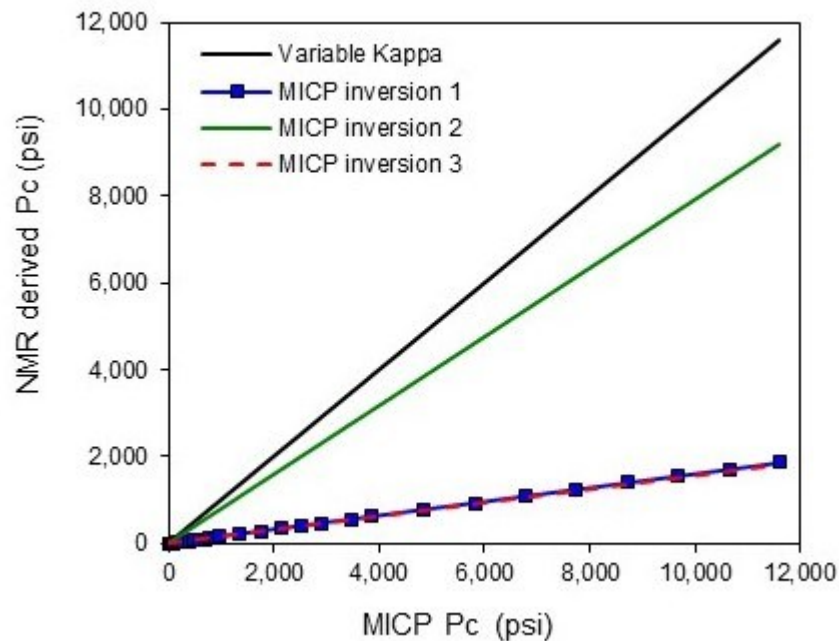


Figure 5-12. Capillary pressure prediction comparison cross-plot. The MICP inversion 1, 2, and 3 corresponds to the groups 1, 2, and 3 reported in Table 5-5.

5.4 Permeability correlations

5.4.1 MICP as input data

Thirteen correlations using MICP data were selected to identify which best predict the absolute core permeability of ZG. Three correlations (Purcell, 1949; Wyllie and Spangler, 1952; Thomeer, 1983) are based on Poiseuille's theory, which models the pore throats as capillary bundles (Table 5-6). The rest of the ten correlations are based on the percolation or characteristic length models that use a characteristic

length (radius or diameter) corresponding to a specific capillary pressure point where the fluid spreads inside the pore throat of the rock (**Table 5-7**). An extended statistical workflow from Comisky et al. (2007) was followed to rank the correlations by calculating the RMSE, R^2 and a standard error (STD x) of the predicted log permeability value (y) for each core log permeability (x) in the correlation (Equation 4–6). The final rank results from the sum of the three rank metrics (**Table 5-8**).

Equation 5–12

$$STDx = \sqrt{\frac{1}{(n-2)} \left[\sum (y - \bar{y})^2 - \frac{[\sum (x - \bar{x})(y - \bar{y})]^2}{\sum (x - \bar{x})^2} \right]}$$

where n is the sample size, y is the predicted value, x is the original value, \bar{x} is the average of the original values and \bar{y} is the average of the predicted values.

The top four correlations are Winland (Kolodzie, 1980), Katz and Thompson (1986; 1987) – these two ranked first, followed by Wells and Amaefule (1985) as second, and Pittman (1992) as third (**Table 5-8**). Winland correlation uses pore throat radius at 35%v/v mercury saturation and porosity to predict gas permeability. Katz and Thompson (1986; 1987) presented three correlations with a particular characteristic length denoted as L_{max} , L_c , and L_{apex} . L_{max} corresponds to the pore throat diameter at threshold pressure, L_c corresponds to 0.43 times L_{max} , and L_{apex} corresponds to the pore throat diameter at Swanson’s (1981) apex point (**Appendix C.2**). The Katz and Thompson correlation that uses L_c and Archie’s (1942) formation factor (R_w/R_o) ranked first with Winland’s correlation. Wells and Amaefule’s correlation uses the apex point of the mercury saturation and capillary pressure ratio from the capillary curve (**Figure 3-20**). Swanson (1981) defined it as the capillary pressure point or pore throat diameter in that mercury flow effectively interconnects the rock pore network (**Section 3.10.3**). Finally, Pittman’s correlation uses the porosity and the apex pore throat radius. The apex pore throat diameter of the ZG dataset ranges from 0.016 to 2.22 μm with an average of 0.14 μm (see **Table 5-3**); this corresponds to a capillary pressure range of 100 to 13,000 psig with an average of 5,400 psig (air-mercury system). This statistical analysis shows that the apex capillary pressure point best correlates with the ZG absolute core permeabilities, further discussed in **Section 5.5.1**.

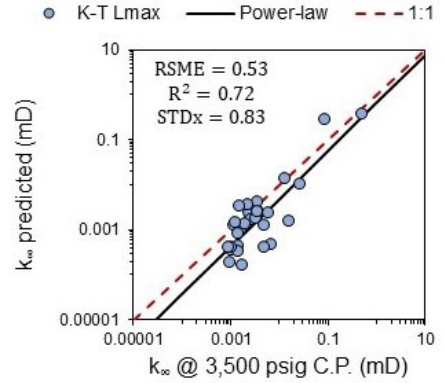
Table 5-6. Selected correlations that follow Poiseuille's theory and their results.

Method	Expression	Cross-plot
Purcell (1949)	$k_{Purcell} = 14254F\phi \int_0^{100} \frac{dS_{Hg}}{P_C^2}$ <p> $k_{Purcell}$ = permeability (mD). F = Purcell's lithological factor (typically 0.216). ϕ = porosity (v/v). S_{Hg} = mercury saturation (%v/v). P_C = capillary pressure (psig). </p>	<p> ● Purcell — Power-law - - - 1:1 RSME = 2.36 $R^2 = 0.07$ STDx = 1.05 </p>
Wyllie and Spangler (1952)	$k_{Wyllie-Spangler} = \frac{10.66 \sigma^2}{k_0 FRF^2 \phi} \int_0^{100} \frac{dS_{Hg}}{P_C^2}$ <p> $k_{Wyllie-Spangler}$ = permeability (mD). S_{Hg} = mercury saturation (%v/v). P_C = capillary pressure (psig). σ = interfacial tension (dynes/cm). k_0 = shape factor (2 for circle). FRF = Archie formation factor (Rw/Ro). </p>	<p> ● Wyllie-Spangler — Power-law - - - 1:1 RSME = 2.09 $R^2 = 0.06$ STDx = 1.00 </p>
Thomeer (1983)	$k_{Thomeer} = 3.8068F_g^{-1.3334} \left(\frac{S_{b\infty}}{P_d}\right)^2$ <p> $k_{Thomeer}$ = permeability (mD). F_g = pore geometrical factor (0.1 used). P_d = displacement pressure (psig). $S_{b\infty}$ = total interconnected pore volume (v/v). </p>	<p> ● Thomeer — Power-law - - - 1:1 RSME = 0.71 $R^2 = 0.69$ STDx = 0.58 </p>

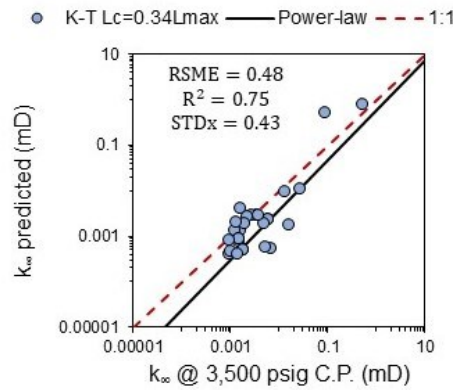
Table 5-7. Selected correlations that follow characteristic length models and their results.

Method	Expression	Cross-plot
Winland (Kolodzie, 1980)	$k_{Winland} = 49.4 R_{35}^{1.7} \phi^{1.47}$ <p> $k_{Winland}$ = permeability (mD). ϕ = porosity (v/v). R_{35} = pore throat radius at 35% mercury saturation (μm). </p>	
Swanson (1981) – air	$k_{Swanson-air} = 399 \left[\frac{S_b}{Pc} \right]_{Apex}^{1.691}$ <p> $k_{Swanson-air}$ = permeability (mD). $[S_b / Pc]_{Apex}$ = mercury saturation and capillary pressure ratio at the apex of capillary pressure curve (v/v/psig). </p>	
Swanson (1981) – brine	$k_{Swanson-brine} = 431 \left[\frac{S_b}{Pc} \right]_{Apex}^{2.109}$ <p> $k_{Swanson-brine}$ = permeability (mD). $[S_b / Pc]_{Apex}$ = mercury saturation and capillary pressure ratio at the apex of capillary pressure curve (v/v/psig). </p>	
Wells and Amaefule (1985)	$k_{W-A} = 30.5 \left[\frac{S_b}{Pc} \right]_{Apex}^{1.56}$ <p> k_{W-A} = permeability (mD). $[S_b / Pc]_{Apex}$ = mercury saturation and capillary pressure ratio at the apex of capillary pressure curve (v/v/psig). </p>	

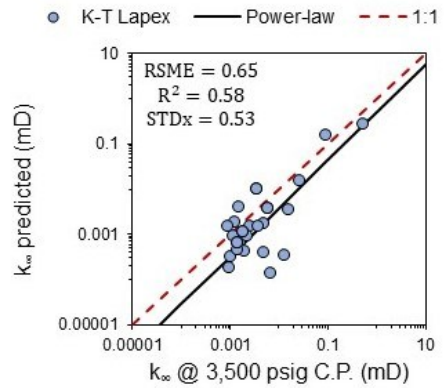
$$k_{K-T L_{max}} = \left[\frac{1013}{226} \right] L_{max}^2 \left[\frac{1}{FRF} \right]$$
 $k_{K-T L_c}$ = permeability (mD).
 L_{max} = characteristic length (μm) at threshold pressure.
 FRF = Archie formation factor (R_w/R_o).
 Katz and Thompson (1986; 1987)
 L_{max}



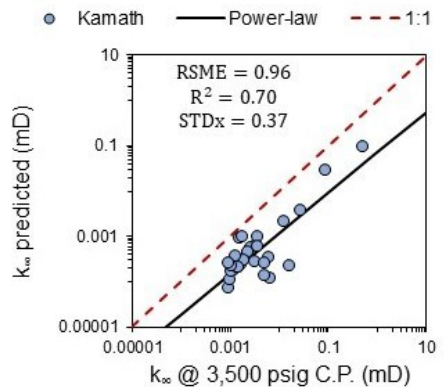
$$k_{K-T L_c} = \left[\frac{1013}{226} \right] L_c^2 \left[\frac{1}{FRF} \right]$$
 $k_{K-T L_e}$ = permeability (mD).
 L_c = characteristic length (μm) equal to $0.34 * L_{max}$.
 FRF = Archie formation factor (R_w/R_o).
 Katz and Thompson (1986; 1987) L_c



$$k_{K-T L_{apex}} = \left[\frac{1013}{226} \right] L_{apex}^2 \left[\frac{1}{FRF} \right]$$
 $k_{K-T L_{apex}}$ = permeability (mD).
 L_{apex} = characteristic length (μm) at apex point defined by Swanson (1981).
 FRF = Archie formation factor (R_w/R_o).
 Katz and Thompson (1986; 1987)
 L_{apex}

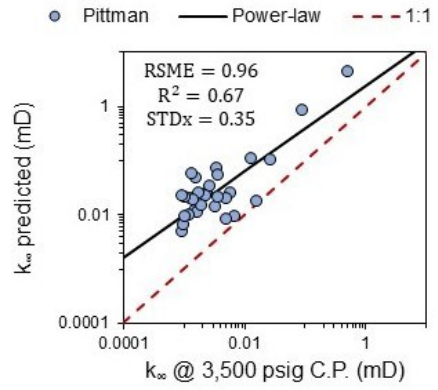


$$k_{Kamath} = 413 \left[\frac{S_b}{P_c} \right]^{1.85} Apex$$
 k_{Kamath} = permeability (mD).
 $[S_b/P_c]_{Apex}$ = mercury saturation and capillary pressure ratio at the apex of capillary pressure curve ($v/v/psig$).
 Kamath (1991)



$$k_{Pittman} = 32.2 R_{apex}^{1.185} \phi^{1.627}$$
 Pittman (1992)

$k_{Pittman}$ = permeability (mD).
 ϕ = porosity (v/v).
 R_{apex} = pore throat radius at $[S_b / Pc]_{Apex}$ (μm).



$$k_{Dastidar} = 4073R_{wgm}^{1.64}\phi^{3.06}$$

Dastidar et al. (2007)

$k_{Dastidar}$ = permeability (mD).
 ϕ = porosity (v/v).
 R_{wgm} = weighted geometric mean of the pore throat radius distribution (μm).

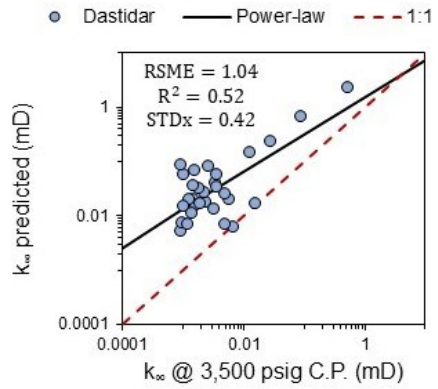


Table 5-8. Ranking summary of selected correlations.

Rank	Correlation	RMSE rank	R ² rank	STDx rank	Sum
1	Winland	2	3	3	8
1	Katz and Thompson L_C	1	1	6	8
2	Wells-Amaefule	7	5	1	13
3	Pittman	6	7	2	15
4	Katz and Thompson L_{max}	3	2	11	16
5	Kamath	9	4	4	17
6	Thomeer	5	6	9	20
6	Katz and Thompson L_{apex}	4	8	8	20
7	Dastidar et al.	10	9	5	24
8	Swanson-air	11	10	7	28
9	Swanson-brine	8	11	10	29
10	Wyllie-Spangler	12	13	12	37
11	Purcell	13	12	13	38

5.4.1.1 Representative pore throat radius of ZG

A further analysis was conducted using multilinear regression (MLR) to identify the characteristic pore throat radius at a specific mercury saturation correlated with ZG core permeability and porosity (Equation 5–13). The Winland correlation, Kolodzie (1980) improved Winland correlation, and Pittman’s (1992) correlations were selected. In addition, an MLR conducted in MS Excel best fitted a pore throat radius at a 35 %v/v mercury saturation (**Table 5-9**). Cross-plots were built comparing the predicted and actual pore throat radius at a specific mercury saturation per correlation (**Appendix C.3**). After statistical and visual analyses were conducted, the most representative pore throat radius is at 25%v/v mercury saturation using the extended Pittman’s (1992) correlation (**Figure 5-13**).

Equation 5–13

$$\log R_i = A + B \log K + C \log \phi$$

where R_i is the pore throat radius at i mercury saturation (μm), K is the absolute permeability (mD), and ϕ is the porosity (%v/v).

Table 5-9. *Winland and Pittman (1992) empirical correlations.*

Correlation	Equation	R²
Best MLR*	$\log R_{35} = 0 - 0.657 + 0.266 \log K + 0.464 \log \phi$	0.917
Winland	$\log R_{35} = 0.732 + 0.588 \log K - 0.864 \log \phi$	0.909
Kolodzie (1980)	$\log R_{35} = 0.9058 + 0.5547 \log K - 0.9033 \log \phi$	0.904
	$\log R_{15} = 0.333 + 0.509 \log K - 0.344 \log \phi$	0.940
	$\log R_{20} = 0.218 + 0.519 \log K - 0.303 \log \phi$	0.939
	$\log R_{25} = 0.204 + 0.531 \log K - 0.350 \log \phi$	0.935
	$\log R_{30} = 0.215 + 0.547 \log K - 0.420 \log \phi$	0.929
	$\log R_{35} = 0.255 + 0.565 \log K - 0.523 \log \phi$	0.914
	$\log R_{40} = 0.360 + 0.582 \log K - 0.680 \log \phi$	0.914
Pittman (1992)	$\log R_{45} = 0.609 + 0.608 \log K - 0.974 \log \phi$	0.915
	$\log R_{50} = 0.778 + 0.626 \log K - 1.205 \log \phi$	0.913
	$\log R_{55} = 0.948 + 0.632 \log K - 1.426 \log \phi$	0.889
	$\log R_{60} = 1.096 + 0.648 \log K - 1.666 \log \phi$	0.846
	$\log R_{65} = 1.372 + 0.643 \log K - 1.979 \log \phi$	0.764
	$\log R_{70} = 1.664 + 0.627 \log K - 2.314 \log \phi$	0.529
	$\log R_{75} = 1.880 + 0.609 \log K - 2.626 \log \phi$	0.193

*MLR = Multilinear Regression.

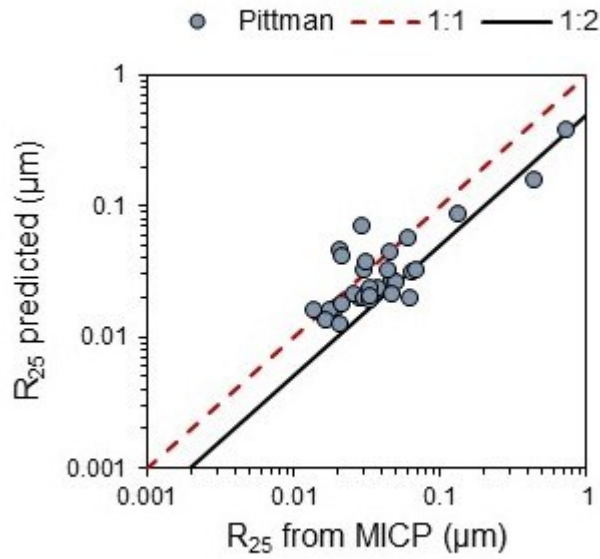


Figure 5-13. Predicted pore throat radius vs Pore throat radius from MICP at a 25 %v/v mercury saturation cross-plot comparing the dataset with Pittman’s (1992) correlation.

5.4.2 NMR as input data

Five correlations using NMR data were selected to identify which best predict the absolute core permeability of ZG. The conventional NMR models of SDR (Schlumberger-Doll-Research) or mean model (Equation 5–14) and Timur-Coates (Equation 5–15) (Coates et al., 1991) were applied using the NMR T_2 geometric mean, and the corresponding T_2 at MICP threshold pressure to analyse which one of these two is more promising as a cut-off boundary. Finally, a correlation named the T_2 summation, proposed by Hossain et al. (2011a) in North Sea greensands, sums all the T_2 distribution data points (Equation 5–16).

Equation 5–14

$$k_{SDR} = C\phi^4 T_{2,geo}^2$$

where k_{SDR} is the permeability (mD), C is a conversion constant, ϕ is the porosity (v/v), and $T_{2,geo}$ is the geometric mean of the NMR T_2 distribution (ms).

Equation 5–15

$$k_{TC} = C\phi^4 \left(\frac{FFI}{BVI} \right)^2$$

where k_{TC} is the permeability (mD), C is a conversion constant, ϕ is the porosity (v/v), FFI is the free fluid index, and BVI is the bulk volume irreducible.

Equation 5–16

$$k_{T2} = C\phi\rho_2^2 \sum_{i=1}^N f_i(T_{2i})^2$$

where k_{T_2} is the permeability (mD), C is a conversion constant, ρ_2 is the surface relaxivity¹ ($\mu\text{m/ms}$), ϕ is the porosity (v/v), and f_i is a fraction of the total amplitude of each T_{2i} .

All the constants, C , per correlation, were found using the least-square method, whereas, for the Timur-Coates model, the best fit was found using the T_2 geometric mean cut-off for the FFI/BVI ratio² (**Figure 5-14**). The same ranking used for the permeability prediction with MICP data was applied (**Table 5-10**) and combined with a visual interpretation (**Figure 5-15**) comparing each correlation with the core permeability. No correlations accurately predicted the absolute permeability of ZG; all showed significant scattering. The SDR model ranked first ($R^2= 0.54$) using the T_2 geometric mean and third using a T_2 cut-off at MICP threshold pressure ($R^2= 0.68$), while the summation model ranked second ($R^2=0.01$). These results are discussed in **Section 5.5.1**.

Table 5-10. Ranking summary of selected correlations.

Rank	Correlation	RMSE rank	R ² rank	STDx rank	Sum
1	SDR with T_2 geometric mean (k_{SDR})	1	2	4	7
2	T_2 summation (k_{T_2})	2	5	1	8
3	SDR with T_2 cut-off at MICP threshold pressure (k_{SDR})	3	1	5	9
4	Timur-Coates with T_2 geometric mean (k_{TC})	4	4	2	10
5	Timur-Coates with T_2 cut-off at threshold pressure (k_{TC})	5	3	3	11

¹ The surface relaxivity was derived from the NMR-MICP scaling factor conversion described in **Section 5.3.3**.

² BVI stands for Bound Volume Irreducible, and FFI stands for Free Fluid Index, respectively (see **Figures 2-2** and **3-25**).

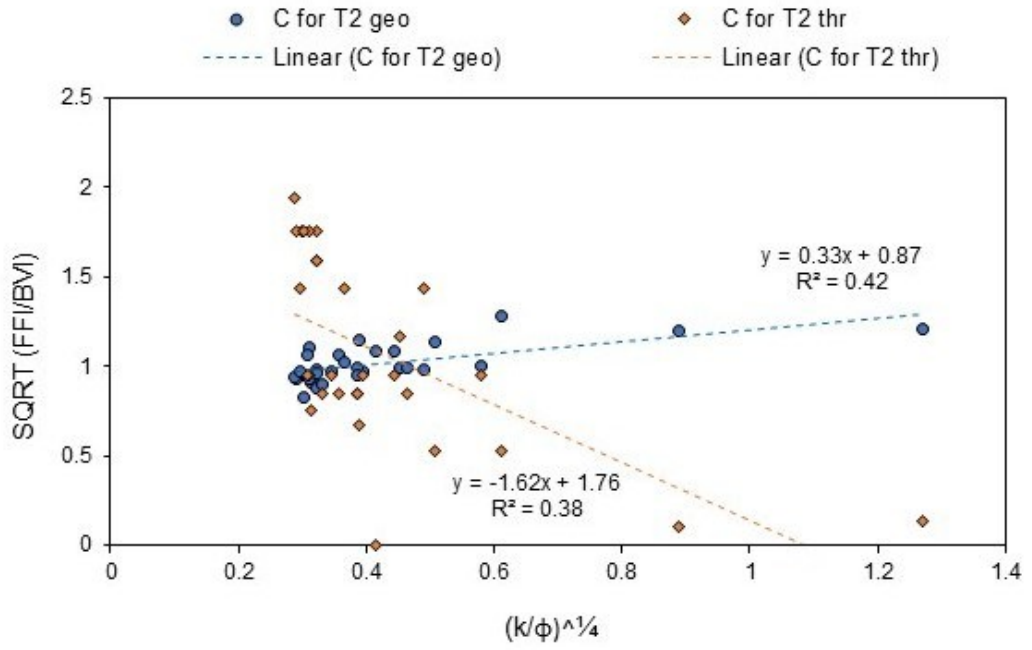


Figure 5-14. Cross-plot used to find the Timur-Coates constant with the least square method.

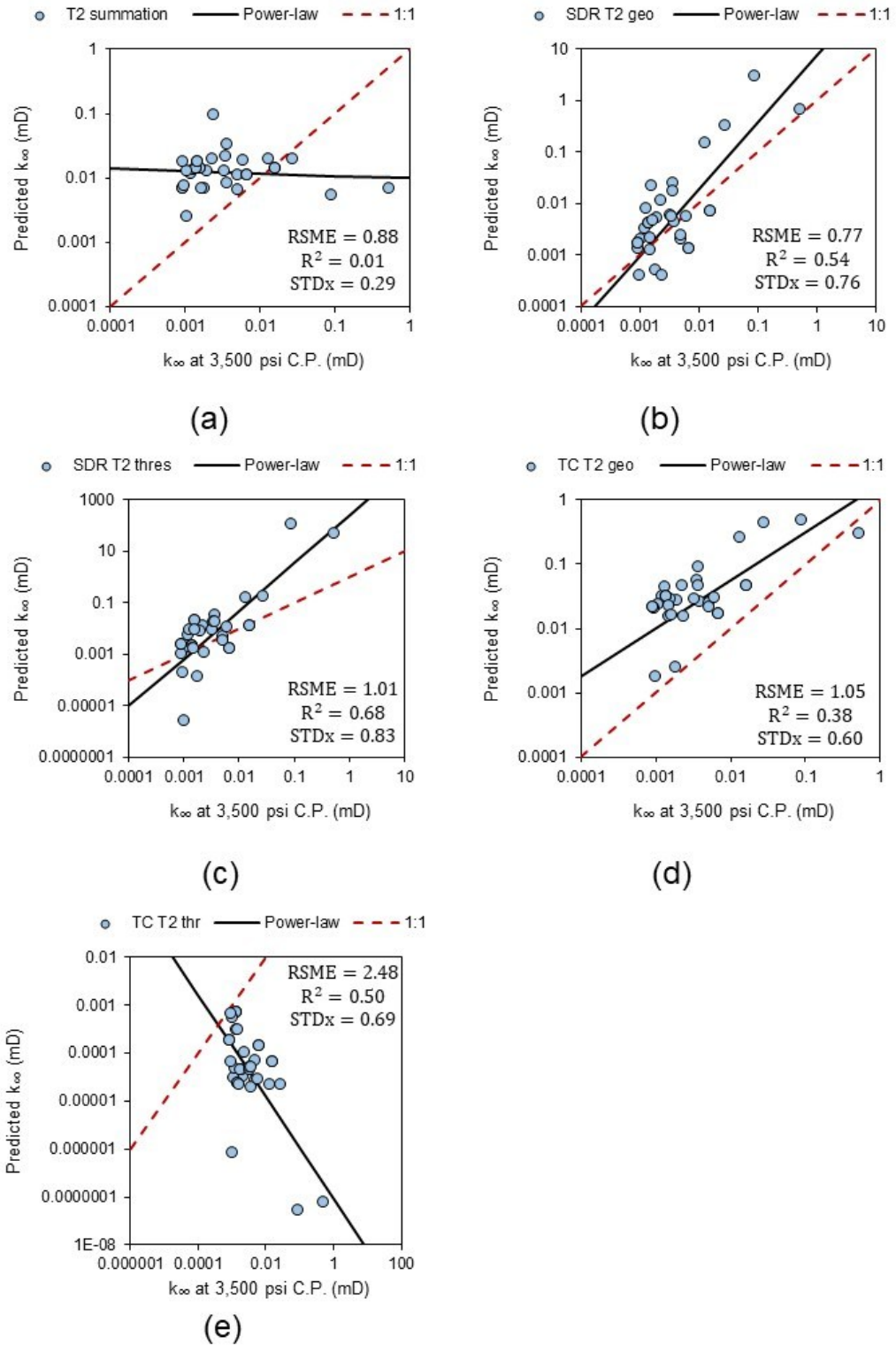


Figure 5-15. Klinkenberg permeability versus NMR predicted permeability from (a) T_2 distribution summation, (b) SDR using the T_2 geometric mean, (c) SDR using the T_2 cut-off at MICP threshold pressure, (d) Timur-Coates using the T_2 geometric mean cut-off, and (e) Timur-Coates using the T_2 cut-off at MICP threshold pressure.

5.5 Discussion

5.5.1 MICP and NMR results

An empirical NMR T_2 cut-off could not be established as no two-phase (air-brine system) experiments were conducted on the cores due to the length of time that would be required. As mentioned in the literature review (**Section 2.3.2**), Dodge et al. (1996) advise using T_2 cut-off values from 10 to 30 ms according to the iron content in greensands. Hossain et al. (2011a) reported lower values of 5.21 and 3.68 ms for two North Sea greensand reservoirs by fixing a T_2 cut-off value at an equivalent capillary pressure of 100 psig (air-brine system). They defined this data point as the separation of the micropores from macropores. These T_2 cut-off values closely align with most of NMR T_2 's highest peak, geometric mean, and threshold pressure ranges in ZG (**Table 5-1**).

Conversely, ZG's average threshold capillary pressure is about 392 psi (air-brine system). An important difference is that the permeability range of the greensand studied by Hossain et al. (2011a) was from 60 to 940 mD. In comparison, the ZG permeability ranges from 790 nD to 2 mD (**Section 4.7.2**). Hence, the T_2 cut-off value equivalent to 100 psig in capillary pressure is not valid for the ZG reservoir as there are no similarities in permeability values and, thus, in flow capacity. Neither the typical T_2 cut-off value of 33 ms for sandstones is correct for the ZG glauconitic cores since this formation is more clayey and denser, with small PSD differing from clean sandstones and shortening the relaxation time in T_2 response. Finally, as a preliminary finding, the threshold or highest peak T_2 values for Groups 1 and 2 with smaller pore distributions can be used as a lower limit boundary for a cut-off (**Section 5.2.1**). In contrast, the traditional T_2 cut-off of 33 ms could be used for the chloritic sandstones (pay sands).

The MICP and NMR techniques proved to be interrelated since their distribution curves are similar per sample (e.g. **Figures 5-9** and **5-10**), using the MICP inversion and variable Kappa methods to convert both curves interchangeably (**Tables 5-4** and **5-5**). The variable Kappa method proved to perfectly match the curves followed by the MICP inversion method with a slope of 0.158 (**Figure 5-12**). An empirical correlation was found to predict the variable scaling factor (psig/ms) following a power-of-law trend with an inverse square root of NMR T_2 with a weighted mean coefficient (A) of 3,258 for ZG reservoir (Equations 5-17 and 5-18).

Equation 5-17

$$\frac{P_c}{T_2} = Kappa = \frac{A}{\sqrt{T_2}}$$

Equation 5–18

$$P_c = \frac{A}{T_2^{1.5}}$$

The PSD distributions from capillary pressure and NMR T_2 showed the same trends. The unimodal small pore curves correspond to high glauconitic micas, smectites, and low chlorite contents. The bimodal big pore curves correspond to high chlorite content and lack of glauconitic particles. A bimodal distribution can be interpreted as natural fracture cores or two distinct pore throats sizing. The MICP PSD of pay sands (**Figure 5-2**) combined with CT and SEM images confirmed a high heterogeneity and complex microstructure (**Chapter 4**), suggesting a meso- and micropores combination instead of being natural fractures. Also, the bimodal small and unimodal small pores NMR T_2 distribution curve peaks concentrate near 1 ms, their capillary pressure curves are higher than the pay sands, and their MICP PSDs are in the nanopore range (**Figure 5-2**), i.e. predominantly glauconite rather than chlorite. The SEM images on these cores presented significant microporosity (**Chapter 4**). Therefore, ZG microporosity controls its glauconitic sandstone capillary pressure and water saturation.

Regarding permeability predictions, the NMR correlations (**Section 5.4.2**) presented scattered results, while the MICP correlations (**Section 5.4.1**) showed promising results. The NMR technology seems to have not proven to be an effective tool for accurately predicting the ZG permeability. The reason is simply that the NMR T_2 distributions in ZG are very short, leading to uncertainty in selecting properly a T_2 cut-off value for applying NMR correlations to predict permeability. Additionally, the pore throat to pore body size ratio may vary between samples, complicating the selection of a consistent T_2 cut-off value. It also seems that the T_2 cut-off selection for the Timur-Coates correlation (Coates et al., 1991) – T_2 geometric mean and at threshold pressure – was not adequate either, as discussed in the opening paragraph of this subsection.

The best-ranked in the MICP correlations were Winland's, Katz and Thompson's, Wells and Amaefule's, and Pittman's (**Table 5-8**). In addition, the extended Pittman's correlation using the pore throat radius at 25 %v/v mercury saturation (R_{25}) best correlates with porosity and permeability with an R^2 of 0.94 (**Table 5-9**). Even though the pore throat radius at 15 %v/v and 20 %v/v mercury saturation presented close R^2 values to 1.0 with Pittman's, their cross-plots were more scattered (**Appendix C.3**). The Katz and Thompson's correlation using a characteristic length or pore throat diameter at the MICP threshold point is discarded due to subjective selection of it. In contrast, the rest of the correlations use a specific equivalent pore throat length (R_i) from the MICP curve.

A further analysis was conducted to compare Pittman's R_{25} , Pittman's R_{apex} , Winland R_{35} and Wells-Amaefule R_{apex} with the dataset to find the best MICP correlation to predict ZG permeability (**Figure 5-16**). The statistical analysis shows that Pittman's correlation at R_{25} predicts it best (**Table 5-11**). This finding agrees with Pittman's (1992) conclusion that the 25 %v/v mercury saturation is the best correlation of pore-throat size with permeability. Therefore, it is concluded that the characteristic pore throat radius of the ZG reservoir is R_{25} and Pittman's correlation at this pore throat radius best predicts gas permeability with porosity.

Table 5-11. Metrics comparison of selected correlations.

Rank	Correlation	R ² Rank	RMSE rank	STDx rank	Sum
1	R_{25} Pittman	1	2	3	6
2	R_{apex} Pittman	3	3	1	7
3	R_{35} Winland	2	4	2	8
4	R_{apex} Wells-Amaefule	4	1	4	9

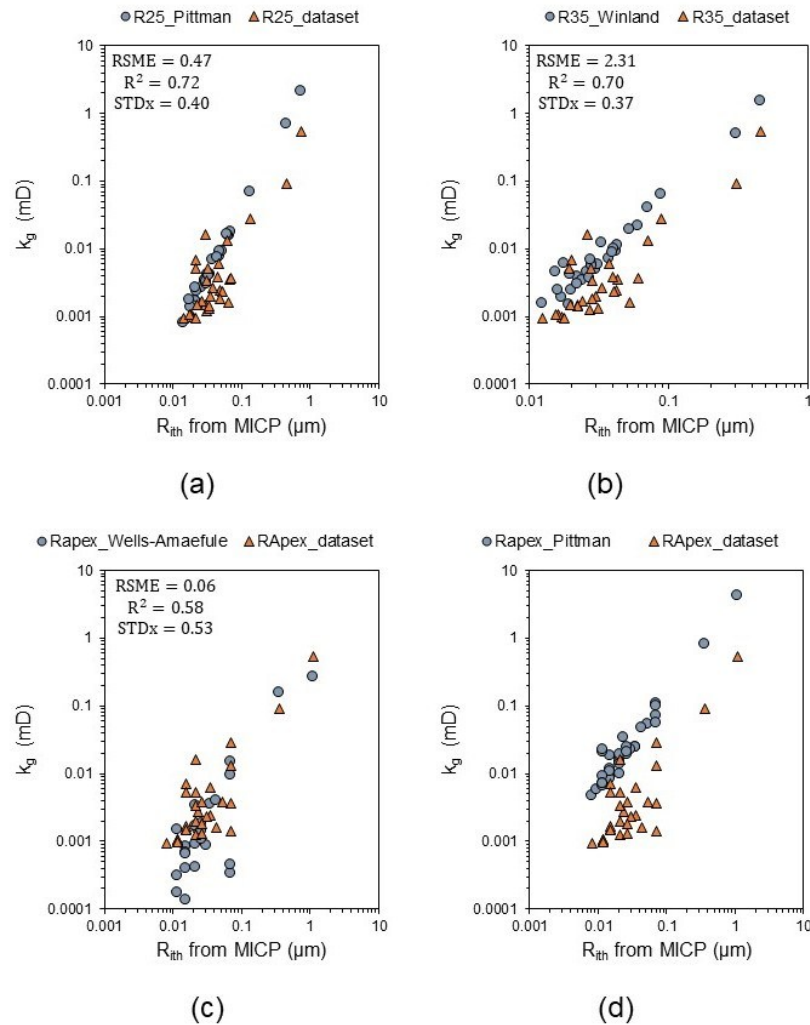


Figure 5-16. Pore throat radius and permeability cross-plot of ZG reservoir cores comparing selected correlations with the dataset: (a) at 25%v/v mercury saturation with Pittman's, (b) at 35%v/v mercury saturation with Winland's, (c) at Apex radius with Wells and Amaefule's, and (d) at Apex radius with Pittman's.

Finally, a regression analysis was conducted with the MICP parameters (P_e , P_d , P_{thr} , P_c at 50%Hg, R_{wgm} , R_{apex} , $PTS_{quartiles}$ and $PTS_{16.50.84}$), including the NMR T_2 geometric mean. Four power-of-law correlations were found with correlational factors, R^2 , between 0.89 and 0.77 (**Figure 5-17**). A very good relationship between R_{wgm} and R_{apex} (with the displacement pressure is in evidence, with R^2 of 0.89 (**Figure 5-17 a**)). In contrast, the capillary pressure at 50% mercury saturation predicts the threshold pressure with R^2 of 0.81 (**Figure 5-17 b**) and the NMR T_2 geometric mean with R^2 of 0.77 (**Figure 5-17 c**). When MICP data are available, these correlations may help predict the displacement and threshold pressures from a new ZG dataset faster and with a consistent bias since their selection is subjective for being a TGS, as well as the NMR T_2 geometric mean of ZG, which may be of use when NMR data is not available.

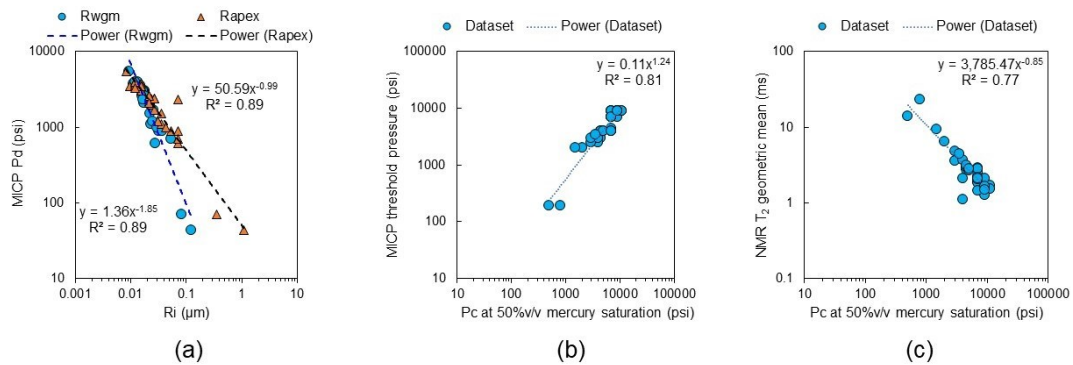


Figure 5-17. Best correlations found with MICP data analysis: (a) MICP displacement pressure vs. the Weighted geometric mean and Apex pore throat radius. (b) MICP threshold pressure vs. Capillary pressure at 50% mercury saturation. (c) NMR T_2 geometric mean vs. Capillary pressure at 50% mercury saturation.

5.5.2 Petrofacies

In **Chapter 4**, three facies were defined according to their mineralogy, core permeability and porosity with ranges of Log FZI values from the FZI method (**Section 4.9.3**). The NMR T_2 distribution (**Figure 5-18**) and derived PSD from MICP (**Figure 5-19**) were added to this grouping to confirm if they can be extended as petrofacies units. Facies 1 is distinctively a petrofacies unit since it corresponds to the chloritic pay sands; its NMR curve is bimodal with PSD predominantly in meso- and micropores. Facies 2 and 3 correspond to the glauconitic sandstones, where the latter presents lower amplitude in the NMR curve as unimodal with PSD predominantly in nanopores. Finally, Facies 3 presents a transitional increase in amplitude and slightly higher NMR T_2 distribution than Facies 2, and its PSD predominates in nanopores with a few micropores. Therefore, since these two have a different PSD distribution, they can be named petrofacies separately. From **Section 5.5.1**, Pittman's (1992) correlation at 25 %v/v mercury saturation gave the

characteristic pore-throat radius ranging from 0.01 to 0.75 μm . So, it was added to the porosity and permeability cross-plot as isolines (**Figure 5-20**).

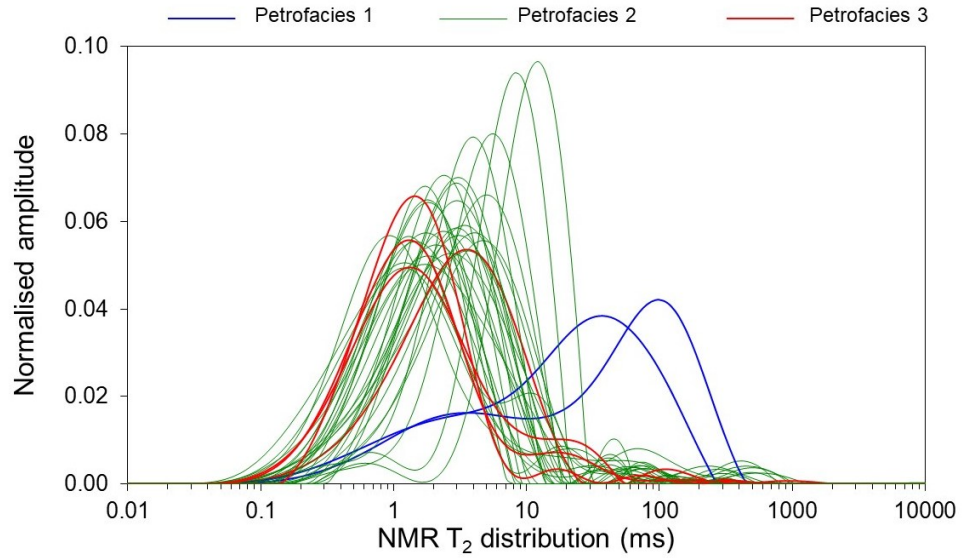


Figure 5-18. NMR T_2 distribution trend per petrofacies.

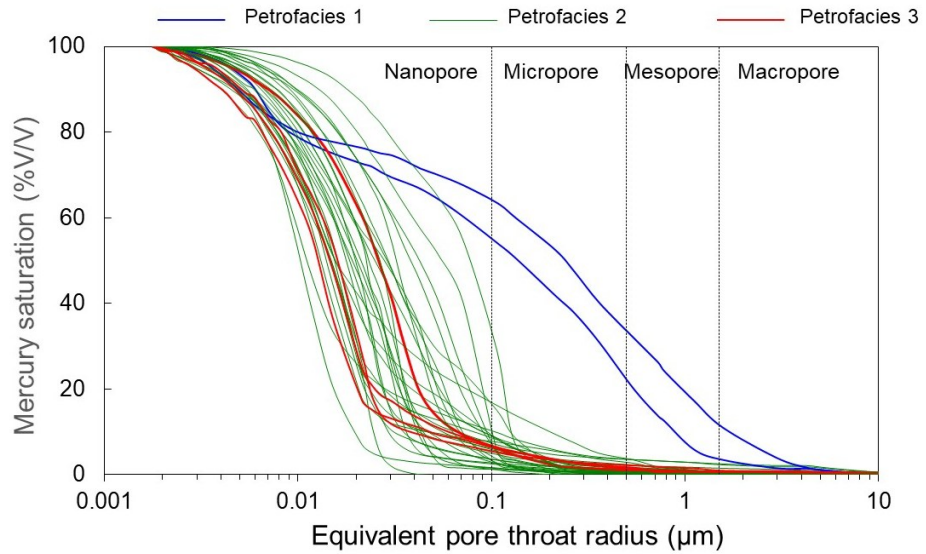


Figure 5-19. Derived PSD from MICP data discriminated per petrofacies.

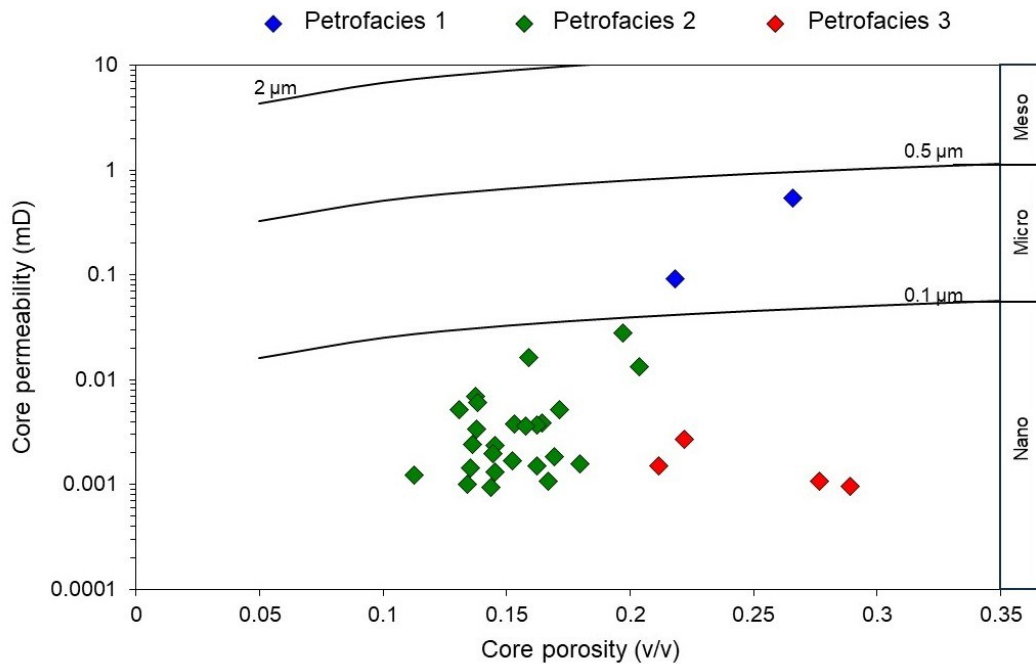


Figure 5-20. Permeability-porosity cross-plot with Pittman's (1992) isolines at equivalent R_{25} values.

Petrofacies 1 is a chloritic sandstone with the highest average iron content (14 %wt), lowest SSA ($3.4 \text{ m}^2/\text{g}$) and a high degree of heterogeneity. Its PSD is bimodal big and small pores. Its capillary pressure curve does not present a visible plateau for the big and small pores range. The entry point for the big pores is about 40 psig, while the small pores are about 1,000 psig in an air-mercury system (**Figure 5-21**). **Petrofacies 2** is predominantly glauconitic mica sandstone with chlorite presence, a moderate degree of heterogeneity from the dataset, the lowest average iron content (7.6 %wt) and the second highest average surface area ($8.9 \text{ m}^2/\text{g}$). Its PSD is unimodal and bimodal, with mostly nanopores. Its capillary pressure plateau averages 6,000 psig in an air-mercury system (**Figure 5-22**). **Petrofacies 3** has the poorest reservoir quality, predominantly glauconitic mica and smectite sandstone with chlorite presence, less degree of heterogeneity from the dataset, second highest average iron content (8 %wt) and the highest average surface area ($11 \text{ m}^2/\text{g}$). Its PSD is unimodal, mainly as nanopores, and its capillary pressure plateaus up to 10,000 psig in an air-mercury system (**Figure 5-23**).

Despite the promising results, it is important to recognise the inherent limitations of the petrofacies workflow. The sample size analysed was limited to two wells, which may not fully represent the spatial and lateral variability of the ZG reservoir throughout the Magallanes basin. The next step is to apply this workflow at the log scale on the wells ENAP1 and ENAP2 to develop a petrophysical model and undergo a validation process in ten uncored wells of the ZG reservoir (**Chapter 7**).

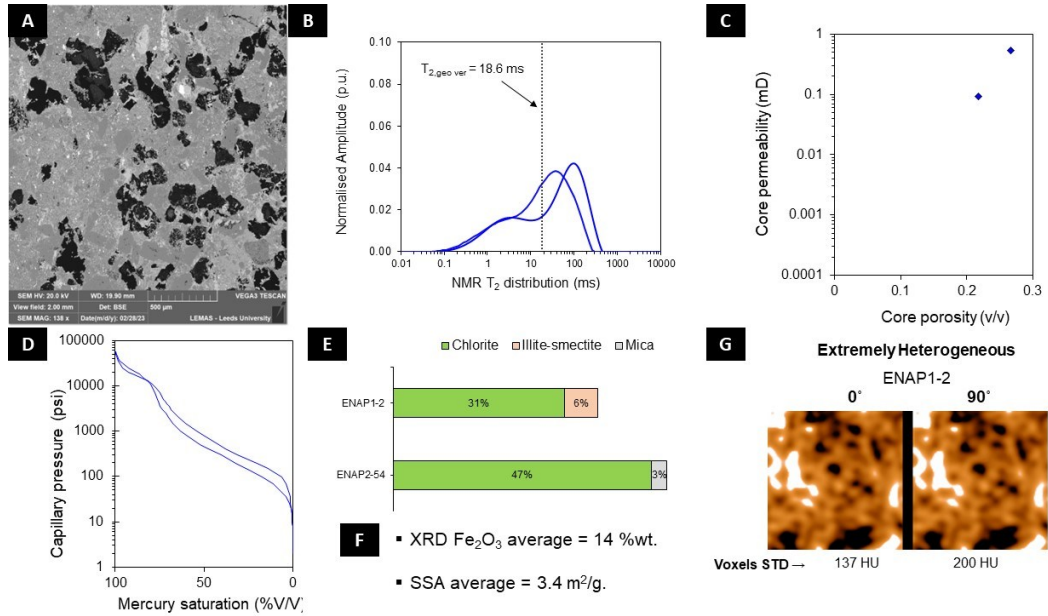


Figure 5-21. Petrofacies 1 features: (A) SEM image of ENAP2-54. (B) NMR T_2 distribution where the average T_2 geometric mean of the cores is indicated. (C) Permeability-porosity cross-plot. (D) Capillary pressure curve as an air-mercury system. (E) XRD mica, illite-smectite, and chlorite content distribution. (F) Average XRF Fe_2O_3 content and SSA. (G) CT image with voxel standard deviation of ENAP1-2.

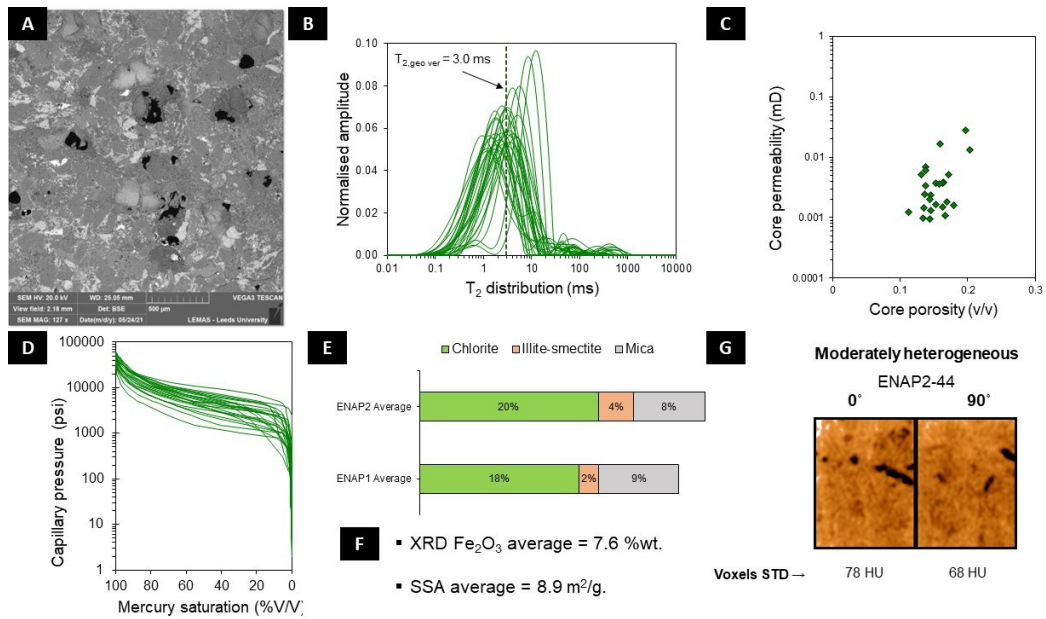


Figure 5-22. Petrofacies 2 features: (A) SEM image of ENAP2-62. (B) NMR T_2 distribution where the average T_2 geometric mean of the cores is indicated. (C) Permeability-porosity cross-plot. (D) Capillary pressure curve as an air-mercury system. (E) XRD mica, illite-smectite, and chlorite content distribution. (F) Average XRF Fe_2O_3 content and SSA. (G) CT image with voxel standard deviation of ENAP2-44.

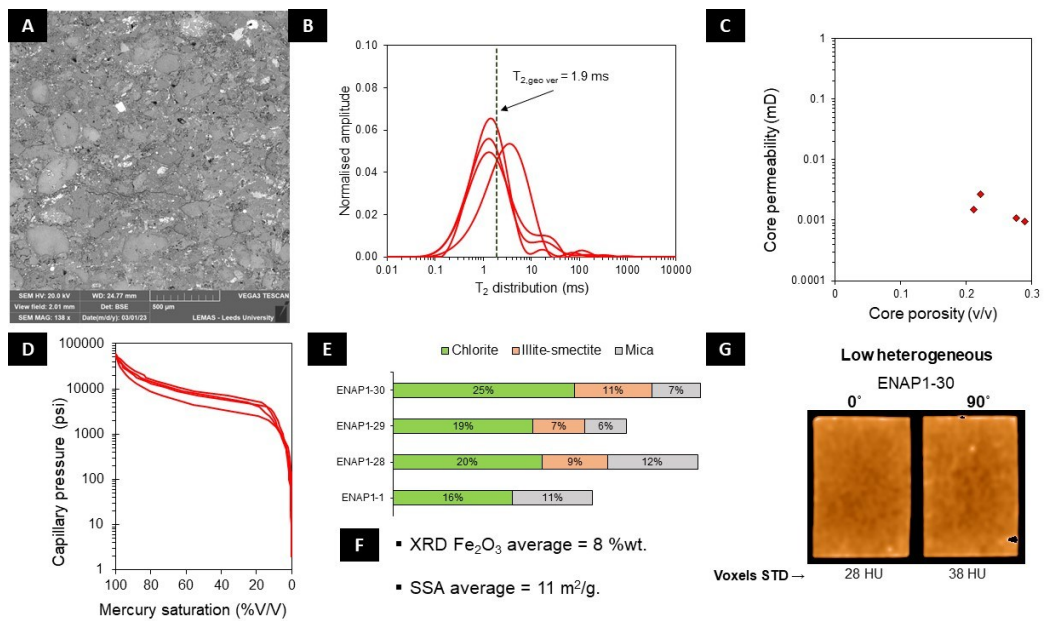


Figure 5-23. Petrofacies 3 features: (A) SEM image of ENAP1-28. (B) NMR T_2 distribution where the average T_2 geometric mean of the cores is indicated. (C) Permeability-porosity cross-plot. (D) Capillary pressure curve as an air-mercury system. (E) XRD mica, illite-smectite, and chlorite content distribution. (F) Average XRF Fe_2O_3 content and SSA. (G) CT image with voxel standard deviation of ENAP1-30.

5.6 Summary

- MICP and NMR Pore Size Distribution (PSD) curves presented the same trends: unimodal small pore, bimodal small pore, and bimodal big pore. The pay sand cores only presented bimodal big pore PSD curve types corresponding to chloritic sandstones, while the other two curve types correspond to glauconitic sandstones.
- Two conversion workflows of NMR-MICP data were achieved, the MICP inversion and variable Kappa, proving that these techniques measure pore throat size (NMR) and radius (MICP). The Kappa method demonstrated the most accuracy by scaling the NMR T_2 parameter as a power-law function (exponent 1.5) and applying a weighted coefficient (3,258) for the ZG reservoir (Equation 5–18), effectively aligning NMR and MICP curves. This outcome suggests a more precise approach to integrating pore size data from both techniques.
- The traditional T_2 cut-off of 33 ms for glauconitic sandstone is incorrect, while the chloritic sandstones (pay sands) may still apply. The NMR T_2 peak and the equivalent to the threshold pressure values may be used as a lower limit boundary cut-off for glauconitic sandstones (Tables C-1 and C-2). Further laboratory analysis of desaturating cores needs to be conducted to confirm this suggestion.
- Microporosity controls capillary pressure and water saturation.

- Pittman's (1992) empirical correlation utilising pore throat radius at 25 %v/v mercury saturation correlated best with porosity and permeability ($R^2=0.94$).
- The characteristic pore throat radius of the ZG reservoir was found to be at 25 %v/v with Pittman's correlation (**Figure 5-16**).
- Two power-of-law correlations using the apex pore throat radius and the weighted geometric mean of the pore throat radius were found to predict MICP displacement pressure ($R^2= 0.89$). Two other power-law correlations were found to predict the MICP threshold pressure ($R^2= 0.81$) and NMR T_2 geometric mean ($R^2= 0.77$) using the MICP at 50 %v/v mercury saturation (**Figure 5-17**).
- No good correlation was found between the Klinkenberg gas permeability and NMR permeability correlations (**Figure 5-15**).
- The identified Facies from Chapter 4 were extended as petrofacies by adding the pore throat distribution from NMR and MICP data (**Section 5.5.2**). The combined MICP and NMR data highlighted the contrasting roles of pore throats (MICP) and pore bodies (NMR) in defining the pore system and its connectivity. Chloritic sandstones (pay sands) showed bimodal PSDs due to significant secondary porosity, with larger pore bodies connected by narrower pore throats. In contrast, glauconitic sandstones exhibited unimodal PSDs, primarily controlled by high clay content and the morphology of glauconitic smectite and mica, which restricted pore connectivity.
- **Petrofacies 1** is a chloritic sandstone with bimodal PSD as small and big pores. The big pores distribution are within the meso and micropores with the highest permeability and porosity; the small pores are within nanopores. This unit has the highest iron content and lowest SSA and is the richest reservoir rock unit.
- **Petrofacies 2** is glauconitic smectite and mica with chlorite presence, moderately heterogeneity degree, lowest iron content but significant, unimodal and bimodal PSD within mostly nanopores. This unit is the second richest reservoir rock unit.
- **Petrofacies 3** is the poorest reservoir quality, with abundant glauconitic mica and smectite presence and unimodal PSD distribution, primarily within nanopores.

Chapter 6

ZG electrical properties and ultrasonic velocities

This chapter presents the measured electrical properties and ultrasonic velocities of the ZG reservoir. It starts by highlighting greensands' electrical and ultrasonic trends, followed by the methodology for measuring the cation-exchange capacity and ultrasonic velocities. Then, it reports the findings and discusses identified relationships and empirical correlations in ZG to assist the well-log interpretation workflow, ending with a summary.

6.1 Introduction

Greensands are often classified as low-resistivity pay zones since their clay minerals can exchange cations with the in-situ formation water, thus adding a second layer of electrical conductivity within the rock framework. Therefore, conventional well-log interpretation can mislead the hydrocarbon zone identification and overestimate water saturation (**Table 2-15**). For this reason, the most used water saturation models for greensands include a clayey term or have a self-compensation coefficient for calibration purposes. The reported values of Archie's coefficients in greensands range from 0.80 to 1.67 for the correlational factor a , 1.18 to 2.09 for the cementation exponent m , and 1.18 to 1.77 for the saturation factor n , respectively (**Table 2-18**). The ENAP company utilises the modified Simandoux model (Bardon and Pied, 1969) with coefficient values of $m=2.09$, $n=1.66$, and $a=1$ (**Section 1.3**). However, the Waxman and Smits (1968) model produced the best fit for the Indonesian greensand reservoirs Res-Q and Res-O, East Java Province (Prayoga et al., 2018). It is noteworthy that none of the water saturation models included greensand reservoirs in their dataset.

Ultrasonic velocity logs are valuable since they calculate Poisson's ratio and Young's modulus. In addition, these body waves can help identify lithology and fluids, thus contributing to reservoir characterisation (e.g. Pickett, 1963; Tatham, 1982; Tosaya, 1982; Hamada, 2004). Some authors have correlated the P-wave and S-wave velocities with porosity (Wyllie et al., 1956; Raymer et al., 1980). Others have also considered the clay content in P-wave and S-wave velocities analyses (Tosaya, 1982; Castagna et al., 1985; Han et al., 1986). For cases when ultrasonic velocities are controlled by porosity as well as clay content, the P-wave and S-wave velocities ratio (V_p/V_s) had proven useful in identifying gas sands in TGS; Gregory (1977), Castagna et al. (1993), and Rojas et al. (2005) agree to use a ratio below 1.5, while Guliyev et al. (2007) reported a ratio below 1.6. Hence, such ratio values can be used as a cut-off to distinguish between sands containing gas and those that do not.

Diaz et al. (2001; 2003) suggest that greensands with good reservoir quality from the Caballos reservoir, Putumayo basin, Colombia have a P-impedance below 12 Mrayls (**Figure 2-31**). Hossain et al. (2012) derived laboratory correlations to predict S-wave velocity from the Vp/Vs velocities ratio logs. Hossain and Cohen (2015) found relationships between the ultrasonic velocities, electrical properties and their diagenetic distribution (**Section 2.3.5**).

This chapter reports the findings related to the first (**SO1**) and second (**SO2**) specific objectives: *identify the key controls on the petrophysical properties of a glauconitic tight sandstones and establish their relationship to the microstructure. Also compare empirical and theoretical water saturation models that include the electrical behaviour of clays and select the best fit for the ZG formation (Section 1.2)*. Two experimental methods were used to derive the cation-exchange capacity of ZG: chemical leaching and multialinity core flooding (**Section 6.2.2**). A standard method was also used to measure ultrasonic velocities on core plugs (**Section 6.2.3**). The electrical resistivity, apparent formation factor, derived Archie's cementation exponent, m , ultrasonic velocities and derived geomechanical properties are reported. The discussion and summary sections focus on the ZG electrical and controls on elastic properties, finding useful relationships for well-log interpretation. **Appendix D** displays the electrical data.

6.1.1 Waxman-Smiths model

Waxman and Smits's (1968) model provides a theoretical and empirical framework to understand the additional conductivity clays contribute to that of a brine-saturated rock. Since the ZG reservoir has significant clay minerals (chlorite and glauconite), the Waxman-Smiths model was selected to study the electrical contribution of ZG clays. This model introduces the shaliness term BQ_v/F^* , which relates the cation exchange capacity, Q_v , with their dependency on the water formation salinity and temperature (Equations 6–1 **Error! Reference source not found.** or 6–2). These are critical factors in accurately determining water saturation in formations with significant clay content.

Equation 6–1

$$C_t = \frac{C_w}{F^*} S_w^n + \frac{BQ_v}{F^*} S_w^{n-1}$$

Equation 6–2

$$\frac{1}{R_t} = \frac{1}{R_w F^*} S_w^n + \frac{BQ_v}{F^*} S_w^{n-1}$$

where Q_v is cation exchange capacity per pore volume unit (meq/cc), B is the equivalent conductance of sodium clay exchange cations (mho·cc/meq·m), and F^* is the intrinsic formation factor for shaly-sand (unitless). R_w is the water resistivity

(ohm·m) at T , the laboratory or formation temperature (Celsius). The Q_v value has to be converted to CEC from mass to volume unit (using Equation 6–3), and B can be estimated using the correlation presented by Juhasz (1981) (Equation 6–4).

Equation 6–3

$$Q_v = \frac{CEC(1 - \phi_t)\rho_g}{100\phi_t}$$

where ϕ_t is total porosity (fraction) at ambient or stress conditions, and ρ_g is grain density (g/cc).

Equation 6–4

$$B = \frac{-1.28 + 0.225T - 0.0059T^2}{1 + R_w^{1.23}(0.045T - 0.27)}$$

This correlation only applies to Na^+ cations; if the formation water has divalent cations (e.g. Ca^{2+} or Mg^{2+}), the value of B may have a $\pm 10\%$ error (McPhee et al., 2015).

6.2 Methodology

The resistivity of brine and brine-saturated rock (**Section 3.12**) was measured at room temperature and converted to reservoir temperature using Arps (1953) (Equation 3–25). The formation factor and Archie's cementation exponent m were derived from the ratio of R_o/R_w (Equation 2–3) and the measured core helium porosity.

6.2.1 Sampling

The ENAP2 samples were selected for the ultrasonic velocity and destructive methods as there was sufficient rock material, while for the multivalency core flooding method, the most permeable and porous core plug from the wells ENAP1 and ENAP2 was selected.

6.2.2 Cation-exchange capacity

6.2.2.1. Chemical leaching method

This method separates the core's clay portion and leaches it with ammonium acetate to release exchangeable cations in solution (Chapman, 1956), which are then analysed using ICP-MS (Induced Coupled Plasma Mass Spectrometry). The same laboratory protocol for clay-XRD sampling was conducted for the clay fraction separation (**Section 3.6.1**). A sedimentation-decantation process after core grinding was repeated at least six times per core to collect 0.5 g of fine grain sample.

The fine-grained samples were transferred to a 50 ml centrifuge tube for the chemical leaching. The leaching involved adding a 15 ml ammonium acetate solution (1 M with

pH 7) and stirring to ensure uniform mixing. The suspension was then centrifuged for 15 minutes at 2,000 rpm, and the supernatant liquid was decanted into a 50 ml volumetric flask three times. The remaining leach solution was made up to the 50 ml mark with distilled water in its centrifuge tube. Fifteen clay samples and one control were analysed with the Thermo Fisher iCAP 7400 Radial ICP-OES equipment at the School of Earth and Environment, University of Leeds, to determine the concentration of the exchangeable cations: Al, Ca, Fe, K, Mg, Mn, and Na. Equations 6–5 and 6–6 were used to calculate the final CEC value (Morgan et al., 1993).

Equation 6–5

$$CEC_i = \frac{V C}{10 M A}$$

Equation 6–6

$$CEC_{Total} = \sum CEC_i$$

where CEC_i and CEC_{Total} are the cation-exchange capacity per cation species and total (meq/100g), V is the solution volume (50 ml of centrifuge tube used), C is the cation concentration in solution (ppm), M is the mass of fine clay (~0.5 g), and A is the atomic mass of cation (AMU).

6.2.2.2. Multisalinity core flooding method

This method follows the Waxman-Smits principle for fully brine-saturated rocks (**Section 6.1.1**): core flooding different brine concentrations and measuring the rock conductivity (C_o) at a constant low flow rate. Since the water formation of the ZG reservoir is freshwater – 12,000 ppm NaCl, the brines used ranged from 20,000 to 0 ppm NaCl, in decreasing salinity order divided into four runs. The experiment setup consisted of a Hassler core holder at 1,500 psig of confining pressure inside a cabinet to maintain a constant temperature of 21°C (**Figure 6-1**). The reported rock resistance was defined at 2 kHz with a phase angle lower than 0.5° (McPhee et al., 2015). The brine conductivity (C_w) inlet and outlet were inline measured during core flooding at a constant low flow rate of 0.09 ml/min. The pressure drop was monitored and used as a control to define a quasi-steady state. Between 20 to 40 pore volumes (PV) were used during flooding before taking final measurements (Lasswell, 2006). Darcy's law was applied to derive the brine permeability during the flooding, and the core was NMR scanned at the beginning and end of the experiment to review changes in the T_2 distribution (Navarro-Perez et al., 2024).

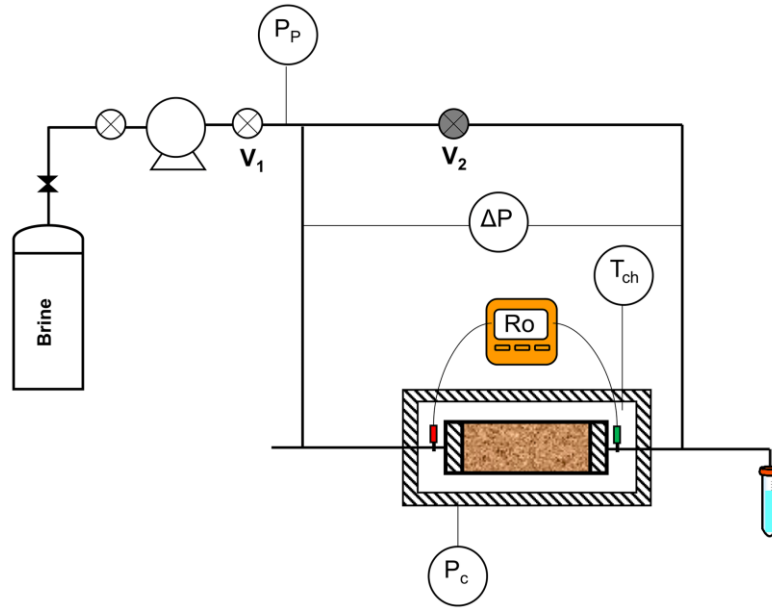


Figure 6-1. Diagram of the multi-salinity experiment. P_p : pore pressure transducer, P_c : confining pressure indicator, ΔP : pressure difference transducer, T_{ch} : chamber temperature, R_o : rock resistance meter, V_1 : pump downstream valve, and V_2 : bypass valve (Navarro-Perez et al., 2024).

The rock conductivity C_o , vs. the brine conductivity C_w , are plotted to derive the CEC. The intercept, BQ_v/F^* (Equation 6–7), is obtained using a linear regression (**Figure 6-2**). Q_v (and CEC) is derived from the slope and the B value of the linear fit. This method presents advantages over direct measurement of CEC since it can be applied under stress and temperature conditions of the reservoir; however, care should be taken when using lower brine salinity (< 50,000 ppm) since clay migration or swelling could occur (McPhee et al., 2015).

Equation 6–7

$$C_o = \frac{C_w}{F^*} + \frac{BQ_v}{F^*}$$

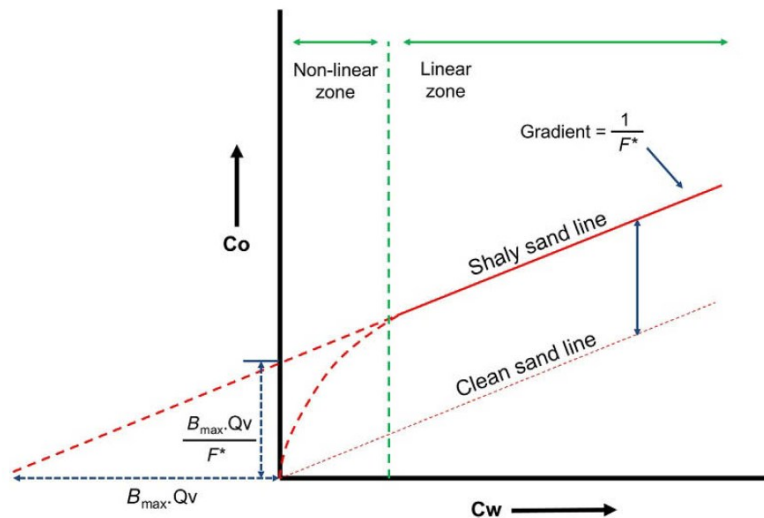


Figure 6-2. Determination of Q_v from multiple salinity tests (McPhee et al., 2015).

6.2.3 Ultrasonic velocities

The 1.5-inch horizontal core plugs from the ENAP2 well were used after finishing the other tests of the core analysis programme (**Section 3.3**). The cores were cleaned with methanol, and notes were taken about the sample state before the test, e.g., on any cracks and irregular shapes. The core plugs were fully brine-saturated with 7% KCl solution. The ultrasonic velocities V_p (P-wave), V_{s1} (S1-wave), and V_{s2} (S2-wave) were measured using the pulse transmission technique following the ISRM³ standard (Aydin, 2014) with a compression testing machine (**Figures 6-3 and 6-4**). Hydrostatic confining pressure was applied on each sample with a loading rate of less than 73 psig/min, and measurements were taken at four confining pressures: 500 psig, 1,450 psig, 2,900 psig, and 4,350 psig, respectively. The frequency used for P-wave velocity was 1 MHz, and that used for S-wave velocities was 0.6 MHz. All measurements were conducted in a loading-unloading loop to monitor hysteresis. The PicoScope 6 software was used for data acquisition of the ultrasonic velocities transit time. The calibration protocol was conducted with aluminium alloy bars as a reference to apply corrections to the measured transit times (**Appendix D.2**). Equation 6–8 was used to calculate the ultrasonic velocities.

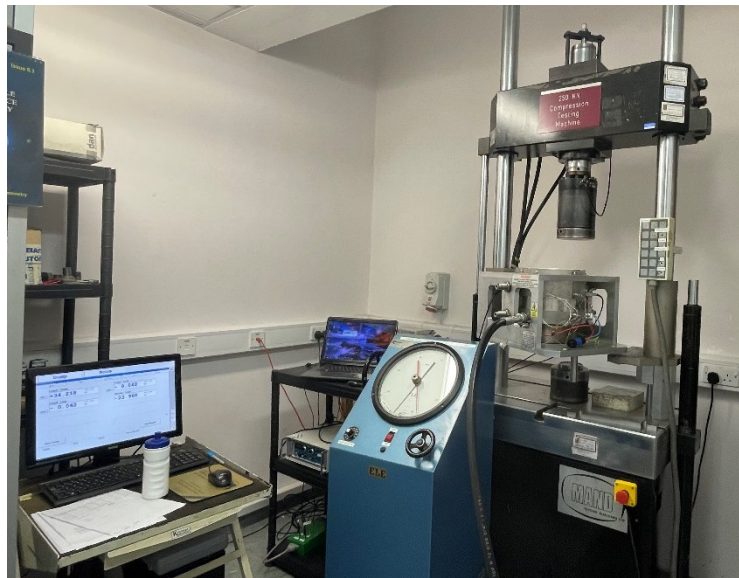


Figure 6-3. Compressive testing machine (maximum of 250 KN) located in the Wolfson Multiphase Flow Laboratory at the University of Leeds, UK.

³International Society for Rock Mechanics.

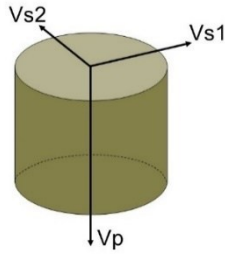


Figure 6-4. Diagram showing compressional or P-wave velocity (V_p) and shear or S-wave velocities (S_1 and S_2) directions.

Equation 6–8

$$v = \frac{L}{(t_{transit} - t_{delay})}$$

where v is the ultrasonic velocity (m/s), L is the length (travel path) of the core plug (m), $t_{transit}$ and t_{delay} are the measured transit time (s) and delay time (s), respectively.

6.3 ZG electrical properties

This section presents the results related to the electrical properties of the ZG formation.

6.3.1 Resistivity, formation factor, and cementation exponent

The ZG rock resistivity ranges from 2.6 to 12.8 ohm·m with an average of 6.0 ohm·m. In contrast, the formation factor ranges from 16 to 76 with an average of 36 at reservoir temperature (average of 96°C for well ENAP1 and 93°C for well ENAP2, respectively) and 1,500 psig of confining pressure (**Table 6-1**). Cross-plots of the log of formation factor confined at 1,500 psig against the log of the helium porosity at ambient stress (**Figure 6-5**) were used to derive m values, which range from 1.66 to 3.08, with an average of 2.02 (**Table 6-2**). Most of the samples (81%) have a m value between 1.8 and 2.0; one sample from the PRT1 unit and three samples from the PRT3 unit have an m value close to 2.4, and the two cores (ENAP1-2 and ENAP2-54) of the PRT3 unit have an m value close to 3. A linear correlation was found with R^2 of 0.66 between the helium porosity and cementation exponent (**Figure 6-6**), where two core plugs (ENAP1-2 and ENAP2-54) of the PRT3 unit deviate with a proportional relationship of 5:6 rather than 1:1 (**Figure 6-7**). In addition, the resistivity of the samples from well ENAP2 was measured at three confining pressures (1,500, 2,500, and 3,500 psig). The resistivities increased by 18% as confining pressure was increased from 1,500 to 3,500 psig (**Table 6-3** and **Figure 6-8**).

Table 6-1. Resistivity, formation factor, and cementation exponent metrics at 1,500 psig confining pressure and reservoir temperature (T_{res}).

Property	Parameter	ENAP1	ENAP2
Ro@T_{res} (ohm·m)	Minimum	2.6	5.2
	Maximum	10.3	12.8
	Average	5.3	7.1
	Standard deviation	1.9	2.1
Formation factor (Ro/Rw)¹	Minimum	16	31
	Maximum	63	76
	Average	32	42
	Standard deviation	12	13

¹ Rw@95°C is 0.16 ohm·m (12,000 ppm NaCl).

Table 6-2. Cementation exponent metrics at 1,500 psig confining pressure using helium porosity.

Property	Parameter	ENAP1	ENAP2
Cementation exponent <i>m</i>	Minimum	1.66	1.78
	Maximum	3.08	2.84
	Average	2.06	1.96
	Standard deviation	0.39	0.26

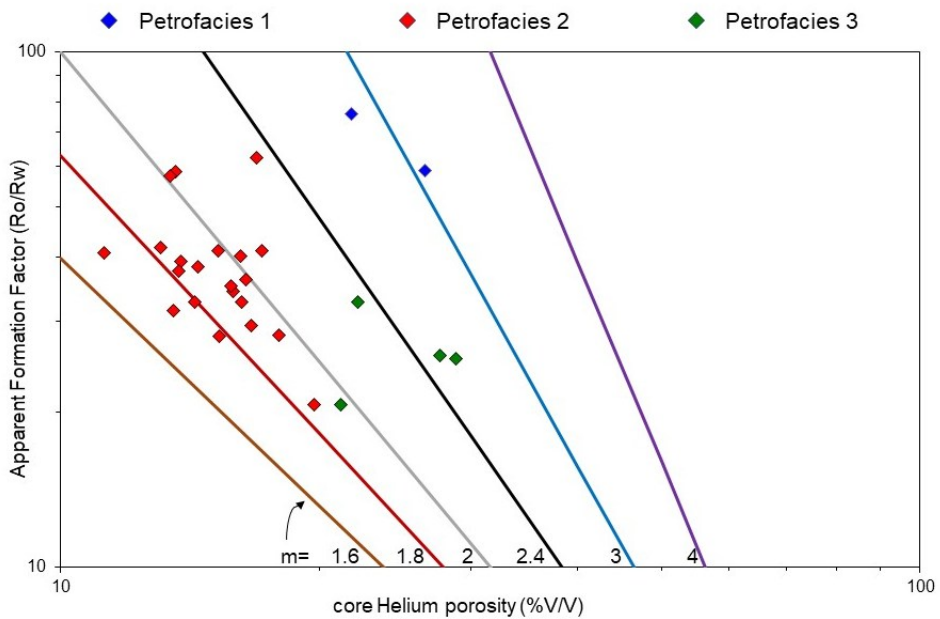


Figure 6-5. Apparent formation factor vs helium porosity cross-plot discriminated by the PRT units.

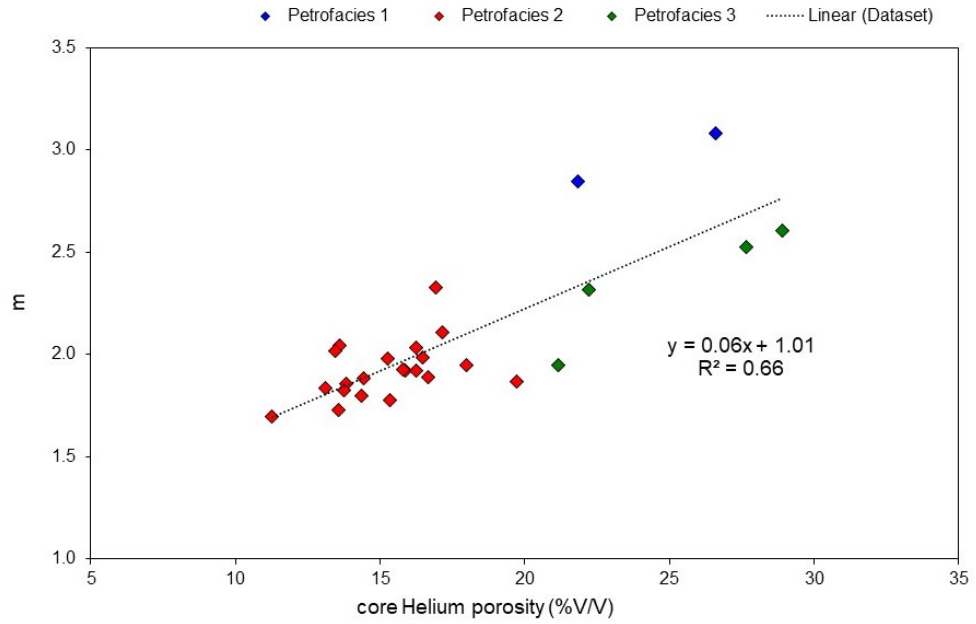


Figure 6-6. Calculated cementation exponent vs helium porosity cross-plot with linear correlation.

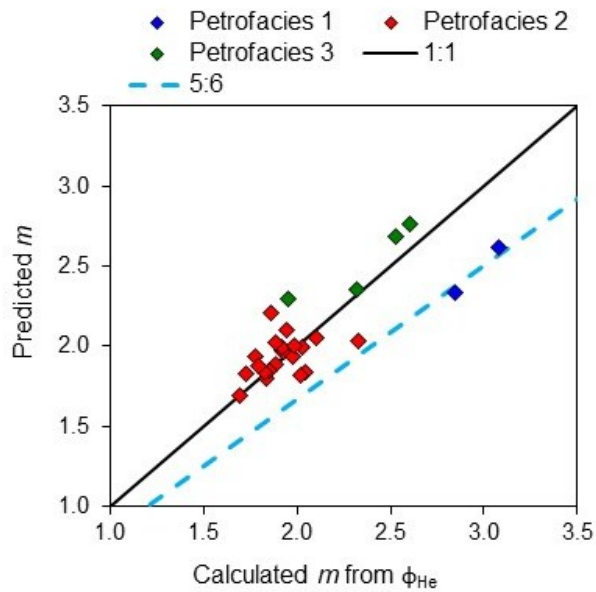


Figure 6-7. Cementation exponent (m) cross-plot: calculated vs predicted from linear correlation, the dark blue data points belong to the pay sands in the PRT3 unit.

Table 6-3. ENAP2 set resistivity metrics measured at three confining pressures.

SAMPLE	PRT	Slope (ohm·m/psig)	Intercept (ohm·m)	R ²	Increase(%) ¹
8	2	0.0003	5.1	0.96	12
17	2	0.0005	4.6	0.98	18
24	2	0.0006	5.9	0.97	18
33	2	0.0005	6.1	0.97	14
44	2	0.0006	9.1	0.96	11
53	2	0.0006	11.9	0.96	9
62	2	0.0003	5.5	0.98	10
38	2	0.0002	5.4	0.99	9
46	2	0.0003	6.6	0.97	8
65	2	0.0002	6.3	0.98	8
76	2	0.0005	9.0	0.97	10
54	3	0.0003	6.6	0.98	7

¹ Increase = (Ro@3,500psig/ Ro@1,500psig) – 1.

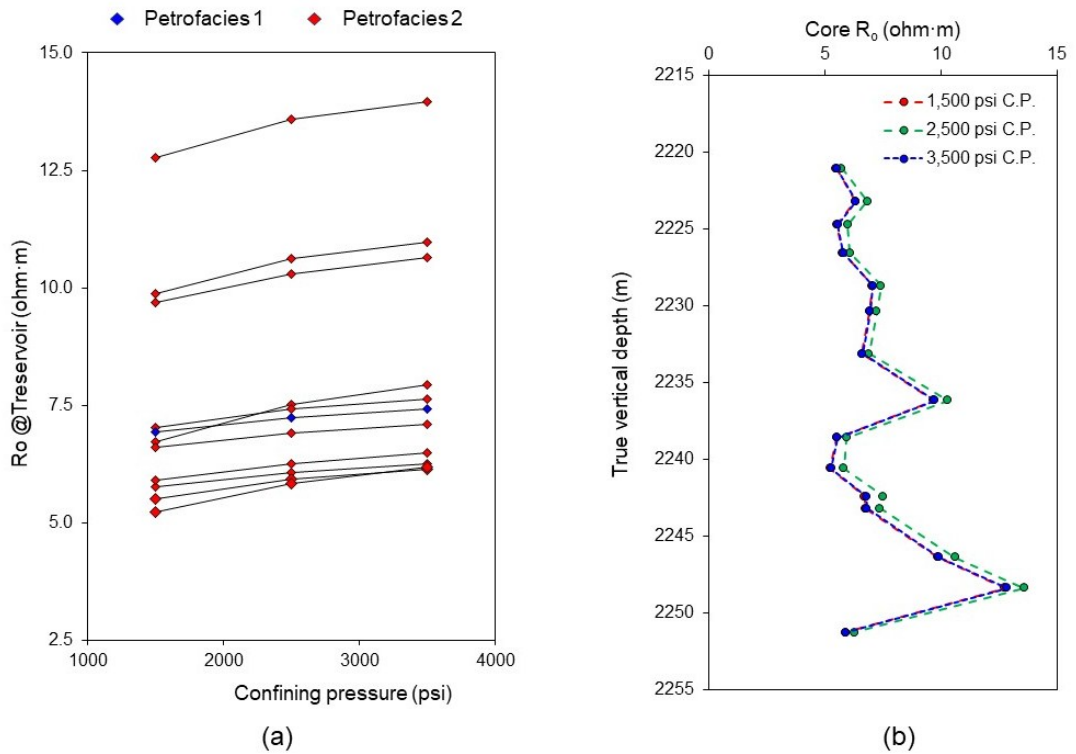


Figure 6-8. Resistivity measurements of ENAP2 set at three confining pressures: (a) cross-plot of rock resistivity to reservoir temperature discriminated by the PRT unit, and (b) cross-plot of the confining pressure resistivities at reservoir temperature vs ENAP2 well depth.

6.3.2 Cation-exchange capacity results

The multivalency core flooding experiment on sample ENAP1-2 followed the Waxman-Smiths model with a linear trend in the highest salinity brines and a non-linear trend towards deionised water (Figure 6-9). This experiment was part of the Navarro-Perez et al. (2024) study comparing three clay-bearing sandstones and their contribution to the geothermal characterisation. The experiment on ENAP1-2 lasted 25 days, and the rock resistivity did not stabilise for the deionised water (DW) run. Its

final conductivity for DW was forecasted to be 0.024 mS/cm, leaving it running for an additional 60 days. The obtained CEC value was 72 meq/100g (Table 6-4).

On the other hand, the obtained CEC values with the chemical leaching method ranged from 18 to 41 meq/100g with an average of 23 meq/100g (Table 6-5). In this method, calcium is the main exchangeable cation with an average of up to 50%, followed by sodium (~29%), magnesium (~15%), and potassium (~5%). Significant amounts of aluminium, iron, and manganese were not absorbed (Figure 6-10). Petrofacies 1 has the highest CEC, followed by petrofacies 2. In addition, three samples containing fractures have moderate CEC values (Figure 6-11).

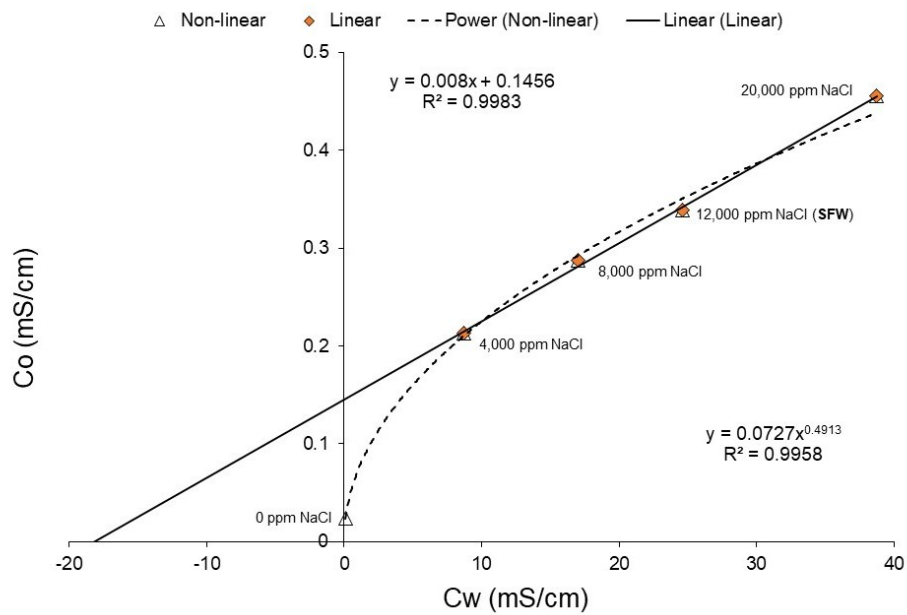


Figure 6-9. Rock (C_o) and brine (C_w) conductivities cross-plot from the multisalinity experiment on ENAP1-2 core (Navarro-Perez et al., 2024).

Table 6-4. CEC results from multisalinity experiment (Navarro-Perez et al., 2024).

SAMPLE	F ¹	Slope	Intercept	Qv (meq/cc)	$\rho_{\text{grain}}(\text{g/cc})^2$	CEC (meq/100g)
ENAP1-2	125	0.008	0.146	5.7	2.89	71.5

¹ Apparent formation factor (inverse slope).

² Derived from helium porosimeter.

Table 6-5. CEC statistics from the destructive method.

Parameter	CEC (meq/100g)	Qv (meq/cc)
Minimum	18	2.6
Maximum	41	5.5
Average	23	3.6
Standard deviation	6	0.9

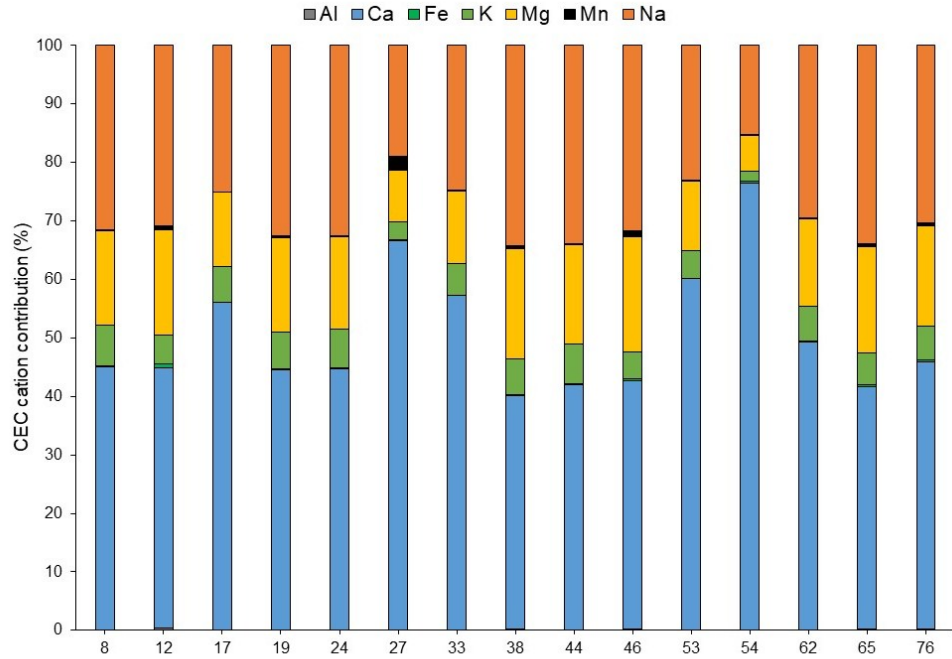


Figure 6-10. Cation contribution in total CEC per sample bar chart with the chemical leaching method.

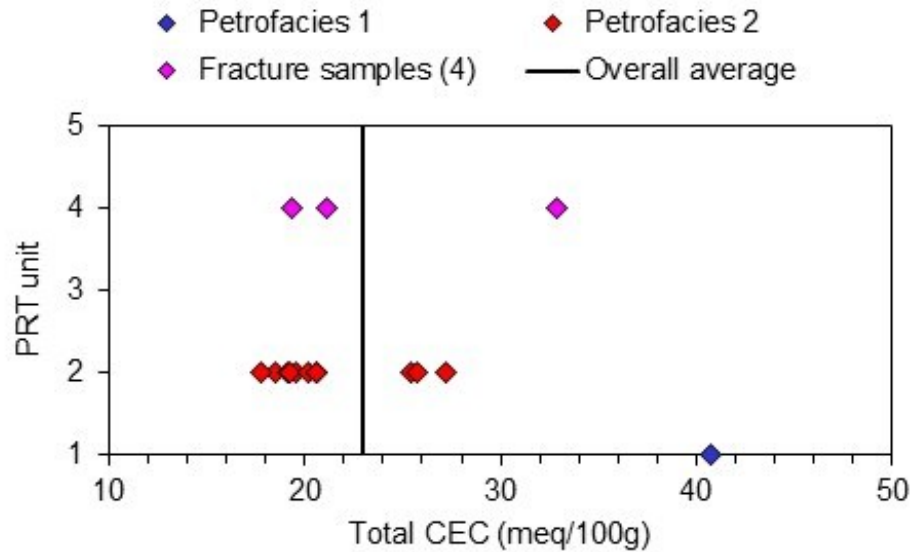


Figure 6-11. Total derived CEC measurements per PRT unit from the chemical leaching method. The black line indicates the average value of 23 meq/100g. Samples ENAP2-12, ENAP2-19, and ENAP2-27 were grouped as fracture samples.

6.4 ZG ultrasonic velocities

This section presents the results related to the ultrasonic velocities of the ZG formation. The measured ultrasonic velocities increased with the confining pressure (Figure 6-12). The average V_p/V_{s1} ratio decreases from 1.85 at 500 psig to 1.77 at

4350 psig (Table 6-6). Linear correlation was applied between Vp and Vs1 at each confining pressure with R² values between 0.71 and 0.82 (Figure 6-13).

Table 6-6. Ultrasonic velocity statistics from ENAP2 set.

Confining pressure	Parameter	Vp (m/s)	Vs1 (m/s)	Vs2 (m/s)	Vp/Vs1
500 psig	Minimum	3,577	1,757	1,814	1.65
	Maximum	4,451	2,632	2,253	2.53
	Average	3,897	2,104	2,050	1.85
	Standard deviation	259	196	127	0.25
1,450 psig	Minimum	3,735	1,885	1,858	1.66
	Maximum	4,190	2,412	2,308	1.93
	Average	3,924	2,168	2,111	1.78
	Standard deviation	140	164	137	0.08
2,900 psig	Minimum	3,873	2,039	1,851	1.67
	Maximum	4,246	2,439	2,353	1.89
	Average	4,018	2,243	2,172	1.77
	Standard deviation	118	128	137	0.05
4,350 psig	Minimum	3,928	2,052	1,901	1.66
	Maximum	4,268	2,453	2,374	1.87
	Average	4,061	2,268	2,197	1.77
	Standard deviation	110	121	129	0.05

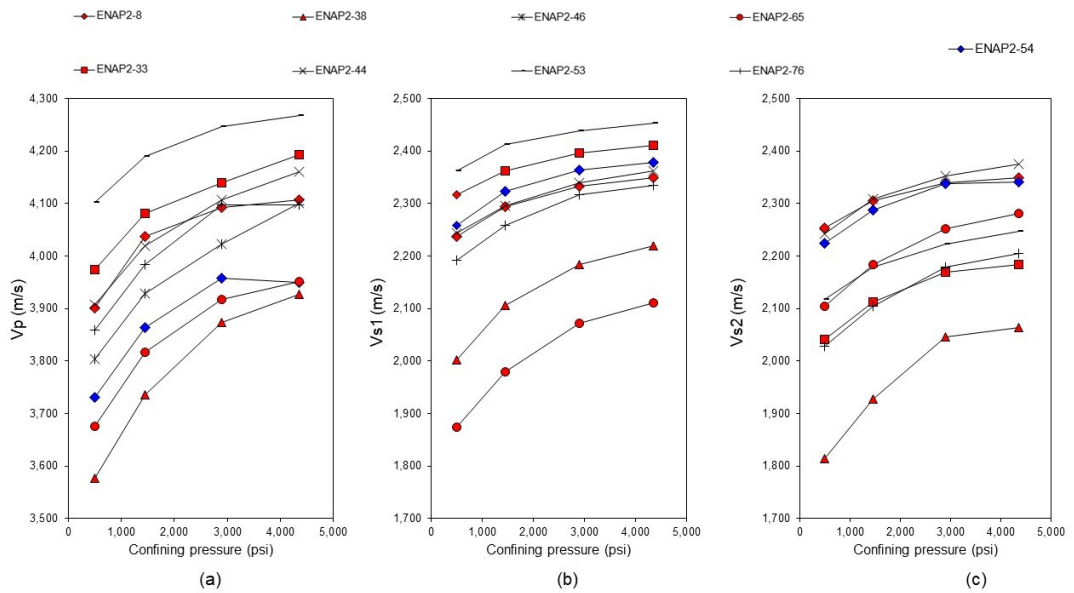


Figure 6-12. Ultrasonic velocities measured at four confining pressure (Table 6-6) for Petrofacies 1 (ENAP2-54) and 2: (a) P-wave velocity, (b) S1-wave velocity, and (c) S2-wave velocity.

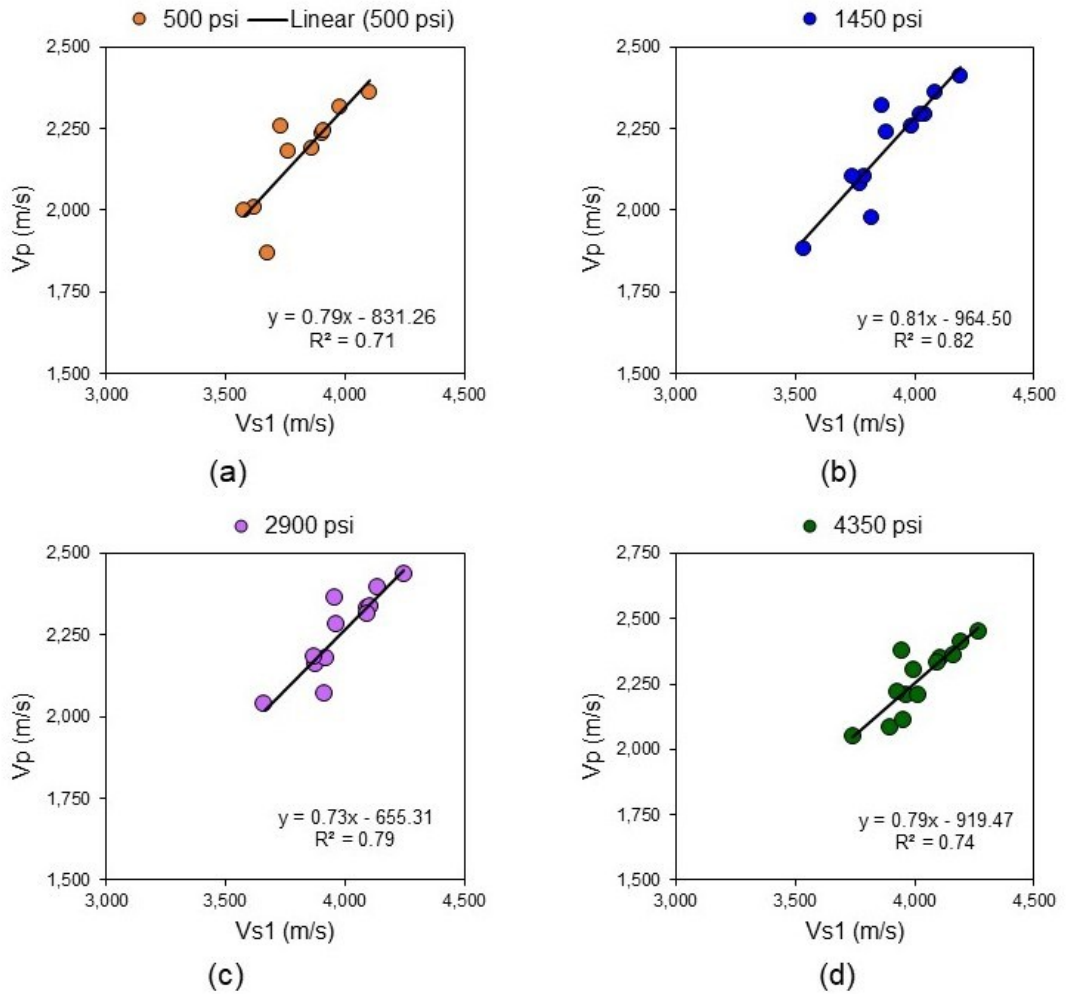


Figure 6-13. P-wave and S1-wave velocities cross-plots at different confining pressures: (a) 500 psig, (b) 1450 psig, (c) 2900 psig, and (d) 4350 psig.

6.5 Discussion

6.5.1 Rock resistivities comparison

ENAP2 core resistivities (R_o) at a confining pressure of 3,500 psig were compared with its well's deep and shallow resistivity logs (**Figure 6-14**). Most laboratory R_o values are 1 ohm·m lower than the resistivity logs, and the pay sand (PRT 1) is 3 ohm·m lower than the shallow resistivity log and 22 ohm·m lower than the deep resistivity log, respectively. This is consistent with PRT1 containing gas on this well, while mudlogging data indicates no gas presence in the non-pay sands. Above 2238 metres, the laboratory R_o values closely cross-match both resistivity logs, indicating a potential water-bearing zone.

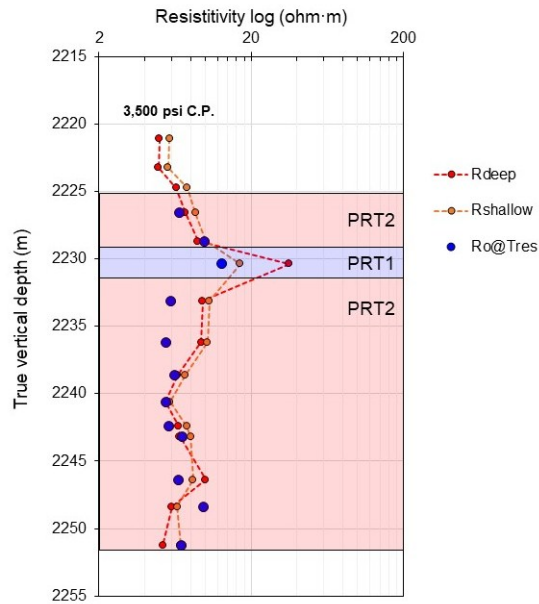


Figure 6-14. Plot comparing the deep and shallow resistivities logs with core resistivity at reservoir temperature per depth and discriminated per PRT (petrofacies) unit (of well ENAP2 with R_o measured at a confining pressure of 3,500 psig).

6.5.2 Cementation exponent correlations and controls

A positive linear correlation was found between the cementation exponent m and porosity, named correlation 1 (Figure 6-6). This correlation trend is similar to the findings of Byrnes et al. (2009) and Cluff et al. (2009) made during studies of the Mesaverde TGS, Western USA, where the m values increase with porosity. Their empirical correlation is a linear correlation between the logarithm of porosity with the cementation exponent. So, this correlation was applied to the dataset with an R^2 of 0.64, named correlation 2 (Figure 6-15). The comparison of both correlations (Figure 6-16 and Table 6-7) agrees with the mentioned studies. For ZG, a variable cementation exponent as a function of porosity is more suitable than a fixed cementation exponent. At a 30% porosity, the m value in correlation 1 is 2.81, while in correlation 2 is 2.49. Thus, the latter correlation controls the calculation range of m better as porosity increases.

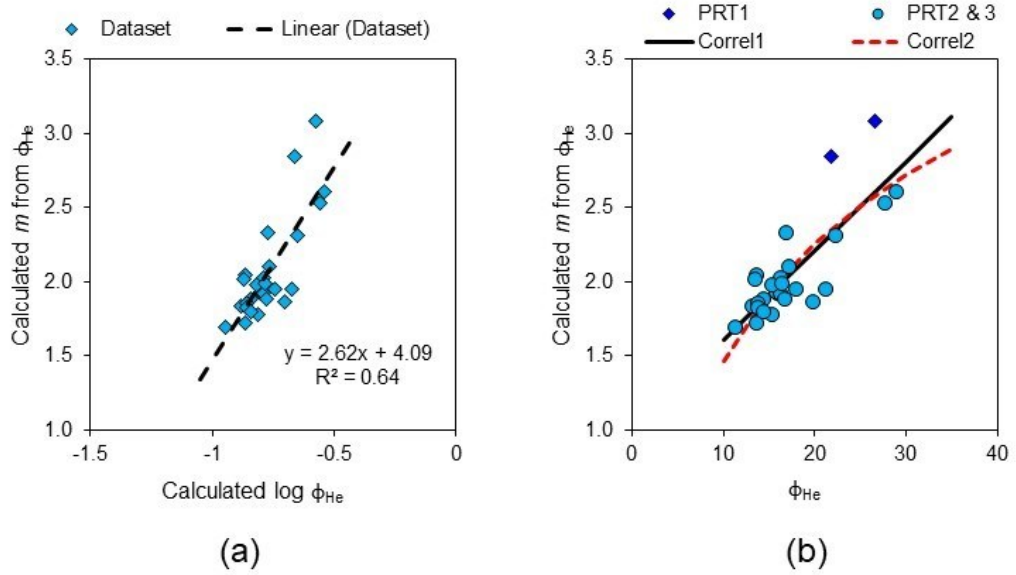


Figure 6-15. Cementation exponent (m) cross-plots with (a) logarithm of core helium porosity with empirical correlation following Cluff et al. (2009); (b) core helium porosity discriminated by PRT units. Correl1 in the black line corresponds to the empirical correlation found in Figure 6-6, and Correl2 in the red dashed line corresponds to the empirical correlation found following Cluff et al. (2009).

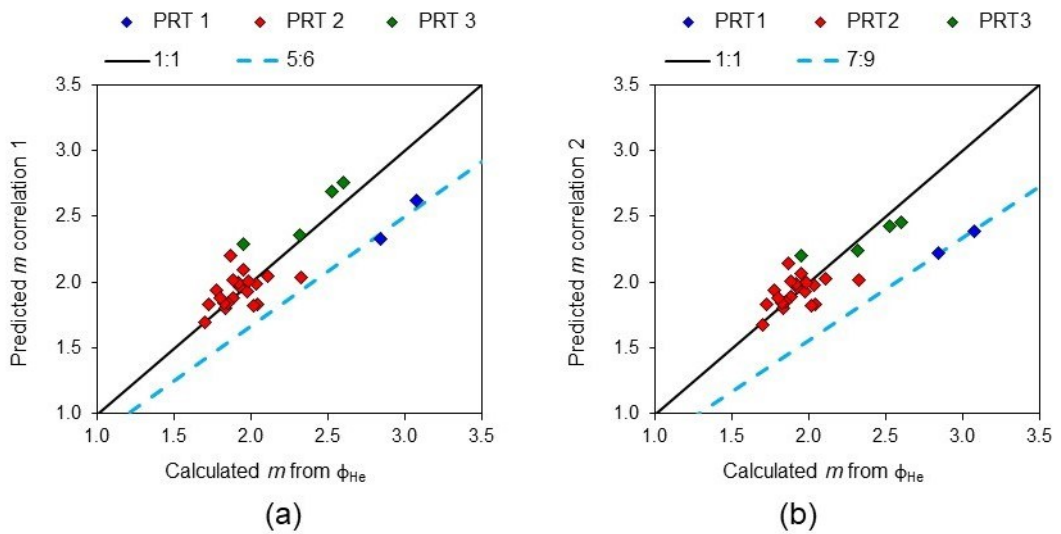


Figure 6-16. Cementation exponent (m) cross-plot (a) calculated vs predicted from correlation found in Figure 6-6; (b) calculated vs predicted from correlation found in following Cluff et al. (2009).

Table 6-7. Statistical comparison of correlations 1 and 2.

Metrics	Correlation 1	Correlation 2
R ²	0.66	0.64
RMSE	0.19	0.22
STD	0.16	0.12

The average value of m (2.02) is very close to 2.09, which ENAP uses in the modified Simandoux model. This average value m (2.02) is within the PRT2 range and increases for the PRT3 (~2.5) and PRT1 (~3.0) units. ZG's mineralogical influences

the cementation exponent. For both lithological units, chloritic (PRT1) and glauconitic (PRT2 and 3), the cementation exponent increases as the iron and chlorite content increases (**Figure 6-17**). The latter is a better discriminator of m , as both lithological units are iron-rich; thus, chlorite content controls m . There is a direct relationship between the degree of heterogeneity from CT images (**Figure 6-18**) and the specific surface area (**Figure 6-19**) with the cementation exponent. These two findings indicate that m varies as the clay type (glauconite or chlorite), and its distribution predominates in the matrix and pore-fillings. Less heterogeneous cores with high specific surface areas correspond to glauconitic sandstones with matrix-supported siltstone, evolved glauconite grains, and lower porosity. More heterogeneous cores with low specific surfaces correspond to chloritic grain-supported sandstones containing plagioclase and significant secondary porosity. Furthermore, following Ziarani and Aguilera's (2012) correlation in TGS, there is a linear relationship between the characteristic length of ZG at r_{25} (**Section 5.5.1**) and the square-root product of the formation factor with Klinkenberg permeability with an R^2 of 0.97 (**Figure 6-20**). Therefore, ZG's electrical properties are controlled by its pore network connectivity and structure, as evidenced by the strong correlation between permeability and characteristic pore length.

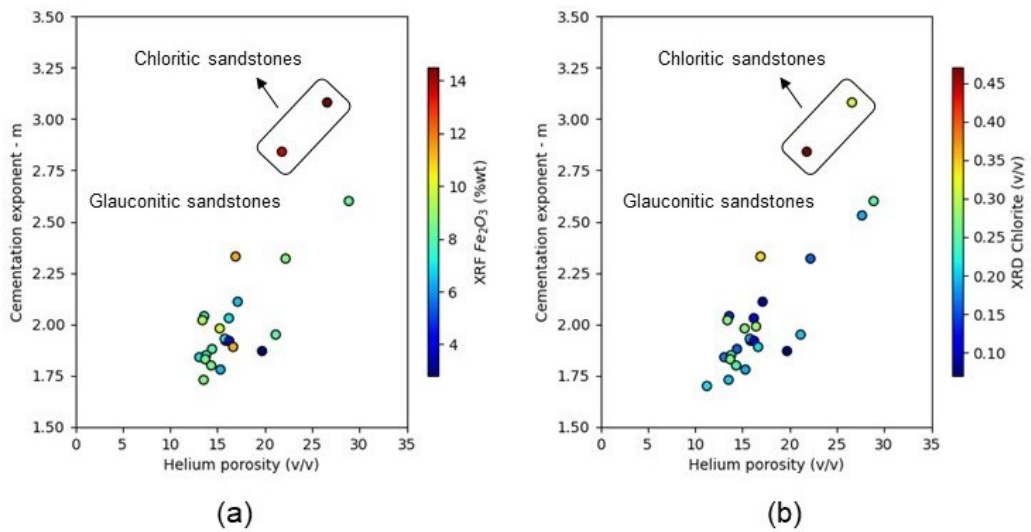


Figure 6-17. Cementation exponent (m) with porosity cross-plots discriminated by (a) XRF iron content and (b) XRD chlorite content.

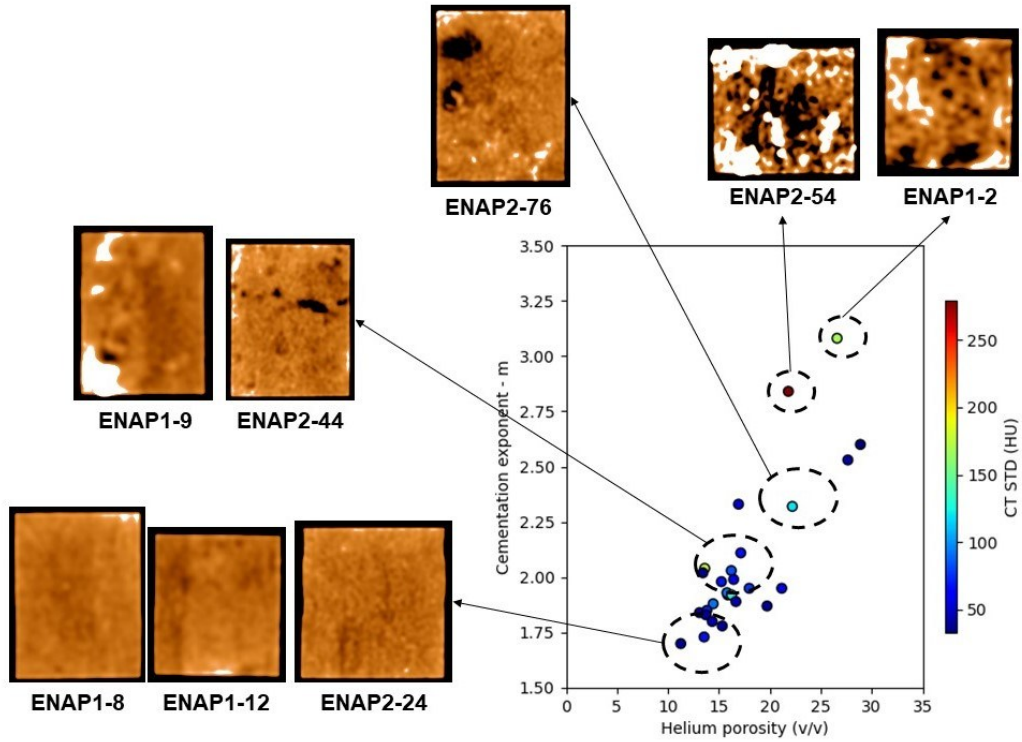


Figure 6-18. Cross-plot of cementation exponent (m) with porosity discriminated by standard deviation counting of voxels from CT scan images. Some CT images are displayed to visualize the trend of the degree of heterogeneity as m increases.

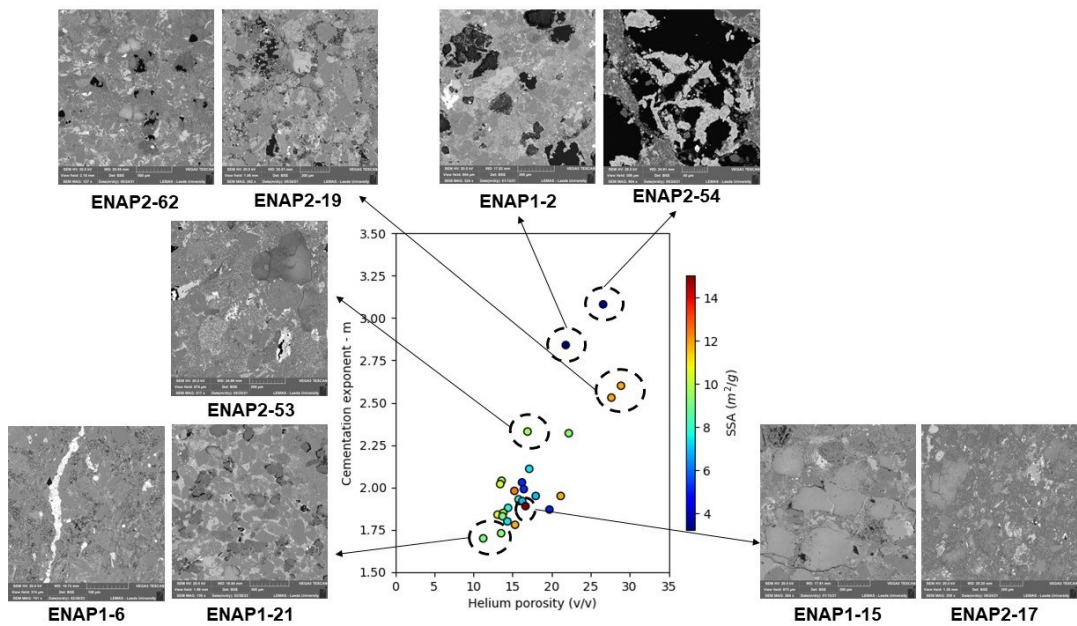


Figure 6-19. Cross-plot of cementation exponent (m) with porosity discriminated by the specific surface area (SSA). Some SEM images are displayed to visualize the grain and pore distribution trend.

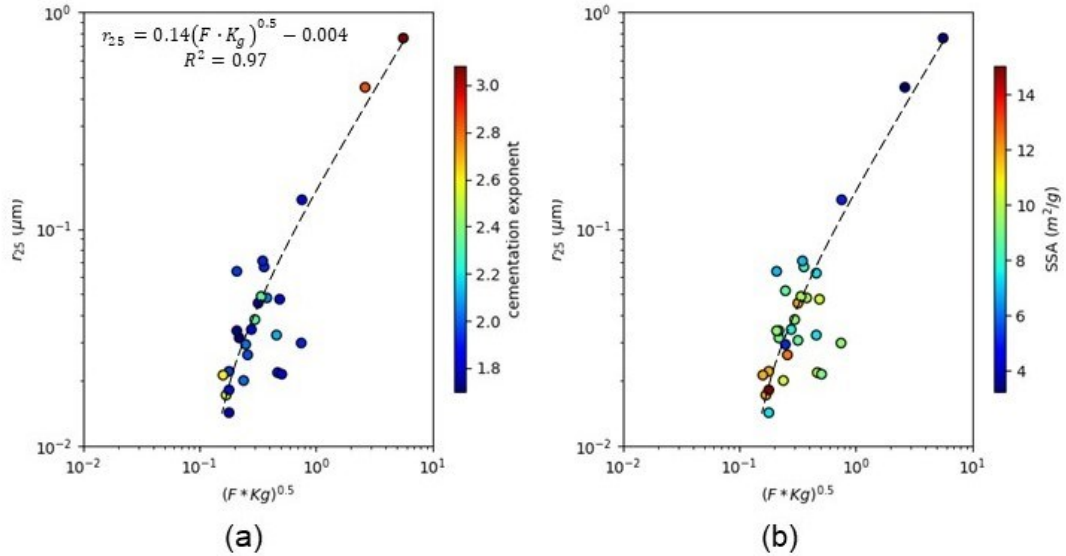


Figure 6-20. Cross-plot of MICP pore-throat radius at 25% mercury saturation (r_{25}) with $(F \cdot K_g)^{0.5}$ following Ziarani and Aguilera (2012) correlation discriminated by (a) the cementation exponent and (b) the specific surface area.

Another interpretation of the variability of m may be related to the electrical efficiency theory (Herrick and Kennedy, 1994), which explains the conductive phase of fully- or partially-saturated rocks with complex pore geometry with an electrical ratio or efficiency (Equation 6–9). It is based on a straight cylindrical tube pore shape aligned with the electrical current direction. In **Chapter 4**, it was argued that the FZI method can be used as a criterion to separate the petrofacies, which is based on Kozeny-Carman’s model of pore throat radius-like cylindrical tube shapes (**Section 4.8.1**). Soleymanzadeh et al. (2021) proposed an Electrical Rock Type (ERT) workflow to predict m values based on the electrical efficiency theory with Byrnes et al. (2009) dataset, following a logarithmic correlation type (Equation 6–10).

Equation 6–9

$$\eta_e = \frac{1}{F\phi}$$

where F is the electrical formation factor, and ϕ is the total porosity (v/v).

Equation 6–10

$$m = \ln \eta_e \frac{1}{\ln \phi} + 1$$

where η_e is the electrical efficiency *Equation 6–9* and ϕ is the total porosity (v/v). The intercept should be equal to 1, which indicates that when $\phi \rightarrow 0$ then $m \rightarrow 1$.

The ERT workflow is simple. The electrical efficiency η_e is calculated with the electrical formation factor and porosity, assuming a normal distribution of $1/\ln \eta_e$ values, and the ERT groups are found. Three ERT groups were identified for the ZG

dataset using 27 data points: ERT0, ERT1, and ERT2 (**Figure 6-21**). ERT0 has the lowest η_e (<10%) and a linear correlation of $R^2=0.95$, followed by ERT1 with η_e up to 18% and a linear correlation of $R^2=0.93$, and ERT2 with η_e up to 25% and a linear correlation of $R^2= 0.56$ (**Figure 6-22**). The intercept values of ERT0 and ERT1 are 1.22 and 0.85, respectively, which are close to 1.0, but the intercept value of ERT2 is 0.19, and for this group, the electrical efficiency theory is inadequate (**Table 6-8**). Nonetheless, it seems this new grouping distinguishes the mineralogical content of ZG rather than the petrofacies units, specifically for the iron, clay, chlorite and plagioclase contents (**Figure 6-23**); this will be further developed in **Chapter 7** with the water saturation model.

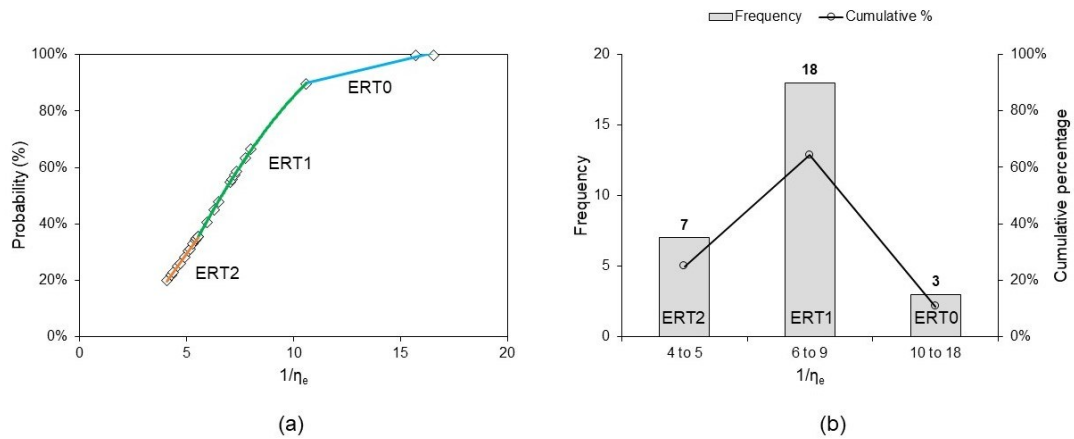


Figure 6-21. (a) Normal probability plot of $(1/\eta_e)$ of the dataset. (b) frequency and cumulative histogram.

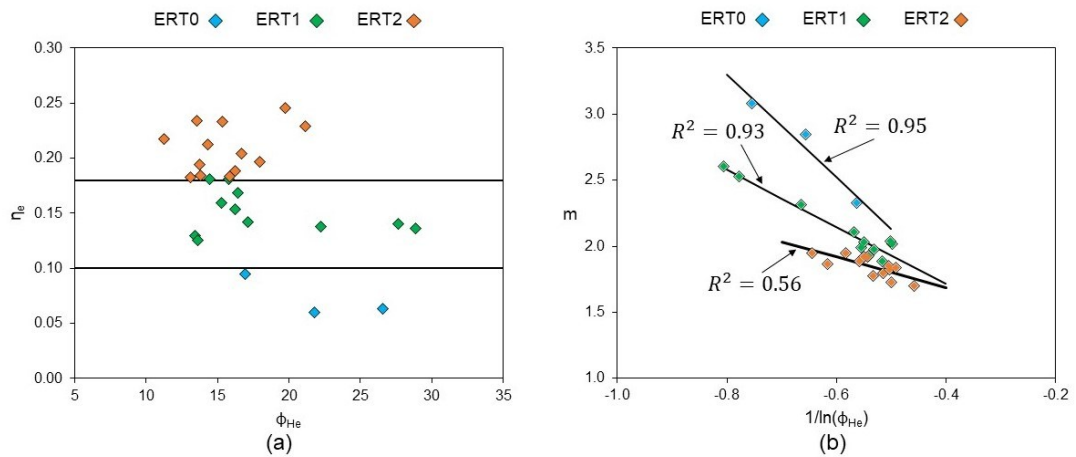


Figure 6-22. (a) Electrical efficiency vs porosity for all ERTs. (b) Cementation exponent vs $1/\ln(\phi_{He})$ for the identified electrical rock types (ERTs).

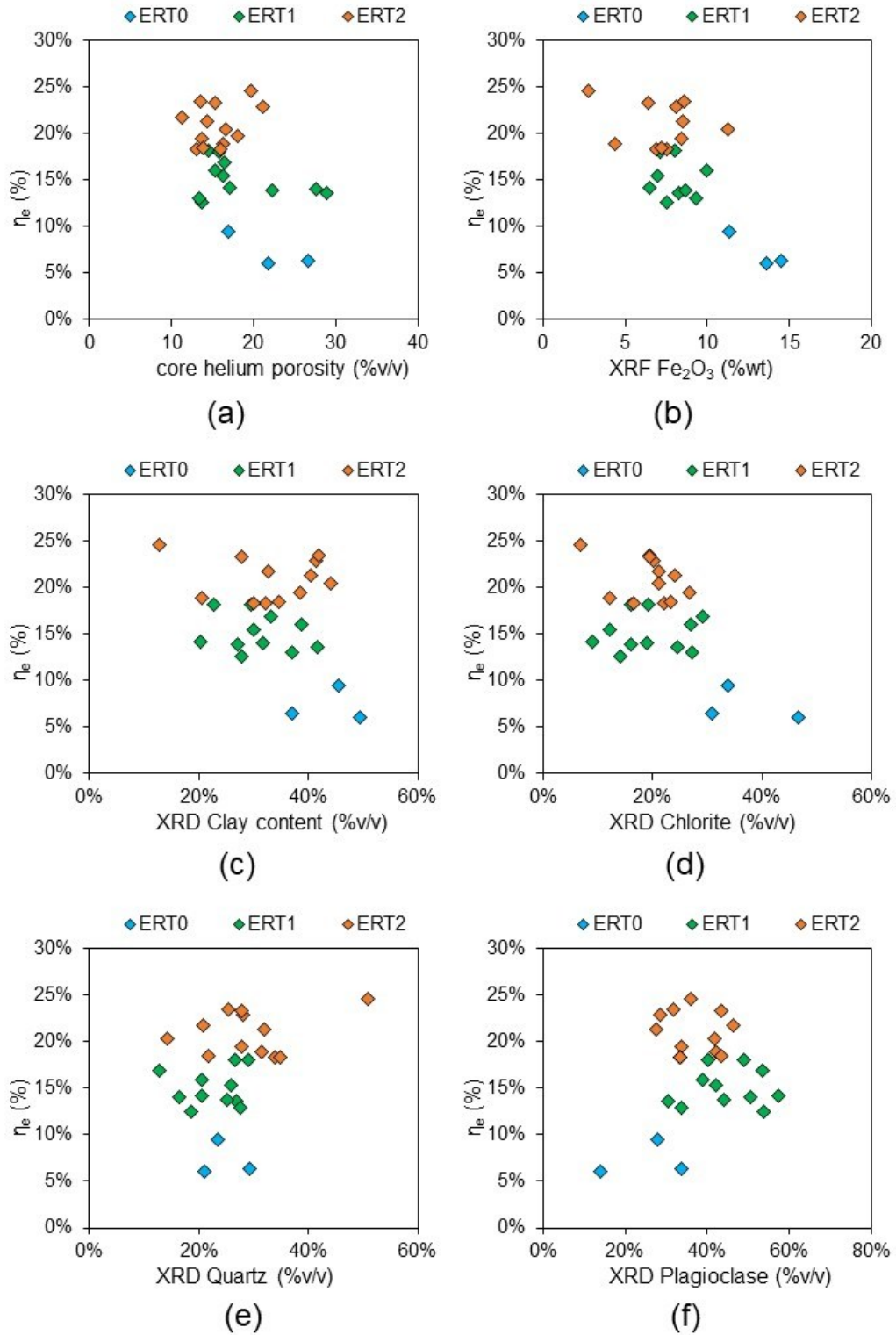


Figure 6-23. Electrical efficiency (η_e) cross-plots with (a) core porosity, (b) iron content, (c) clay content, (d) chlorite content, (e) quartz content, and (f) plagioclase content.

Table 6-8. Fitted equations with the ERT workflow.

ERT class	Equation	R ²	RMSE	m range
ERT0	$m = -1.16 \frac{1}{\ln \phi} + 1.22$	0.95	0.07	2.1 – 3.3
ERT1	$m = -2.16 \frac{1}{\ln \phi} + 0.85$	0.93	0.06	1.7 – 2.6
ERT2	$m = -3.90 \frac{1}{\ln \phi} + 0.19$	0.56	0.05	1.7 – 2.0

Finally, **Table 6-3** and **Figure 6-8** show that within the range of confining pressure tested, ZG's rock resistivity increases linearly with confining pressure. So, the ENAP2 set laboratory Ro values were compared with its derived Archie cementation exponent at the three measured confining pressures (1,500, 2,500, and 3,500 psig), showing a linear increase (**Figure 6-8 a**) with a stress effect of until 3% from 1,500 to 3,500 psig of confining pressure (**Figure 6-8 b**). Hence, the *m* values of the found correlations (**Figure 6-15**) must be corrected.

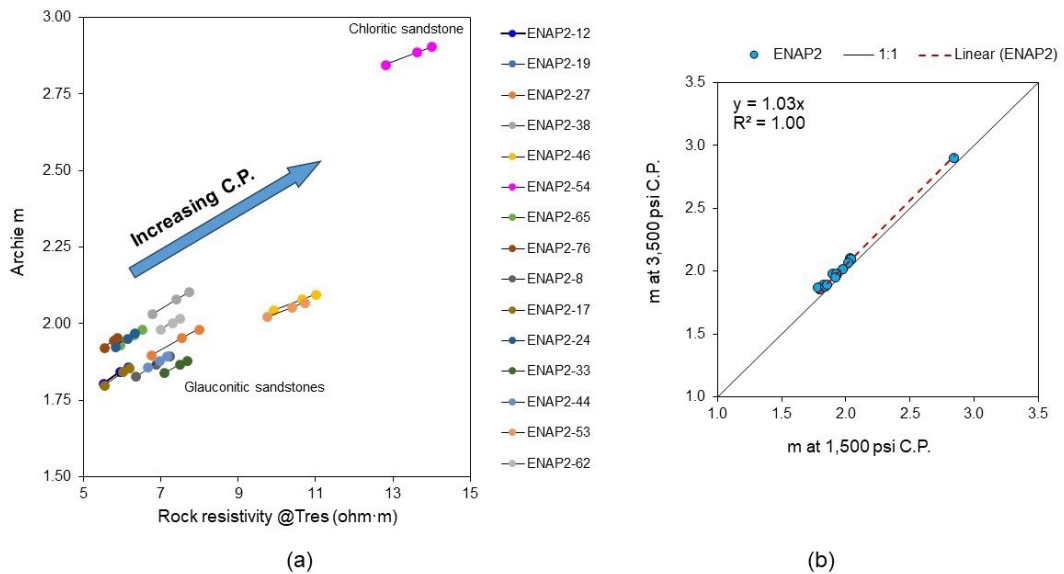


Figure 6-24. Cross-plots of ENAP2 set: (a) cementation exponent (*m*) vs rock resistivity at the measured three confining pressures and (b) comparison of measured cementation exponent at 1,500 psig C.P. vs 3,500 psig C.P.

6.5.3 Cation-exchange capacity comparison

CEC measurements from both methods differ significantly. In practice, the chemical leaching method outperforms the multialinity method because it is simply faster. The multialinity method is inadequate for TGSs since their permeabilities are low to ultra-low. Therefore, it takes longer to reach a quasi-steady state for measurement reading.

Using the multisalinity method for the selected sample, ENAP1-2 (pay sand), it took 25 days to core flood four brine concentrations. Nevertheless, the obtained data is valuable since the experiment setup is the closest to replicating the reservoir conditions of ZG (pressure only). In addition to the electrical resistance of rock and pore water measurements, the brine permeability and pore size distribution were also determined. Permeability impairment increased as salinity decreased. However, an odd permeability increase was observed in the change from 8,000 to 4,000 ppm NaCl, possibly due to the rearrangement of pores due to clay migration or swelling. This hypothesis is accepted since the NMR T_2 distribution trend from the first run with 12,000 ppm NaCl increases to a quasi-bimodal pore size distribution at the last run with deionised water (DW) (Figure 6-25).

Power-law correlations between the pore water conductivity with the apparent formation factor and the cementation exponent were investigated. For the selected sample, the derived cementation exponent ranges from 2.8 to 3.4 at low salinity (Figure 6-26). These correlations may assist in deriving F and m between 20,000 to 4,000 ppm NaCl at 25°C for ZG because ENAP assumes that the salinity of in-situ formation water is 12,000 ppm NaCl. The fact is that the ZG reservoir still does not produce water on the surface. The low water volume recovered from cores in the laboratory analyses (using Dean Stark and Karl Fischer titration methods) was not enough to accurately determine the formation of water salinity due to them being mixed with mud. The assumption of using 12,000 ppm NaCl lies in the average range from the reports of laboratory services companies and the expertise of ENAP petrophysicists.

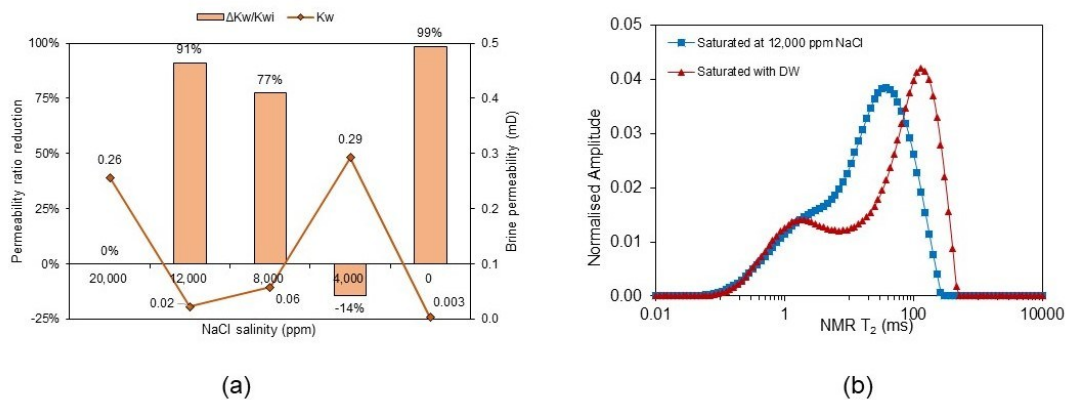


Figure 6-25. Plots from multisalinity experiment on ENAP1-2: (a) permeability ratio reduction trend, (b) NMR T_2 distribution trend (modified from Navarro-Perez et al., 2024).

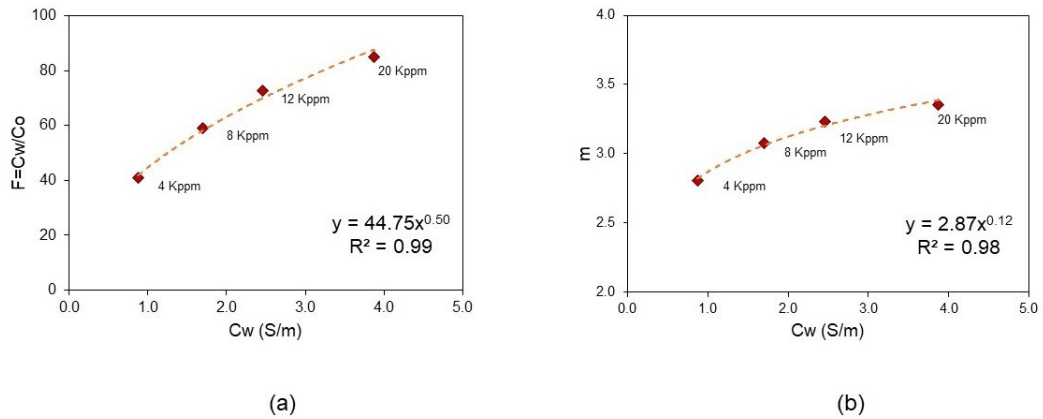


Figure 6-26. Pore water conductivity (C_w) cross-plots from multivalency experiment in ENAP1-2: (a) apparent formation factor, (b) cementation exponent.

The highest CEC value, 41 meq/100g, corresponds to sample ENAP2-54 (pay sand), which is 30.5 meq/100g units lower than ENAP1-2 (pay sand) from the multivalency method. In comparison, the literature reports CEC values between 5 to 40 meq/100g for greensands (**Section 2.3.7**). Potential reasons why the ZG pay sand CEC values from both laboratory methods differ greatly are:

- i. The chemical leaching method comes from soil laboratory standards, that is, unconsolidated rock particles; when destroying cores with significant clay portions, the surface area may increase if clay portions are broken and, therefore, overestimate CEC results (McPhee et al., 2015). The pay sand cores have the lowest specific surface area values ($\sim 4 \text{ m}^2/\text{g}$).
- ii. Due to rock availability, both methods could not be conducted for the same sample, e.g. ENAP1-2. ZG rock microstructure is complex, and each core is different so no fundamental comparison can be made.
- iii. The sampling in ENAP2 was sufficient as bulk, but only a small quantity could be gathered as a fine portion with the sedimentation-decantation process. As the methodology (**Section 6.2.2.1**) stated, six sedimentation-decantation batches per core were performed to collect 0.5 g. Ideally, the laboratory protocol requires 1 g of fine portion (Chapman, 1956).

Finally, there is no laboratory standard for measuring CEC in oil and gas industry cores; other methods that destroy cores are titration with $\text{BaCl}_2/\text{MgSO}_4$ or adsorption of methylene blue (e.g. Rihayat et al., 2018). Hence, each laboratory selects which CEC method to use, resulting in different results from the same reservoir cores with no comparison baseline. This is a fact for other measurements such as porosity and permeability (e.g. Chhatre et al., 2017; Luffel and Howard, 1998). Further investigation needs to be conducted to determine an adequate CEC protocol for complex TGSs such as ZG. For now, the multivalency method is more appropriate to simulate the rock at in-situ confining pressures, and the chemical leaching method is

suitable for identifying the cations release of the ZG clay fine portion. However, the results may not be representative due to a lack of accuracy and different test conditions.

6.5.4 ZG ultrasonic correlations and controls

ENAP2 ultrasonic velocities sets were compared with traditional empirical correlations in sandstones in three types: (i) V_p as a function of V_{s1} , (ii) V_p as a function of porosity, and (iii) V_p as a function of porosity and clay content. For the first type, **Figure 6-13** points out a clear linear relationship between V_p and V_{s1} , so the dataset was compared with Castagna et al. (1985) mudrock line correlation (Equation 6–11) with the two highest confining pressure applied, 2,900 and 4,350 psig, respectively (**Figure 6-27**). The obtained R^2 values of 0.79 and 0.74 of the prediction using the mudrock line are the same as the empirical linear correlations found in **Figure 6-13**. Thus, the ZG V_p and V_s have a linear relationship that follows the mudrock line like other worldwide shales, siltstones, and mudstone reservoirs (**Figure 6-28**).

Equation 6–11

$$V_p \text{ (m/s)} = 1.16V_s + 1360$$

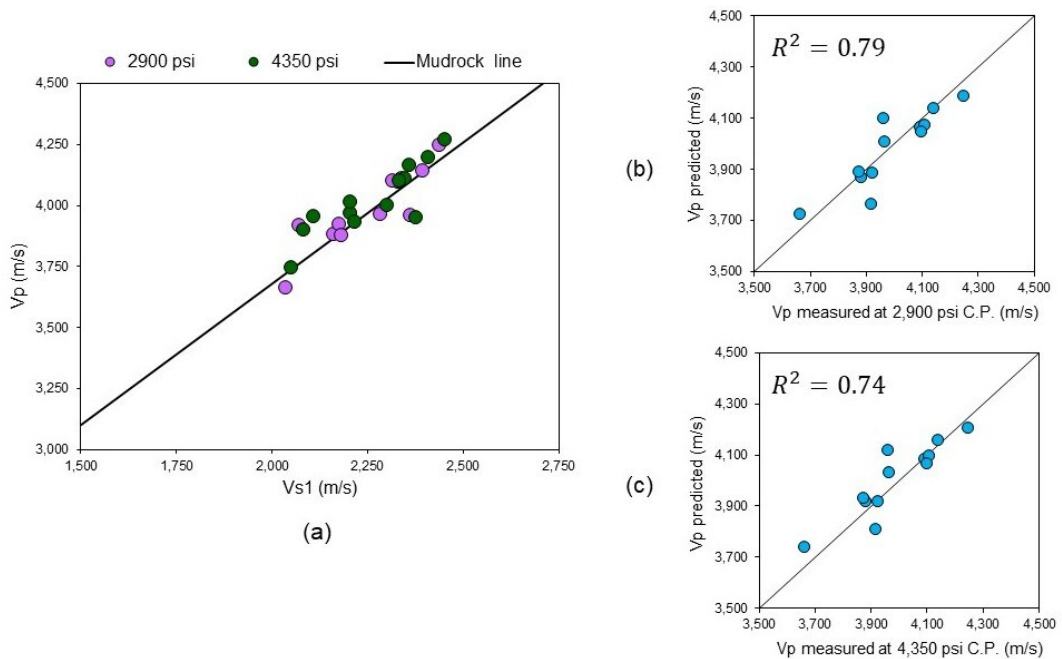


Figure 6-27. (a) V_{s1} vs V_p discriminated at confining pressures of 2,900 and 4,350 psig, respectively, and compared with Castagna et al. (1985) mudrock line. (b) Cross-plot of measured vs predicted V_p at 2,900 psig CP with Castagna et al. (1985) mudrock line. (c) Cross-plot of measured vs predicted V_p at 4,350 psig CP with Castagna et al. (1985) mudrock line.

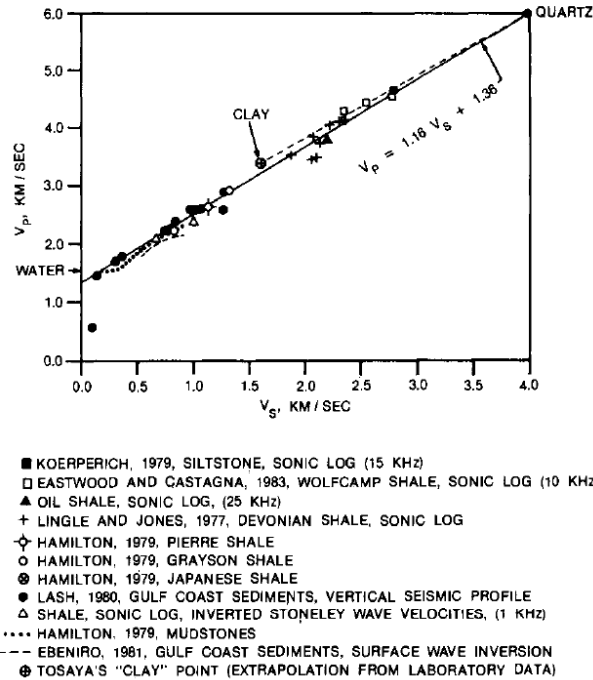


Figure 6-28. *V_s and V_p for worldwide mudrocks from in-situ sonic and field seismic measurements from Castagna et al.'s (1985) study.*

The most common relationships between V_p and porosity are Wyllie et al. (1956) and Raymer et al. (1980), shown in Equations 6–12 and 6–13. The V_{p_f} value used was 1,621 m/s, calculated with an empirical correlation (Equation D–2). The V_{p_m} value was 5,372 m/s, calculated from the Voight-Reuss-Hill average (Equation D–6) and Voight and Reuss bounds with the QXRD data and literature minerals pure values (Mavko et al., 2009). Both correlations are within the ZG glauconitic sandstone range, and an empirical linear correlation was found, but the chloritic sandstone ENAP2-54 does not follow the compared correlations (**Figure 6-29**). The obtained R^2 values (0.52 and 0.53) only included the glauconitic sandstones. ENAP2-54 corresponds to pay sand and differs from the other cores within its microstructure. It is characterised by a high presence of secondary pores, lack of glauconite, and the presence of grain-supported sandstone with plagioclase and chlorite dominance in the matrix (**Figure 4-4 A**). Thus, the compressional wave transmission in ZG's chloritic sandstones is easier and faster, while it is lower in ZG's glauconitic sandstone. The latter is a matrix-supported sandstone with significant microporosity, meaning that pores are isolated, hence leading to poor interconnectivity. Also, they have more glauconite, meaning they have a lower elastic modulus, affecting the compressional wave transmission.

Equation 6–12

$$\frac{1}{V_p} = \frac{\phi}{V_{p_f}} + \frac{(1 - \phi)}{V_{p_m}}$$

Equation 6–13

$$Vp = (1 - \phi)^2 Vp_m + \phi Vp_f, \quad \phi < 37\%$$

where Vp , Vp_f , and Vp_m are the P-wave velocities of the formation, fluid, and rock matrix, respectively (m/s), and ϕ is porosity (v/v).

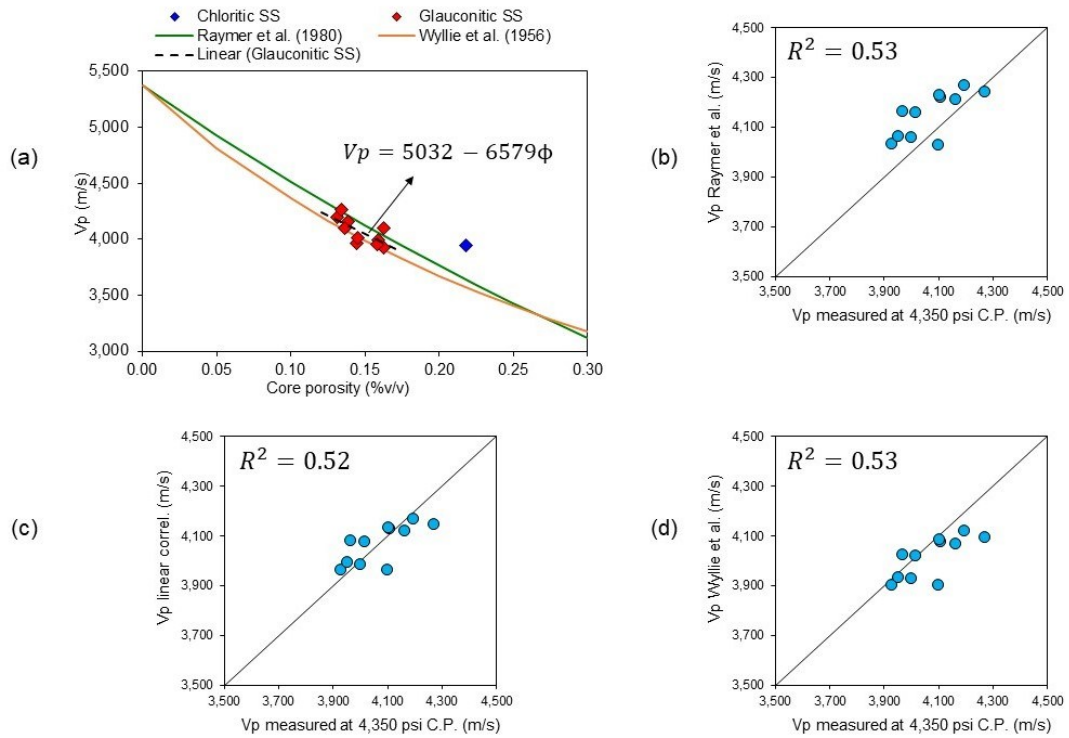


Figure 6-29. (a) Core porosity vs Vp cross-plot discriminated by lithological units at 4,350 psig C.P. and compared with Wyllie et al. (1958) and Raymer et al. (1980) correlations. A linear empirical correlation is shown. (b) Cross-plot of measured vs predicted Vp with Raymer et al. (1980) correlation. (c) Cross-plot of measured vs predicted Vp with linear empirical correlation. (d) Cross-plot of measured vs predicted Vp with Wyllie et al. (1958) correlation. The chloritic sample ENAP2-54 was not added in the cross-plots (b), (c), and (d).

The selected correlations of Vp as a function of porosity and clay content are Tosaya (1982), Castagna et al. (1985), and Han et al. (1986), shown in **Table 6-9**. None of these correlations represent reasonable fits for ZG’s glauconitic sandstone cores (**Figure 6-30**). A multilinear regression (MLR) with MS Excel was compared with the dataset with an R^2 value of 0.52 (**Figure 6-31**). The obtained MLR equation indicates that the clay content seems irrelevant as a third term to predict Vp since its coefficient is one order of magnitude lower than the porosity coefficient and intercept values.

Table 6-9. Selected correlations of V_p as a function of porosity (ϕ) and clay content (C).

Reference	Equation
Tosaya (1982)	$V_p \text{ (m/s)} = 5,800 - 8,600\phi - 2,400C$
Castagna et al. (1985)	$V_p \text{ (m/s)} = 5,810 - 9,420\phi - 2,210C$
Han et al. (1986)	$V_p \text{ (m/s)} = 5,590 - 6,930\phi - 2,180C$

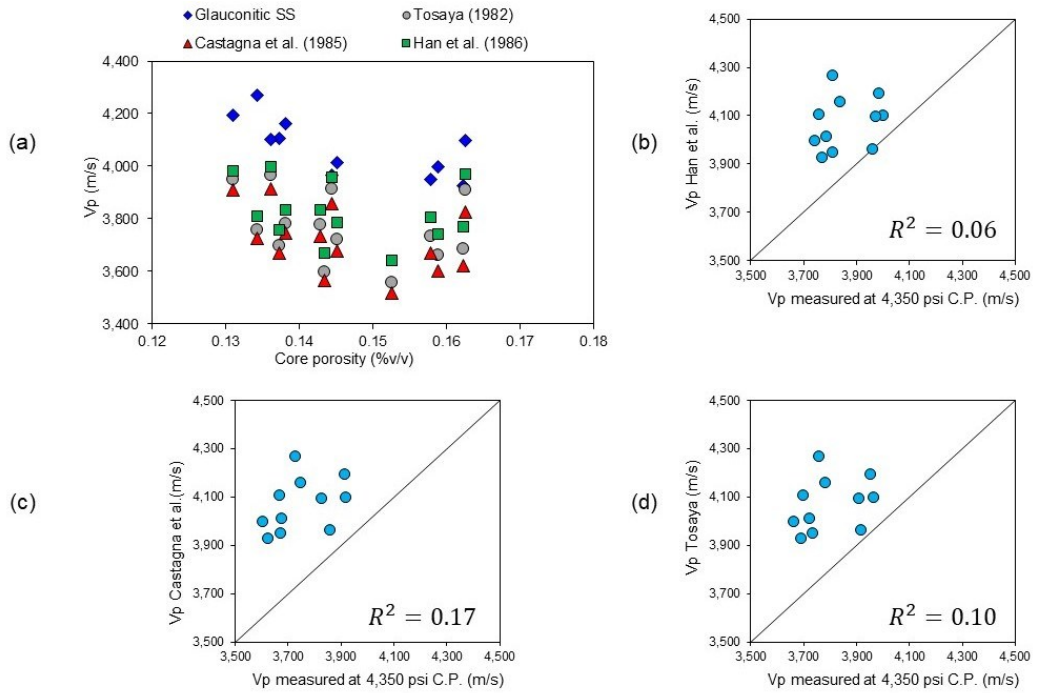


Figure 6-30. (a) Core porosity vs V_p cross-plot discriminated by glauconitic sandstone cores at 4,350 psig C.P. and compared with selected correlations. (b) Cross-plot of measured vs predicted V_p with Han et al. (1986) correlation. (c) Cross-plot of measured vs predicted V_p with Castagna et al. (1958) correlation. (d) Cross-plot of measured vs predicted V_p with Tosaya (1982) correlation.

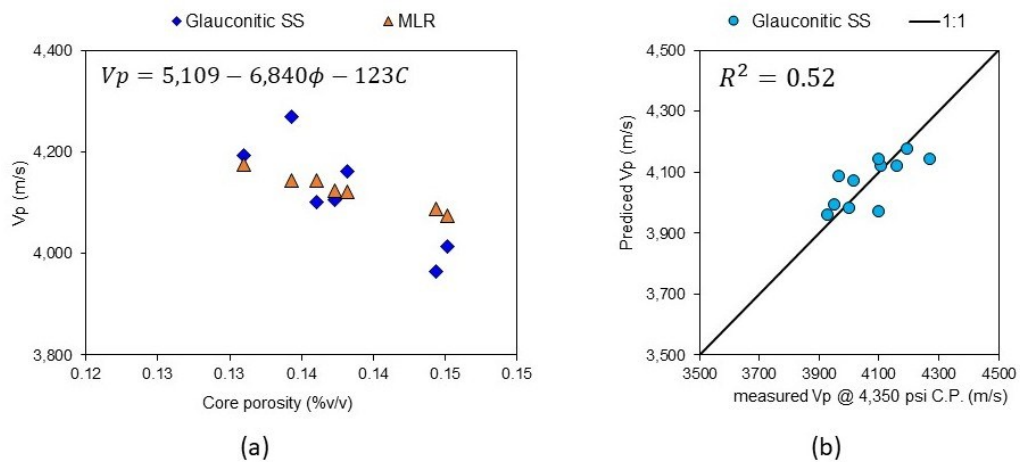


Figure 6-31. (a) Core porosity vs V_p cross-plot discriminated by glauconitic sandstone cores at 4,350 psig C.P. and compared with multilinear regression (MLR) equation. (b) Cross-plot of measured vs predicted V_p with MLR correlation.

The ultrasonic velocities controls in ZG's glauconitic sandstones:

- i. The total clay content for ZG's glauconitic sandstone, there higher the clay content, the lesser the total porosity and the higher the Vp (**Figure 6-32**).
- ii. The microstructure features of ZG's glauconitic sandstone are distinctive. The higher the degree of heterogeneity and glauconitization process, the lower the Vp (**Figure 6-33**). Less heterogeneous cores present isolated secondary pores and pore-fillings and slightly evolve glauconitic grains related to trend to the specific surface area (**Figure 6-33**).

A trend in chloritic sandstone could not be found, as only one core was available (ENAP2-54). However, the data interpretation shows that this peculiar lithological unit has greater secondary pores, a lack of glauconite minerals, the highest iron content, and the lowest specific surface area (**Figures 6-32 and 6-33**); these control its Vp value.

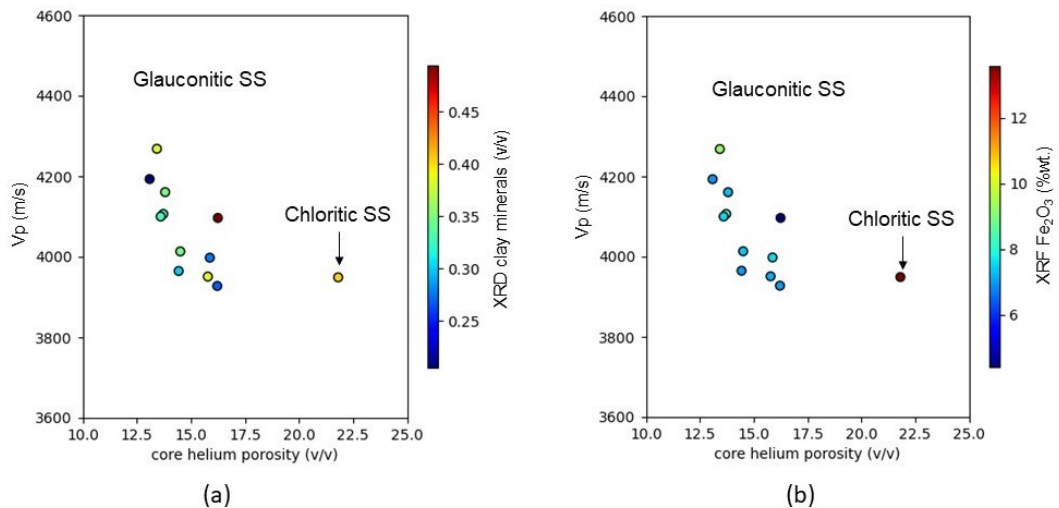


Figure 6-32. Core helium porosity vs Vp cross-plots at a confining pressure of 4,350 psig discriminated by (a) XRD clay minerals and (b) XRF iron content.

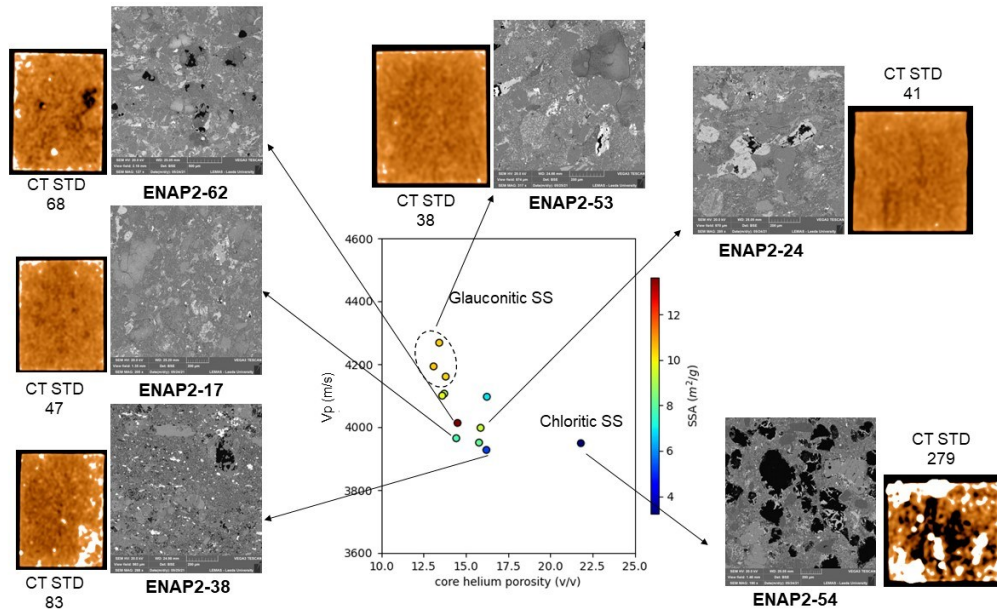


Figure 6-33. Core helium porosity vs Vp cross-plot with some SEM images at a scale of 200 μm and CT scan images of cores.

On another hand, the V_p/V_{s1} ratio values at 4,350 psig C.P. were correlated with parameters such as cementation exponent, rock resistivity, clay content, core permeability with mineralogical content and derived Poisson's ratio (**Figure 6-34**). A cut-off V_p/V_{s1} ratio between 1.66 and 1.74 seems to separate the pay sand from the glauconitic sandstones (ENAP2-54 V_p/V_{s1} value is 1.66). This range is higher than the reported values of 1.5 (Gregory, 1977; Castagna et al., 1993; Rojas et al., 2005) and 1.6 (Guliyev et al., 2007) for TGS. The laboratory measurements were made under brine saturation and not gas saturation. These differences in saturation conditions could affect the in situ V_p/V_{s1} ratio. The proposed cut-off range is a potential marker to separate the pay zone in the ZG formation using the V_p/V_{s1} log, which is further assessed in **Chapter 7**.

Finally, the Poisson's ratio, Young's Modulus, Shear Modulus and Impedance were derived from the ultrasonic data (**Table 6-10**) (equations are available in **Appendix D.3**). ENAP2 Poisson's ratio ranges from 0.22 to 0.30, averaging 0.26. These values are within representative values for soft sandstone (0.2-0.35) and shale (0.28-0.43) (Lake, 2007). The only ZG literature reference of geomechanical properties comes from Britt et al. (2016), who reported ZG static Young's Modulus ranging from 2.2 to 7.4 MMPsig from compressional test; in comparison, the derived ENAP2 static Young's Modulus ranges from 3.7 to 5.1 MMPsig. Only two fairly good correlations were found considering all ENAP2 dataset: Poisson's ratio vs XRD plagioclase content as a positive linear trend ($R^2= 0.66$) and Impedance from Vp vs helium porosity as a power-of-law ($R^2= 0.72$) (**Figure 6-35**). In other words, as the plagioclase content increases, the clay content decreases, and Poisson's ratio increases, implying that the plagioclase minerals contribute to the greater resistance to lateral deformation relative to axial deformation under rock compression (See Equation D-2 in **Appendix D.3**). This also implies that as porosity increases, the Impedance from Vp decreases, i.e. an inverse relationship, indicating a potential decrease in bulk density and stiffness in ZG (See Equation D-10 in **Appendix D.3**).

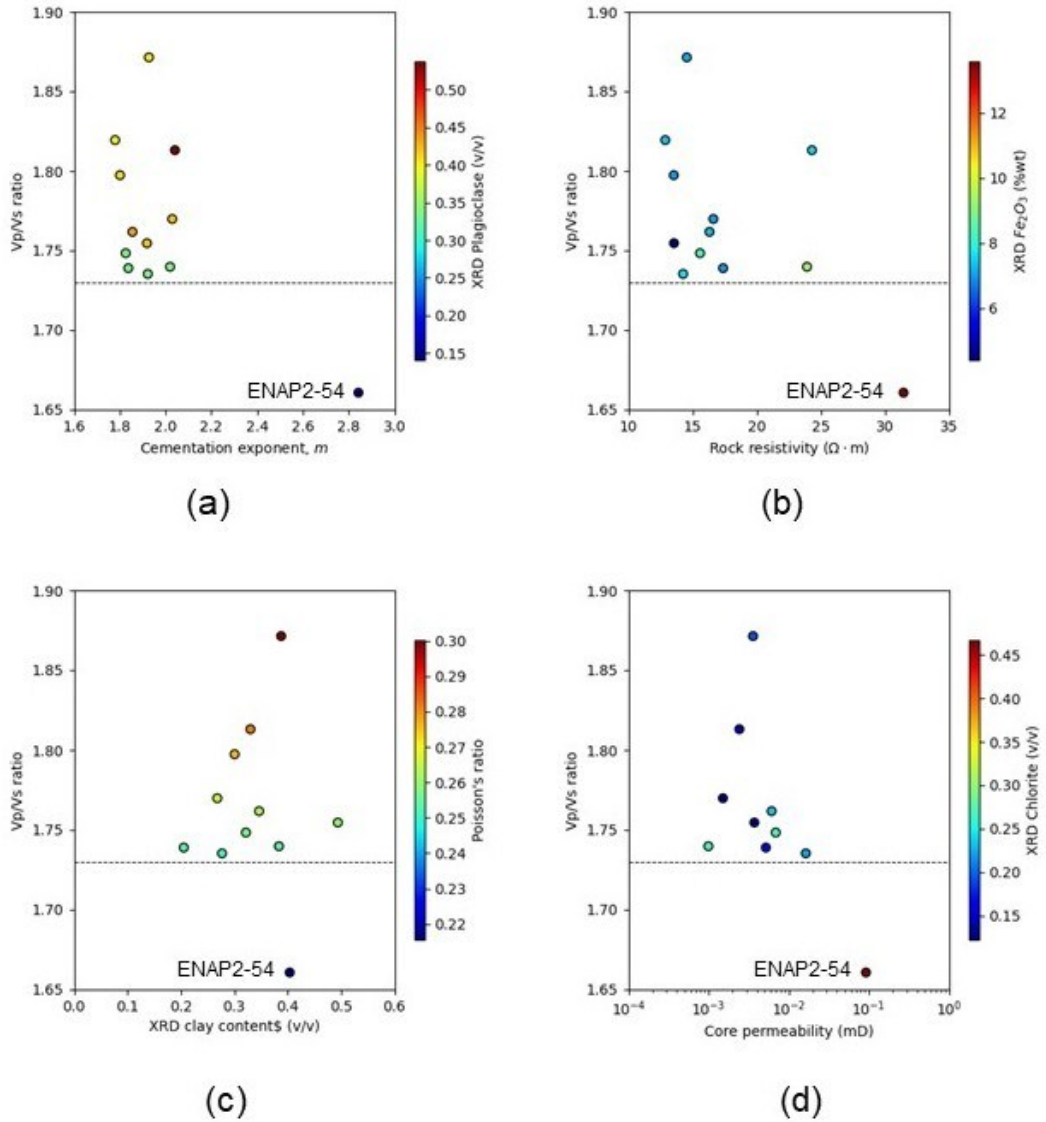


Figure 6-34. *Vp/Vs1 ratio cross-plots at a confining pressure of 4,350 psig: (a) cementation exponent vs Vp/Vs1 discriminated by the plagioclase content; (b) rock resistivity vs Vp/Vs1 discriminated by the iron content; (c) clay content vs Vp/Vs1 discriminated by the Poisson's ratio; (d) core permeability vs Vp/Vs1 discriminated by the chlorite content.*

Table 6-10. *ENAP2 geomechanical parameters statistics at a confining pressure of 4,350 psig.*

Static parameter	Bulk density (kg/m ³)	Poisson's ratio	Young's Modulus (MMPsig)	Shear Modulus (MMPsig)	Impedance from Vp (Mrayl ¹)
Minimum	2,160	0.22	3.7	1.4	8.5
Maximum	2,374	0.30	5.1	2.0	10.0
Average	2,292	0.26	4.4	1.7	9.3
Standard deviation	59	0.02	0.4	0.2	0.4

¹ Mrayl unit = 1x10⁶ Kg/m²·m/s.

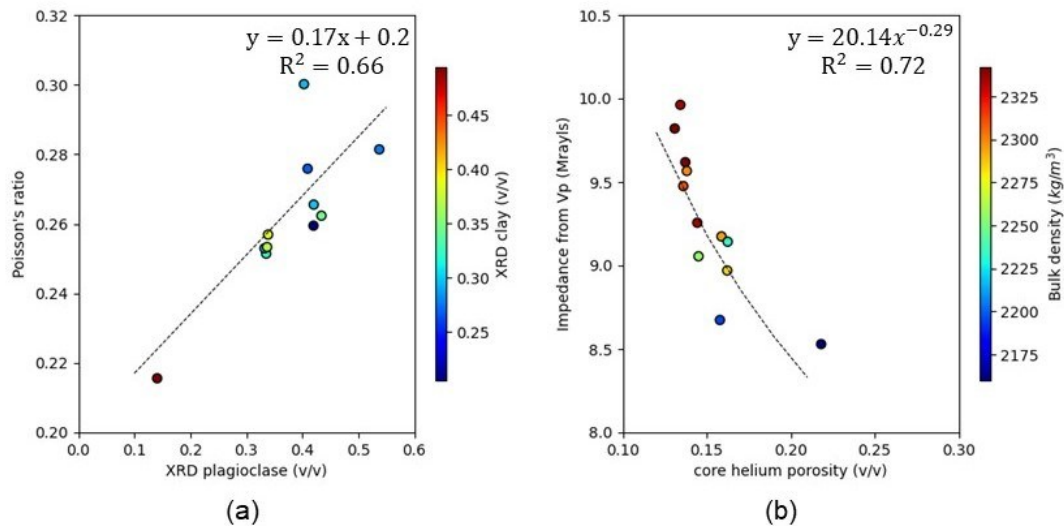


Figure 6-35. Geomechanical properties cross-plots at a confining pressure of 4,350 psig: (a) plagioclase content vs Poisson's ratio discriminated by clay content; (b) core helium porosity vs Impedance from V_p discriminated by bulk density.

6.6 Summary

This chapter highlights the relationships between rock resistivity, cementation exponents, and cation-exchange capacity (CEC) in the ZG reservoir. It further informs reservoir characterisation and complements the petrophysical insights developed in previous chapters. The findings emphasise the role of chlorite and glauconite in controlling the electrical and elastic properties in governing the reservoir's behaviour under various conditions.

- ZG rock resistivity and formation factor at 12,000 ppm NaCl averages 6.0 $\text{ohm}\cdot\text{m}$ and 36, respectively, at reservoir temperature (93-96°C) and confining pressure of 1,500 psig (**Section 6.3.1**).
- ENAP2 set rock resistivities increased by 18% by increasing confining pressure from 1,500 to 3,500 psig (**Table 6-3** and **Figure 6-8**). The latter rock resistivities subset closely matches the deep and shallow resistivity log readings above 2,238 metres vertically (**Figure 6-14**), indicating a potential water-bearing zone.
- The cementation exponent in ZG ranged from 1.8 and 2.0 for glauconitic sandstones and reached a value of 3.0 for chloritic sandstones (pay sands) at a confining pressure of 1,500 psig. The higher the value of the cementation exponent, the higher the iron, total clay, and chlorite content is and the lower the quartz content (**Figure 6-17**).
- The overall average of m 2.02 is very close to the value of 2.09 that ENAP uses in the modified Simandoux water saturation model.
- The derived value of m at 1,500 psig C.P. needs a factor of 1.03 to be at reservoir conditions, i.e. a C.P. of 3,500 psig (**Figure 6-24**).

- The helium core porosity and cementation exponent m showed a linear correlation with an R^2 of 0.66 (**Figure 6-6**). However, it underestimated the PRT1 m value by 17% (1/6) (**Figure 6-7**). This finding indicates that Archie's (1942) model does not apply to this reservoir (**Section 6.5.2**).
- A second correlation was found between the logarithm of porosity and m with an R^2 of 0.65 (**Figure 6-15**), agreeing with the studies of Byrnes et al. (2009) and Cluff et al. (2209) in the Mesaverde TGS. This correlation seems to better control the upper bound of m than the previously mentioned, where at a 30%v/v of porosity, the m value is 2.49.
- A third correlation was found using the Electrical Rock Type (ERT) workflow (Soleymanzadeh et al., 2021). Three groups were categorised in the ZG dataset according to electrical efficiency: ERT0 had the lowest η_e (<10%) and a linear correlation of $R^2=0.95$, followed by ERT1 with η_e up to 18% and a linear correlation of $R^2=0.93$, and ERT2 with η_e up to 25% and a linear correlation of $R^2=0.56$ (**Figure 6-21**). ERT0 corresponds to pay sand samples. These groups distinguish the mineralogical content of ZG better than PRT units (**Figure 6-23**).
- ZG's chlorite content controls the cementation exponent. m increases with iron and chlorite content and degree of heterogeneity and decreases with specific surface area (**Figures 6-17, 6-18, and 6-19**).
- Using Ziarani and Aguilera's (2012) correlation, a strong relationship ($R^2= 0.97$) between ZG's characteristic length at r_{25} and the square-root product of the formation factor with Klinkenberg permeability was found (**Figure 6-20**). This finding indicates that the pore throat interconnectivity also controls ZG's electrical properties.
- Cation-exchange capacity was measured using two different methods: multivalency core flooding and chemical leaching. The first is based on the Waxman and Smits (1968) model by core flooding different brines and measuring the rock resistance. The second method is based on Chapman (1965) by destroying the core and leaching it with ammonium acetate to release exchangeable cations (**Section 6.2.2**).
- The multivalency method followed the Waxman-Smits premise with a linear trend in the highest salinity brines and a non-linear trend towards deionised water (**Figure 6-9**). The obtained CEC value was 72 meq/100g in a pay sand sample (ENAP1-2).
- The chemical leaching method identified the presence of seven cations, of which calcium contributed the most (~50%), followed by sodium (~29%), magnesium (~15%), and potassium (~5%); these elements have only one valence of cation associated (Ca^{2+} , Na^+ , Mg^{2+} , and K^+). Aluminium, iron, and manganese did not

significantly contribute to the final CEC values (**Figure 6-10**). The final CEC values range from 18 to 41 meq/100g, averaging 23 meq/100g.

- It has been proven with both methods that the pay sands have the highest CEC values. The CEC value from the chemical leaching method is 41 meq/100g, corresponding to sample ENAP2-54, which is 30.5 meq/100g lower than ENAP1-2 from the multisalinity method.
- In practice, the chemical leaching method outperforms the multisalinity method because it is faster. Nevertheless, the obtained data is valuable since the experiment setup is the closest to replicating the reservoir conditions of ZG (pressure only). Not only were the electrical resistance of rock and pore water measured, but also the brine permeability and NMR T_2 distribution were determined, showing permeability impairment as brine salinity decreased (**Figure 6-25**).
- Two power-law correlations were found to predict the apparent formation factor and cementation exponent with the pore water conductivity (C_w) (**Figure 6-26**). These correlations may assist in deriving F and m between 20,000 to 4,000 ppm NaCl at 25°C for ZG.
- Further investigation is needed to determine an adequate CEC protocol for complex TGSs such as ZG. For now, the multisalinity method is more appropriate for simulating the rock at in-situ confining pressures, and the chemical leaching method is suitable for identifying the cations release of the ZG clay fine portion.
- The ZG ultrasonic velocities increased as the confining pressure rose (500 to 4,350 psig). V_p ranged from ~3,500 to 4,300 m/s, V_{s1} ranged from ~1850 to 2,500 m/s, and V_{s2} ranged from 1,800 to 2,400 m/s (**Figure 6-12**).
- At each confining pressure, linear correlations with R^2 values between 0.71 and 0.82 were found between V_p and V_{s1} (**Figure 6-13**).
- ZG's V_p and V_s have a linear relationship that follows the mudrock line (Castagna et al., 1985) like other worldwide shales, siltstones, and mudstone reservoirs (**Figure 6-28**).
- Both Wyllie et al. (1956) and Raymer et al. (1980) correlations proved reasonably good predictions for ZG's glauconitic sandstones V_p as a function of porosity with R^2 value 0.53 (**Figure 6-29**). The theoretical V_p values of brine (1,621 m/s) and rock matrix (5,372 m/s) were adequate for the selected correlations.
- Tosaya (1982), Castagna et al. (1985), and Han et al. (1986) correlations were selected to compare the prediction of ZG's glauconitic sandstones V_p as a function of porosity and clay. Neither was proven to be close to the laboratory measurements (**Figure 6-30**), but a multilinear regression with an R^2 of 0.52 was a better fit (**Figure 6-31**).

- Total clay content and microstructure features such as degree of heterogeneity, glauconitization process and specific surface area control the ultrasonic velocities in ZG's glauconitic sandstones (**Figures 6-32 and 6-33**).
- The chloritic pay sand core ENAP2-54 showed the opposite trend that ZG's glauconitic sandstones. Its V_p is higher with high iron and chlorite content, attributed to its secondary pores and grain-support matrix (**Figures 6-32 and 6-33**).
- The overall V_p/V_s ratio is 1.79; at the three highest confining pressures (1,450 – 2,900 – 4,350 psig), the average V_p/V_s ratio is 1.77 (**Table 6-6**). A cutoff ratio between 1.66 and 1.74 was determined to separate the pay chloritic sand from glauconitic sandstones (**Figure 6-34**), which will be helpful for the well-log interpretation using the V_p/V_s log.
- The dynamic Poisson's ratio for samples from well ENAP2 ranged from 0.22 to 0.30, averaging 0.26, and dynamic Young's Modulus ranged from 3.7 to 5.1 MMPsig (**Table 6-10**).
- A linear correlation ($R^2= 0.66$) was found between the Poisson's ratio with plagioclase content (**Figure 6-35 a**), implying that the plagioclase minerals contribute to the greater resistance to lateral deformation relative to axial deformation under compression.
- A power law relationship (with $R^2= 0.72$) was found between the impedance of V_p and porosity (**Figure 6-35 b**), indicating a potential decrease in bulk density and stiffness in ZG. This observation suggests that sediment compaction and diagenesis have significantly influenced the pore structure and mineral composition due to the reduction of the pore space, tightening of grains and increasing mineral cementation, particularly in deeper core locations. This explanation agrees with the findings of **Chapter 4**, which indicated that the deeper the core location, the more evolved the glauconitic grains are.

Chapter 7

Improved petrophysical interpretation of the ZG

This chapter presents the petrophysical evaluation of ZG with a well-logging methodology for twelve wells. It starts by summarising the greensand effects in logs and the features in ZG, followed by the methodology. Then, it reports and discusses the results and findings of the clay volume, porosity, permeability, and water saturation models. In addition, it estimates the net pay. The discussion focused on the selection criteria compared with the literature and empirical correlations found in previous chapters, ending with a summary.

7.1 Introduction

This chapter builds upon the results and findings presented in Chapters 4 to 6 to improve the petrophysical evaluation of the ZG reservoir using well-logging methodologies for twelve wells. The mineralogical and microstructural insights from **Chapter 4**, particularly the identification of chlorite and glauconite as key controls on porosity and permeability, inform the selection of lithological markers and petrophysical models. The pore size distribution data and permeability correlations from **Chapter 5** provide critical calibration points for the permeability and water saturation models used here, highlighting the significance of chloritic and glauconitic petrofacies in reservoir characterization. The electrical and elastic property relationships established in **Chapter 6**, including the influence of chlorite and glauconite on resistivity and cementation exponents, are integrated into the interpretation of well logs to address challenges posed by greensands. This chapter leverages these findings to develop and validate models for clay volume, porosity, permeability, and water saturation, with an estimation of net pay and a comparative analysis against literature and empirical correlations.

A characteristic of greensands is their high glauconite, which contains significant potassium, resulting in higher gamma-ray log readings than quartz-rich sandstones. Glauconite also has a high iron content, which increases the neutron and photoelectric log readings because of their large thermal neutron absorption cross-section and high atomic number; hence, porosity derived from the neutron log is overestimated, while the photoelectric log may assist as a lithological marker. Since greensands grain density is higher than quartz, the porosity derived from the bulk density log is also overestimated if not correctly calibrated. Consequently, the typical bulk density and neutron logs crossover to identify hydrocarbons in gas reservoirs might not occur in greensands. Similarly, the clay minerals in greensands decrease resistivity log readings due to their significant cation-exchange capacity, which may

lead to the hydrocarbon zone being interpreted as being water-saturated (**Table 2-15**). In addition, Archie's (1942) empirical model overestimates the water saturation since it does not consider the additional electrical contribution of clay minerals. Therefore, shaly-sand water saturation models are preferred for use in greensands.

The ZG formation exhibits an unusual gamma-ray pattern, with a bell-shaped curve over the pay sand (chloritic sandstones) area, followed by a funnel-shaped trend. Its deep resistivity log contrasts the gamma-ray shape like a mirror effect (**Figure 1-6**). ENAP defines glauconitic sandstones as having a gamma-ray reading of less than 65 API units and siltstone between 65 and 100 API units, even though glauconite typically shows a high gamma-ray signature (**Section 2.3.6**). The photoelectric factor log is used complementary to separate the sandy and clayey zones, i.e. separate the chloritic and glauconitic sandstone, respectively. In contrast, the Vp/Vs log separates the pay sand with a lower value than 1.75. The NMR tool calibrates core porosity, and the modified Simandoux model estimates the water saturation profile (**Section 1.3**).

This chapter reports the findings related to the second (**SO2**) and third specific (**SO3**) objectives: *compare empirical and theoretical water saturation models that include the electrical behaviour of clays and select the best fit for the ZG formation, and propose an integrated workflow for establishing a suitable petrophysical model in the ZG formation* (**Section 1.2**). The results, correlations and findings from **Chapters 4, 5, and 6** are used in this last results chapter to help calibrate and build an improved petrophysical model through well-log interpretation. The methodology (**Section 7.2**) presents the steps for the petrophysical evaluation in twelve wells that produce tight gas from ZG for building suitable clay volume, porosity, permeability, and water saturation models (**Section 7.3**). The discussion and summary sections compare this project's results with ENAP reports and literature, highlighting their similarities and differences. **Appendix E.6** displays the final petrophysical evaluation of the ten uncored wells.

7.2 Methodology

The petrophysical evaluation workflow involved conducting a well-log interpretation in seven steps (**Figure 7-1**) using the software Interactive Petrophysics – IP – v2024 (<https://www.geoactive.com/interactive-petrophysics>):

1. Environmental correction & qualitative control: All log data needed to be processed through an environmental correction according to the logging tool used, such as the standoff position, tool diameter, and whether the mud used is barite, among other things. The qualitative control identified missing data,

outliers, or affected data by hole conditions. The environmental corrections and Log QC modules of IP were used.

2. Clay volume model: Gamma-ray and PEF logs were selected as single clay indicators, while the bulk density and neutron porosity logs were selected as double clay indicators. The key wells used the XRD core data and the CMR (Combined Magnetic Resonance) tool for clay volume calibration. The formulas used are shown in **Appendix D.2**.
3. Porosity model: The Basic Log Analysis Function module in IP derived porosity logs from bulk density, neutron porosity, and sonic logs, respectively. Each synthetic porosity log was compared with core helium and NMR porosity data for the calibration process. The formulas used are shown in **Appendix E.4**.
4. Permeability model: The empirical correlation (Equation 7–1) found in **Section 4.9.3** was applied to compute the gas permeability, and a cut-off criterion of $\text{Log FZI} > -1.25$ was used to identify the Petrofacies 1 that corresponds to the pay sand unit (Equation 4–4).
5. Water saturation model: Archie's (1942) and three shaly-sand water saturation models were selected to find ZG's most suitable water-saturation profile. The Indonesian (Poupon and Leveaux, 1971), modified Simandoux (Bardon and Pied, 1969) and Waxman-Smits (1968) models; their equations are shown in **Appendix E.5**. The saturation exponent n was fitted with Pickett's (1973) plot and compared with ENAP's reported value. Water and clay resistivities were defined according to laboratory and ENAP's reported values. The correlations found in **Chapter 6** to derived m as a function of porosity were compared against the petrofacies units' average values and ENAP's reported value of 2.09 (**Section 6.5.2**). $\text{Log FZI} > -1.25$ criteria and V_p/V_s ratio between 1.70 and 1.75 were assessed as reservoir markers and compared to the gas produced from the chromatography report.
6. Pay zone: The Cut-off and Summations module in IP was used to identify and quantify the net reservoir and pay per well using the same cut-off criteria of ENAP (Gonzalez-Gonzalez et al., 2018); $V_{cl} \leq 50\%v/v$, $\Phi \geq 6\%v/v$, and $S_w \leq 65\%v/v$.

Equation 7–1

$$k_g = 1 \times 10^{-5} e^{36.89\phi}$$

where k_g is the gas permeability (mD), and Φ is the selected porosity log (v/v).

The minimum curvature method was selected in IP software to compute the true vertical depth (TVD) per well using the deviation data available (**Table 7-1**). The output TVD log results from a circular arc that passes through the two stations at the

measured station angles (e.g. Farah, 2013). The core data was entered as array curves with an upscaling factor of 6 for the ENAP1 well and 2 for the ENAP2 well (Z dimension in IP), which relates the core depth location and the log interval step depth and shifted for proper data fitting.

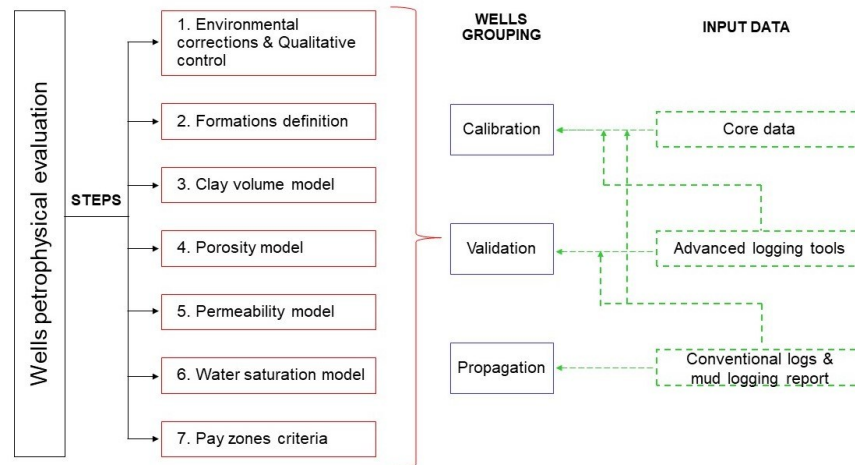


Figure 7-1. Petrophysical evaluation workflow diagram.

Table 7-1. ZG wells formation depth interest and inclination angle.

Well	Interest interval depth (MD*)	Deviation angle range (degrees)
ENAP1	2049 – 2186	1.0 – 1.3
ENAP2	2027 – 2260	11.6 – 12.9
WX1	1958 – 2363	0.3 – 0.8
WX2	1942 – 2180	0.3 – 0.5
WX3	2159 – 2274	2.5 – 3.0
WX4	2075 – 2223	0.2 – 0.7
WX5	2108 – 2352	1.0 – 3.3
WX6	2207 – 2336	0.1 – 0.7
WX7	2049 – 2181	1.5 – 2.1
WX8	2113 – 2278	1.3 – 2.5
WX9	2224 – 2380	1.9 – 2.0
WX10	2069 – 2251	2.5 – 3.6

*MD = measured depth (metres).

The twelve wells were grouped following Carrizo et al.'s (2021) three distinct categories (**Table 7-2**), following a logical well-log interpretation framework: calibration, validation, testing and evaluation. The key wells, ENAP1 and ENAP2, have the most complete data: core data, conventional logs and advanced logging technologies. These wells form the calibration group, calibrating the petrophysical model with the core data after proper upscaling. The next step is the validation with wells WX1 to WX3 with no core data but the same log data to validate the accuracy and robustness of the petrophysical model. The final step is the propagation with wells WX4 to WX10 with only the conventional logs to test and evaluate the applicability of the petrophysical model.

Table 7-2. ZG wells grouping according to Carrizo et al.'s (2021) definitions.

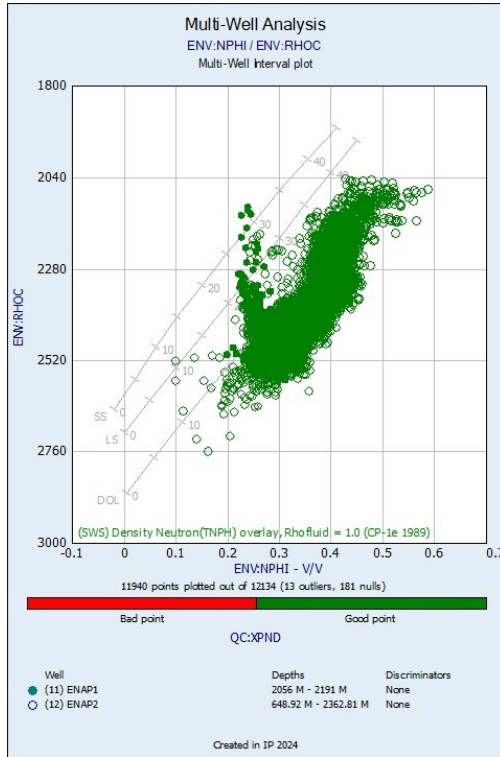
Well	Group	Workflow step	Input information
ENAP1	Key	Calibration	Laboratory data, conventional logs, mud logging report, and NMR, CMR and NGS tools.
ENAP2			
WX1	Validator	Validation	Conventional logs, mud logging report, and NMR, CMR and NGS tools.
WX2			
WX3			
WX4			
WX5			
WX6	Propagation	Testing and evaluation	Conventional logs and mud logging report.
WX7			
WX8			
WX9			
WX10			

7.3 Petrophysical evaluation results

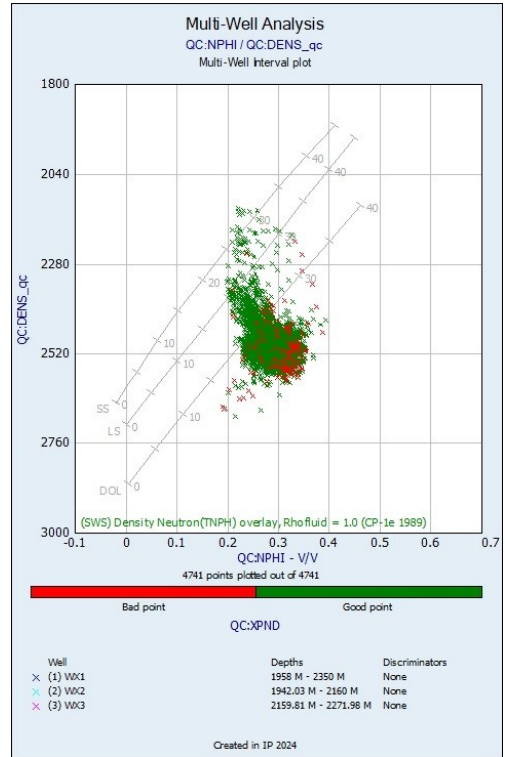
7.3.1 Environmental correction & qualitative control

Environmental corrections were conducted in IP with the Schlumberger Corrections algorithm based on the Schlumberger (1989) green book volume 1 in all conventional logs, excepting the resistivities since the AIT (Array Induction Imager) tool of Schlumberger provides five resistivity measurements at 10, 20, 30, 60, and 90 inches of depth of investigation enabling accuracy in characterising the shallow invaded zone and determining the true resistivity of the formation. The qualitative control identified bad data points in the logs, followed by a quick-look interpretation of the difference between the calliper and bit size log to detect if such data was due to caving or mud invasion. The bulk density and neutron porosity cross-plot with the flag values of bad holes indicate that there is no bad data for the key wells and little bad data for the validator and propagation wells (**Figure 7-2**).

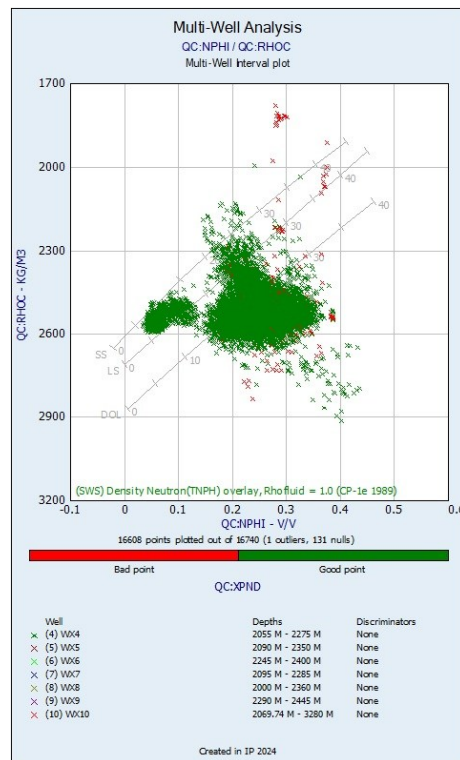
No significant caving or mud invasion was found that may affect the log readings through the quick-look interpretation in all wells (**Appendix E.1**). For the key wells (**Figures 7-3** and **7-4**), the gross pay sand was identified with preliminary cutoff values of 80 API and 1.75 for the gamma-ray and VPVS logs, respectively; supported by the trends of SP and PEF, the crossover between the invaded formation and deep resistivities indicating porous rock filled with fluids, and the crossover bulk density-neutron porosity indicating a gas effect.



(a)



(b)



(c)

Figure 7-2. Bulk density and neutron porosity cross-plot of calibration (a), validation (b), and propagation (c) groups.

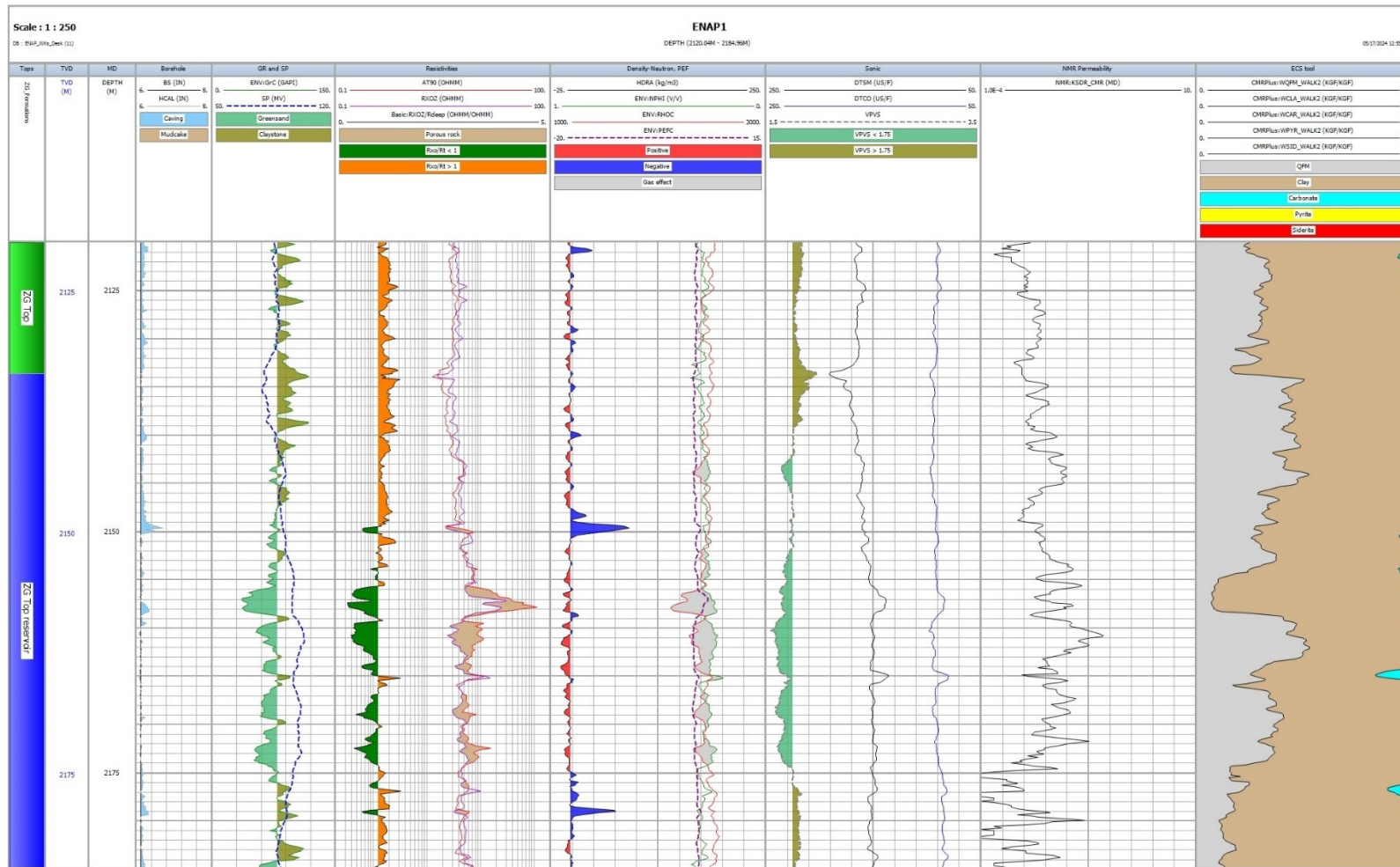


Figure 7-3. Quick-look interpretation of ENAP1 well. Track1: ZG formations name. Track2: True vertical depth (m). Track3: Measured depth (m). Track4: Borehole, BS= Bit size 6.12", HCAL= calliper. Track5: GrC=gamma-ray, SP=spontaneous potential. The preliminary cutoff value for greensand and claystone is 80 API. Track6: AT90=deep resistivity, RXOZ=invaded formation resistivity, and RXOZ/Rdeep ratio. Porous rock shading occurs in the crossover from RXOZ to AT90. Track7: DTSM=compressional transit time, DTCD=shear transit time, VPVS< 1.75 identifies the pay zone (ENAP cut-off). Track8: SDR permeability model from NMR tool. Track9: mineralogy logs derived from the CMR tool.

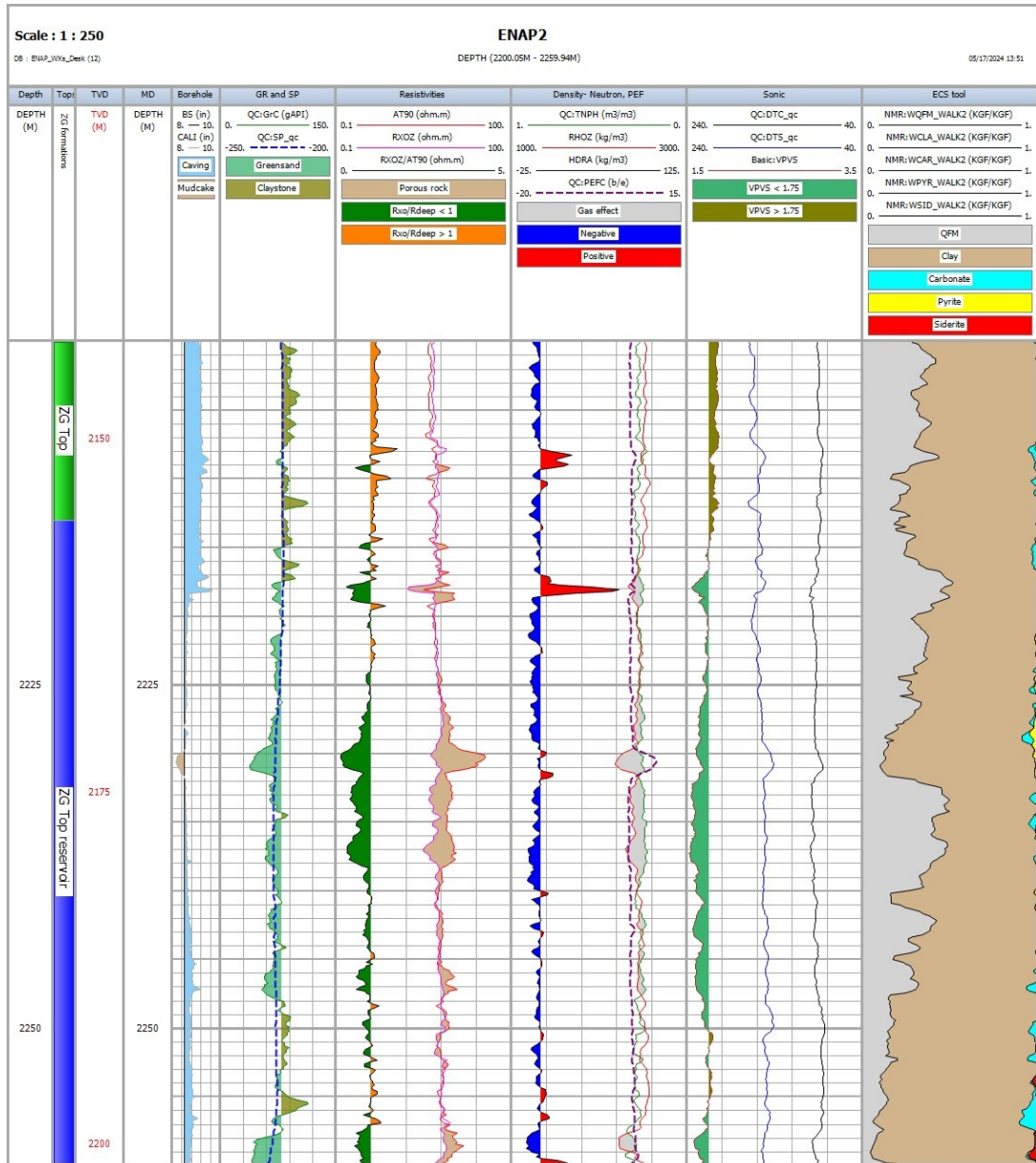


Figure 7-4. Quick-look interpretation of ENAP2 well. Track1: ZG formations name. Track2: True vertical depth (m). Track3: Measured depth (m). Track4: Borehole, BS= Bit size 6.12", HCAL= calliper. Track5: GrC=gamma-ray, SP=spontaneous potential. The preliminary cutoff value for greensand and claystone is 80 API. Track6: AT90=deep resistivity, RXOZ=formation resistivity, and RXOZ/Rdeep ratio. Porous rock shading occurs in the crossover from RXOZ to AT90. Track7: DTSM=compressional transit time, DTCO=shear transit time, VPVS < 1.75 identifies the pay zone (ENAP cut-off). Track8: mineralogy logs derived from the CMR tool.

7.3.2 Clay volume model

Each subzone of ZG formation per well was divided according to the trend of conventional logs, primarily from the gamma-ray and the deep resistivity tools. The density-neutron crossover occurred in all wells to identify the gas effect, corresponding to the lowest gamma-ray and highest photoelectric factor readings. Therefore, the pay sands area was easy to identify. After statistical revision of gamma-ray counting API values in the key and validator wells (**Figure 7-5** and **Table**

7-3), the values of 40 and 130 API were selected as the clean sandstone and clay formation representative values to use in the linear method for clay volume estimation (**Section E.2**~~Error! Reference source not found.~~). Only the photoelectric factor, as a single indicator, was used in the pay sands subzone with values of 2.5 and 6.25 barns/e as representative values of the clean sandstone and clay formations (Equation E-2) since the other indicators failed to estimate the clay volume with the mineralogical data calibration process. The double indicator, density-neutron, parameters (Equation E-3) were selected according to its cross-plot by defining the clean sandstone line or two endpoints and the clay point (**Figure 7-6**). This indicator with the gamma-ray was used for most of the subzones to derive the final clay volume in clayey formations. The calibration process was successful (**Figures 7-7** and **7-8**) and confirmed with the validation and propagation groups (**Appendix E.3**).

ENV:GrC (GAPI)

Active Zones : W:11 Z:1, 2, 3, 4, 5 W:12 Z:1, 2, 3, 4, 5 W:1 Z:1, 2, 3, 4, 5, 6 W:2 Z:1, 2, 3, 4, 5, 6 W:3 Z:1, 2, 3, 4

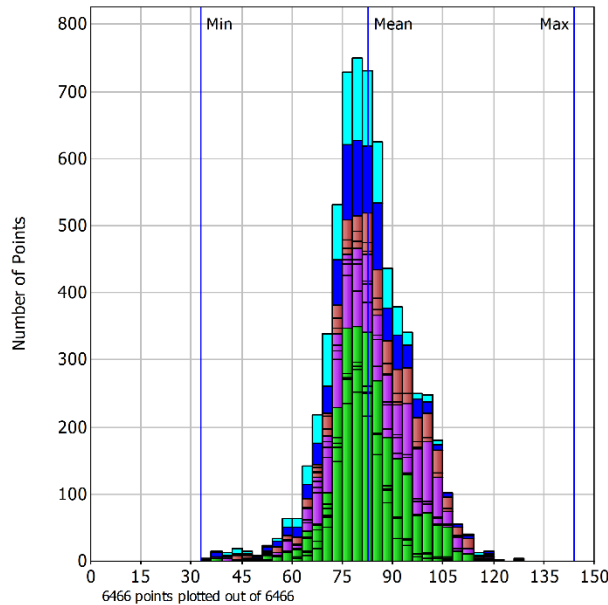


Figure 7-5. Gamma-ray readings of wells ENAP1 (blue), ENAP2 (light blue), WX1 (green), WX2 (purple), and WX3 (red-brown) histogram. The average minimum, maximum, and mean values lines are shown.

Table 7-3. Gamma-ray (GR) average statistics from key and validator wells.

Parameter (API)	Pay sands	Clay sandstone
Average GR minimum	37	56
Average GR maximum	76	116
Average GR standard deviation	12	11
Average GR Mean	50	80
Average GR 10% percentile	38	66
Average GR 50% percentile	47	79
Average GR 90% percentile	65	93

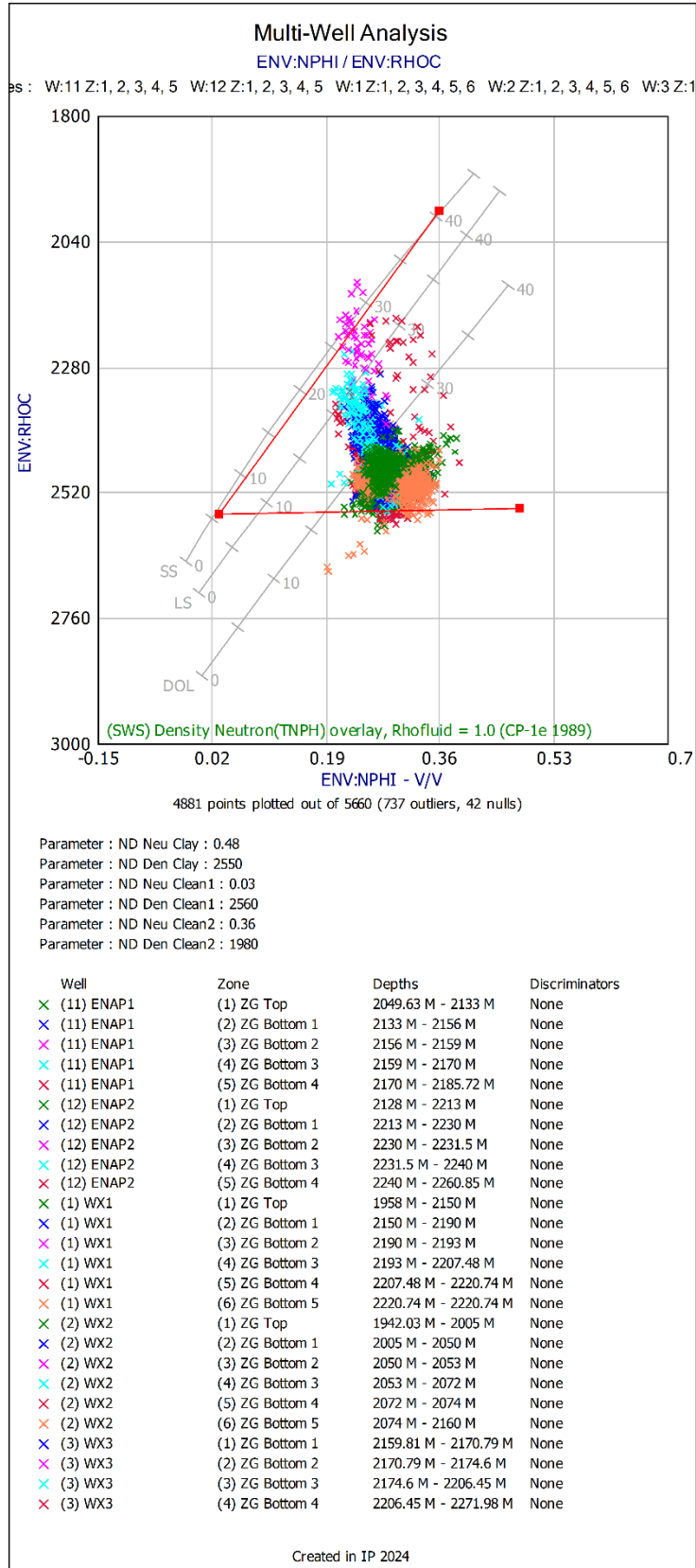


Figure 7-6. Neutron porosity (v/v) and bulk density (kg/m³) cross-plot of key and validators wells per subzone. The pay sands are coloured in magenta and were not considered to establish the clean sandstone line. The grey isolines stand for sandstones (SS), limestone (LS) and dolomite (DOL).

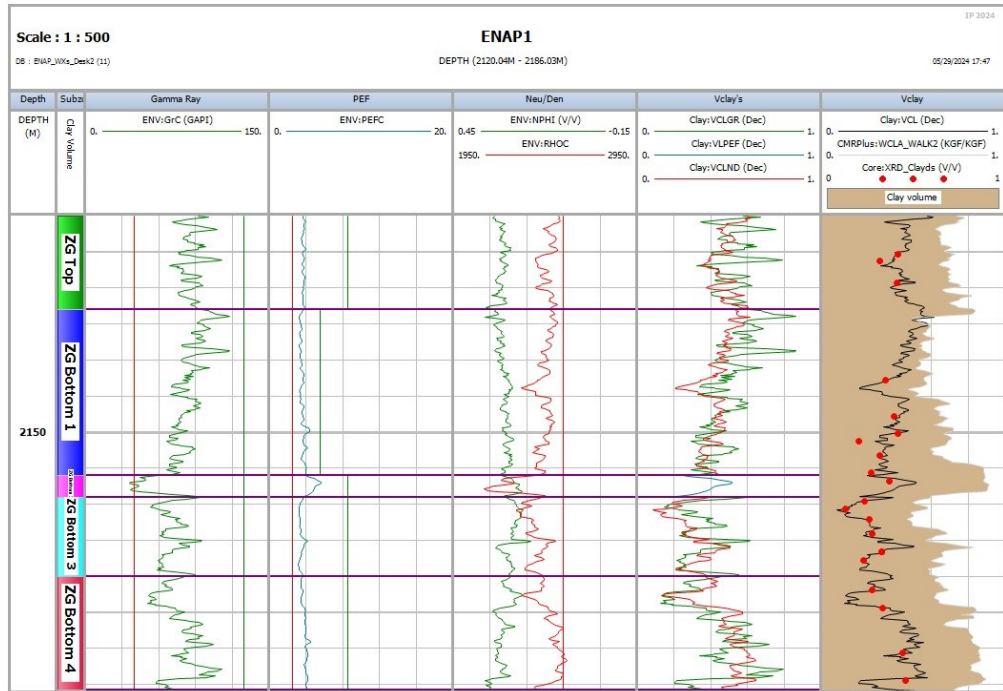


Figure 7-7. Clay volume estimation of ENAP1 well. Track 1: True vertical depth (m). Track 2: ZG subzones name. Track 3: Gamma-ray log (API). Track 4: Photoelectric factor log (barns/e). Track 5: Bulk density (kg/m^3) and neutron porosity (v/v) logs. Track 6: Clay volume estimation from each selected indicator. Track 7: Final clay volume in black line (VCL). XRD core data in red dots. Clay volume derived from the CMRPlus tool (kgf/kgf).

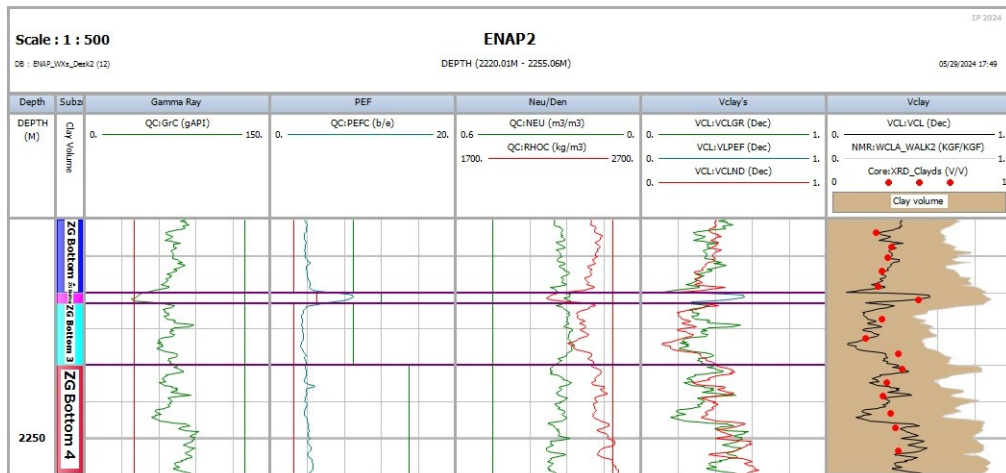


Figure 7-8. Clay volume estimation of ENAP2 well. Track 1: True vertical depth (m). Track 2: ZG subzones name. Track 3: Gamma-ray log (API). Track 4: Photoelectric factor log (barns/e). Track 5: Bulk density (kg/m^3) and neutron porosity (v/v) logs. Track 6: Clay volume estimation from each selected indicator. Track 7: Final clay volume in black line (VCL). XRD core data in red dots. Clay volume derived from the CMRPlus tool (kgf/kgf).

7.3.3 Porosity model

The setting parameters per synthetic porosity log were (Figure E-12):

- Density porosity: $2,728 \text{ kg}/\text{m}^3$ as matrix density (Section 4.5.2) and $1,000 \text{ kg}/\text{m}^3$ as fluid density since ZG is a freshwater reservoir (12,000 ppm NaCl).

- Neutron porosity: Converted to sandstone units since its input was in limestone units.
- Sonic porosity: 56.75 $\mu\text{s}/\text{ft}$ as matrix transit time and 270 $\mu\text{s}/\text{ft}$ as fluid transit time and a compaction factor of 1.6 for glauconitic sandstone and 0.8 for chloritic sandstone using Wyllie's time average formula (Equation E-5). The matrix transit time was converted from the Voight-Reuss-Hill average method in **Chapter 6** (i.e., 5,375 m/s), while the fluid transit time corresponds to pure water from Serra (1984). Lastly, the compaction factor was fixed for data fitting.

The three synthetic porosity logs were compared with core helium and NMR data (Figures 7-9 and 7-10). The porosity logs derived from bulk density and sonic logs better fit the core data. Also, the NMR porosity log (TCMR) from the CMR tool was compared with the core data, and it best fitted with the sonic porosity log instead of the density porosity log. The neutron porosity log greatly overestimated the ZG porosity and was discarded in the validation process (Figure 7-11).

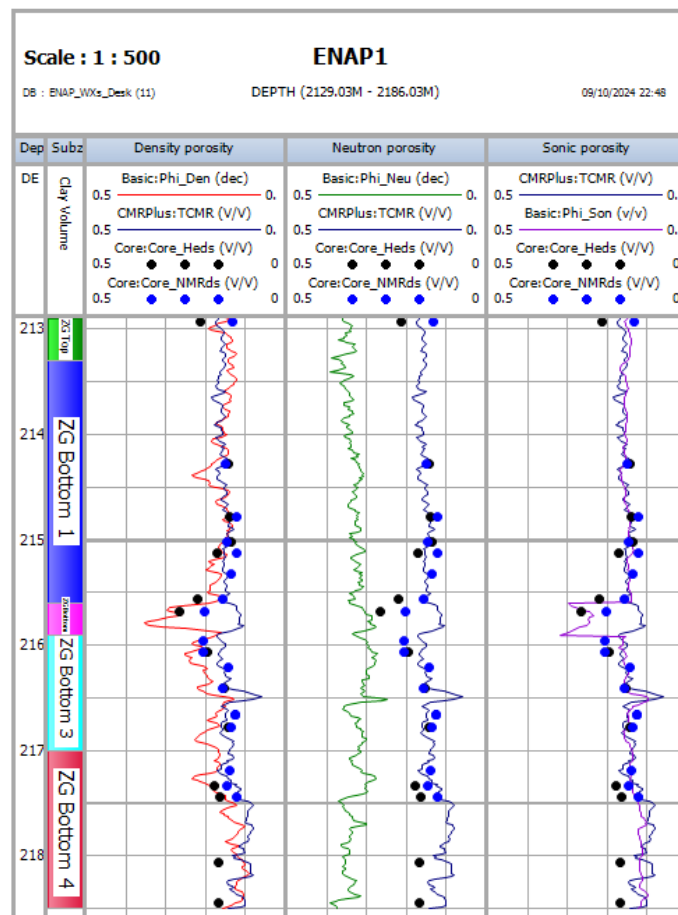


Figure 7-9. Porosity logs vs core porosity of ENAP1 well. Track 1: True vertical depth (m). Track 2: ZG subzones name. Track 3: Density porosity (red), NMR porosity (blue), core helium porosity (black dot), core NMR porosity (blue dot). Track 4: Neutron porosity (green). Track 5: Sonic porosity (purple).

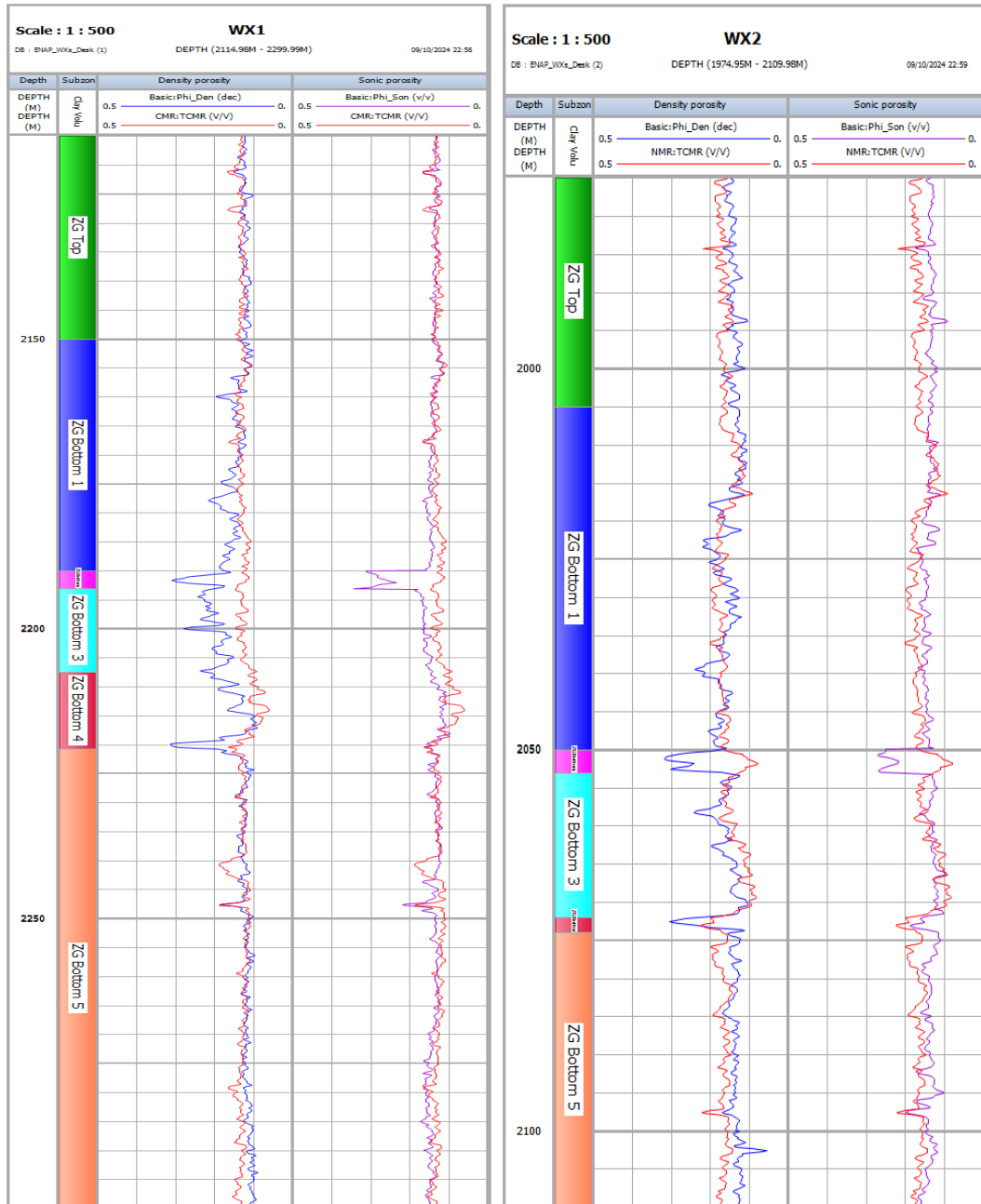


Figure 7-11. Porosity logs vs core porosity of WX1 and WX2 wells. Track 1: True vertical depth (m). Track 2: ZG subzones name. Track 3: Density porosity (blue), NMR porosity (red). Track 4: Sonic porosity (purple), NMR porosity (red).

7.3.4 Permeability model

The permeability synthetic log was compared with core gas permeability in the key wells. For ENAP1 well, the NMR permeability correlations of Timur-Coates and SDR were available from the CMR tool (Figures 7-12 and 7-13). The Log FZI > -1.25 criteria was compared with the subzone definition of the clay volume model in all wells, confirming the identification of Petrofacies 1 (Figure 7-14).

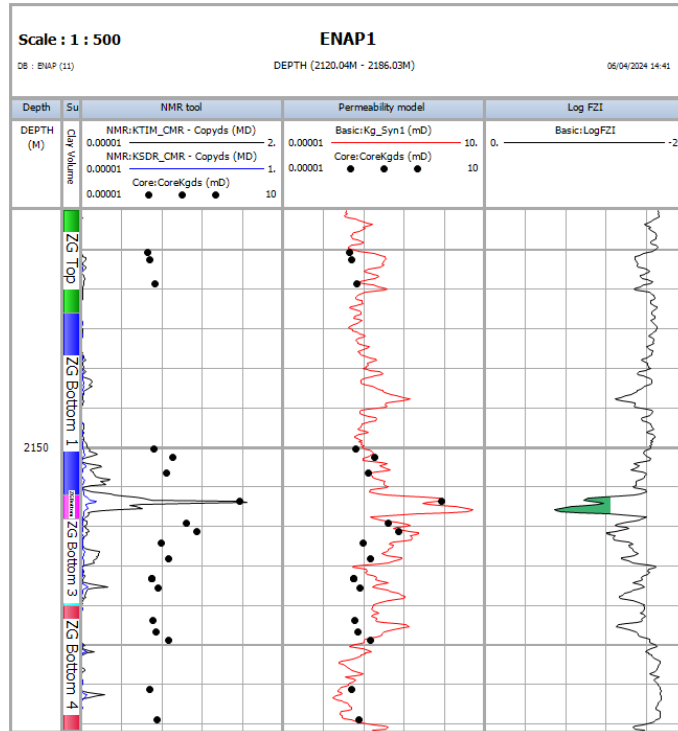


Figure 7-12. Permeability model of ENAP1 well. Track 1: True vertical depth (m). Track 2: ZG subzones name. Track 3: NMR porosity log from Timur-Coates (black), NMR porosity log from SDR (blue), core permeability (black dot). Track 4: Synthetic permeability log (red). Track 5: Computed Log FZI (black) with a cutoff value -1.25.

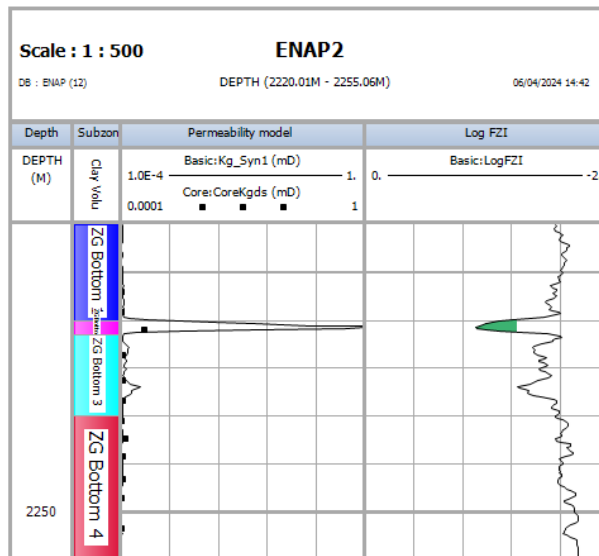


Figure 7-13. Permeability model of ENAP2 well. Track 1: True vertical depth (m). Track 2: ZG subzones name. Track 3: core permeability (black dot), synthetic permeability log (black). Track 4: Computed Log FZI (black) with a cutoff value -1.25.

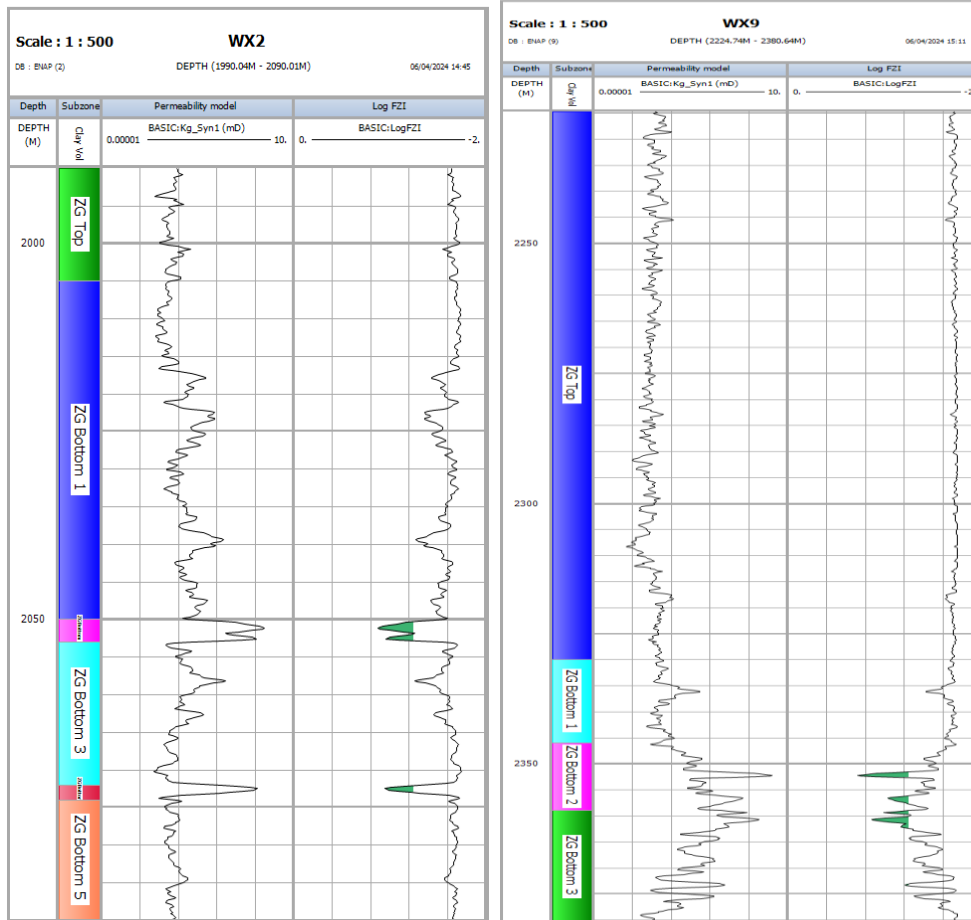


Figure 7-14. Permeability model of WX2 (validator) and WX9 (propagation) wells. Track 1: True vertical depth (m). Track 2: ZG subzones name. Track 3: Synthetic permeability log (black). Track 4: Computed Log FZI (black) with a cutoff value -1.25.

7.3.5 Water saturation model

Two of the three correlations between cementation exponent and porosity from **Chapter 6 (Figure 6-6 and Table 6-8)** were compared with the average m values in ZG: 3 for the pay sand area and 2.02 for the rest of the formation. The latter is preferred when there is no total core porosity data (**Figure 6-17**). This selection criteria is discussed in **Section 7.4.4**. An overall saturation exponent n value of 1.66 was selected, the same used by ENAP (**Figure 7-15**). The Indonesian and modified Simandoux were the most suitable water saturation models in the calibration process since both are V_{shale} models where the only parameter (clay resistivity, R_{cl}) was easily tuned (**Figure 7-16**). The latter is preferred as the Indonesian is more sensitive to the clay resistivity, clay volume and water resistivity parameters (see **Section 7.4.4**). **Table 7-4** shows the input parameters of the four selected water saturation models. The top subzone of ZG was forced as 100% water based on the mudlogging data, which showed no gas detection. However, it is important to note that while the mudlog data suggest no gas, the zone could still contain gas below the critical saturation level as it is clay-bearing. There are four identified reservoir markers,

namely: photoelectric factor log, total gas production from mudlogging data, Log FZI and Vp/Vs cut-off values, shown in **Figure 7-16**.

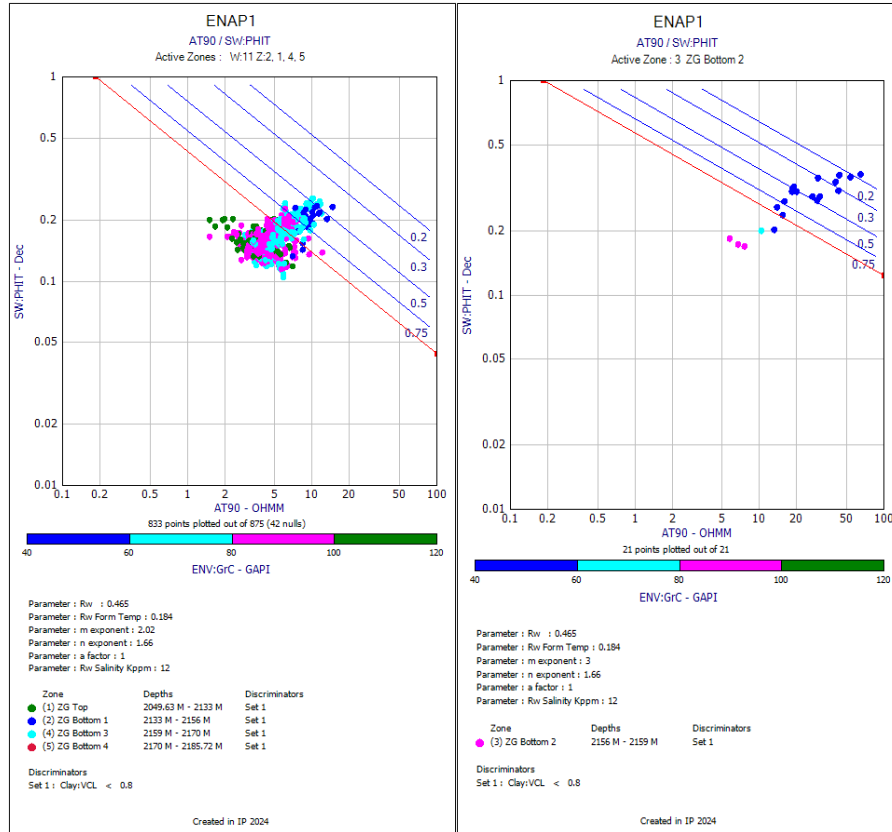


Figure 7-15. Pickett's plot of well ENAP1. The left side shows the glauconitic sandstone subzones with $m=2.02$, and the right side shows the chloritic sandstone subzone with $m=3.0$. The X-axis shows the deep resistivity log, and the Y-axis shows the total porosity log, which is discriminated by gamma-ray log readings from 40 to 120 API.

Table 7-4. Input parameters used at selected water saturation models.

Parameter	Unit	Input
a	Unitless	1
m	Unitless	2.02 and 3 (pay sand)
n	Unitless	1.66
Water resistivity (R_w)	ohm·m	0.47 @ 25°C
Mud filtrate resistivity (R_{mf})	ohm·m	0.12 @ 21°C
True resistivity (R_t)	ohm·m	AT90 log
Clay volume (V_{cl})	v/v	Vcl log
Porosity (Φ)	v/v	Density porosity log
Clay resistivity (R_c)	Minimum	ohm·m 3.21 @ 96°C
	Average	ohm·m 3.72 @ 96°C
	Maximum	ohm·m 4.00 @ 96°C
Equivalent conductance of clay cations (B)	mho/meq	1
Cation exchange capacity from core data*	meq/ml	Qv_correl log
Cation exchange capacity* from log data (Q_v)	a	Unitless 3.44 to 9.97
	b	Unitless -19.60 to -80.30

*Parameters used in Equation E-10.

7.3.6 ZG's net pay

The identification of the net pay is consistent with the location of the Petrofacies (PTR) 1 unit and was defined using the methodology described in **Section 7.2**. Specifically, the net pay was determined using ENAP's (Gonzalez-Gonzalez et al., 2018) cut-off criteria: clay volume (VCL) \leq 50%v/v, density porosity (Φ) \geq 6%v/v, and water saturation (Sw) \leq 65%v/v.. The input logs were (i) the clay volume (VCL) from the clay volume model, (ii) the density porosity log (*PhiDen*) from the porosity model, and (iii) the water saturation log (*SW_ModSimandoux*) from the water saturation model. The first three were used to identify the net reservoir, while the water saturation cut-off was added to identify the pay zones.

Figure 7-17 shows the net reservoir and pay zones from wells ENAP1 and ENAP2, while **Table 7-5** shows the quantification of net pay from the interpreted twelve wells. Finally, **Figure 7-18** displays the key wells' petrophysical evaluation; the rest are available in **Appendix E.6**.

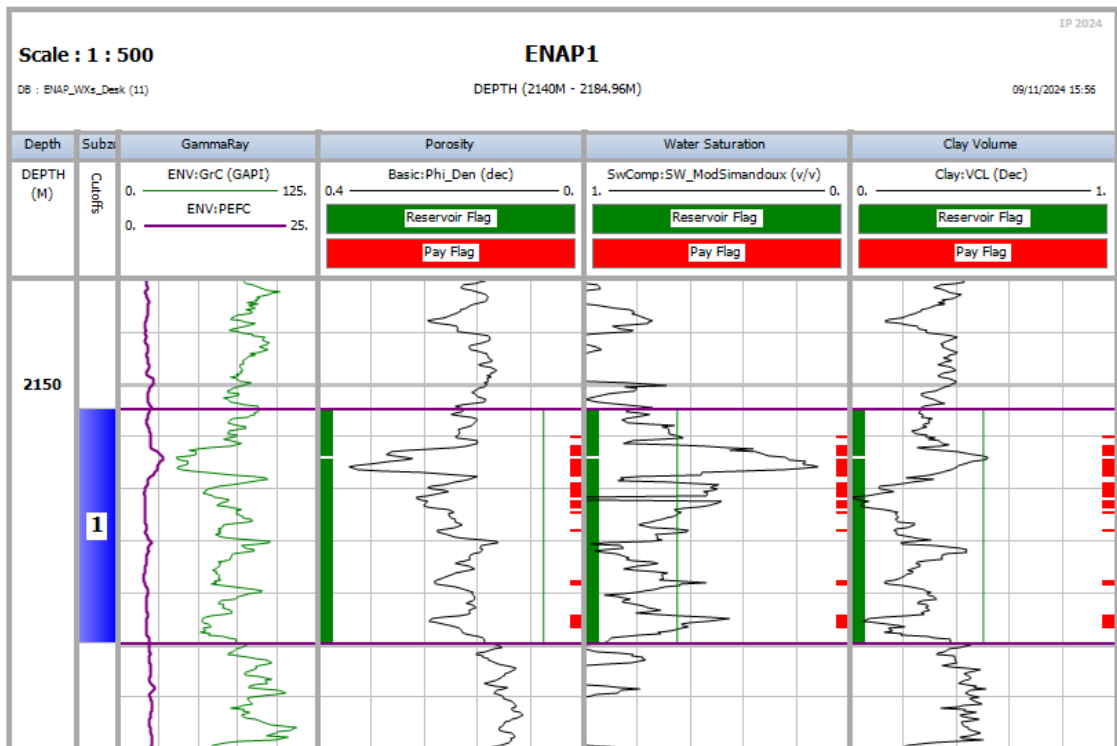


Figure 7-17. Net pay (red) and reservoir (green) location in well ENAP1. Track 1: True vertical depth (m). Track 2: ZG subzone name. Track 3: Gamma-ray (green) and photoelectric factor (purple) logs. Track 4: Porosity (v/v). Track5: Water saturation (v/v). Track6: Clay volume (v/v).

Table 7-5. Net pay intervals with their average porosity, clay volume, and water saturation per well.

Well	Top (MD)	Bottom (MD)	Net pay (MD)	N/G (%)	Average (%v/v)		
					ϕ	Vcl	Sw
ENAP1	2152.35	2174.75	7.47	33	24	46	22
ENAP2	2216.05	2238.91	3.51	15	23	52	21
WX1	2152.01	2225.62	5.79	8	22	59	11
WX2	2045.97	2057.86	0.91	8	25	46	44
WX3	2167.74	2197.91	6.71	22	21	56	32
WX4	2174.44	2215.29	22.71	56	18	52	25
WX5	2201.27	2257.5	14.17	25	19	56	26
WX6	2264.21	2334.77	31.39	44	19	45	27
WX7	2126.59	2175.66	17.98	37	20	50	26
WX8	2220.93	2277.62	26.67	47	18	47	32
WX9	2334.31	2378.2	31.85	73	20	40	30
WX10	2180.84	2225.5	19.66	44	18	55	29

*MD = measured depth (metres).

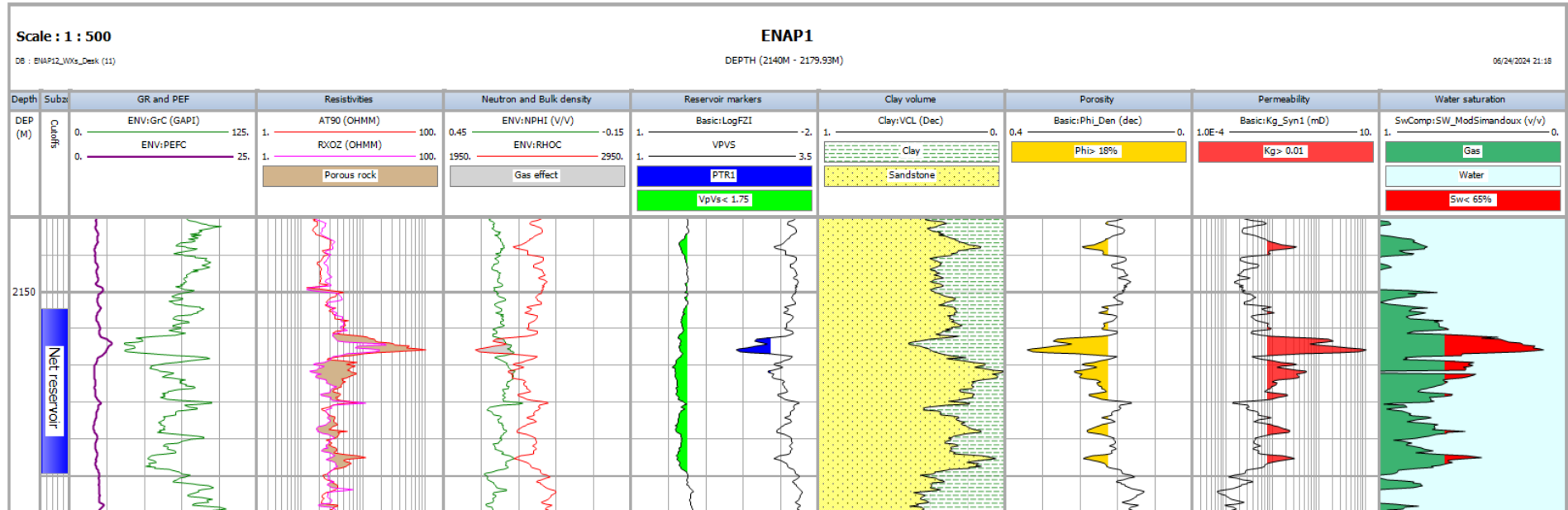


Figure 7-18. Petrophysical evaluation of well ENAP1: Track 1: True vertical depth (m). Track 2: Subzone name. Track 3: Gamma-ray (green) and photoelectric factor (purple) logs. Track 4: Deep resistivity (red) and formation resistivity (magenta) logs. Porous rock shading in light brown occurs in the crossover from RXOZ to AT90. Track5: Neutron porosity (green) and bulk density (red) logs. Gas effect shading in light grey occurs in the crossover from RHOC to NPHI. Track6: Reservoir markers Log FZI (black) displays the PTR1 facies location shading in blue, and Vp/Vs ratio (blue) displays pay sand location shading in lime. Track7: Clay and sandstone lithology. Track8: Total porosity (black). A cut-off value of 18%v/v in shading gold. Track9: Permeability (black). A cut-off value of 0.01 mD in shading red. Track10: Water saturation (black). Gas saturation shading in green, water saturation in light blue, and a cut-off value of Sw= 65%v/v in red.

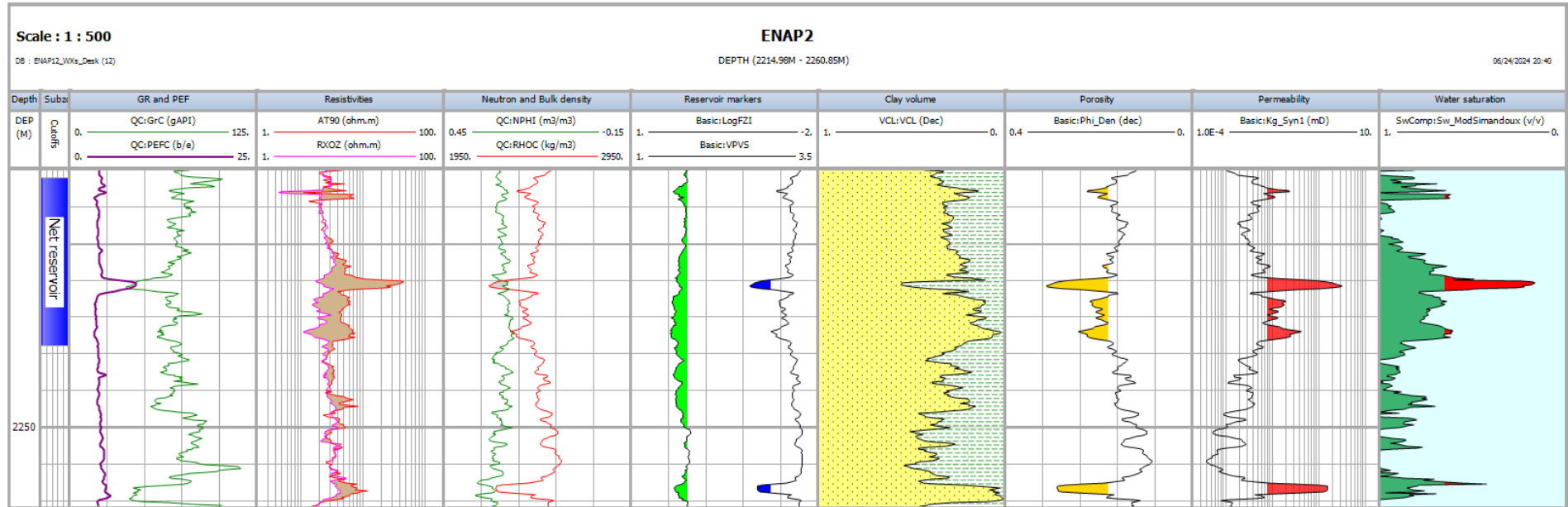


Figure 7-19. Petrophysical evaluation of well ENAP2: Track 1: True vertical depth (m). Track 2: Subzone name. Track 3: Gamma-ray (green) and photoelectric factor (purple) logs. Track 4: Deep resistivity (red) and formation resistivity (magenta) logs. Porous rock shading in light brown occurs in the crossover from RXOZ to AT90. Track5: Neutron porosity (green) and bulk density (red) logs. Gas effect shading in light grey occurs in the crossover from RHOC to NPHI. Track6: Reservoir markers Log FZI (black) displays the PTR1 facies location shading in blue and Vp/Vs ratio (blue) displays pay sand location shading in lime. Track7: Clay and sandstone lithology. Track8: Total porosity (black). A cut-off value of 18%v/v in shading gold. Track9: Permeability (black). A cut-off value of 0.01 mD in shading red. Track10: Water saturation (black). Gas saturation shading in green, water saturation in light blue, and a cut-off value of Sw= 65%v/v in red.

7.4 Discussion

7.4.1 Controls on clay volume

The photoelectric factor (PEF) log is the recommended single indicator to estimate clay volume in chloritic sandstone zones ($GR < 50$ API), as it is sensitive to the rock's mineralogy and the iron content, including contributions from the chlorite, glauconite, and pyrite. This finding agrees with the ENAP report (Gonzalez-Gonzalez et al., 2018) and literature (Patchett et al., 1993; Klein et al., 2006), as the PEF log provides more reliable estimation in these zones compared to other logs by directly responding to the specific lithology unit. The gamma-ray log measures natural radioactivity, which tends to be higher in clay-rich formations due to the presence of potassium and thorium. The bulk density-neutron indicator logs complement the Vcl estimation by providing additional insight into the porosity and mineral composition cross-plot (**Figure 7-6**), helping to differentiate between clay and non-clay subzones. The calibration process in the key wells (**Figures 7-7** and **7-8**) resulted in a 15% for well ENAP1 and a 54% prediction of XRD core data for well ENAP2 (**Table 7-6** and **Figure 7-20**). Potential reasons for the poor match in well ENAP1 are (1) the geological variability is more complex than ENAP2 as CT scan and SEM images showed, the first presented a higher degree of heterogeneity, and (2) due to the previous explanation, ENAP1 has more statistical outliers than ENAP1.

Finally, the division of subzones is straightforward as ZG presents a signature trend in gamma-ray and resistivity logs; above it, the gamma-ray log has a bell pattern, and below the pay sand, a funnel pattern, and the resistivity log shows a mirror effect (e.g. **Figure 1-6**). In **Chapter 6**, it was found that a cut-off ratio between 1.70 and 1.74 of this parameter may separate the pay sand (**Figure 6-34**). ENAP petrophysicists use a cut-off value of 1.75. After assessing the ranges of 1.70 and 1.75, it is concluded that the value of 1.75 identifies the net reservoir zone and not the pay sand. Instead the photoelectric factor log is a pay sand marker since it increases at the chloritic sandstone area only (**Figure 7-21**).

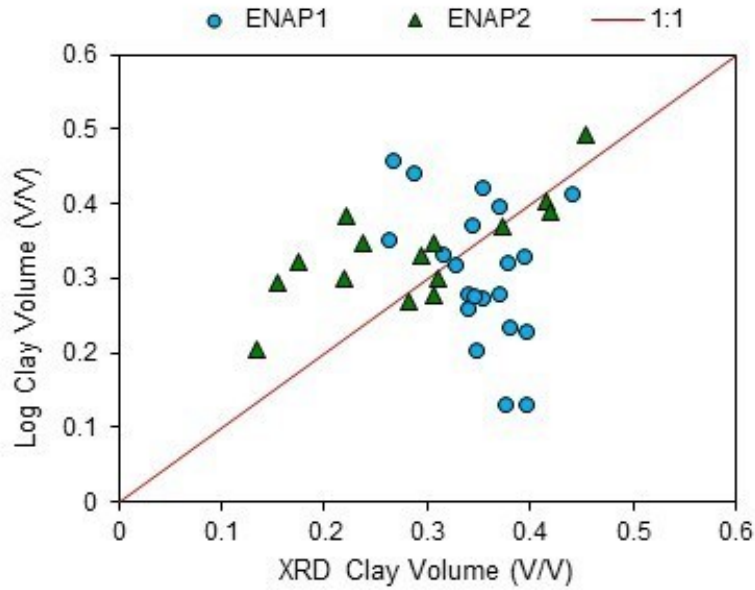


Figure 7-20. Clay volume plot comparison of XRD (X-axis) with log data (Y-axis).

Table 7-6. Statistical metrics of clay volume estimation in key wells.

Well	R ²	RMSE
ENAP1	0.15	0.11
ENAP2	0.54	0.08

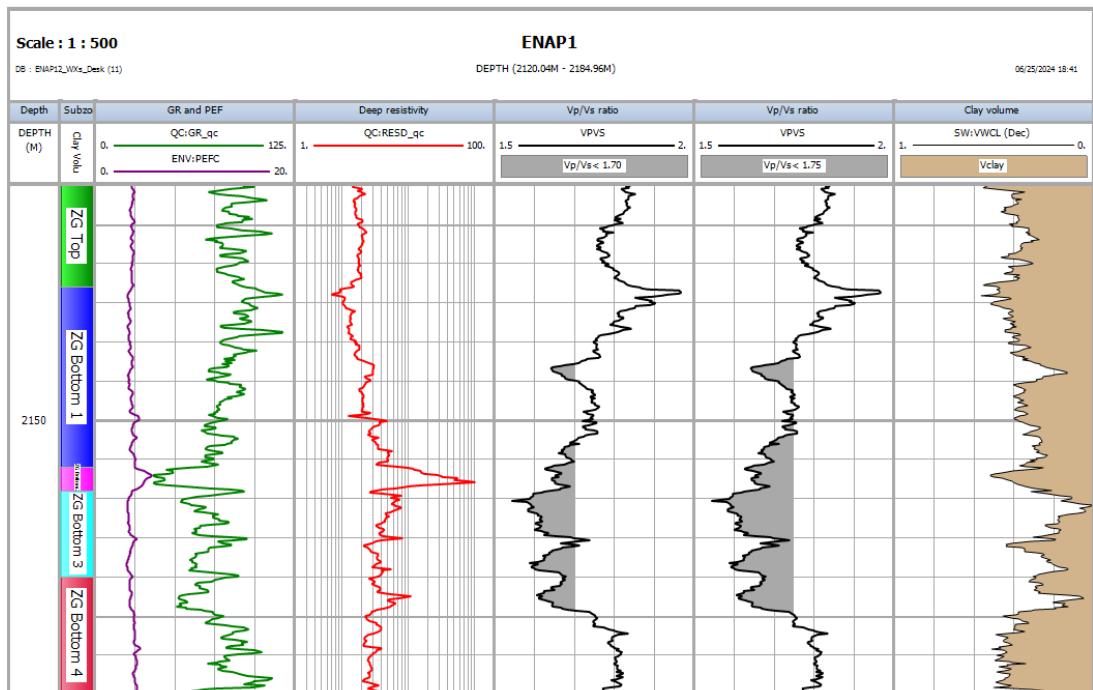


Figure 7-21. Well ENAP1. Track 1: True vertical depth (m). Track 2: ZG subzone name. Track 3: Gamma-ray (green) and photoelectric factor (purple) logs. Track 4: Deep resistivity (ohm·m). Track 5: Vp/Vs ratio log with grey shading below 1.70. Track 6: Vp/Vs ratio log with grey shading below 1.75. Track 7: Clay volume (v/v).

7.4.2 Porosity and permeability estimates from log data

The derived porosity from the bulk density log (Equation E-4) best represents the ZG total porosity after calibration with core helium porosity. The derived porosity from the sonic log (Equation E-5) is a second alternative for effective porosity as it is better calibrated with core NMR porosity and NMR logging tool. Finally, the derived porosity from the neutron log overestimated the total porosity (**Figures 7-9 and 7-10**).

From the literature, the density porosity method underestimates greensands porosity (Patchett et al., 1993; Diaz et al., 2001; Hossain et al., 2011b). Also, ENAP uses the NMR tool to calibrate core porosity with the sonic method (Gonzalez-Gonzalez et al., 2018). The statistics (**Table 7-7**) show that the density method is the best in predicting total porosity using a grain density of 2,728 kg/m³, followed by the sonic method in predicting interconnected porosity, as it is fairly close to the NMR logging tool (**Figure 7-22**). Conversely, for the pay sand zone (chloritic sandstone), the sonic method predicts best the core helium porosity (**Figure 7-23**). Notably, the bulk density log is not run in most wells operated by ENAP due to budget constraints, or the quality can be very low. Therefore, the sonic method from Wyllie's equation is recommended for such wells.

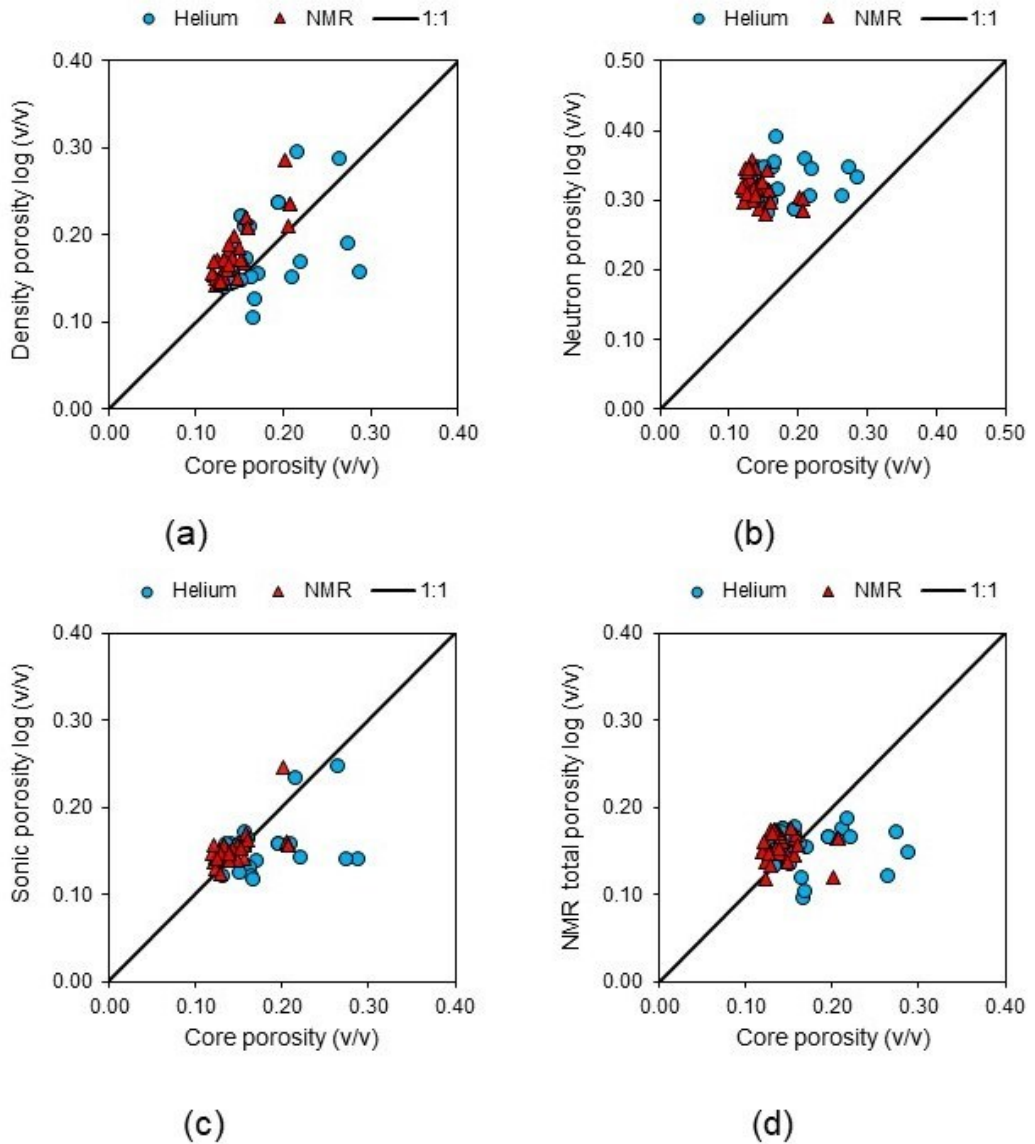


Figure 7-22. Porosity plots comparison: core porosity (X-axis) with porosity log data (Y-axis): (a) density method, (b) neutron method, (c) sonic method, and (d) NMR tool.

Table 7-7. Statistical metrics of porosity estimation in key wells ENAP1 and ENAP2.

Core porosity	Log porosity	ENAP1		ENAP2	
		R ²	RMSE	R ²	RMSE
Helium	Density	0.08	0.05	0.84	0.03
NMR	Density	0.69	0.04	0.66	0.03
Helium	Sonic	0.12	0.05	0.74	0.01
NMR	Sonic	0.34	0.02	0.34	0.02
Helium	Neutron	0.00	0.13	0.08	0.15
NMR	Neutron	0.42	0.16	0.25	0.15
Helium	NMR	0.07	0.06	0.27	0.02
NMR	NMR	0.01	0.03	0.08	0.01

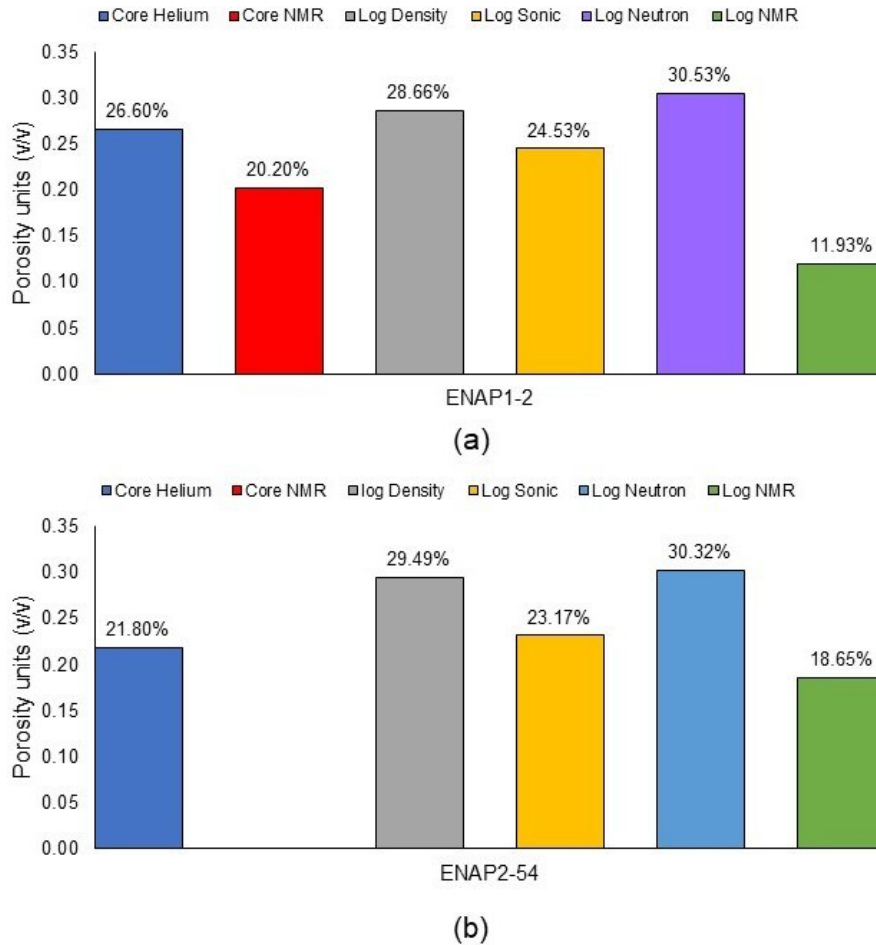


Figure 7-23. Bar chart comparison of pay sand samples' core and log porosity data: (a) ENAP1-2, (b) ENAP2-54.

In the previous chapters, several correlations were found to predict permeability with porosity, equivalent pore-throat radius and mercury saturation from capillary pressure data, and NMR correlations. The simpler the correlation, the fewer uncertainties and constraints are added. This is the reason to have selected Equation 7–1 (**Section 4.9.3**) with an R^2 of 0.64 (**Tables 4-15** and **4-16**). In addition, a good reservoir marker was found based on the FZI method using porosity and permeability as inputs (Equation 4–4) to locate the Petrofacies 1 unit with $\text{Log FZI} > -1.25$ (**Figures 7-12, 7-13** and **7-14**). While Log FZI is derived from porosity and permeability, its utility lies in its ability to provide a more refined delineation of reservoir units, particularly in confirming the top and bottom depths of pay sands. This approach complements the permeability model by offering a clearer differentiation of Petrofacies units, enhancing the log-scale interpretation.

7.4.4 Estimates of water saturation from log data

The average values of the cementation exponent m (3 and 2.02) were compared with the two correlations found in **Chapter 6**. The first one is a linear correlation as a function of total porosity (**Figure 6-6**), while the second is a logarithmic correlation

based on the Electrical Rock Type (ERT) workflow of Soleymanzadeh et al. (2021). The first equation from **Table 6-8** corresponds to a m range of 2.1 – 3.3. These three options for the cementation exponents produce similar results using the modified Simandoux model (**Figure 7-24**). After statistical (**Table 7-8**) and visual comparison (**Figure 7-25**) of the correlations with the average m values. It is recommended to use the selected average m values if the pay sand area has been securely identified and correlation 2 if the calibration process has been executed on the total core porosity. The saturation exponent n could not be empirically determined as no two-phase (air-brine system) experiments were conducted on the core analysis programme due to the time required in a tight rock (e.g. McPhee et al., 2015). Therefore, using Pickett's plot, ENAP's value of 1.66 was ensured after proper data fit (**Figure 7-15**).

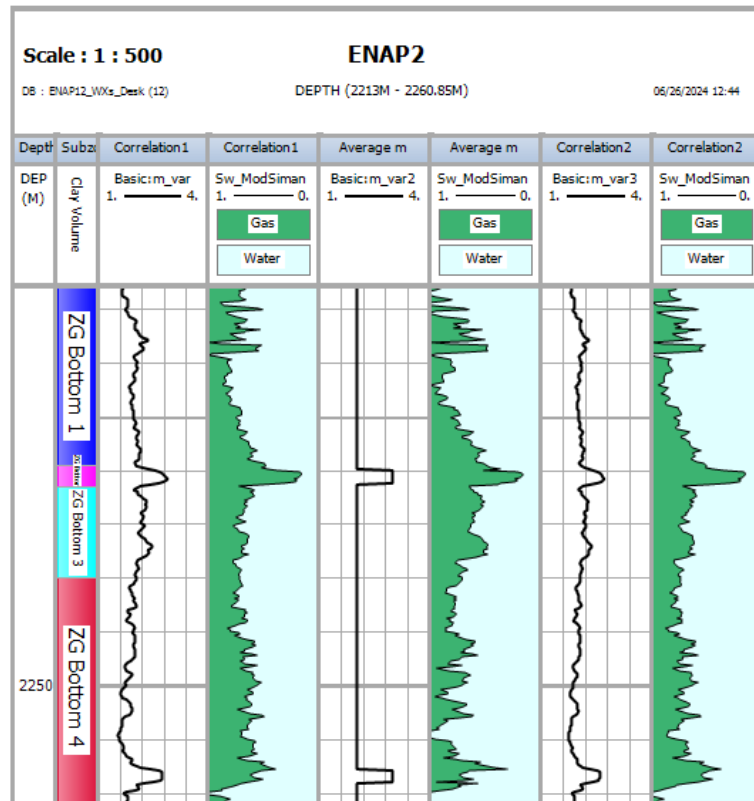


Figure 7-24. Well ENAP2. Track 1: True vertical depth (m). Track 2: ZG subzone name. Track 3: cementation exponent m (black) log from correlation 1 (linear). Track 4: Water saturation log using correlation 1 and the modified Simandoux model. Track5: cementation exponent m (black) log from average values. Track6: Water saturation log using average values of m and the modified Simandoux model. Track7: cementation exponent m (black) log from correlation 2 (natural logarithmic). Track8: Water saturation log using correlation 2 and the modified Simandoux model.

Table 7-8. Statistical metrics of cementation exponent correlations with the average values in key wells ENAP1 and ENAP2.

Correlation	ENAP1		ENAP2	
	R ²	RMSE	R ²	RMSE
1 – linear	0.64	0.12	0.54	0.12
2 – ERT	0.82	0.08	0.78	0.08

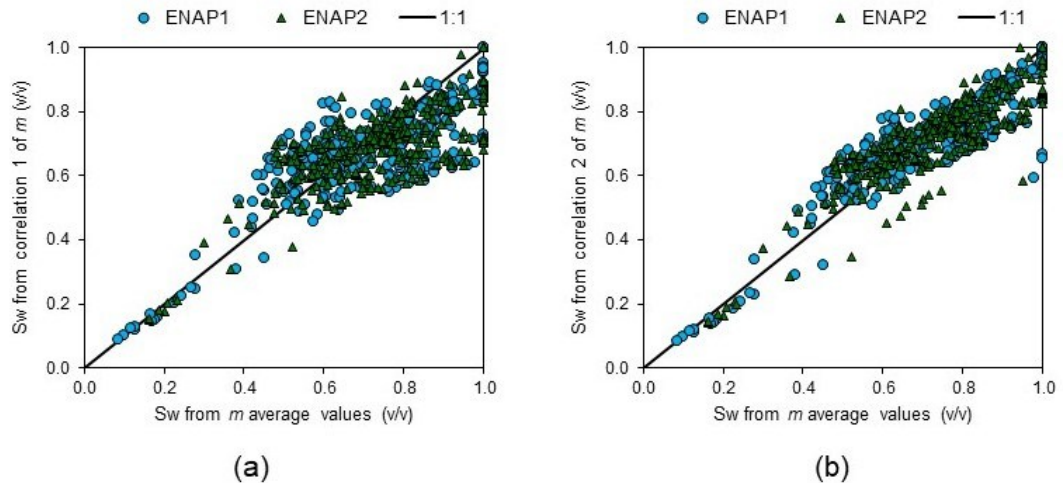


Figure 7-25. Cross-plot comparison of water saturation log values with the average m values (X-axis) and on the Y-axis: (a) Correlation 1 (linear). (b) Correlation 2 (ERT).

The water saturation model could not be calibrated with Sw_i core values since no laboratory analysis was used to determine the in situ water volume in the provided samples. The reason is that in tight rocks there is a high uncertainty in the laboratory using the traditional Dean-Stark extraction or retort methods to determine the water volume. The results are biased due to high clay content, especially if illite-smectite minerals are present, and there is a great possibility of losing water droplets in the distillation process (API RP40, 1989). In addition, the service laboratory of ENAP uses the Karl-Fisher method (titration after core cleaning), an expensive method with proper solvent and storage handling that may give better results. Still, these methods use solvents that intrude the core pore spaces, meaning that the technique may not recover the bound water volumes since it has been proven that ZG is mostly comprised of nanopores (e.g. **Figure 5-2**) with significant microporosity (**Section 4.3.2**). Instead, the Wolfson laboratory uses the NMR spectrometer to scan the sealed core (as received) to quantify the amount of in situ pore volume. This approach was conducted on ENAP1 sidewall core plugs, as **Figure 3-3** explained. The output pore volume (V_i) was divided with the brine-saturated NMR pore volume (PV) after the cleaning process (**Section 3.11**) to compute a likely Sw_i core value. However, the obtained Sw_i core values did not contribute to the calibration of the water saturation model (**Figure 7-26**). This is because the NMR tool measures hydrogen atoms in fluids (water, gas and mud filtrate). As a result, the NMR measurements may not accurately reflect the actual water saturation in cores.

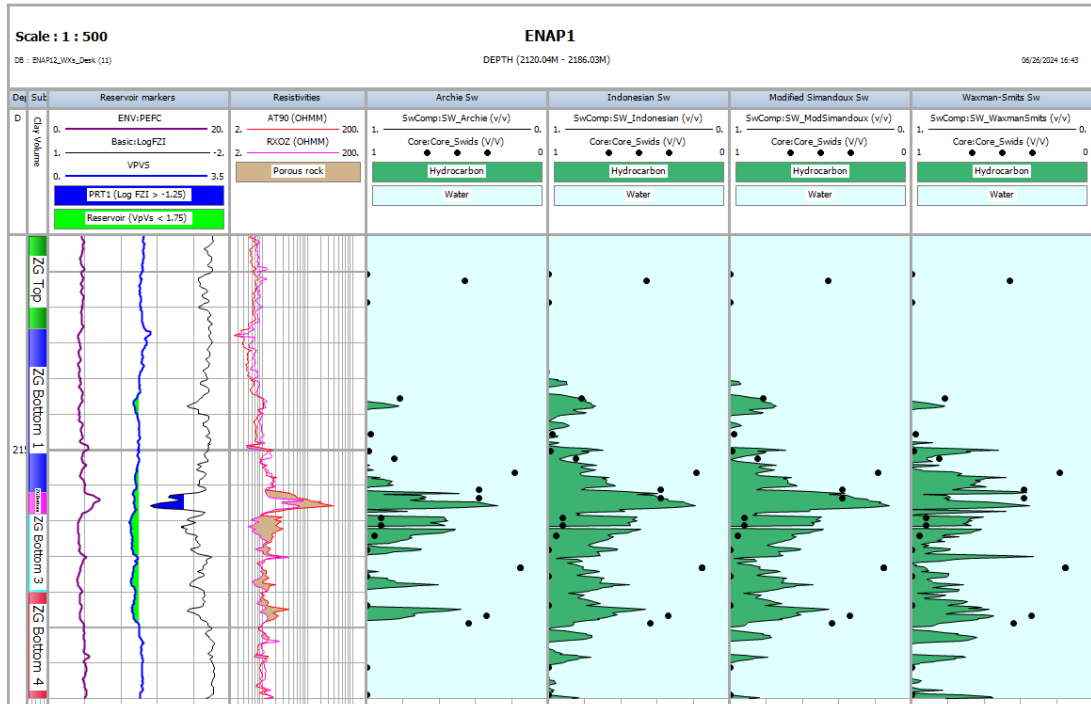


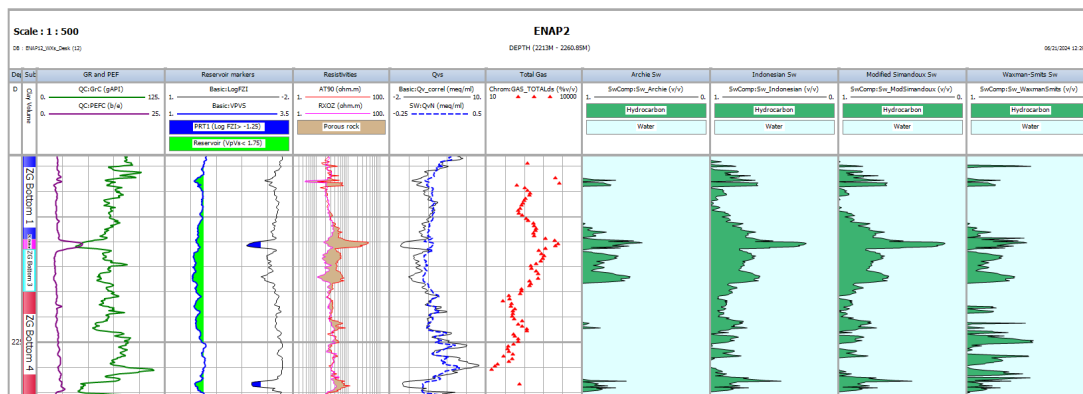
Figure 7-26. Well ENAP1. Track 1: True vertical depth (m). Track 2: ZG subzone name. Track 3: Photoelectric factor (purple), Vp/Vs ratio (blue), and Log FZI (black) logs. Track 4: Deep (red) and formation (magenta) resistivity logs. Track 5: Water saturation log with Archie's model. Track 6: Water saturation log with the Indonesian model. Track 7: Water saturation log with the modified Simandoux model. Track 8: Water saturation log with the Waxman-Smits model.

The literature reported using the modified Simandoux, Waxman-Smits, and pseudo Archie in greensands (**Section 2.3.7**). The first two are shaly-water saturation models typically classified as *Vsh* and double-layer models, respectively (e.g. Worthington, 1985). The *Vsh* models have empirically expanded Archie's (1942) correlation by implicitly adding a shaliness/clayey term to include the clay-bound water and minerals portion. In contrast, the double-layer models are based on theory and empirical data to explain the additional electrical charge of clay minerals as an ionic double-layer phenomenon, typically expressed in the *Qv* or *CEC* parameter (see **Section 2.2.1**). The Indonesian model was also selected since it is used on tight sandstones and freshwater formations with less than 40,000 ppm NaCl (Poupon and Leveaux, 1971; Geloil, 2020).

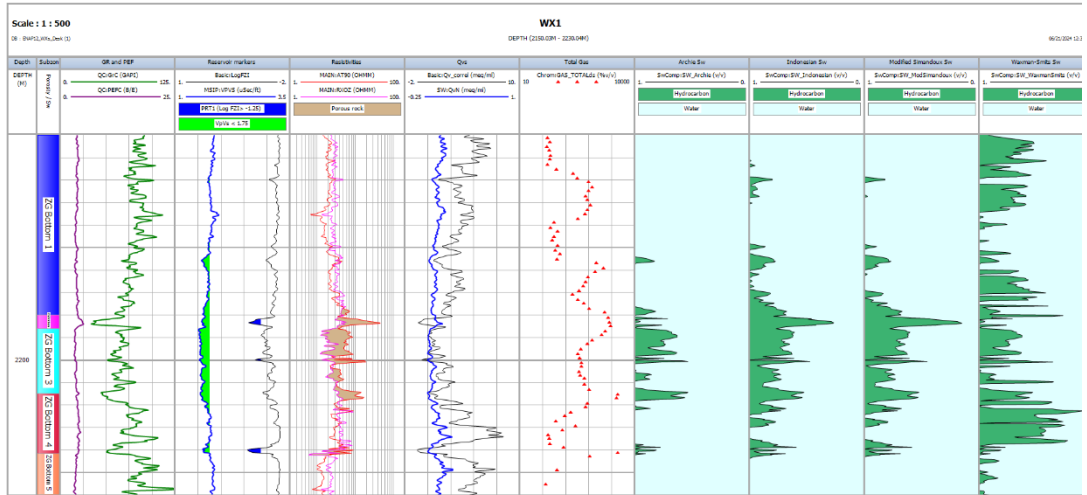
After defining the input parameters to compute the selected water saturation models. The selection of the best water saturation models laid using the markers of Vp/Vs ratio < 1.75, Log FZI > -1.25, total gas production from mudlogging data, and the shifts of the photoelectric factor and gamma-ray logs (**Figure 7-27**). Archie's model was discarded as it underestimated the Sw profile the most, as demonstrated by its consistently lower Sw estimated compared to the other models attributed to not considering in its model a clay effect (Track 8 in **Figure 7-27**). The clay presence increases the bound water content, which Archie's model overlooks, leading to

inaccurate Sw estimations. The Waxman-Smiths provided a poor estimation due to computational issues explained in the next paragraph. In contrast, the Indonesian and modified Simandoux models computed similar good Sw log profiles.

The Waxman-Smiths presented computing issues due to three additional parameters (see Equation E-9): Sw_b (bound water saturation), B (equivalent conductance of clay cations) and Q_v (cation exchange capacity). While the first parameter is automatically computed by IP, the other two are user-defined. The B parameter was initially computed at reservoir temperature using Juhasz's (1981) correlation **Error! Reference source not found.**, yielding a value of 11 mho/meq. However, this value was deemed unrealistic and generated a noisy Sw log. Given the computational issues with the model, a decision was made to fix B at the default value of IP at 1 mho/meq. Q_v in IP follows Juhasz's (1981) correlation (Equation E-10) using the slope and intercept of a and b of a linear correlation through the $1/\Phi_T$ vs Q_v app cross-plot. The log data of the key wells were used to derive the a and b coefficients (**Figure 7-28**) and compared with the output Q_v empirical correlation of core data from the chemical leaching experiment (**Figure 7-29**). This latter cross-plot differs greatly from the logging cross-plot of the ENAP2 well (**Figure 7-28 a**). This mismatch may be due to differences in the conditions under which the laboratory experiments and logging measurements were conducted, such as scale effects or variations in the rock's physical properties. Therefore, the decision was made to use log-derived values to maintain consistency with the well data and ensure better alignment with the field conditions. Further laboratory data, however, is still necessary to refine these parameters and improve the calibration of the Waxman-Smiths model.



(a)



(b)

Figure 7-27. Wells ENAP2 (a) and WX1 (b). Track 1: True vertical depth (m). Track 2: ZG subzone name. Track 3: Photoelectric factor (purple) and gamma-ray (green) logs. Track 4: Reservoir markers Log FZI (black) displays the PTR1 facies location shading in blue, and the Vp/Vs ratio (blue) displays the PTR1 facies location shading in lime. Track 5: Porous rock shading in light brown occurs in the crossover from RXOZ to AT90. Track6: Cation-exchange capacity curves used in the Waxman-Smits model, from core data (black) and log data (blue). Track7: total gas production from mudlogging data (red triangles). Track8: Sw Archie's model. Track9: Sw Indonesian model. Track10: Sw Modified Simandoux model. Track11: Sw Waxman-Smits model.

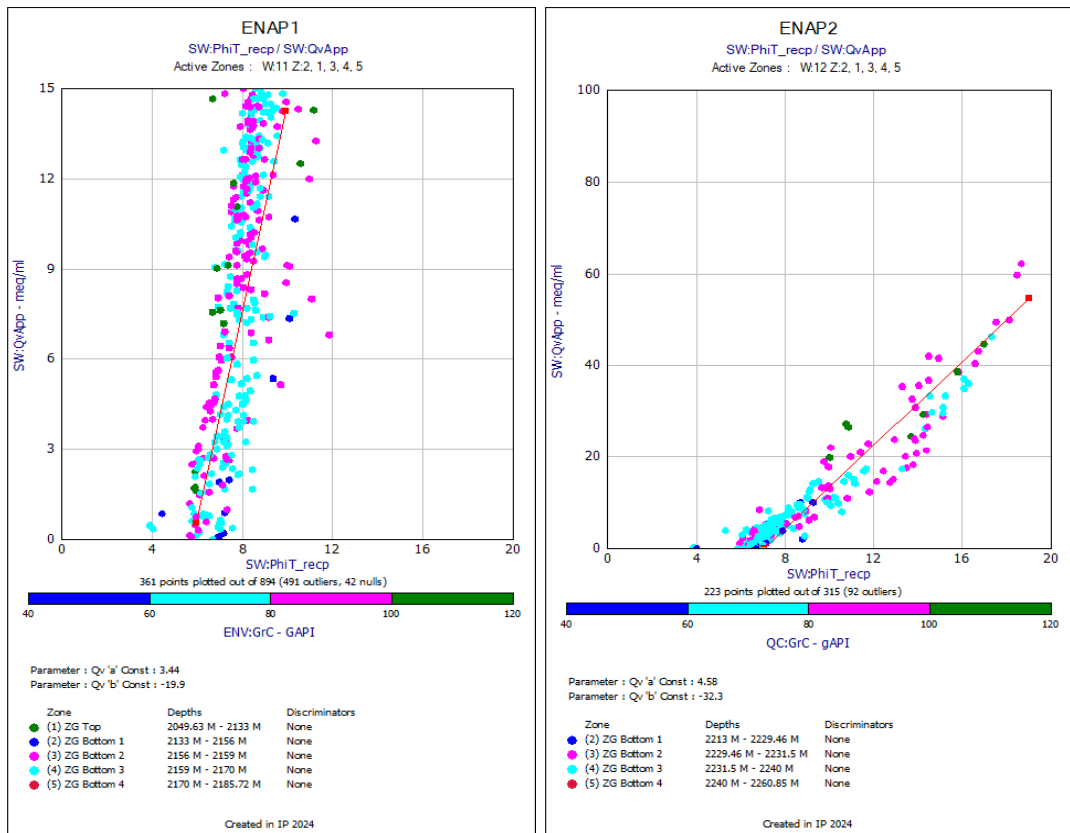


Figure 7-28. $1/\Phi_T$ vs Q_{vapp} , cross-plot of wells ENAP1 (left) and ENAP2 (right), discriminated by gamma-ray log readings.

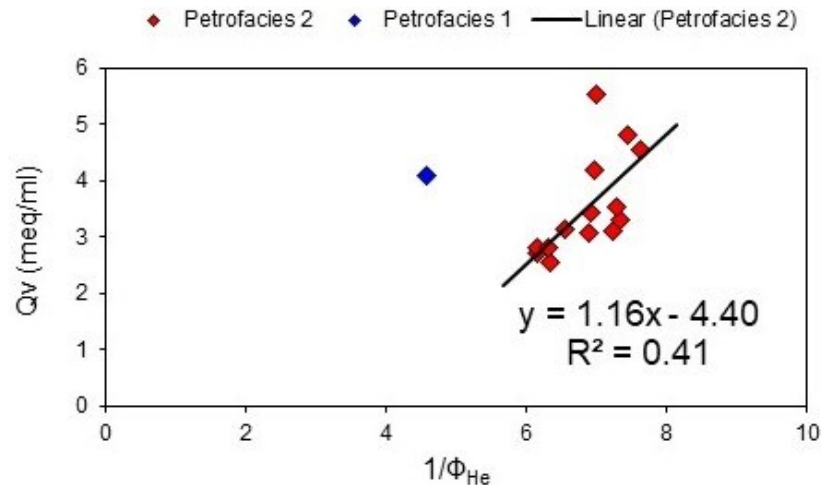


Figure 7-29. $1/\Phi_T$ vs Q_{vapp} cross-plot of well ENAP2 with core data. Linear correlation does not consider the PTR1 unit.

Finally, the Indonesian and modified Simandoux computed consistent S_w log profiles that contrasted fairly good with the selected markers. ENAP uses the latter, and after consultation, the petrophysicists have not considered the Indonesian model in their petrophysical evaluation. Their S_w values differ in the pay sand zone (see magenta data points in **Figure 7-30**), where the modified Simandoux is 15% lower than the Indonesian (**Figure 7-31**). A sensitivity analysis was therefore conducted by selecting sample ENAP1-2 (pay sand core) data, varying clay resistivity (R_{cl}), water resistivity (R_w), and clay volume (V_{cl}) parameters, and computing the change in S_w per model (**Figure 7-32**). For both models, the tuning parameter is the R_{cl} , and this is the most sensitive, with an average absolute error of ~ 0.05 v/v in S_w , followed by R_w and V_{cl} , respectively (**Table 7-9**). The difference lies in the quadratic expression of the Indonesian model in these three parameters and that the V_{cl} depends on a power-law function to prevent an overestimation of S_w when clay content is high (Equation E-8). In addition, the ZG's R_{cl}/R_w ratio at reservoir temperature (96°C) is about 8, which is considerably low. Since it is a freshwater reservoir, it does fall within the two criteria for using the Indonesian model. As Poupon and Leveaux (1971) stated in their conclusion paper, "Of the equations studied, Eq. 2 seems to account best for the effect of clay in the range of 40% to 90% on the resistivity of a shaly formation, particularly in the case of low R_{clay}/Q ratios which often are encountered when formation-water salinity is rather low (less than about 40,000 ppm)". ZG's clay portion is a third of its mineralogy.

Furthermore, for this particular sample, the S_{wi} core value derived with the NMR spectrometer is closer to the Indonesian rather the modified Simandoux model (**Table 7-10**). At the end of this project, there was not enough core data to verify whether the modified Simandoux or Indonesian model was the best fit for ZG's S_w profile.

Therefore, it is recommended to explore further the application of the Indonesian model in ZG with *Swi* core values from the laboratory.

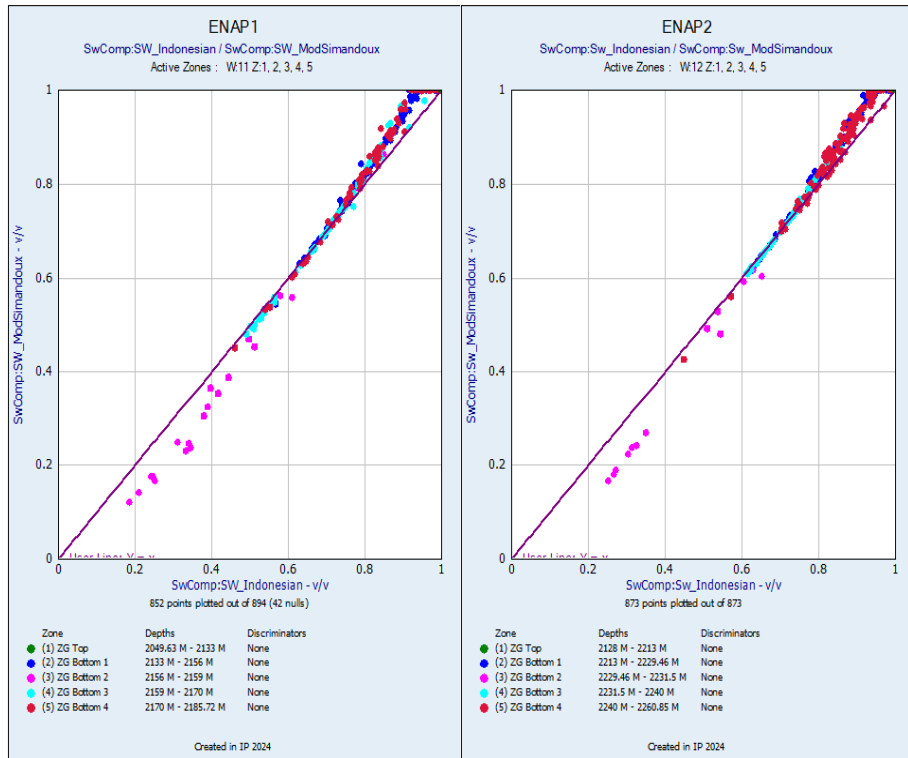


Figure 7-30. Computed Indonesian *Sw* (X-axis) vs computed modified Simandoux *Sw* (Y-axis) of key wells ENAP1 (left) and ENAP2 (right), discriminated by subzones. Note the underestimation of the Indonesian in subzone ZG bottom2, which corresponds to the pay sand location.

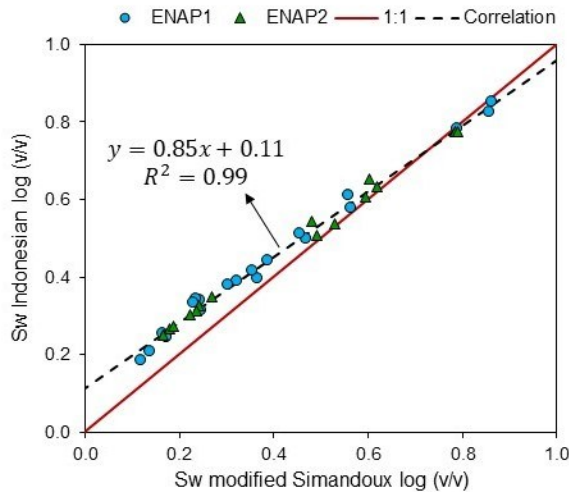
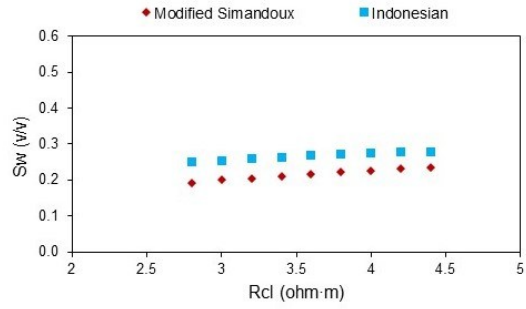
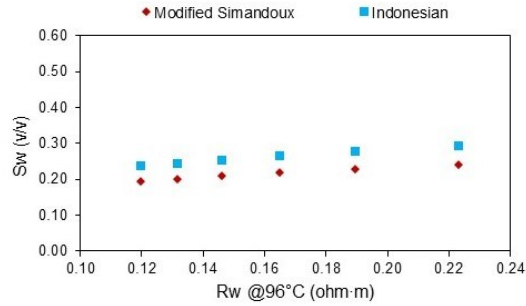


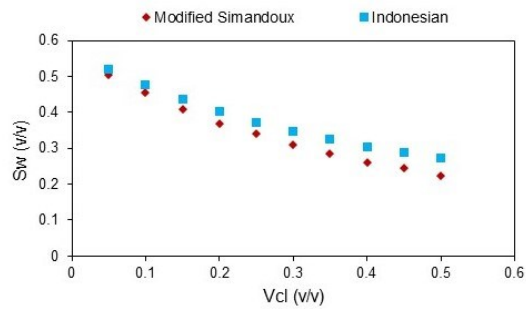
Figure 7-31. Cross-plot of *Sw* log profiles of modified Simandoux (X-axis) vs Indonesian (Y-axis) of the pay sand area of key wells.



(a)



(b)



(c)

Figure 7-32. Sensitivity analysis cross-plots: (a) varying clay resistivity, Rcl. (b) varying water resistivity, Rw. (c) varying clay volume, Vcl.

Table 7-9. Absolute error in sensitivity analysis for sample ENAP1-2.

Parameter (v/v)	$\Delta Sw = Sw_{Ind} - Sw_{ModSim} $ (v/v)		
	Varying Rcl (ohm-m)	Varying Rw (ohm-m)	Varying Vcl (v/v)
Minimum	0.043	0.042	0.015
Maximum	0.057	0.052	0.048
Median	0.052	0.046	0.035
Average	0.051	0.046	0.035

Table 7-10. Swi comparison of core and saturation models for ENAP1-2.

Parameter	Sw (v/v)
Swi core	0.38
Indonesian model	0.38
Modified Simandoux model	0.31

7.5 Summary

- The gamma-ray log with 40 and 130 API endpoint values is recommended to derive the clay volume in glauconitic sandstone sections. Also, the double indicator of bulk density and neutron logs are recommended in such zones (**Figure 7-6**).
- The photoelectric factor log with endpoint values of 2.5 and 6.25 barns/e is recommended as a single indicator to derive the clay volume in chloritic sandstones based on its ability to distinguish between key lithological units—chloritic sandstones with higher PEF values and glauconitic sandstones with lower PEF values. The PEF measurements for chlorite (4.59 barns/e) and glauconite (7.42 barns/e) reflect this variation, with the selected endpoint values capturing the range of mineral compositions in these units. Field data support this approach and align with the mineralogical properties of the pay sand zone (**Figures 7-7 and 7-8**).
- The density method is recommended to derive the total porosity log with a matrix density of 2,728 kg/m³ and a fluid density of 1,000 kg/m³, as this method provides reliable porosity estimates for the specific lithology in ZG. The matrix density of 2,728 kg/m³ is representative of the glauconite and chlorite minerals present in the formation from laboratory data. The fluid density of 1,000 kg/m³ corresponds to pure water as this is a freshwater formation.
- If the bulk density log is not available, then the sonic method is recommended to derive the total porosity log using Wyllie's time average formula (Equation E-5) with a matrix transit time of 56.75 µs/ft and a fluid transit time of 270 µs/ft as fluid (**Figure 7-22**). Although both Wyllie et al. (1956) and Raymer et al. (1980) correlations provided reasonably good predictions for ZG's glauconitic sandstones, the Wyllie method is preferred here due to its better performance, as indicated by an R² value of 0.53 (Chapter 6, Figure 6-29). In this current chapter, the Wyllie method has been improved by adding a compaction factor of 0.8 for chloritic sandstone and 1.6 for glauconitic sandstone.
- The exponential correlation (Equation 7-1) is preferred to compute the permeability model in ZG (**Figures Figure 7-12 and 7-13**) because it achieved the best fit, with an R² value of 0.63, outperforming other models analysed in **Section 4.9.3**. This correlation demonstrates the highest predictive accuracy for permeability, making it the most reliable choice for this formation.
- Four marker logs were found to identify the net reservoir: the photoelectric factor log, the total gas production from mudlogging data, the Vp/Vs ratio log and a correlation from the FZI method described in **Section 4.9.3**. The latter uses a Log FZI > -1.25 criterion to identify the pay sand zone or petrofacies (PTR) 1.

- The V_p/V_s ratio cut-off value of 1.75 is confirmed to identify the chloritic sandstones or PTR 1, where zones with V_p/V_s ratio lower than 1.75 correspond to the net reservoir (**Figure 7-21**). While **Chapter 6** identified a range of 1.70 to 1.74 for the pay sand, 1.75 better distinguishes the net reservoir zone from glauconitic sandstones with higher V_p/V_s ratios. This is further supported by characteristic gamma-ray and resistivity log trends, and the photoelectric factor log serves as the final pay sand marker.
- The cementation exponent m input must vary in the pay sand zone to a value of 3, while for the rest of ZG, a value of 2.02 is suitable. In addition, the logarithmic correlation based on the Electrical Rock Type (ERT) workflow of Soleymanzadeh et al. (2021) proved to be useful as a varying m in function of total porosity (**Table 7-8**).
- The Pickett's plot was used to confirm ENAP's saturation exponent value of 1.66, as no two-phase (air-brine) experiments were conducted to empirically determine n due to the time required for tight rock systems (e.g., McPhee et al., 2015). Therefore, ENAP's value was adopted after proper data fitting (**Figure 7-15**).
- The Sw_i core values obtained from the NMR spectrometer were not directly useful for calibrating the water saturation model, as the NMR tool measures hydrogen atoms in all fluids stored in cores (water, gas, and mud filtrate), which may not accurately reflect the in situ Sw_i in tight rocks (**Figure 7-26**). However, for sample ENAP1-2, a pay sand, the NMR results helped confirm that the Indonesian (Poupon and Leveaux, 1971) and modified Simandoux (Bardon and Pied, 1969) models best represent ZG's Sw log profile (**Table 7-10**).
- The Waxman-Smiths (1968) model showed promise due to the electrical rock resistivity behaviour in the multivalinity experiment in **Chapter 6**; Q_v values from core data differed significantly from those derived from log data (**Figures 7-28** and **7-29**), likely due to differences in measurement conditions, such as scale effects or rock property variations. These discrepancies highlight the need for further investigation to improve this model calibration in ZG.
- The modified Simandoux and the Indonesian saturation models presented similar values in glauconitic sandstones and clayey sections but differed in the pay sand area. The modified Simandoux computed 15% lower Sw than the Indonesian in such an area.
- According to Poupon and Leveaux's (1971) conclusions, the ZG formation meets two criteria of the Indonesian model: R_{cl}/R_w ratio is considerably low, and it is a freshwater reservoir (i.e. 12,000 ppm NaCl).
- At the end of this project, there was not enough core data to verify whether the modified Simandoux or Indonesian model was the best fit for ZG's Sw profile.

Therefore, it is recommended to explore further the application of the Indonesian model in ZG with Swi core values from the laboratory.

Chapter 8

Conclusions and recommendations

This chapter presents the key conclusions of the conducted investigation and recommendations for further work.

8.1 Conclusions

This dissertation investigates the Chilean reservoir ZG from a petrophysical perspective, lithologically described as a greensand. The petrophysical characterisation employed a systematic methodology, including a core analysis programme (**Chapter 3**), laboratory methods to study the ZG electrical behaviour and elasticity (**Chapter 6**), and well-log interpretation (**Chapter 7**). Three specific objectives (SOs) were proposed (**Section 1.2**) to identify the petrophysical key controls, rock's microstructure relationships, the best-fit water saturation model, and an improved petrophysical modelling workflow for the particular case of ZG, located at the Magallanes basin, Tierra del Fuego island.

The key conclusions drawn for this investigation include:

- The lithological composition of ZG exerts primary control over its pore system, influencing fluid storage and fluid properties. Glauconite and chlorite are the main clay minerals in ZG that control its petrophysical properties. Together, these comprise a third of ZG's mineralogy. This finding agrees with the literature review mind map (**Figure 2-36**). Both minerals influence ZG's petrophysical properties by impacting specific surface area, pore structure, and permeability. Chlorite, with its pore-lining morphology, enhances pore preservation and improves reservoir quality, whereas glauconite contributes to the reduction of permeability due to its association with nanopores and higher specific surface. These minerals also significantly affect rock conductivity, permeability, and elasticity, as demonstrated by secondary porosity formation in chloritic sandstones, which plays a major role in enhancing reservoir quality (**Figure 4-4 A**). This conclusion is further supported by the correlation between mineralogy and pore-throat structure (**Section 5.5.2 Petrofacies**).
- The core analysis programme results (**Chapters 4 and 5**) indicate two particular lithology units: glauconitic and chloritic sandstone with the following features.
 - a) The glauconitic sandstones present moderate iron due to the presence of glauconite, chlorite, and pyrite. They exhibit moderate heterogeneity and a narrow pore size distribution (PSD) predominately within the nanopores range. Their air-mercury capillary pressure curves indicate a high threshold value of up to 2,000 psig. These rocks have a higher specific surface area (~10 m²/g) compared to the chloritic sandstones, with moderate to high

porosity (11 – 29%v/v) and ultra-low to low permeability (0.001 – 0.03 mD). This unit corresponds to poor reservoir quality.

- b) The chloritic sandstones present the highest iron content due to chlorite and pyrite minerals with a small presence of glauconite. They have a high heterogeneity degree and wide bimodal PSD within the meso- and micropores range. Their air-mercury capillary curves have low threshold values of less than 200 psig. These rocks have a lower specific surface area (~4 m²/g) compared with the glauconitic sandstone, high porosity (22 – 27%v/v), and low permeability (0.01 – 1 mD). This unit corresponds to the pay sands or richer reservoir quality.
- The pore system in ZG is primarily controlled by lithological heterogeneity, where chloritic sandstones exhibit a bimodal pore size distribution conducive to enhanced fluid flow, while glauconitic sandstones have a predominance of nanopores that limit flow and storage capacity. Key microstructure relationships were found between the clay minerals and specific surface area (**Figure 4-7**), total porosity and gas permeability (Equation 7–1). Additionally, 50%v/v mercury saturation correlates with the NMR T₂ geometric mean (**Figure 5-17**), and Pittman's (1992) correlation relates the equivalent pore-throat radius at 25%v/v mercury saturation with porosity and permeability (**Table 5-11**). The latter confirms that the ZG's characteristic pore-throat length is at this mercury saturation intrusion (**Figure 5-16**).
 - ZG is a tight rock where its permeability is stress sensitive, especially in the range k_g < 0.01mD at increasing confining pressure (**Figure 4-14**), and its porosity is not (**Section 4.7.2**). Thus, a conversion factor in permeability needs to be applied when converting permeability measurements taken at ambient conditions to those measured in situ. This adjustment is necessary for stress sensitivity in tight formations where permeability decreases under confining pressure (**Figure 4-13**).
 - Three hydraulic units were identified using the Flow Zone Indicator (FZI) method (Amaefuele et al., 1993) based on Kozeny-Carman's permeability model, further classified as petrofacies or petrophysical rock typing (PRT) units with PSDs (**Sections 4.9.3** and **5.5.2**, respectively). Chloritic pay sands correspond to PRT1 units, while glauconitic sandstones are separated into PTR2 and PRT3 units. The latter corresponds to rock units with ultra-low permeability. The Log FZI parameter, derived from well logs using porosity and permeability, assists in separating the PRT1 unit from the rest, thus identifying the richer reservoir rocks. This method is valuable as it integrates multiple log responses to distinguish pay zones more effectively than porosity or permeability alone (**Figures 7-12** and **7-13**).
 - The traditional NMR T₂ cut-off of 33 ms for sandstones is only valid for chloritic pay sands. For glauconitic sandstones, the NMR T₂ distribution is shorter (0.1 to

25 ms), as observed in the core analysis of ZG (**Figure 5-1**), making this traditional cut-off value unrealistic. The differences in NMR responses reflect variations in pore structure and fluid mobility within the two lithological units, with chloritic sandstones supporting enhanced fluid flow due to larger pore spaces. The threshold pressure values can be used as a lower boundary for glauconitic sandstones to distinguish reservoir quality. For instance, threshold pressures above 2,000 psig indicate glauconitic sandstones with lower permeability, while lower threshold pressures (near 200 psig) define more permeable chloritic sands (**Figure 5-2**). This capillary pressure point can be derived from the variable Kappa method to convert from MICP to NMR (Equation 5–18).

- ZG electrical resistivities at 12,000 ppm NaCl indicate two distinct cementation exponents m for the identified lithology units: 2.02 for glauconitic sandstones and 3.0 for chloritic sandstones (PTR1). The results highlight that lithology and microstructure are critical factors controlling the electrical behaviour in ZG, particularly the role of pore-lining chlorite in preserving pore structures. The microstructure, particularly the large secondary pores and pore-lining chlorite, primarily controls the electrical behaviour in ZG rather than the type and distribution of clay minerals. In the PRT1 unit, chlorite pore-lining helps to preserve the pores, enhancing reservoir quality (**Figures 4-4; 4-5 B and H**), resulting in a combination of high porosity and formation factor (**Figure 6-5**). In addition, a correlation based on Soleymanzadeh et al. (2021) workflow, applying the electrical efficiency theory (Herrick and Kennedy, 1994), offers a useful alternative for varying the cementation exponent m , as opposed to relying solely on the linear correlation from **Chapter 6 (Figure 7-25)**.
- The selected methods to derive ZG's cation-exchange capacity (CEC) cannot be compared as they measure this parameter differently. On the one hand, the chemical leaching method (Chapman, 1965) identifies the cations that interchange with brine, and the sum is a total CEC. Here, ZG CEC ranged from 18 to 41 meq/100g and it identified that calcium contributed half to the CEC, followed by sodium and magnesium. On the other hand, the multivalency experiment, based on the Waxman-Smits (1968) model, extrapolates CEC from resistivity (conductivity) measurements of rock and core-flooding brine. Only a pay sand sample could run, giving a CEC value of 72 meq/100g. The discrepancy between these methods suggest the need for standardised protocols or cross-validation techniques to reconcile differences in measured CEC values. The findings indicate that CEC plays a crucial role in water saturation modelling at freshwater salinity due to its influence on rock conductivity and clay-bound water content. The multivalency experiment in Chapter 6 demonstrates how variations in CEC affect formation resistivity and, consequently, S_w calculations (**Figure**

7-27). Furthermore, the clayey tight sandstone cores in the Navarro-Perez et al. (2024) study showed significant permeability reductions under changing salinity conditions, emphasising the impact of CEC on formation damage.

- In well-log interpretation, four reservoir markers identify the net reservoir in ZG: the photoelectric factor (PEF) log showing a great increase, the total gas production from mudlogging data, the Log FZI > -1.25 criterion, and the V_p/V_s ratio > 1.75. The latter was confirmed after data processing of ultrasonic velocities in the core (**Figure 6-34**). The Log FZI criterion integrates both porosity and permeability, providing a more comprehensive identification of reservoir quality (PRT1 unit) than porosity alone. The clay volume model uses the gamma-ray logs as a single indicator and bulk density-neutron logs as the second indicator in glauconitic sandstones. In chloritic sandstones, the PEF log is the sole indicator for estimating the clay volume (**Section 7.4.1**). The total porosity model is derived with the density method; if it is not available, then the sonic method can be applied with the Wyllie et al. (1956) formula with a compaction factor of 0.8 and 1.6 for the glauconitic and chloritic sandstones, respectively (**Section 7.3.3**). The permeability model is derived from the empirical correlation found in **Chapter 4 (Section 7.3.4)**.
- The Indonesian (Poupon and Leveaux, 1971) and modified Simandoux (Bardon and Pied, 1969) models are the best-fit water saturation (S_w) models for ZG; the modified Simandoux model presents a 15% S_w lower in the pay sand area. This conclusion is based on S_w log comparisons with core-derived S_{wi} values and observed resistivity trends (**Figure 7-32** and **Table 7-9**). However, additional laboratory measurements are required to validate these models further (**Section 7.4.4**).

8.2 Recommendations for further work

Based on the findings of this investigation, the following recommendations for further research are proposed:

- In the XRD interpretation, a customised workflow needs to be elaborated to confirm glauconitic mica and smectite minerals following Odin and Matter's (1981) guidelines since the glauconite first-order basal reflection of the 10 Å peak overlaps between illite and expandable mixed layers (**Section 4.9.1**).
- The ZG permeability is controlled by its complex microstructure features, such as pore throat lack of interconnectivity and significant microporosity. It is recommended to investigate using advanced visualisation techniques such as Wood's metal immersion combined with SEM or others to understand further the impact of the mentioned microstructural features on permeability and porosity.

- Due to time constraints, the relative permeability of ZG was not determined, as no two-phase experiments were conducted in this research. The primary challenge is that the ultra-low permeability of ZG complicates the laboratory procedures and extends the experimentation timing. For instance, the current laboratory service at ENAP employs the Welge method to estimate the relative permeability using absolute permeabilities of brine and gas. However, this theoretical correlation requires validation with empirical data. Therefore, it is recommended to investigate further and develop empirical methods to measure the relative permeability in ZG and to compare such empirical results with the Welge method.
- The ZG reservoir is a unique rock type. Further investigation can be made into analysing in more detail the effects of NMR T_1 and T_2 distributions with the iron within the glauconite and chlorite mineral content, as several authors have reported the paramagnetic effects of iron content in greensands (e.g. LaTorraca et al., 1995; Saidian and Prasad, 2015). Dodge et al. (1995) reported an indirect relation between the NMR T_2 cut-off value and iron content (**Table 2-10**). However, there is a knowledge gap in the definition of an NMR T_2 cut-off value to identify the mobile gas volume in ZG; thus, it is recommended to NMR scan desaturating cores at different brine saturation degrees to build an empirical NMR T_2 distribution curve and contrast it with the suggested brine-saturated NMR T_2 peak or threshold pressure values as the lower limit.
- Further investigation is needed to determine an adequate cation-exchange capacity (CEC) protocol for complex TGSs such as ZG, as the selected methods are not comparable. For now, the multivalency method is more appropriate for simulating the rock at in-situ confining pressures, and the chemical leaching method is suitable for identifying the cations released from the ZG clay fine portion. Although the Waxman-Smiths (1968) model was a promising saturation model, there still needs to be more certainty in the true values of Sw_b (bound water saturation), B (equivalent conductance of clay cations) and Q_v (cation exchange capacity). Moreover, more core data is needed to comprehend further which method actually measures the CEC, as other electrical components might be involved.
- Further investigation in the laboratory is needed to find more reliable Sw_i core values in ZG that can help calibrate the water saturation model. This issue is common in unconventional resources like tight rocks. Since two shaly-sand water saturation models were found best to predict ZG's (Indonesian and modified Simandoux), it is recommended to assess the Indonesian model since it meets the two criteria of Poupon and Leveaux's (1971): R_c/R_w ratio is considerably low, and it is a freshwater reservoir (i.e. 12,000 ppm NaCl).

- The next step is to work with ENAP company to apply the proposed petrophysical evaluation workflow in the rest of the ZG wells and move to the reservoir modelling approach with open-source software such as OPM-flow (<https://opm-project.org/>). This researcher and ENAP intend to continue collaborating to enhance the petrophysical characterisation of formations in the Magallanes basin, thus contributing to the academia and industry spheres to offer knowledge and expertise to local decision-makers.

List of References

- A Dictionary of Chemistry. [Online]. 2020. *Magnetism*. [Accessed 19 June 2023]. Available from: <https://www.oxfordreference.com/view/10.1093/acref/9780198841227.001.0001/acref-9780198841227-e-2587>
- Abd El-Rahman, M.K. 2006. Degritting of glauconite clay by different techniques for use in water treatment as as fertiliser. *Mineral Processing and Extractive Metallurgy*. **115** (3), pp. 145-149. Available from: <https://doi.org/10.1179/174328506X109095>
- Abousrafa, E.M., Somerville, J.M., Hamilton, S.A., Olden, P.W.H., Smart, B.D.G. and Ford, J. 2009. Pore geometrical model for the resistivity of brine saturated rocks. *Journal of Petroleum Science and Engineering*. **65**(3-4), pp. 113-122. Available from: <https://doi.org/10.1016/j.petrol.2008.12.009>
- Abudelgawad, G., Page, A.L. and Lund, L.J. 1975. Chemical weathering of glauconite. *Soil Science Society of America Journal*. **39** (3), pp. 567-571.
- Adisoemarta, P.S., Anderson, G.A., Frailey, S.M., and Asquith, G.B. 2000. Historical use of m and a in well log interpretation: is conventional wisdom backwards? *SPE Permian Basin Oil and Gas Recovery Conference*. Midland, Texas: SPE, p. SPE-59699. Available from: <https://doi.org/10.2118/59699-MS>
- Ahmed, T. 2019. *Reservoir Engineering Handbook*. 5th ed. Gulf Professional Publishing.
- Aimar, E., Cevallos, M., Cangini, A., Mas-Cattapan, F. and Vega, V. 2018. Extension y desarrollo de los reservorios de baja permeabilidad del yacimiento Campo Indio, Formación Magallanes (Maastrichtiano Tardío-Daniano), Cuenca Austral Argentina. *10° Congreso de Exploración y Desarrollo de Hidrocarburos*. Mendoza, Argentina: IAPG.
- Akai, T., Takakuwa, Y., Sato, K., and Wood, J. M. 2016. Pressure dependent permeability of tight rocks. *SPE Low-Permeability Reservoirs Symposium*. Denver, Colorado: SPE, p. SPE-180262. Available from: <https://doi.org/10.2118/180262-MS>
- Alderton, D.. 2021. Glauconites. In: Alderton, D. and Scott, A.E. eds. *Encyclopedia of Geology*. Academy Press, pp. 374-378.

- Allaby, M. 2019. *A dictionary of plant sciences*. 4th ed. Oxford: Oxford University Press.
- Alqatrani, G. Britt, L.K, Otzen, M., Guzman, M., Kusanovic, G. and Dunn-Norman, S. 2016. A statistical approach to fracture optimization of the glauconite formation in Southern Chile. *SPE Asia Pacific Hydraulic Fracturing Conference*. Beijing: SPE, p. SPE-181864-MS. Available from: <https://doi.org/10.2118/181864-MS>
- Alqatrani, G. Britt, L.K, Otzen, M., Guzman, M., Kusanovic, G. and Dunn-Norman, S. 2018. Fracture optimization of an unconventional gas resource in Southern Chile. *SPE International Fracturing Technology Conference and Exhibition*. Muscat, Oman: SPE, p. SPE-191428-18IHFT-MS. Available from: <https://doi.org/10.2118/191428-18IHFT-MS>
- Amaefule, J.O., Altunbay, M., Tiab, D., Kersey, D.G. and Keelan, D.K. 1993. Enhanced reservoir description: using core and log data to identify hydraulic (flow) units and predict permeability in uncored intervals/wells. *SPE Annual Technical Conference and Exhibition*. Houston, Texas: SPE, p. SPE-26436-MS. Available from: <https://doi.org/10.2118/26436-MS>
- Amaefule, J.O., Wolfe, K., Walls, J.D., Ajufo, A.O. and Peterson, E. 1986. Laboratory determination of effective liquid permeability in low-quality reservoir rocks by the pulse decay technique. *SPE California Regional Meeting*. Oakland, California: SPE, p. SPE-15149-MS. Available from: <https://doi.org/10.2118/15149-MS>
- Amann-Hildenbrand, A., Dietrichs, J. P. and Krooss, B. M. 2016. Effective gas permeability of Tight Gas Sandstones as a function of capillary pressure—a non-steady-state approach. *Geofluids*. **16**(3), pp. 367-383. Available from: <https://doi.org/10.1111/gfl.12155>
- API RP40. 1998. *Recommended Practices for Core Analysis*. 2nd ed. API, Washington, DC.
- Archie, G. E. 1942. The electrical resistivity log as an aid in determining some reservoir characteristics. *Transactions AIME* **146**(01). pp. 54-62. Available from: <https://doi.org/10.2118/942054-G>
- Arps, J.J. 1953. The effect of temperature on the density and electrical resistivity of sodium chloride solutions. *Journal of Petroleum*

Technology. **5**(10), pp. 17-20. Available from:
<https://doi.org/10.2118/953327-G>

Asquith, G.B. 1990. *Log evaluation of shaly sandstones a practical guide*. American Association of Petroleum Geologists.

Atahualpa, G., 2013. *Efecto de la glauconita en las propiedades petrofísicas del reservorio arenisca "T" Superior del Bloque Tarapoa*. Geology Engineering thesis, Universidad Central de Ecuador.

Aydin, A. 2014. Upgraded ISRM suggested method for determining sound velocity by ultrasonic pulse transmission technique. In: Ulusay, R. (eds) *The ISRM Suggested Methods for Rock Characterization, Testing and Monitoring: 2007-2014*. Cham: Springer International Publishing, pp. 95-99. Available from: https://doi.org/10.1007/978-3-319-07713-0_6

AZO materials. (2023). *Micromeritics AutoPore V Series Porosimeters*. Available from: <https://www.azom.com/equipment-details.aspx?EquipID=3277%20>

Baker, J. C., Uwins, P. J. R. and Hamilton, P. J. 1997. Freshwater sensitivity of glauconitic hydrocarbon reservoirs. *Journal of Petroleum Science and Engineering*. **18**(1-2), pp. 83-91. Available from: [https://doi.org/10.1016/S0920-4105\(96\)00076-9](https://doi.org/10.1016/S0920-4105(96)00076-9)

Bansal, U., Banerjee, S. and Nagendra, R. 2020. Is the rarity of glauconite in Precambrian Bhuima Basin in India related to its chloritization? *Precambrian Research*. **336**, p. 105509. Available from: <https://doi.org/10.1016/j.precamres.2019.105509>

Baptist, O.C. and Sweeney, S.A. 1954. The effect of clays on the permeability of reservoir sands to waters of different saline contents. *Clays and Clay Minerals*. **3**, pp. 505-515.

Bardon, C. and Pied, B. 1969. Formation water saturation in shaly sands. *SWPLA 10th Annual Logging Symposium*. Houston, Texas: SPWLA, p. SWPLA-1969-Z.

Barton, C. D. and Karathanasis, A. D. 2002. Clay minerals. In: Dekker, M. *Encyclopedia of soil science*. New York, USA: Rattan Lal, comp., pp. 187-192.

Berg, R.R. 1975. Capillary pressures in stratigraphic traps 1. *AAPG Bulletin*. **59**(6), pp. 939-956.

- Britt, L.K., Otzen, G., Guzman, M., Kusanovic, G., Alqatrani, G. and Dunn-Norman, S. 2016. Hydraulic fracturing of a clay rich formation in Southern Chile: the challenges & successes. *SPE Asia Pacific Hydraulic Fracturing Conference*. Beijing, China: SPE, p. SPE-181808-MS. Available from: <https://doi.org/10.2118/181808-MS>
- Broger, K. and Syhlonyk, G. 1995. Glauconite sandstone exploration: a case study from the Lake Newell project, Southern Alberta, Canada.
- Brunauer, S., Emmett, P. H., and Teller, E. 1938. Adsorption of gases in multimolecular layers. *Journal of the American Chemical Society*. **60**(2), pp. 309-319.
- Burst, J.F. 1958. Mineral heterogeneity in "glauconite pellets". *The American Mineralogist: Journal of Earth and Planetary Materials*. **43**(5-6), pp. 481-497.
- Bush, D.C. and Jenkins, R.E. 1970. Proper hydration of clays for rock property determinations. *Journal of Petroleum Technology*. **22**(07), pp. 800-804.
- Byrnes, A., Cluff, R., Webb, J., Victorine, J., Stalder, K., Osburn, D., Knoderer, A., Metheny, O., Hommertzheim, T., Byrnes, J. and Krygowski, D., 2008. *Analysis of critical permeability, capillary pressure and electrical properties for Mesaverde tight gas sandstones from western us basins*. University Of Kansas Center For Research Incorporated.
- Cade, C.A, Evans, I.J. and Bryant, S.L. 1994. Analysis of permeability controls: a new approach. *Clay Minerals*. **29**(1994), pp. 491-501.
- Carpenter, A.B. 1978. Origin and chemical evolution of brines in sedimentary basins. *SPE Annual Fall Technical Conference and Exhibition*. Houston, Texas: SPE, p. SPE-7504-MS.
- Carrizo, N., Santiago, E. and Saldungaray, P. 2021. An Integrated Petrophysical Characterization of a Siliciclastic Tight Gas Reservoirs in Neuquén Basin, Western Argentina. *SPWLA 62nd Annual Logging Symposium*. Virtual: SPWLA, p. SPWLA-2021-0044. Available from: <https://doi.org/10.30632/SPWLA-2021-0044>
- Castagna, J. P., Batzle, M. L., and Eastwood, R. L. 1985. Relationships between compressional-wave and shear-wave velocities in clastic silicate rocks. *Geophysics*. **50**(4), pp. 571-581.
- Castagna, J. P., Batzle, M. L., Kan, T. K., and Backus, M. M. 1993. Rock physics—The link between rock properties and AVO response. *Offset-*

dependent reflectivity—Theory and practice of AVO analysis: SEG. **8**, pp. 135-171.

- Chapman. 1956. Cation-exchange capacity. In: C.A. Black (ed.). *Methods of soil analysis - Chemical and microbiological properties*. Agronomy 9:891-901.
- Chehrazi, A., Rezaee, R. and Rahimpour, H. 2011. Pore-facies as a tool for incorporation of small-scale dynamic information in integrated reservoir studies. *Journal of Geophysics and Engineering.* **8**(2), pp. 202-224. Available from: <https://doi.org/10.1088/1742-2132/8/2/008>
- Chen, T. and Stagg, P.W. 1984. Semilog analysis of the pulse-decay technique of permeability measurements. *Society of Petroleum Engineers Journal.* **24**(06), pp.639–642. Available from: <https://doi.org/10.2118/11818-PA>
- Chhatre, S.S., Sahoo, H., Leonardi, S., Vidal, K., Rainey, J., Braun, E.M. and Patel, P. 2017. A blind study of four digital rock physics vendor labs on porosity, absolute permeability, and primary drainage capillary pressure data on tight outcrop rocks. Annual Symposium of the Society of Core Analysts. Vienna, Austria.
- Cimbalnikova, A. 1970. Index of refraction and density of glauconites. *Cas. Mineral. Geol. Csekosl.* **15**, pp. 335-345.
- Cimbalnikova, A. 1971a. Chemical variability and structural heterogeneity of glauconites. *American Mineralogist: Journal of Earth and Planetary Materials.* **56**(7-8), pp. 1385-1392.
- Cimbalnikova, A. 1971b. Influence of 10Å/14Å interlayering on the layer charge of glauconites. *American Mineralogist: Journal of Earth and Planetary Materials.* **56**(7-8), pp. 1393-1398.
- Clavier, C., Coates, G. and Dumanoir, J. 1984. Theoretical and experimental bases for the dual-water model for interpretation of shaly sands. *Society of Petroleum Engineers Journal.* **24**(02), 153-167. Available from: <https://doi.org/10.2118/6859-PA>
- Cluff, R. M., Byrnes, A. P., Whittaker, S., and Krygowski, D. 2008. Evidence for a Variable Archie Porosity Exponent 'm' and Impact on Saturation Calculations for Mesaverde Tight Gas Sandstones: Piceance, Uinta, Green River, Wind River, and Powder River Basins. *In Proceedings of the AAPG Rocky Mountain Section Meeting.*

- Cluff, R.M. and Byrnes, A.P. 2010. Relative permeability in tight gas sandstone reservoirs - the "permeability jail" model. *SPWLA 51st Annual Logging Symposium*. Perth, Australia: SPWLA, p. SPWLA-20120-58470.
- Coates, G.R., Xiao, L. and Prammer, M.G. 1999. *NMR logging principles and applications*. Houston: Elsevier Science.
- Comisky, J.T., Newsham, K.E., Rushing, J.A. and Blasingame, T.A. 2007. A comparative study of capillary-pressure-based empirical models for estimating absolute permeability in tight gas sands. *SPE Annual Technical Conference and Exhibition*. Anaheim, California: SPE, p. SPE-110050.
- Comisky, J.T., Santiago, M., McCollom, B., Buddhala, A. and Newsham, K.E. 2017. Sample size effects on the application of mercury injection capillary pressure for determining the storage capacity of tight gas and oil shales. *Canadian Unconventional Resources Conference*. Calgary, Alberta: SPE, p. SPE-149432-MS. Available from: <https://doi.org/10.2118/149432-MS>
- Cui, X., Bustin, A.M.M. & Bustin, R.M. 2009. Measurements of gas permeability and diffusivity of tight reservoir rocks: different approaches and their applications. *Geofluids*. **9**(3), pp. 208-223. Available from: <https://doi.org/10.1111/j.1468-8123.2009.00244.x>
- Daneshfar, R. and Moghadasi, J. 2017. Clay swelling: a critical review of 50 years of research. *6th International Conference on Oil, Gas, Refining & Petrochemical with focus relationship between Government, University & Industry*. Shiraz, Iran.
- Darcy, H. 1856. *Les fontaines publiques de la ville de Dijon: exposition et application*. Victor Dalmont, Paris.
- Dastidar, R., Sondergeld, C. H. and Rai, C. S. 2007. An improved empirical permeability estimator from mercury injection for tight clastic rocks. *Petrophysics*. **48**(03), pp. 186–190.
- de Carvalho, R., Ferreira, E. L. and Rodrigues, M., 2015. Design of experiments to evaluate clay swelling inhibition by different combinations of organic compounds and inorganic salts for application in water base drilling fluids. *Applied Clay Science*. **105-106**, pp. 124-130. Available from: <https://doi.org/10.1016/j.clay.2014.12.029>

- Deer, W.A., Howie, R.A. & Zussman, J. 2013. *An introduction to the rock-forming minerals*. 5th ed. Mineralogical Society of Great Britain and Ireland.
- Diaz, E., Prasad, M., Gutierrez, M.A., Dvorkin, J. and Mavko, G. 2001. Elastic properties of glauconite and glauconitic sandstone reservoirs. *SEG Annual Meeting*. San Antonio, Texas: SEG, p. SEG-2001-1772.
- Diaz, E., Prasad, M., Mavko, G. and Dvorkin, J. 2003. Effect of glauconite on the elastic properties, porosity and permeability of reservoir rocks. *The Leading Edge*. **22**(1), pp. 42-45. Available from: <https://doi.org/10.1190/1.1542755>
- DNPuq. 2023. *Capillary pressure curve from mercury intrusion method*. [Online]. [Accessed 05 December 2023]. Available from: https://commons.wikimedia.org/wiki/File:Capillary_pressure_curve_01.svg
- Dodge, W.S., Shafer, J.L., Klimentidis, R.E. 1996. Capillary pressure: the key to producible porosity. *37th SPWLA Annual Logging Symposium*. New Orleans, Louisiana: SPWLA, p. SPWLA-1996-J.
- Doveton, J.H. 2014. *Principles of mathematical petrophysics*. Oxford: University Press.
- Doveton, J.H. 2018. Chapter 24 Mathematical minerals: a history of petrophysical petrography. In: Daya Sagar B., Cheng Q., Agterberg F. (eds) *Handbook of Mathematical Geosciences*. Springer, Cham. Available from: https://doi.org/10.1007/978-3-319-78999-6_24
- Durand, C., Cerepi, A. and Brosse, E. 2000. Effect of pore-lining chlorite on petrophysical properties of low-resistivity sandstone reservoir. *2000 SPE Annual Technical Conference and Exhibition*. Dallas, Texas: SPE, p. SPE-63070. Available from: <https://doi.org/10.2118/72179-PA>
- Dvorkin, J., and A. Nur. 1996. Elasticity of high-porosity sandstones: Theory for two North Sea datasets. *Geophysics*. **61**, pp. 1363–1370.
- El-Amamy, M.M., Page, A.L. and Abudelgawad, G. 1982. Chemical and mineralogical properties of glauconitic soils as related to potassium depletion. *Soil Science Society of America Journal*. **46**(2), pp. 426-430.
- Elementary Engineering Library. 2020. *Clay mineralogy*. [Online]. [Accessed 31 May 2022]. Available from: <https://www.elementaryengineeringlibrary.com/civil-engineering/soil-mechanics/soil-mineralogy-clay-mineralogy>

- ENAP. 2020. *Memoria anual ENAP 2019*. Available from: https://www.enap.cl/pag/729/1887/memoria_2019
- Eslinger, E. and Pevear, D. 1988. *Clay minerals for petroleum geologists and engineers, SEPM Short Course 22*. Society for Sedimentary Geology, Tulsa, OK.
- Ethier, V.G. and King, H.R. 1991. Reservoir quality evaluation from visual attributes on rock surfaces: methods of estimation and classification from drill cuttings or cores. *Bulletin of Canadian Petroleum Geology*. **39**(3), pp. 233-251. Available from: <https://doi.org/10.35767/gscpgbull.39.3.233>
- EU Joint Research Centre. (n.d.). *BCR-172 quartz (2.50 m²/g) (nitrogen BET specific surface area)*. [Online]. [Accessed 11 September 2023]. Available from: <https://crm.jrc.ec.europa.eu/p/q/quartz+/BCR-172-QUARTZ-2-50-m2-g-nitrogen-BET-specific-surface-area/BCR-172>
- Farah, F.O., 2013. Directional well design, Trajectory and survey calculations, with a case study in Fiale, Asal rift, Djibouti. *Geothermal Training Programme*. **27**, pp.27-34.
- Farahani, M., Aghaei, H. and Asadolahpour, S.R. 2019. Sensitivity of unsteady-state gas-water relative permeability to experimental artefacts and interpretation techniques; case study from a gas reservoir in south Iran. *Journal of Natural Gas Science and Engineering*. **71**, p. 102998. Available from: <https://doi.org/10.1016/j.jngse.2019.102998>
- Florence, F.A., Rushing, J.A., Newsham, K.E. and Blasingame, T.A. 2007. Improved Permeability Prediction Relations for Low-Permeability Sands. Rocky Mountain Oil & Gas Technology Symposium. Denver, Colorado: SPE, p. SPE-107954-MS. Available from: <https://doi.org/10.2118/208976-MS>
- Garamendi, R. and Atau, H. 1999. Estrategia de explotacion en reservorios de bajo restablecimiento de presion. *INGEPET 1999*. Lima, Peru.
- Garay Andrade, C., Sanz Vera, J., Salas, F., Pucci, C., Castro, A., Bastos, V., Schubert, E. and Theuveny, B. 2022. Enhancement of production data in tight gas reservoir through an automated multiphase measurement skid for remote operation. *SPE Canadian Energy Technology Conference*. Calgary, Alberta: SPE, p. SPE-208976-MS. Available from: <https://doi.org/10.2118/208976-MS>

- Geloil. 2020. *The Indonesian Poupon-Leveaux water saturation equation*. [Online]. [Accessed 10 September 2020]. Available from: https://geoloil.com/Indonesia_SW.php
- Geoactive Limited. 2024. *Interactive Petrophysics* (6.0.0). [Software]. [Accessed 1 May 2024].
- Geology.com. 2023. *Chlorite*. [Online]. [Accessed 25 April 2023]. Available from: <https://geology.com/minerals/chlorite.shtml>
- Glover, P.W.J. 2015. 11.04 - Geophysical properties of the near surface earth: electrical properties. In: Schubert, G. ed. *Treatise on Geophysics*. 2nd ed. Elsevier, pp. 89-137.
- Gong, W., You, L., Xu, J., Kang, Y., and Zhou, Y. 2022. Experimental study on the permeability jail range of tight gas reservoirs through the gas-water relative permeability curve. *Frontiers in Physics*. **10**, p. 923762. Available from: <https://doi.org/10.3389/fphy.2022.923762>
- Gonzalez-Gonzalez, A., Valderrama, J. M., Gschaider, C. T., Carcamo, R. A., Verdugo-Dobronic, M., Canessa, N. D., Perez-Perez, A., Velasquez-Arauna, A., Sanchez-Ojeda, J., Ahumada-Villar, M. and Gonzalez-Vidal, M. 2018. Desarrollo del play tight gas zona glauconítica, Bloque Arenal, Cuenca de Magallanes - Chile: caso estudio. *10° Congreso de Exploración y Desarrollo de Hidrocarburos*. Mendoza, Argentina: IAPG.
- Gray, D.H. and Rex, R.W. 1966. Formation damage in sandstones caused by clay dispersion and migration. *Clays and Clays Minerals*. **14**, pp. 355-366. Available from: <https://doi.org/10.1346/CCMN.1966.0140131>
- Gregory, A. R. 1976. Fluid saturation effects on dynamic elastic properties of sedimentary rocks. *Geophysics*. **41**(5), pp. 895-921.
- Guanochanga, J., 2013. *Modelo geológico, caracterización petrofísica y cálculo de reservas, en la Arenisca "T" Superior del Campo Mariann 4A y Mariann Norte en el Bloque Tarapoa*. Geology Engineering thesis, Universidad Central de Ecuador.
- Guisse, P., Grattoni, C., Allshorn, S., Fisher, Q.J. and Schiffer, A. 2017. Stress sensitivity of mercury injection measurements. *International Symposium of the Society of Core Analysts*. Vienna: SCA, p. SCA217-011.
- Guliyev, E. and Davis, T.L. 2007. Interpretation of Vp/Vs velocity ratio for improved tight gas sandstone reservoir characterization, Rulison field,

- Colorado. *SEG Annual Meeting*. San Antonio, Texas: SEG, p. SEG-2007-1451.
- Gunter, G.W., Viro, E.J. and Wolgemuth, K. 2012. Identifying value added opportunities by integrating well log interpretation, petrophysical rock types and flow units: introducing a new multi-component stratigraphic modified Lorenz method. *SPWLA 53rd Annual Logging Symposium*. Cartagena, Colombia: SPWLA, p. SPWLA-2012-170.
- Hamada, G.M. 2004. Reservoir fluids identification using Vp/Vs ratio. *Oil & Gas Science and Technology*. **59**(6), pp. 649-654. Available from: <https://doi.org/10.2516/ogst:2004046>
- Han, D.H., Nur, A. and Morgan, D., 1986. Effects of porosity and clay content on wave velocities in sandstones. *Geophysics*. **51**(11), pp.2093-2107.
- Harder, H. 1969. Boron content of sediments as a tool in facies analysis. *Sedimentary Geology*. **4**(1-2), pp. 153-175.
- Hartmann, D.J. and Coalson, E.B., 1990. *Evaluation of the Morrow Sandstone in Sorrento Field, Cheyenne County, Colorado*.
- Haskett, S.E., Narahara, G.M. and Holditch, S.A. 1988. A method for the simultaneous determination of permeability and porosity in low-permeability cores. *SPE Form Eval*. **3**(03), pp.651–658. Available from: <https://doi.org/10.2118/15379-PA>
- Hatcher, G. B., Chen, H., Rahman, S. S. and Hogg, P. F. 1996. Evaluating formation damage risks in a glauconitic sandstone reservoir: a case history from the offshore North West Shelef of Australia. *SPE Asia Pacific Oil and Gas Conference*. Adelaide, Australia: SPE, p. SPE-37014. Available from: <https://doi.org/10.2118/37014-MS>
- Haynes, W.M. 2016. *CRC Handbook of Chemistry and Physics 97th edition*. (W. M. Haynes, ed.). Boca Raton, FL: Taylor and Francis, an imprint of CRC Press.
- Herrick, D.C. and Kennedy, W.D., 1994. Electrical efficiency—A pore geometric theory for interpreting the electrical properties of reservoir rocks. *Geophysics*. **59**(6), pp.918-927. Available from: <https://doi.org/10.1190/1.1443651>
- Hook, J.R. 2003. An introduction to porosity. *Petrophysics*. **44**(03), pp. 205-212.

- Hossain, Z. 2011. *Rock-physics modelling of the North Sea greensand*. PhD Dissertation, Technical University of Denmark.
- Hossain, Z. and Cohen, A.J. 2012. Relationship among porosity, permeability, electrical and elastic properties. 2012 SEG Annual Meeting. Las Vegas, Nevada: SEG, p. SEG-2012-1496.
- Hossain, Z. and Zhou, Y. 2015. Petrophysics and rock physics modeling of diagenetically altered sandstone. *Interpretation*. **3**(01), pp. 107-120. Available from: <https://doi.org/10.1190/INT-2014-0048.1>
- Hossain, Z., Fabricius, I. L. and Christense, H. F. 2009. Elastic and nonelastic deformation of greensand. *The Leading Edge*. **28**(1), pp. 86-88. Available from: <https://doi.org/10.1190/1.3064151>
- Hossain, Z., Mukerji, T., Dvorkin, J. and Fabricius, I. L. 2011a. Rock physics model of glauconite greensand from the North Sea. *Geophysics*. **76**(6), pp. E199-E209. Available from: <https://doi.org/10.1190/geo2010-0366.1>
- Hossain, Z., Grattoni, C. A., Solymar, M. and Fabricius, I. L. 2011b. Petrophysical properties of greensand as predicted from NMR measurements. *Petroleum Geoscience*. **17**, pp. 111-125. Available from: <https://doi.org/10.1144/1354-079309-038>
- Hossain, Z., Mukerji, T. and Fabricius, I. L. 2012. Vp-Vs relationship and amplitude variation with offset modeling of glauconitic greensand. *Geophysical Prospecting*. **60**(1), pp. 117-137. Available from: <https://doi.org/10.1111/j.1365-2478.2011.00968.x>
- Hower, J. 1961. Some factors concerning the nature and origin of glauconite. *American Mineralogist: Journal of Earth and Planetary Materials*. **46**(3-4_Part_1), pp. 313-334.
- Hugget, J.M. 2021. Glauconites. In: Alderton, D. and Scott, A.E. ed(s). *Encyclopedia of Geology*. Academy Press, pp. 334-340.
- Jaeger, J. C., Cook, N. G. W. and Zimmerman, R. W. 2007. *Fundamentals of rock mechanics*. 4th edition. Oxford: Blackwell Publishing.
- Jait, D. M., Cevallos, M., Molinari, M. L., Cangini, A., Mas-Cattapan, F. and Vega, V. 2018. Exploración y desarrollo de reservorios de baja permeabilidad de la Formación Magallanes en el Bloque El Cerrito, Cuenca Austral, Argentina. *10° Congreso de Exploración y Desarrollo de Hidrocarburos*. Mendoza, Argentina: IAPG.

- Jones, F.O. 1964. Influence of chemical composition of water on clay blocking of permeability. *Journal of Petroleum Technology*. **16**(04), pp. 441-446. Available from: <https://doi.org/10.2118/631-PA>
- Jones, F.O. and Owens, W.W. 1980. A laboratory study of low-permeability gas sands. *Journal of Petroleum Technology*. **32**(09), pp.1631-1640. Available from: <https://doi.org/10.2118/7551-PA>
- Jones, S.C. 1997. A technique for faster pulse-decay permeability measurements in tight rocks. *SPE Formation Evaluation*. **12**(01), pp.19-25. Available from: <https://doi.org/10.2118/28450-PA>
- Juhasz, I. 1988. Porosity systems and petrophysical models used in formation evaluation. In: *Society of Petrophysicists and Well Log Analysts, London Chapter, Porosity Seminar*.
- Kamath, J. 1992. Evaluation of accuracy of estimating air permeability from mercury-injection data. *SPE Formation evaluation*. **7**(04), pp. 304-310. Available from: <https://doi.org/10.2118/18181-PA>
- Katz, A. J. and Thompson, A. H. 1986. Quantitative prediction of permeability in porous rock. *Physical review B*. **34**(11), p. 8179. Available from: <https://doi.org/10.1103/PhysRevB.34.8179>
- Katz, A. J. and Thompson, A. H. 1987. Prediction of rock electrical conductivity from mercury injection measurements. *Journal of Geophysical Research: Solid Earth*. **92**(B1), pp. 599-607. Available from: <https://doi.org/10.1029/JB092iB01p00599>
- Kennedy, W.D. and Herrick, D.C. 2012. Conductivity models for Archie rocks. *Geophysics*. **77**(3), pp. WA109-WA128. Available from: <https://doi.org/10.1190/geo2011-0297.1>
- Kenyon, W.E. 1997. Petrophysical principals of applications of NMR logging. *The Log Analyst*. **38**(02).
- Khilar, K.C. and Fogler, H.S. 1983. Water sensitivity of sandstones. *Society of Petroleum Engineers*. **23**(01), pp. 55-64.
- Klein, J. D., Little, L., Scheihing, M. and Seifert, D. 2006. Formation evaluation and permeability prediction in a highly heterogeneous reservoir: the Kuparuk C-Sand. *SWPLA 47th Annual Logging Symposium*. Veracruz, Mexico: SPWLA, p. SPWLA-2006-FFF.

- Klinkenberg, L. J. 1941. The permeability of porous media to liquid and gases. *Drilling and Production Practice. American Petroleum Institute.* pp. 200-213.
- Knapp, L.J., Nanjo, T., Uchida, S., Haeri-Ardakani, O., and Sanei, H., 2018. Investigating Influences on Organic Matter Porosity and Pore Morphology in Duvernay Formation Organic-Rich Mudstones. *SPWLA 24th Formation Evaluation Symposium.* Chiba, Japan: SPWLA, p. SPWLA-JFES-2018-B.
- Kolodzie Jr, S. 1980. Analysis of pore throat size and use of the Waxman-Smits equation to determine OOIP in Spindle Field, Colorado. *55th Annual Fall Technical Conference and Exhibition of the SPWLA.* Dallas, Texas: SPWLA, p. SPE-9382.
- Kozeny, J. 1927. Ueber kapillare Litung des Wassers im Boden. *Sitzungsberichte der Kaiserlichen Akademie der Wissenschaften, Wien.* **136**, pp. 271-306.
- Krinsley, D.H., Pye, K., Boggs, S. Jr. And Tovey, N.K. 1998. Backscattered Scanning Electron Microscopy and Image Analysis of Sediments and Sedimentary Rocks. Cambridge: Cambridge University Press.
- Krishnan, K.M. 2021. *Principles of materials characterization and metrology - 10. Scanning Electron Microscopy.* [Online]. Oxford University Press, pp. 413-433. [Accessed 28 June 2023]. Available at: <https://app.knovel.com/hotlink/pdf/id:kt012RLKI1/principles-materials/scanning-electron-microscopy>
- Kundt, A. and Warburg, W. 1875. Über reibung und Wärmeleitung verdünnter Gase. *Poggendorfs Annalen der Physick und Chemie.* **155**, p. 337.
- Lake, L.W. ed., 2007. *Petroleum Engineering Handbook: Reservoir Engineering and Petrophysics (Vol. 5).* Richardson, USA: Society of Petroleum Engineers.
- Langmuir, I. 1918. The adsorption of gases on plane surfaces of glass, mica and platinum. *Journal of the American Chemical Society.* **40**(9), pp. 1361-1403.
- Laplace, P. 1806. Supplement to the tenth edition. *Méchanique céleste 10.*
- Lasswell, P.M., 2006. Core analysis for electrical properties. *Petrophysics-The SPWLA Journal of Formation Evaluation and Reservoir Description.* **47**(03).

- LaTorraca, G.A., Dunn, K.J. and Bergman, D.J. 1995. Magnetic susceptibility contrast effects on NMT T2 logging. *SPWLA 36th Annual Logging Symposium*. Paris: SPWLA, p. SPWLA-1995-JJ.
- Lenormand, R. 2003. Interpretation of mercury injection curve derive pore size distribution. *International Symposium of the Society of Core Analysts*. Pau, France: SCA, p. SCA2003-52.
- Lever, A. and Dawe, R.A. 1987. Clay migration and entrapment in synthetic porous media. *Marine and Petroleum Geology*. **4**(2), pp, 112-118.
- López-Quirós, A., Sánchez-Navas, A., Nieto, F. and Escutia, C. 2020. *New insights into the nature of glauconite*. *American Mineralogist*. **105**(5), pp.674-686. Available from: <https://doi.org/10.2138/am-2020-7341>
- Luffel, D.L. and Howard, W.E., 1988. Reliability of laboratory measurement of porosity in tight gas sands. *SPE formation evaluation*. **3**(04), pp.705-710.
- Madsen, F.T. and Muller-Vonmoos, M. 1989. The swelling behaviour of clays. *Applied Clay Science*. **4**(1989), pp. 143-156.
- Markley, M., Seminario, F., Gabulle, J. and Luquez, J. 2010. Microporosity and laminations in Non-Archie reservoirs create challenges for water-saturation computation and reserves evaluation: Camisea, Peru. *SPE Latin American & Caribbean Petroleum Engineering Conference*. Lima: SPE, p. SPE-139424. Available from: <https://doi.org/10.2118/139424-MS>
- Marshall, D., Gardners, J.S., Mardon, D. and Coates, G.R. 1999. Method for correlating NMR relaxometry and mercury injection data. *International Symposium of Society of Core Analysts*. SCA, p. SCA-9511.
- Mavko, G., T. Mukerji, and J. Dvorkin. 2009. *The rock physics handbook: Tools for seismic analysis of porous media*. 2nd ed. Cambridge: University Press.
- McPhee, C., Reed, J. and Zubizarreta, I. 2015. *Core Analysis: a best practice guide*, 64. Elsevier.
- Menger, S. and Prammer, M. 2002. Developments in NMR logging, in M. Lovell and N. Parkinson, eds., *Geological applications of well logs: AAPG Methods in Exploration No. 13*, p. 55-59.
- Merck. 2023. *Dichloromethane SDS*. [Online]. [Accessed 18 May 2023]. Available from:

https://www.merckmillipore.com/GB/en/product/msds/MDA_CHEM-106454?Origin=PDP

- Mindlin, R. D. 1949. Compliance of elastic bodies in contact. *Journal of Applied Mechanics and Technical Physics*. **16**(3), pp. 259–268.
- Mo, F., Peng, X., Devegowda, D., Du, Z., Qi, Z., Tang Y., and Fang, F. 2020. Permeability jail for two-phase flow in tight sandstones: formulation, application and sensitivity studies. *Journal of Petroleum Science and Engineering*. **184**, (2020), 106583. Available from: <https://doi.org/10.1016/j.petrol.2019.106583>
- Mohnke, O., and Yaramanci, R.D. 2008. Pore size distributions and hydraulic conductivities of rocks derived from Magnetic Resonance Sounding relaxation data using multi-exponential decay time inversion. *Journal of Applied Geophysics*. **66**(3-4), pp. 73-81. Available from: <https://doi.org/10.1016/j.jappgeo.2008.05.002>
- Montaron, B. 2008. Connectivity theory - a new approach to modelling "non-Archie" rocks. SPWLA 49th Annual Logging Symposium. Austin, Texas: SPWLA, p. SPWLA-2008-GGGG.
- Morgan, D.J., Highley, D.E. and Bloodworth, A.J., 1993. Industrial Minerals laboratory Manual-Bentonite. *British Geological Survey, Technical report WG/93/20 Mineralogy and Petrology Series*, pp.1-125.
- Mortensen, J., Engstrøm, F. and Lind, I. 1998. The relation among porosity, permeability, and specific surface of chalk from the Gorm field, Danish North Sea. *SPE Reservoir Evaluation and Engineering*. **1**, pp. 245-251.
- Moss, A. K., Benson, T., and Barrow, T. 2019. An Investigation into Different Correlation Methods between NMR T2 Distributions and Primary Drainage Capillary Pressure Curves Using an Extensive Sandstone Database. *E3S Web of Conferences*. **89**(2019), pp. 02003. Available from: <https://doi.org/10.1051/e3sconf/20198902003>
- MyScope. 2023. *Beam/specimen interactions - scanning electron microscopy*. [Online]. [Accessed 28 June 2023]. Available from: https://myscope.training/#/SEMlevel_2_9
- Navarro-Perez, D., Fisher, Q., Allshorn, S., Grattoni, C. and Lorinczi, P., 2024. Multi-salinity core flooding study in clay-bearing sandstones, a contribution to geothermal reservoir characterisation. *Advances in Geosciences*. **62**, pp.71-80. Available from: <https://doi.org/10.5194/adgeo-62-71-2024>

- Neasham, J.W. 1977. The morphology of dispersed clay in sandstone reservoirs and its effect on sandstone shaliness, pore space and fluid flow properties. *SPE Annual Fall Technical Conference and Exhibition*. Denver, Colorado: SPE, p. SPE-6858-MS. Available from: <https://doi.org/10.2118/6858-MS>
- Newman, A. C. D. and Brown, G. 1987. The chemical constitution of clays. In: A.C.D. Newman (Editor). *Chemistry of clays and clay minerals, Ch. 1 Mineral. Soc. Monogr.* **6**, pp.1-128.
- Newsham, K.E., Rushing, J.A., Lasswell, P.M., Cox, J.C. and Blasingame, T.A. 2004. A comparative study of laboratory techniques for measuring capillary pressures in tight gas sands. *SPE Annual Technical Conference and Exhibition*. Houston, Texas: SPE, p. SPE-89866. Available from: <https://doi.org/10.2118/89866-MS>
- Odin, G.S. and Fullagar, P.D. 1988. Geological significance of the glaucony facies. In: G.S. Odin (Editor), *Green Marine Clays, Ch. C4. Developments in Sedimentology*. Amsterdam: Elsevier.
- Odin, G.S. and Letolle, R. 1980. Glauconitization and phosphatization environments: a tentative comparison. *SEPM Special Publications*. **29**(1980), pp. 227-237.
- Odin, G.S. and Matter, A. 1981. De glauconiarum origin. *Sedimentology*, **28**(5), pp. 611-641.
- Odom, I.E. 1984. Glauconite and celadonite minerals. *Reviews in Mineralogy and Geochemistry*. **13**(1), pp. 545-584.
- Palacky, G.J. 1988. Resistivity characteristics of geologic targets. *Electromagnetic Methods in Applied Geophysics*. **2**(3), p. 53.
- Patchett, J. G., Wiley, R. and El Bahr, M. 1993. Modeling the effects of glauconite on some openhole logs from the lower Senonian in Egypt. *SPWLA 34th Annual Logging Symposium*. Calgary: SPWLA, p. SWPLA-1993-RR.
- Peng, S., Zhang, T., Loucks, R.G. and Shultz, J. 2017. Application of mercury injection capillary pressure to mudrocks: conformance and compression corrections. *Marine and Petroleum Geology*. **88**, pp. 30-40. Available from: <https://doi.org/10.1016/j.marpetgeo.2017.08.006>
- Pettijohn, F. J., Potter, P. E., and Siever, R. 1973. *Sand and sandstone*. Springer Science & Business Media.

- Pickett, G. R. 1963. Acoustic character logs and their applications in formation evaluation. *Journal of Petroleum Technology*. **15**(06), pp. 659-667.
- Pickett, G.R., 1973. Pattern recognition as a means of formation evaluation. *The Log Analyst*. **14**(04), pp. 3-11.
- Pinto, J., Vallejos, D. and Gonzalez, A. 2022. Geología sedimentaria y diagenesis del reservorio gasifero no convencional Paleoceno de la "zona glauconítica", Bloque Arenal, Tierra del Fuego, Chile. 11° *Congreso de Exploracion y Desarrollo de Hidrocarburos*. Mendoza: IAPG.
- Pires, L.O., Fiorelli, G.L., Winter, A., and Trevisan, O.V., 2017. Petrophysical Characterization of Carbonates Heterogeneity. *Offshore Technology Conference*. Rio de Janeiro: OTC, p. OTC-28098-MS. Available from: <https://doi.org/10.4043/28098-MS>
- Pittman, E. D. 1992. Relationship of porosity and permeability to various parameters derived from mercury injection-capillary pressure curves for sandstone. *AAPG Bulletin*. **76**, pp. 191-198.
- Pittman, E. D., 1979. Porosity, diagenesis and productive capability of sandstone reservoirs. *The Society of Economic Paleontologists and Mineralogists (SEPM) Special Publication*. **26**, pp. 159-173.
- Porras, J.C. and Campos, O. 2001. Rock typing: a key approach for petrophysical characterization and definition of flow units, Santa Barbara field, Eastern Venezuelan Basin. *SPE Latin American and Caribbean Petroleum Engineering Conference*. Buenos Aires: SPE, p. SPE-69458. Available from: <https://doi.org/10.2118/69458-MS>
- Porras, J.C., Barbato, R. and Khazen, L. 1999. Reservoir flow units: a comparison between three different models in the Santa Barbara and Pirital fields, North Monagas Area, Eastern Venezuelan Basin. *SPE Latin American and Caribbean Petroleum Engineering Conference*. Caracas: SPE, p. SPE-53671. Available from: <https://doi.org/10.2118/53671-MS>
- Poupon, A. and Leveaux, J. 1971. Evaluation of water saturations in shaly formations. *Trans. SPWLA 12th Ann. Logging Symp.*, O1-2. (Full text in Shaly Sand Reprint volume, SPWLA, Houston, pp IV 81-95).
- Pratama, E., Ismail, M.S. and Ridha, S. 2017. An integrated workflow to characterize and evaluate low resistivity pay and its phenomenon in a

- sandstone reservoir. *Journal of Geophysics and Engineering*. **14**(3), pp. 513-519. Available from: <https://doi.org/10.1088/1742-2140/aa5efb>
- Prayoga, O. A., Wicaksono, B., Setyoko, S., Wibowo, A., Wijaksono, E., Sulistyono, Momem, M. and Zulmi, I. 2018. Integrated analysis for reservoir characterization of low resistivity glauconitic shaly sand reservoir of Miocene Ngryong Sandstone: implications for saturation modelling at low contrast hydrocarbon pay zone. *2nd SPWLA Asia Pacific Technical Symposium*. Bogor, Java: SPWLA, p. SPWLA-2018-1810.
- Purcell, W. R. 1949. Capillary pressures-their measurement using mercury and the calculation of permeability therefrom. *Journal of Petroleum Technology*. **1**(02), pp. 39-48.
- Raymer, L.L., Hunt, E.R. and Gardner, J.S., 1980, July. An improved sonic transit time-to-porosity transform. In *SPWLA Annual Logging Symposium* (pp. SPWLA-1980). SPWLA.
- Revil, A. and Mahardija, H, 2013. Coupled hydromechanical and electromagnetic disturbances in unsaturated porous materials. *Water Resources Research*. **49**(2), pp. 744-766. Available from: <https://doi.org/10.1002/wrcr.20092>
- Rietveld, H.M. 1969. A profile refinement method for nuclear and magnetic structures. *Journal of Applied Crystallography*. **2**(2), pp. 65-71.
- Rietveld, H.M. 1969. A profile refinement method for nuclear and magnetic structures. *Journal of Applied Crystallography*. **2**(2), pp. 65-71.
- Rihayat, T., Salim, S., Arlina, A., Fona, Z., Jalal, R., Alam, P.N., Sami, M., Syarif, J. and Juhan, N., 2018, March. Determination of CEC value (cation exchange capacity) of bentonites from North Aceh and Bener Meriah, Aceh Province, Indonesia using three methods. In *IOP Conference Series: Materials Science and Engineering* (Vol. 334, No. 1, p. 012054). IOP Publishing.
- Rojas, E., Davis, T.L., Batzle, M., Prasad, M. and Michelena, R.J., 2005, November. Vp-Vs ratio sensitivity to pressure, fluid, and lithology changes in tight gas sandstones. In *SEG International Exposition and Annual Meeting* (pp. SEG-2005). SEG.
- Rueslåtten, H., Eidsemo, T. & Slot-Petersen, C. 1998b. NMR studies of iron-rich sandstone oil reservoir. *International Symposium of Society of Core Analysts*. SCA, p. SCA-9821.

- Saidian, M. and Prasad, M. 2016. Effect of mineralogy on nuclear magnetic resonance surface relaxivity: a case study of Middle Bakken and Three Forks formations. *Fuel*. **161**(2015), pp. 197-206. Available from: <https://doi.org/10.1016/j.fuel.2015.08.014>
- Sampath, K. and Keighin, C.W. 1982. Factors affecting gas slippage in tight sandstones of cretaceous age in the Uinta basin. *Journal of Petroleum Technology*. **34**(11), pp. 2715-2720. Available from: <https://doi.org/10.2118/9872-PA>
- Sander, R., Pan, Z. & Connell, L.D. 2017. Laboratory measurement of low permeability unconventional gas reservoir rock: a review of experimental methods. *Journal of Natural Gas Science and Engineering*. **37**(2017), pp. 248-279. Available from: <https://doi.org/10.1016/j.jngse.2016.11.041>
- Schlömer, S. and Krooss, B. M. 1997. Experimental characterisation of the hydrocarbon sealing efficiency of cap rocks. *Marine and Petroleum Geology*. **14**(5), pp. 565-580.
- Schlumberger, 2020. The Schlumberger Oilfield Glossary website. Available from: <https://www.glossary.oilfield.slb.com/en/>
- Schlumberger. 1989. *Log Interpretation, Principles/Applications*. Schlumberger Wireline and Testing.
- Schlumberger. 1997. *Log interpretation charts*. Houston: Schlumberger Wireline & Testing.
- Schlumberger. 2006. ECS elemental capture spectroscopy sonde. [Online]. [Accessed 26 February 2021]. Available from: <https://www.slb.com/-/media/files/fe/brochure/ecs-brochure>
- Schlumberger. 2014. CMR-Plufs combinable magnetic resonance tool. [Online]. [Accessed 26 February 2021]. Available from: <https://www.slb.com/-/media/files/fe/product-sheet/cmr-plus-ps>
- Schlumberger. 2016. The defining series: Basic well log interpretation. [Online]. [Accessed 01 September 2020]. Available from: <https://www.slb.com/resource-library/oilfield-review/defining-series/defining-log-interpretation>
- Schowalter, T.T. 1979. Mechanics of secondary hydrocarbon migration and entrapment 1. *AAPG Bulletin*. **63**(5), pp. 723-760.

- Serra, O. 1984. Fundamentals of well-log interpretation. *Part 1: The acquisition of logging data, 15A*. Elsevier.
- Seyama, H., Soma, M., and Theng, B.K.G. 2013. X-ray photoelectron spectroscopy. In: Bergaya, F., Theng, B.K.G. and Lagaly, G. ed. *Developments in Clay Science*. Elsevier, p. 865.
- Shanley, K.W., Cluff, R.M., and Robinson, J.W. 2004. Factors controlling prolific gas production from low-permeability sandstone reservoirs: implications for resource assessment, prospect development, and risk analysis. *AAPG Bulletin*. **88**(August 2004), pp. 1083-1121.
- Simpson, G.A., Fishman, N.S. and Hari-Roy, S. 2018. New Nuclear Magnetic Resonance Log T2 Cut-off Interpret Parameters for the Unconventional Tight Oil of the Bakken Petroleum System Using 2-D NMR Core Laboratory Measurements on Native State and Post-Cleaned Core Samples. *SPWLA 59th Annual Logging Symposium*. London: SPWLA, p. SPWLA-2018-GGGG.
- Slot-Petersen, C., Eidesmo, T., White, J. and Rueslatten, H.G. 1998. NMR formation evaluation applications in a complex low-resistivity hydrocarbon reservoir. *SPWLA 39th Annual Logging Symposium*. Keystone, Colorado: SPWLA, p. SPWLA-1998-TT.
- Sneider, R. M. 2003. Worldwide examples of low resistivity pay. *Houston Geological Society Bulletin*. **45**, pp. 47-59.
- Sneider, R. M. and King, H.R. 1984. Reservoir rock detection and characterisation. In: Elmsworth, Case Study of a Deep Basin Gas Field, J.A. Masters (ed.). *American Association of Petroleum Geologist, Memor 38*, pp. 205-282.
- Sneider, R. M., and King, H.R., Hawkes, H.E. and Davis, T.B. 1983. Methods for detection and characterization of reservoir rock, deep basin gas area, western Canada. *Journal of Petroleum Technology*. **35**(09), pp. 1725-1734.
- Soeder, D. J. 1986. Laboratory drying procedures and the permeability of tight sandstone core. *SPE Formation Evaluation*. **1**(01), pp. 16-22.
- Soleymanzadeh, A., Helalizadeh, A., Jamialahmadi, M. and Soulgani, B.S., 2021. Development of a new model for prediction of cementation factor in tight gas sandstones based on electrical rock typing. *Journal of Natural Gas Science and Engineering*. **94**, p.104128. Available from: <https://doi.org/10.1016/j.jngse.2021.104128>

- Svendsend, H.E. 2019. *MICP-Based rock typing of complex, multi-modal formations in Edvard Grieg Field*. Master thesis, Universitetet I Stavanger.
- Svendsend, H.E. 2019. *MICP-Based rock typing of complex, multi-modal formations in Edvard Grieg Field*. Master's thesis, University of Stavanger.
- Swanson, B. F. 1981. A simple correlation between permeabilities and mercury capillary pressures. *Journal of Petroleum Technology*. **33**(12), pp. 2498-2504.
- Swanson, B.F. 1985. Microporosity in reservoir rocks: its measurement and influence on electrical resistivity. *The Log Analyst*. **26**(6), pp. 42-70.
- Sweeney, S.A. and Jennings, Jr. 1960. Effect of wettability on the electrical resistivity of carbonate rock from a petroleum reservoir. *The Journal of Physical Chemistry*. **64**(5), pp. 551-553.
- Taber, D.R., Vickers, M.K., and Winn Jr., R..D. 1995. The definition of the Albian 'A' Sand reservoir fairway and aspects of associated gas accumulation in the North Celtic Sea Basin. *Geological Society, London, Special Publications*. **93**(1), pp. 227-244. Available from: <https://doi.org/10.1144/GSL.SP.1995.093.01.16>
- Tao, S., Gao, L. and Pan, Z. 2019. Swelling of clay minerals and its effect on coal permeability and gas production: a case study of southern Qinshui Basin, China. *Energy Science & Engineering*. **7**(2), pp. 515-528. Available from: <https://doi.org/10.1002/ese3.301>
- TARR. 2023. New TESCAN Vega3 XMU scanning electron microscope. [Online]. [Accessed 28 June 2023]. Available from: <https://www.tarrc.co.uk/pages/NewSEM2015.htm>
- Tatham, R.H.1982. Vp/Vs and lithology. *Geophysics*. **47**(3), pp. 336-344. Available from: <http://dx.doi.org/10.1190/1.1441339>
- Tedrow, J.C. 2002. *Greensand and greensand soils in New Jersey: a review*. Rutgers, The State University of New Jersey.
- Thomas, E.C. and Stieber, S.J. 1975. The distribution of shale in sandstones and its effect upon porosity. *SPWLA 16th Annual Logging Symposium*. New Orleans, Louisiana: SPWLA, p. SPWLA-1975-T.
- Thomas, W. H., Ringen, J. K. and Rasch, S. O. 2003. Effect of glauconite on petrophysical properties as revealed by core analysis. *International*

Symposium of the Society of Core Analysts. Pau, France: SCA, p. SCA2003-32.

- Thomeer, J. 1983. Air permeability as a function of three pore-network parameters. *Journal of Petroleum Technology*. **35**(04), pp. 809-814. Available from: <https://doi.org/10.2118/10922-PA>
- Thompson, G.R. and Hower, J. 1975. The mineralogy of glauconite. *Clays and Clays Mineral*. **23**, pp. 289-300.
- Tiab, D. and Donaldson, E.C. 2012. *Petrophysics - theory and practice of measuring rock and fluid transport properties*. 3rd ed. Elsevier.
- Timur, A. 1968. An investigation of permeability, porosity, and residual water saturation relationships. *SPWLA 9th Annual Logging Symposium*. New Orleans, Louisiana: SPWLA, p. SPWLA-1968-J.
- Tosaya, C. A. 1982. *Acoustical properties of clay-bearing rocks*. PhD thesis, Stanford University.
- Urban, E. and Aguilera, R. 2015. Determination of principal in-situ stress magnitude from well logs in unconventional reservoirs: a practical application in Willesden Green Field, Canada. *SPE Latin American and Caribbean Petroleum Engineering Conference*. Quito: SPE, p. SPE-177261-MS. Available from: <https://doi.org/10.2118/177261-MS>
- Vallabhaneni, S., Saraf, R. and Priyadarshy, S., 2019. Machine-learning-based petrophysical property modeling. *SPE Europec featured at 81st EAGE conference and exhibition*. London: SPE, p. SPE-195436-MS. Available from: <https://doi.org/10.2118/195436-MS>
- Van Houten, F. B. and Purucker, M.E. 1984. Glauconitic peloids and chamositic ooids - favorable factors, constraints, and problems. *Earth-Science Reviews*. **20**(03), pp. 211-243. Available from: [https://doi.org/10.1016/0012-8252\(84\)90002-3](https://doi.org/10.1016/0012-8252(84)90002-3)
- Van Olphen, H. 1977. *An introduction to clay colloid chemistry: for clay technologists, geologists, and soil scientists*. 2nd edition. New York: Wiley.
- Van Olphen, H. and Fripiat, J.J. 1979. Data handbook for clay materials and other non-metallic minerals. *Soil Science*. **131**(1), p. 62.
- Vanderlinde, W. 2019. Scanning electron microscopy. In: Gandhi, T. ed. *Microelectronics failure analysis desk reference*. [Online]. 7th Edition. ASM International, pp. 413-433. Available at:

<https://app.knovel.com/hotlink/pdf/id:kt0121SDO3/microelectronics-failure/microelect-scanning-electron>

- Volokitin, Y., Looyestijn, W., Slijkerman, W. and Hofman, J. 1999. Constructing capillary pressure curves from NMR log data in the presence of hydrocarbons. *SPWLA 40th Annual Logging Symposium*. Oslo: SPWLA, p. SPWLA-1999-KKK.
- Washburn, E.W. 1921. The dynamics of capillary flow. *Physical Review*. **17**(3), p. 273.
- Waxman, M. H. and Smits, L. J. M. 1968. Electrical conductivities in oil-bearing shaly sands. *Society of Petroleum of Engineering Journal*. 8(02), pp. 107-122. Available from: <https://doi.org/10.2118/1863-A>
- Weaver, C.E. 1989. *Clays, muds, and shales*. The Netherlands: Elsevier.
- Webmineral. 2019. *Mineralogy database*. [Online]. Available from: <https://www.webmineral.com/>
- Wells, J.D. and Amaefule, J.O. 1985. Capillary pressure and permeability relationships in tight gas sands. *SPE/DOE Low Permeability Gas Reservoir Symposium*. Denver, Colorado: SPE, p. SPE-13879. Available from: <https://doi.org/10.2118/13879-MS>
- Wentworth, C.K. 1922. A scale of grade and class terms for clastic sediments. *The journal of geology*. **30**(5), pp. 377-392.
- Wiley, R. and Patchett, J.G. 1990. CNL neutron porosity modeling, a step forward. *The Log Analyst*. **31**(03), pp. 133-149.
- Wilson, L., Wilson, M.J., Green, J. and Patey, I. 2014. The influence of clay mineralogy on formation damage in North Sea reservoir sandstone: a review with illustrative examples. *Earth-Science Reviews*. **134** (2014), pp. 70-80. Available from: <https://doi.org/10.1016/j.earscirev.2014.03.005>
- Wilson, M.D. 1982. Origins of clays controlling permeability and porosity in tight gas sands. *Journal of Petroleum Technology*. **34**(12), pp. 2871-2876. Available from: <https://doi.org/10.2118/9843-PA>
- Wilson, M.D. and Pittman, E.D. 1977. Authigenic clays in sandstones: recognition and influence on reservoir properties and paleoenvironmental analysis. *Journal of Sedimentary Research*. **47**(1), pp. 3-31. Available from: <https://doi.org/10.1306/212F70E5-2B24-11D7-8648000102C1865D>

- Withjack, E.M., Devier, C. and Michael, G. 2003. The role of x-ray computed tomography in core analysis. *SPE Western Regional/AAPG Pacific Section Joint Meeting*. Long Beach, California: SPE, p. SPE-83467. Available from: <https://doi.org/10.2118/83467-MS>
- Worden, R.H., Griffiths, J., Wooldridge, L.J., Utley, J.E.P., Lawan, A.Y., Muhammed, D.D., Simon, N. and Armitage, P.J.. 2020. Chlorite in sandstones. *Earth-Science Reviews*. **204**, p. 103105. Available from: <https://doi.org/10.1016/j.earscirev.2020.103105>
- Worthington, P. F. 1985. The evolution of shaly-sand concepts in reservoir evaluation. *The Log Analyst*. **26**(01) pp. 23-40.
- Worthington, P. F. 2000. Recognition and evaluation of low-resistivity pay. *Petroleum Geoscience*. **6** (1), pp. 77-92. Available from: <https://doi.org/10.1144/petgeo.6.1.77>
- Worthington, P. F. 2009. Net pay—what is it? What does it do? How do we quantify it? How do we use it? *SPE Asia Pacific Oil and Gas Conference & Exhibition*. Jakarta: SPE, p. SPE-123561. Available from: <https://doi.org/10.2118/123561-MS>
- Worthington, P. F., Pallatt, N. and Toussaint-Jackson, J.E. 1989. Influence of microporosity on the evaluation of hydrocarbon saturation. *SPE Formation Evaluation*. **4**(02) pp. 203-209. Available from: <https://doi.org/10.2118/14296-PA>
- Worthington, P.F. 1993. The uses and abuses of the Archie equations, 1: The formation factor-porosity relationship. *Journal of Applied Geophysics*. **30**(3), pp.215-228. Available from: [https://doi.org/10.1016/0926-9851\(93\)90028-W](https://doi.org/10.1016/0926-9851(93)90028-W)
- Wyllie, M. R. J. and Spangler, M. B. 1952. Application of electrical resistivity measurements to problem of fluid flow in porous media. *AAPG Bulletin*. **36**(2), pp. 359-403.
- Wyllie, M.R.J. and Gardner, G.H.F. 1958. The generalized Kozeny-Carman equation. *II WorldOil*.
- Wyllie, M.R.J., Gregory, A.R. and Gardner, L.W., 1956. Elastic wave velocities in heterogeneous and porous media. *Geophysics*. **21**(1), pp.41-70. Available from: <https://doi.org/10.1190/1.1438217>
- Xiao, J., Wang, J. and Sun, X. 2017. Fines migration: problems and treatments. *Oil and Gas Research*. **3**(1), p. 123.

- Yang, X. F., Ma, Z. Z., Zhou, Y. B., Zhang, Z.W., Liu, Y. M., Wang, D.D. and Zhao, Y. B. 2019. Reservoir characteristics and hydrocarbon accumulation of the glauconitic sandstone in the Tarapoa Block, Oriente Basin, Ecuador. *Journal of Petroleum Science and Engineering*. **173**, pp. 558-568. Available from: <https://doi.org/10.1016/j.petrol.2018.10.059>
- Young, T. 1805. An essay on the cohesion of fluids. *Proceeding of the Royal Society of London Series I*. **1**, pp. 171-172.
- Zhang, Y. J., Lollback, P. A., Rojahn, J. S., Salisch, H. A. and Stuart, W. J. 1996. A methodology for estimating permeability from well logs in a formation of complex lithology. *SPE Asia Pacific Oil and Gas Conference and Exhibition*. Adelaide: SPE, p. SPE-37025-MS. Available from: <https://doi.org/10.2118/37025-MS>
- Zhang, Y., Salisch, H. A. and Arns, C., 2000. Permeability evaluation in a glauconite-rich formation in the Carnarvon Basin, Western Australia. *Geophysics*. **65** (1), pp. 46-53. Available from: <https://doi.org/10.1190/1.1444724>
- Ziarani, A. S. and Aguilera, R. 2012. Pore-throat radius and tortuosity estimation from formation resistivity data for tight-gas sandstone reservoirs. *Journal of Applied Geophysics*. **83**, pp. 65-73. Available from: <https://doi.org/10.1016/j.jappgeo.2012.05.008>

Appendix A: NMR empirical calibration curves

A.1 Number of scans

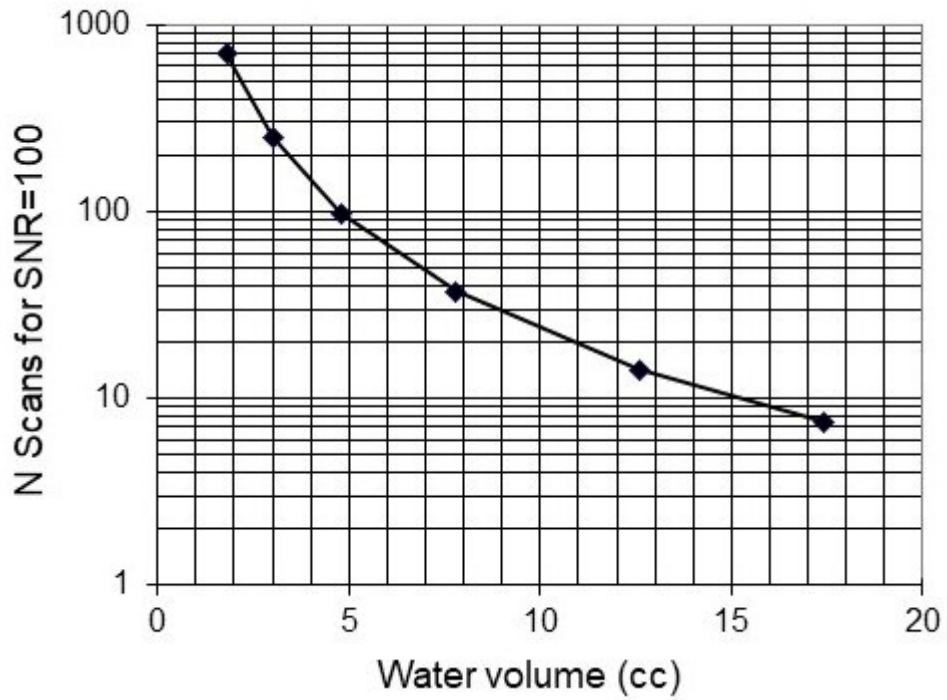


Figure A-1. Cross-plot of number of scans versus water volume.

A.2 Signal-to-Noise

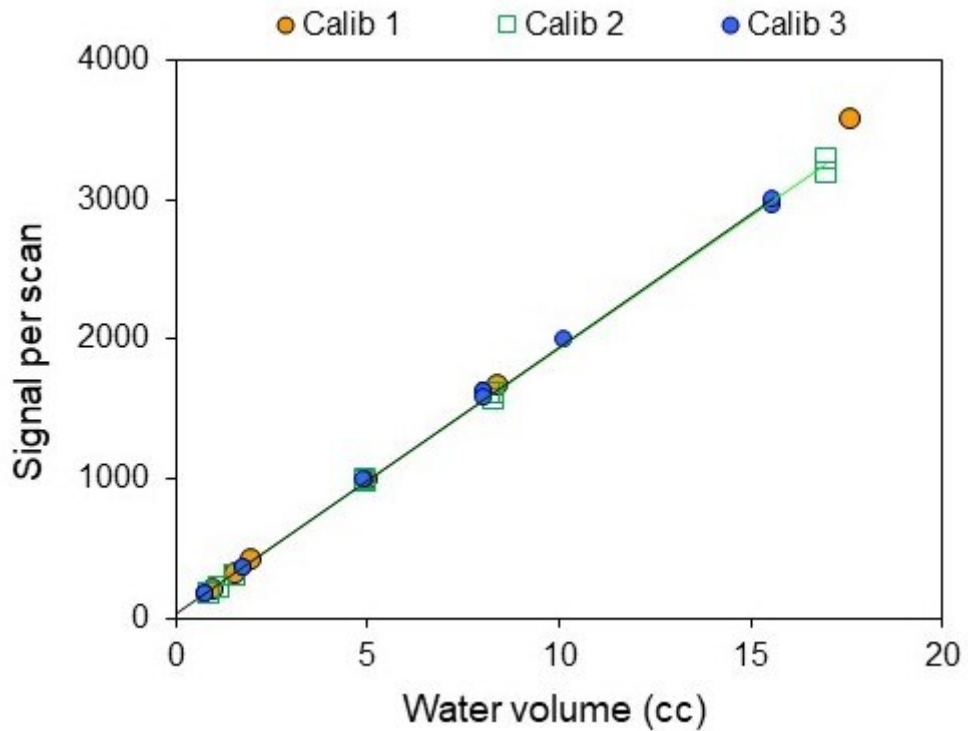


Figure A-2. Cross-plot of signal per scan versus water volume.

A.3 Hydrogen index correction

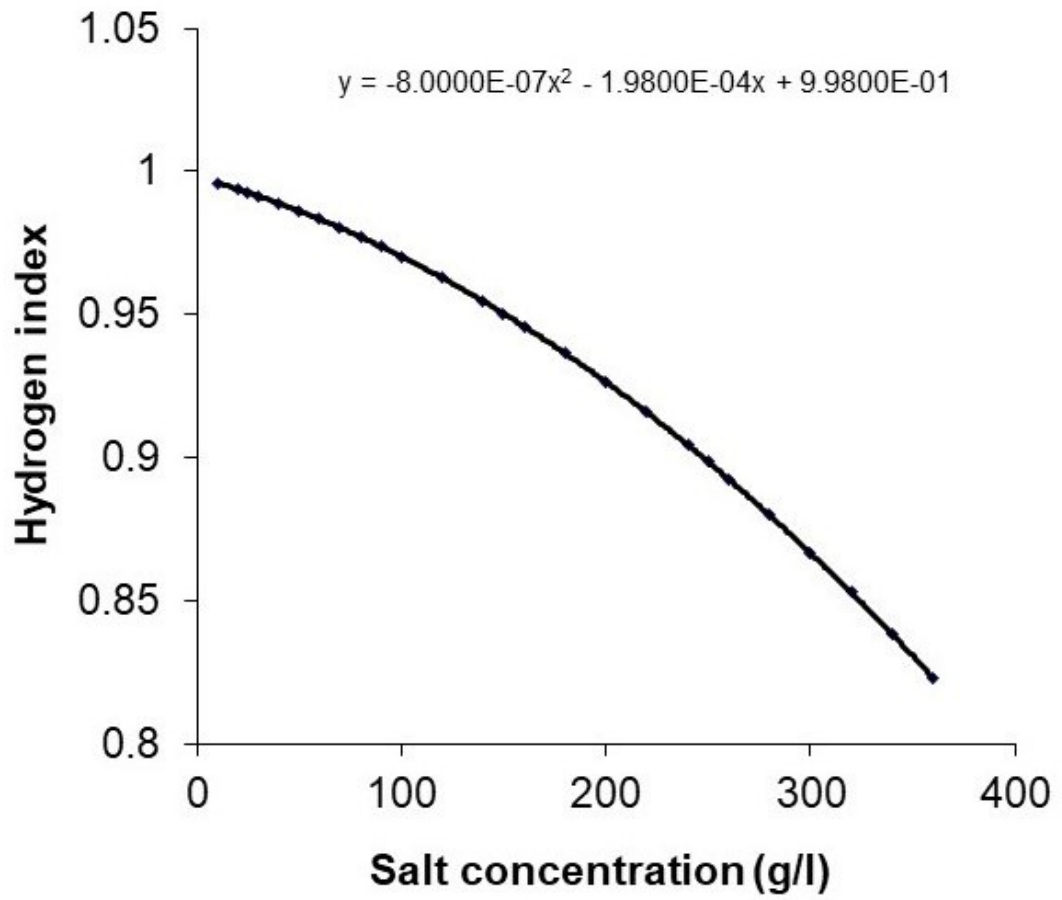


Figure A-3. Cross-plot of hydrogen index and salt concentration.

Appendix B: Core analysis data

B.1 Master list

Table B-1. Master list table of ENAP1 core plugs XRD analysis and CT voxels standard deviation.

Sample	XRD (%V/V)							CT STD (HU)
	Quartz	Plagioclase	Mica	Illite - smectite	Chlorite ³	Pyrite	Calcite	
ENAP1-1 ¹	25.1	44.1	10.89	0.0	16.2	1.9	0.0	119
ENAP1-2	29.2	33.8	0.00	6.0	31.0	0.0	0.0	168
ENAP1-6	29.5	44.2	9.09	0.0	16.7	0.5	0.0	71
ENAP1-8	20.8	46.2	11.39	0.0	21.3	0.3	0.0	40
ENAP1-9	26.6	49.0	5.71	0.9	16.2	1.7	0.0	91
ENAP1-12	30.3	40.6	0.00	0.0	27.4	0.5	1.3	45
ENAP1-13 ²								77
ENAP1-14	12.8	53.5	3.92	0.0	29.2	0.5	0.0	63
ENAP1-15	14.2	41.7	22.93	0.0	21.1	0.0	0.0	47
ENAP1-17	43.2	33.3	7.56	1.4	14.3	0.4	0.0	45
ENAP1-18	50.8	36.0	4.93	0.9	7.0	0.4	0.0	41
ENAP1-21	23.4	28.0	11.71	0.0	33.9	0.2	2.7	55
ENAP1-22	24.6	42.3	10.48	7.7	13.7	1.2	0.0	71
ENAP1-23	20.6	57.4	4.48	6.6	9.1	1.8	0.0	67
ENAP1-24	25.4	31.8	13.68	8.6	19.6	0.9	0.0	68
ENAP1-25	24.9	34.7	9.22	9.9	21.2	1.0	0.0	47
ENAP1-27	34.1	28.9	7.12	13.7	14.1	1.3	0.7	52
ENAP1-28	28.1	28.7	12.23	8.9	20.2	0.8	1.1	60
ENAP1-29	16.4	50.5	5.74	7.0	19.0	1.5	0.0	44
ENAP1-30	26.8	30.6	6.60	10.6	24.5	0.2	0.7	33
ENAP1-31	27.8	43.4	8.39	0.0	19.4	0.7	0.4	42

¹ 1.89%v/v of barite.

² Not enough sample for XRD analysis.

³ Summation of XRD kaolinite and chlorite.

Table B-2. Master list table of ENAP2 core plugs XRD analysis and CT voxels standard deviation.

Sample	XRD (%V/V)							CT STD (HU)
	Quartz	Plagioclase	Mica	Illite - smectite	Chlorite	Pyrite	Calcite	
ENAP2-8	27.7	33.9	11.0	0.6	26.8	0.0	0.0	39
ENAP2-12	29.2	41.0	10.8	4.8	11.3	3.0	0.0	231
ENAP2-17	31.9	27.7	15.4	0.9	24.1	0.0	0.0	47
ENAP2-19	24.4	40.0	6.9	13.2	14.6	1.0	0.0	50
ENAP2-24	33.8	33.6	8.0	2.0	22.2	0.4	0.0	41
ENAP2-27	16.5	48.4	8.1	9.2	15.9	2.1	0.0	296
ENAP2-33	35.0	33.3	4.5	9.0	16.6	0.4	1.3	46
ENAP2-38	25.8	42.1	4.5	13.2	12.2	1.6	0.7	83
ENAP2-44	21.8	43.4	10.7	0.7	23.3	0.2	0.0	73
ENAP2-46	18.5	53.8	5.0	8.5	14.2	0.0	0.0	176
ENAP2-53	27.6	33.7	9.7	0.1	27.2	0.3	1.5	38
ENAP2-54	21.1	14.1	2.7	0.0	46.7	0.5	14.9	279
ENAP2-62	20.5	38.9	9.7	2.0	27.1	0.1	1.7	69
ENAP2-65	29.0	40.3	5.5	4.7	19.3	0.8	0.4	91
ENAP2-76	31.4	42.0	6.2	2.2	12.2	0.5	5.6	128

Table B-3. Master list table of ENAP1 core plugs XRF analysis.

Sample	XRF (%wt)										
	SiO ₂	TiO ₂	Al ₂ O ₃	Fe ₂ O ₃	MnO	MgO	CaO	Na ₂ O	K ₂ O	P ₂ O ₅	SO ₃
ENAP1-1	62.8	0.6	13.8	8.7	0.1	1.9	1.2	4.5	1.7	0.1	1.0
ENAP1-2	59.7	0.8	12.3	14.5	0.9	3.2	1.3	3.5	0.5	0.1	0.5
ENAP1-6	67.1	0.7	13.6	6.1	0.05	2.2	1.2	4.7	1.7	0.1	0.3
ENAP1-8 ¹											
ENAP1-9	64.0	0.7	13.7	8.1	0.05	2.0	1.3	4.9	1.6	0.1	0.7
ENAP1-12	65.4	0.8	12.8	7.7	0.06	2.5	1.9	4.0	1.6	0.1	0.5
ENAP1-13 ¹											
ENAP1-14 ¹											
ENAP1-15	58.0	0.8	14.8	11.3	0.07	3.2	1.5	4.6	2.6	0.1	0.1
ENAP1-17	73.3	0.6	10.5	5.1	0.04	1.7	1.0	3.6	1.5	0.1	0.2
ENAP1-18	77.8	0.5	9.5	2.8	0.02	0.9	0.7	3.8	1.4	0.1	0.5
ENAP1-21	59.9	0.6	12.4	11.3	0.08	3.2	2.8	3.4	1.6	0.1	0.5
ENAP1-22 ¹											
ENAP1-23	62.4	0.8	15.2	6.5	0.04	1.8	1.5	5.6	1.4	0.1	0.4
ENAP1-24	58.4	0.7	16.2	8.6	0.07	2.7	2.0	4.7	1.8	0.1	0.5
ENAP1-25	61.7	0.8	14.6	8.0	0.07	2.7	2.4	3.1	2.2	0.1	0.8
ENAP1-27	65.1	0.6	13.4	7.2	0.05	2.1	1.9	2.6	2.1	0.1	0.6
ENAP1-28	63.9	0.6	13.8	8.1	0.05	2.3	2.0	2.9	2.3	0.1	0.7
ENAP1-29 ¹											
ENAP1-30	62.3	0.7	14.8	8.5	0.06	2.9	2.2	2.8	2.2	0.1	0.3
ENAP1-31	66.8	0.7	13.3	6.4	0.05	2.0	1.2	4.7	1.6	0.1	0.2

¹ Not enough sample for XRD analysis.

Table B-4. Master list table of ENAP2 core plugs XRF analysis.

Sample	XRF (%wt)										
	SiO ₂	TiO ₂	Al ₂ O ₃	Fe ₂ O ₃	MnO	MgO	CaO	Na ₂ O	K ₂ O	P ₂ O ₅	SO ₃
ENAP2-8	62.8	0.8	14.1	8.4	0.07	3.4	2.1	3.1	1.9	0.1	0.2
ENAP2-12	65.4	0.7	13.8	7.0	0.04	1.8	1.8	3.8	1.7	0.1	0.5
ENAP2-17	65.4	0.6	12.6	8.5	0.06	3.0	1.8	2.5	2.2	0.1	0.2
ENAP2-19	62.2	0.8	15.3	7.4	0.06	2.6	2.1	3.7	2.0	0.2	0.5
ENAP2-24	66.1	0.7	12.8	7.6	0.06	2.6	1.8	3.4	1.6	0.1	0.2
ENAP2-27	58.0	0.9	16.3	8.7	0.06	2.7	2.4	4.6	1.7	0.3	0.5
ENAP2-33	67.1	0.7	12.5	6.9	0.05	2.5	2.3	3.1	1.7	0.1	0.2
ENAP2-38	63.2	0.8	14.7	7.0	0.05	2.2	1.9	4.0	1.7	0.2	0.4
ENAP2-44	64.2	0.7	14.3	7.2	0.05	2.7	1.9	4.4	1.5	0.2	0.2
ENAP2-46	61.4	0.8	15.1	7.5	0.05	2.2	1.6	5.2	1.4	0.2	0.6
ENAP2-53	63.8	0.8	12.4	9.3	0.07	2.8	2.1	3.7	1.6	0.1	0.3
ENAP2-54	48.4	0.5	8.7	13.6	0.09	3.1	13.4	1.8	0.1	0.2	1.5
ENAP2-62	59.7	0.9	14.3	10.0	0.07	3.4	2.5	4.0	1.5	0.3	0.1
ENAP2-65	64.8	0.8	13.2	7.1	0.06	2.5	2.1	3.9	1.3	0.4	0.6
ENAP2-76	65.5	0.7	12.3	4.0	0.14	1.7	4.9	4.1	1.3	0.2	1.0

Table B-5. Master list table of ENAP1 core plugs specific surface area, bulk density, grain density, helium and brine porosities.

Sample	SSA _{BET} (m ² /g)	Bulk density (g/cc)		Grain density (g/cc)	Porosity (%v/v)	
		Calliper	Mercury		Helium	Brine
ENAP1-1	9.4	2.29	2.31	2.97	22.2	16.7
ENAP1-2	3.5	2.10	2.12	2.89	26.6	¹
ENAP1-6	8.6	2.26	2.28	¹	¹	15.5
ENAP1-8	9.1	2.31	2.33	2.63	11.3	14.3
ENAP1-9	7.6	2.30	2.32	2.71	14.4	14.7
ENAP1-12	7.8	2.27	2.29	¹	¹	15.3
ENAP1-13	6.9	2.02	2.24	2.48	18.0	18.0
ENAP1-14	5.3	2.29	2.32	2.78	16.5	15.1
ENAP1-15	15.0	2.36	2.39	2.87	16.5	14.3
ENAP1-17	7.4	2.09	2.12	¹	¹	21.3
ENAP1-18	5.1	2.08	2.11	2.63	19.7	20.1
ENAP1-21	9.8	2.26	2.28	2.74	16.9	17.0
ENAP1-22	8.8	2.27	2.31	¹	¹	14.9
ENAP1-23	7.4	2.32	2.35	2.84	17.2	12.4
ENAP1-24	9.4	2.25	2.32	2.72	13.5	15.8
ENAP1-25	9.7	2.32	2.35	2.74	14.1	14.8
ENAP1-27	11.8	2.24	2.32	2.67	14.3	16.4
ENAP1-28	11.8	2.29	2.32	2.95	21.2	15.8
ENAP1-29	11.8	2.31	2.32	¹	27.7	15.8
ENAP1-30	11.8	2.29	2.33	¹	28.9	15.5
ENAP1-31	11.8	2.22	2.24	2.65	15.3	16.7

¹ Outlier.

Table B-6. Master list table of ENAP2 core plugs specific surface area, bulk density, grain density, helium and brine porosities.

Sample	SSA _{BET} (m ² /g)	Bulk density (g/cc)		Grain density (g/cc)	Porosity (%v/v)	
		Calliper	Mercury		Helium	Brine
ENAP2-8	9.1	2.33	2.36	2.74	13.73	13.95
ENAP2-12	7.6	2.32	2.35	2.74	14.44	14.76
ENAP2-17	7.4	2.32	2.35	2.74	14.35	14.71
ENAP2-19	13.6	2.30	2.33	2.72	14.52	15.84
ENAP2-24	9.4	2.26	2.29	2.72	15.88	15.99
ENAP2-27	11.8	2.36	2.41	2.80	14.29	14.65
ENAP2-33	10.5	2.32	2.36	2.71	13.10	13.55
ENAP2-38	5.2	2.29	2.32	2.76	16.22	15.44
ENAP2-44	10.4	2.28	2.32	2.69	13.82	14.35
ENAP2-46	9.7	2.31	2.34	2.71	13.61	13.93
ENAP2-53	10.4	2.35	2.37	2.74	13.43	13.33
ENAP2-54	3.2	2.15	2.19	2.80	21.82	22.36
ENAP2-62	12.5	2.28	2.32	2.74	15.25	15.21
ENAP2-65	8.1	2.23	2.26	2.69	15.79	14.51
ENAP2-76	6.9	2.24	2.26	2.70	16.25	16.05

Table B-7. Master list table of ENAP1 core plugs MICP and NMR porosities, Klinkenberg permeability at three confining pressures (C.P.), and brine permeability measured at 1,500 psig C.P.

Sample	Porosity (%v/v)		Klinkenberg permeability (mD)			Brine permeability (mD)
	MICP	NMR	1,500 psig C.P.	2,500 psig C.P.	3,500 psig C.P.	
ENAP1-1	15.6	15.6	0.0027 ¹			0.00083
ENAP1-2	20.7	20.2	0.56	0.54	0.54	0.065
ENAP1-6	14.5	14.3	0.0036	0.0025	0.0024	0.00065
ENAP1-8	13.2	12.5	0.00079	0.00098	0.0012	0.00022
ENAP1-9	14.0	13.7	0.0020	0.0020	0.0020	0.00033
ENAP1-12	14.5	14.1	0.0016	0.0015	0.0013	0.00019
ENAP1-13	16.7	14.8	²	²	0.0016	0.00048
ENAP1-14	13.0	12.3	0.0044	0.0040	0.0039	0.00041
ENAP1-15	13.2	³	0.0039	0.0020	0.0011	0.00012
ENAP1-17	20.4	20.6	0.013	0.014	0.013	0.0050
ENAP1-18	20.1	20.8	0.028	0.028	0.028	0.015
ENAP1-21	17.4	³	0.0036	0.0025	0.0018	0.00019
ENAP1-22	13.8	13.8	0.0057	0.0049	0.0034	0.00027
ENAP1-23	13.6	12.1	0.007	0.0059	0.0052	0.00021
ENAP1-24	15.4	14.8	0.0020	0.0018	0.0014	0.00030
ENAP1-25	12.2	12.3	0.32	0.20	0.14	0.0012
ENAP1-27	13.1	14.9	0.14	0.087	0.060	0.0044
ENAP1-28	13.7	13.3	0.0029	0.0020	0.0015	0.00015
ENAP1-29	15.0	13.8	0.0039	0.0019	0.0011	0.00065
ENAP1-30	13.9	13.1	0.0025	0.0011	0.00096	0.00011
ENAP1-31	16.4	15.8	0.0025	0.0032	0.0038	0.0015

¹ Only at this confining pressure the core plug could be measured.

² Klinkenberg permeability could not be established.

³ Outlier.

Table B-8. Master list table of ENAP2 core plugs MICP and NMR porosities, Klinkenberg permeability at three confining pressures (C.P.), and brine permeability measured at 1,500 psig C.P.

Sample	Porosity (%v/v)		Klinkenberg permeability (mD)			Brine permeability (mD)
	MICP	NMR	1,500 psig C.P.	2,500 psig C.P.	3,500 psig C.P.	
ENAP2-8	11.9	12.1	0.014	0.011	0.0069	0.00068
ENAP2-12	13.0	13.5	0.85	0.53	0.49	2.86 ¹
ENAP2-17	12.2	13.0	0.0021	0.0011	0.00095	0.00022
ENAP2-19	11.9	13.0	2.15	1.56	1.14	0.0071
ENAP2-24	14.4	15.2	0.027	0.022	0.016	0.0020
ENAP2-27	10.9	12.0	0.88	0.60	0.40	0.087
ENAP2-33	12.3	12.6	0.015	0.0089	0.0052	0.00012
ENAP2-38	14.0	13.3	0.0024	0.0019	0.0015	0.0010
ENAP2-44	13.3	13.8	0.0082	0.0075	0.0061	0.00017
ENAP2-46	13.6	²	0.0033	0.0027	0.0024	0.00003
ENAP2-53	11.9	²	0.0027	0.0016	0.0010	0.00002
ENAP2-54	14.9	²	0.10	0.098	0.092	0.0041
ENAP2-62	13.8	12.9	0.0032	0.0024	0.0017	0.00003
ENAP2-65	16.2	15.9	0.0042	0.0038	0.0036	0.00040
ENAP2-76	16.6	16.0	0.0042	0.0039	0.0037	0.00012

¹ This core plug presented a failure after the saturation process, affecting the measurement. The steady-state technique was only used on this sample.

² Outlier.

B.2 QXRD and XRF trends versus depth

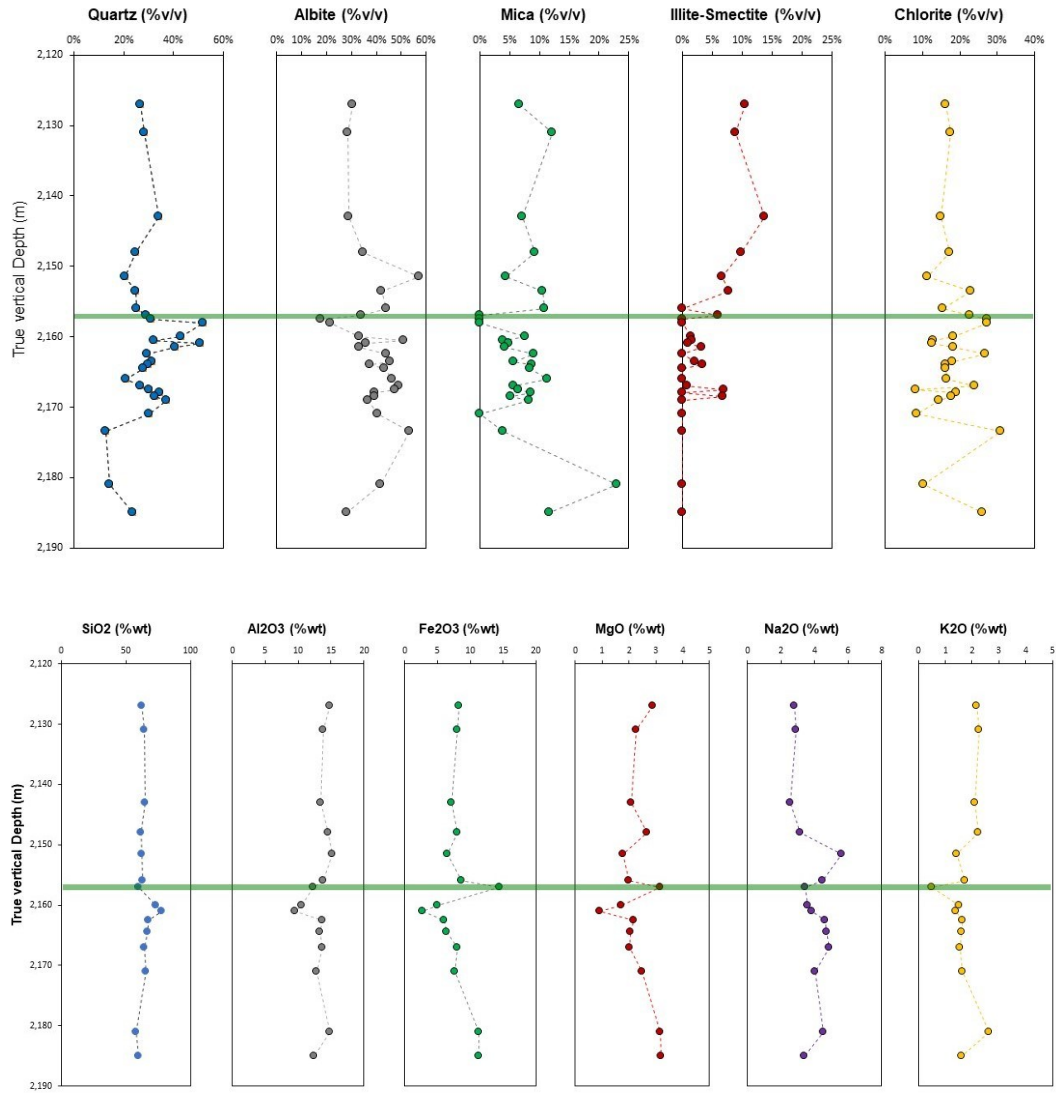


Figure B-1. ENAP1 mineralogy (top) and major chemical components (bottom) against depth. The green rectangle indicates the location of the pay sand core.

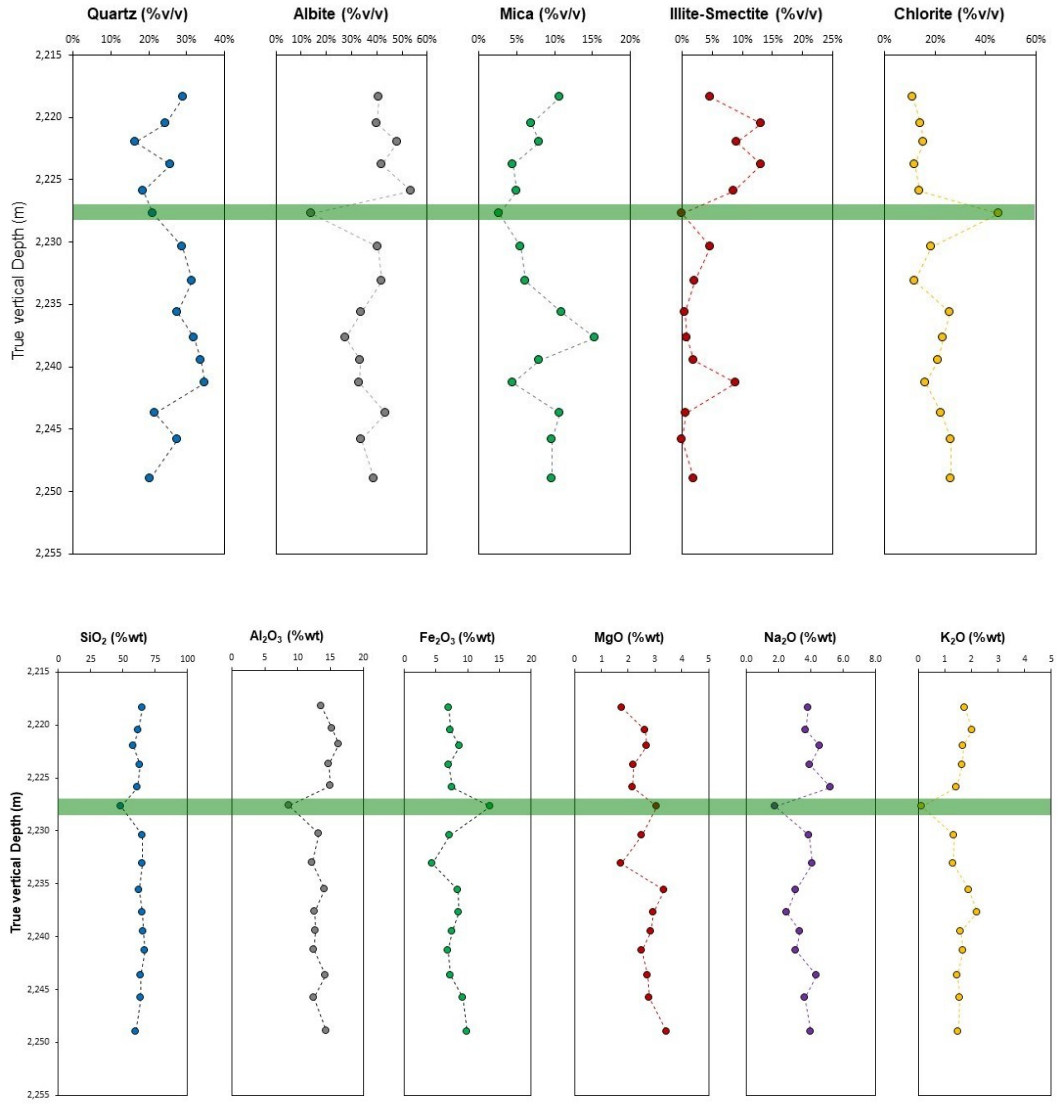


Figure B-2. ENAP2 mineralogy (top) and major chemical components (bottom) against depth. The green rectangle indicates the location of the pay sand core.

Appendix C: MICP and NMR data

C.1 Master list.

Table C-1. Master list table of ENAP1 core plugs NMR relevant output data.

Sample	PSD curve	Scaling factor ($\mu\text{m}/\text{ms}$)	Surface relaxivity ($\mu\text{m}/\text{ms}$)	T ₂ geometric (ms)	T ₂ at P _{thr} (ms)	T ₂ at higher peak (ms)
ENAP1-1	USP	0.005	5.0	3.0	2.7	3.5
ENAP1-2	BBP	0.002	2.0	14.1	114.2	37.7
ENAP1-6	USP	0.004	4.0	3.7	3.7	5.3
ENAP1-8	USP	0.003	3.3	2.6	3.3	3.5
ENAP1-9	USP	0.003	3.3	2.7	3.3	3.1
ENAP1-12	USP	0.003	3.3	3.2	3.3	4.0
ENAP1-13	USP	0.003	3.3	4.8	4.4	4.6
ENAP1-14 ¹						
ENAP1-15	USP	0.003	3.3	1.6	1.5	5.3
ENAP1-17	BSP	0.003	3.3	6.4	6.6	8.1
ENAP1-18	BSP	0.003	3.3	9.3	6.6	12.3
ENAP1-21	USP	0.003	3.3	2.8	1.5	3.1
ENAP1-22	USP	0.003	3.3	2.8	3.3	2.7
ENAP1-23	USP	0.003	3.3	2.2	3.3	3.1
ENAP1-24	USP	0.003	3.3	2.1	1.5	1.8
ENAP1-25	USP	0.003	3.3	1.6	1.5	1.5
ENAP1-27	USP	0.003	3.3	2.1	1.5	2.0
ENAP1-28	BSP	0.004	4.0	1.4	1.6	1.5
ENAP1-29	BSP	0.003	3.3	1.7	1.5	1.3
ENAP1-30	BSP	0.004	4.0	1.5	1.3	1.3
ENAP1-31	USP	0.003	2.5	4.5	5.1	5.3

USP = Unimodal small pore. BSP = Bimodal small pore. BBP = Bimodal big pore.

¹ This core plug presented a failure after the saturation process; therefore, it was not considered for NMR T₂ measurements.

Table C-2. Master list table of ENAP2 core plugs NMR relevant output data.

Sample	PSD curve	Scaling factor ($\mu\text{m}/\text{ms}$)	Surface relaxivity ($\mu\text{m}/\text{ms}$)	T ₂ geometric (ms)	T ₂ at P _{thr} (ms)	T ₂ at higher peak (ms)
ENAP2-8	USP	0.003	3.3	1.7	1.9	1.8
ENAP2-12	BSP	0.004	4.0	1.9	1.6	1.8
ENAP2-17	USP	0.002	2.5	1.7	2.0	1.8
ENAP2-19	USP	0.004	4.0	1.5	1.2	1.2
ENAP2-24	USP	0.003	3.3	2.6	3.3	3.0
ENAP2-27	BSP	0.005	5.0	1.3	1.0	1.0
ENAP2-33	USP	0.003	2.5	2.2	2.6	2.3
ENAP2-38	BSP	0.004	4.0	1.8	1.6	1.3
ENAP2-44	BSP	0.004	4.0	2.8	3.7	3.5
ENAP2-46	USP	0.010	10.0	1.1	1.8	1.2
ENAP2-53	USP	0.003	3.3	2.1	1.5	1.8
ENAP2-54	BBP	0.002	1.7	23.1	134.3	100.0
ENAP2-62	USP	0.002	2.5	2.9	4.0	3.1
ENAP2-65	USP	0.004	4.0	2.1	3.7	2.3
ENAP2-76	USP	0.005	5.0	3.6	3.6	4.0

USP = Unimodal small pore. BSP = Bimodal small pore. BBP = Bimodal big pore.

Table C-3. Master list table of ENAP1 core plugs MICP relevant output data.

Sample	P _e (psig)	P _d (psig)	P _{thr} (psig)	R _{apex} (μm)	R _{wgm} (μm)	PTS _Q	PTS _{16.50.84}
ENAP1-1	10	2,000	4,000	0.02	0.02	1.7	5,996
ENAP1-2	10	50	200	1.11	0.12	5.2	6,196
ENAP1-6	20	1,200	3,000	0.03	0.03	1.7	5,663
ENAP1-8	10	2,300	4,000	0.02	0.02	1.8	8,330
ENAP1-9	2	2,200	4,000	0.02	0.02	1.6	6,330
ENAP1-12	25	2,400	4,000	0.03	0.02	1.4	6,163
ENAP1-13	100	1,000	3,000	0.04	0.03	1.9	4,497
ENAP1-14 ¹							
ENAP1-15	25	4,000	9,000	0.01	0.01	1.4	10,663
ENAP1-17	70	900	2,000	0.07	0.04	1.7	3,496
ENAP1-18	5	700	2,000	0.07	0.05	1.9	2,330
ENAP1-21	40	2,400	9,000	0.03	0.02	2.3	8,663
ENAP1-22	800	2,600	4,000	0.02	0.02	1.6	6,330
ENAP1-23	40	2,100	4,000	0.02	0.02	1.8	8,330
ENAP1-24	40	2,300	9,000	0.07	0.02	1.9	8,996
ENAP1-25	40	3,500	9,000	0.01	0.01	1.4	10,330
ENAP1-27	200	3,600	9,000	0.01	0.02	1.3	8,496
ENAP1-28	10	3,500	7,000	0.02	0.02	1.6	9,829
ENAP1-29	20	4,000	9,000	0.01	0.01	1.5	12,996
ENAP1-30	10	3,300	9,000	0.01	0.01	1.4	10,163
ENAP1-31	15	1,700	3,500	0.03	0.03	1.7	4,996

P_e = entry pressure. P_d = displacement pressure. P_{thr} = threshold pressure. R_{apex} = apex pore throat radius. R_{wgm} = weighted geometric mean pore throat radius. PTS_Q = Pore throat size sorting at the squared root of the third and first capillary pressure quartiles (psig^{1/2}). PTS_{16.50.84} = Pore throat size sorting at three capillary pressures located at extremes and centre (psig).

¹ This core plug was not measured with the MICP technique.

Table C-4. Master list table of ENAP2 core plugs MICP relevant output data.

Sample	P _e (psig)	P _d (psig)	P _{thr} (psig)	R _{apex} (μm)	R _{wgm} (μm)	PTS _Q	PTS _{16,50,84}
ENAP2-8	2,500	3,800	7,000	0.02	0.01	1.5	10,663
ENAP2-12	5	3,000	7,000	0.02	0.02	1.4	7,996
ENAP2-17	140	5,500	9,000	0.01	0.01	1.3	11,996
ENAP2-19	10	3,500	9,000	0.01	0.01	1.5	11,156
ENAP2-24	15	2,600	4,000	0.02	0.02	1.7	9,496
ENAP2-27	10	3,100	9,000	0.02	0.02	1.6	10,163
ENAP2-33	25	3,500	7,000	0.02	0.01	1.5	8,829
ENAP2-38	10	3,000	7,000	0.02	0.02	1.7	8,162
ENAP2-44	10	1,100	3,000	0.04	0.02	2.1	6,495
ENAP2-46	500	1,500	2,500	0.04	0.02	1.9	6,329
ENAP2-53	5	3,800	9,000	0.01	0.01	1.4	10,496
ENAP2-54	10	70	200	0.36	0.08	5.5	5,329
ENAP2-62	10	3,000	4,500	0.02	0.02	1.6	7,996
ENAP2-65	5	620	3,000	0.07	0.03	2.1	5,497
ENAP2-76	10	900	2,500	0.05	0.03	1.9	4,497

P_e = entry pressure. P_d = displacement pressure. P_{thr} = threshold pressure. R_{apex} = apex pore throat radius. R_{wgm} = weighted geometric mean pore throat radius. PTS_Q = Pore throat size sorting at the squared root of the third and first capillary pressure quartiles (psig^{1/2}). PTS_{16,50,84} = Pore throat size sorting at three capillary pressures located at extremes and centre (psig).

¹ This core plug was not measured with the MICP technique.

C.2 Apex position of the ZG dataset.

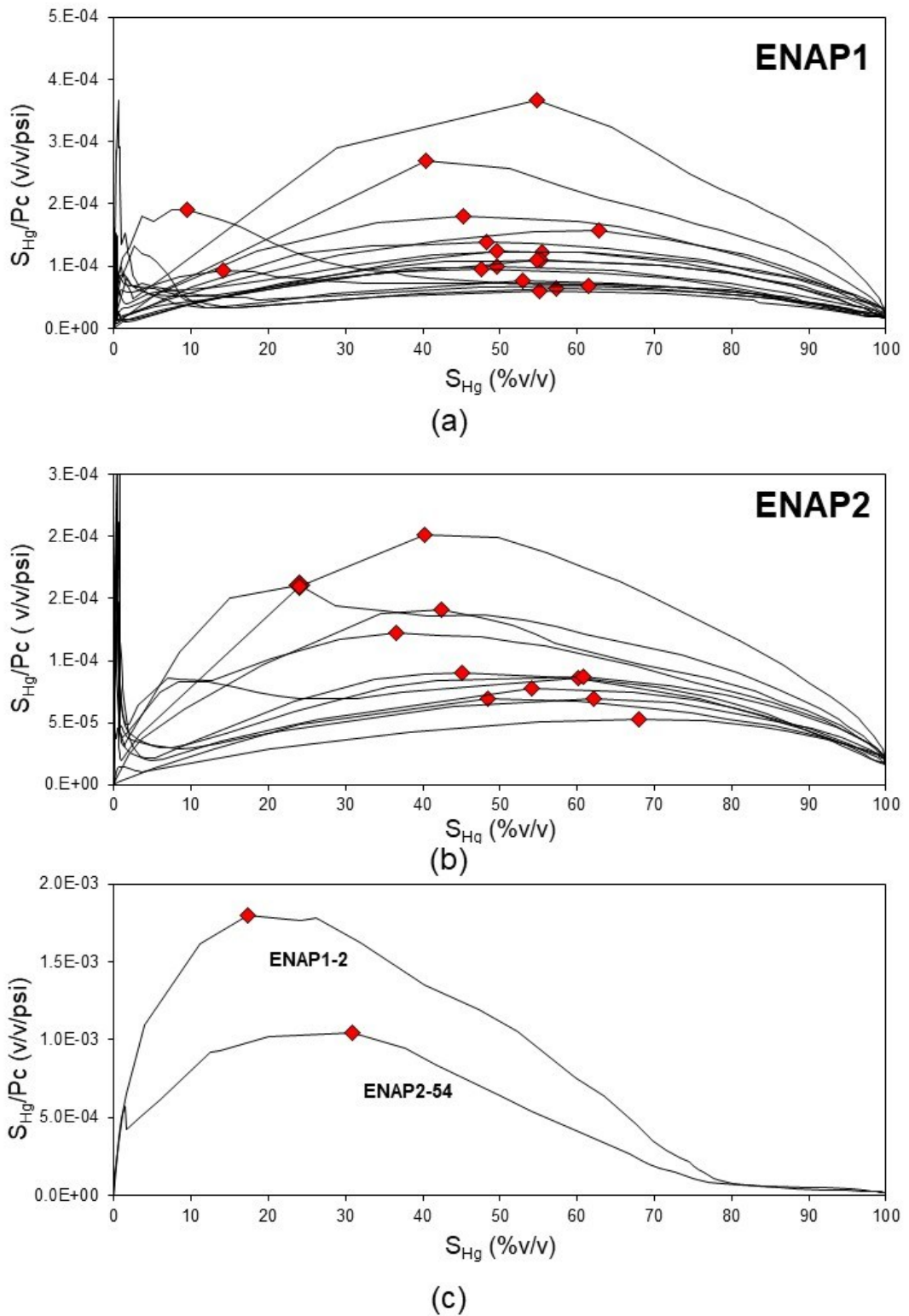


Figure C-1. Apex position of the ZG dataset using Pittman's (1992) workflow.

C.3 Cross-plot comparison on equivalent pore-throat radius correlations.

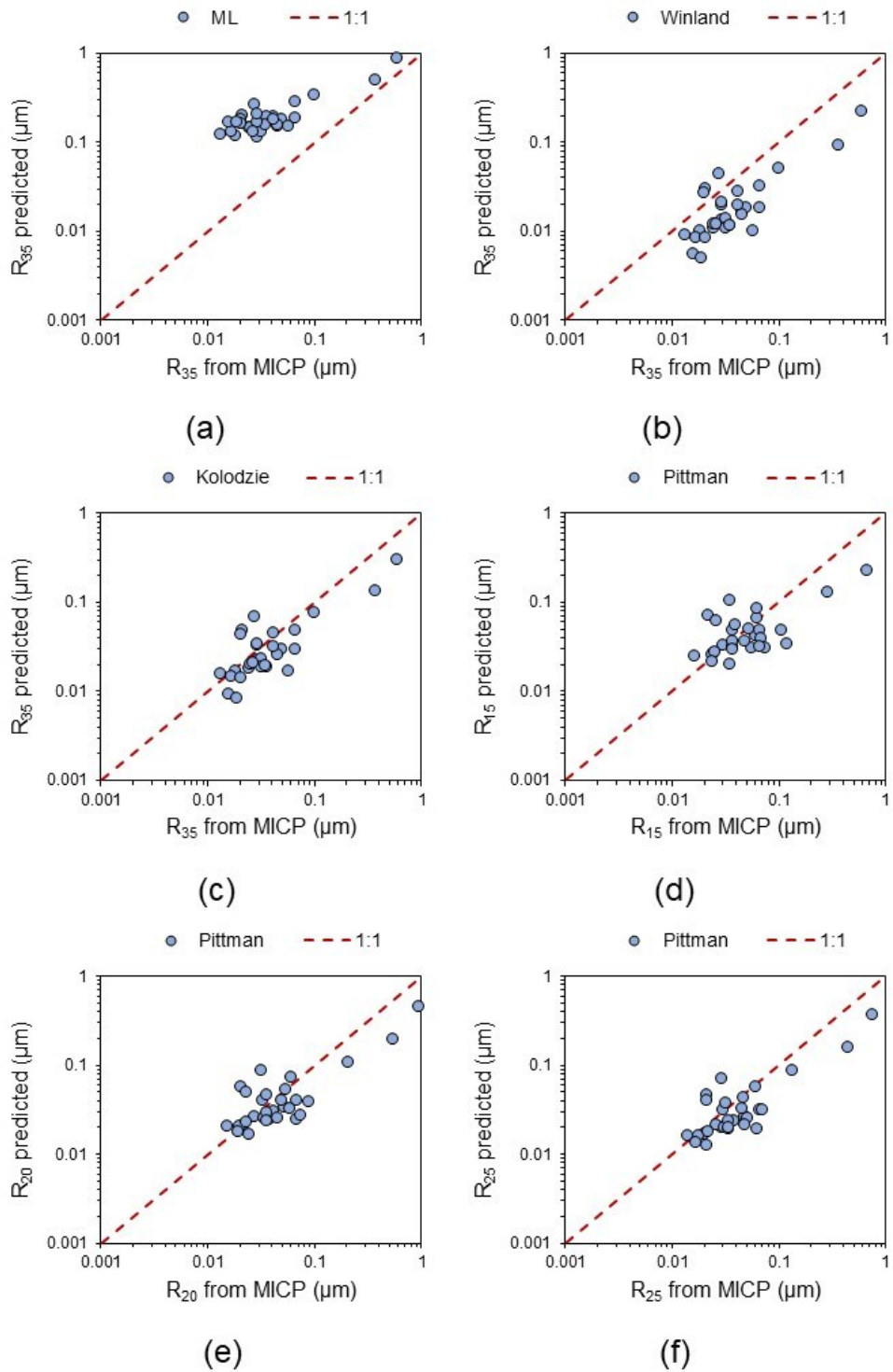


Figure C-2. (a) Predicted vs actual pore-throat radius at 35%v/v mercury saturation with MLR in MS Excel. (b) Predicted vs actual pore-throat radius at 35% mercury saturation with Winland's correlation. (c) Predicted vs actual pore-throat radius at 35%v/v mercury saturation with Kolodzie's correlation. (d) Predicted vs actual pore-throat radius at 15%v/v mercury saturation with Pittman's correlation. (e) Predicted vs actual pore-throat radius at 20%v/v mercury saturation with Pittman's correlation. (f) Predicted vs actual pore-throat radius at 25%v/v mercury saturation with Pittman's correlation.

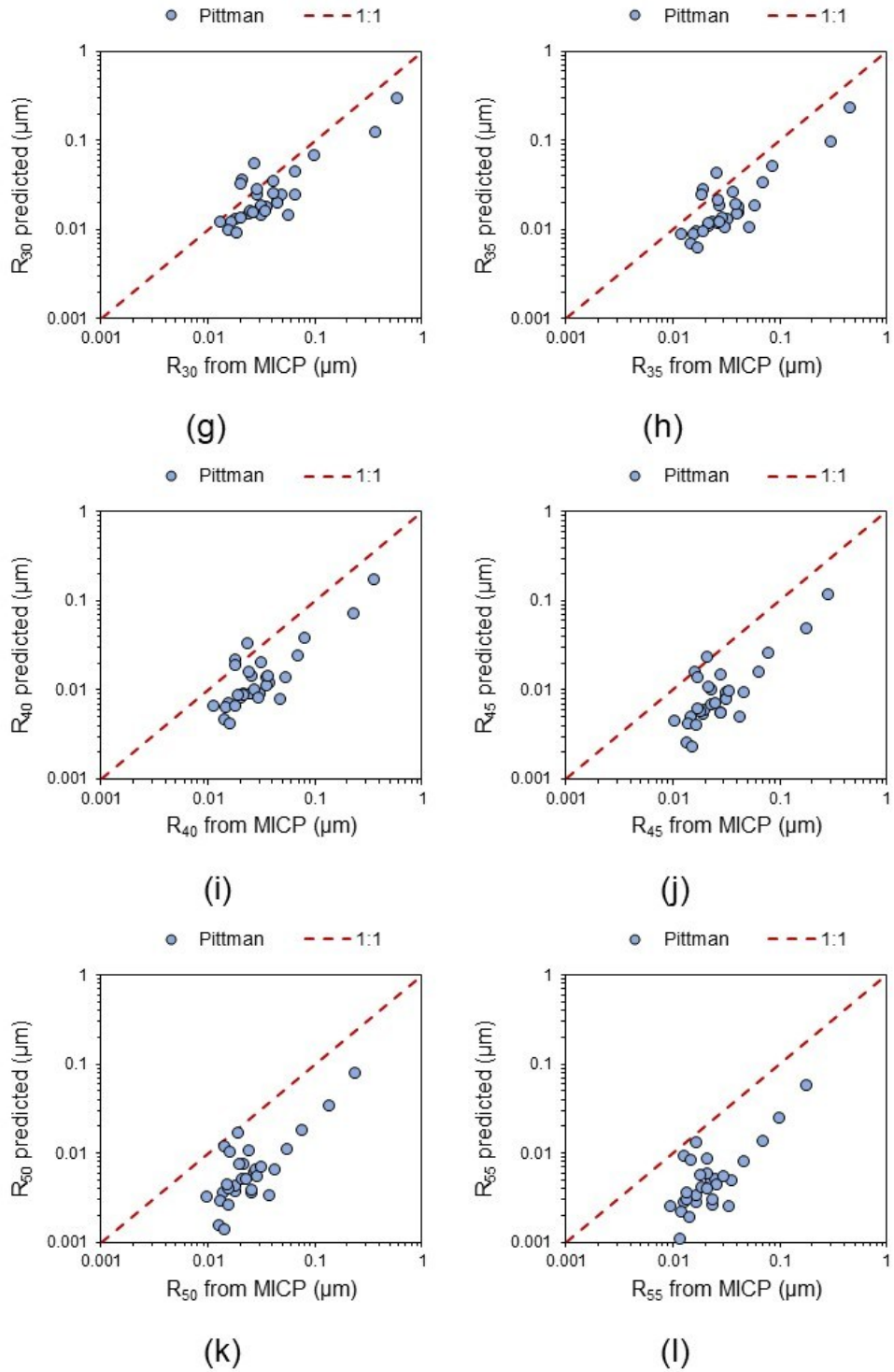


Figure C-3. (g) Predicted vs actual pore-throat radius at 30%v/v mercury saturation with Pittman's correlation. (h) Predicted vs actual pore-throat radius at 35%v/v mercury saturation with Pittman's correlation. (i) Predicted vs actual pore-throat radius at 40%v/v mercury saturation with Pittman's correlation. (j) Predicted vs actual pore-throat radius at 45%v/v mercury saturation with Pittman's correlation. (k) Predicted vs actual pore-throat radius at 50%v/v mercury saturation with Pittman's correlation. (l) Predicted vs actual pore-throat radius at 55%v/v mercury saturation with Pittman's correlation.

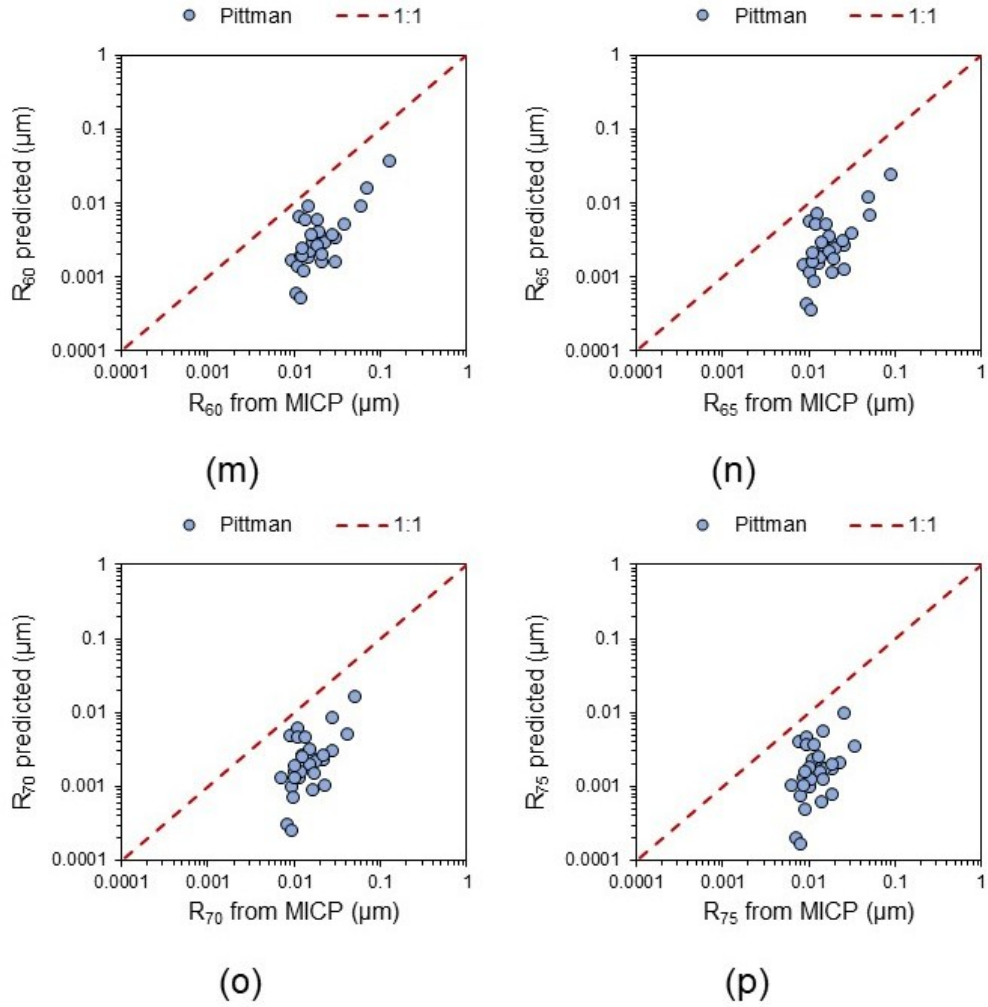


Figure C-4. (m) Predicted vs actual pore-throat radius at 60%v/v mercury saturation with Pittman's correlation. (n) Predicted vs actual pore-throat radius at 65%v/v mercury saturation with Pittman's correlation. (o) Predicted vs actual pore-throat radius at 70%v/v mercury saturation with Pittman's correlation. (p) Predicted vs actual pore-throat radius at 75%v/v mercury saturation with Pittman's correlation.

Appendix D: Electrical and ultrasonic data

D.1 Electrical data at a confining pressure of 1,500 psig.

Table D-1. Master list table of ENAP1 core plugs electrical data.

Sample	Depth (m)	Log Rdeep (ohm·m)	Log Rshallow (ohm·m)	Log CTEM (°C)	Ro@res ¹ (ohm·m)	F ²	m ³
ENAP1-1	2,156	13.2	10.6	96.08	5.4	33	2.32
ENAP1-2	2,157	30.5	27.7	96.08	9.8	59	3.08
ENAP1-6	2,162	8.2	7.2	96.36	4.2	26	
ENAP1-8	2,166	5.4	5.0	96.36	6.7	41	1.70
ENAP1-9	2,167	6.8	6.2	96.36	6.3	38	1.88
ENAP1-12	2,171	6.5	5.7	96.36	6.0	36	
ENAP1-13	2,172	8.9	8.1	96.36	4.6	28	1.95
ENAP1-14	2,173	8.5	7.3	96.36	5.9	36	1.99
ENAP1-15	2,180	5.6	5.6	96.36	4.8	29	1.89
ENAP1-17	2,159	10.5	8.4	96.08	2.6	16	
ENAP1-18	2,161	11.5	10.0	96.36	3.4	21	1.87
ENAP1-21	2,184	6.3	6.0	96.36	10.3	63	2.33
ENAP1-22	2,153	6.8	7.4	96.08	4.9	30	
ENAP1-23	2,151	5.4	5.2	96.08	6.7	41	2.11
ENAP1-24	2,150	6.3	6.3	96.08	5.2	32	1.73
ENAP1-25	2,148	4.8	4.9	96.08	4.5	27	1.69
ENAP1-27	2,142	4.5	4.4	96.08	4.2	25	1.66
ENAP1-28	2,130	4.5	4.3	95.80	3.4	21	1.95
ENAP1-29	2,127	4.4	4.3	95.80	4.2	26	2.53
ENAP1-30	2,127	4.9	4.4	95.80	4.2	25	2.60
ENAP1-31	2,164	7.7	7.1	96.36	4.6	28	1.78

¹ Converted rock resistivity from 25°C to reservoir temperature using Arps's equation. These measurements were conducted at a confining pressure of 1,500 psig.

² Calculated as the ratio of Ro/Rw. The value of Rw is 0.016 ohm·m at the average reservoir temperature (12,000 ppm NaCl).

³ Calculated as $-\text{Log}(F)/\text{Log}(\Phi_{\text{He}})$. Some helium porosities of the ENAP1 set were discarded as outliers.

Table D-2. Master list table of ENAP2 core plugs electrical data.

Sample	Depth (m)	Log Rdeep (ohm·m)	Log Rshallow (ohm·m)	Log CTEM (°C)	Ro@res ¹ (ohm·m)	F ²	m ³
ENAP2-8	2,238	2.3	2.2	93.33	6.3	38	1.83
ENAP2-12	2,221	2.8	2.8	92.93	5.5	33	1.80
ENAP2-17	2,240	2.1	2.2	93.33	5.5	33	1.80
ENAP2-19	2,223	2.7	2.7	92.93	5.2	31	1.78
ENAP2-24	2,242	5.5	4.0	93.33	5.8	34	1.92
ENAP2-27	2,224	2.9	2.8	93.13	6.7	40	1.90
ENAP2-33	2,243	2.6	2.3	93.53	7.0	42	1.84
ENAP2-38	2,226	2.6	2.6	93.13	6.8	40	2.03
ENAP2-44	2,246	2.4	2.6	93.53	6.6	39	1.85
ENAP2-46	2,228	2.7	2.6	93.13	9.9	59	2.04
ENAP2-53	2,248	2.6	2.5	93.53	9.7	58	2.02
ENAP2-54	2,230	2.7	2.4	93.13	12.8	76	2.84
ENAP2-62	2,251	2.2	2.1	93.53	6.9	41	1.98
ENAP2-65	2,233	2.5	2.4	93.33	5.9	35	1.93
ENAP2-76	2,236	2.7	2.4	93.33	5.5	32	1.92

¹ Converted rock resistivity from 25°C to reservoir temperature using Arp's equation. These measurements were conducted at a confining pressure of 1,500 psig.

² Calculated as the ratio of Ro/Rw. The value of Rw is 0.016 ohm·m at the average reservoir temperature (12,000 ppm NaCl).

³ Calculated as $-\text{Log}(F)/\text{Log}(\Phi_{\text{He}})$.

D.2 Calibration information for ultrasonic velocities.

The calibration protocol consists of a system delay correction by determining the delay time (and derived velocity) of a solid body's measured wave transit time. This delay was determined by measuring the transit time at zero and for aluminium alloy bars. A cross-plot between the measured transit time (x-axis) and length (y-axis) is built and fit to a linear correlation (**Figure D-1**).

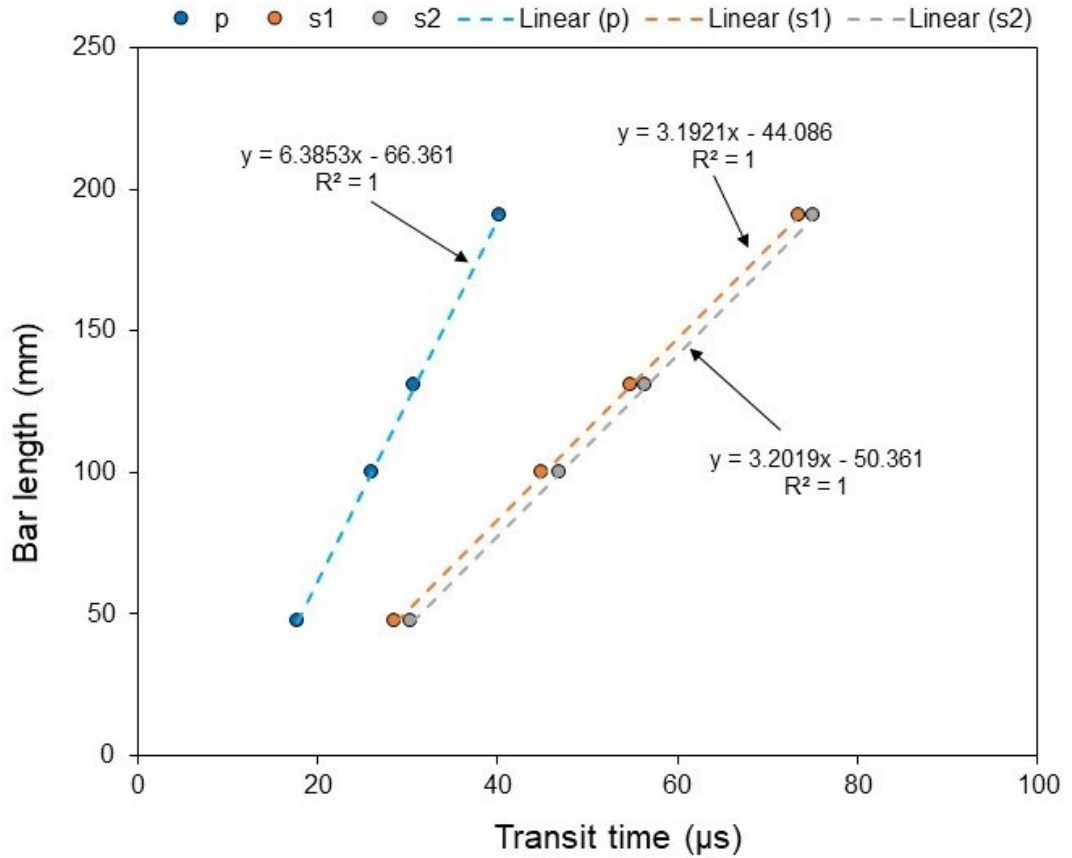


Figure D-1. Calibration cross-plot with aluminium alloy bars.

Equation D-1

$$t_{delay} = -\frac{b}{m}$$

where t_{delay} is the delay time (μs), b and m are the linear correlation intercept (mm) and slope (mm/ μs).

Table D-3. Calibration data.

Point	Bar length (mm)	P-wave (μs)	S1-wave (μs)	S2-wave (μs)
Zero	0	10.59	14.00	15.75
1	41	17.78	28.64	30.45
2	100	26.08	45.04	47.00
3	130	30.83	54.80	56.53
4	190	40.23	73.49	75.21
t_{delay}		10.39	13.81	15.73

D.3 Derived ultrasonic and geomechanical properties equations

Equation D-2

$$V_B = V_W + S(1170 - 9.6T + 0.055T^2 - 8.5 \times 10^{-5}T^3 + 2.6P - 0.0029TP - 0.0476P^2) + S^{3/2}(780 - 10P + 0.16P^2) - 1820S^2$$

where V_B and V_W are the brine and pure water acoustic velocity (m/s), S is the brine salinity as in fractions of one (parts per million divided by 10^6), P is the in-situ pressure (MPa), and T is the in-situ temperature (Celsius). Note: the selected salinity was 12,000 ppm NaCl, and the pressure and temperature conditions were 30 MPa (4,350 psig) and 93.27 °C.

Equation D-3

$$V_W = \sum_{i=0}^4 \sum_{j=0}^3 \omega_{ij} T^i P^j$$

where V_W is the brine and pure water acoustic velocity (m/s), ω_{ij} are coefficients listed in *Table D-4*, T is the in-situ temperature (Celsius degrees), and P is the in-situ pressure (MPa).

Table D-4. Listed ω_{ij} coefficients.

$\omega_{00}= 1402.85$	$\omega_{01}= 1.524$	$\omega_{02}= 3.437 \times 10^{-3}$	$\omega_{03}= -1.197 \times 10^{-5}$
$\omega_{10}= 4.871$	$\omega_{11}= -0.0111$	$\omega_{12}= 1.739 \times 10^{-4}$	$\omega_{13}= -1.628 \times 10^{-6}$
$\omega_{20}= -0.04783$	$\omega_{21}= 2.747 \times 10^{-4}$	$\omega_{22}= -2.135 \times 10^{-6}$	$\omega_{23}= 1.237 \times 10^{-8}$
$\omega_{30}= 1.487 \times 10^{-4}$	$\omega_{31}= -6.503 \times 10^{-7}$	$\omega_{32}= -1.455 \times 10^{-8}$	$\omega_{33}= 1.327 \times 10^{-10}$
$\omega_{40}= -2.197 \times 10^{-7}$	$\omega_{41}= 7.987 \times 10^{-10}$	$\omega_{42}= 5.230 \times 10^{-11}$	$\omega_{43}= -4.614 \times 10^{-13}$

Equation D-4

$$M_V = \sum_{i=1}^n f_i M_i$$

where M_V is the Voigt upper bound to predict elastic properties, f_i is the volumetric fraction (v/v) of the i^{th} phase, and M_i is the elastic properties of the i^{th} phase.

Equation D-5

$$\frac{1}{M_R} = \sum_{i=1}^n \frac{f_i}{M_i}$$

where M_V is the Reuss upper bound to predict elastic properties, f_i is the volumetric fraction (v/v) of the i^{th} phase, and M_i is the elastic properties of the i^{th} phase.

Equation D-6

$$M_{VRH} = \frac{M_V + M_R}{2}$$

where M_{VRH} is the Voigt-Reuss-Hill average elastic property.

Equation D-7

$$v = \frac{0.5 \left(V_p / V_{s1} \right)^2 - 1}{\left(V_p / V_{s1} \right)^2 - 1}$$

where v is Poisson's ratio (unitless), V_p and V_{s1} are the P-wave and S1-wave velocities, respectively (m/s).

Equation D-8

$$G = \frac{\rho_b (V_{s1})^2}{6894.76 \cdot 10^6}$$

where G is the shear or G modulus (MMpsig), ρ_b is the rock bulk density (kg/m^3), and V_{s1} is the S1-wave velocity (m/s).

Equation D-9

$$E = 2G(1 + v)$$

where E is the Young's modulus (MMpsig).

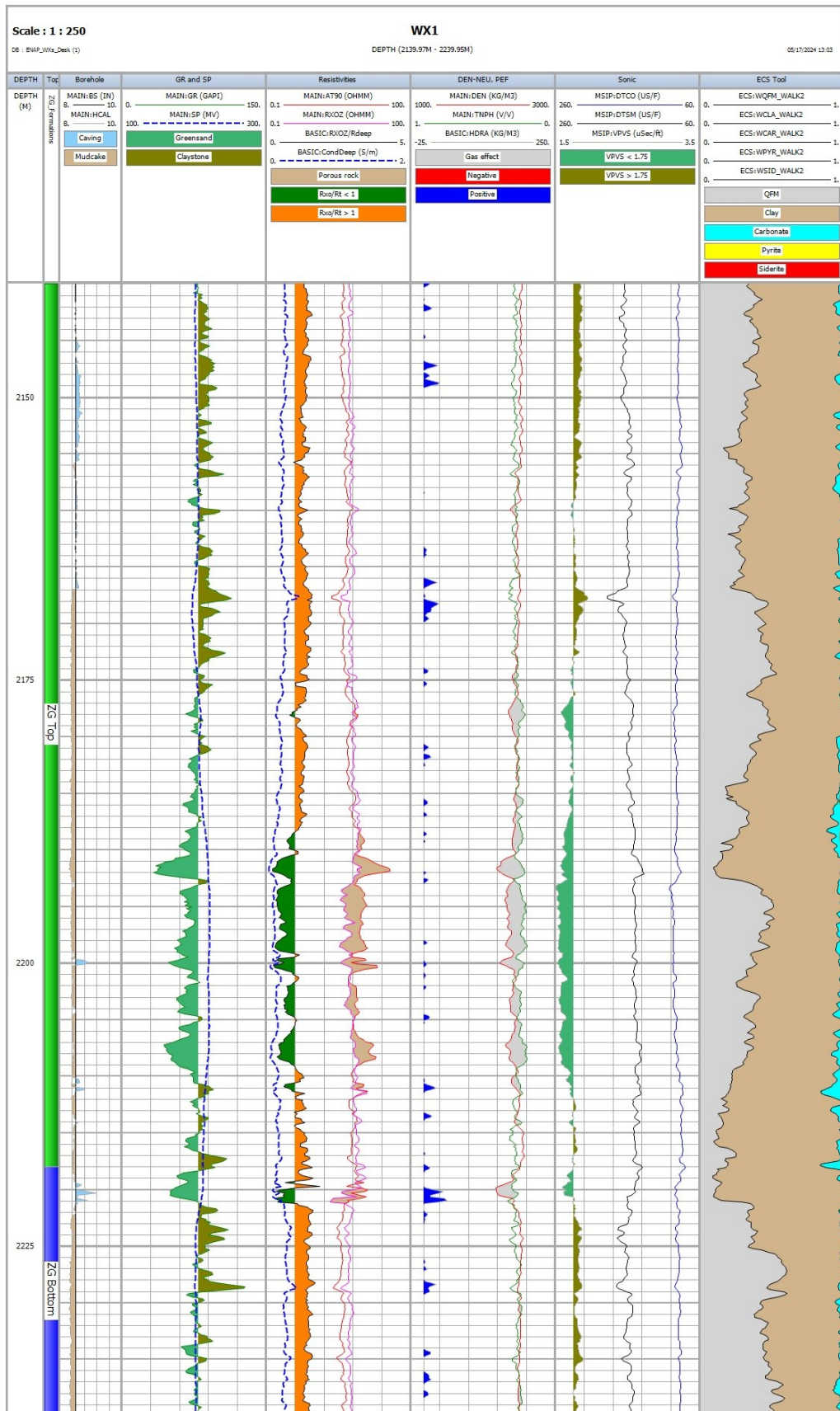
Equation D-10

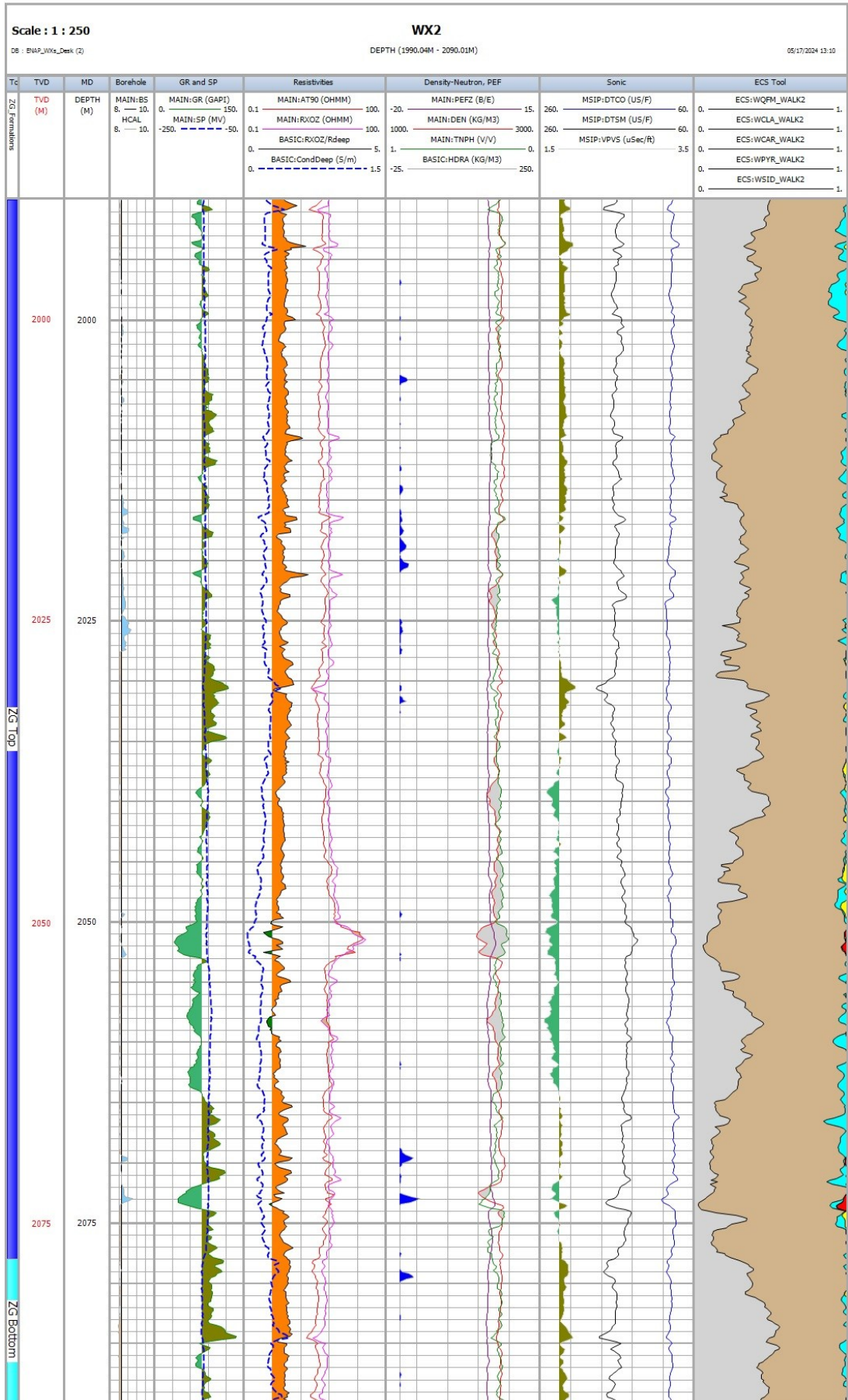
$$Z = \frac{\rho_b V_p}{10^6}$$

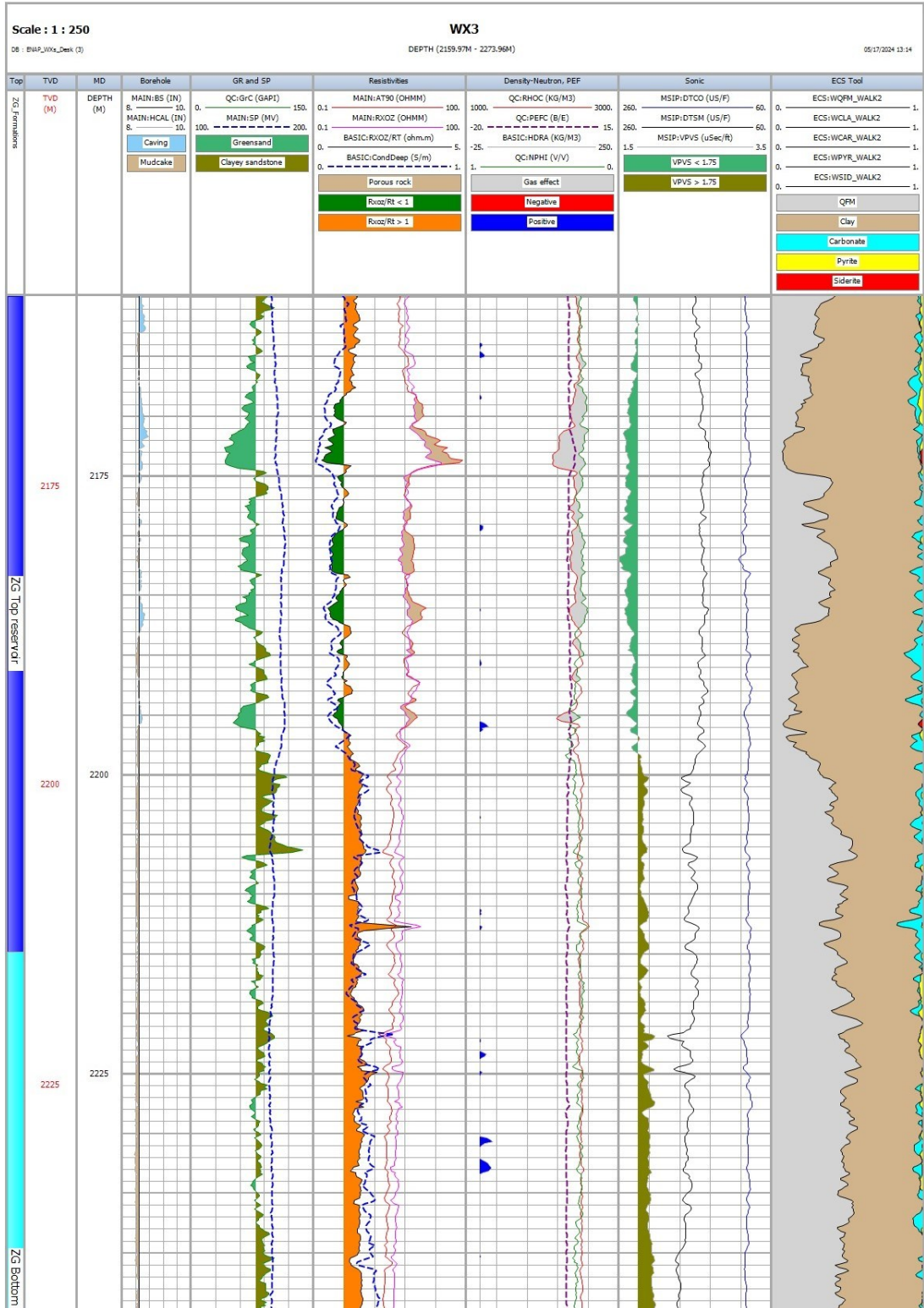
where Z is the impedance from V_p (Mrayls), ρ_b is the rock bulk density (kg/m^3), and V_p is the P-wave velocity (m/s).

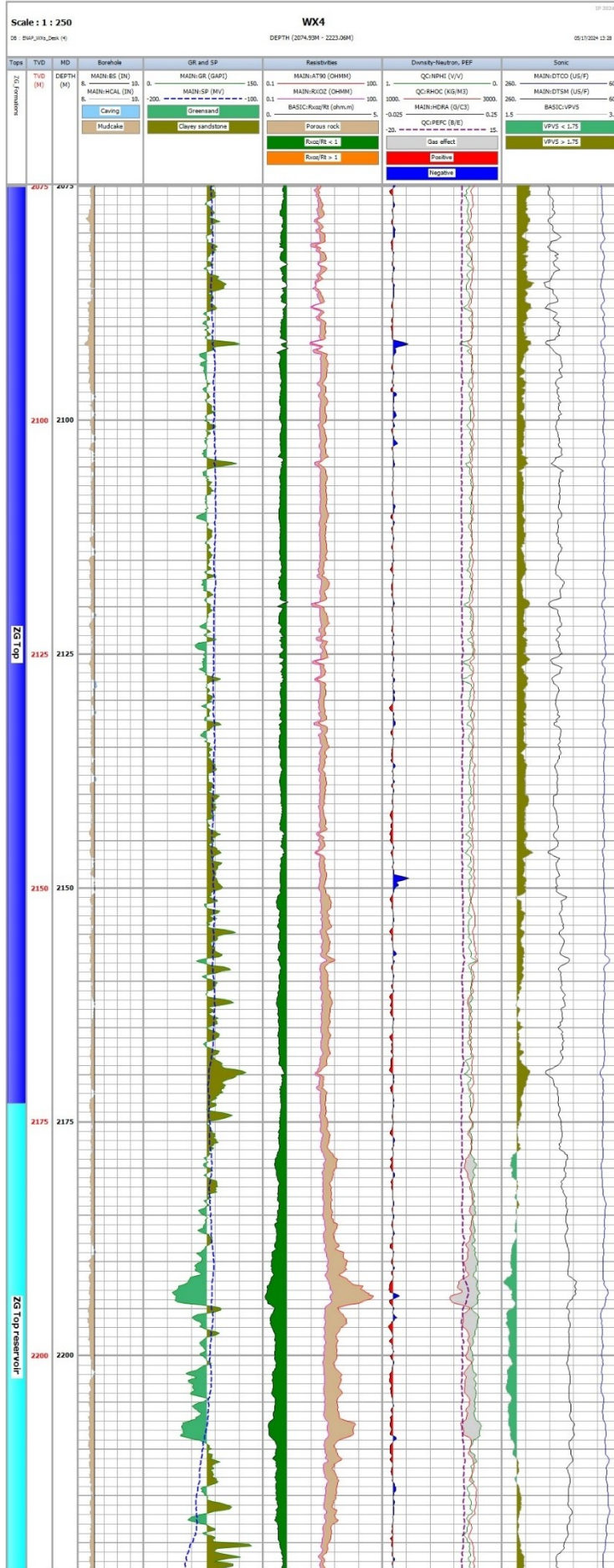
Appendix E: Petrophysical evaluation data

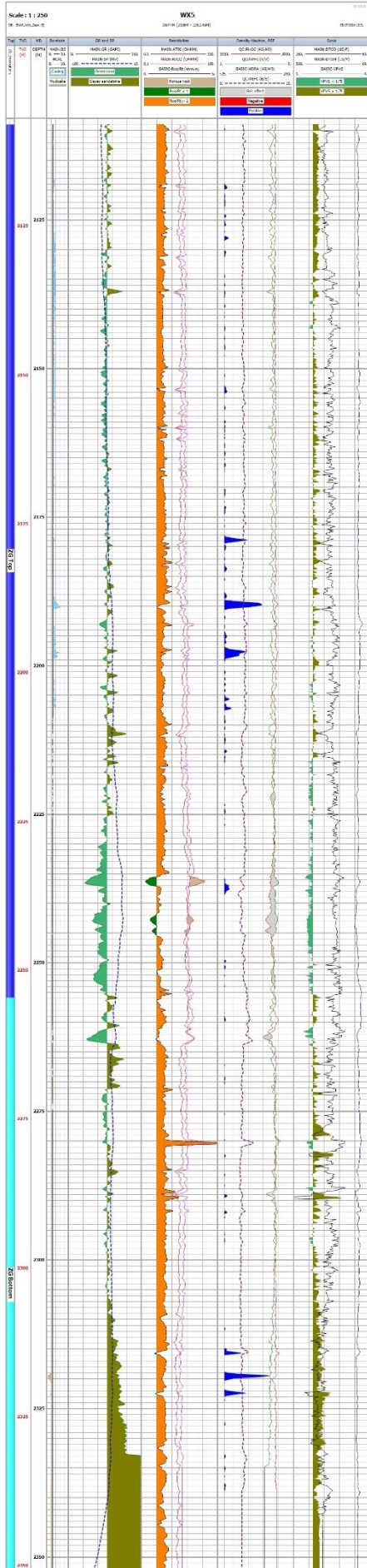
E.1 Quick-look petrophysical interpretation of wells WX1 to WX10.

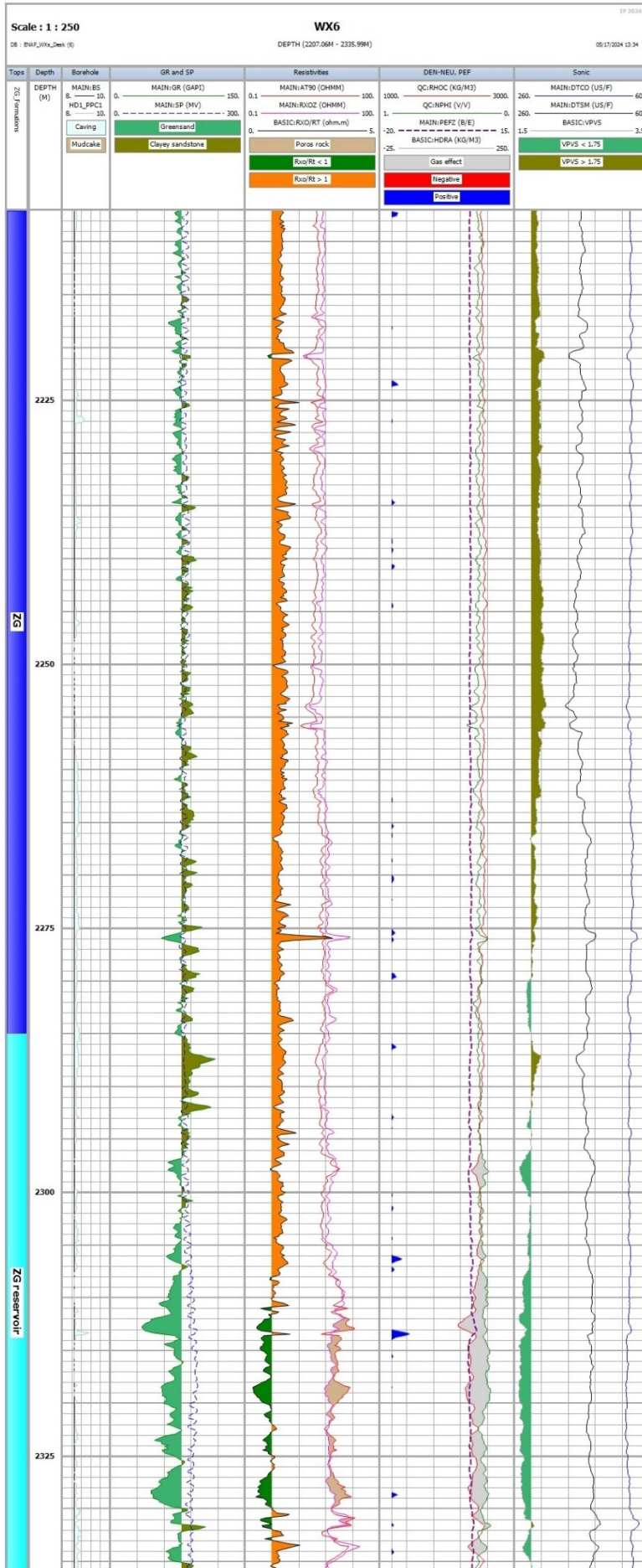


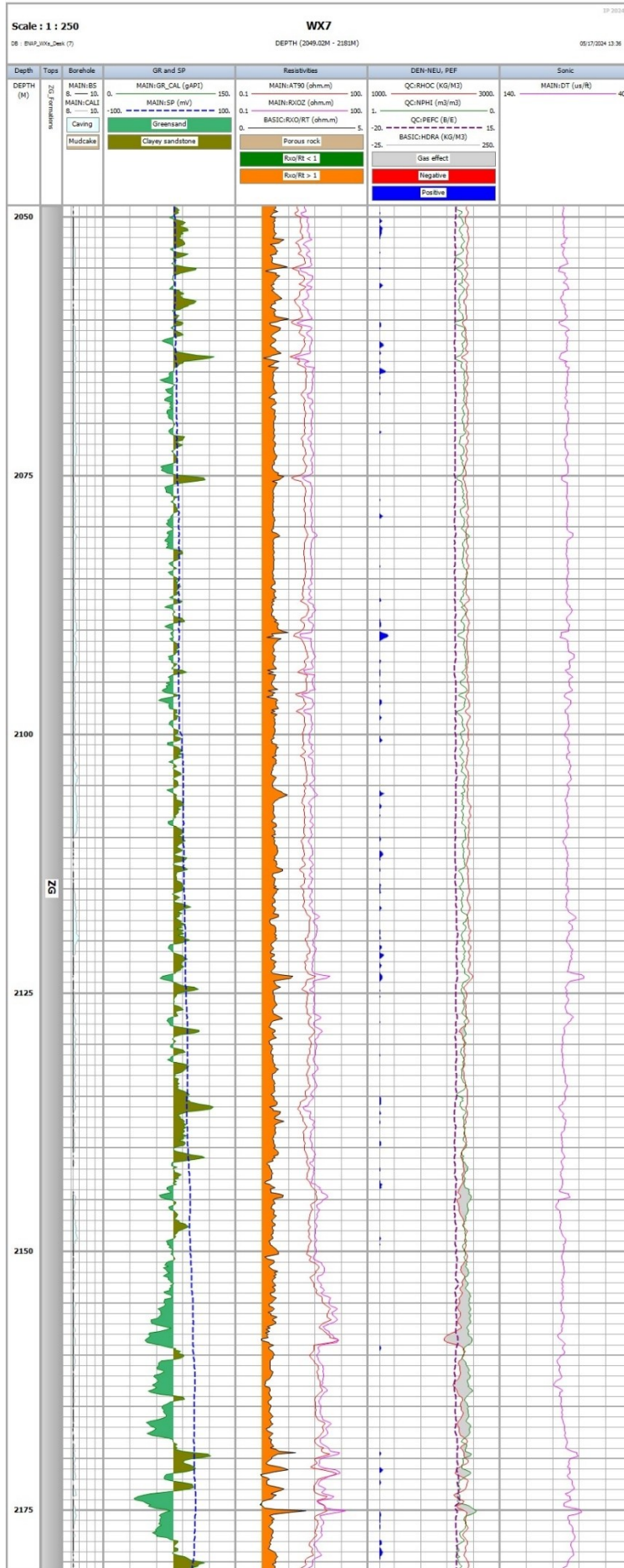


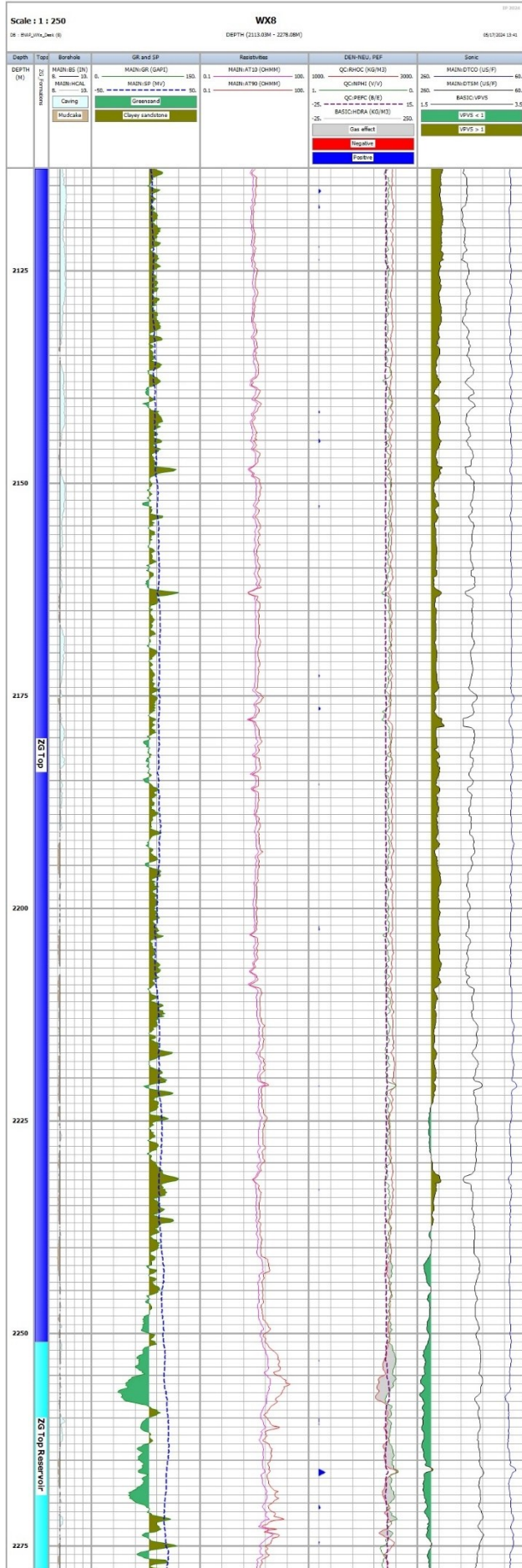


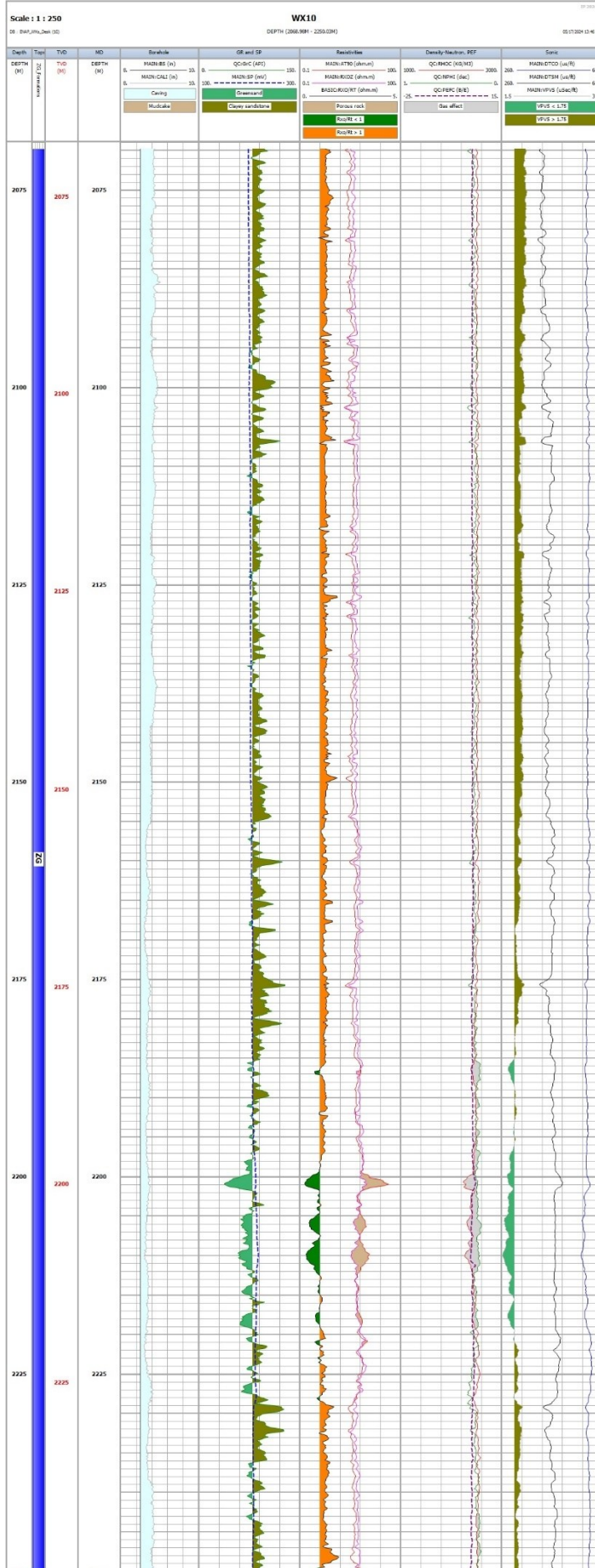












E.2 Clay volume equations.

Equations Equation E–1, Equation E–2, and Equation E–3 show the derived clay volume using gamma-ray, photoelectric factor, and density-neutron logging tools. The clean and clay gamma-ray and photoelectric factor values were selected according to the calibration with XRD core data in key wells and validated with wells WX1 to WX3. The double indicator's clay point and clean sandstone line are selected according to the bulk density and neutron porosity cross-plot (**Figure E-1**).

Equation E–1

$$Vcl_{GR} = \frac{GR - GR_{clean}}{GR_{clay} - GR_{clean}}$$

Where Vcl_{GR} is the clay volume index derived from the gamma-ray tool (v/v), GR , GR_{clean} and GR_{clay} are the gamma-ray log readings at the depth of interest, clean sandstone (mean minimum) and clay formation (mean maximum) baselines, respectively.

Equation E–2

$$Vcl_{PEF} = \frac{PEF - PEF_{clean}}{PEF_{clay} - PEF_{clean}}$$

where Vcl_{PEF} is the clay volume index derived from the photoelectric factor tool (v/v), PEF , PEF_{clean} , and PEF_{clay} are the photoelectric factor log readings at the depth of interest, clean sandstone (mean minimum) and clay formation (mean maximum) baselines, respectively.

Equation E–3

$$Vcl_{ND} = \frac{(Den_{cl2} - Den_{cl1})(Neu - Neu_{cl1}) - (Den - Den_{cl1})(Neu_{cl2} - Neu_{cl1})}{(Den_{cl2} - Den_{cl1})(Neu_{clay} - Neu_{cl1}) - (Den_{clay} - Den_{cl1})(Neu_{cl2} - Neu_{cl1})}$$

where Vcl_{ND} is the clay volume index derived from the bulk density and neutron porosity tools (v/v). Den , Den_{clay} , Den_{cl1} and Den_{cl2} are the bulk density log readings at a depth of interest, clay formation, and clean sandstone endpoints 1 and 2, respectively. Neu , Neu_{clay} , Neu_{cl1} and Neu_{cl2} are the neutron porosity log readings at the depth of interest, clay formation, and clean sandstone endpoints 1 and 2, respectively.

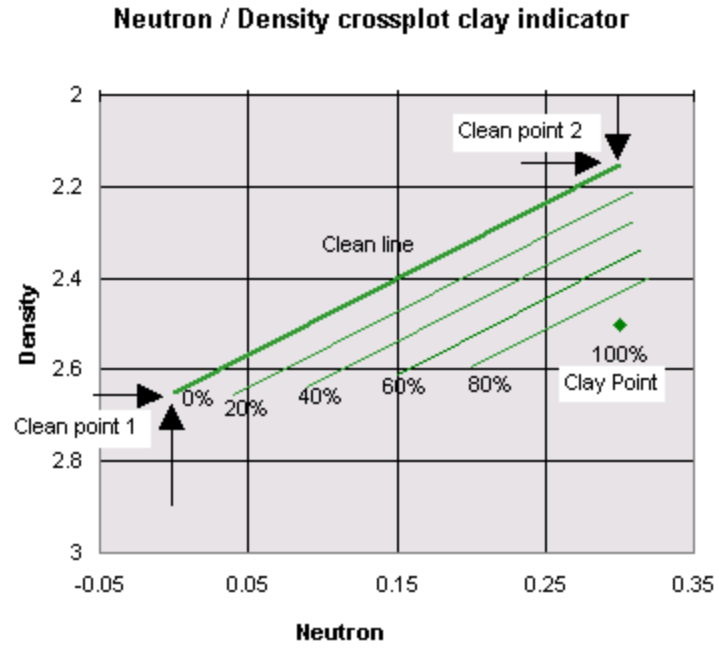


Figure E-1. Diagram of bulk density (g/cc) and neutron porosity (v/v) cross-plot to define the clean sandstone endpoints 1 and 2 with the clay point (Geoactive Ltd., 2024).

E.3 Clay volume estimation of wells WX1 to WX10.

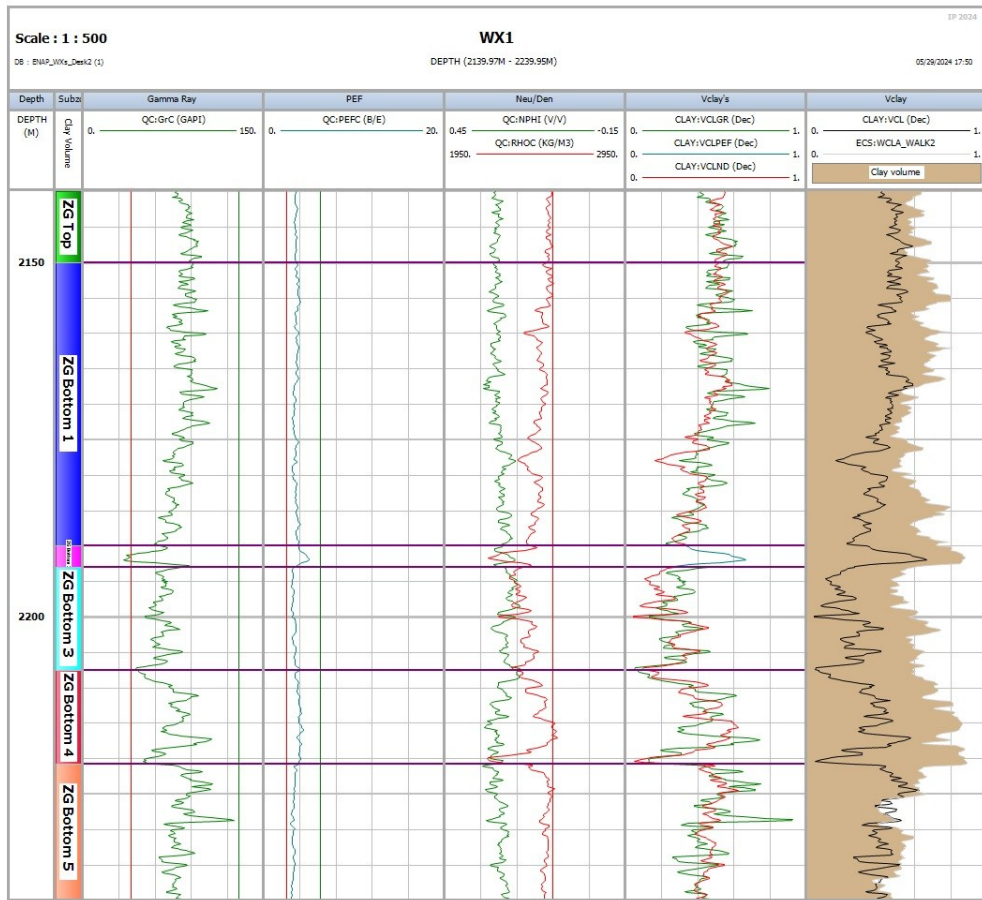


Figure E-2. Clay volume estimation of WX1 well. Track 1: Depth (m). Track 2: ZG subzones name. Track 3: Gamma-ray log (API). Track 4: Photoelectric factor log (barns/e). Track 5: Bulk density (kg/m³) and neutron porosity (v/v) logs. Track 6: Clay volume estimation from each selected indicator. Track 7: Final clay volume in black line (VCL). Clay volume derived from the CMRPlus tool (kgf/kgf).

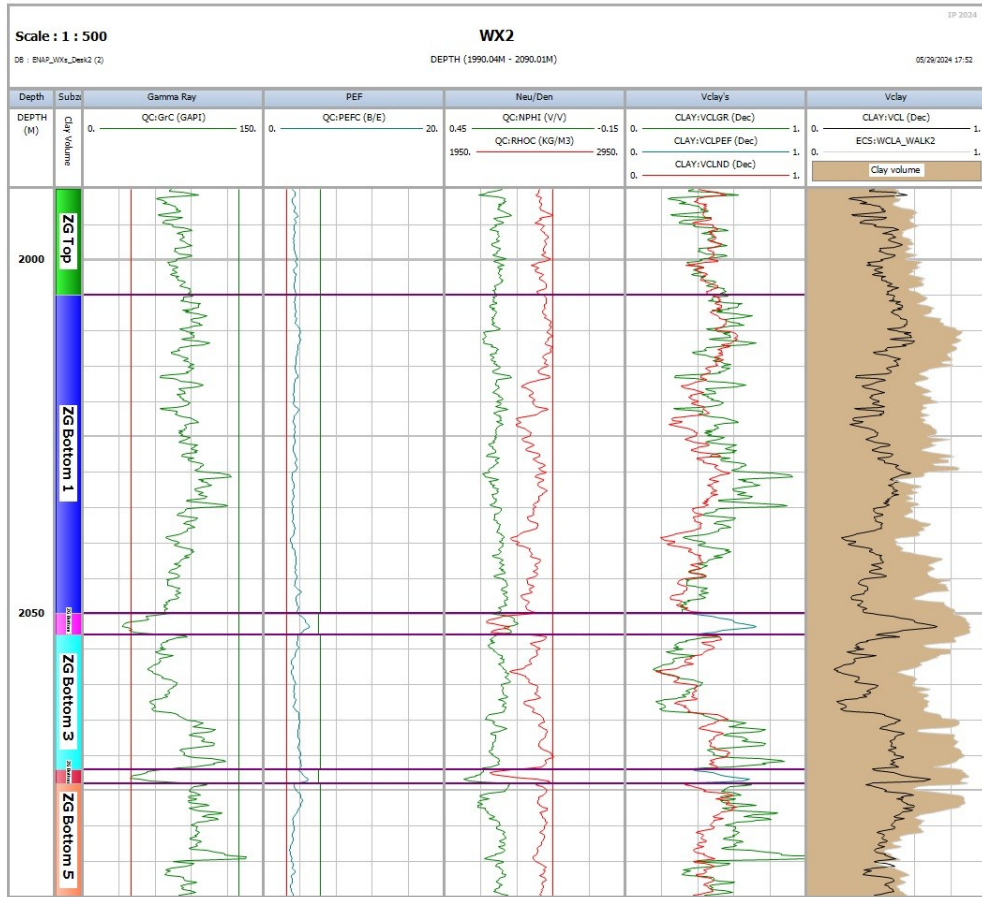


Figure E-3. Clay volume estimation of WX2 well. Track 1: Depth (m). Track 2: ZG subzones name. Track 3: Gamma-ray log (API). Track 4: Photoelectric factor log (barns/e). Track 5: Bulk density (kg/m³) and neutron porosity (v/v) logs. Track 6: Clay volume estimation from each selected indicator. Track 7: Final clay volume in black line (VCL). Clay volume derived from the CMRPlus tool (kgf/kgf).

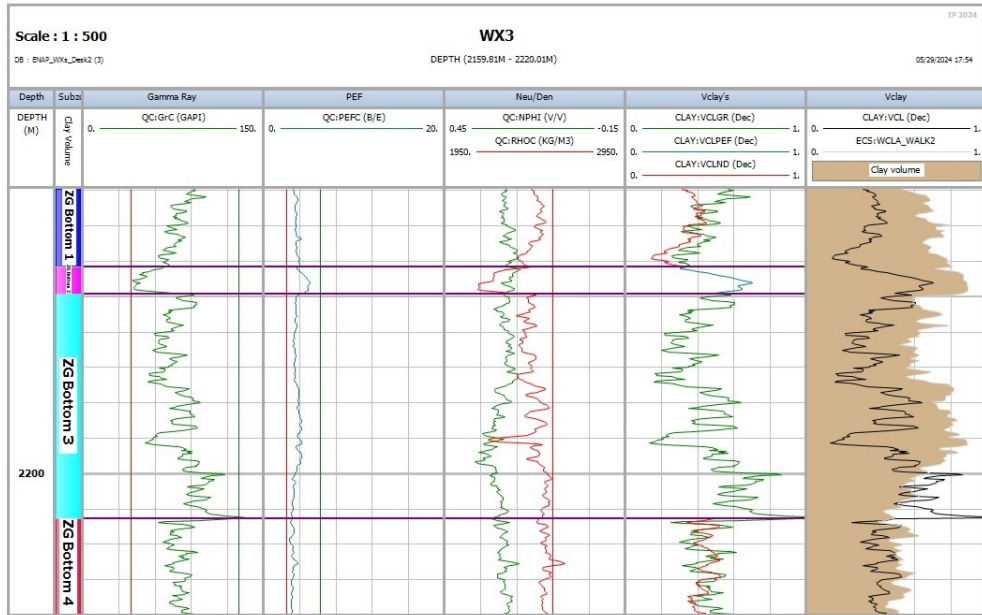


Figure E-4. Clay volume estimation of WX3 well. Track 1: Depth (m). Track 2: ZG subzones name. Track 3: Gamma-ray log (API). Track 4: Photoelectric factor log (barns/e). Track 5: Bulk density (kg/m³) and neutron porosity (v/v) logs. Track 6: Clay volume estimation from each selected indicator. Track 7: Final clay volume in black line (VCL). Clay volume derived from the CMRPlus tool (kg/kgf).

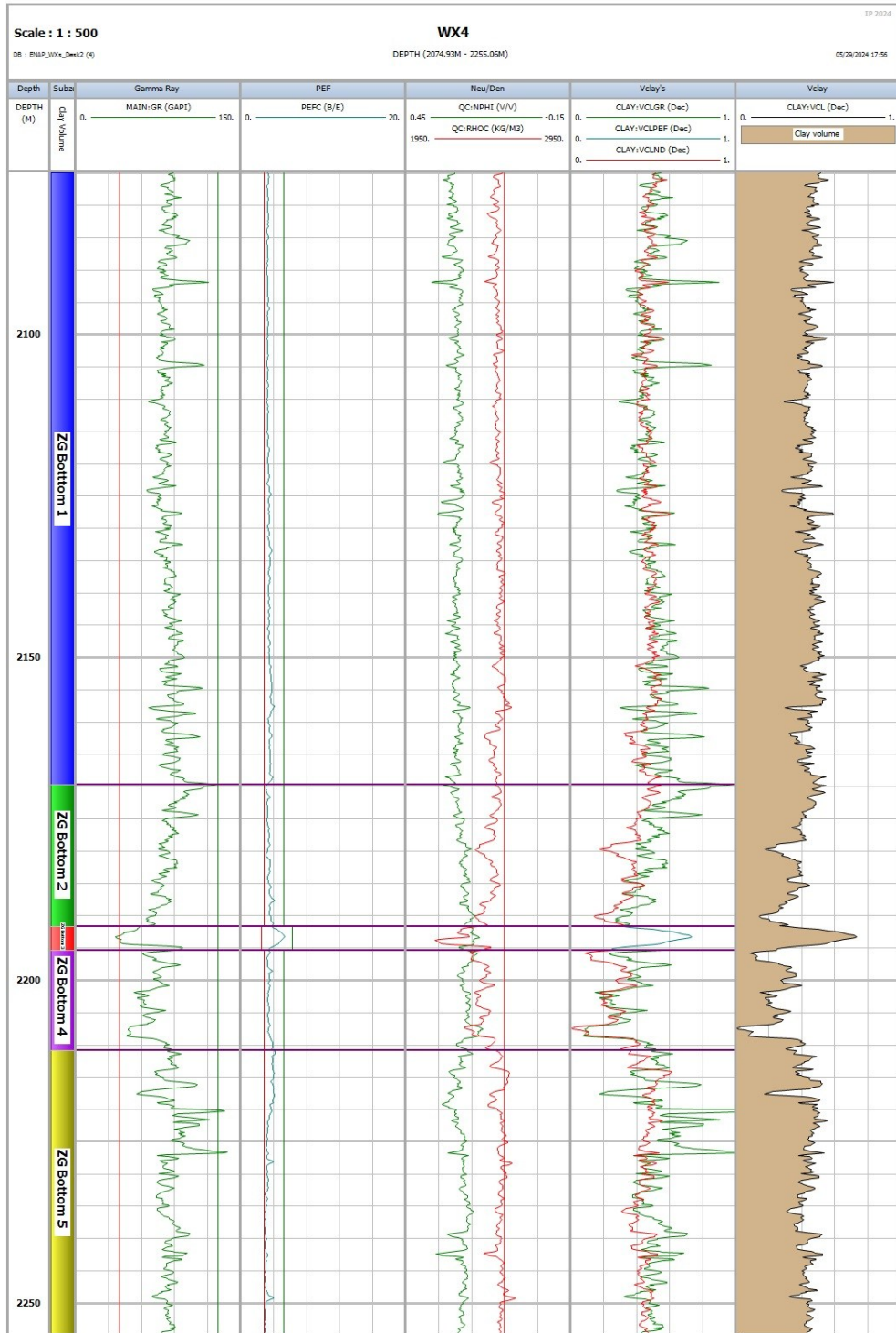


Figure E-5. Clay volume estimation of WX4 well. Track 1: Depth (m). Track 2: ZG subzones name. Track 3: Gamma-ray log (API). Track 4: Photoelectric factor log (barns/e). Track 5: Bulk density (kg/m³) and neutron porosity (v/v) logs. Track 6: Clay volume estimation from each selected indicator. Track 7: Final clay volume in black line (VCL).

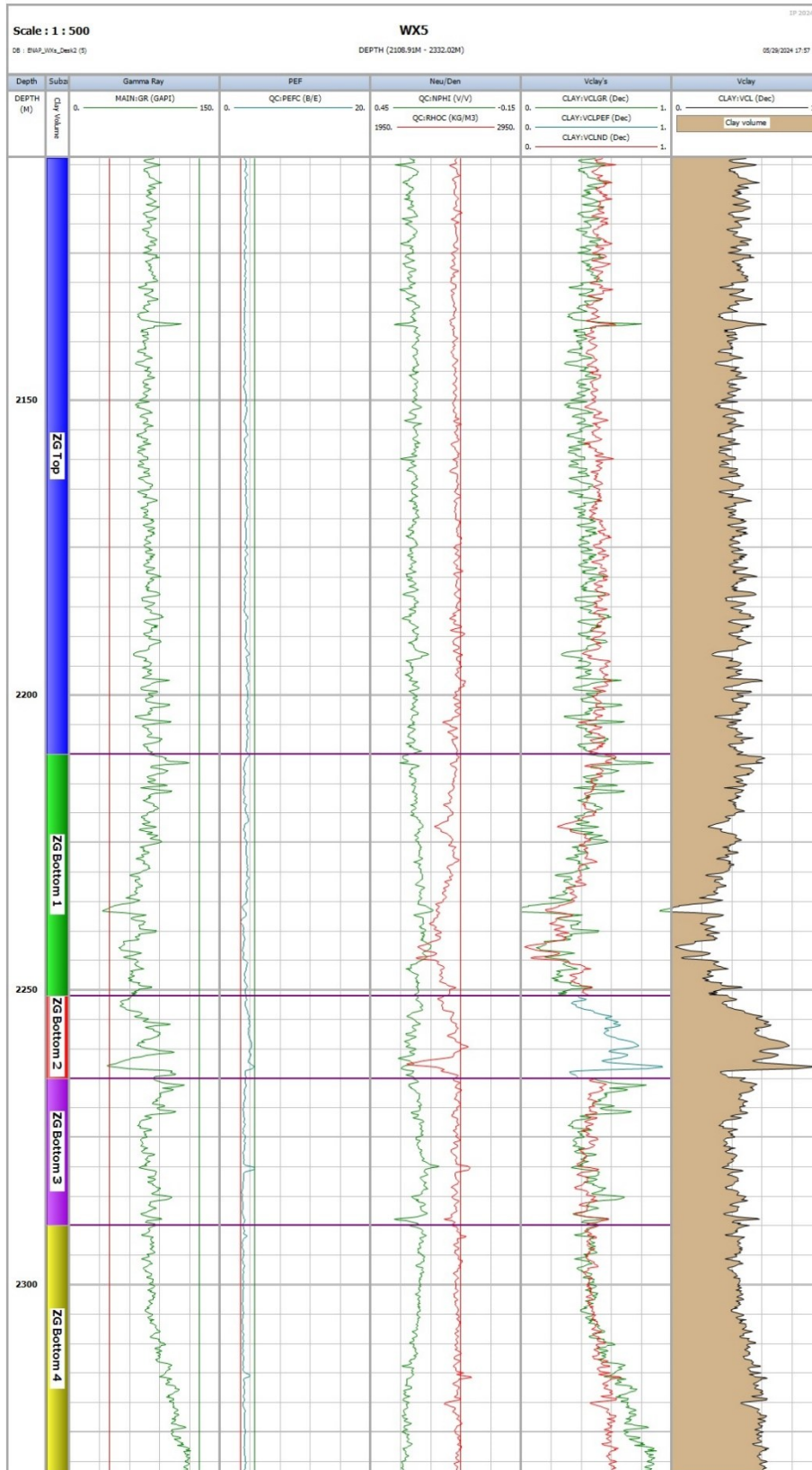


Figure E-6. Clay volume estimation of WX5 well. Track 1: Depth (m). Track 2: ZG subzones name. Track 3: Gamma-ray log (API). Track 4: Photoelectric factor log (barns/e). Track 5: Bulk density (kg/m^3) and neutron porosity (v/v) logs. Track 6: Clay volume estimation from each selected indicator. Track 7: Final clay volume in black line (VCL).

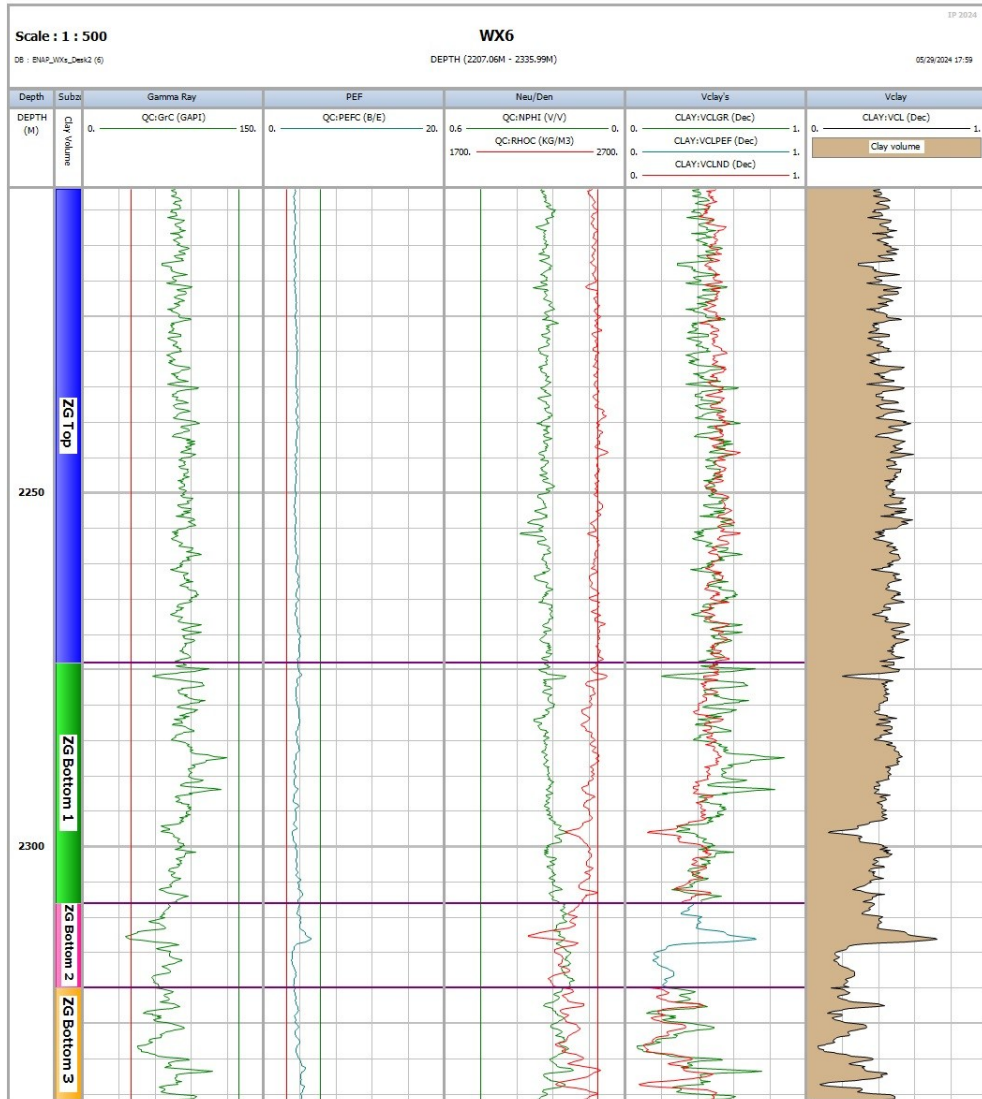


Figure E-7. Clay volume estimation of WX6 well. Track 1: Depth (m). Track 2: ZG subzones name. Track 3: Gamma-ray log (API). Track 4: Photoelectric factor log (barns/e). Track 5: Bulk density (kg/m³) and neutron porosity (v/v) logs. Track 6: Clay volume estimation from each selected indicator. Track 7: Final clay volume in black line (VCL).

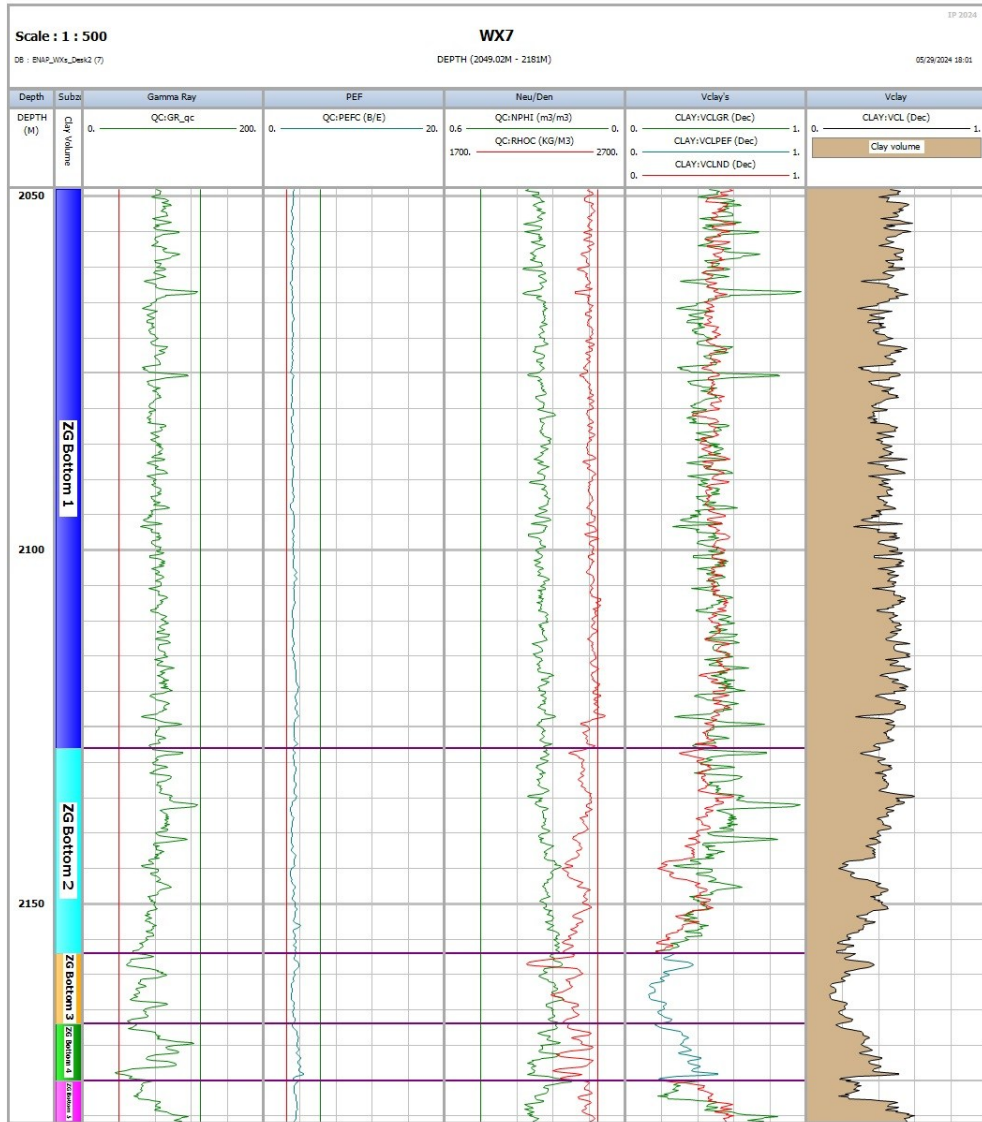


Figure E-8. Clay volume estimation of WX7 well. Track 1: Depth (m). Track 2: ZG subzones name. Track 3: Gamma-ray log (API). Track 4: Photoelectric factor log (barns/e). Track 5: Bulk density (kg/m³) and neutron porosity (v/v) logs. Track 6: Clay volume estimation from each selected indicator. Track 7: Final clay volume in black line (VCL).

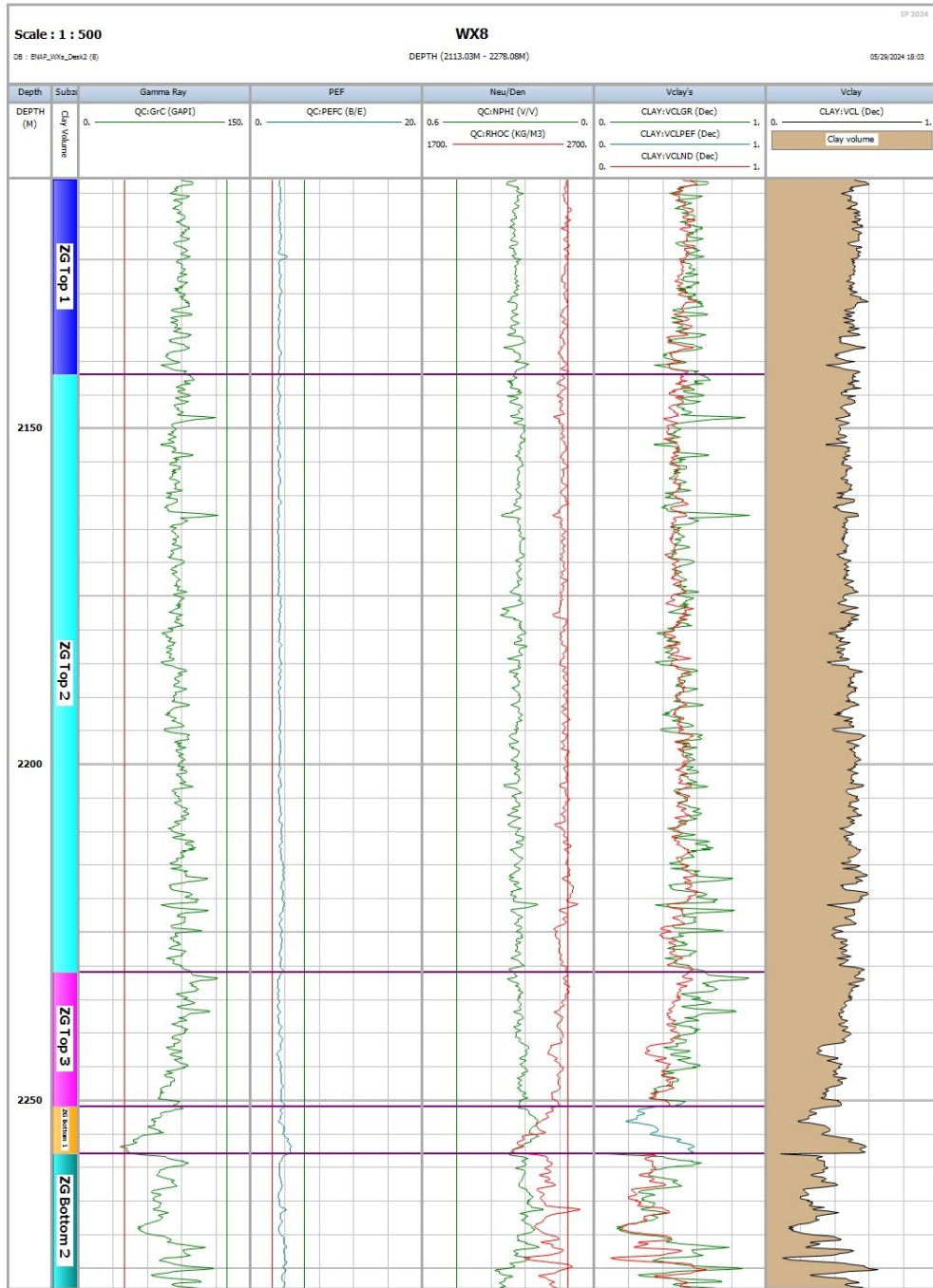


Figure E-9. Clay volume estimation of WX8 well. Track 1: Depth (m). Track 2: ZG subzones name. Track 3: Gamma-ray log (API). Track 4: Photoelectric factor log (barns/e). Track 5: Bulk density (kg/m³) and neutron porosity (v/v) logs. Track 6: Clay volume estimation from each selected indicator. Track 7: Final clay volume in black line (VCL).

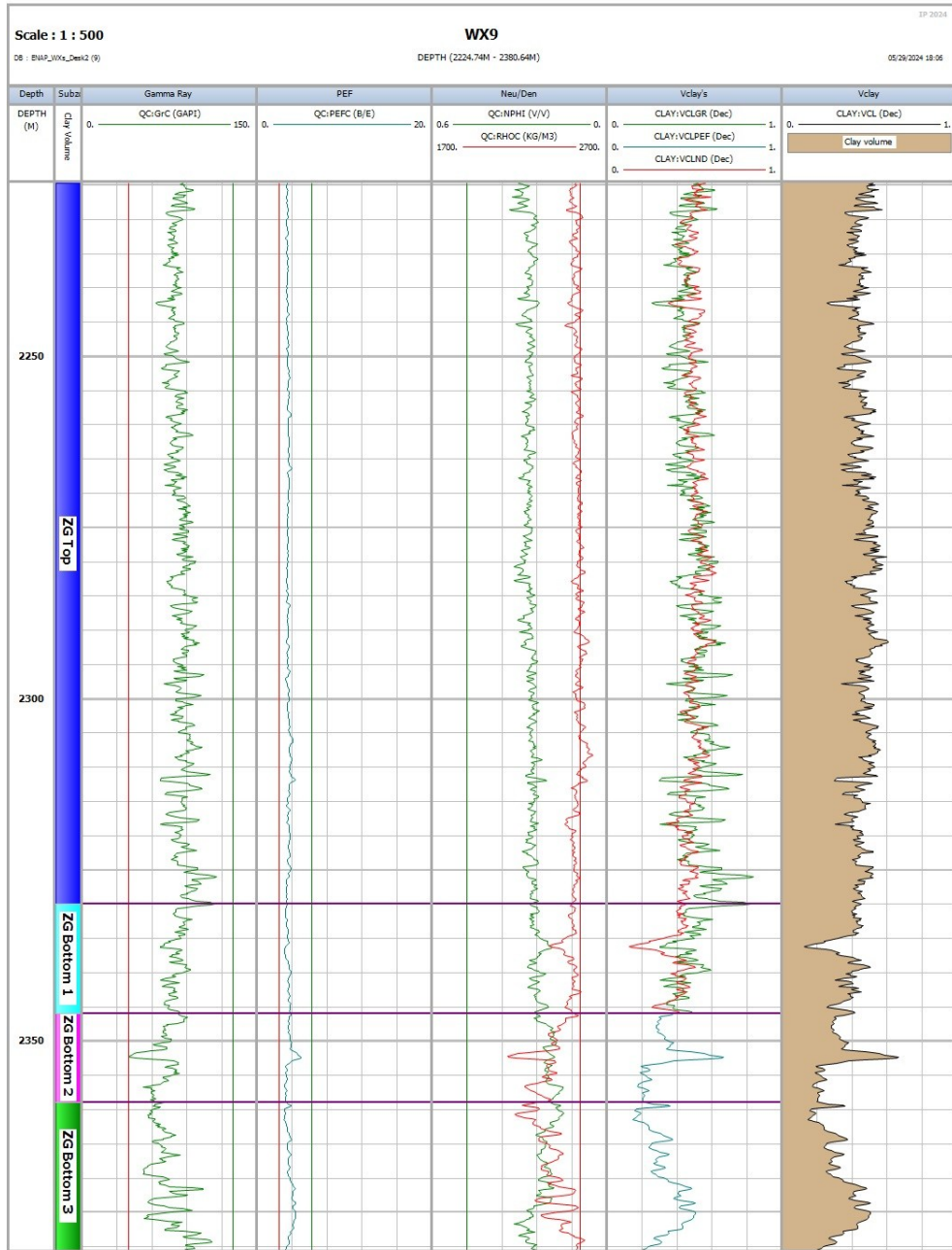


Figure E-10. Clay volume estimation of WX9 well. Track 1: Depth (m). Track 2: ZG subzones name. Track 3: Gamma-ray log (API). Track 4: Photoelectric factor log (barns/e). Track 5: Bulk density (kg/m^3) and neutron porosity (v/v) logs. Track 6: Clay volume estimation from each selected indicator. Track 7: Final clay volume in black line (VCL).

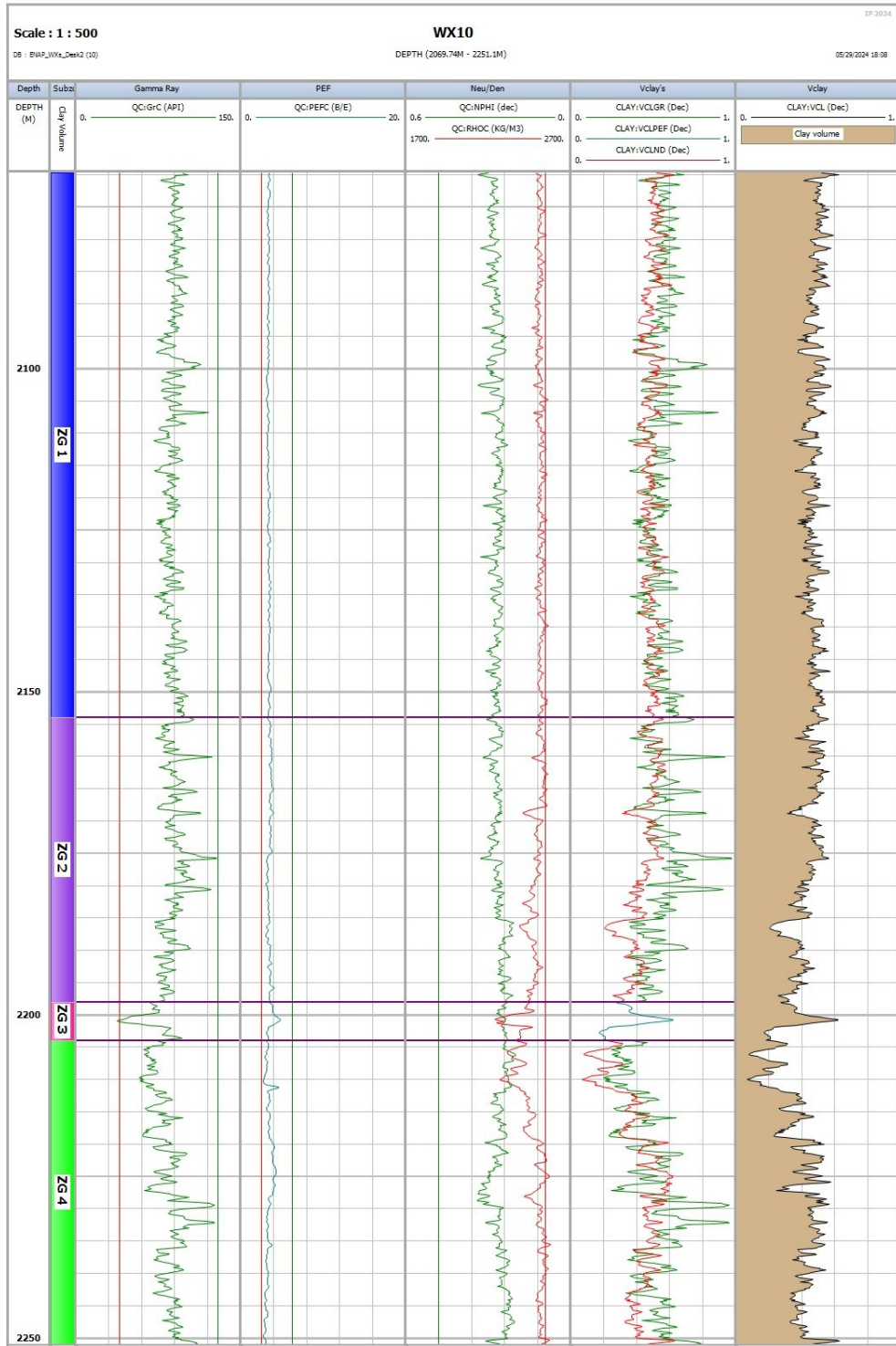


Figure E-11. Clay volume estimation of WX10 well. Track 1: Depth (m). Track 2: ZG subzones name. Track 3: Gamma-ray log (API). Track 4: Photoelectric factor log (barns/e). Track 5: Bulk density (kg/m^3) and neutron porosity (v/v) logs. Track 6: Clay volume estimation from each selected indicator. Track 7: Final clay volume in black line (VCL).

E.4 Log porosity equations.

Equations Equation E–4 and Equation E–5 show the porosity derived from bulk density and sonic velocity logs. The neutron porosity log is converted according to input and output lithology and the type of neutron tool. The CNL (Compensated Neutron Log) tool from Schlumberger was used for the case study. The input parameters and settings are shown in **Figure E-12**.

Equation E–4

$$\phi_D = \frac{(Rho_m - Rho_b)}{(Rho_m - Rho_{fluid})}$$

where Rho_{ma} , Rho_b , and Rho_{fluid} are matrix, bulk, and fluid densities (kg/m^3). Φ_D is the density porosity (v/v).

Equation E–5

$$\phi_S = \frac{(DT - DT_m)}{(DT_{fluid} - DT_m) \times Cp}$$

where DT_{ma} , DT , and DT_{fluid} are matrix, bulk, and fluid sonic transit time ($\mu s/ft$). Cp is a compactor factor (unitless), and Φ_S is the sonic porosity (v/v).

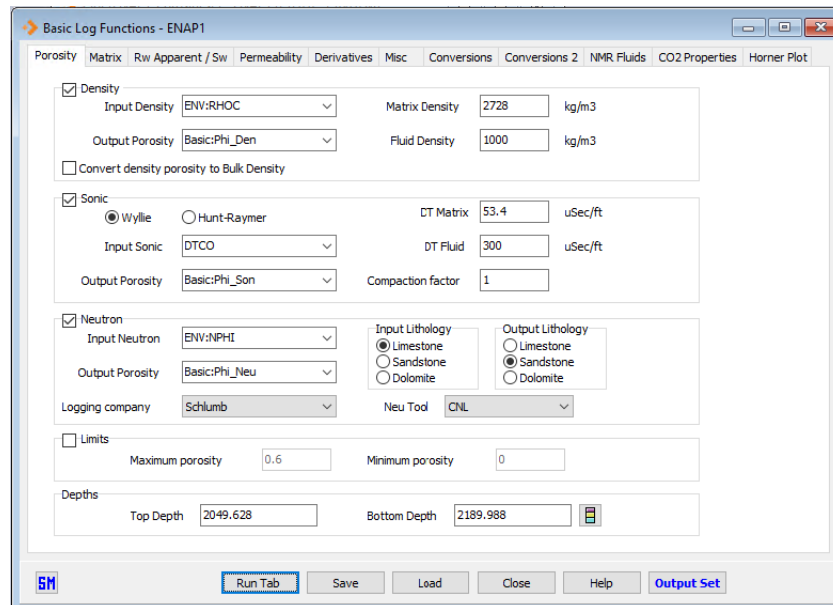


Figure E-12. Screenshot of the Porosity tab from the Basic Log Analysis Function module in IP (Geoactive Ltd., 2024).

E.5 Water saturation equations.

Archie's (1942):

Equation E–6

$$Sw = \sqrt[n]{\frac{a R_w}{R_t \phi_T^m}}$$

The modified Simandoux (Bardon and Pied, 1969):

Equation E-7

$$\frac{1}{Rt} = \frac{\phi^m Sw^n}{a Rw (1 - Vcl)} + \frac{Vcl Sw}{Rcl}$$

The Indonesian (Poupon and Leveaux, 1971):

Equation E-8

$$\frac{1}{\sqrt{Rt}} = \left(\sqrt{\frac{\phi^m}{a Rw}} + \frac{Vcl^{(1-(Vcl/2))}}{\sqrt{Rcl}} \right) Sw^{n/2}$$

The Waxman-Smits (1968):

Equation E-9

$$\frac{1}{Rt} = \frac{\phi_T^m SwT^n}{a Rw} \left(1 + B Qv \frac{Rw}{SwT} \right)$$

$$SwT = Sw(1 - Swb) + Swb$$

Where:

m = Cementation factor (unitless).

n = Saturation exponent (unitless).

a = Tortuosity factor (unitless).

Vcl = Wet clay volume (v/v).

Sw = Effective water saturation (v/v).

Swb = Bound water saturation (v/v).

SwT = Total water saturation (v/v).

Rw = Formation water resistivity (ohm·m).

Rt = Input resistivity curve (ohm·m).

Rcl = Resistivity of the clay (ohm·m).

Qv = Cation exchange capacity per unit total pore volume (meq/ml).

B = Equivalent conductance of clay cations (mho/meq).

In IP software, Qv is either entered as a curve or is calculated from ϕ_T using two coefficients, a and b , through the $1/\phi_T$ vs Qv app cross-plot.

Equation E-10

$$Qv = \frac{a}{\phi_T} + b$$

B is either an entered parameter or it is calculated from Juhasz (1981):

Equation E-11

$$B = \frac{-1.28 + 0.225 T - 0.0004059 T^2}{1 + R_w^{1.25}(0.045 T - 0.27)}$$

where T is the formation temperature (Celsius degrees).

E.6 Petrophysical evaluation of wells WX1 to WX10.

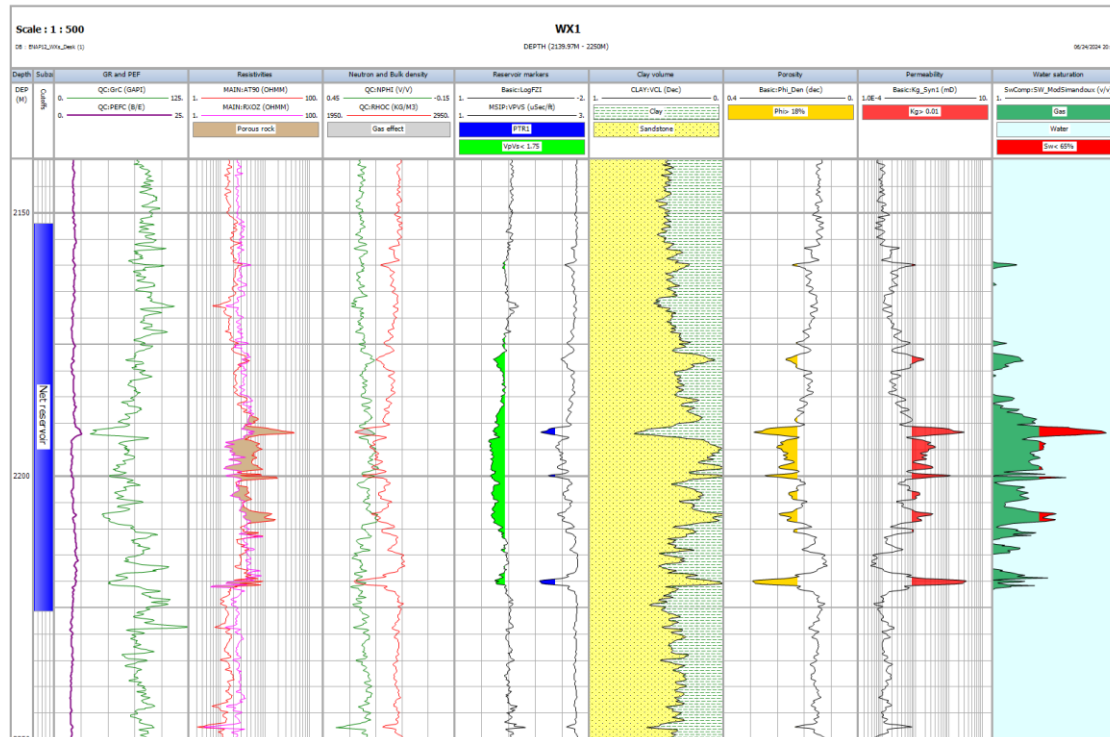


Figure E-13. Petrophysical evaluation of well WX1: Track 1: True vertical depth (m). Track 2: Subzone name. Track 3: Gamma-ray (green) and photoelectric factor (purple) logs. Track 4: Deep resistivity (red) and formation resistivity (magenta) logs. Porous rock shading in light brown occurs in the crossover from RXOZ to AT90. Track5: Neutron porosity (green) and bulk density (red) logs. Gas effect shading in light grey occurs in the crossover from RHOC to NPHI. Track6: Reservoir markers Log FZI (black) displays the PTR1 facies location shading in blue, and Vp/Vs ratio (blue) displays pay sand location shading in lime. Track7: Clay and sandstone lithology. Track8: Total porosity (black). A cut-off value of 18%v/v in shading gold. Track9: Permeability (black). A cut-off value of 0.01 mD in shading red. Track10: Water saturation (black). Gas saturation shading in green, water saturation in light blue, and a cut-off value of Sw= 65%v/v in red.

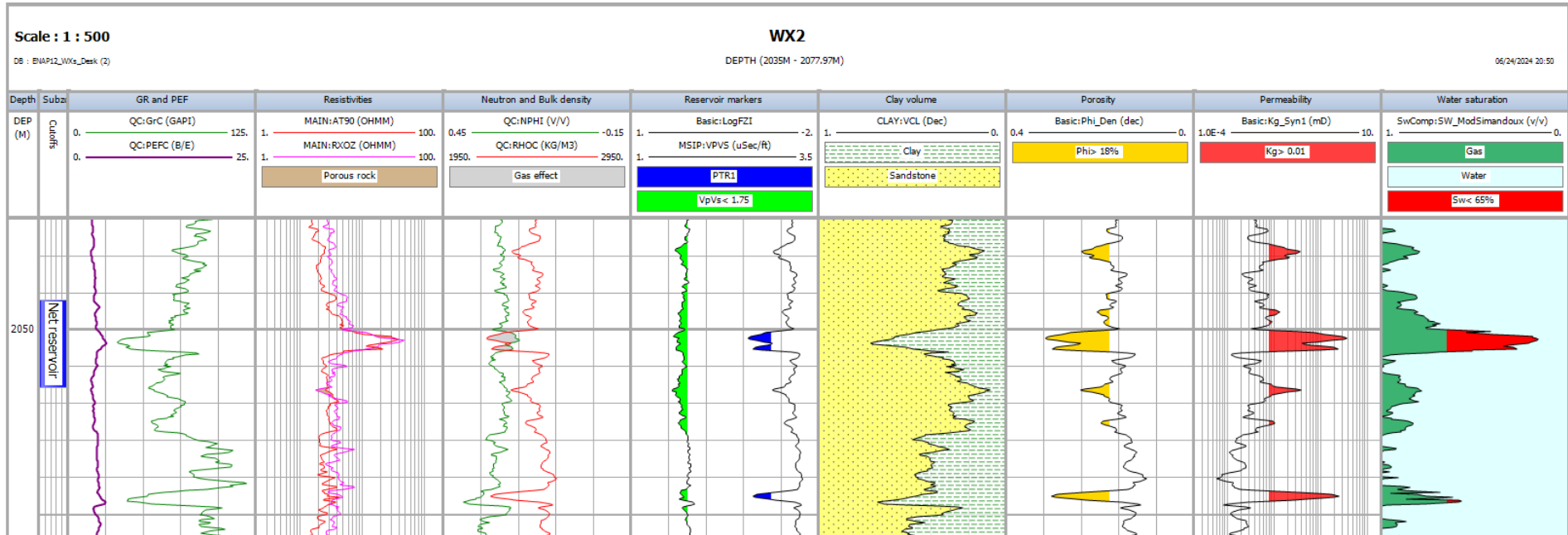


Figure E-14. Petrophysical evaluation of well WX2: Track 1: True vertical depth (m). Track 2: Subzone name. Track 3: Gamma-ray (green) and photoelectric factor (purple) logs. Track 4: Deep resistivity (red) and formation resistivity (magenta) logs. Porous rock shading in light brown occurs in the crossover from RXOZ to AT90. Track5: Neutron porosity (green) and bulk density (red) logs. Gas effect shading in light grey occurs in the crossover from RHOC to NPHI. Track6: Reservoir markers Log FZI (black) displays the PTR1 facies location shading in blue, and Vp/Vs ratio (blue) displays pay sand location shading in lime. Track7: Clay and sandstone lithology. Track8: Total porosity (black). A cut-off value of 18%v/v in shading gold. Track9: Permeability (black). A cut-off value of 0.01 mD in shading red. Track10: Water saturation (black). Gas saturation shading in green, water saturation in light blue, and a cut-off value of Sw= 65%v/v in red.

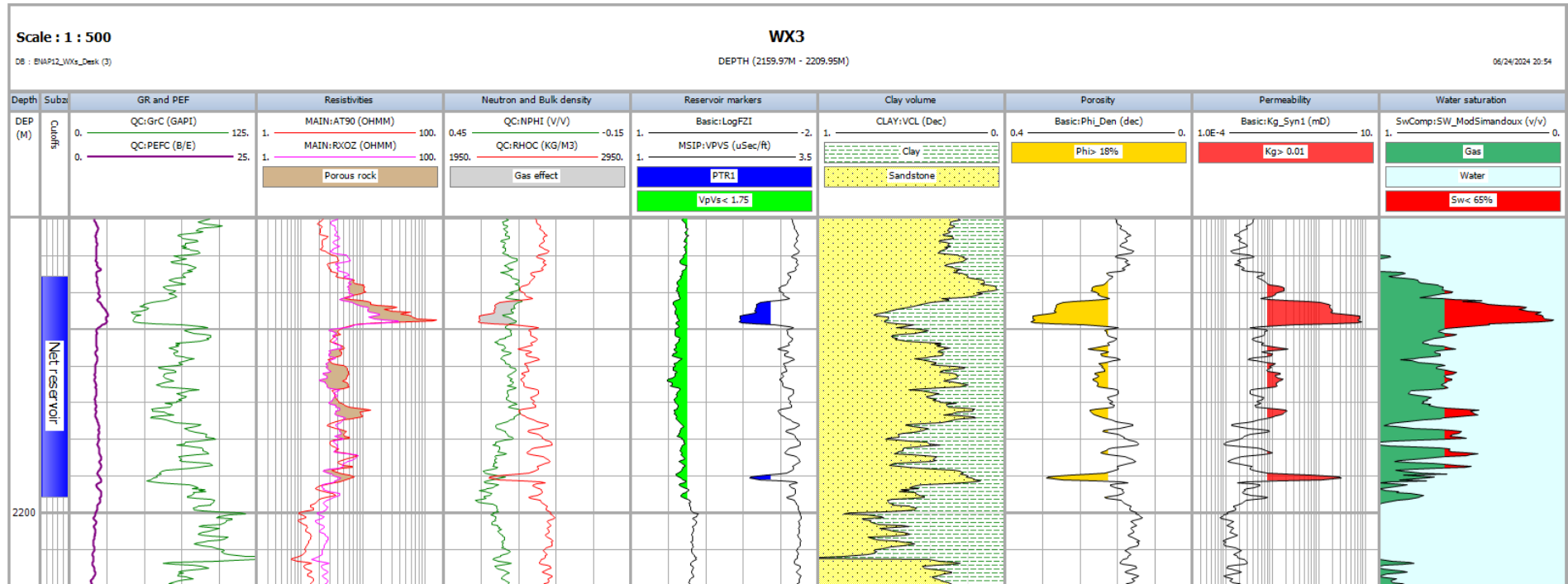


Figure E-15. Petrophysical evaluation of well WX3: Track 1: True vertical depth (m). Track 2: Subzone name. Track 3: Gamma-ray (green) and photoelectric factor (purple) logs. Track 4: Deep resistivity (red) and formation resistivity (magenta) logs. Porous rock shading in light brown occurs in the crossover from RXOZ to AT90. Track5: Neutron porosity (green) and bulk density (red) logs. Gas effect shading in light grey occurs in the crossover from RHOC to NPHI. Track6: Reservoir markers Log FZI (black) displays the PTR1 facies location shading in blue, and Vp/Vs ratio (blue) displays pay sand location shading in lime. Track7: Clay and sandstone lithology. Track8: Total porosity (black). A cut-off value of 18%v/v in shading gold. Track9: Permeability (black). A cut-off value of 0.01 mD in shading red. Track10: Water saturation (black). Gas saturation shading in green, water saturation shading in light blue, and a cut-off value of Sw= 65%v/v in red.

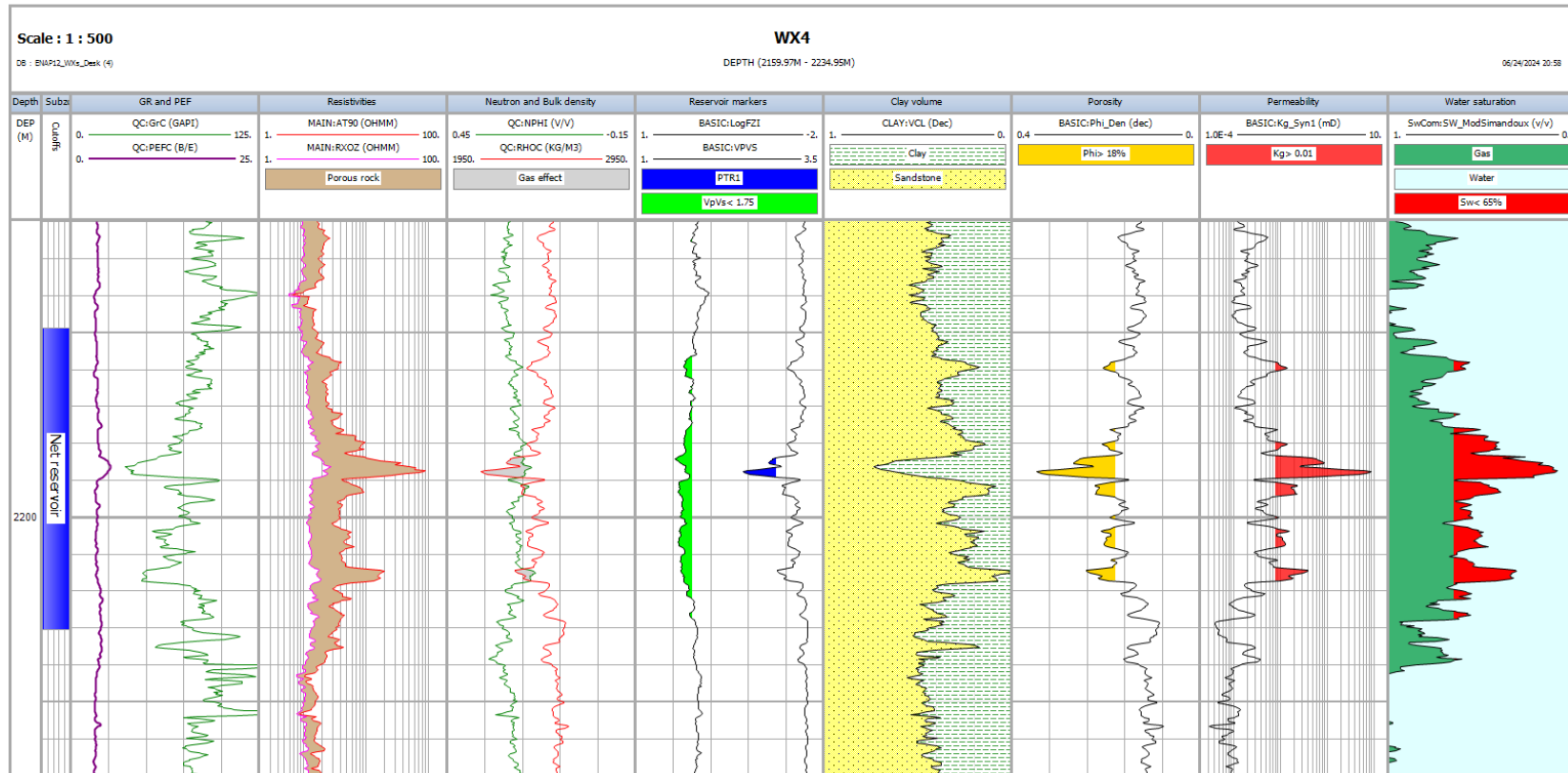


Figure E-16. Petrophysical evaluation of well WX4: Track 1: True vertical depth (m). Track 2: Subzone name. Track 3: Gamma-ray (green) and photoelectric factor (purple) logs. Track 4: Deep resistivity (red) and formation resistivity (magenta) logs. Porous rock shading in light brown occurs in the crossover from RXOZ to AT90. Track5: Neutron porosity (green) and bulk density (red) logs. Gas effect shading in light grey occurs in the crossover from RHOC to NPHI. Track6: Reservoir markers Log FZI (black) displays the PTR1 facies location shading in blue, and Vp/Vs ratio (blue) displays pay sand location shading in lime. Track7: Clay and sandstone lithology. Track8: Total porosity (black). A cut-off value of 18%v/v in shading gold. Track9: Permeability (black). A cut-off value of 0.01 mD in shading red. Track10: Water saturation (black). Gas saturation shading in green, water saturation in light blue, and a cut-off value of Sw= 65%v/v in red.

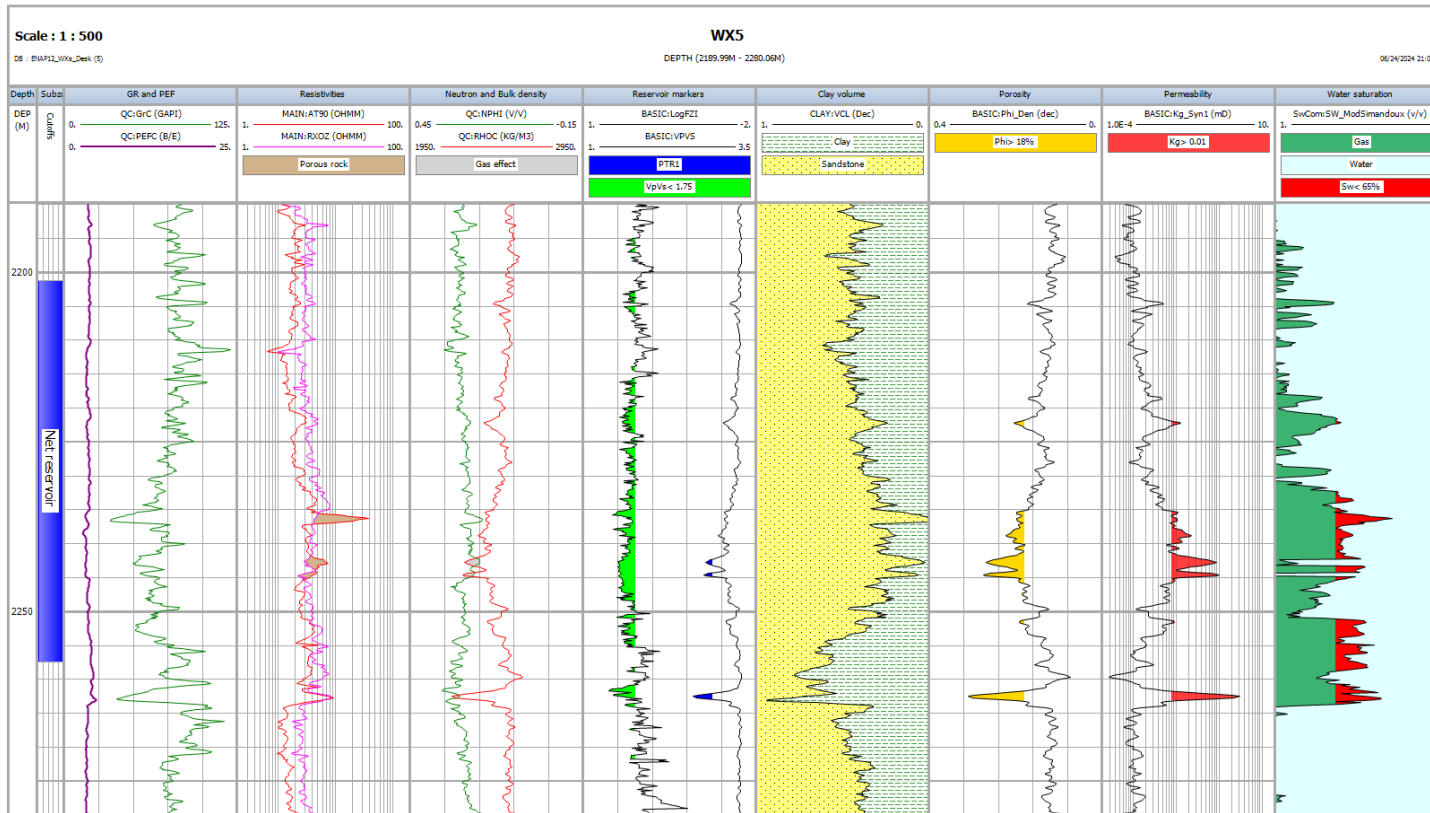


Figure E-17. Petrophysical evaluation of well WX5: Track 1: True vertical depth (m). Track 2: Subzone name. Track 3: Gamma-ray (green) and photoelectric factor (purple) logs. Track 4: Deep resistivity (red) and formation resistivity (magenta) logs. Porous rock shading in light brown occurs in the crossover from RXOZ to AT90. Track5: Neutron porosity (green) and bulk density (red) logs. Gas effect shading in light grey occurs in the crossover from RHOC to NPHI. Track6: Reservoir markers Log FZI (black) displays the PTR1 facies location shading in blue, and Vp/Vs ratio (blue) displays pay sand location shading in lime. Track7: Clay and sandstone lithology. Track8: Total porosity (black). A cut-off value of 18%v/v in shading gold. Track9: Permeability (black). A cut-off value of 0.01 mD in shading red. Track10: Water saturation (black). Gas saturation shading in green, water saturation in light blue, and a cut-off value of Sw= 65%v/v in red.

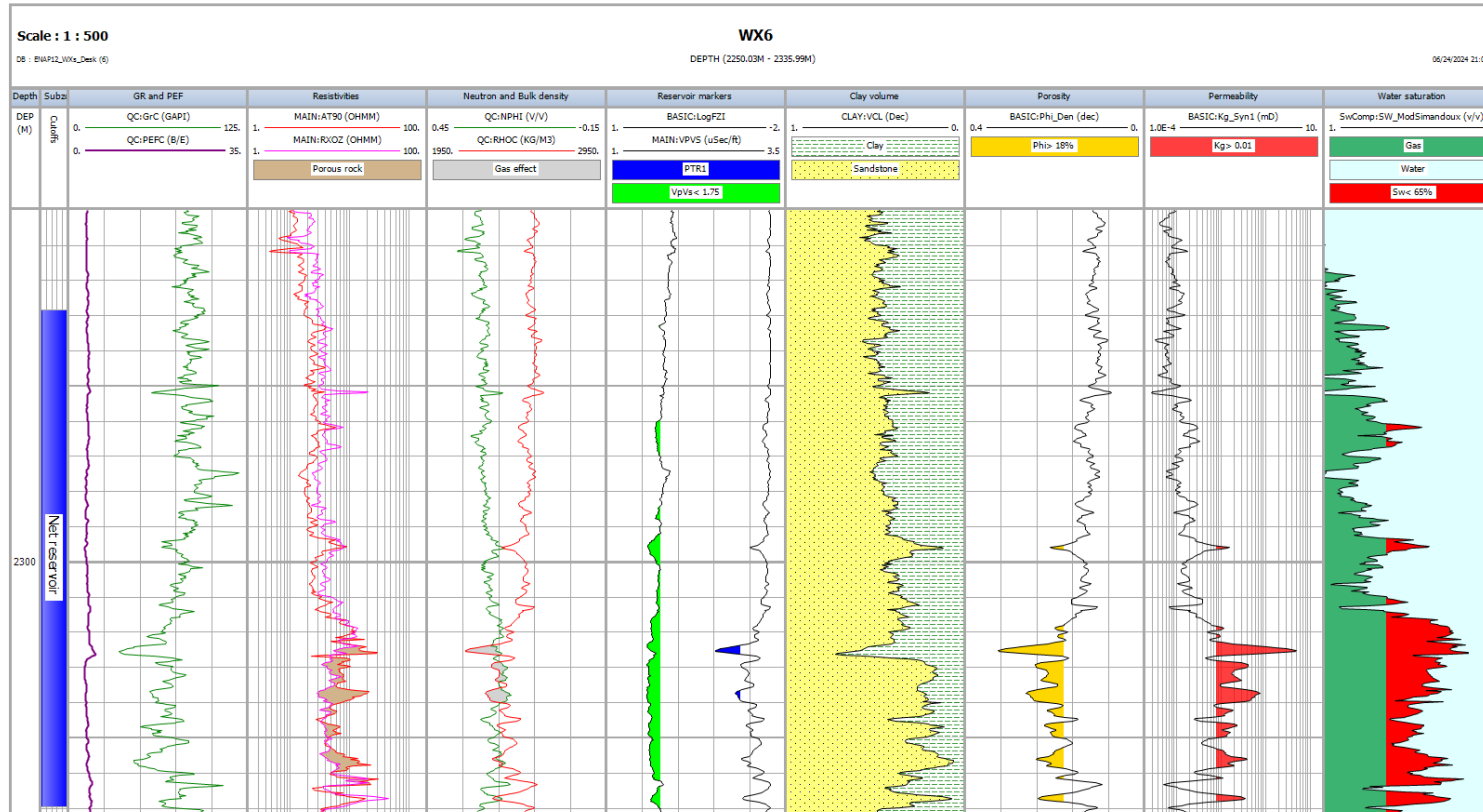


Figure E-18. Petrophysical evaluation of well WX6: Track 1: True vertical depth (m). Track 2: Subzone name. Track 3: Gamma-ray (green) and photoelectric factor (purple) logs. Track 4: Deep resistivity (red) and formation resistivity (magenta) logs. Porous rock shading in light brown occurs in the crossover from RXOZ to AT90. Track5: Neutron porosity (green) and bulk density (red) logs. Gas effect shading in light grey occurs in the crossover from RHOC to NPHI. Track6: Reservoir markers Log FZI (black) displays the PTR1 facies location shading in blue, and Vp/Vs ratio (blue) displays pay sand location shading in lime. Track7: Clay and sandstone lithology. Track8: Total porosity (black). A cut-off value of 18%v/v in shading gold. Track9: Permeability (black). A cut-off value of 0.01 mD in shading red. Track10: Water saturation (black). Gas saturation shading in green, water saturation in light blue, and a cut-off value of Sw= 65%v/v in red.

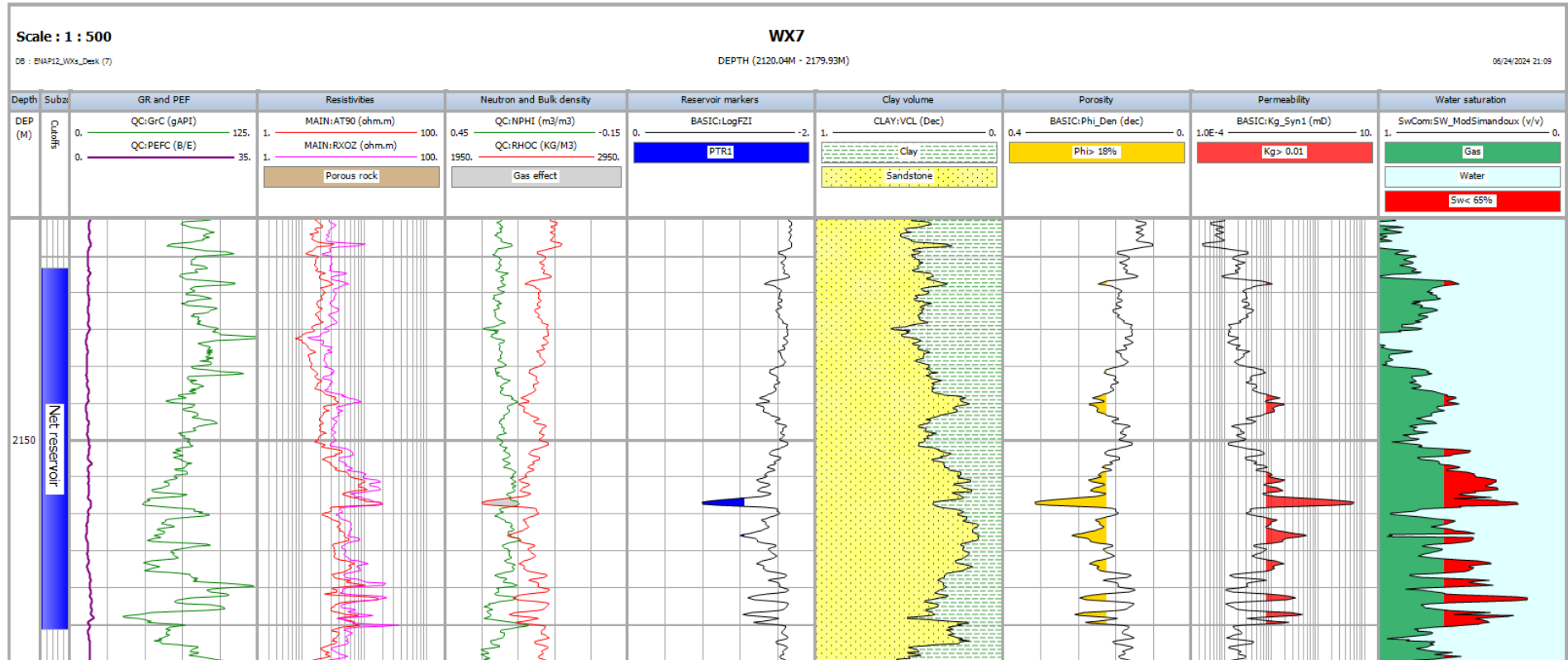


Figure E-19. Petrophysical evaluation of well WX7: Track 1: True vertical depth (m). Track 2: Subzone name. Track 3: Gamma-ray (green) and photoelectric factor (purple) logs. Track 4: Deep resistivity (red) and formation resistivity (magenta) logs. Porous rock shading in light brown occurs in the crossover from RXOZ to AT90. Track5: Neutron porosity (green) and bulk density (red) logs. Gas effect shading in light grey occurs in the crossover from RHOC to NPHI. Track6: Reservoir markers Log FZI (black) displays the PTR1 facies location shading in blue, and Vp/Vs ratio (blue) displays pay sand location shading in lime. Track7: Clay and sandstone lithology. Track8: Total porosity (black). A cut-off value of 18%v/v in shading gold. Track9: Permeability (black). A cut-off value of 0.01 mD in shading red. Track10: Water saturation (black). Gas saturation shading in green, water saturation in light blue, and a cut-off value of Sw= 65%v/v in red.

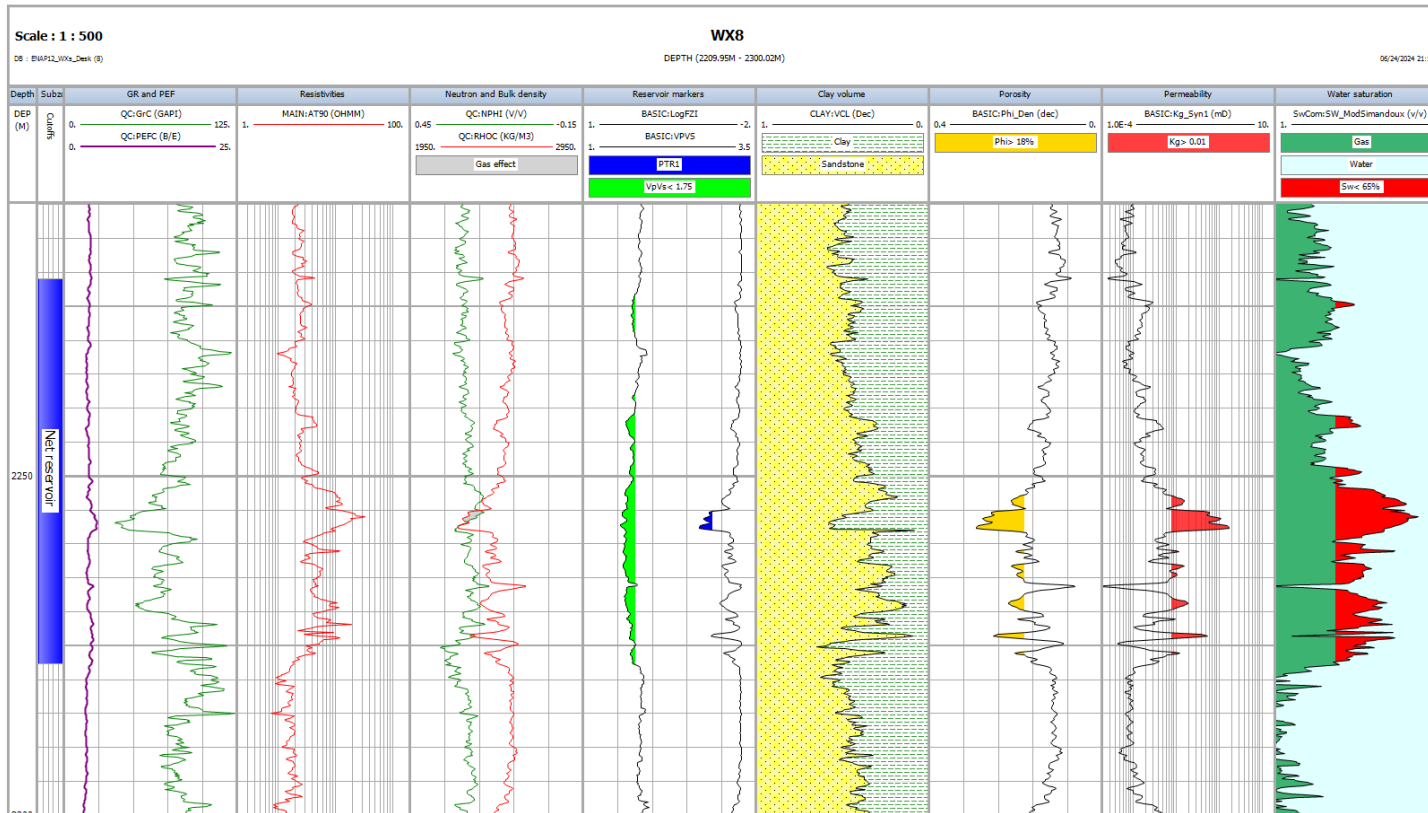


Figure E-20. Petrophysical evaluation of well WX8: Track 1: True vertical depth (m). Track 2: Subzone name. Track 3: Gamma-ray (green) and photoelectric factor (purple) logs. Track 4: Deep resistivity (red) and formation resistivity (magenta) logs. Porous rock shading in light brown occurs in the crossover from RXOZ to AT90. Track5: Neutron porosity (green) and bulk density (red) logs. Gas effect shading in light grey occurs in the crossover from RHOC to NPHI. Track6: Reservoir markers Log FZI (black) displays the PTR1 facies location shading in blue, and Vp/Vs ratio (blue) displays pay sand location shading in lime. Track7: Clay and sandstone lithology. Track8: Total porosity (black). A cut-off value of 18%v/v in shading gold. Track9: Permeability (black). A cut-off value of 0.01 mD in shading red. Track10: Water saturation (black). Gas saturation shading in green, water saturation in light blue, and a cut-off value of Sw= 65%v/v in red.

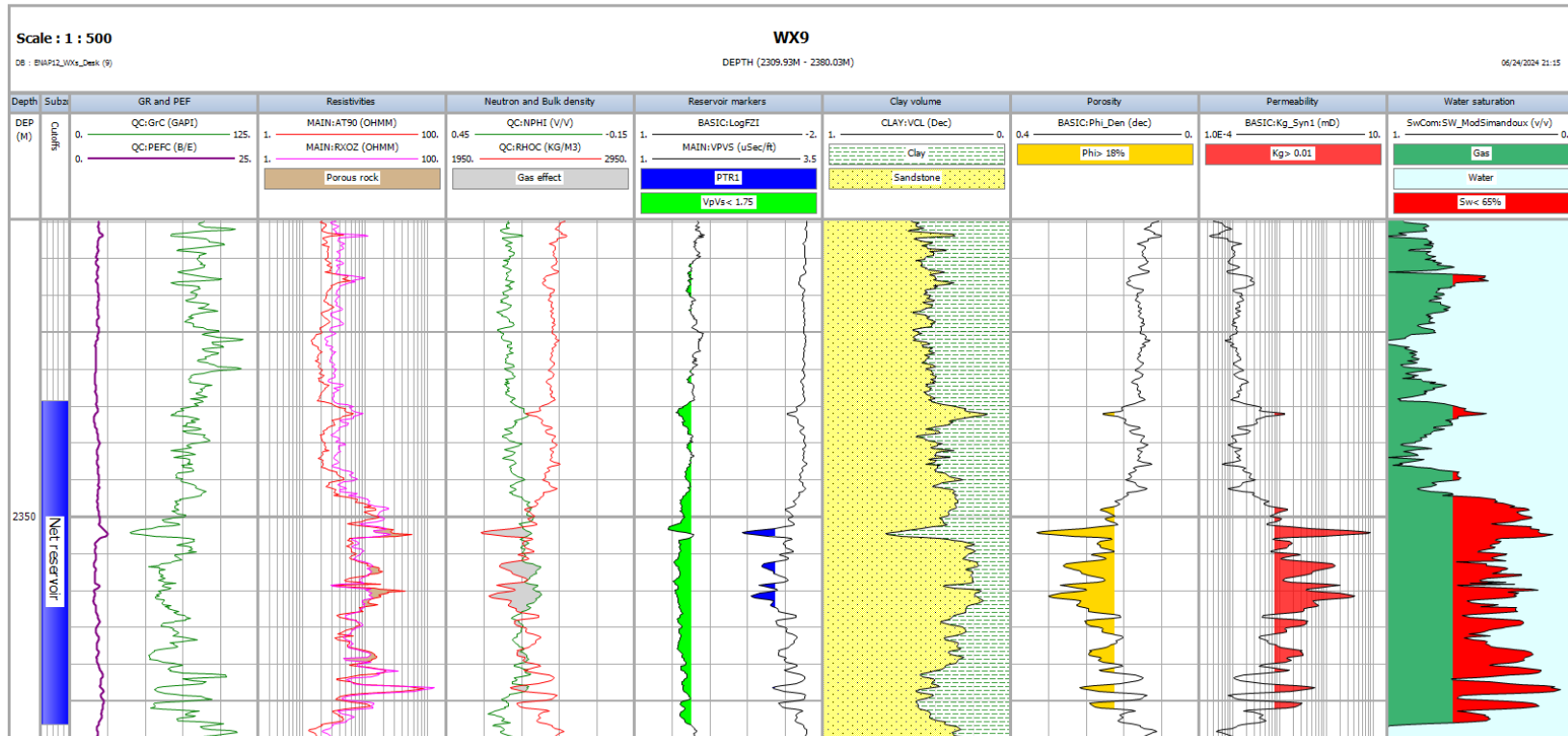


Figure E-21. Petrophysical evaluation of well WX9: Track 1: True vertical depth (m). Track 2: Subzone name. Track 3: Gamma-ray (green) and photoelectric factor (purple) logs. Track 4: Deep resistivity (red) and formation resistivity (magenta) logs. Porous rock shading in light brown occurs in the crossover from RXOZ to AT90. Track5: Neutron porosity (green) and bulk density (red) logs. Gas effect shading in light grey occurs in the crossover from RHOC to NPHI. Track6: Reservoir markers Log FZI (black) displays the PTR1 facies location shading in blue, and Vp/Vs ratio (blue) displays pay sand location shading in lime. Track7: Clay and sandstone lithology. Track8: Total porosity (black). A cut-off value of 18%v/v in shading gold. Track9: Permeability (black). A cut-off value of 0.01 mD in shading red. Track10: Water saturation (black). Gas saturation shading in green, water saturation in light blue, and a cut-off value of Sw= 65%v/v in red.

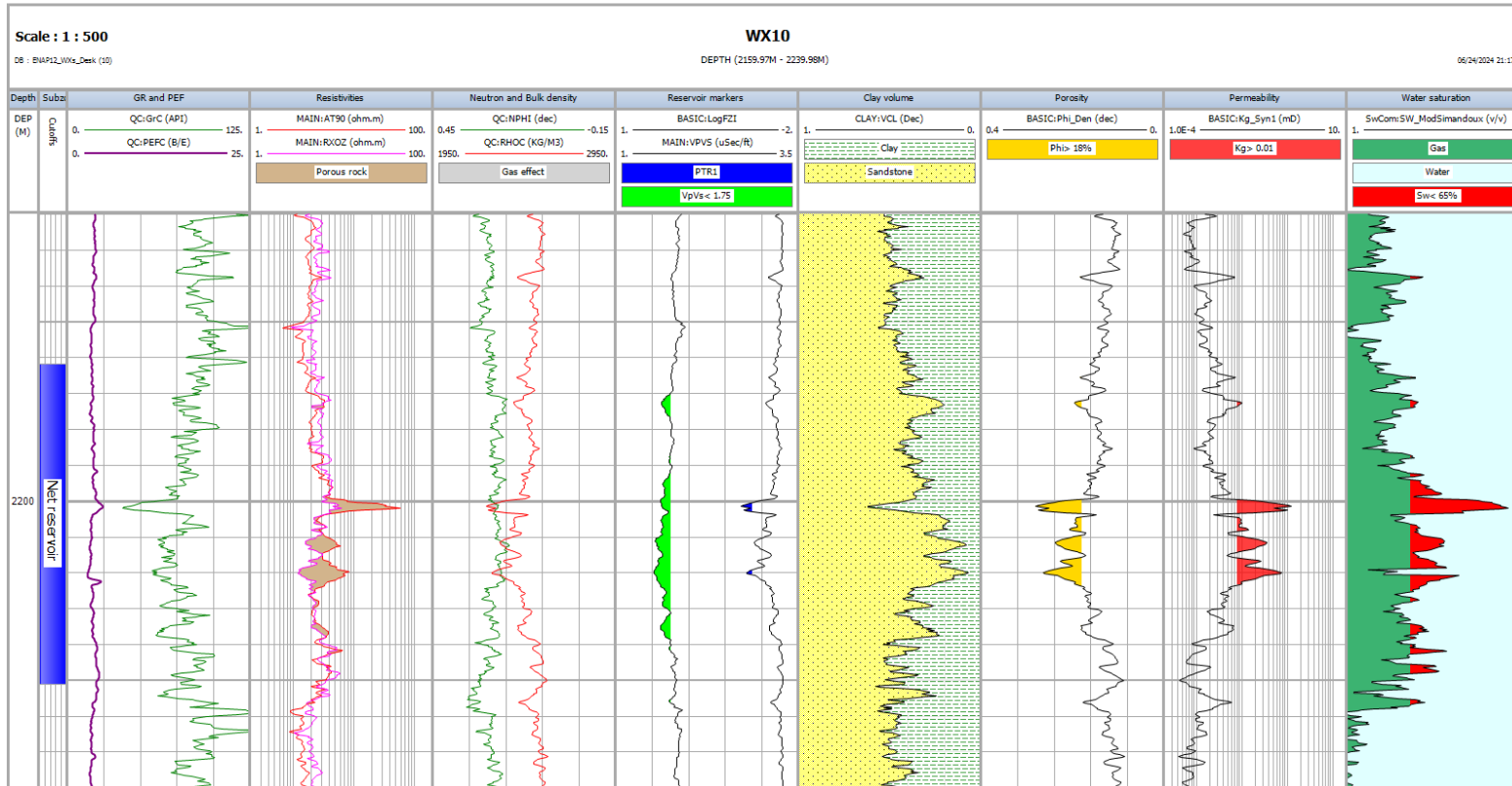


Figure E-22. Petrophysical evaluation of well WX10: Track 1: True vertical depth (m). Track 2: Subzone name. Track 3: Gamma-ray (green) and photoelectric factor (purple) logs. Track 4: Deep resistivity (red) and formation resistivity (magenta) logs. Porous rock shading in light brown occurs in the crossover from RXOZ to AT90. Track5: Neutron porosity (green) and bulk density (red) logs. Gas effect shading in light grey occurs in the crossover from RHOC to NPHI. Track6: Reservoir markers Log FZI (black) displays the PTR1 facies location shading in blue, and Vp/Vs ratio (blue) displays pay sand location shading in lime. Track7: Clay and sandstone lithology. Track8: Total porosity (black). A cut-off value of 18%v/v in shading gold. Track9: Permeability (black). A cut-off value of 0.01 mD in shading red. Track10: Water saturation (black). Gas saturation shading in green, water saturation in light blue, and a cut-off value of Sw= 65%v/v in red.